NNT : 2025AIXM0058

THÈSE DE DOCTORAT

Soutenue à Aix-Marseille Université
le 18 mars 2025

Azat GAINUTDINOV

Mécanismes synaptiques et de réseau des ondes aiguës précoces dans l'hippocampe du rongeur en periode néonatal

Discipline
Biologie santé

Spécialité
Neurosciences

École doctorale
ED 658 – Sciences du vivant

Laboratoire/Partenaires de recherche
Institut de Neurobiologie de la Méditerranée (INMED UMR 1249)

Composition du jury

Dirk ISBRANDT Rapporteur
Professeur, DZNE – Allemagne, Cologne

Anton SIROTA Rapporteur
Professeur, LMU - Allemagne, Munich

Matthew COLONNESE Examinateur Professeur, GWU - États-Unis, Washington, D.C.

Christophe PORCHER Président du jury
Professeur d'université, INMED - Marseille

Roustem KHAZIPOV Directeur de thèse
Directeur de Recherche, INMED - Marseille

Agnès BAUDE Co-directrice de thèse
Chargée de Recherche, INMED - Marseille

Affidavit

I, undersigned, Azat Gainutdinov, hereby declare that the work presented in this manuscript is a collective research, carried out under the scientific supervision of Roustem Khazipov and Agnés Baude, in accordance with the principles of honesty, integrity and responsibility inherent to the research mission. The research work and the writing of this manuscript have been carried out in compliance with both the French national charter for Research Integrity and the Aix-Marseille University charter on the fight against plagiarism.

This work has not been submitted previously either in this country or in another country in the same or in a similar version to any other examination body.

In accordance with the principles of transparency and academic integrity, I hereby declare that, as a non-native English speaker, I have utilized artificial intelligence tools (deepl.com) exclusively for the purposes of grammar and spell checking, as well as for translating certain texts to English. I affirm that no AI-generated content has been employed to produce any knowledge or results presented in this dissertation.

Marseille, 13 Janvier 2024



Cette œuvre est mise à disposition selon les termes de la Licence Creative Commons Attribution - Pas d'Utilisation Commerciale - Pas de Modification 4.0 International.

Liste de publications et participation aux conférences

Liste des publications réalisées dans le cadre du projet de thèse :

1. Gainutdinov, A., Shipkov, D., Sintsov, M., Fabrizi, L., Nasretdinov, A., Khazipov, R., & Valeeva, G. (2023). Somatosensory-Evoked Early Sharp Waves in the Neonatal Rat Hippocampus. *International Journal of Molecular Sciences*, *24*(10), 8721. https://doi.org/10.3390/ijms24108721
2. Frolova, A., Gainutdinov, A., Juzekaeva, E., Safeeva, L., Valeeva, G., & Khazipov, R. (2023). Development of GABAergic Inhibition Associated with Entorhinal Input in Granular Cells of the Dentate Gyrus. In Journal of Evolutionary Biochemistry and Physiology (Vol. 59, Issue 6, pp. 2390–2398). Pleiades Publishing Ltd. https://doi.org/10.1134/s002209302306039x

Participation aux conférences au cours de la période de thèse :

1. GDR NeuralNet 2022 (poster) 11th annual meeting, 21–23 September 2022, Lyon
2. Neurodays 2023, 16–17 November 2023
3. GDR NeuralNet 2023 (poster) 12th annual meeting, 11–13 October 2023, Marseille
4. Neurodays 2024, 21–23 November 2024

Résumé

Dans l'hippocampe des rongeurs nouveau-nés, les ondes aigües précoces (« early sharp waves, eSPWs ») représentent le premier patron d'activité organisée, apparaissant sous forme de bouffées d'activité récurrente de réseau neuronal. Cette thèse explore les mécanismes à l'origine de la génération des eSPWs, et leurs corrélats synaptiques dans le contexte de la maturation développementale de l'inhibition hippocampique.

L'étude commence par examiner le rôle de la stimulation somatosensorielle dans l'induction des eSPWs. Les expériences ont démontré que la stimulation électrique sous-cutanée induit des eSPWs, avec des caractéristiques temporelles et spatiales similaires à celles des événements spontanés. Les profils de densité des sources de courant (CSD) ont révélé l'implication des voies temporo-ammonique et perforante, reliant les entrées sensorielles externes à l'activité hippocampique.

La dynamique temporelle des réponses synaptiques lors des eSPWs *in vivo* et pendant les réponses évoquées par la stimulation des voies temporo-ammonique et perforante dans les préparations *in vitro* a été analysée à l'aide d'enregistrements en patch-clamp dans les régions CA1 et du gyrus denté (DG). L'analyse a montré que les courants postsynaptiques excitateurs (EPSCs) précèdent les courants postsynaptiques inhibiteurs (IPSCs) de plusieurs dizaines de millisecondes, créant une large fenêtre d'intégration pour les entrées excitatrices. Ce décalage se réduit à mesure que les synapses inhibitrices mûrissent, reflétant la progression développementale de l'inhibition "feedforward".

Enfin, une analyse immunohistochimique a cartographié la distribution et la mise en place développementale des futures synapses inhibitrices à parvalbumine dans la région CA1 de l'hippocampe. Les résultats de cette analyse suggèrent que les synapses établies par les interneurones à parvalbumin sur les dendrites se forment plus précocement que les synapses périsomatiques.

Dans l'ensemble, ces résultats indiquent un rôle clé des entrées excitatrices externes dans l'activation du réseau neuronal hippocampique immature et suggèrent également un développement tardif de l'inhibition dans l'hippocampe, ce qui, ensemble, crée les conditions d'une activité en bouffée dans l'hippocampe au cours des premiers stades du développement.

Mots-clés: ondes aigües précoces, hippocampe néonatal, stimulation somatosensorielle, dynamique synaptique, courants synaptiques, interneurones à parvalbumine, développement de l'hippocampe, inhibition feedforward, cortex entorhinal

Abstract

In the neonatal rodent hippocampus, early sharp waves (eSPWs) represent the first organized activity pattern, emerging as transient, recurrent bursts of neuronal network activity. This thesis investigates the mechanisms underlying eSPW generation, and their synaptic correlates in context of developmental maturation of hippocampal inhibition.

The study begins by exploring the role of somatosensory stimulation in evoking eSPWs. Experiments demonstrated that electrical stimulation of whisker pads and limbs reliably induces eSPWs, showing temporal and spatial characteristics similar to spontaneous events. The current-source density (CSD) profiles revealed the involvement of temporoammonic and perforant pathways, linking external sensory inputs to hippocampal activity.

The temporal dynamics of synaptic responses during eSPWs *in vivo* and during responses evoked by stimulation of the temporo-ammonic and perforant pathways in the *in vitro* preparations were analysed using patch-clamp recordings in the CA1 and DG regions. Analysis revealed that excitatory postsynaptic currents (EPSCs) precede inhibitory postsynaptic currents (IPSCs) by tens of milliseconds, creating a broad integration window for excitatory input. This delay narrows as inhibition matures, aligning with the developmental progression of feedforward inhibition (FFI).

Finally, immunohistochemical analysis mapped the distribution and developmental placement of future parvalbumin inhibitory synapses in the CA1 region of the hippocampus. The results of this analysis suggest that dendritic synapses made by parvalbumin interneurons form earlier than perisomatic synapses.

Taken together, these results indicate a key role for external excitatory inputs in the activation of the immature hippocampal neuronal network and also suggest a delayed development of inhibition in the hippocampus, which together create conditions for bursting activity in the hippocampus during early development.

Key words: early sharp waves, neonatal hippocampus, somatosensory stimulation, synaptic dynamics, synaptic currents, parvalbumin interneurons, hippocampal development, feedforward inhibition, entorhinal cortex

Remerciements

I would like to thank my advisors Dr. Rustem Khazipov and Dr. Agnés Baude for their guidance during my PhD. studies.

I would like to thank those who worked with me on the articles of this dissertation:

Dmitrii Shipkov, Mikhail Sintsov, Lorenzo Fabrizi, Azat Nasretdinov, Guzel Valeeva, Daria Vinokurova, Anastasia Frolova, Elvira Juzekaevaa, Lyia Safeeva, Ilgam Khalilov, Rin Kikuchi, Marie Giorgi-Kurz, Robin F Dard, Michel Picardo.

I am grateful to Dr. Rosa Cossart for having accepted me at INMED, as well as Dr. Marat Minlebaev and Dr. Dmitrii Suchkov who were of helpful advice during my whole stay.

Finally, this work would not be possible without being granted by French Government, ANR AAPG 2021 « Internalisation des fonctions cognitives dans le système entorhinal-hippocampique des rongeurs » (acronyme Devhippo).

Table des matières

Affidavit **2**
Liste de publications et participation aux conférences **3**
Résumé **4**
Abstract **4**
Remerciements **6**
Table des matières **7**
Table des figures **11**
List of abbreviations **14**
1. Problem statement **16**
1.1. Research questions 17
1.2. Research objectives 17
1.3. Key propositions 18
2. Introduction **19**
2.1. Hippocampal structure 19
2.1.1. Subiculum and entorhinal cortex 20
2.1.2. Cornu ammonis 21
2.1.3. Dentate gyrus 21
2.2. Connections 22
2.2.1. Perforant and temporoammonic pathways 22
2.2.2. Commissural/associative pathway 23
2.2.3. Local circuits 25
2.3. Cells of hippocampus 27
2.3.1. Excitatory neurons 27
2.3.2. Interneurons 28
2.4. Hippocampal development 32
2.4.1. Growth of the structure 32
2.4.2. Neurogenesis in hippocampus 33
2.5. Network activity patterns 36
2.5.1. Network activity in adult hippocampus 36
2.5.2. Network activity in developing hippocampus 47
2.6. Feedforward inhibition 58
2.6.1. Feedforward inhibition in adult brain 59
2.6.2. Feedforward inhibition in developing brain 60
3. Methods **70**
3.1. Electrophysological approaches to study population patterns of activity 70
3.1.1. Local Field Potential 70

3.1.2. Current Source Density analysis 72
3.1.3. Multi-unit activity (MUA) 73
3.1.4. Patch-clamp electrophysiology 73
3.2. Confocal immunolocalization of Synaptotagmin isoform Syt2 76
3.2.1. Immunocytochemistry 77
3.2.2. Confocal microscopy 79
3.3. Software built for analysis 81
3.3.1. Easy Viewer: a tool for analyzing multichannel electrophysiological signals 81
3.3.2. Synapto Catcher: a software for analyzing microscopic images 84
4. Results 87
4.1. Article 1. Somatosensory-Evoked Early Sharp Waves in the Neonatal Rat Hippocampus 87
4.1.1. Abstract 87
4.1.2. Introduction 88
4.1.3. Results 89
4.1.4. Discussion 96
4.1.5. Materials and Methods 98
4.1.6. References 100
4.2. Article 2. (in preparation) Temporal Window of Integration during Early Sharp Waves in the CA1 hippocampus of neonatal rats 105
4.2.1. Abstract 105
4.2.2. Introduction 105
4.2.3. Materials and Methods 107
4.2.4. Results 108
4.2.5. Author Contributions 112
4.2.6. Funding sources 112
4.2.7. Conflict of Interest 112
4.2.8. Data Availability Statement 112
4.2.9. References 112
4.3. Article 3. Development of GABAergic Inhibition Associated with Entorhinal Input in Granular Cells of the Dentate Gyrus 116
4.3.1. Abstract 116
4.3.2. Graphical abstract 117
4.3.3. Introduction 117
4.3.4. Materials and methods 118
4.3.5. Results 119
4.3.6. Discussion 120
4.3.7. Authors' contribution 124
4.3.8. Funding 124
4.3.1. Ethics approval and consent to participate 124

4.3.1. Conflict of interest 124
4.3.2. References 124
4.4. Article 4. (in preparation) Development of inhibition associated with the Entorhinal Cortex input in the CA1 hippocampus of neonatal rats 128
4.4.1. Introduction 129
4.4.2. Materials and Methods 130
4.4.3. Results 131
4.4.4. Funding sources 137
4.4.5. Conflict of Interest 137
4.4.6. Data Availability Statement 137
4.4.7. References 137
4.5. Article 5. (in preparation) Distribution of synapses along the radial axis of the CA1 hippocampus 141
4.5.1. Abstract 141
4.5.2. Introduction 141
4.5.3. Materials and methods 142
4.5.4. Results 144
4.5.5. Discussion 150
4.5.6. Sequential maturation and functional implications 150
4.5.7. Developmental differences among layers 150
4.5.8. Comparison with previous studies 150
4.5.9. Mechanistic insights and future directions 151
4.5.10. Limitations and considerations 151
4.5.11. Conclusion 151
4.5.12. Author contributions 151
4.5.13. Funding sources 152
4.5.14. Conflict of interest 152
4.5.15. Data availability statement 152
4.5.16. References 152
5. Discussion 154
5.1. The role of sensory signals in generating eSPW 154
5.2. Age-dependent changes in inhibitory activity 155
5.3. Mechanisms behind delayed GABA in neonates 155
5.4. Absence of GABA-silent cells in in vivo CA1 156
5.5. Absence of GABA-silent cells in the dentate gyrus 157
5.6. Timing differences in GABA and glutamate synapse formation 157
5.7. Delayed feedforward GABAergic transmission in neonatal DG, CA1, and neocortex: Evidence for a universal developmental principle 158
5.8. Spatial organization of synapses and maturation of inhibition 159
5.9. Study limitations 159
5.10. Conclusions 159

6. Copyright permissions for figures 161
7. References 168
ANNEXES 191

Table des figures

Figure 1. Schematic drawing of the hippocampal formation. 19
Figure 2. Cross-sectional diagram of the entorhinal cortex (EC). 20
Figure 3. Topographic organization of downstream pathways from EC. 22
Figure 4. Ventral hippocampal commissure. 23
Figure 5. Commissural path (only ipsilateral to contralateral connections are represented). 24
Figure 6. Trisynaptic loop. 25
Figure 7. Hippocampal connections. 26
Figure 8. Feedback excitation and inhibition of dentate gyrus. 26
Figure 9. Feedforward excitation and inhibition of dentate gyrus. 27
Figure 10. Morphology of hippocampal principal cells. 28
Figure 11. Summary of all described IN subtypes in hippocampal subfield CA. 29
Figure 12. IN subtypes of the dentate gyrus. 31
Figure 13. Mouse Hippocampus Development. 33
Figure 14. The axes of the mouse hippocampus and its characteristic PCs. 34
Figure 15. CA1 pyramidal neurons. 35
Figure 16. Timetable of neurogenesis. 35
Figure 17. Sharp wave in adult animal. 37
Figure 18. Response to ventral hippocampal commissure stimulation. 38
Figure 19. Response to perforant path stimulation. 38
Figure 20. Example of sharp wave in adult rat with superimposed ripple. 39
Figure 21. Ripple oscillations in rat pups do not appear until after the second week of life. 40
Figure 22. Ripple oscillations in mice hippocampus do not appear until postnatal day 10. 40
Figure 23. Example of dentate spikes type 1 and 2. 41
Figure 24. Hippocampal bursts in freely moving rat pups (P4 to P6). 49
Figure 25. Recording of SPWs preceded by startles in a head-fixed P2 rat. 50
Figure 26. Activity bursts in MEC layer 3 precede eSPWs in neonatal rats. 51
Figure 27. Single unit activity in hippocampus and MEC L3 in relation to eSPWs. 52
Figure 28. Single unit firing properties with regards to eSPWs. 52
Figure 29. Comparison of eSPWs with adult SPWs. 54
Figure 30. Unitary discharges and evoked potentials in response to tooth pulp (TP) and acoustic (click) stimulations. 55
Figure 31. Hippocampal responses to somatosensory stimulation in the urethane-anaesthetized rat. 56
Figure 32. Hippocampal MUA responses to somatosensory stimulation 57

Figure 33. Feedforward inhibition (FFI). 58
Figure 34. Coincidence detection in PCs is abolished by $GABA_AR$ antagonists. 59
Figure 35. Feed-forward inhibitory inputs selectively impinge on the soma of PCs. 60
Figure 36. Synaptic mechanisms of early gamma oscillations. 61
Figure 37. Developmental increase in $GABA_A$ receptor-mediated transmission in response to thalamocortical input. 62
Figure 38. Age-related increase in thalamic input to fast-spiking (FS) interneurons compared to stellate cells (SC). 63
Figure 39. Development of connection probability and strength between fast-spiking (FS) interneurons and stellate cells (SC) across early postnatal days. 64
Figure 40. Developmental changes in BC signaling. 65
Figure 41. Developmental changes in IPSCs at BC synapses in the dentate gyrus. 66
Figure 42. CA1 dynamics and movement during early postnatal development. 67
Figure 43. Recruitment of CA1 glutamatergic and GABAergic neurons. 68
Figure 44. Development of perisomatic GABAergic innervation in CA1 region. 69
Figure 45. A model illustrating the generation of LFP from a population of identical neurons. 70
Figure 46. Examples of commonly used single unit and LFP recording devices. 71
Figure 47. An example of a silicon probe inserted into the principal barrel of a P6 rat. 71
Figure 48. Example of CSD profiles derived from spatially resolved LFP recordings. 72
Figure 49. Example of MUA extraction from the high-frequency components of extracellular data. 73
Figure 50. Patch-clamp procedure and configurations. 74
Figure 51. Example of patch-clamp in whole-cell current-clamp configuration. 75
Figure 52. Example of collecting information about synaptic currents using the low chloride concentration method. 76
Figure 53. Synaptic vesicle fusion. 77
Figure 54. The principle of antibody-based immunocytochemistry. 78
Figure 55. The working principle of a confocal microscope. 79
Figure 56. Validation of the overlap between immunohistochemical and genetic methods for localizing PV+ interneurons. 80
Figure 57. Example of a confocal image with fluorophore markers. 80
Figure 58. Main interface of the EasyViewer program. 81
Figure 59. Easy Viewer's filtering settings. 82
Figure 60. Automatic event detection settings. 83
Figure 61. Event-based signal averaging showing activity dynamics with CSD. 83
Figure 62. Image preparation and stacking settings in Synapto Catcher. 84
Figure 63. ROI selection and customization interface. 85
Figure 64. Filtering and binarization parameters. 85
Figure 65. Object identification and counting results. 86

Figure 66. Results gallery. 86
Figure 67. Spontaneous early sharp waves (eSPWs) and hippocampal responses evoked by electrical stimulation of skin in neonatal rat pup. 90
Figure 68. Somatosensory-evoked hippocampal eSPW response properties. 91
Figure 69. Current-source density (CSD) profile of spontaneous and stimulus-evoked eSPWs. 92
Figure 70. The relative magnitude of spontaneous and stimulus-evoked eSPWs. 93
Figure 71. Time relations between three main current sink observed during spontaneous and stimulusevoked eSPWs. 94
Figure 72. Multiple unit activity (MUA) recorded in CA1 pyramidal cell layer and DG granular cell layer during spontaneous and stimulus-evoked eSPW. 95
Figure 73. Synaptic correlates of eSPWs. 109
Figure 74. Examples of IPSC and EPSC bursts in a CA1 pyramidal cell during eSPWs. 109
Figure 75. Averaged EPSC and IPSC components of eSPWs. 110
Figure 76. Age-dependence of the EPSC and IPSC components half-rise times. 110
Figure 77. Perforant path stimulationevoked EPSCs and IPSCs in GCs at different postnatal ages. 122
Figure 78. Agedependence of the PPevoked EPSCs and IPCSs delays in GCs. 123
Figure 79 Angular bandle – evoked responses in the CA1 area of the neonatal rat intact hippocampus in vitro. 132
Figure 80 High incidence of ecIPSCs failure in neonatal CA1 pyramidal cells. 134
Figure 81. Long and variable ecIPSC delays in neonatal CA1 hippocampus. 135
Figure 82. Image processing example: filtering and binarization of synaptotagmin-2 (Syt-2) staining within the stratum oriens (SO) at two developmental ages (P5 and P21). 144
Figure 83. Syt-2 staining within Stratum Pyramidale. 145
Figure 84. Syt-2 staining within Stratum Oriens. 146
Figure 85. Syt-2 staining within Stratum Radiatum. 147
Figure 86. Syt-2 axon terminal density (%Area) within SP (stratum pyramidale), SO (stratum oriens) and SR (stratum radiatum) at postnatal day 5. 148
Figure 87. Axon terminal density (%Area) in hippocampal CA1 sublayers during postnatal development (P5, P11, P15, P21 and adult). 149
Figure 88. Hypothetical scheme of connections at early postnatal age (P5). 149

List of abbreviations

- AAC - Axo-axonic Cells
- ADA - Apical Dendrite-Associated Interneurons
- AMPA - Alpha-Amino-3-Hydroxy-5-Methyl-4-Isoxazolepropionic Acid
- BC - Basket Cells
- CA - Cornu Ammonis
- CCK - Cholecystokinin
- CH - Cortical Hem
- CR - Cajal-Retzius Cells
- CRH - Corticotropin-Releasing Hormone
- CSD - Current-Source Density
- DAPI - 4',6-Diamidino-2-Phenylindole
- DG - Dentate Gyrus
- DI - Dendrite-Innervating Cells
- DNE - Dentate Neuroepithelium
- DS - Dentate Spike
- ECG - Electroencephalogram
- EC - Entorhinal Cortex
- EMG - Electromyography
- EPSC - Excitatory Postsynaptic Current
- EPSP - Excitatory Postsynaptic Potential
- eSPW - Early Sharp Wave
- FFII - Feedforward Inhibition
- FP - Forepaw
- FS - Fast-Spiking
- GABA - Gamma-Aminobutyric Acid
- GABAA - GABA Type A Receptor
- GC - Granule Cells
- GDP - Giant Depolarizing Potential
- GFP - Green Fluorescent Protein
- HICAP - Hilar Commissural/Associational Path Cells
- HIL - Hilar-Associated Interneurons
- HIPP - Hilar Perforant Path Cells
- HNE - Hippocampal Neuroepithelium
- HP - Hindpaw
- IN - Interneuron
- IPSC - Inhibitory Postsynaptic Current
- IPSP - Inhibitory Postsynaptic Potential
- ISI - Interstimulus Interval
- LEC - Lateral Entorhinal Cortex
- LFP - Local Field Potential
- MF - Mossy Fibers

- MEC - Medial Entorhinal Cortex
- ML - Molecular Layer
- MOPP - Molecular Layer Perforant Path-associated Interneurons
- MUA - Multiunit Activity
- OLM - Oriens-Lacunosum Moleculare Cells
- OML - Outer Molecular Layer Cells
- PC - Principal Cell
- PCL - Pyramidal Cell Layer
- PETH - Peri-Event Time Histogram
- PMTH - Peri-Movement Time Histogram
- PN - Pyramidal Neurons
- PP - Perforant Pathway
- PV - Parvalbumin
- PW - Principal Whisker
- REM - Rapid Eye Movement
- ROI - Region of Interest
- SC - Schaffer Collateral
- SCA - Schaffer Collateral-Associated Interneurons
- SD - Standard Deviation
- SG - Slow Gamma
- SLM - Stratum Lacunosum-Moleculare
- SNARE - Soluble NSF Attachment Protein Receptor
- SO - Stratum Oriens
- SP - Stratum Pyramidale
- SPW - Sharp Wave
- SR - Stratum Radiatum
- SUB - Subiculum
- SW - Slow Wave
- SWP - Sharp Wave Potential
- Syt-2 - Synaptotagmin 2
- TA - Temporoammonic
- TML - Total Molecular Layer Cells
- TP - Temporoammonic Pathway
- VIP - Vasoactive Intestinal Peptide
- VZ - Ventricular Zone
- WH - Whisker Pad

1. Problem statement

In the immature hippocampus, a key brain structure involved in learning and memory processes, neural network activity demonstrates discontinuous temporal organization: most activity is synchronized in Early Sharp Waves (eSPWs) that represent the earliest organized pattern of activity in the developing hippocampus of newborn rodents (Leinekugel et al., 2002; Valeeva and Janackova et al., 2019; Murata and Colonnese 2020; Graf et al., 2021, Cossart and Khazipov, 2022, Marguet et al., 2015, Mohns et al., 2007). Although the electrophysiological characteristics of eSPWs resemble those of sharp waves and ripples (SWRs) in adults, the mechanisms underlying their generation differ. Adult SWRs are spontaneous, top-down generated events, while eSPWs emerge in a bottom-up manner, associated with inputs from the entorhinal cortex (EC) and activated by myoclonic movements in newborn rodents. It has been suggested that triggering of eSPWs by movements involves somatosensory feedback (Mohns et al., 2007; Valeeva and Janackova et al., 2019), raising a hypothesis that direct somatosensory stimulation can trigger eSPWs, similarly to the effects of myoclonic movements. The hypothesis that direct-somatosensory stimulation can elicit eSPWs requires verification. Confirmation of this hypothesis could demonstrate that external excitatory inputs from the EC play a primary role in generating eSPWs in vivo. This further raises a question of an interplay between excitatory and inhibitory inputs in the generation of eSPWs. While gamma-aminobutyric acid-mediated (GABAergic) synapses are established on hippocampal neurons during development first and well before the glutamatergic synapses (Tyzio et al., 1999), dynamics of activation of glutamatergic and GABAergic synaptic inputs during eSPWs remains elusive. For example, delayed recruitment of feedforward GABAergic inhibition has been shown during activation of thalamic inputs in the neonatal somatosensory cortex (Daw et al., 2007; Minlebaev et al., 2011). If inhibitory postsynaptic current (IPSC) dynamics similarly lag at long delays behind excitatory postsynaptic current (EPSC) dynamics during activation of EC inputs, this could explain global and long-lasting excitation in the hippocampal network during eSPWs (Valeeva and Janackova et al., 2019; Dard et al., 2022), as well as lack of pair-pulse inhibition in the hippocampus of neonatal rodents (Harris and Teyler, 1983; Michelson et al., 1989). Along with this hypothesis, biphoton imaging of presynaptic terminals of interneurons in the pyramidal cell layer revealed near silence of perisomatic inhibition in the neonatal mouse hippocampus following neonatal movements (Dard et al., 2022). This finding aligns with the observation of very few perisomatic GABAergic synapses during immunochemical staining for their markers, such as glutamate decarboxylase (GAD), synapsin, and synaptotagmin-2 (Syt-2), and through electron microscopy during the first postnatal week (Schwartzkroin et al., 1981; Dupuy and Houser, 1996; Rozenberg et al., 1989; Tyzio et al., 1999; Dard et al., 2022). Collectively, these observations necessitate studying the

relative behavior of IPSCs and EPSCs in the neonatal hippocampal neurons during activation of EC inputs and during eSPWs. Consequently, the anatomical development of GABAergic synapses on CA1 pyramidal cells becomes an important question. It is known in adults that hippocampal inputs via the temporoammonic pathway (TA) and perforant pathway (PP) are modulated by feedforward inhibition mediated by diverse GABAergic interneurons, notably fast-spiking parvalbumin (PV) perisomatic basket cells, which provide rapid and powerful somatic inhibition, establishing a precise temporal integration window (Freund and Katona, 2007; Pouille and Scanziani, 2001; Klausberger and Somogyi, 2008). Studying the development of the distribution of PV interneuron terminals could help explain why GABAergic inhibition is weak at younger ages.

1.1. Research questions

1. The possibility of triggering eSPWs in the neonatal rodent hippocampus through direct somatosensory stimulation.
2. Dynamics of synaptic responses (IPSCs and EPSCs) during actication of EC inputs and during eSPWs in the hippocampal neurons of neonatal rodents .
3. Examination of the developmental distribution of PV interneuron terminals in the hippocampus.

1.2. Research objectives

1. **Assessing the possibility of triggering eSPWs with direct somatosensory stimulation.**
   To determine whether direct somatosensory stimuli can evoke eSPWs with characteristics like spontaneous eSPWs associated with myoclonic movements, subcutaneous electrical stimulation of whisker pad in neonatal rats (P5–P6) has been used under urethane anesthesia in vivo to suppress movement responses. Hippocampal activity was recorded using 16-channel silicon electrodes placed along the CA1-DG axis. The characteristics of evoked eSPWs were compared to spontaneous ones using current source density (CSD) profiles, amplitude, duration, and spatiotemporal characteristics of LFP and MUA.
2. **Investigation of synaptic currents during eSPWs in the CA1 hippocampus.**
   To study the dynamics of interactions between EPSCs and IPSCs in the CA1 hippocampus during eSPWs, patch-clamp recordings from pyramidal cells (P3–P7) were conducted in urethane-anesthesized rats in vivo. A low-chloride intracellular solution is used to separate excitatory and inhibitory currents. Analysis included temporal characteristics of the currents—latency, duration, and amplitude—as well as duration of the integration window during postnatal development.
3. **Characterization of synaptic currents in the dentate gyrus (DG) during perforant path stimulation.**
   To understand the age-related dynamics of EPSCs and IPSCs in granule cells of the DG in association with the EC input, perforant path stimulation was employed in

hippocampal slices of rats in vitro. Patch-clamp recordings allowed measurement of EPSC and IPSC latency, jitter, and amplitude across different ages (P2–P62). These data were used to evaluate developmental changes in the integration window associated with the maturation of inhibitory mechanisms in the DG.

4. **Examining the development of inhibitory mechanisms associated with inputs from the EC in CA1 hippocampal pyramidal cells.**
   The question of how delayed maturation of inhibitory currents affects the integration of excitatory inputs from the EC has been addressed by analyzing the temporal characteristics of EPSCs and IPSCs in CA1 pyramidal cells during temporoammonic pathway stimulation in the intact mouse hippocampus in vitro. Recordings were performed, focusing on latency and jitter changes in IPSCs and EPSCs during different ages (P1–P11). These data were used to study changes in the integration window as inhibitory mechanisms develop.

5. **Study of the developmental distribution of future PV interneuron terminals in CA1 hippocampal layers.**
   To understand the developmental spatial distribution of inhibitory synapses from future PV interneurons in the hippocampus, an analysis was conducted at different stages of the postnatal development. Immunohistochemical methods using the Syt-2 marker as a reliable indicator of future PV interneurons were employed. Synapse density was studied in the stratum oriens, pyramidale, and radiatum layers at postnatal ages from P5 to P21. The results provide insight into the sequential development of inhibitory mechanisms and their contribution to hippocampal functional maturity.

1.3. Key propositions

1. **Somatosensory stimulation as a trigger for eSPWs:** Early sharp waves (eSPWs) in the hippocampus of neonatal rats can be induced by direct somatosensory stimulation.

2. **Synaptic currents and signal integration in CA1 and DG:** eSPW generation is driven by excitatory EPSCs dominating at early stages, while inhibitory IPSCs are activated with a delay, broadening the signal integration window in CA1 and DG during early postnatal development.

3. **Distribution of PV interneuron terminals in CA1:** The maturation of inhibitory mechanisms in the hippocampus is associated with the sequential development of future PV interneuron terminal distribution first in dendritic compartments of CA1 pyramidal cells.

2. Introduction

To ensure the subject of the study is clear and well-defined, we will structure the introduction by dedicating time to a comprehensive overview of the hippocampus. We will begin with a detailed examination of the hippocampal structure, exploring its anatomical organization, connections with other brain regions, and the characteristics of its diverse populations of nerve cells. Following this foundational discussion, we will delve into the patterns of activity within the hippocampal network, including both spontaneous and coordinated neural dynamics. Along the way, we will aim to highlight key elements and mechanisms that are particularly relevant to the objectives of this study, providing a thorough context that will guide our exploration and help us achieve the research goals.

2.1. Hippocampal structure

The hippocampal region is a key part of the cerebral cortex, made up of connected structures: the parahippocampal gyrus (entorhinal cortex, presubiculum, and parasubiculum), subiculum, and hippocampus proper (cornu ammonis) and dentate gyrus (Figure 1).

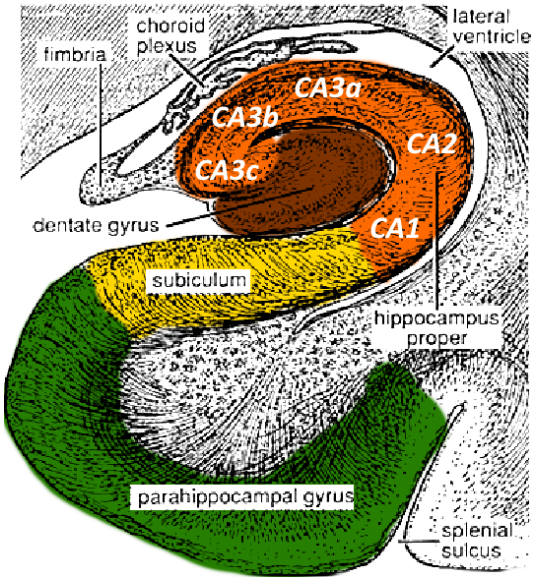

Figure 1. Schematic drawing of the hippocampal formation.
The hippocampal formation consists of the dentate gyrus (dark orange), hippocampus proper (pale orange), and subiculum (yellow). The latter is continuous with entorhinal cortex covering the parahippocampal gyrus (green). The hippocampus proper (cornu ammonis) may be divided into four regions (CA1…CA3 a, b, c). Output axons (blue) from the hippocampal formation run superficially in the alveus and then in the fimbria. The subiculum conveys reciprocal connections between the hippocampus and entorhinal cortex. The hippocampus forms a partial wall of the lateral ventricle, which contains a choroid plexus. From Kiernan, 2012.

Next, we will take a closer look at the connections and cells of the hippocampus. We will pay most attention to EC, CA, and DG structures.

2.1.1. Subiculum and entorhinal cortex

The subiculum is a transitional field between the three-layered CA1 (archicortex) and the six-layered entorhinal cortex (neocortex) (El Falougy et al., 2006). The subiculum represents the major output from the hippocampus. In turn, the subiculum receives input from the superficial layers of the entorhinal cortex and CA1. Therefore, subicular neurons (mostly pyramidal cells) receive synaptic input from axons from both areas, with the projections from entorhinal cortex being limited to the more distal dendrites. The subiculum also receives input from many of the brain structures that project to the entorhinal cortex. Pyramidal cells in the subiculum form both local collaterals (targeting other pyramidal cells within the subiculum) and projecting collaterals that target layer V of the entorhinal cortex and the pre- and parasubiculum. The subiculum also projects to many other brain areas, including the medial prefrontal cortex and many other (sub) cortical structures (Fröhlich, 2016).

Entorhinal cortex (EC) (Figure 2) contains six layers that, except for layer I, are substantially different from those found in the neocortex. Differences in appearance and cellular arrangements within these layers allow for a subdivision into lateral, intermediate and medial parts. Layer II contains the cell bodies of large stellate cells, which are grouped into islands in the lateral and intermediate EC; in medial EC, they form a continuous layer. Layer II is separated from layer III by a cell-sparse zone. Layer III contains medium-sized pyramidal cells. Layer IV is a cell-sparse zone (lamina dissecans) with few scattered large pyramidal cells. Layer V-VI contains relatively densely packed medium and small-sized neurons (Bayer et al., 1993).

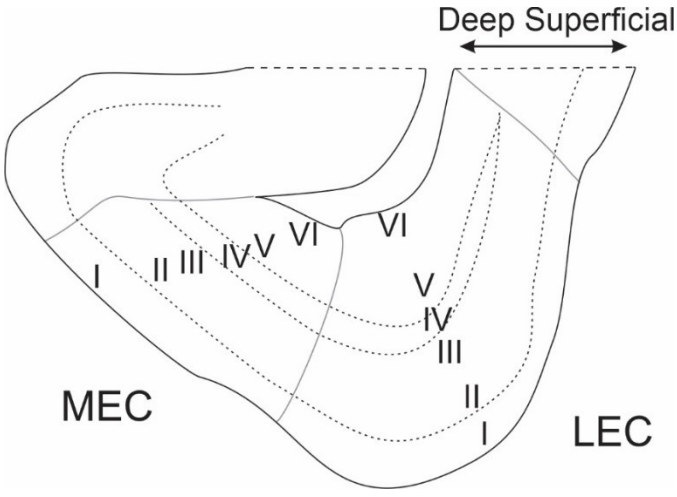

Figure 2. Cross-sectional diagram of the entorhinal cortex (EC).

This cross-sectional diagram illustrates the structural organization of the entorhinal cortex (EC), with a focus on its various subregions. The diagram differentiates the medial entorhinal cortex (MEC) and the lateral entorhinal cortex (LEC). The cortical layers within these areas are labeled with Roman numerals (I-VI), representing the different depths from superficial to deep, as indicated by the directional arrow. From van Strien et al., 2009.

2.1.2. Cornu ammonis

The Cornu Ammonis (CA) region of the hippocampus is traditionally subdivided into four distinct areas: CA1, CA2, CA3(a, b, c), Hilius. Each area has unique cellular compositions and structures. For instance, in the **CA1 region**, densely packed pyramidal neurons are aligned in a single layer. These neurons are notable for their thick apical dendrites that extend into the stratum radiatum and basal dendritic trees that project into the stratum oriens. Their axons subsequently project to the subiculum as well as other hippocampal regions, thereby influencing a range of neural circuits. In contrast, the **CA2 region** is a smaller area where pyramidal cells, although similar in appearance to those in CA1, exhibit distinct connectivity and specific molecular markers. CA2 neurons typically have unique input–output relationships, often receiving inputs from the entorhinal cortex while projecting to the CA3 region. Moving on to the **CA3 region**, it houses large pyramidal neurons that are less densely packed than those in CA1. These neurons display extensive basal and apical dendritic trees, receive mossy fiber inputs from the dentate gyrus, and send projections to CA1 and other regions through Schaffer collaterals. Furthermore, within the CA3 region—often divided into subregions labeled CA3(a, b, c)—one encounters the Hilus or polymorphic layer, which is characterized by a variety of cell types including polymorphic, fusiform, and modified pyramidal cells. Among these cells, the excitatory mossy cell is the most common; it receives inputs from granule cells via mossy fibers and projects its axons to the dentate molecular layer and fimbria (Amaral, 1978).

2.1.3. Dentate gyrus

The dentate gyrus is organized into layers that can be distinguished based on cell type and density. The outermost layer, known as the molecular layer, predominantly contains the dendrites of granule cells and various interneurons, and it also receives incoming axonal projections from the entorhinal cortex via the perforant path. Just beneath the molecular layer lies the granule cell layer, which is densely populated by granule cells—small neurons with compact cell bodies. These granule cells not only receive input from the entorhinal cortex but also send their axonal projections, known as mossy fibers, to the CA3 region, thereby contributing to the intrinsic circuitry of the hippocampus.

The dentate gyrus is also unique because adult neurogenesis occurs throughout the lifespan in both rats and humans. Granule neurons formed during juvenile and adult periods come from scattered precursor cells in the subgranular zone (Bayer et al., 1993).

2.2. Connections

2.2.1. Perforant and temporoammonic pathways

The perforant path is the projection from the entorhinal cortex (EC) to the hippocampus, connecting to the dentate gyrus, all subdivisions of Ammon's horn, and the subiculum (Andersen et al., 2009, see Figure 3). It connects the entorhinal cortex (EC) layer 2 (L2) to the dentate gyrus (DG) and CA3 region. From there, signals are transmitted from the dentate granule cells to CA3 pyramidal cells and then to the proximal dendrites of CA1 pyramidal cells in the stratum radiatum (SR). The perforant path interacts with the temporoammonic pathway, which projects from EC layer 3 (L3) to the distal dendrites of CA1 pyramidal cells in the stratum lacunosum-moleculare (sl-m). During hippocampal activity, such as MEC bursts/eSPW sequences, these pathways are co-activated, driving excitation of CA1 neurons (Ylinen et al., 1995; Csicsvari et al., 2000; Buzsaki, 2015).

Recent conceptualizations suggest that direct EC projections to CA3 and CA1 also function in a feedforward manner, modulating activity projected along the trisynaptic pathway. The direct perforant path projections to the hippocampal pyramidal subfields, especially CA1, have been less studied, but it has been shown that EC stimulation can evoke short-latency spikes in CA1 units, indicating monosynaptic activation via the perforant path (Soltesz and Jones, 1995).

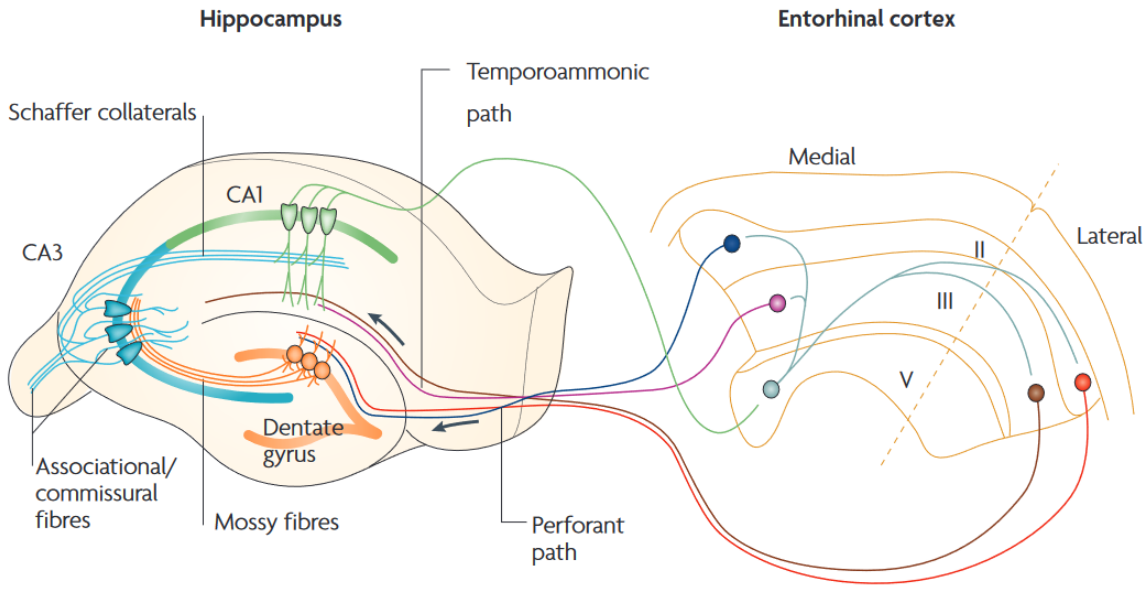

Figure 3. Topographic organization of downstream pathways from EC.
From Neves et al., 2008.

2.2.2. Commissural/associative pathway

Commissural axons project through the hippocampal commissure to the opposite hippocampal formation and form synapses on the proximal dendritic regions of hippocampal target cells, specifically in the inner third of the molecular layer of the dentate gyrus and the stratum radiatum and oriens of Ammon's horn. In rats, the molecular layer of the dentate gyrus receives topographically organized input from cells in the hilar region of the opposite dentate gyrus (Deller et al., 1995, see Figure 4)

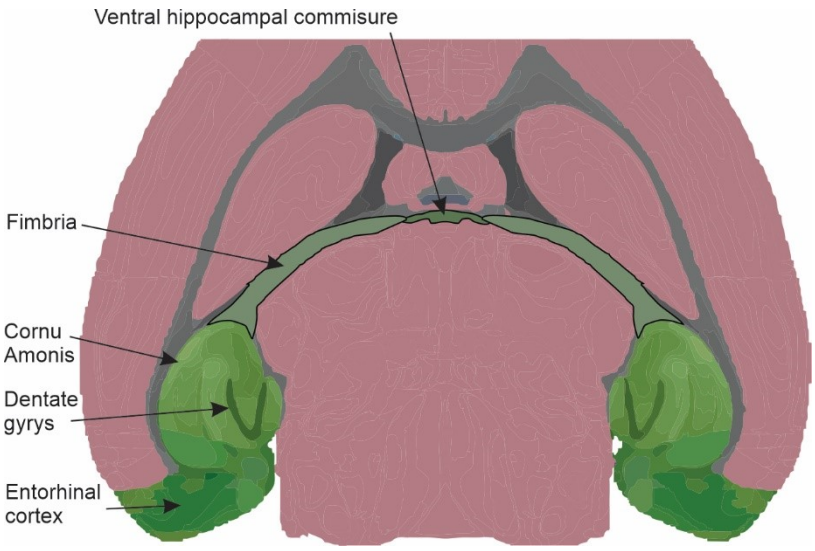

Figure 4. Ventral hippocampal commissure.
This horizontal section of the rodent brain highlights the ventral hippocampal commissure and related hippocampal structures. Ventral hippocampal commissure is a prominent bundle of nerve fibers that connects the hippocampal formations of the left and right hemispheres, enabling interhemispheric communication. Fimbria is a fiber tract extending from the hippocampus, through which the ventral hippocampal commissure facilitates the connection between the hippocampi.

Commissural fibers originating from CA3 pyramidal neurons project to the CA3 and CA1 fields of Ammon's horn. There is also a connection between contralateral CA1 fields, but it is weaker compared to the extensive connections originating from CA3 (Groen and Wyss, 1990, see Figure 5).

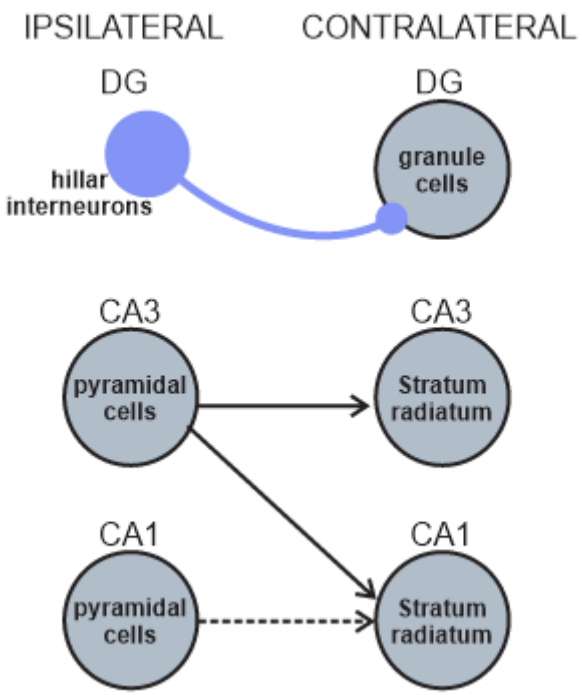

Figure 5. Commissural path (only ipsilateral to contralateral connections are represented). Inspired by Janáčková, 2013.

Neurons projecting to the contralateral hippocampus develop relatively late. In mice, the first commissural axons reach Ammon's horn at E18 and the dentate gyrus at P2. Synapses form only after birth (Blackstad, 1956; Fricke and Cowan, 1978; Super and Soriano, 1994). At P2, 60% of commissural axons target GABA-positive elements, and by P5, this is still the case for half of the connections. However, in the adult hippocampus, GABA-immunoreactive targets of commissural axon terminals represent less than 4% (Super et al., 1998). These GABAergic cells do not act as transient targets for incoming commissural fibers, as commissural axons still end up in the correct layer even in DLX1/2 mutant mice, which lack hippocampal interneurons (Pleasure et al., 2000). Additionally, the layer specificity of entorhinal and commissural connections does not depend on the temporal arrival of the fibers (Frotscher et al., 1995). Commissural fibers are guided to the inner molecular layer by positional cues on proximal segments of granule cell dendrites, which rely on the correct lamination of granule cells. The lamination of granule cells depends on the extracellular matrix protein reelin (Gebhardt et al., 2002; Zhao et al., 2003).

2.2.3. Local circuits

Local circuits determine the output pattern in brain structures receiving multiple inputs. The internal circuit of the hippocampus, known as the trisynaptic loop, was traditionally viewed as a unidirectional glutamatergic connection among three major cell groups: granule cells of the dentate gyrus, pyramidal cells of CA3, and pyramidal cells of CA1. All three fields receive glutamatergic input from the entorhinal cortex via the perforant path (Andersen et al., 1966, see Figure 6).

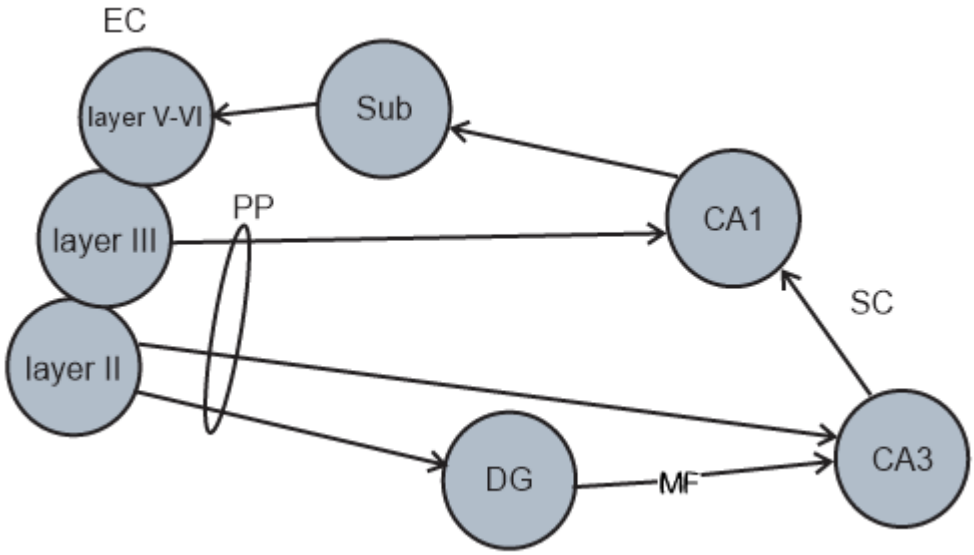

Figure 6. Trisynaptic loop.
PP perforant pathway, MF mossy fibres, SC Schaffer collaterals, Sub subiculum. Inspired by Janáčková, 2013.

More recent studies have revealed the existence of feedback connections between CA3 and the dentate gyrus (DG), which include both excitatory and inhibitory connections, as well as inhibitory connections between the entorhinal cortex (EC) and the DG (see Figure 7).

In slice preparations, stimulating the CA3 region induces inhibitory postsynaptic potentials in granule cells. It is hypothesized that this inhibition is mediated by the excitation of dentate gyrus basket cells and other interneurons by the recurrent CA3 collaterals (Scharfman, 1993; Kneisler and Dingledine, 1995). Sinks in the inner molecular layer occur during hippocampal sharp waves, indicating retrograde excitation of granule cells (Buzsaki, 1986). When GABAA inhibition is pharmacologically blocked, or during stimulation-induced afterdischarges, epileptic population bursts in CA3 and hilar mossy fibers also result in granule cell discharge (Scharfman, 1994; Bragin et al., 1997). This afterdischarge-induced recruitment of granule cells persists even after the bilateral removal of the entorhinal cortex (Bragin et al., 1997). These in vitro and in vivo experiments suggest that the CA3-dentate gyrus feedback can lead to both suppression and excitation of granule cells (Penttonen et al., 1997, see Figure 8).

In summary, these observations explain the mechanism of bidirectional activation of the dentate gyrus, which involves activation from the entorhinal cortex (EC) via the perforant path, as well as activation via recurrent collaterals from CA3 (Penttonen et al., 1997).

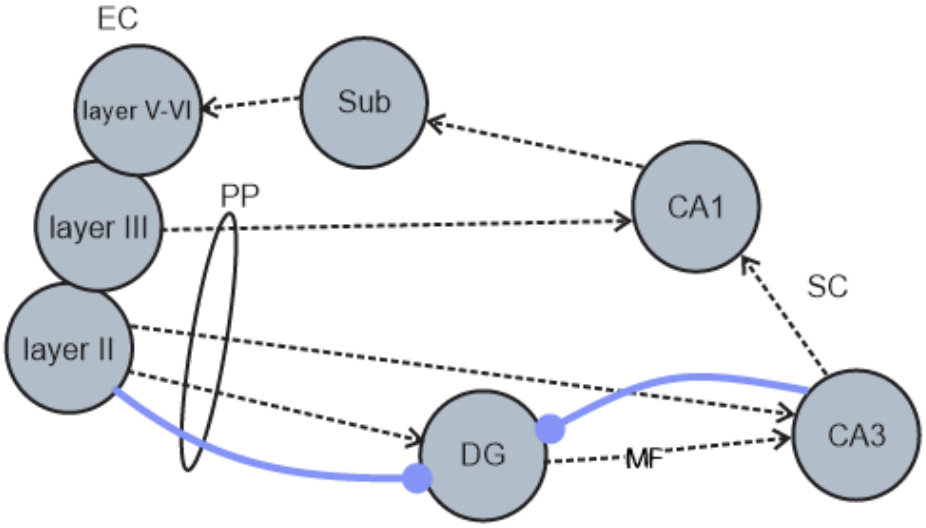

Figure 7. Hippocampal connections.
Inhibitory (blue line) and recurrent connections within hippocampal formation. Trisynaptic loop connections in dotted lines. Inspired by Janáčková, 2013.

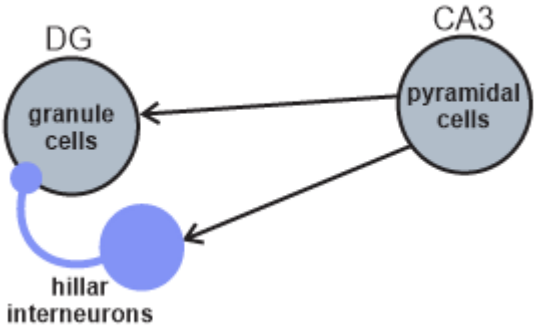

Figure 8. Feedback excitation and inhibition of dentate gyrus.
Inspired by Janáčková, 2013.

As for the mechanism of anterograde inhibition, MOPP (molecular layer perforant path-associated) cells have been shown to connect to granule cells using retrograde transsynaptic tracing. Paired whole-cell recordings of a MOPP cell and a granule cell, while stimulating the perforant path, revealed that both cells received excitatory postsynaptic potentials (EPSPs). However, because MOPP cells have a higher resting membrane potential, they were preferentially recruited (Li et al., 2013). Thus, in adults, the entorhinal cortex exerts an inhibitory effect on the dentate gyrus (Figure 9).

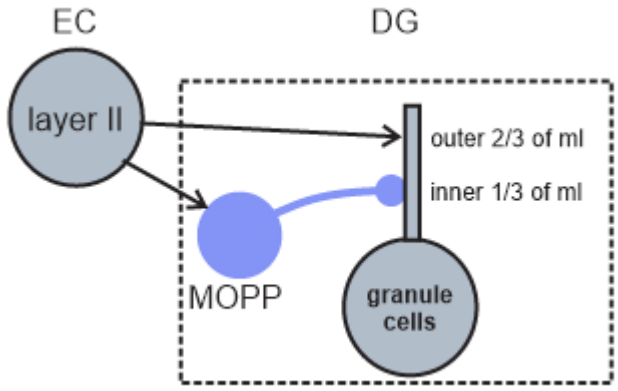

Figure 9. Feedforward excitation and inhibition of dentate gyrus.
MOPP molecular layer perforant path-associated cells, GC granule cells. Inspired by Janáčková, 2013.

2.3. Cells of hippocampus

2.3.1. Excitatory neurons

2.3.1.1. Pyramidal cells of Cornu ammonis

Pyramidal cells in the Cornu Ammonis (CA) regions of the hippocampus exhibit distinct morphological features (See Figure 10). These neurons typically have a triangular-shaped soma with a large apical dendrite that extends towards the molecular layer and several basal dendrites that spread horizontally. The cell bodies of CA1 pyramidal cells have a diameter of ~15 μm (Vida et al., 2018). They form a dense and well-defined stratum pyramidale (sPyr). sPyr in CA2 and CA3 is less compact than in CA1 region. The resting membrane potential is about −60 mV (Vazetdinova et al., 2022). Excitatory synapses are primarily glutamatergic, located on dendritic spines, while inhibitory synapses are GABAergic and found on the soma and proximal dendrites (Gulyas et al., 1999).

2.3.1.2. Granule cells of Dentate gyrus

Granule cells (GC) in the Dentate Gyrus (DG) of the hippocampus exhibit distinct morphological features. In the DG, GC form a dense layer known as the granule cell layer. Mature GCs have small, round, or ovoid cell bodies with a diameter of ~10 μm and are located densely packed in the GC layer (Vida et al., 2018). These neurons typically have a prominent apical dendrite that extends towards the molecular layer and numerous shorter basal dendrites. The resting membrane potential typically is about -75 mV (Mishra and Narayanan, 2020; Scharfman, 1995). Excitatory and inhibitory synapses are arranged similarly to CA.

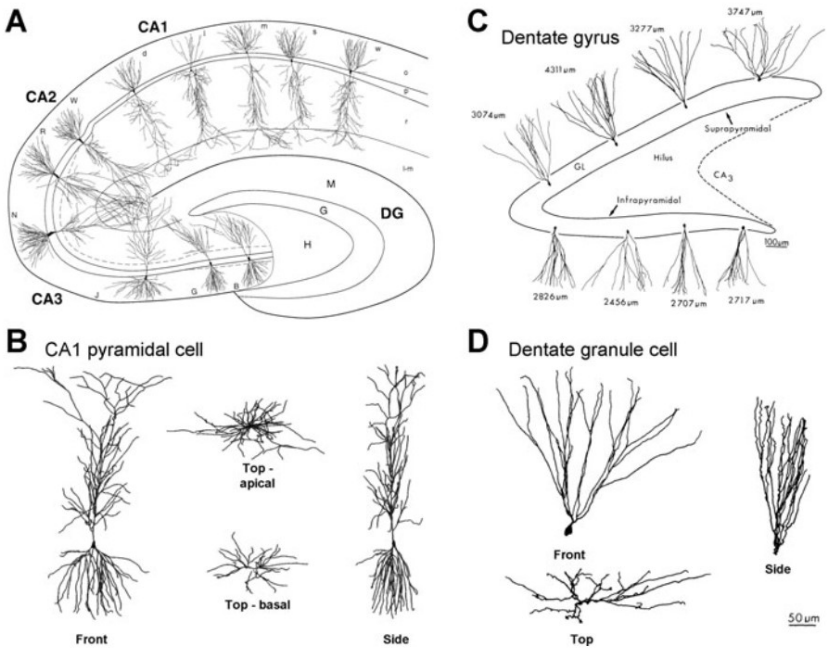

Figure 10. Morphology of hippocampal principal cells.

(a) Pyramidal cells of the CA1, CA2, and CA3 area. (b) Three-dimensional structure of a CA1 pyramidal cell illustrated from frontal, side, and top views. (c) Morphological diversity of DG GCs. Values adjacent to the cells indicate the total dendritic length. Note the difference between the upper (suprapyramidal) and lower (infrapyramidal) blades. (d) Three-dimensional structure of a GC illustrated from frontal, side, and top views. From Vida et al., 2018.

2.3.2. Interneurons

Subgroups of GABAergic interneurons innervate specific parts of excitatory neurons. Inhibitory synapses on cell bodies and axon initial segments are ideally located to control the genesis of action potentials, while those targeting dendrites of principal cells may control dendritic calcium spikes (Miles et al., 1996). Local GABAergic interneurons regulate the firing rate of principal cells, modulate their spike timing, and synchronize their activity (Klausberger and Somogyi, 2008).

2.3.2.1. Interneuron subtypes in Cornu ammonis

There are various types of interneurons, each differing in morphology, electrophysiological, and neurochemical characteristics (Booker and Vida, 2018; Petilla Interneuron Nomenclature Group et al., 2008). The types of interneurons in CA are listed below. Figure 11 shows the scheme of their location in the hippocampal layers.

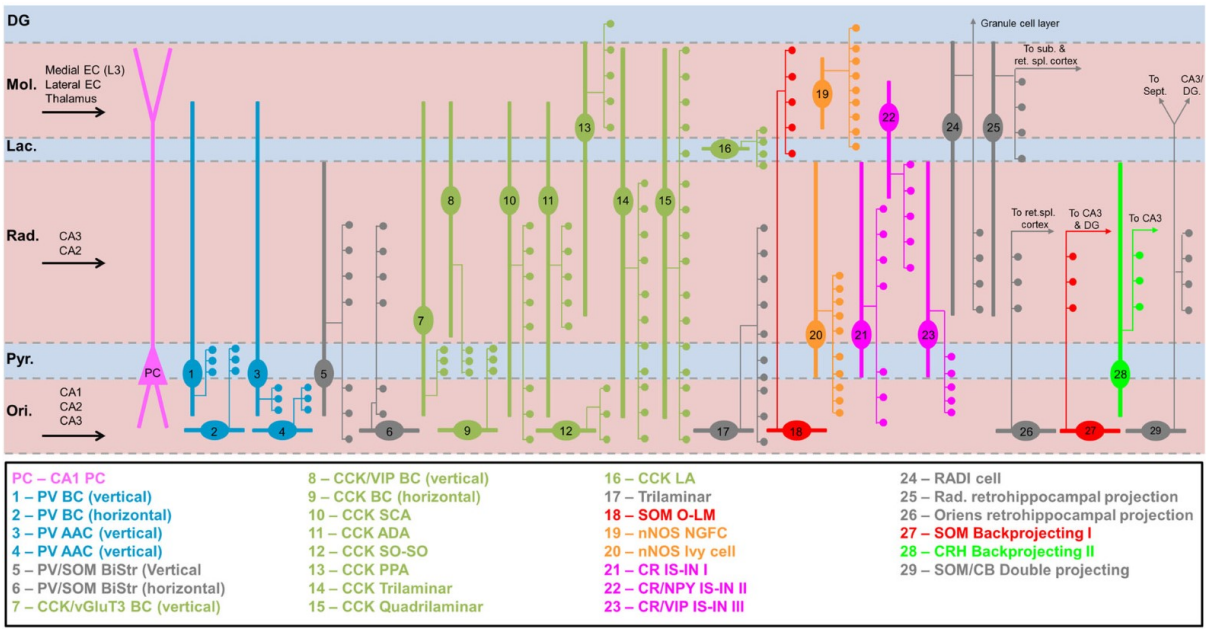

Figure 11. Summary of all described IN subtypes in hippocampal subfield CA.

Schematic overview of known morphological and neurochemical IN subtypes in CA1. Somatodendritic domains (thick lines), axonal locations (thin lines) and major terminal fields (circles) are shown with respect to regional layers (thin dashed lines). Afferent inputs are indicated with black arrows. Layers: Ori, str. oriens; Pyr, str. pyramidale; Rad., str. radiatum; Lac., str. lacunosum; Mol., str. moleculare; DG, dentate gyrus. From Booker and Vida, 2018.

Somatic (Perisomatic)–Targeting Interneurons

Perisomatic inhibitory interneurons comprising basket cells (BC) target PC somata and proximal dendrites. PV BCs are fast-spiking with low membrane resistance, vertically oriented dendrites, and a high number of excitatory synapses. PV BCs are essential for rapid inhibition. PV BCs in CA2 have dendritic and axonal arbors that extend beyond the subfield borders, innervating CA1 and/or CA3 PCs. Regular-spiking in nature, CCK BCs have spike train adaptation and form large amplitude IPSCs, highly expressing CB1 cannabinoid receptors.

Axo-Axonal Interneurons (AAC)

Targeting PC axon initial segments, axo-axonic cells are part of the perisomatic inhibitory interneurons.

Dendritic–Targeting Interneurons

Bistratified cells (BiStr) are characterized by their horizontally oriented dendrites, enabling them to provide robust feedback inhibition in CA1 pyramidal cells by forming up to ten synaptic contacts. In a related group, **SOM oriens/lacunosum-moleculare cells** (SOM OLM) are typically located at the stratum oriens/alveus border and serve as prototypical feedback interneurons; their horizontally oriented dendrites run parallel to the alveus. Another morphologically diverse group is represented by **CCK dendrite-innervating cells** (CCK DI), which are the most varied DI cells in CA1 with at least seven subtypes. These cells exhibit regular spiking and consistent spike train adaptation. Within this category, Schaffer collateral-associated interneurons have axons that form synapses in the stratum radiatum, primarily targeting large caliber apical dendrites, and

are noted for their high expression of CB1 receptors and VGluT3. Similarly, apical dendrite-associated interneurons also form synapses in the stratum radiatum with large caliber apical dendrites and share the expression of CB1 receptors and VGluT3. Along the same lines, stratum oriens–stratum oriens interneurons possess a horizontal multipolar dendritic tree with axonal arbors confined to the stratum oriens, where they function as strong feedback elements. Expanding on the diversity, CCK trilaminar interneurons feature an inverted pyramidal-shaped soma in the stratum radiatum, with axon terminals distributing across the radiatum, oriens, and pyramidale layers. Moreover, quadrilaminar interneurons are distinguished by their ovoid somata at the stratum radiatum/ lacunosum-moleculare border, and they extend their axonal ramifications across the radiatum, lacunosum-moleculare, pyramidale, and oriens layers. In addition, perforant path-associated interneurons contribute to feedforward inhibition by targeting dentate granule cells and interneuron dendrites in the outer two-thirds of the molecular layer, while lacunosum-associated interneurons have their somata at the stratum radiatum/lacunosum-moleculare border with dendrites and axons that span all layers. Moving beyond these cell groups, **neurogliaform cells** (NGFCs) , which express neuronal nitric oxide synthase (nNOS), are typically found in the distal stratum radiatum and lacunosum-moleculare. In contrast, **Ivy cells** form a population of slow-spiking GABAergic neurons that produce robust disinhibition within the hippocampal network. Finally, **trilaminar cells**, located in the stratum oriens, possess long and dense axons that extend through the stratum oriens, pyramidale, and radiatum, potentially establishing connections with both CA3 and the dentate gyrus.

Interneuron-Specific Interneurons (IS-INs)

IS-IN type I interneurons express calretinin (CR) but not vasoactive intestinal peptide (VIP). They have small, round somata and possess vertical dendrites, which primarily serve to inhibit the dendritic domains of other interneurons. In contrast, **IS-IN type II** interneurons are characterized by the expression of both CR and VIP. These cells inhibit other interneurons and are known to form mutual inhibitory synapses, establishing a more interconnected network of local inhibition. Meanwhile, **IS-IN type III** interneurons are similar in many respects to type II cells; however, they lack detailed morphological and neurochemical descriptions, which leaves some aspects of their function and connectivity less understood.

Additional Specialized and Long-Range–Projecting Interneurons

RADI cells are notable for having a large proportion of their axon terminals situated in the stratum radiatum, where they specifically target the apical dendrites of CA2 pyramidal cells. In contrast, **oriens/retrohippocampal projection interneurons** extend their projections to the medial septum, thereby providing strong inhibition to septal glutamatergic neurons. Similarly, **radiatum/retrohippocampal projection interneurons** feature dendritic and axonal projections that span both the stratum radiatum and retrohippocampal regions, indicating their involvement in broader network modulation. Additionally, **backprojecting interneurons** can be separated into two distinct types: Backprojecting I interneurons, which are characterized by their

expression of somatostatin (SOM), and Backprojecting II interneurons, which are defined by corticotropin-releasing hormone (CRH) expression. Moreover, there exists a group of **double projecting interneurons** that send axonal projections to both local and distant hippocampal regions, thus integrating multiple circuits within the hippocampus. Among the interneurons unique to CA2 are the **stratum pyramidale–stratum radiatum cells** (SP-SR), which are characterized by distinctive axonal and dendritic morphologies that set them apart from other interneuron subtypes. Further contributing to the diversity of hippocampal interneurons are the **mossy fiber–associated cells**, which have their somata positioned in the stratum lucidum and exhibit vertically or radially oriented beaded dendrites localized to both the stratum oriens and radiatum. Complementing this group are the **spiny stratum lucidum cells** that express calretinin (CR) and possess somata along with densely spiny dendrites running parallel to the stratum pyramidale. Finally, the **CR/SOM hippocampo-septal cells**, which reside in the stratum lucidum and co-express both SOM and CR, extend their influence by targeting interneurons in all layers of CA3 as well as in the hilus of the dentate gyrus.

2.3.2.2. Interneuron subtypes in Dentate gyrus

Below is a list of interneuron subtypes in hippocampal DG. Figure 12 also shows their location in the hippocampal layers.

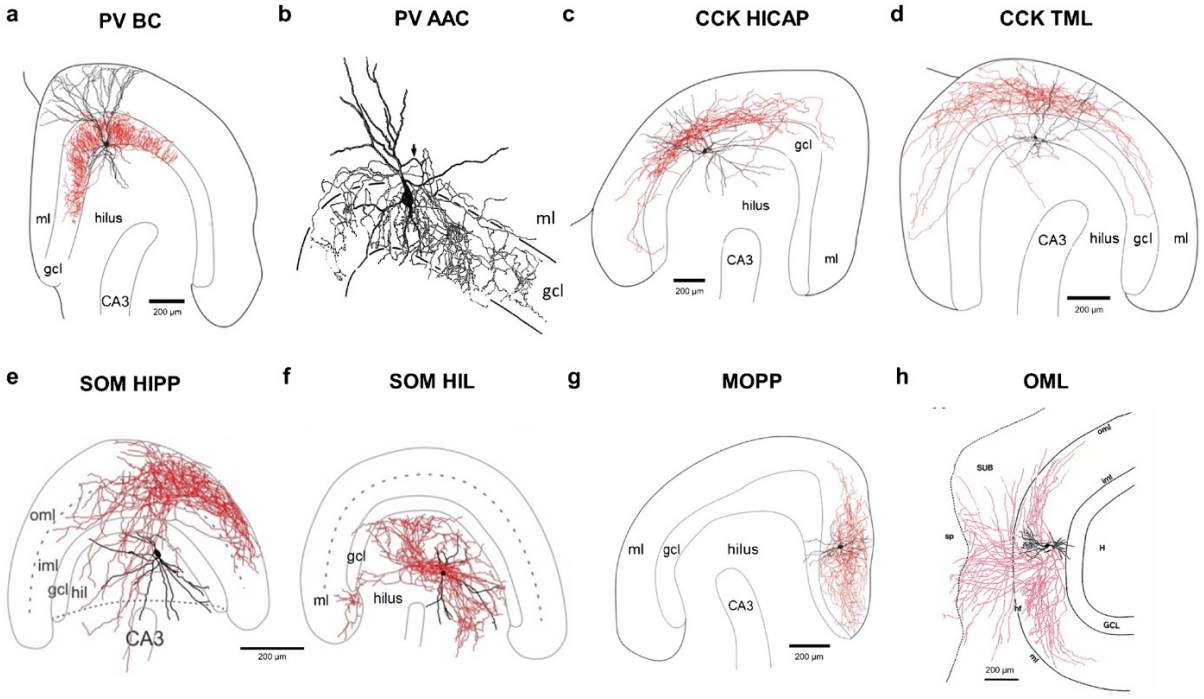

Figure 12. IN subtypes of the dentate gyrus.

Examples of morphological subtypes of identified IN in the DG of mice and rats. All panels except for b show soma and dendrites in black and axon in red. b Dendrites as thick black lines and axon as thin lines. From Booker and Vida, 2018.

a) **PV BCs:** PV basket cells in DG are similar to those in CA1 and CA3, characterized by fast-spiking properties and high density in the granule cell layer.

b) **PV AAC:** Parvalbumin-expressing axo-axonic cells (PV AACs) in the dentate gyrus are inhibitory interneurons that target the axon initial segments of granule cells

c) **CCK hilar commissural/associational path:** HICAP cells in DG have vertically oriented dendrites and form dense synapses in the inner molecular layer.

d) **CCK total molecular layer cells:** TML cells in DG have pyramidal-shaped somata and form synapses in the molecular layer, providing feedforward and feedback inhibition.

e) **SOM hilar perforant path cells:** HIPP cells have horizontal dendrites in the hilus and form synapses in the outer molecular layer.

f) **SOM hilar-associated INs:** HIL cells with dendrites in the hilus and axons providing strong perisomatic inhibition.

g) **Molecular layer perforant path cells:** MOPP cells have somata in the outer molecular layer and form pure feedforward inhibition in dentate granule cells.

h) **Outer molecular layer cells:** OML cells have axons in the outer molecular layer and subiculum, forming symmetrical output synapses on spiny dendrites.

2.4. Hippocampal development

2.4.1. Growth of the structure

The nervous system is one of the first systems to start developing during the embryonic period and the last to fully develop after birth. Neurulation begins in the trilaminar embryo when the central part of the ectoderm forms the neural plate, which folds into the neural tube. This tube will eventually become the entire central nervous system. During development, the front part, called the telencephalon, will form the cerebral cortex, basal ganglia, and limbic system.

The hippocampal formation, part of the limbic system, is created by the infolding of the archicortex into the ventricle (See Figure 13). Its three-layered structure indicates it was, along with the olfactory cortex, one of the first types of cortices to develop in early nervous systems (Gilbert and Singer, 2010). Its development begins at E14-16 when the neuroepithelium in the upper middle wall of the telencephalon curves into the lateral ventricle, creating a distinct area of the cortical sheet called the hippocampal primordium. This primordium will become the subiculum, Ammon's horn, and dentate gyrus. The hippocampal primordium is next to the entorhinal cortex primordium, which is located more towards the back (Bayer, 1980).

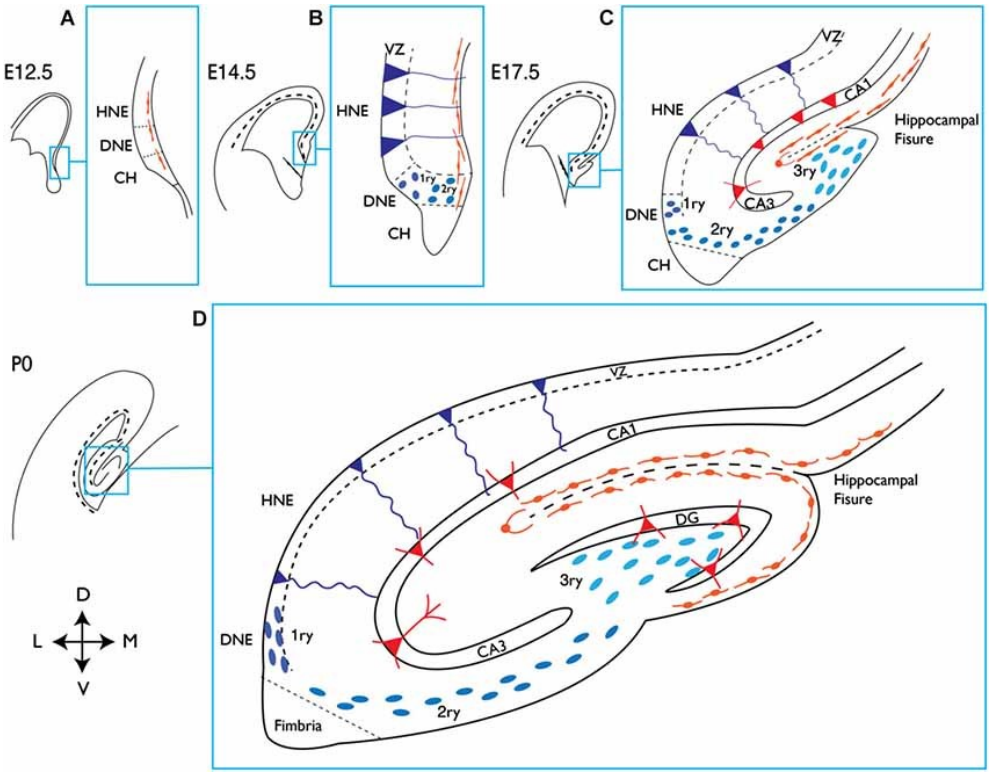

Figure 13. Mouse Hippocampus Development.

It outlines various embryonic stages and birth (P0), highlighting the hippocampus via magnified areas (blue squares). (A) At E12.5, the tentative DNE sits between HNE and CH, producing Cajal-Retzius cells (orange). (B) At E14.5, primary matrix dentate precursors (dark blue circles) are in the VZ, migrating towards the cortex, forming the secondary matrix (blue circles). HNE's VZ radial glial precursors (dark blue and triangular body shape) will generate hippocampal neurons. (C) At E17.5, the hippocampal fissure forms, and dentate precursor cells accumulate there, shaping the tertiary matrix (light blue). Cajal-Retzius cells (orange) follow the fissure, aiding in neuron migration. (D) At birth, the DG begins to form with granule neurons (red triangles) appearing first in the upper blade. The migration of Cajal-Retzius cells fosters the formation of the lower DG blade. While primary and secondary matrix precursor cells will soon vanish, tertiary matrix cells continue to divide and produce granule neurons postnatally. From Urbán and Guillemot, 2014.

2.4.2. Neurogenesis in hippocampus

Understanding the migration and formation of neurons within the hippocampus provides valuable information about its development. The following sections will discuss the neurogenesis and migration patterns of pyramidal, granular and interneuron cells, highlighting key timelines, migration dynamics, and developmental gradients (See Figure 14 and Figure 15).

2.4.2.1. Pyramidal Cells Development

Pyramidal cells in the Ammon's horn begin to be generated from the second week of embryonic development (E14 – E20). Cells in the CA3 region are produced earlier (peaking on E17) than those in the CA1 region (peaking on E18-19). However, CA1 pyramidal cells reach their final positions earlier than CA3 cells. This may be because CA1 cells have a shorter distance to migrate from the Ammonic neuroepithelium, whereas CA3 cells must travel around Ammon's horn (Altman and Bayer, 1990). Similar to the

neocortex, deeper pyramidal cells are born earlier than those in the superficial layer, affecting how their connections form (Deguchi et al., 2011).

Migration Dynamics: Multiple migration modes, speeds, and routes have been reported depending on birthdate. Early-born pyramidal neurons migrate faster than later-born ones, which take 7–9 days to reach their final destinations, as they remain frozen for ~3 days in CA1 and 4 days in CA3 in the multipolar state (Cossart and Khazipov, 2022).

Distal-proximal (transverse) axis: CA2 neurons and those in the subiculum are born first, followed by distal CA1 and distal CA3. CA1c (closer to CA2) and CA3c (closer to the dentate gyrus) are the last regions of Ammon's horn to be born, just before the dentate gyrus, which continues adding new neurons into adulthood.

Superficial-deep (radial) axis: Successive generations of glutamatergic neurons occupying the principal pyramidal and granule cell layers of the hippocampus migrate past the existing earlier-born neurons, creating layers in an "inside-out" fashion. Superficial neurons (closer to the stratum radiatum) are generally born later than deep neurons (closer to the stratum oriens). This deep-to-superficial gradient is less pronounced in CA3 than in CA1 (Cossart and Khazipov, 2022).

Dorsal-ventral (long) axis: There is no obvious developmental gradient of neurogenesis along the dorsoventral axis in the CA1 region, unlike CA3 or the entorhinal cortex, where ventral neurons are born significantly later than dorsal ones (Cossart and Khazipov, 2022).

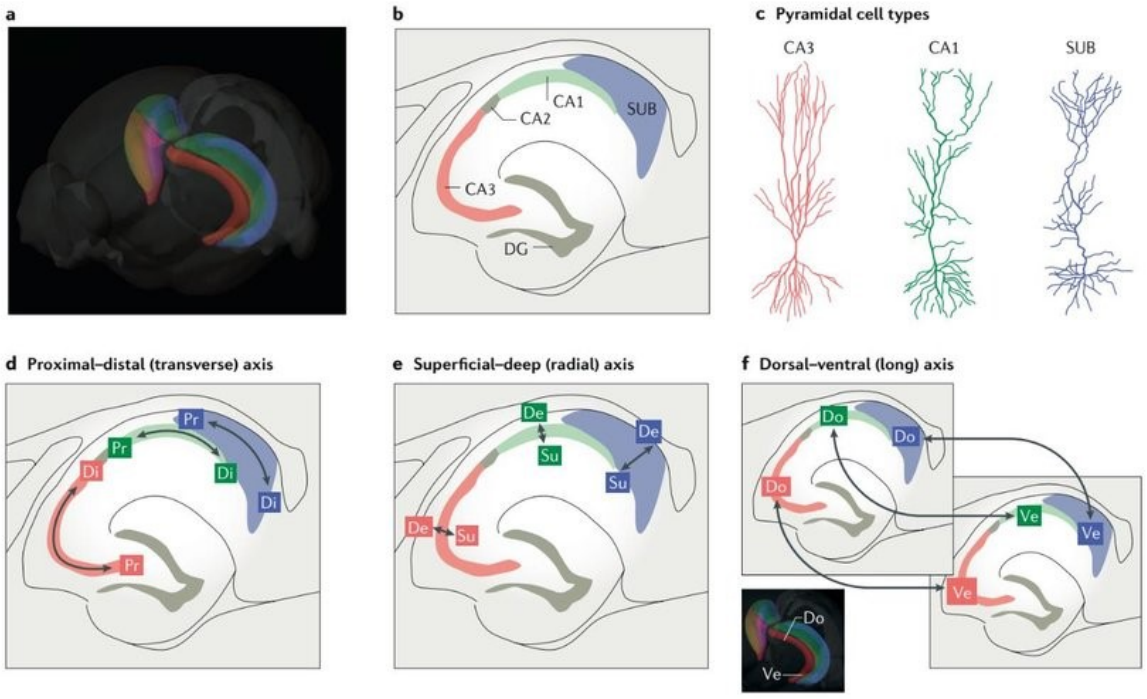

Figure 14. The axes of the mouse hippocampus and its characteristic PCs.

a: A 3D render of the mouse brain prepared with the Allen Brain Explorer 2 showing the CA3 in red, CA1 in green and the subiculum (SUB) in blue. b: A cross section of the hippocampal long axis with labelled regions. c:

characteristic CA1, CA3 and SUB cells illustrating the morphological differences between the three types. d-f: schematic illustrations of the three hippocampal spatial axes; d: proximal-distal (Pr-Di), e: superficial-deep (Su-De) and f: dorso-ventral (Do-Ve). From Cembrowski and Spruston, 2019.

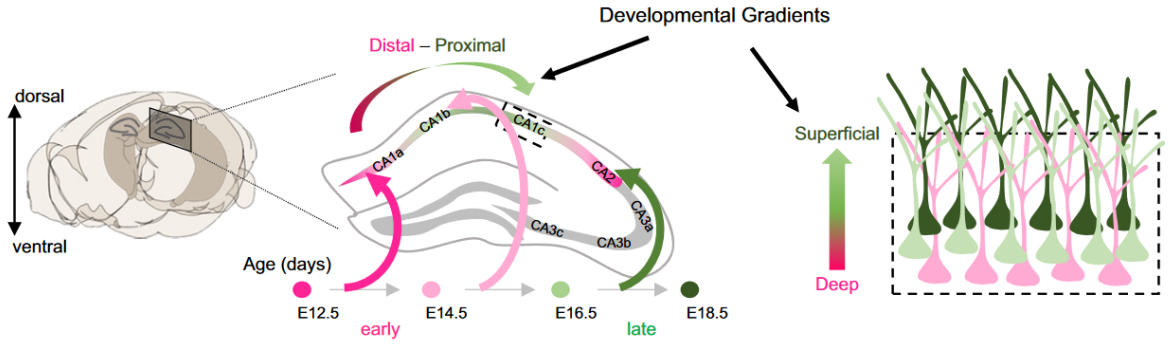

Figure 15. CA1 pyramidal neurons.
Schematic cartoon illustrates the distribution of CA1 pyramidal neurons (PN) along the transverse and radial (inset) axes according to their presumed birthdate (from embryonic day (E)12.5 to E18.5 in mice). Early born PNs (ebPNs) are represented in pink and later-born PNs (lbPNs) in green. From Cossart and Khazipov, 2022.

2.4.2.2. Granule Cells Development

Origin and Development: The granule cells of the dentate gyrus originate from the dentate neuroepithelium, specifically a region called the "dentate notch" (Altman and Bayer, 1990). These granule cells are known for their notably late development (Bayer, 1980), making the dentate gyrus the last hippocampal structure to form. Around 85% of these neurons are generated after birth in mice and rats (Figure 16), mainly during the first postnatal week. Neurogenesis slows down in the second and third postnatal weeks, with the dentate gyrus appearing mature by P21. Most dentate granule neurons settle from older, superficial layers to younger, deeper ones, opposite to the gradients seen in the neocortex layers (Bayer, 1980).

	CA1	CA3ab	CA3c	DG GC
E16	■	■		
E17	■	■	■	
E18	■	■	■	
E19	■	■	■	
E20			■	
E21-E22				
P0-P3				■
P4-P7				■
P8-P11				■
P12-P15				■

Figure 16. Timetable of neurogenesis.
Black shows the presence of neurogenesis. It can be seen that among the areas of the hippocampus proper, granule cells in the dentate gyrus begin neurogenesis later than the others. Data from Bayer et al., 1993.

2.4.2.3. Interneuron Development

Generation and Migration Paths: Interneurons that will populate the hippocampus are generated in the medial and caudal ganglionic eminences, located in the ventral wall of the telencephalon. In rats, these interneurons are produced between E13-18, with

those for Ammon's horn being generated earlier than those for the dentate gyrus (Amaral and Kurz, 1985). These interneurons migrate tangentially through the cortex, traveling within either the marginal zone or the subventricular layer, and then switch to a radial migration direction to reach the hippocampal primordium by E15 in mice (Manent et al., 2006). Interneurons from the caudal ganglionic eminence populate the strata lacunosum moleculare and deep radiatum, while those from the medial ganglionic eminence populate all layers, with a preference for strata pyramidale and oriens (Tricoire et al., 2011).

Timing and Layer Settling: The peak genesis of interneurons occurs before that of principal neurons; however, this does not mean they reach their final layer and functional connections in the network before the excitatory cells do (Danglot et al., 2006).

2.5. Network activity patterns

2.5.1. Network activity in adult hippocampus

2.5.1.1. Sharp waves

Sharp waves are large amplitude (1-3 mV) aperiodic potentials in the CA1 pyramidal cell field's stratum radiatum (See Figure 17). They represent massive synaptic excitation and synchronous discharge of pyramidal cell populations, generated in the CA3 region and invading the entire hippocampal formation (Buzsaki, 1986). Sharp waves are observed during slow-wave sleep, motionless wakefulness, drinking, face washing, grooming, and eating. Their endogenous origins are supported by several key findings: they occur most frequently when the animal has minimal environmental interaction (Buzsaki et al., 1983); neurons in layers II-III of the entorhinal cortex are relatively silent during sharp waves (Chrobak and Buzsaki, 1994); lesions in the entorhinal cortex do not abolish sharp waves and instead increase hippocampal sharp wave-associated population bursts (Suzuki and Smith, 1988; Bragin et al., 1995); and sharp waves are also observed in hippocampal slices from adult brains (Kranig et al., 2013).

Cellular Mechanisms of Sharp Waves

Studies in vitro show that sharp waves initiate in a small group of CA3 pyramidal cells (maximum in CA3b). AMPA receptor-mediated excitation is necessary to generate sharp waves, but phasic GABAA receptor-mediated current is also essential. Perisomatic inhibitory cells inhibit sharp wave initiation while bursting but enhance its occurrence in the following second (Colgin et al., 2005; Ellender et al., 2010). Blocking both phasic and tonic GABAA receptor-mediated inhibition transforms sharp waves into epileptiform bursts (Ellender and Paulsen, 2010). Behavior of populations of neurons is studied using electrophysiological methods recording simultaneously large numbers of active cells and methods recording unitary action potentials. Combination of those methods, together

with analyses of the signal describing movements of charges across the plasma membrane (current source and sink analysis) and correlation methods to find dependence between signals, serve to elucidate the way cell populations in different brain structures communicate. More recently, optical methods that enable recording of hippocampal activity using intracellular calcium or voltage sensitive dyes have been introduced, but these will not be discussed here.

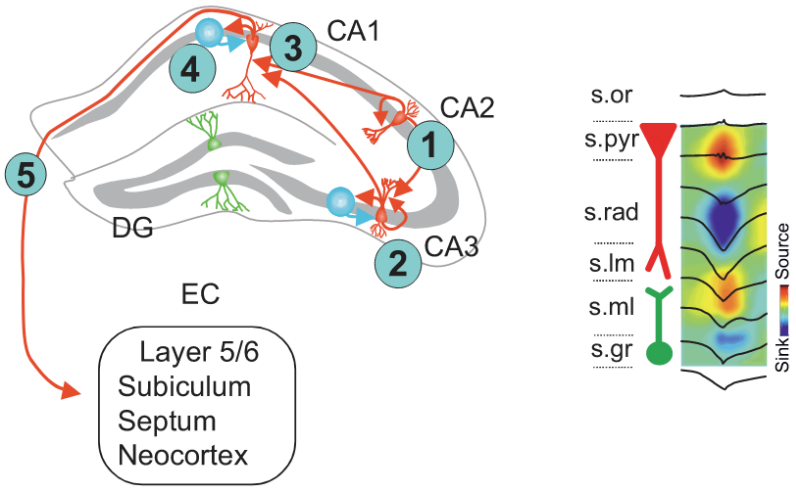

Figure 17. Sharp wave in adult animal.
Amplitude depth profiles in CA1-dentate gyrus show maximal sinks in stratum radiatum. From Cossart and Khazipov, 2022.

Direct stimulation of Schaffer collaterals in the ventral hippocampal commissure produces evoked potentials that have a similar shape and current-source density (CSD) analysis to spontaneous sharp waves (Figure 18). From surface to depth, the analysis shows:

a. A sink, likely caused by commissural/associational excitatory postsynaptic potentials (EPSPs) on the basal dendrites of pyramidal cells.

b. A sink corresponding to the population spike, indicating the collective firing of pyramidal cells.

c. A source following the population spike, due to recurrent inhibitory postsynaptic potentials (IPSPs).

d. A sink from commissural/associational EPSPs on the apical dendrites of pyramidal cells.

e. Sinks due to commissural/associational EPSPs on granule cells in the ectal and endal blades of the dentate gyrus

f. Sinks presumably due to EPSPs from medial entorhinal afferents (Brankack et al., 1993).

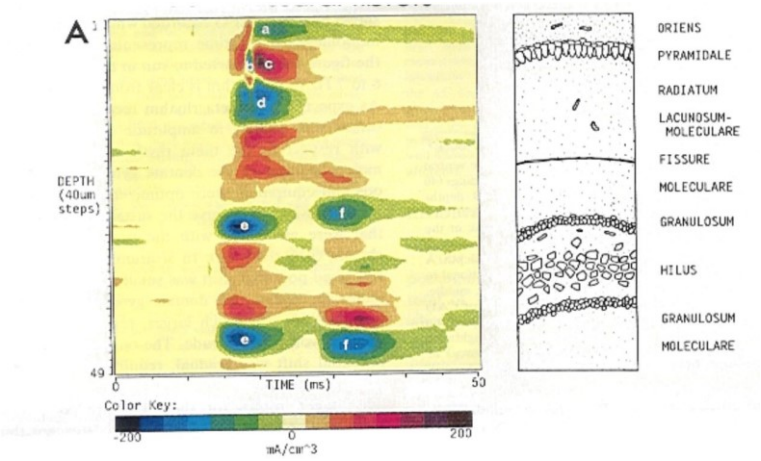

Figure 18. Response to ventral hippocampal commissure stimulation.
Current source density analysis following stimuli to the ventral hippocampal commissure and scheme of corresponding cell layers. From Brankack et al., 1993.

In contrast, the response to stimulation of the perforant path reveals the most prominent sinks and sources as follows (Figure 19):

a. A sink due to the direct termination of perforant path fibers on CA1 pyramidal cells.

b. Sinks resulting from medial perforant path EPSPs in the ectal and ental blades of the dentate gyrus.

c. Sources presumably due to IPSPs on the somata of granule cells.

b. Examining the CSD analyses of evoked potentials thus aids in localizing specific layers within the hippocampus and understanding the distinct contributions of different pathways to hippocampal activity.

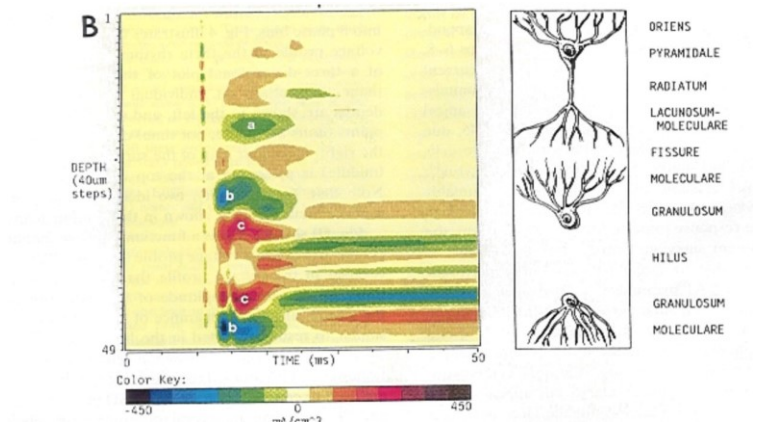

Figure 19. Response to perforant path stimulation.
Current source density analysis following stimuli to the perforant path and pyramidal and granule cell layout. From Brankack et al., 1993.

Sharp waves propagate to the subiculum and deep layers of the entorhinal cortex but are not recorded in the superficial layers (Chrobak and Buzsaki, 1996). Sharp waves have also been recorded in other species, notably in humans (Freemon and Walter, 1970).

2.5.1.2. Ripples

Ripples are a series of 3-13 (typically 5-8) high-frequency (140-200 Hz) waves, usually with a spindle shape. The polarity of these waves reverses across the pyramidal layer of CA1, and unit action potentials are mainly superimposed on the negative portions of these high-frequency waves (Suzuki and Smith, 1988; Buzsaki et al., 1992, see Figure 20).

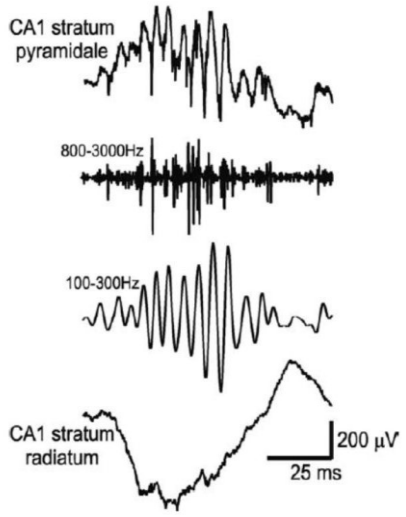

Figure 20. Example of sharp wave in adult rat with superimposed ripple.

Top and bottom traces are simultaneously recorded wide band traces from pyramidal layer and stratum radiatum, respectively. Note oscillatory pattern in the pyramidal layer, accompanied by an increase in local unit activity (second trace, 0.5-5 kHz) and consist of 5-15 wavelets within approximatively 70 ms (i.e. 140-200 Hz, filtered, third trace). From Buhl and Buzsaki, 2005.

Mechanism of Initiation

Three mechanisms have been proposed for initiating ripples. One possibility is that the synchronous discharge of CA3 and/or CA1 pyramidal cells leads to a transient, coordinated activation of CA1 basket and chandelier cells, which in turn produce a rhythmic oscillatory pattern in CA1 pyramidal neurons (Ylinen et al., 1995; Brunel and Wang, 2003). Alternatively, ripple initiation could be attributed to interneuron synchrony mediated by dendro-dendritic and dendro-somatic gap junctions between interneurons; however, subsequent studies have demonstrated that ripples persist unaltered in mice lacking these gap junctions (Ylinen et al., 1995; Draguhn et al., 1998; Buhl et al., 2003), thereby challenging this hypothesis. A third proposed mechanism suggests that gap junctions between the axons of pyramidal cells serve as the trigger for ripple initiation (Draguhn et al., 1998; Schmitz et al., 2001).

Emergence of ripples during development

Sharp wave-associated ripples appear by the end of the second postnatal week and gradually increase in frequency until P18 (Buhl and Buzsaki, 2005). Once ripples emerge,

the intra-ripple frequency reaches adult values (see Figure 21). Another study observed ripples in pups as young as P7 (Mohns et al., 2007).

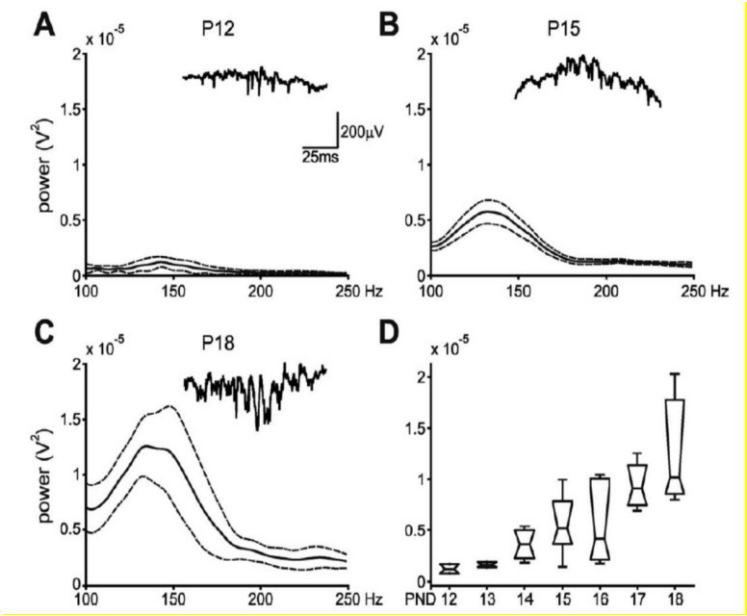

Figure 21. Ripple oscillations in rat pups do not appear until after the second week of life.
(A-C) Multitaper analysis of wide-band detected SW-associated activity for three selected age groups in freely moving animals. Solid/dotted lines: mean ± S.E.M. Insets examples of SW-ripple for each age group; black trace: wide band recording from CA1 sp. (D) Group results. Peak power in the 140-200 Hz frequency band across all age groups. Note the increase in power of the peak ripple frequency as the age increases. Horizontal lines indicate the mean at each age. From Buhl and Buzsaki, 2005.

Similar determination but in mice (4 to 12-day-old) was perormed by Pochinok et al., 2024. It was shown that ripples are robustly detected and induced by light stimulation of channelrhodopsin-2-transfected CA1 pyramidal neurons only from postnatal day 10 (P10) onwards (See Figure 22).

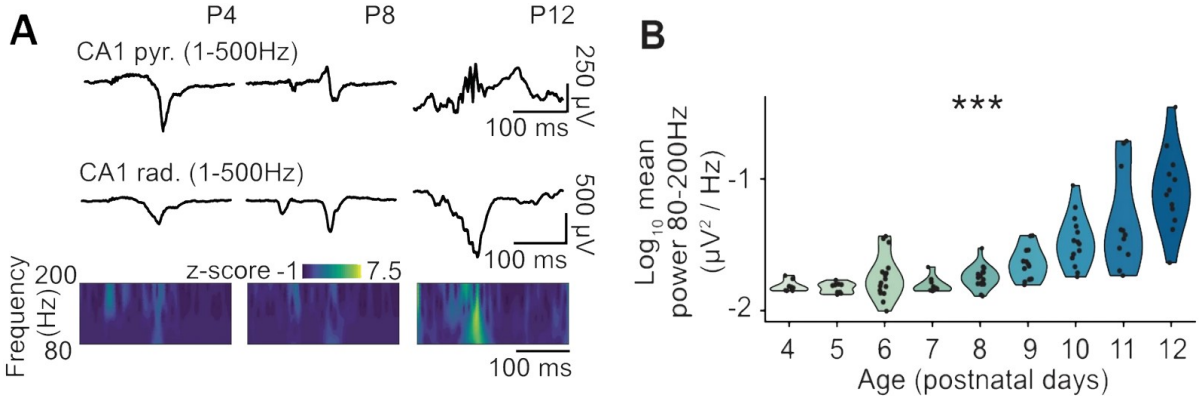

Figure 22. Ripple oscillations in mice hippocampus do not appear until postnatal day 10.
A Characteristic SPW and SPW-R events extracellularly recorded in the stratum pyramidale and stratum radiale of the hippocampal CA1 area of P4, P8, and P12 mice displayed together with the wavelet spectrum of the LFP at identical timescale. B Violin plot displaying the power in the 80-200 Hz frequency band across age (n = 111 mice). From Pochinok et al., 2024.

2.5.1.3. Sharp wave related gamma oscillations, “gamma tails”

Sharp waves can be followed by gamma frequency range oscillations (60-100 Hz), known as "gamma tails." Gamma tails are observed in normal adult behaving rats, with their frequency increasing after bilateral entorhinal cortex lesions (Traub et al., 1996).

Mechanism of Initiation

In vitro preparations show that transient gamma oscillations can be elicited by synchronizing pyramidal cell population bursts through partial blockade of GABAA receptors, increasing the amplitude and duration of pyramidal EPSCs, along with ectopic axonal action potentials or partial blockade of AMPA receptors on interneurons.

Therefore, it is proposed that gamma tails might be initiated either by NMDA receptor-mediated excitation of the interneuron pool (Sah et al., 1990; Traub et al., 1994), or through metabotropic glutamate receptor-mediated excitation of interneurons (Miles and Poncer, 1993; McBain et al., 1994; Poncer et al., 1995).

Emergence of gamma tails during development

According to Mohns et al., 2007 gamma tails closely associated with sharp waves, first emerge around postnatal day 6 and persist through at least postnatal day 18.

2.5.1.4. Dentate spikes

Dentate spikes (Figure 23) are large amplitude (2-4 mV), short duration (<30 ms) field potentials occurring sparsely (1-2 per minute) particularly in the dentate gyrus (DG). There are two primary types of dentate spikes: Type 1 Dentate Spikes (DS1), initiated by inputs from the lateral entorhinal cortex II (LECII) and Type 2 Dentate Spikes (DS2), initiated by inputs from the medial entorhinal cortex II (MECII). Both types identified in the rat (Bragin et al., 1995) and the mouse (Buzsaki et al., 2003).

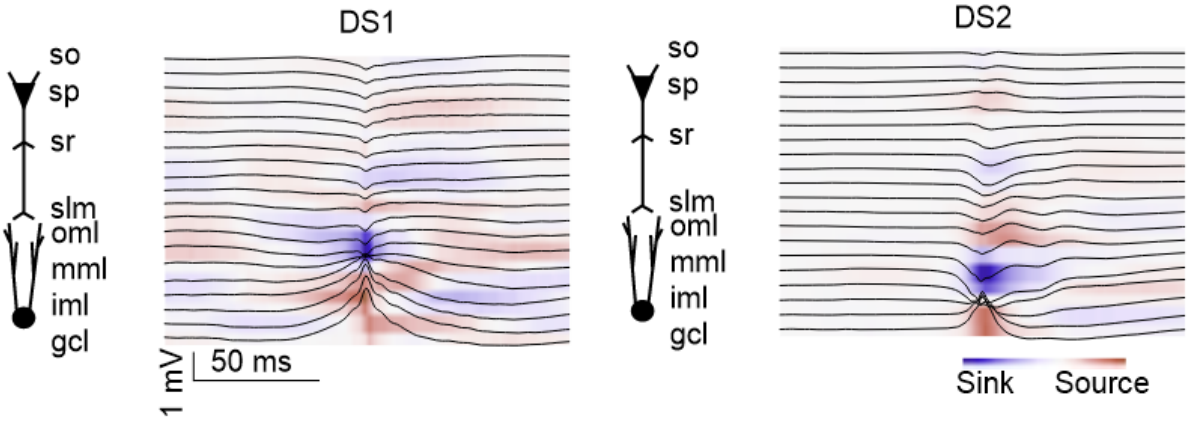

Figure 23. Example of dentate spikes type 1 and 2.

The figure shows current source density (CSD) maps for two types of dentate spikes (DS1 and DS2) recorded in the dentate gyrus. DS1 displays a primary sink in the oml (outer molecular layer), while DS2 shows a primary sink in mml (middle molecular layer) From Farrell et al., 2024.

Mechanism of Initiation

DS2 events are characterized by synchronization between MECII-originating slow gamma (SG) oscillations in DG and CA3-originating SG oscillations in CA1 at the DS2 peak (Dvorak et al., 2021; Farrell et al., 2024). This synchronization promotes excitation-inhibition cofiring within and across the DG→CA3→CA1 pathway. The initiation of these spikes involves extrahippocampal control signals from the entorhinal cortex, specifically through the perforant path projection to DG. Current source density (CSD) analysis reveals distinct anatomical and temporal properties for DS1 and DS2. DS2 sinks occur at middle molecular layers (mml), while DS1 sinks are found at outer molecular layers (oml).

Emergence of dentate spikes during development

Although specific data on the emergence of dentate spikes during the neonatal period is not available, it is worth highlighting that the development of neural networks and synaptic connections in the dentate gyrus continues throughout the first weeks of life, and early forms of neural activity may differ from mature patterns. This idea is further elaborated upon in the discussion section of this dissertation, where we consider the potential relationship between DS2 and the early sharp waves (eSPWs).

2.5.1.5. Theta oscillations

Hippocampal theta oscillation, also known as rhythmical slow activity, is a large amplitude, relatively slow (6-10 Hz), highly regular rhythm that occurs when the animal is engaged in motor behavior and during REM sleep (Vanderwolf, 1969). Theta oscillation is most regular in frequency and largest amplitude in the str. lacunosum-moleculare of the hippocampal CA1 region.

The extracellular currents underlying theta waves are generated mainly by the entorhinal input, CA3 (Schaffer) collaterals, and voltage-dependent Ca2+ currents in pyramidal cell dendrites. The entorhinal cortex contributes via excitatory signals transmitted to the distal dendrites of CA1 pyramidal cells. The CA3 recurrent network of pyramidal cells and possibly hilar mossy cells forms an intrahippocampal oscillator. The extrahippocampal (entorhinal) and intrahippocampal (CA3) theta oscillators can be relatively independent. After surgical removal of the entorhinal cortex, all remaining theta appears to depend on the integrity of the CA3 region (Buzsaki, 2002).

Mechanism of Initiation

Theta rhythms in the hippocampus are primarily generated by the coordinated activity of excitatory pyramidal neurons and inhibitory interneurons. Pyramidal neurons in the CA1 and CA3 regions of the hippocampus exhibit rhythmic firing patterns that are phase-locked to theta oscillations. This synchronized activity is thought to be driven by inputs from the entorhinal cortex, which provides excitatory drive at theta frequencies (Ylinen et al., 1995).

Interneurons, particularly parvalbumin-positive (PV+) basket cells, play a crucial role in the generation and maintenance of theta rhythms. These interneurons provide inhibitory input to pyramidal neurons, creating a feedback loop that contributes to the rhythmic oscillatory activity. The interaction between excitatory and inhibitory neurons forms the basis of the local circuit oscillations observed in the hippocampus (Ylinen et al., 1995).

Cholinergic input from the medial septum is another critical factor in the modulation of theta rhythms. Acetylcholine (ACh) release in the hippocampus enhances the excitability of pyramidal neurons and modulates the activity of interneurons. This cholinergic modulation is essential for the initiation and maintenance of theta oscillations. Studies have shown that the blockade of cholinergic receptors significantly disrupts theta rhythms, highlighting the importance of this neuromodulatory system (Vandecasteele et al., 2014).

Gap junctions may contribute to the synchronization of theta rhythms by facilitating rapid signal transmission and coordinated inhibitory neuron activity in the hippocampal network (Bocian and Kowalczyk, 2012).

Emergence of theta oscillations during development

In the adult rodent, CA1 theta oscillations are supported by the interplay between inputs from the septum, MEC, and CA3 with local and long-range GABAergic neurons and resonant intrinsic firing properties. The development of theta oscillations in the hippocampus was first described by LeBlanc and Bland (Leblanc and Bland, 1979) in the form of intermittent bursts of activity within the theta-frequency range occurring in CA1 and DG from P8-9 during movement and starting from P10 during RUN/REM states or following cholinergic-agonist application. Starting from P8–10, theta-coherent activities synchronize the hippocampus, red nucleus, LEC, prefrontal cortex, and ventromedial thalamus (Hartung et al., 2016, Ahlbeck et al., 2018, Brockmann et al., 2011, Del Rio-Bermudez et al., 2017). From P10 to P23–28, theta oscillations increase in amplitude and frequency from 4 to 7 Hz. The exact network mechanisms underlying emergence and developmental changes in hippocampal theta oscillations, which likely involve maturation of theta-generative properties in CA3 and EC networks, local, notably inhibitory CA1 circuits, as well as cholinergic and noradrenalinergic control remain an open question for future investigations (Cossart and Khazipov, 2022).

2.5.1.6. Gamma oscillations

The second type of synchronization mechanism seen in the hippocampus during alert behaviors is the relatively fast gamma oscillation (25-140 Hz). Although gamma and theta oscillations frequently co-occur, with gamma exhibiting its largest amplitude when nested within slower theta oscillations, they are generated independently (Leung, 1992; Stumpf, 1965). Gamma is an intrinsic rhythm that persists even after damage to the septal and all subcortical inputs to the hippocampus (Buzsaki et al., 1983).

Mechanism of Initiation

Two independent gamma generators have been identified in behaving animals. The first, located in the CA3-CA1 region, is intrahippocampal in origin. In contrast, the second gamma generator originates in the dentate gyrus, where its activity is driven by input from the entorhinal cortex (Bragin et al., 1995; Csicsvari et al., 2003).

Hippocampal gamma oscillations can also be induced in vitro by applying drugs that activate muscarinic, kainate, or metabotropic glutamate receptors or by tetanic stimulation patterns (Whittington et al., 1995; Whittington et al., 2001; Fisahn et al., 1998; Towers et al., 2002; Hajos et al., 2004). Gamma occurs in bursts at specific times of the theta cycle, and not all principal cells are involved in gamma firing, suggesting it serves to select particular cell subsets for processing (Lisman and Idiart, 1995; Jensen and Colgin, 2007; Senior et al., 2008).

Cellular Involvement in Gamma Oscillations Both pyramidal cells and interneurons are activated during gamma oscillations. Pyramidal cells fire action potentials around the negative peak of the oscillation (on average 0.03 ± 0.65 ms after the negative peak of the oscillation). Perisomatic inhibitory cells are also tightly coupled to the phase of the oscillation, firing 1.97 ± 0.95 ms after the negative peak of the oscillation (Hajos et al., 2004).

Functional Significance of Gamma Oscillations Due to their high frequency, gamma oscillations are ideally suited for operations requiring high precision neuronal coordination. These operations include rapid selection of inputs, filtering out unnecessary inputs, grouping neurons into functional ensembles, retrieving memories needed to perform previously learned tasks, and determining which aspects of an experience will be remembered (Colgin and Moser, 2010).

Emergence of gamma oscillations during development

Precursors of gamma oscillations, beta-gamma oscillations (at a frequency of 20–30 Hz) were first observed at P5 in short bursts during active and, to a lesser extent, quiet sleep (Marguet et al., 2015; Karlsson et al., 2006, Mohns and Blumberg, 2008). These beta-gamma hippocampal network oscillations increase in amplitude and frequency (toward the gamma frequency range) with age, and become modulated by theta rhythms starting from P8 (Mohns and Blumberg, 2008). By P10, the gamma rhythm was nearly continuous (Lahtinen et al., 2002; Karlsson et al., 2006).

The above was confirmed in a study by (Tsintsadze et al., 2015). They investigated the developmental features of kainate-induced oscillations (KA-Os) in the CA3 region of rat hippocampal slices, which are directly linked to inhibition-based gamma oscillations. Inhibition-based gamma oscillations can be reliably induced in hippocampal and neocortical slices both in vitro and in vivo during exposure to cholinergic agents or glutamate receptor agonists, including kainate.

Their findings revealed that up to postnatal day P5, the bath application of kainate failed to evoke detectable oscillations. However, starting from P5, kainate (300 nM) reliably induced oscillations in the CA3 pyramidal cell layer, with their amplitude and frequency progressively increasing with age. Initially, these oscillations were weak, slow

(20–25 Hz, beta range), and poorly synchronized with CA3 units and synaptic currents. Over the second postnatal week, the LFP power, unit synchronization, and the frequency of KA-Os increased, reaching gamma frequencies (30–40 Hz) by P15–21 (Tsintsadze et al., 2015).

2.5.1.7. Pathological high frequency oscillations

Ictal-pHFOs and their mechanisms during development

According to Le Van Quyen et al., 2006, the generation of ictal pathological high-frequency oscillations (ictal-pHFOs) during early development is distinct from both interictal-pHFOs and normal HFOs (ictal - during seizures; interictal - between seizures; normal - seen in processes like SWR). Ictal-pHFOs are primarily driven by the excitatory action of GABA in immature neural networks. GABAergic depolarization facilitates synchronized firing of interneuron networks, producing high-frequency bursts (>80 Hz) that correspond to ictal-pHFOs observed at seizure onset (Khalilov et al., 2005). These oscillations are specific to pathological conditions and do not occur under normal physiological circumstances.

Before P6, when glutamatergic synapses are insufficiently mature to generate higher-frequency normal HFOs (>60 Hz), ictal-pHFOs rely on GABAergic excitation and gap junctions between interneurons, which are prevalent during early stages (Zsiros and Maccaferri, 2005). Seizures can amplify ictal-pHFO generation by downregulating KCC2 cotransporters, increasing intracellular chloride levels, and further enhancing the excitatory effects of GABA (Rivera et al., 2004).

After P6, as glutamatergic synapses and NMDA receptor functionality mature, ictal-pHFOs transition to mechanisms involving higher-frequency oscillations (>60 Hz), which are no longer solely reliant on GABAergic excitation (Khalilov et al., 2005). These developmental mechanisms distinguish ictal-pHFOs from normal HFOs, which depend on the balanced interaction of glutamatergic and inhibitory GABAergic networks in mature neural circuits.

Very fast ictal -pHFOs (200–500 Hz), often observed in mature networks, arise due to mechanisms such as recurrent excitatory synaptic transmission and axo-axonic gap junctions in pyramidal neurons, which are hallmark features of pathological activity but are not involved in generating normal HFOs (Traub et al., 2002). These mechanisms highlight how interictal-pHFOs in adults depend on distinct, seizure-specific processes.

Interictal-pHFOs in adult networks

In animal models of chronic hippocampal epilepsy, pathological high-frequency oscillations (interictal-pHFOs) with spectral frequencies in the range of 250–600 Hz occur in the dentate gyrus, CA1, CA3 areas of the hippocampus, subiculum, and entorhinal cortex. These interictal-pHFOs are observed only in rats that exhibit recurrent spontaneous seizures and not in those that have been subjected to an epileptic insult but do not exhibit epileptic seizures (Bragin et al., 1999). Interictal-pHFOs reflect

synchronized burst firing of principal cells within small, localized neuronal clusters, which may represent the epileptogenic zone. These oscillations are typically observed at sites of seizure onset and are correlated with seizure frequency, with a higher number of interictal-pHFO-generating sites being associated with increased seizure frequency (Bragin et al., 2003; Bragin et al., 2010). Furthermore, interictal-pHFOs in human patients with mesio-temporal lobe epilepsy share similarities with those observed in epileptic rats, including frequency, duration, and their association with the seizure onset zone (Staba et al., 2002).

2.5.1.8. Place cells

Place cells, which are pyramidal neurons in the hippocampus, fire when an animal is in a specific location within its environment, effectively creating a cognitive map of the spatial environment. These cells were first discovered by O'Keefe and Dostrovsky, 1971. Place cells are mainly located in the CA1 and CA3 regions of the hippocampus, and their firing fields are stable over time. The activity of place cells is influenced by a variety of factors, including visual cues, internal cues such as the animal's speed and direction of movement, and other sensory inputs.

In addition to their role in representing current spatial positions, place cells participate in the phenomena of replay and preplay. Replay occurs when sequences of place cell activity, corresponding to an animal's previous movements, are reactivated during rest or sleep, aiding in memory consolidation. During replay, communication appears to predominantly flow from the hippocampus to the neocortex to strengthen memory traces (Ji and Wilson, 2007). Preplay, in contrast, involves the predictive activation of place cell sequences before an animal explores a new path. This anticipatory activity is suggested to involve hippocampal signals influencing cortical areas, potentially priming them for the processing of future events (Dragoi and Tonegawa, 2011). These processes highlight the bidirectional and temporally distinct communication roles of the hippocampus in coordinating past and future spatial representations with cortical networks.

Emergence of place cells during development

At P15, the first internal representations are observed in CA1 in the form of unstable place cells. After P17, preplay and sharp wave ripples replaying single locations start being observed. A few days later, the trajectories depicted within replay and preplay progressively represent longer trajectories (Scott et al., 2011; Farooq and Dragoi, 2019; Muessig et al., 2019; Cossart and Khazipov, 2022).

2.5.1.9. Grid cells

Grid cells, found in the medial entorhinal cortex (MEC), exhibit multiple firing fields that are arranged in a hexagonal grid pattern covering the entire environment. They were discovered by Edvard and May-Britt Moser in 2005 (Hafting et al., 2005). These cells provide a metric for space, which complements the positional information provided by place cells. Grid cells are thought to play a key role in path integration, which allows an

animal to keep track of its position by integrating information about its movements over time. This path integration is essential for navigation, especially in the absence of external cues (Cossart and Khazipov, 2022).

Emergence of grid cells during development

Grid cells mature later than hippocampal place cells, with adult-like grid cell firing present around 3–4 weeks of age (Langston et al., 2010; Cossart and Khazipov, 2022). Grid firing begins to appear on postnatal day 19, with the development of grid cells occurring suddenly rather than gradually. When these cells emerge, their activity patterns already resemble those of mature forms. Grid cells exhibit adult-like firing fields that tessellate into a coherent map of the local environment. This map is universal, preserving its internal structure across different environments. Additionally, in young rats, as in adults, grid cells encode information about direction and speed (Wills et al., 2012).

2.5.2. Network activity in developing hippocampus

2.5.2.1. Synchronous plateaus assemblies (SPAs)

SPAs are the first coherent electrical patterns to appear around birth. They represent calcium plateaus in groups of neurons connected by gap junctions (Crepel et al., 2007; Allene et al., 2012). By the end of the first postnatal week, SPAs are gradually replaced by synapse-driven network patterns like GDP or eSPW.

2.5.2.2. Giant Depolarizing Potentials (GDPs) in the neonatal hippocampus in vitro

Giant Depolarizing Potentials (GDPs) are network activities of hippocampal pyramidal cells driven by synapses. They result mainly from excitatory GABAergic and, to a lesser extent, glutamatergic currents (Ben-Ari et al., 1989; Khazipov et al., 1997; Leinekugel et al., 1997; Cherubini et al., 1990). GDPs are generated in CA3 and propagate to CA1 (Garaschuk et al., 1998). Interneurons in CA3 stratum radiatum also play a role in GDP generation, with activation determined by excitatory GABAergic connections between interneurons and glutamatergic connections from pyramidal cells (Khazipov et al., 1997). Both AMPA and NMDA receptors contribute to GDP generation. The depolarization necessary to activate NMDA receptors is provided by AMPA and GABAA receptor activation. NMDA receptors further depolarize and excite interneurons, increasing GABA release. The physiological role of GDPs is unknown, but similar synchronous activity is seen in other developing brain structures and may aid in network formation by increasing calcium ion concentration in postsynaptic cells (Leinekugel et al., 1995; Cash et al., 1996; Durand and Konnerth, 1996). GDPs, being the first observed network activity in vitro, are hypothesized to be counterparts of sharp waves observed in vivo. This hypothesis is supported by the finding that the NKCC1 blocker bumetanide, which eliminates GABA depolarizing actions and suppresses GDPs in vitro, also suppresses

sharp waves in neonatal rat hippocampus in vivo (Sipila et al., 2006). However, there is no direct evidence for the presence of GDP in vivo.

In the developing hippocampus, the cellular mechanisms underlying the excitatory role of GABA are closely linked to the balance of chloride ion transporters, specifically the cation-chloride cotransporters NKCC1 and KCC2. The balance between the NKCC1 and KCC2 transporters dictates the excitatory and inhibitory roles of GABA (Kahle et al., 2008). During early development, neurons exhibit high intracellular chloride concentrations, primarily due to the activity of the NKCC1 transporter, which imports chloride ions into the cell. This high chloride concentration leads to a depolarizing, and thus excitatory, effect when GABA binds to its receptors (Yamada et al., 2004). The NKCC1 transporter is highly expressed in immature neurons, contributing to the maintenance of this depolarizing action of GABA. Thus, high chloride concentration in the developing hippocampus leads to the excitatory effect of GABA, and consequently, excitatory GABAergic connections between interneurons, leads to synchronous activation of SR-CA3 interneurons and therefore the generation of GDPs. GDPs go away with age because there is a developmental upregulation of the KCC2 transporter, which exports chloride ions out of the cell. This process gradually reduces the intracellular chloride concentration, shifting the GABAergic response from excitatory to inhibitory (Zhang et al., 2006).

2.5.2.3. Early Sharp Waves (eSPWs) in neonatal hippocampus in vivo

In neonatal rodent CA1, neuronal network activity is characterized by discontinuous temporal organization reminiscent of "trace discontinu" or "trace alternant" described in preterm human EEG, with most of neuronal activity synchronized in the intermittent bursts separated by long (lasting from several seconds to tens of seconds) periods of silence. In this regard, temporal organization of the early hippocampal activity is similar to that observed during the neonatal period in rodents' neocortex, spinal cord, thalamus and other brain regions (Colonnese and Khazipov 2012). As well as in other brain structures, the early form of hippocampal bursting activity displays quite unique developmental features. In the neonatal rodent (rat and mouse) CA1 hippocampus, the hippocampal activity bursts are associated with sharp LFP waves, which are negative below the CA1 pyramidal cell layer (PCL) and reverse at the PCL, and are often followed by "tails" of units (Leinekugel et al., 2002; Mohns et al., 2007; Mohns and Blumberg, 2008; Marguet et al., 2015; Valeeva and Janackova et al., 2019; Cossart and Khazipov, 2022, see Figure 24).

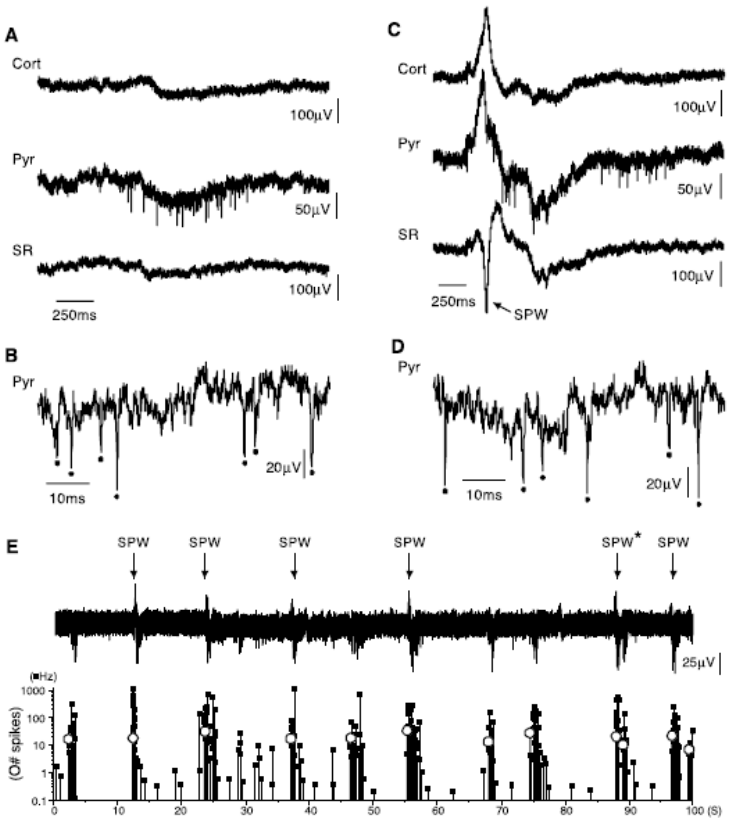

Figure 24. Hippocampal bursts in freely moving rat pups (P4 to P6).

(A) Multiple-unit burst discharge in CA1 pyramidal layer (Pyr) and Þeld activity in the neocortex (Cort) and stratum radiatum (SR). Part of the burst is expanded in (B), showing single units (dots). (C) Field SPW (arrow) associated burst recorded from the same three sites as in (A). Part of the burst is expanded in (D), showing single units (dots). (E) Filtered trace (.200 Hz) of multiunit activity in CA1 pyramidal layer. Arrows indicate simultaneously recorded Þeld SPWs. Below the trace is the corresponding multiple unit activity over time. Each vertical line terminated with a black square represents the Þring of one spike (height proportional to the instantaneous frequency of spikes). Vertical lines terminated with a white circle correspond to multiunit bursts (heights proportional to the number of spikes in the burst). Note that population-Þeld SPWs (arrows) co-occur with multiunit bursts. The SPW burst marked by an asterisk corresponds to the event illustrated in (C). From Leinekugel et al., 2002.

Although this pattern has certain electrographic resemblance of adult SPWs (Buzsaki, 2015) and this term has been used in its initial descriptions, it has some unique features and important difference in the generative mechanisms from adult SPWs, and therefore, in the current literature, it is most often referred to as early sharp waves (eSPWs). As said above, eSPWs share some similarities with adult SPWs, though they lack ripple oscillations, which only emerge during the second postnatal week along with a development of perisomatic inhibition (Leinekugel et al., 2002; Buhl and Buzsaki, 2005; Pochinok et al., 2024). Similar to adult SPWs, eSPWs display high levels of bilateral synchronization (Valeeva and Nasretdinov et al., 2019). eSPWs initiation and propagation display longitudinal gradient, with eSPWs most often initiated in the septal pole and propagating towards the temporal pole at high speed of ~250 mm/s (Valeeva et al., 2020), which is only slightly slower than speed of longitudinal propagation of adult SPWs

(~350 mm/s) (Patel et al., 2013). However, despite of these similarities, eSPWs differ from adult SPWs in their generative mechanisms.

Indeed, adult SPWs are spontaneous network discharges that are internally generated in the hippocampal CA2/CA3 network and propagate to CA1, and from CA1 to a variety of extrahippocampal targets. In contrast, eSPWs are externally driven events, whose generation involves inputs from EC. Indeed, while adult SPWs are associated with the main sink in SR, current source density profile of eSPWs is characterized by two prominent sinks located in SR and SLM indicating a co-activation of intrahippocampal inputs from CA3 together with EC inputs, respectively. Also, while neurons in superficial EC layers (which are source for temporoammonic and perforant inputs to hippocampus) are silent during adult SPWs, neurons both in L2 (source of PP input) and in L3 (source of TA input) are both activated during eSPWs, and their activation precedes activation of CA1 during eSPWs. Also, while neurons in deep EC layers (one of CA1 targets) fire at delay from CA1 neurons during adult SPWs, they fire before CA1 neurons (and even shortly before L2 and L3 EC neurons) during eSPWs in the neonatal rats (Shipkov et al., 2024). Finally, while adult SPWs occur during sleep and periods of immobility, eSPWs are highly correlated with physiological myoclonic movements, characteristic of active sleep during the neonatal period in rodents. Indeed, vast majority of bursts of activity in EC, and following EC bursts-driven eSPWs, are reliably preceded by myoclonic movements (See Figure 25, Figure 26, Figure 27, Figure 28).

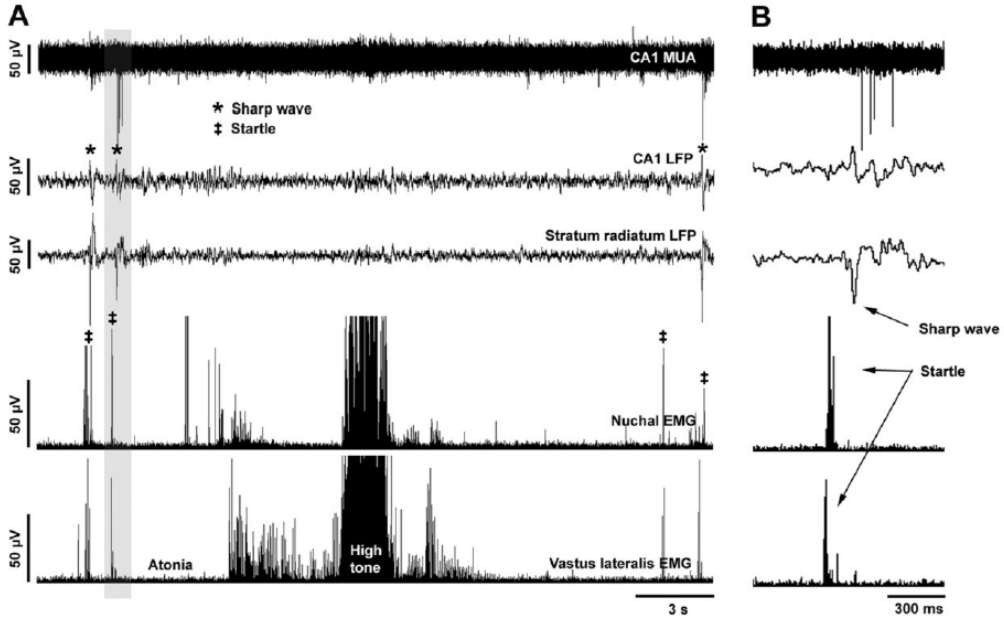

Figure 25. Recording of SPWs preceded by startles in a head-fixed P2 rat.

Traces from top: CA1 multiunit activity (MUA; filter: 500-5000 Hz); local field potentials (LFP) recorded from CA1 and stratum radiatum (filter: >100 Hz); EMG activity in the nuchal and vastus lateralis muscles. Individual instances of SPWs and startles are indicated. (B) Shaded area from (A) expanded to reveal temporal structure of the startle-SPW complex in detail. From Karlsson et al., 2006.

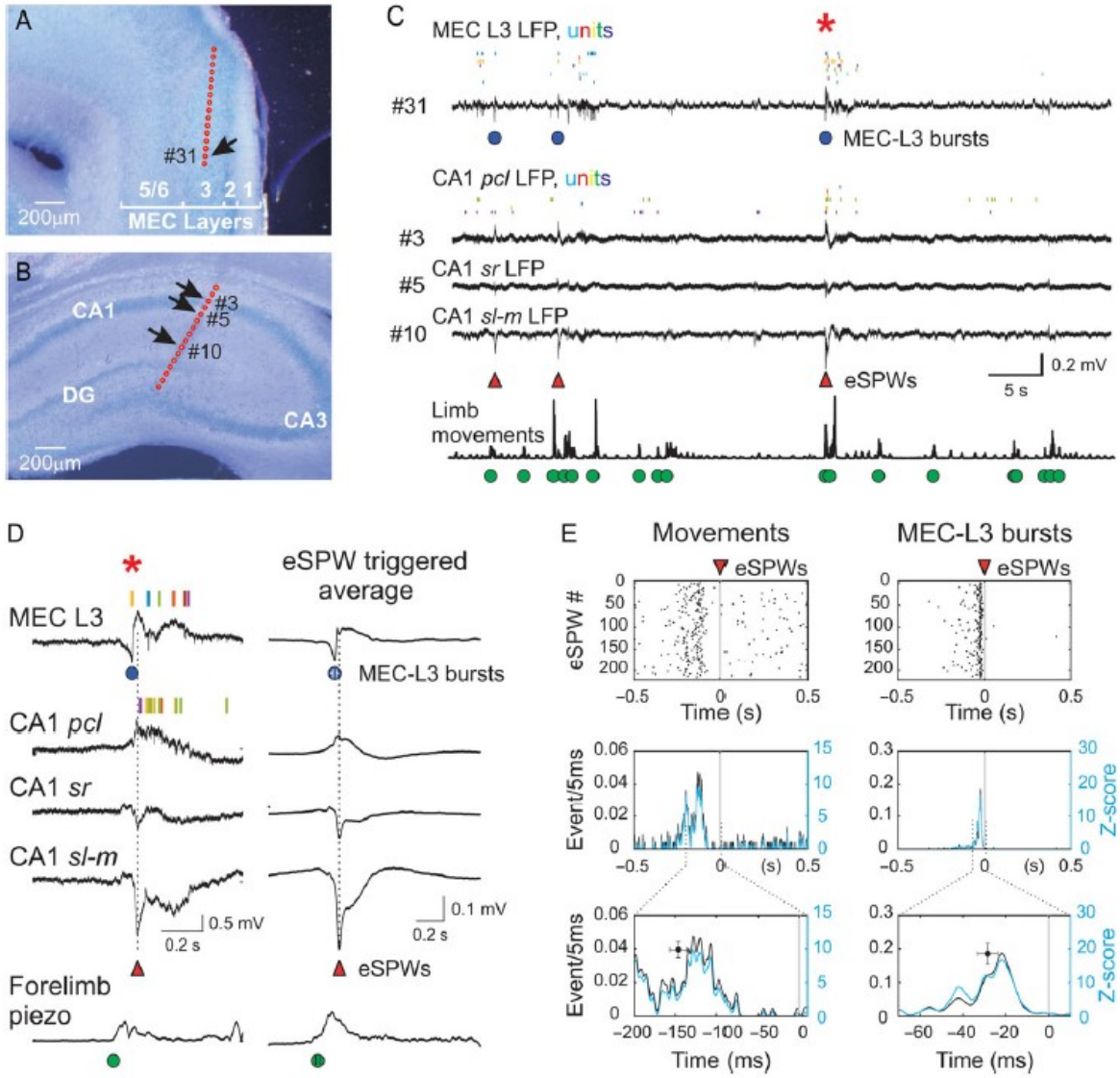

Figure 26. Activity bursts in MEC layer 3 precede eSPWs in neonatal rats.

Recording sites of the DiI-stained multielectrode arrays overlaid on a cresyl violet stained sagittal MEC slice (A) and coronal hippocampal slice (B) in a P5 pup. (C) Simultaneous LFP recordings (black traces) in MEC (recording site # 31 on A), CA1 pyramidal cell layer (PCL), stratum radiatum (SR) and lacunosum-moleculare (sl-m) from the recording sites # 3, 5 and 10 in (B), respectively. Bottom, movement recording averaged over three piezo channels. Action potentials from individual clustered unit are represented by vertical lines in distinct colors. eSPWs are indicated by red triangles, MEC L3 burst times by blue circles, and myoclonic movements by green circles. (D) A MEC L3 burst/eSPW complex from panel (C) (red asterisk) and eSPW-triggered LFP average (right) on expanded time scale. Right, eSPW-triggered average traces for the whole session. The circles below average traces show group averages of delays between MEC L3 bursts and eSPWs (blue; mean ± SD; n = 198 events recorded from four P4–6 rats), and between movement onset and eSPW (green; mean ± SD; n = 180 events recorded from four P4–6 rats). (E) eSPW-triggered raster plots (top) and PETHs (middle-bottom) for forelimb movements (left) and MEC L3 bursts (right). Bottom and middle PETHs are identical, but on a different time scale. Z-scores are computed from shuffled data. Circles at the bottom plots show Z-score peak value and time (mean ± SD) from four P4–6 animals. From Valeeva and Janackova et al., 2019.

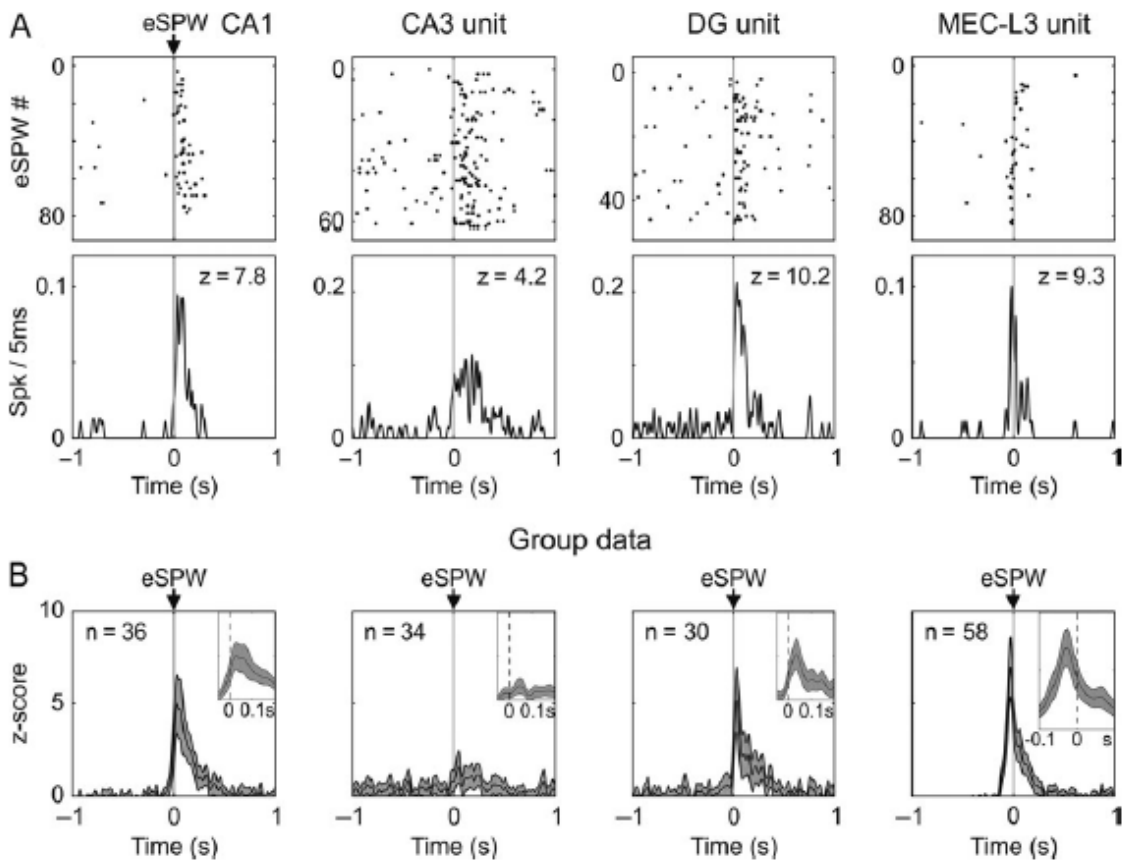

Figure 27. Single unit activity in hippocampus and MEC L3 in relation to eSPWs.

(A) Raster plots (top) and PETHs of individual cells aligned to eSPW times. CA1 and MEC L3 cells were recorded simultaneously. (B) Average PETHs from all selected cells in each structure expressed as a z-score from shuffled data. Insets are zoomed versions at an expanded time scale. n, number of cells. From Valeeva and Janackova et al., 2019.

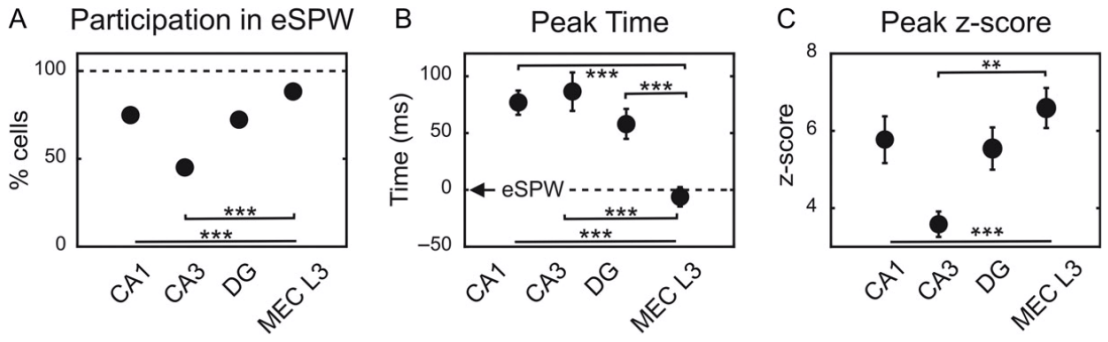

Figure 28. Single unit firing properties with regards to eSPWs.

(A) Percentage of units with significant PETH peaks (z > 1.65). (B) Average time of peak firing of single units relative to eSPWs. (C) Average z-scores at peak firing. Error bars correspond to standard error of the mean. From Valeeva and Janackova et al., 2019.

The following network model of entorhinal–hippocampal eSPWs in neonatal rats has been proposed (Valeeva and Janackova et al., 2019). In this model, the EC drives the hippocampus and the early entorhinal–hippocampal communication is embedded into a large-scale bottom-up circuit processing somatosensory feedback resulting from neonatal movements. This network diagram describes a sequence of events which link myoclonic movements and eSPWs (See Figure 29). All starts in the spinal cord, where the network bursts in motoneurons ignite myoclonic movements (1), which in turn generate sensory feedback and activate secondary sensory neurons in the spinal cord (Petersson et al., 2003; Inacio et al., 2016) (2). Sensory feedback from movements triggers, in a topographic manner, activity bursts - early gamma oscillations and spindle-bursts - in the primary somatosensory cortex (S1) (3) (Yang et al., 2009; Mohns and Blumberg, 2010; McVea et al., 2012; Akhmetshina et al., 2016; Dooley et al., 2020). Information from S1 is further conveyed, presumably via perirhinal cortex, to the EC where it initiates an activity burst (4) (Mohns and Blumberg, 2008; Valeeva and Janackova et al., 2019). Bursts in superficial EC layers further send information to hippocampus via two pathways: (i) the TA input from EC L3 to the distal apical dendrites of CA1 pyramidal cells (5), which activation generates a sl-m sink and (ii) PP input from EC L2 to the dentate gyrus (DG) (6) and CA3 (7). Presumably, CA3 activation is amplified by a recurrent excitatory CA3-CA3 synapses, and further conveyed through Schaffer collaterals to CA1, where is generates a SR sink (8).

This bottom-up model is consistent with the hypothesis that EC, and more precisely, stellate cells, provide an activity-dependent instructive signal that drives maturation sequentially and unidirectionally through the intrinsic circuits of the entorhinal–hippocampal network during the postnatal period (Donato et al., 2017). It seems that this model of the early hippocampal function, embedded into the large-scale network processing the sensory feedback from movements, is also in agreement with the bottom-up operation of many other brain networks including, besides the above mentioned S1 activity bursts driven by movements (Khazipov et al., 2004; Yang et al., 2009; Mohns and Blumberg, 2010; Akhmetshina et al., 2016), retinal wave driven activities in visual thalamus-cortex (Hanganu et al., 2006; Colonnese and Khazipov, 2010; Ackman et al., 2012; Zhang et al., 2012), cochlear burst-driven activity in auditory system (Tritsch et al., 2007; Wang et al., 2015; Babola et al., 2018).

The hypothesis above assuming that somatosensory feedback binds myoclonic movements with eSPWs implies that direct somatosensory stimulation should be also capable of evoking eSPWs, by analogy to spindle-bursts and early gamma oscillations that can be evoked by sensory stimulation in somatosensory cortex in the absence of movements (Khazipov et al., 2004; Yang et al., 2009; Mohns and Blumberg, 2010; Minlebaev et al., 2011; Akhmetshina et al., 2016). This hypothesis is in keeping with the fact that eSPWs become less frequent and dissociate from myoclonic movements but persist in the “cerveau isole” after severing external inputs through a supracollicular transection (Karlsson et al., 2006), indicating that they are internally-generated events and that sensory input plays only a triggering role.

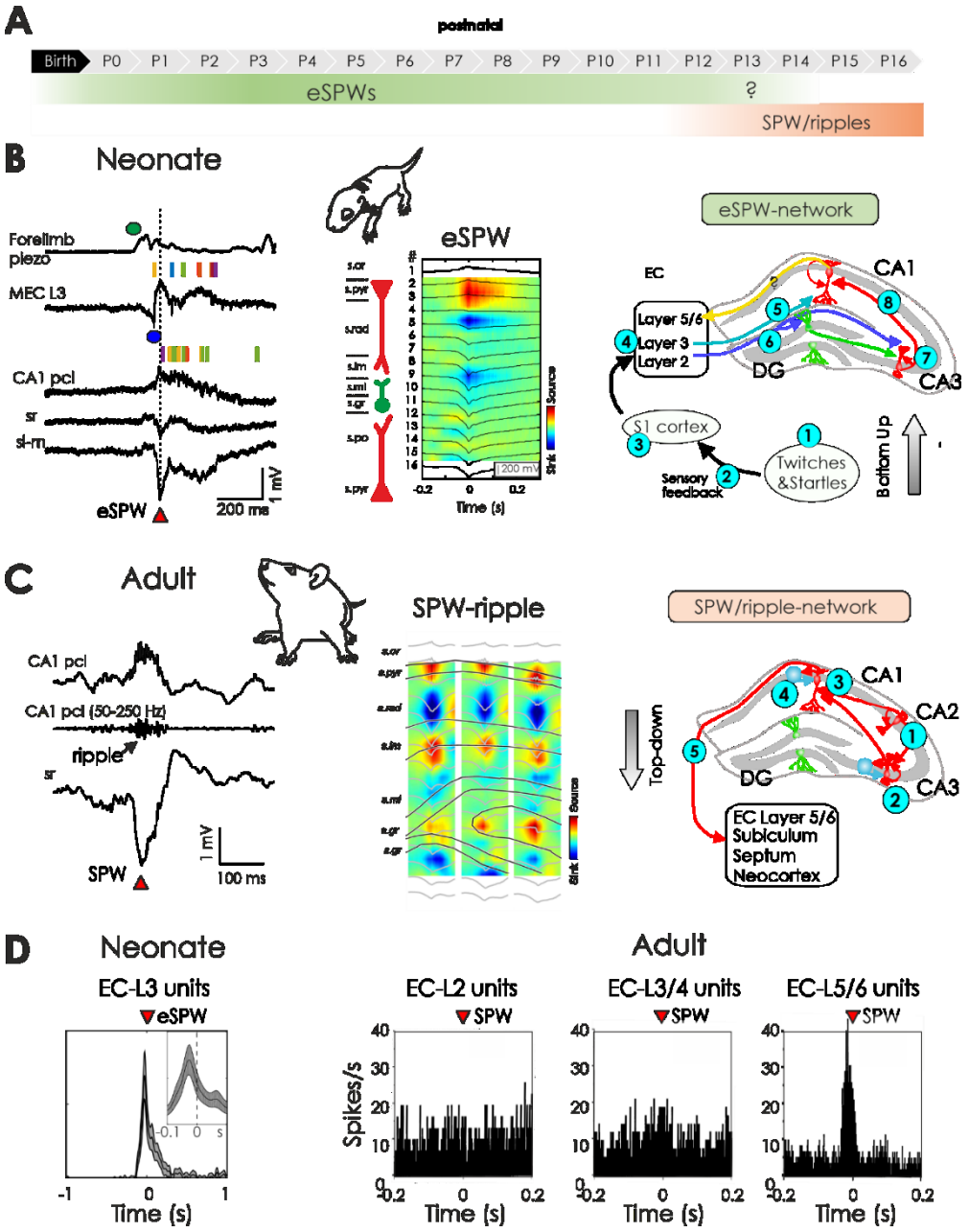

Figure 29. Comparison of eSPWs with adult SPWs.

A: timeline of eSPWs and SPW/ripples. B, left: example traces of the forelimb twitch (green circle), population burst in MEC-L3 (blue circle) and eSPWs (red triangle) recorded from the CA1 pyramidal cell layer (PCL), stratum radiatum (SR), and stratum lacunosum-moleculare (SLM) in a P5 rat pup. Vertical color bars above traces indicate single unit activity. P, postnatal; E embryonic. B, middle: corresponding current-source density of eSPWs with the most prominent sinks in SR and around the hippocampal fissure; s.pyr., stratum pyramidale; s.gr, stratum granule; st.or, stratum oriens. B, right: eSPW network model. Note that sequential activation of various structures in this scheme follows the bottom-up information transfer from the spinal cord to hippocampus. C, left: example traces of adult SPW/ripple in CA1 PCL and SR. C, middle: current-source density of SPWs with the most prominent sink in CA1 SR. C, right: SPW network model. Note that SPWs are internally generated in the hippocampus and support top-down information transfer from the hippocampus to the extrahippocampal targets. D, left:eSPWs are preceded by activation of MEC-L3 units in neonatal rat pups, whereas adult SPWs are associated with activation of neurons only in the hippocampal output deep entorhinal cortex (EC) layers. s.po, stratum polymorphum; s.ml, stratum moleculare. From Cossart and Khazipov, 2022.

In adults, somatosensory, auditory and visual stimuli evoke LFP responses in hippocampus and modulate hippocampal neurons firing (Deadwyler et al., 1981; Brankack and Buzsaki, 1986; Vinogradova, 2001; Pereira et al., 2007; Bellistri et al., 2013; O'Keefe and Krupic, 2021, see Figure 30). Current source density (CSD) profile of somatosensory evoked local field potential (LFP) responses revealed activation of temporoammonic and perforant pathways with characteristic sinks in the CA1 stratum lacunosum-moleculare and molecular layer of dentate gyrus, respectively (Brankack and Buzsaki, 1986; Bellistri et al., 2013).

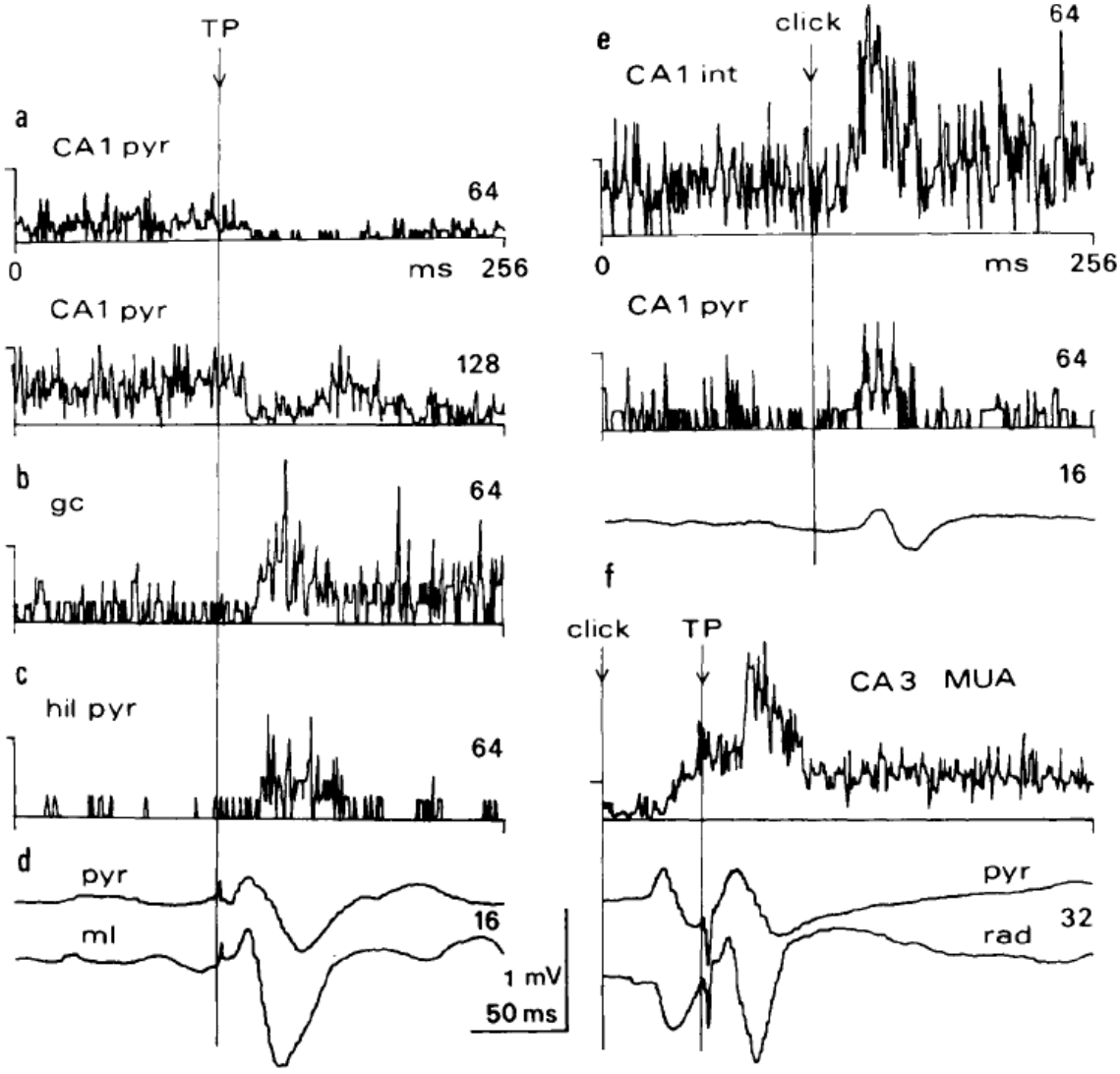

Figure 30. Unitary discharges and evoked potentials in response to tooth pulp (TP) and acoustic (click) stimulations.

a: two pyramidal cells (pyr) illustrating pure inhibition and inhibition-excitation sequence, respectively. The granule cell (gc) and the hilar pyramidal cell (hil pyr) were recorded in different experiments. Evoked field responses (d) were obtained in the same track as in a. e: peristimulus histograms of a CA1 interneuron (int) and an adjacent pyramidal cell and evoked potential in response to click stimuli, f: additive effect of acoustic and tooth pulp stimulation on multiple unit activity (MUA) in CA3a. Figures above the averages indicate the number of samples. Calibration: 5 units per bin. From Brankack and Buzsaki, 1986.

These responses were also associated with activation of granular cells in DG and variable, but predominantly inhibitory effects on CA1 pyramidal neurons (Bellistri et al., 2013, see Figure 31 and Figure 32). Somatosensory-evoked responses in the hippocampus of neonatal rats remain largely unexplored, however. This question is tightly related to a hypothesis above that, according to a scheme of eSPWs genesis, somatosensory stimulation should be capable of evoking eSPWs in the absence of movements. To this aim, we examined the responses evoked by somatosensory stimulation in the hippocampus of neonatal rat pups in the Article 1.

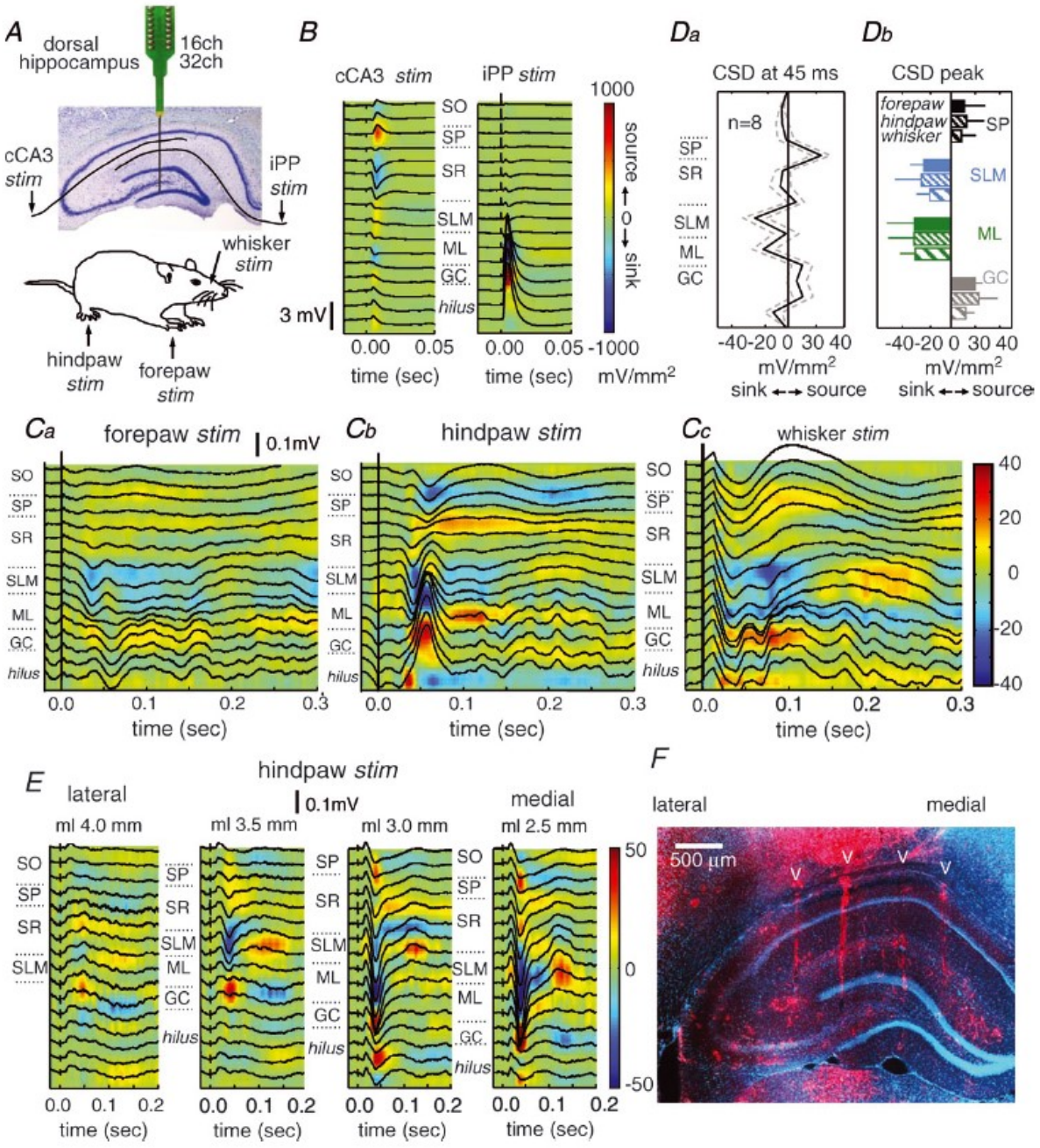

Figure 31. Hippocampal responses to somatosensory stimulation in the urethane-anaesthetized rat

A, multi-site (16 or 32 channel) silicon probes were used to record from the dorsal hippocampus of anaesthetized rats submitted to stimulation of either the contralateral forepaw, hindpaw or the whisker pad. Stimulation of the contralateral CA3 region (cCA3) and the ipsilateral perforant pathway (iPP) were used for

localization purposes. B, local field potentials and current source density (CSD) maps (underlying colour maps) of the hippocampal responses to cCA3 and iPP facilitated the localization of hippocampal strata. Mean responses from 10 stimuli in one representative rat. Current sources are represented in red while current sinks are blue. SO, stratum oriens, SP, stratum pyramidale, SR, stratum radiatum, SLM, stratum lacunosum molecular, ML, molecular layer, GC, granule cell layer. C, mean local field potentials and CSD maps of the hippocampal responses recorded in one rat to stimulation of the forepaw (Ca), hindpaw (Cb) and the whisker pad (Cc). Means obtained by averaging responses to 100 individual stimuli. Da, average CSD depth profile at 45 ms. Data from n = 8 stimulation sessions with similar spatial sampling. Db, mean CSD responses recorded at different hippocampal strata after somatosensory stimulation of the forepaw (FP, dark), hindpaw (HP, thin dashed) and the whisker pad (WH, thick dashed). Means obtained from different stimulation sessions: n = 14 SP (black; 3 FP, 7 HP, 4 WH), n = 15 SLM (blue; 3 FP, 8 HP, 4 WH), n = 28 ML (green; 10 FP, 11 HP, 7 WH) and n = 28 GC (grey; same numbers as ML). E, mediolateral recordings obtained by parallel insertion of two 16-channel silicon shanks separated by 500 µm. F, the fluorescent dye DiI (red) was applied to the probe at the end of experiments for localization purposes. Cell nuclei were stained with bisbenzimide (blue). From Bellistri et al., 2013.

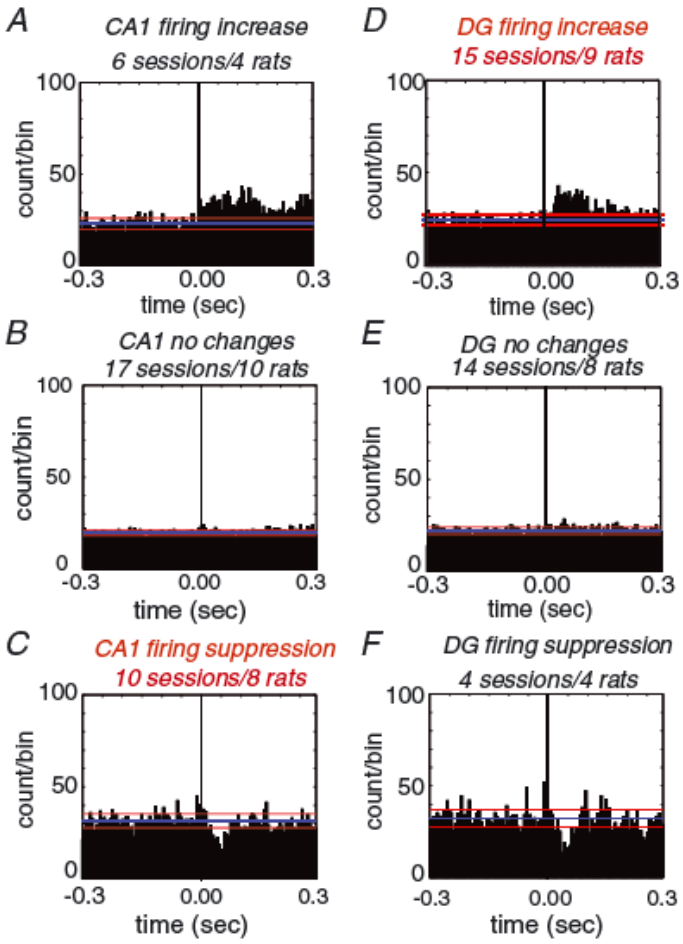

Figure 32. Hippocampal MUA responses to somatosensory stimulation

All histograms represent cumulative data. A, MUA recordings obtained from the stratum pyramidale of the CA1 region in 6 stimulation sessions from 4 rats exhibited significant firing increase after somatosensory stimulation. The blue and red lines mark the mean and standard deviation of the baseline firing rate, respectively. B, no statistically significant changes were found in 17 sessions from 10 rats. C, firing suppression was observed in 10 stimulation sessions (8 rats). D, in the granular layer of the dentate gyrus (DG), significant increases of MUA were observed in 15 stimulation sessions from 9 rats. E, no significant changes were seen in 14 sessions (8 rats). F, firing suppression in the DG was evident in only 4 stimulation sessions from 4 rats. From Bellistri et al., 2013.

The parsimonious scheme linking the movements and hippocampal eSPWs is primarily based on feedforward excitatory connections whereas internally generated networks, notably inhibitory ones, appear to play limited roles at the early developmental stages. It has been further suggested that development of perisomatic inhibition underlies disengagement of hippocampal network from the external influence from movements switching from global excitation in neonates to global inhibition in adults at around P9-10 (Dard et al., 2022), as well as transformation of eSPWs to adult SPWs with ripples at around the same age (Pochinok et al., 2024). See also below, Chapter on Development of Feedforward Inhibition, and Articles 3 and 4, describing development of EC-input associated inhibition in DG and CA1, and Article 5, describing development of topography of synapses established by future PV interneurons in CA1).

2.6. Feedforward inhibition

Feedforward inhibition (FFI) is a neural mechanism that helps regulate information flow and maintain balance within neural circuits in the brain. It occurs when an excitatory input to a principal cell also activates an inhibitory interneuron, which then sends inhibitory signals to the same principal cell (Figure 33). This process ensures that the principal cell's activity is modulated, preventing later signals from slipping through the narrow window of opportunity. FFI mechanism can be found in various brain regions like the hippocampus, thalamus, cortex, and cerebellum. FFI maintain temporal precision, prevent runaway excitation, and ensure proper synaptic integration (Pouille and Scanziani, 2001; Daw et al., 2006).

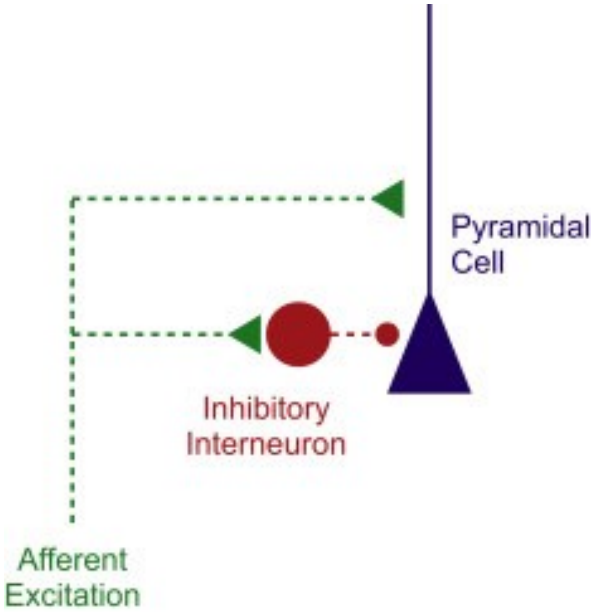

Figure 33. Feedforward inhibition (FFI).
The diagram illustrates FFI, where an excitatory signal activates both a pyramidal neuron (Pyr) and an inhibitory interneuron. The inhibitory interneuron then suppresses the activity of the pyramidal neuron. From Fröhlich, 2016.

2.6.1. Feedforward inhibition in adult brain

2.6.1.1. Feed-forward inhibition is responsible for coincidence detection

The simultaneous activation of two independent synaptic pathways converging onto a principal hippocampal neuron could induce an action potential if the stimuli arrive within a narrow temporal window of less than two milliseconds (Pouille and Scanziani, 2001). This was systematically tested by varying the interstimulus interval (ISI) between the two inputs and recording the neuron's firing probability (See Figure 34). The findings revealed a sharp decline in the probability of spike generation as the ISI increased.

It was further observed that the application of GABAA receptor antagonists, such as bicuculline or SR95531, significantly broadened the temporal integration window. Under normal conditions, the temporal window for spike generation was narrow (~1.4 ms), but this window expanded to ~16.7 ms when GABA(A) receptors were blocked. This pharmacological manipulation also led to a decrease in the precision of spike timing, with neurons firing at a greater delay following the stimulus (~8.2 ms in control conditions, ~16.8 ms in the presence of GABAAR antagonist). and with increased variability (jitter) in spike timing (~0.5 ms in control conditions, ~1.4 ms with GABAAR antagonists). These results suggest that GABAergic feed-forward inhibition plays a critical role in enforcing the temporal fidelity of synaptic integration, ensuring that neurons fire spikes with precise timing relative to the synaptic input (Pouille and Scanziani, 2001).

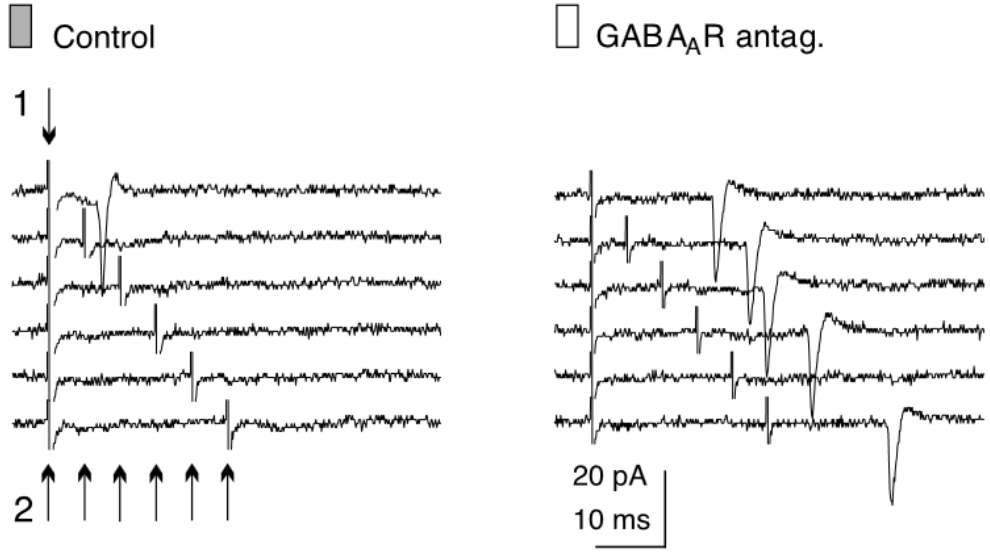

Figure 34. Coincidence detection in PCs is abolished by GABA$_A$R antagonists.
Current traces showing cell-attached recordings from CA1 PCs upon stimulation of two Shaffer collateral pathways. Each sweep shows a different interstimulus interval (ISI) between pathways. In control conditions, a spike is triggered only upon simultaneous stimulation of pathways 1 and 2. In bicuculline, spikes are also triggered with larger ISIs. From Pouille and Scanziani, 2001.

2.6.1.2. Involvement of perisomatic projecting PV interneurons in feedforward inhibition

Different classes of GABAergic interneurons selectively innervate different subcellular compartments of PCs (Freund and Buzsaki, 1996). Parvalbumin-positive basket cells (PV BC) target the soma (perisomatic projecting) and proximal dendrites of pyramidal neurons, modulating their activity.

The study by Pouille and Scanziani, 2001 demonstrated the involvement of PV interneurons in feed-forward inhibition. Signals were recorded from both the soma and dendrites of pyramidal cells (Figure 35) during responses to Schaffer collateral stimulation. Inhibition was observed to be stronger in the soma than in the dendrites, resulting in a much narrower temporal integration window in the soma compared to the dendrites, where inhibition was less pronounced (Pouille and Scanziani, 2001).

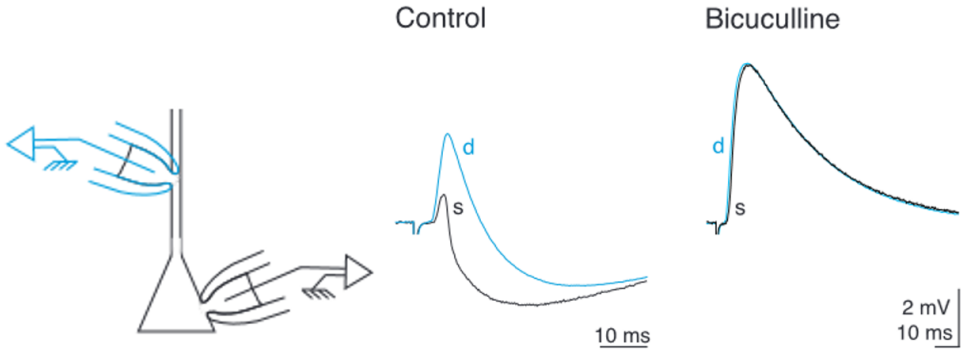

Figure 35. Feed-forward inhibitory inputs selectively impinge on the soma of PCs.
Voltage traces showing somatic (s, black) and dendritic (d, blue) responses to Schaffer collateral stimulation, in control conditions and in bicuculline From Pouille and Scanziani, 2001.

2.6.2. Feedforward inhibition in developing brain

2.6.2.1. Somatosensory cortex

In neonatal rats, the developmental trajectories of FFI and the synchronization of early gamma oscillations (EGOs) within the thalamocortical system exhibit parallel progressions during the first postnatal week (Minlebaev et al., 2011, see Figure 36). EGOs are rhythmic brain activity patterns (around 30-100 Hz) in newborn rats that occur in response to sensory inputs, such as whisker deflections, and are observed as oscillatory responses in LFP of the corresponding sensory cortex area. Initially, during the early postnatal days (P2 to P3), EGOs are predominantly driven by gamma-rhythmic excitatory postsynaptic currents (EPSCs) in the granular (Gr, LIV)) layer of the barrel cortex, with inhibitory postsynaptic currents (IPSCs) being sparse and appearing late in the oscillation cycle.

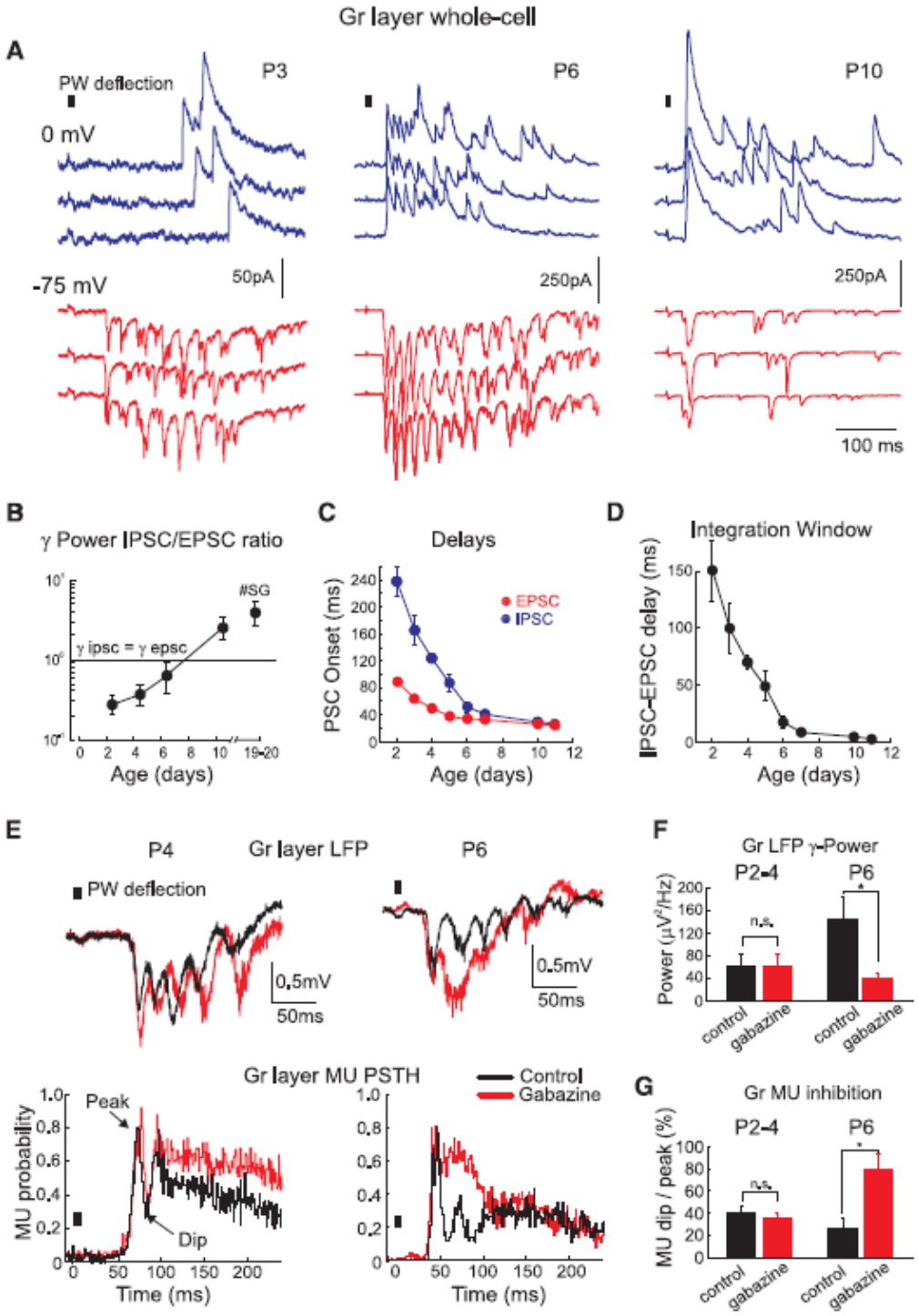

Figure 36. Synaptic mechanisms of early gamma oscillations.

(A) Whole-cell responses evoked by PW stimulation in Gr neurons at different ages recorded in voltage clamp to separate IPSCs (blue top traces at 0 mV) and EPSCs (red bottom traces at –75 mV). (B) Age dependence of the IPSC/EPSC gamma power ratio in Gr cells (P2 to P11) (n = 33 cells) and SG cells (P19 to P20) (n=5 cells). (C) Age dependence of EPSCs and IPSCs onset delay in Gr cells from PW stimulus onset. (D) Age dependence of the integration window, defined as the difference between EPSCs and IPSCs onset delay. (E) (Top) PW-evoked Gr LFP responses in P4 and P6 rats before (black traces) and after (red traces) epipial application of the g-aminobutyric acid type A receptor blocker gabazine (50 mM). (Bottom) Corresponding Gr MUA PSTHs. (F and G) Summary plots of the effects of gabazine on (F) PW-evoked Gr LFP gamma power at P2 to P4 (n= 5) and P6 (n = 4), and (G) MUA dip-to-peak ratio [as shown in (E)] From Minlebaev et al., 2011.

However, as development progresses, particularly by the end of the first postnatal week (P5 to P7), local inhibitory circuits, including those involved in FFI, become increasingly recruited into the generation of EGOs. This transition is characterized by a notable increase in the rhythmicity of IPSCs during EGOs, as evidenced by a delayed onset of IPSCs relative to EPSCs, with the temporal delay decreasing significantly—from over 100 milliseconds at P2-P3 to ~6 milliseconds by P7-P11. The necessity of cortical inhibition for sustaining EGOs becomes apparent by P6, as evidenced by experiments showing that pharmacological blockade of cortical inhibition with gabazine has minimal impact on EGOs at P2 to P4 but significantly reduces their occurrence at P6. The gradual maturation of inhibitory circuits, including FFI, is therefore crucial for the proper development of these early neural networks, allowing for the precise temporal binding required for sensory processing in the mature brain.

Similar findings were also made in developing barrel cortex in thalamocortical slices in vitro, which also supported the idea that the maturation of feedforward inhibition in layer IV barrel cortex occurs between P3–5 and P7–9 (Daw et al., 2007, See Figure 37 and Figure 38).

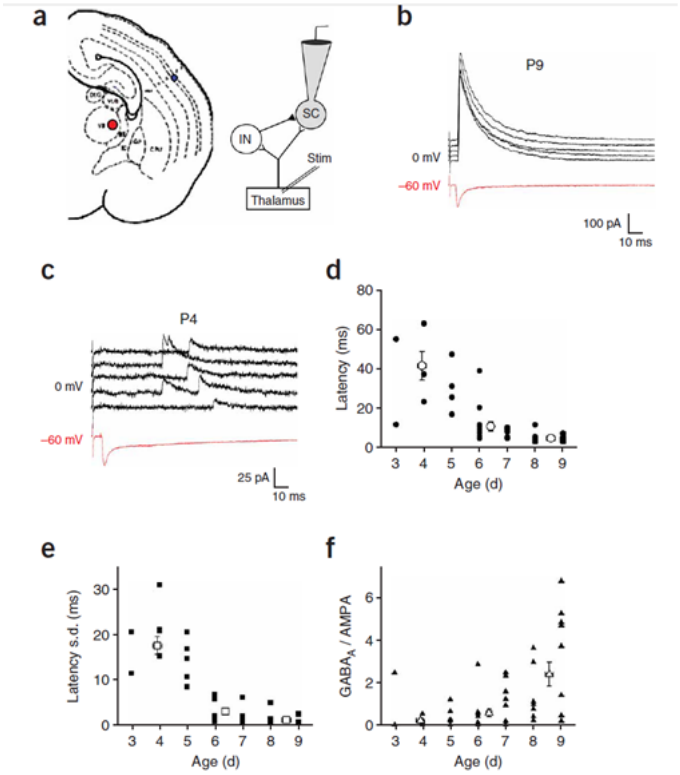

Figure 37. Developmental increase in GABAA receptor-mediated transmission in response to thalamocortical input.

a: Experimental setup showing whole-cell recordings from stellate cells with thalamic stimulation. b: Thalamocortical-evoked inhibitory postsynaptic currents (IPSCs) recorded at P9, showing responses at 0 mV and -60 mV holding potentials. c: Similar IPSC recordings at P4, demonstrating weaker and less reliable responses compared to P9. d, e: Latency and variability of GABAA receptor-mediated postsynaptic currents over age, indicating a decrease in latency with maturation. f: Ratio of GABAA to AMPA receptor-mediated responses, showing increased GABAA involvement with age. From Daw et al., 2007.

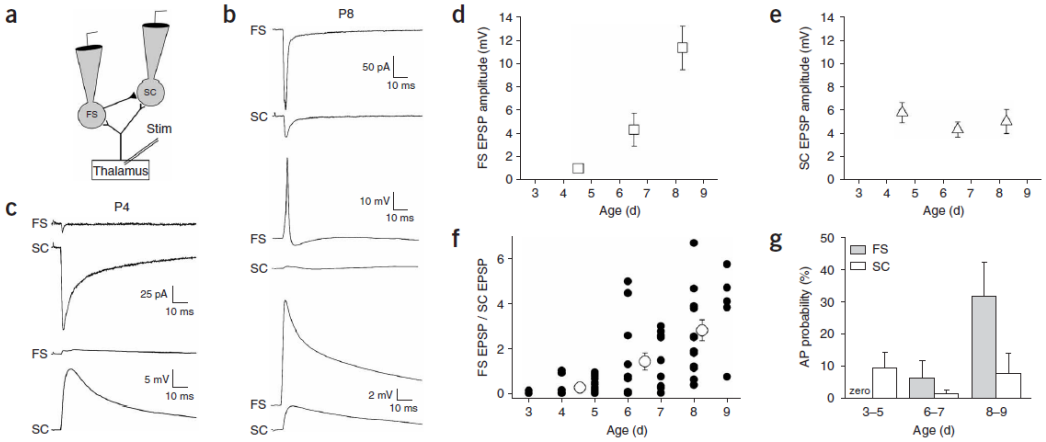

Figure 38. Age-related increase in thalamic input to fast-spiking (FS) interneurons compared to stellate cells (SC).

a: Experimental setup showing simultaneous whole-cell recordings from a fast-spiking interneuron and a stellate cell with thalamic stimulation. b: Thalamocortical excitatory postsynaptic currents (EPSCs) and corresponding voltage changes (EPSP or action potential) recorded in FS interneuron and SC pair at P8. Traces are shown at resting potential and at a hyperpolarized potential (-70 mV). c: Similar recordings as in (b) but at P4, showing weaker responses compared to P8. d, e: Amplitude of thalamocortical EPSPs in FS interneurons (d) and SCs (e) across different ages at -70 mV holding potential, indicating developmental changes in EPSP strength. f: Ratio of thalamocortical EPSP amplitude between FS interneurons and SCs across age groups, showing increased relative input to FS interneurons with age. g: Probability of action potential firing in response to thalamic stimulation at resting membrane potential in FS interneurons (gray) and SCs (open), illustrating higher excitability in FS interneurons as development progresses. From Daw et al., 2007.

During this period, the development of fast-spiking interneurons (FS INs) plays a role in establishing inhibitory circuits. Young basket cells (BCs) and FS INs initially integrate asynchronous inputs, generating low-frequency trains of action potentials that elicit weak and slow IPSCs in their target neurons. This results in a slow form of inhibition. By P7–9, a large, reliable IPSC is evoked by thalamic stimulation shortly after EPSC, indicating the maturation of fast inhibitory synaptic output (Daw et al., 2007). During this time, mature BCs begin to detect coincident excitatory inputs, generating high-frequency trains of action potentials and producing a fast inhibitory synaptic output. This provides phasic inhibition with high temporal precision to their targets, significantly contributing to the speed and temporal precision of both feedforward and feedback inhibition. Fast-spiking interneurons become important mediators of feedforward inhibition in the layer IV barrel cortex by the end of the first postnatal week. An individual FS interneuron can powerfully inhibit an individual stellate cell (Daw et al., 2007). There is also a developmental increase in the probability of evoking an action potential in FS INs by thalamocortical input, which remains low at P3–5 and P6–7 but increases significantly at P8–9 (Daw et al., 2007). In neonates (P3–5), the amplitude of unitary IPSCs is small, typically less than 5 pA. However, the size of the unitary IPSCs increases significantly around P7, and by P8–9, their amplitude is approximately five times larger than that at P3–5 (Daw et al., 2007). Of important note, connectivity probability between BC to stellate cells displayed increase from 7% at P3-5 to 30% at P8-9 (see Figure 39).

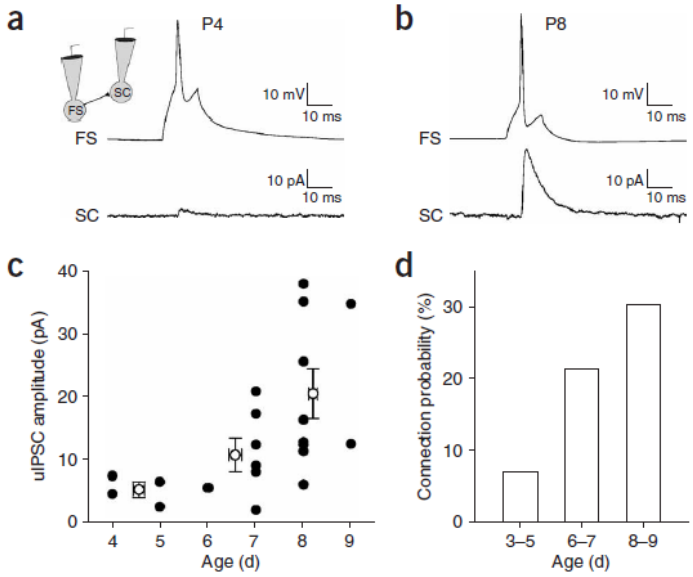

Figure 39. Development of connection probability and strength between fast-spiking (FS) interneurons and stellate cells (SC) across early postnatal days.

a: Action potential induced in a fast-spiking interneuron (top) and corresponding inhibitory postsynaptic potential (IPSP) recorded in a synaptically connected stellate cell at P4. Inset illustrates the experimental setup. b: Example of unitary FS interneuron-to-stellate cell connection at P8, showing stronger IPSP compared to P4. c: Amplitude of unitary inhibitory postsynaptic currents (uIPSCs) between FS interneurons and stellate cells over age (P3-P9). Filled symbols represent individual recordings; open symbols indicate mean values for age groups. d: Connection probability between FS interneurons and stellate cells increases with age, showing a trend toward stronger synaptic connectivity by the end of the first postnatal week. From Daw et al., 2007.

2.6.2.2. Hippocampus

Initial studies in hippocampal slices from neonatal rodents and primates emphasized early development of GABAergic synapses, prior to formation of glutamatergic synapses (Tyzio et al., 1999; Khazipov et al., 2001). Together with depolarizing and excitatory actions of GABA, which GABA exerts in neonatal slices in vitro, and the roles of depolarizing GABA in the generation of the hippocampal network discharges during neonatal period, so-called Giant Depolarizing Potentials (GDPs) (Ben-Ari et al., 1989), this has led to the hypothesis that GABA is the primary excitatory neurotransmitter driving primitive forms of the network activity in the neonatal hippocampus (Ben-Ari et al., 2007). However, more recent work suggested that GABA exerts mainly inhibitory actions in the neonatal cortical and hippocampal networks in vivo (Kirmse et al., 2015; Valeeva et al., 2016; Graf et al., 2021, but see also Murata and Colonnese, 2020). Regardless of the polarity of GABA actions, several lines of evidence indicate that GABAergic control over hippocampal activity in the neonates is limited, notably due to the delayed development of perisomatic FFI.

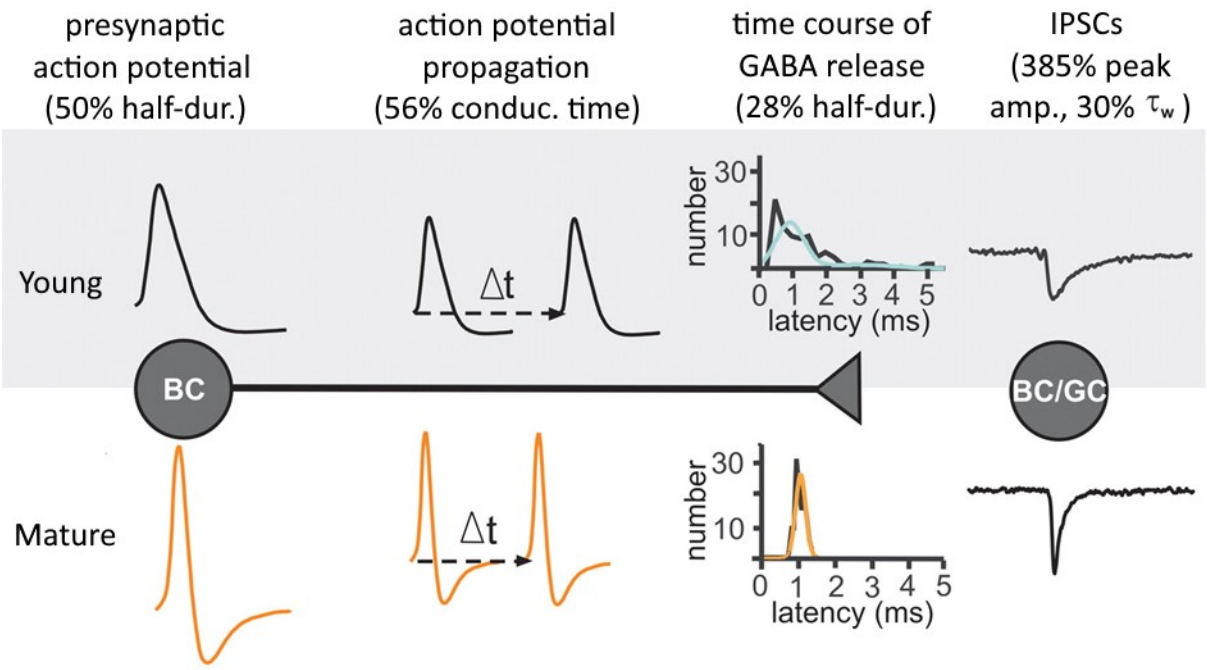

Figure 40. Developmental changes in BC signaling.

Schematic illustration of the sequence of events involved in the generation of inhibitory signals at BC output synapses in the young and the mature dentate gyrus of GAD67–GFP mice. From left to right: a somatic action potential, axonal action potential propagation, time course of quantal transmitter release, and unitary IPSCs in young (top) and mature (bottom) networks are shown. The percent change of the given property of BC signaling at young (P6 –P10) and mature (P18 –P25) developmental stages is shown in brackets. Note that the combination of changes in these parameters underlies the emergence of fast signaling properties in BCs during development. See Results and Discussion for details. half-dur., Half-duration; conduc.time, conduction time; peak amp., peak amplitude. From Doischer et al., 2008.

In a pivotal study, Doischer and colleagues (Doischer et al., 2008) have demonstrated that in the mice DG, basket cells undergo marked changes in their morphological, intrinsic, and synaptic properties during a postnatal period between P6 to P25 (Figure 40 and Figure 41). In parallel with a growth of dendritic and axonal arbor, BCs displayed a developmental increase in the speed of their membrane time constant, action potential waveform, and axonal conduction velocity, as well as an increase in the connectivity between BCs and DG granular cells and between BCs, precision, strength, and reliability of transmitter release at BC output synapses. Also, kinetics of unitary IPSCs become rapid. The authors concluded that these concerted developmental changes convert BCs from slow to fast signaling devices during the late postnatal period. These findings also raise a hypothesis that FFI, which is supported by BCs, is delayed in development. Exploration of this question in relation to the inhibition associated with the EC input to CA1 and DG is presented in this manuscript in the Articles-3 and 4, respectively.

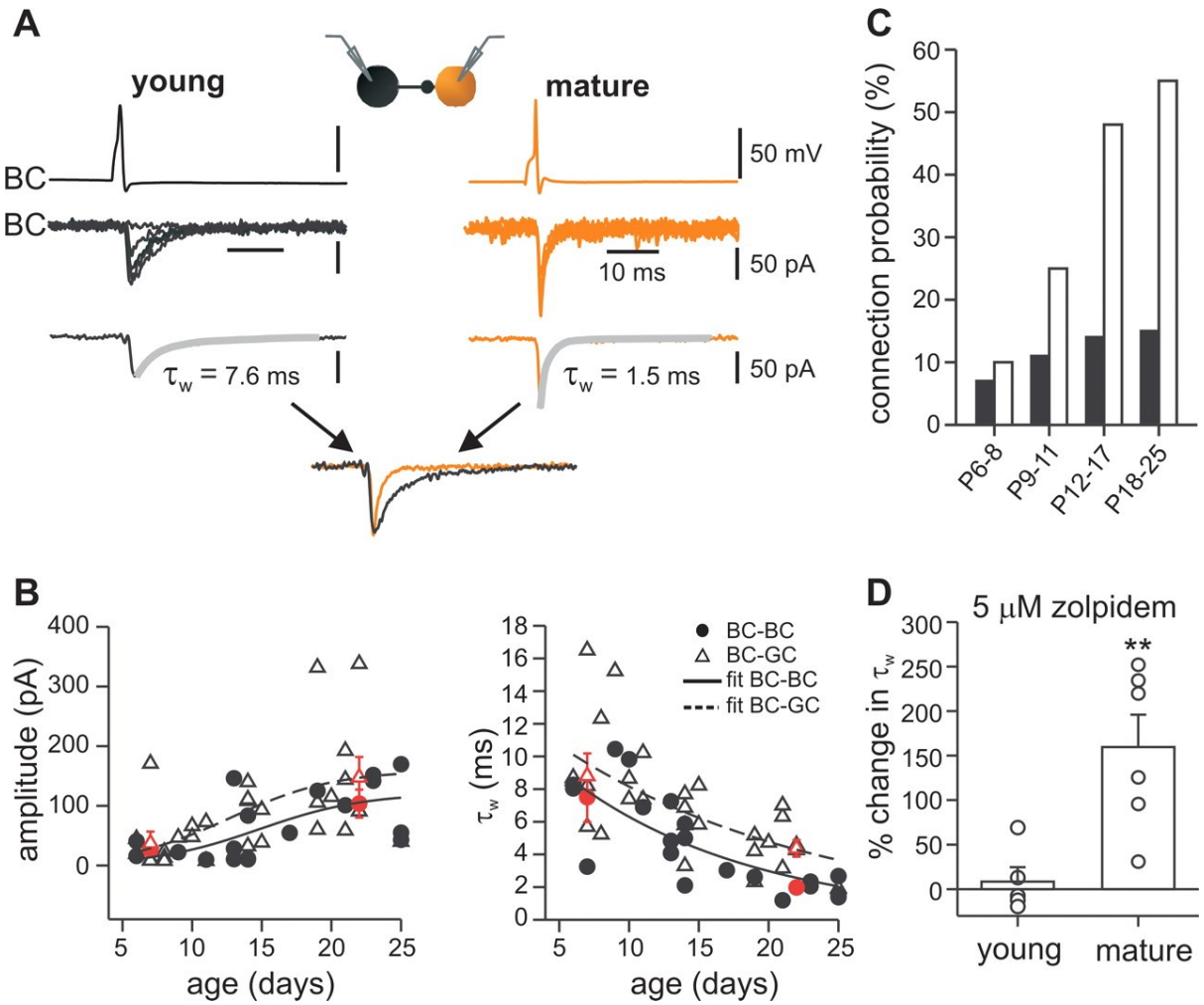

Figure 41. Developmental changes in IPSCs at BC synapses in the dentate gyrus.

A: Example recordings of IPSCs in BC-BC pairs from young (P6, left, black) and mature (P21, right, orange) cells. Top traces show presynaptic action potentials, middle shows superimposed IPSC traces (6 traces), and bottom shows averaged IPSCs (30 traces) with decay phases fit to a double-exponential function. Normalized and superimposed traces illustrate faster decay in mature BCs (τw = 1.5 ms) compared to young BCs (τw = 7.6 ms). B: Summary plots showing developmental trends in peak amplitude (left) and amplitude-weighted decay time constants (τw, right) for BC-BC (filled circles) and BC-GC (open triangles) pairs across postnatal ages. Data fits (sigmoidal for amplitude, exponential for τw) indicate increases in strength and speed of IPSCs with age. C: Connection probability between BCs (filled bars) and between BCs and granule cells (GCs, open bars) across age groups (P6–P25). Connection likelihood increases with age, peaking between P18–P25. D: Effect of 5 μM zolpidem, a benzodiazepine type I receptor agonist, on the decay time constant (τw) of IPSCs evoked by extracellular axon stimulation. Zolpidem increases τw in mature BCs ($P > 0.01$), but has no significant effect in young BCs, highlighting age-dependent modulation. From Doischer et al., 2008.

Along with these observations, studies by Dard and colleagues (Dard et al., 2022) using dynamic biphoton calcium imaging in CA1 mouse hippocampus in vivo revealed robust activation of CA1 pyramidal cells following neonatal movements during the first postnatal week, and developmental switch in this excitatory response to inhibition at around P9-10 (See Figure 42). While interneurons were activated following movements both before and after the switch, the authors did not observe activation of perisomatic rings of GABAeric axon terminals in CA1 pyramidal cell layer in the neonatal mice. Around

postnatal day 9 or 10, there was a rapid increase in the development of GABAergic connections targeting the somatic regions of pyramidal neurons. investigated the anatomical progression of somatic GABAergic innervation within the CA1 pyramidal layer from postnatal day 3 (P3) to day 11 (P11), with a particular focus on the contributions from putative parvalbumin-expressing basket cells (PVBCs), which are the primary source of this innervation. To achieve this, they utilized immunohistochemistry to detect Synaptotagmin2 (Syt2), a well-established marker for parvalbumin-positive inhibitory boutons in cortical areas (See figure Figure 43, Sommeijer and Levelt, 2012).

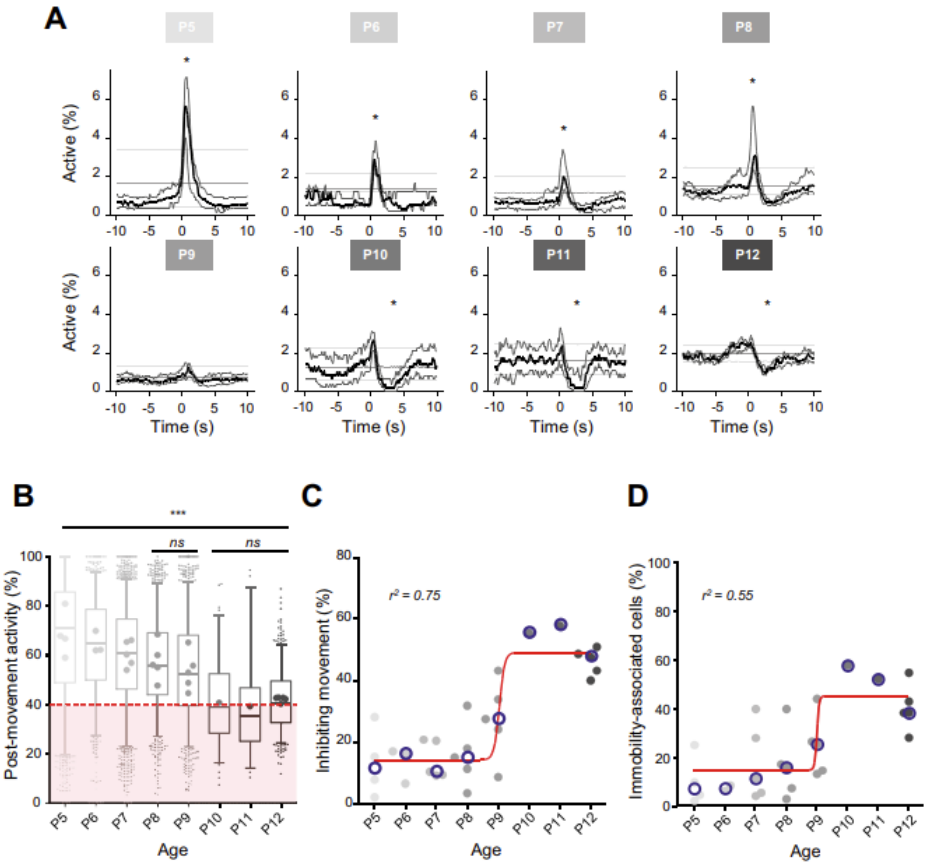

Figure 42. CA1 dynamics and movement during early postnatal development.

A: Peri-movement time histograms (PMTH) showing the percentage of active CA1 cells around movement onset across different ages. The dark line represents the median, with gray lines indicating the 25th and 75th percentiles. Thin gray lines represent the 5th, median, and 95th percentiles from surrogate data for comparison. Black asterisks highlight values that exceed the surrogate data range. B: Distribution of post-movement neural activity by age. Box plots display activity following movements for each age group, with whiskers representing the 5th and 95th percentiles. Large colored dots show average activity for each mouse, color-coded from light gray (P5) to black (P12). The red-shaded area highlights movements classified as "inhibiting". From Dard et al., 2022.

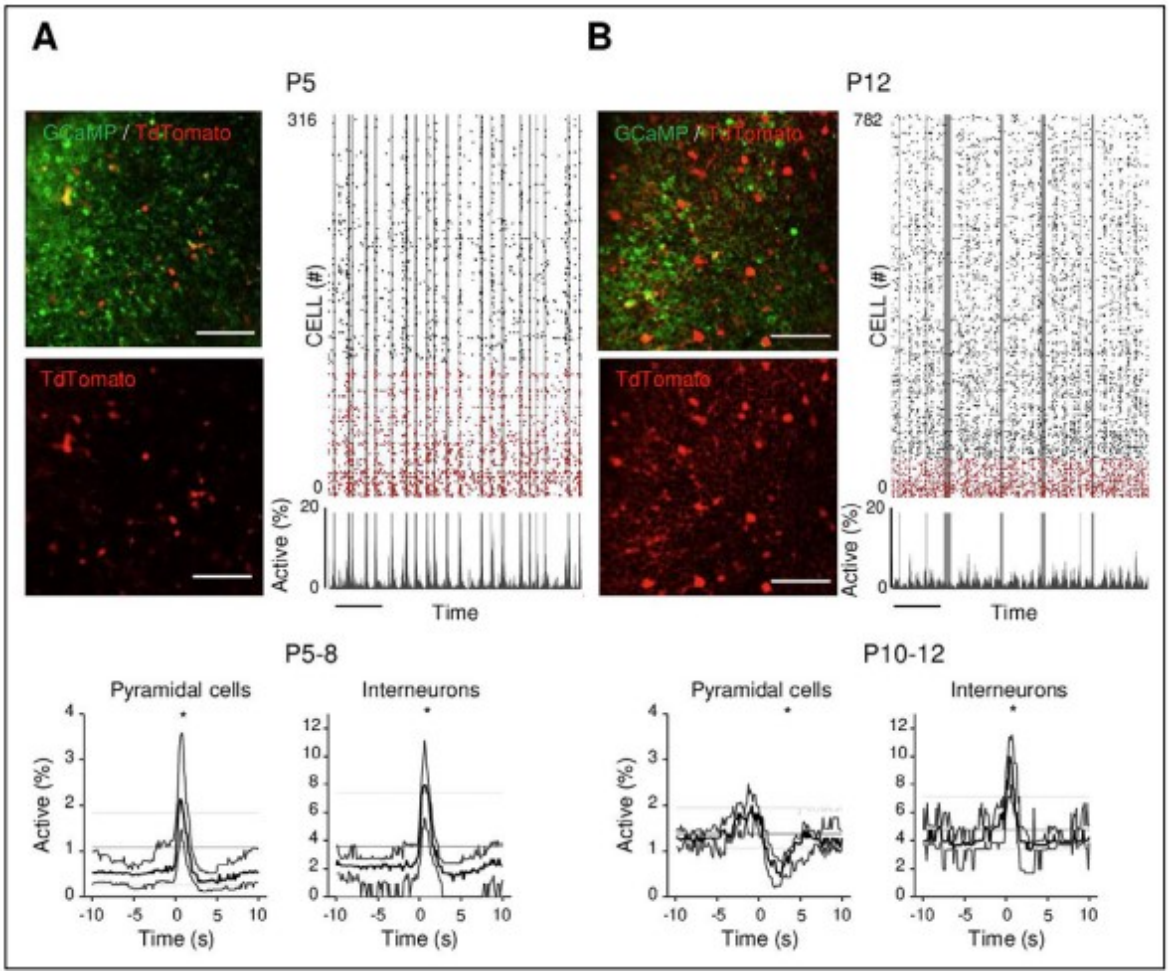

Figure 43. **Recruitment of CA1 glutamatergic and GABAergic neurons.**

A: Imaging and raster plot from P5 mouse showing CA1 pyramidal cells (black) and interneurons (red) in the stratum pyramidale, with neurons sorted by cell type. Gray lines indicate mouse movements. B: Similar data from a P12 mouse, illustrating increased recruitment with age. Bottom panels: Peri-movement time histograms (PMTH) for pyramidal cells and interneurons, grouped by age (P5–8 and P10–12), show distinct activity patterns, with increased and more synchronized activity in older mice, especially in pyramidal cells. From Dard et al., 2022.

Dard and colleagues measured the extent of Syt2 labeling in the pyramidal cell layer at various developmental stages (See Figure 44). They found that from P3 to P7, PV innervation remained relatively stable and low (median values: P3: 0.34%; P5: 0.57%; P7: 0.49%, based on data from three mice per group). However, a notable increase in the density of Syt2-positive labeling occurred after P9 (P9: 1.03%; P11: 1.48%, three mice per group). Through this study, Dard and colleagues demonstrated the growth of synapses from PV interneurons in the pyramidal layer. Of note, development of perisomatic inhibition at around P9-10 identified in this study nicely matches the onset of ripple oscillations, which are associated with SPWs in adult hippocampus (Leinekugel et al., 2002; Buhl and Buzsaki, 2005; Pochinok et al., 2024).

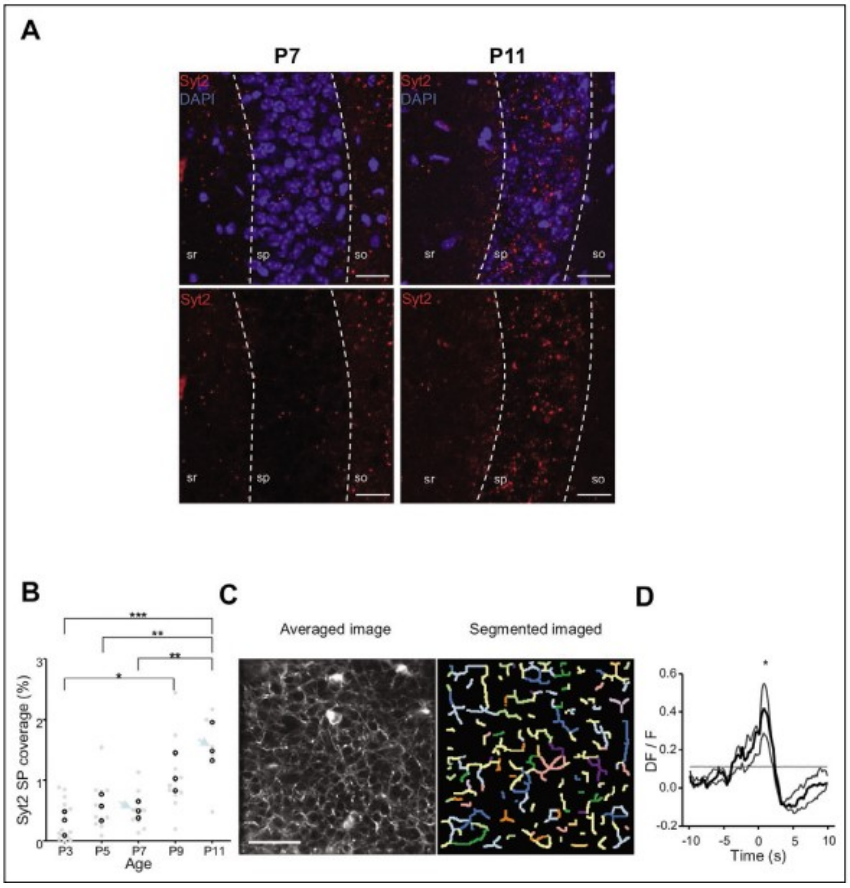

Figure 44. Development of perisomatic GABAergic innervation in CA1 region.

A: Confocal images of CA1 at P7 and P11, showing synaptotagmin-2 (Syt2) staining (red) in the stratum pyramidale (sp), with DAPI staining (blue) for cell nuclei. Increased Syt2 coverage is visible at P11. B: Quantification of Syt2 coverage in the pyramidal cell layer (sp) over postnatal days, showing an increase with age. C: Example of a segmented CA1 field in a P9 mouse, highlighting pyramidal cell structures after injection with a GCaMP6s calcium indicator. D: Peri-movement time histogram (PMTH) of calcium fluorescence change (ΔF/F) aligned to movement onset, showing increased perisomatic activity in response to movement. From Dard et al., 2022.

Because global activation of CA1 following movements in neonatal mice likely involves eSPWs, which are reliably triggered by movements in the neonates (Karlsson et al., 2006; Valeeva and Janackova et al., 2019), these findings suggest that GABAergic inhibition fails suppressing the CA1 population discharges associated with the eSPWs. Because EC input to CA1 plays important role in eSPWs genesis, these findings also indicate on a relative immaturity of the inhibition associated with the EC input to CA1 in the neonatal CA1. While the study by Dard et al., 2022 unraveled deficits of perisomatic inhibition as underlying mechanism, more detailed descriptions of the dynamics of GABAergic inputs relatively glutamatergic inputs during eSPWs and EC-evoked responses are required for better understanding of cellular and network functions in the neonatal hippocampus, In this aim, patch-clamp recordings from CA1 neurons with a voltage-separation of GABAergic and glutamatergic conductances were performed during eSPWs in vivo, and during EC-evoked responses in vitro, and the results are presented in Articles 2 and 4, respectively.

3. Methods

3.1. Electrophysiological approaches to study population patterns of activity

The behavior of neuron populations is studied using electrophysiological methods that record activity from large numbers of cells simultaneously, as well as methods that record individual action potentials. By combining these techniques with analyses of signals describing the movement of charges across the plasma membrane (current source and sink analysis) and correlation methods to determine dependencies between signals, researchers can understand how cell populations in different brain structures communicate. Recently, optical methods for recording hippocampal activity using intracellular calcium or voltage-sensitive dyes have been introduced, but these are not discussed here.

3.1.1. Local Field Potential

Local Field Potential (LFP) is an electrical signal resulting from the activity of a large number of neurons. It is recorded using extracellular electrodes placed near a population of neurons (See Figure 45). The unfiltered signal from such an electrode reflects the sum of action potentials from cells within approximately 50-350 μm from the tip of the electrode (Legatt et al., 1980; Gray and Maldonado et al., 1995) and slower ionic events from within 0.5–3 mm from the tip of the electrode (Juergens et al., 1999). LFP reflects integral currents across the membranes of nearby neurons, which are generated by postsynaptic currents, both excitatory and inhibitory, as well as intrinsic neuronal conductance associated with ion fluxes through membrane channels.

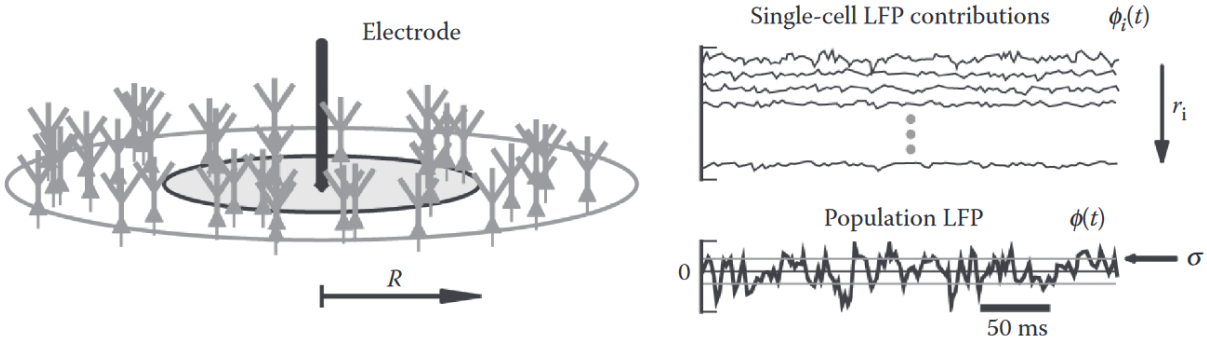

Figure 45. A model illustrating the generation of LFP from a population of identical neurons.
Cells are homogeneously distributed on a disc of radius R with, in this case, the tip of the electrode in the center. The sum of LFP contributions ϕi(t) of individual cells at distances ri from the population center results in a population LFP ϕ(t). From Einevoll et al., 2013.

Various tools are used to record LFPs (see Figure 46). The most common microelectrodes are thin metal wires made of tungsten, platinum, or steel that are embedded in brain tissue to record localized activity. Multi-electrode systems such as the Utah Array or Neuropixels, which include multiple electrodes and allow simultaneous recording of signals from different parts of the brain, are also used, which is particularly useful for studying network interactions (see Figure 47). Flexible polymer electrodes are increasingly being used due to their biocompatibility and ability to minimize tissue damage, making them suitable for long-term recordings.

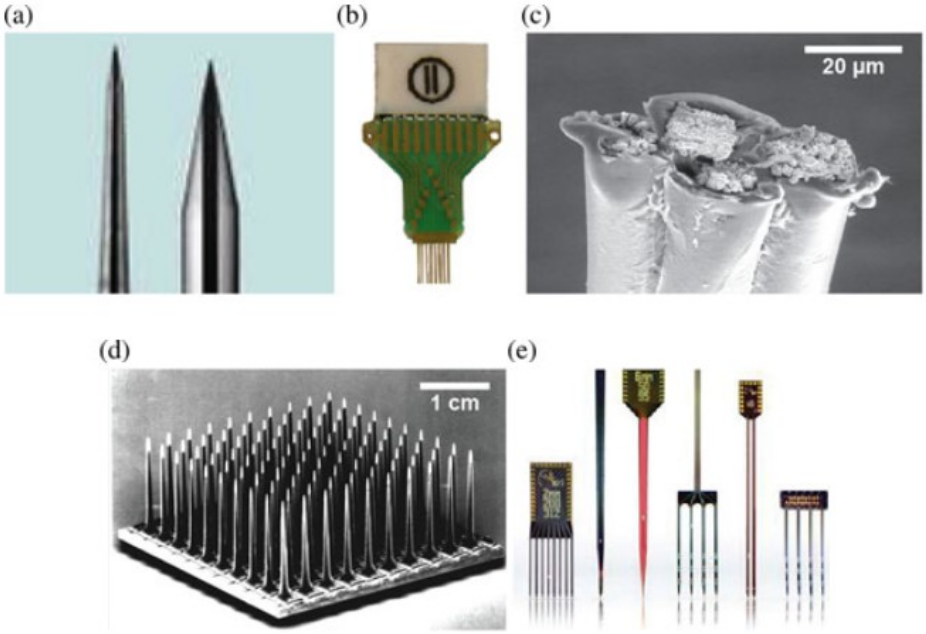

Figure 46. Examples of commonly used single unit and LFP recording devices.
(a) Silica-encapsulated tungsten electrodes (Thomas Recording GmbH). (b) Tungsten microwire array (Tucker-Davis Technologies Inc.). (c) Tetrode microwire bundle (Dr. T. Davidson, Stanford University). (d) Silicon ”Utah” multielectrode array (Blackrock Inc.). (e) Silicon multitrode probes (Neuronexus Inc.). From Pashaie et al., 2014.

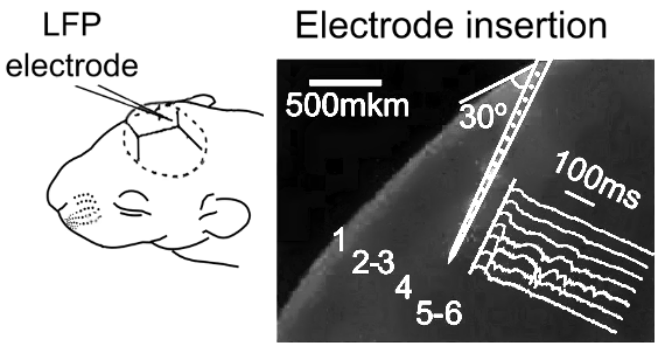

Figure 47. An example of a silicon probe inserted into the principal barrel of a P6 rat.
From Sintsov et al., 2017.

3.1.2. Current Source Density analysis

Inwardly directed currents, such as excitatory postsynaptic currents or currents through sodium and calcium channels, cause a transient depletion of positive charges in the extracellular space, reflected as a negative-going LFP signal, an active sink. Outwardly directed transmembrane currents, such as inhibitory postsynaptic currents and currents via voltage-gated potassium channels, cause a transient accumulation of positive charges or depletion of negative charges, generating a local positively-going LFP signal, an active source. The LFP signal also contains passive sinks and sources propagating from distant sites. Distinction between active and passive LFP components can be achieved through current-source density (CSD) analysis.

CSD analysis provides detailed information about neuronal activity using extracellular recording methods, especially in layered structures like the hippocampus, see Figure 48. CSD is explicitly derived from the spatial derivatives of the extracellular LFP signals measured by an array of electrodes. By examining the voltage gradients recorded at multiple depths, it becomes possible to estimate where current enters or exits the tissue. A source is equivalent to current injected into the extracellular medium, and a sink to current absorbed from the medium into a cell. CSD analysis can identify active synaptic sites (both excitatory and inhibitory). CSD measures the amplitude of the current source or sink at a given point, varying with current size and electrode distance. The model assumes homogeneous and stationary electrical properties of the extracellular medium and that current sources are dipoles (Nicholson and Freeman, 1975; Bedard and Destexhe, 2011).

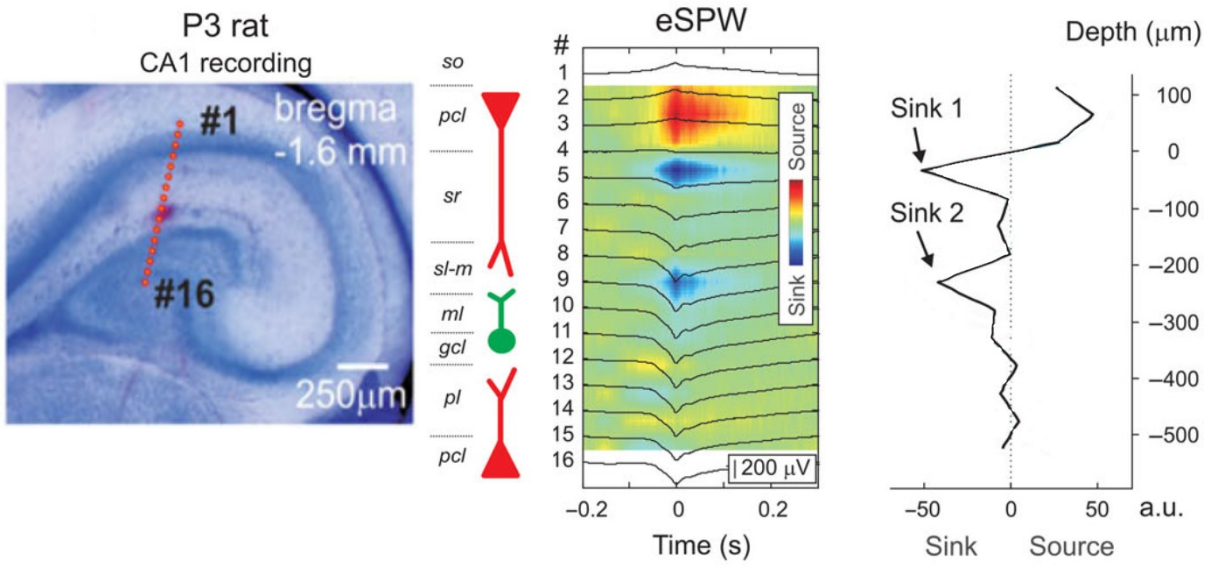

Figure 48. Example of CSD profiles derived from spatially resolved LFP recordings.

The figure shows electrode placements (#1–#16) across hippocampal layers in a rat CA1 region (left), a color-coded CSD map with sources (red) and sinks (blue) over time of eSPW onset (middle), and the depth profile of CSD highlighting current sinks and sources within specific layers (right). Adapted from Valeeva and Janackova et al., 2019.

3.1.3. Multi-unit activity (MUA)

Multi-Unit Activity (MUA) reflects the high-frequency components of extracellular recordings (including those from which LFPs are derived, see Figure 49) and is associated primarily with the firing of multiple nearby neurons. By applying high-pass filters to the same extracellular data used to obtain LFP signals, the spiking activity of a population of neurons can be isolated, resulting in MUA. While LFP captures the slower, subthreshold synaptic and dendritic processes, MUA provides a direct measure of aggregate neuronal firing, offering a complementary view of local network dynamics. Both LFP and MUA are thus extracted from the same extracellular recordings, but focus on different frequency bands and underlying physiological processes.

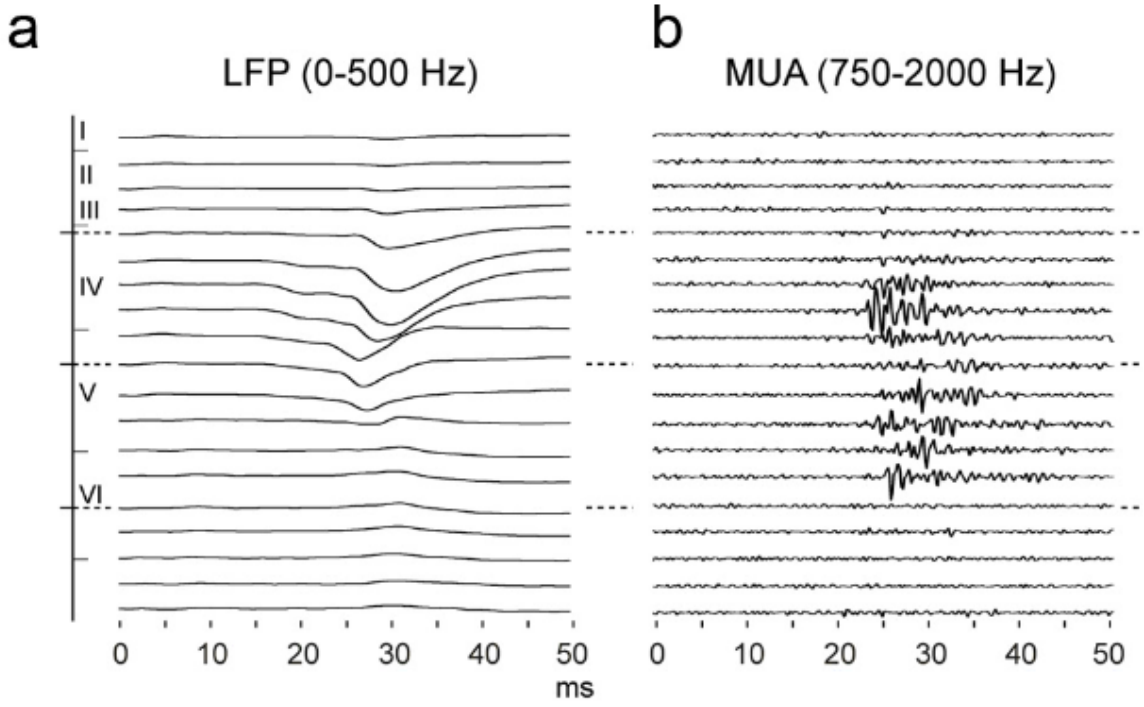

Figure 49. Example of MUA extraction from the high-frequency components of extracellular data.
Example voltage trace in a P10 rat's S1 cortex, recorded in response to a single sweep contralateral whisker deflection and showing the low (LFP; calibration, 1 mV)- and high (MUA without rectification; calibration, 50uV)-frequency components of the poststimulus response. From Quairiaux et al., 2011.

3.1.4. Patch-clamp electrophysiology

Patch-clamp is a powerful electrophysiological technique used to study the electrical properties of individual cells and ion channels. This method allows high-resolution current recordings of whole cells, excised cellular patches, and even single-channel events (Neher and Sakmann, 1976).

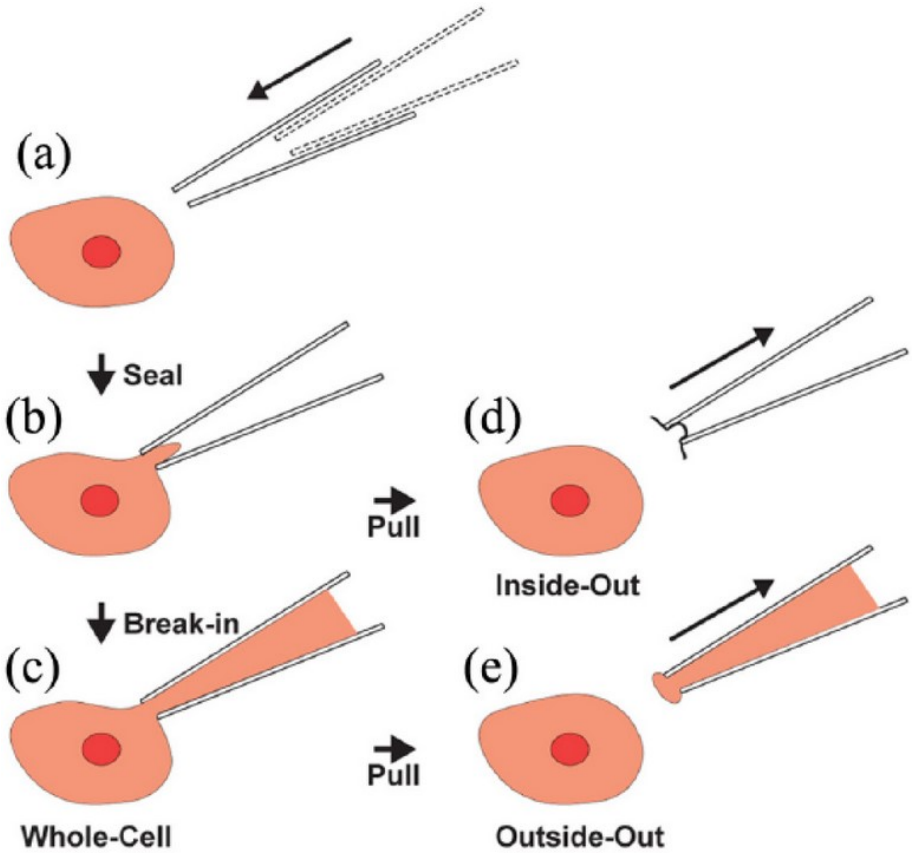

Figure 50. Patch-clamp procedure and configurations.

(a) The glass micropipette approaches the target cell. (b) Cell-attached: the micropipette is sealed onto a patch of cell membrane. (c) Whole-cell: the membrane patch is ruptured, and contact with the intracellular space is established. (d) Inside-out: if after sealing, the pipette is rapidly withdrawn, a patch of membrane remains attached to the tip, exposing the intracellular surface of the membrane to the medium. (e) Outside-out: if the pipette is gently withdrawn from a whole-cell configuration, a piece of membrane remains attached to the tip, forming a patch where the original extracellular side of the membrane remains in contact with the extracellular media, while the internal part of the membrane is in contact with the internal part of the pipette. From Annecchino and Schultz, 2018.

Patch-clamp is a versatile electrophysiological technique that can be conducted in various configurations, including cell-attached, whole-cell, inside-out, and outside-out patches (See Figure 50 and Figure 51). It allows researchers to control either the voltage across the membrane (voltage clamp) or the current passing through it (current clamp), facilitating detailed studies of ion channel behavior (Sakmann and Neher, 1984). Widely applied in the investigation of excitable cells like neurons, cardiomyocytes, and muscle fibers, as well as non-excitable cells, the technique has become a cornerstone in cellular physiology research, as outlined by (Sigworth and Neher, 1980). The patch-clamp method offers exceptional resolution, making it possible to study both single ion channel currents and the combined activity of multiple channels. In the whole-cell configuration, the pipette solution can diffuse into the cytoplasm, enabling the introduction of drugs or manipulation of intracellular targets (Marty and Neher, 1983).

Patch-clamp has significantly contributed to understanding of ion channel function, cellular excitability, and synaptic transmission. It has become an essential tool in neuroscience, pharmacology, and drug discovery.

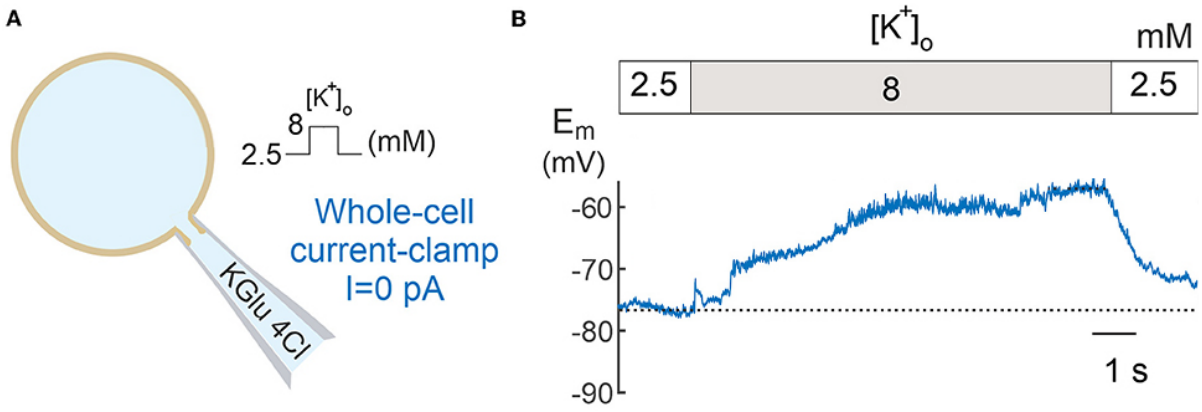

Figure 51. Example of patch-clamp in whole-cell current-clamp configuration.

(A) Scheme of recordings. (B) Example of the response to an increase in [K+]o from 2.5 to 8 mM in the bath solution during whole-cell recording in a L5 pyramidal neuron. From Vazetdinova et al., 2022.

Whole-cell recordings with low chloride concentration for separating synaptic currents

Whole-cell recordings with low chloride enables the separate study of excitatory and inhibitory synaptic currents in neurons based on their reversal potentials.

Using an intracellular solution with low chloride ion concentration (4.2 mM), the equilibrium potential for GABAergic currents (E) is set at approximately -70 mV, minimizing their contribution at this potential. Maintaining the membrane potential at this level allows isolated recording of excitatory postsynaptic currents (EPSC) mediated by glutamate receptor activation. Conversely, maintaining the potential at 0 mV, the reversal potential for excitatory currents, enables recording of inhibitory postsynaptic currents (IPSC) associated with GABA receptor activation.

For example, this method was employed in the study by Khalilov et al., 2015 (see Figure 52), to record the dynamics of GABA- and glutamate-mediated currents in CA3 pyramidal cells of the hippocampus in newborn rats. Recordings were performed at the reversal potential for glutamate currents (0 mV) and GABA currents (-70 mV).

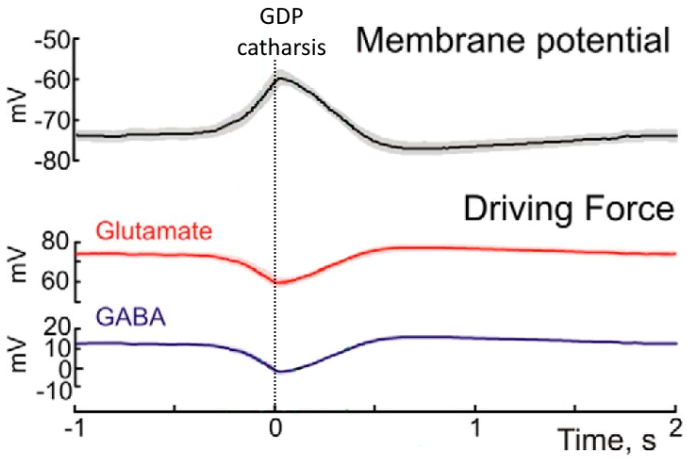

Figure 52. Example of collecting information about synaptic currents using the low chloride concentration method.

Dynamic changes in GABAergic and glutamatergic currents in CA3 pyramidal cells during GDPs (t = 0, s). Average membrane potential during GDPs obtained during gramicidin perforated patch recordings. And driving forces for glutamate and GABA(A) receptor mediated synaptic currents during GDPs. From Khalilov et al., 2015.

3.2. Confocal immunolocalization of Synaptotagmin isoform Syt2

Neurotransmitter release during synaptic transmission is tightly regulated by the coordinated action of specialized proteins in response to an influx of calcium ions. The fusion of the synaptic vesicle with the plasma membrane is primarily mediated by the SNARE complex, consisting of proteins such as synaptobrevin, syntaxin, and SNAP-25 (Chen et al., 1999; Hu et al., 2003). Synaptotagmin acts as a calcium sensor that triggers the rapid fusion of these membranes upon calcium binding (Pang et al., 2006). Synaptotagmin is characterized by an N-terminal transmembrane region and two C2 domains (C2A and C2B) that bind calcium ions (see Figure 53). In Article 5 of the current work, we used synaptotagmin in its Syt2 isoform as a reliable marker for parvalbumin-positive inhibitory boutons (Sommeijer and Levelt, 2012, Harris et al. 2018).

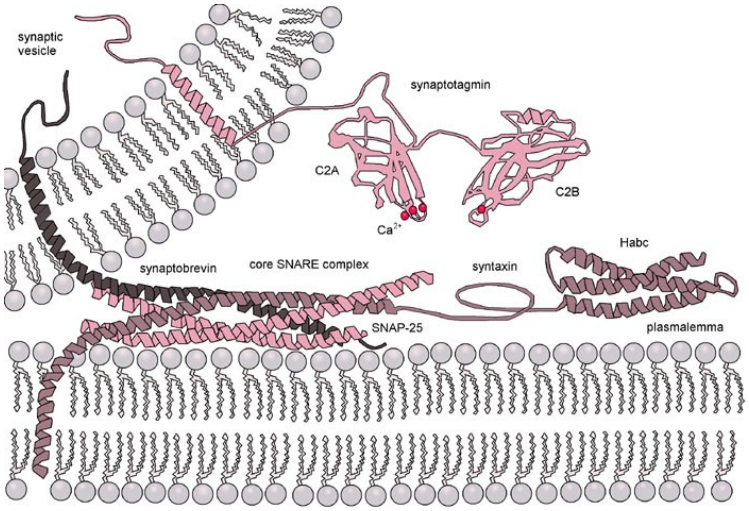

Figure 53. Synaptic vesicle fusion.

The synaptic vesicle is shown at the top, with synaptobrevin embedded in its membrane. The SNARE complex, formed by synaptobrevin, syntaxin, and SNAP-25, spans the gap between the vesicle and the plasma membrane at the bottom. Synaptotagmin is displayed with its C2A and C2B domains, each capable of binding calcium ions (Ca^{2+}), which are essential for triggering the fusion event. The Habc domain of syntaxin is also shown, folded near the plasma membrane. From Chapman, 2002.

To study the synaptic terminals of parvalbumin-positive (PV+) interneurons, such as basket cells, the method of immunohistochemistry combined with confocal microscopy is often used. This approach enables visualization of proteins involved in the functional aspects of synaptic transmission, such as Synaptotagmin-2 (Syt2), a marker associated with rapid neurotransmitter release. The key steps are described below: preparation of tissue sections and immunohistochemistry, ensuring high specificity in protein detection.

3.2.1. Immunocytochemistry

Immunocytochemistry is used for the specific visualization of proteins in tissues using antibodies.

Preparation of Tissue Sections

To study brain tissues, they are fixed to prevent the degradation of cellular structures. This process includes perfusion of animals with a fixative solution (e.g., 4% paraformaldehyde in phosphate buffer), which replaces blood with the fixative to preserve the tissue. After extraction, the brain is further fixed in the same solution, treated with a cryoprotectant (e.g., 30% sucrose) to prevent damage during freezing, and then sectioned into thin slices (e.g., 50 µm) using a cryostat. These slices preserve microstructures, including synaptic terminals, for subsequent analysis.

The simplified workflow for preparing tissue sections is as follows:

Anesthesia → Perfusion with fixative → Brain extraction → Post-fixation in PFA → Sucrose treatment → Freezing → Sectioning → Storage.

Antibody-Based Immunocytochemistry

Immunocytochemistry relies on two types of antibodies: primary antibodies that recognize the target protein and secondary antibodies that amplify the signal and provide fluorescence (see Figure 54).

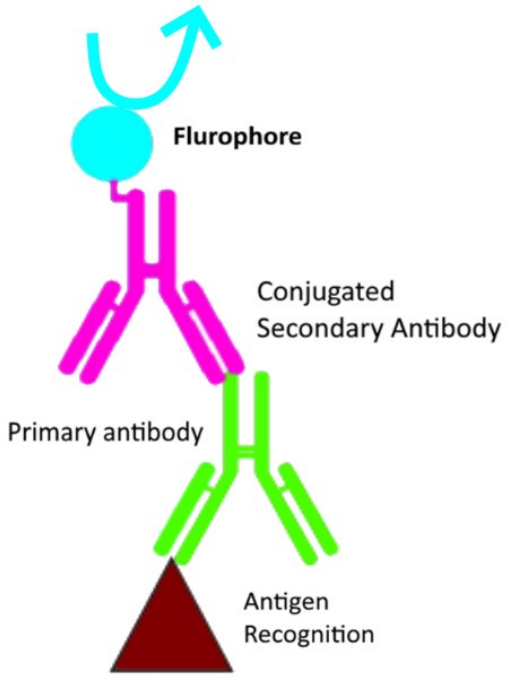

Figure 54. The principle of antibody-based immunocytochemistry.
The primary antibody (green) specifically binds to the target protein (antigen), depicted as a red circle. The secondary antibody (pink), conjugated with a fluorophore (blue circle), binds to the primary antibody. The fluorophore emits light when excited by a laser, allowing visualization of the target protein in the sample. From Rohilla et al. 2020.

Blocking Non-Specific Binding

Before applying antibodies, tissue sections are treated with a blocking solution containing a detergent (e.g., PBS with Triton-X) and serum (e.g., 10% normal donkey serum). This step prevents non-specific binding of antibodies to other proteins in the tissue, ensuring accurate visualization.

Incubation with Primary Antibodies

Primary antibodies bind to the target protein (such as Syt2) with high specificity. This is achieved because primary antibodies recognize unique epitopes of the protein (specific amino acid sequences or structures). These antibodies are typically produced by immunizing animals (e.g., mice) with peptides corresponding to the structure of the target protein.

Incubation with Secondary Antibodies

Secondary antibodies bind to primary antibodies by interacting with their universal Fc region. They carry a fluorescent tag (e.g., Alexa 647), which enables visualization. A

single secondary antibody can bind to multiple primary antibodies, amplifying the signal. Secondary antibodies are universal and can be used with any primary antibody produced in the same species (e.g., mouse-derived antibodies).

Fluorescence of Secondary Antibodies

The fluorescent tag emits light when excited by a laser of a specific wavelength (e.g., 647 nm). This allows precise localization of target proteins in the tissue.

3.2.2. Confocal microscopy

Confocal microscopy is used to capture fluorescent signals with high precision. The microscope focuses the laser on a thin layer of tissue (e.g., 1 µm), minimizing light scattering from other layers (see Figure 55). This, for example, enables detailed imaging of synaptic terminals, such as those of PV+ interneurons expressing Syt2. High-resolution objectives (e.g., 40×/1.4 oil) and optimized scanning parameters (e.g., z-step of 1 µm) allow for 3D reconstructions and accurate localization of terminals within the tissue.

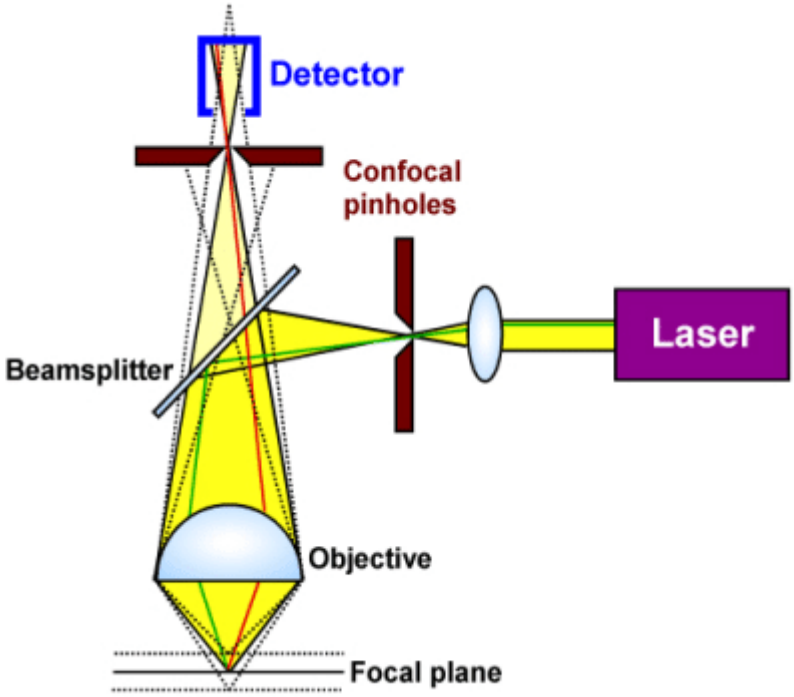

Figure 55. The working principle of a confocal microscope.
A laser beam passes through a beamsplitter, which directs it into the objective lens. The objective focuses the beam onto a specific focal plane of the sample. Light emitted or reflected from the focal plane passes back through the confocal pinhole, which blocks scattered light from other planes, and reaches the detector. This process ensures high-resolution and high-contrast imaging by restricting visualization to the focal region. From Debarnot et al., 2019.

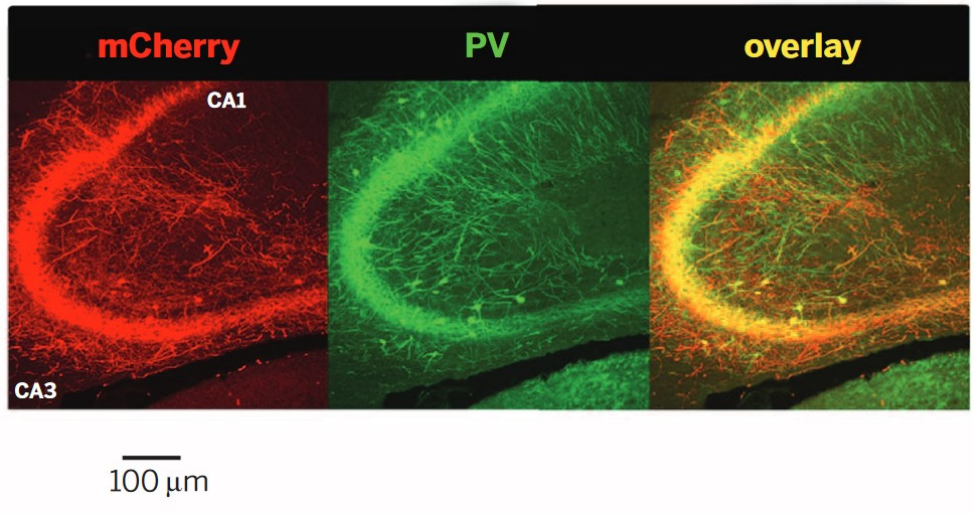

Figure 56. Validation of the overlap between immunohistochemical and genetic methods for localizing PV+ interneurons.

The red channel (mCherry) represents genetically labeled Parvalbumin+ cells, while the green channel (PV) shows their immunoreactivity. The overlay demonstrates colocalization, confirming the accuracy of both approaches. From **Hu et al., 2014**.

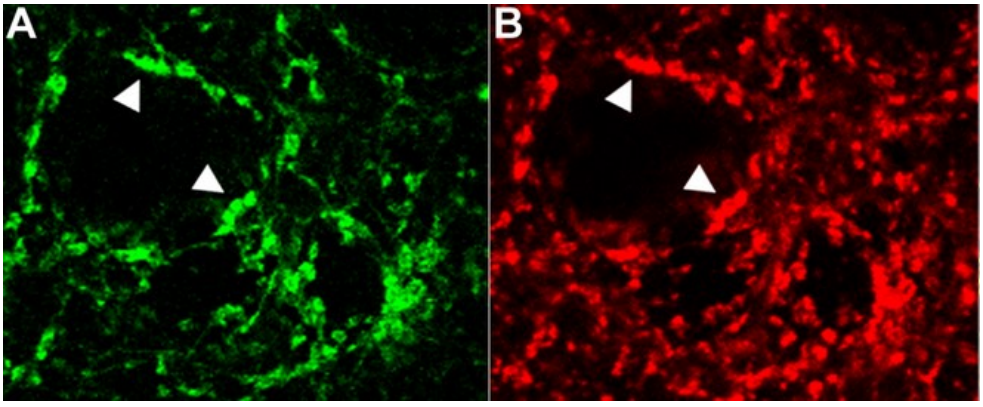

Figure 57. Example of a confocal image with fluorophore markers.

The image demonstrates the expression of Synaptotagmin-2 (Syt2) and vesicular GABA transporter (VGAT) in layers 2–3 of the visual cortex. Panel A (green) shows the distribution of Syt2 in synaptic terminals, highlighted by arrowheads. Panel B (red) illustrates VGAT expression in the same regions. A key point emphasized in the article is that Syt2 almost always colocalizes with VGAT in these layers. From Sommeijer and Levelt, 2012.

The confocal immunolocalization method may be assessed in combination with genetic labeling. For example, in Figure 56, PV+ interneurons appear to colocalize with genetically expressed mCherry, indicating the potential interchangeability of these methods. These methods provide highly specific detection and visualization of synaptic terminals of inhibitory neurons (see Figure 57). Immunocytochemistry, based on the interaction of primary and secondary antibodies, combined with confocal microscopy, enables the study of microanatomy and molecular mechanisms of inhibitory transmission with a high level of detail.

3.3. Software built for analysis

3.3.1. Easy Viewer: a tool for analyzing multichannel electrophysiological signals

The EasyViewer software (developed by the author of this dissertation) was used for processing and analyzing multichannel electrophysiological signals. The program effectively managed large datasets and enabled accurate analysis of the temporal and spatial characteristics of the signals. The main functionalities of the program are detailed below.

Signal visualization

The software provides data visualization with options for adjusting time ranges, sampling frequencies, and channel offsets. These manipulations allow analysts to detect significant patterns, such as amplitude changes or temporal correlations between channels. This functionality is particularly useful for identifying specific activity related to experimental conditions (see Figure 58).

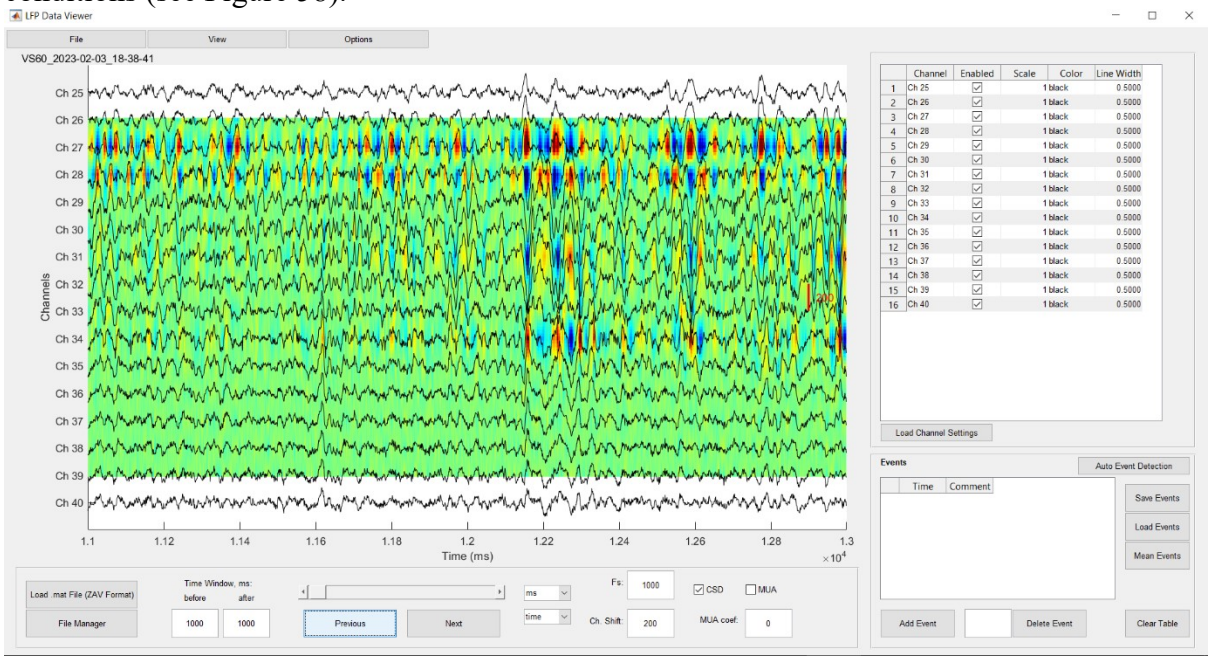

Figure 58. Main interface of the EasyViewer program.
The figure demonstrates the program's capabilities for signal visualization with adjustable time ranges and scaling options, as well as CSD analysis of the displayed signals.

Signal processing

The program supports filtering using bandpass, low-pass, and high-pass filters, as well as mean subtraction to eliminate background noise (see Figure 59). Additionally, the software

performs Current Source Density (CSD), Independent Component Analysis (ICA), and Principal Component Analysis (PCA) to identify spatial and temporal signal characteristics.

It allows data manipulation, including merging data from different recordings into a single trace, adding data to new channels, replacing existing data, or integrating data into any part of a recording. These features simplify the analysis of complex multichannel data and facilitate detailed comparative studies.

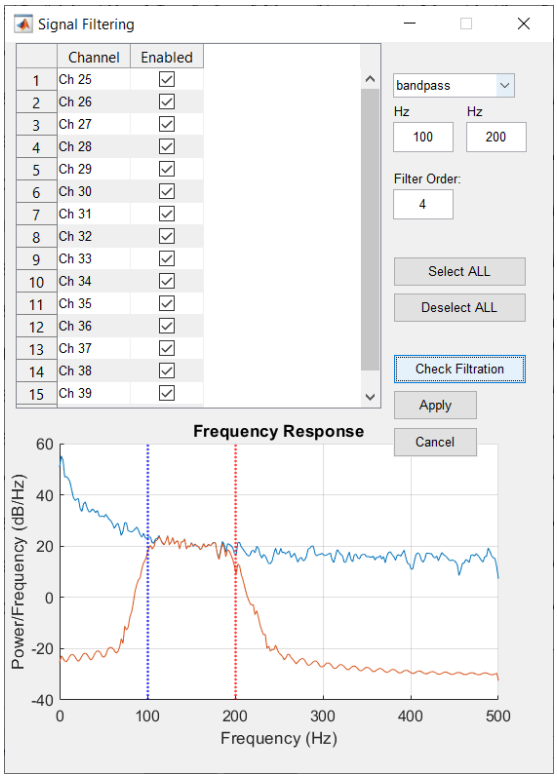

Figure 59. Easy Viewer's filtering settings.

Event management

The program provides manual and automatic event addition to a list for further processing based on amplitude thresholds, time intervals, and smoothing settings. Event timings and their properties were saved for subsequent analysis. This enables precise identification of specific phenomena and their association with other data (see Figure 60).

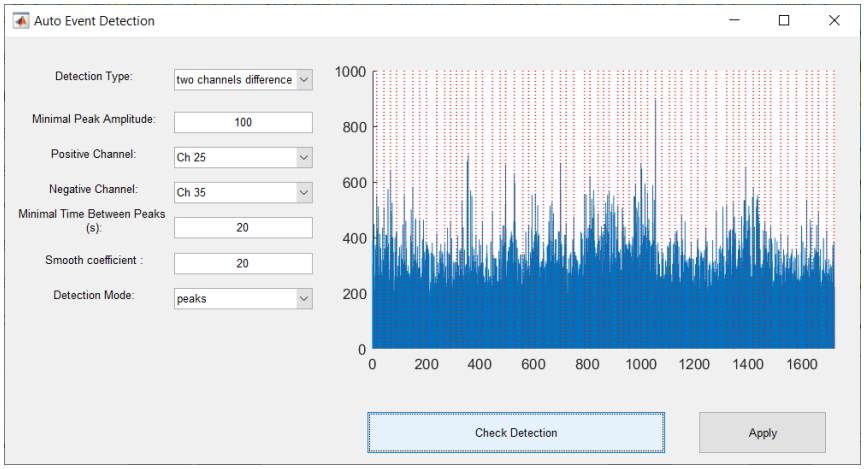

Figure 60. Automatic event detection settings.

The blue trace shows the amplitude of all detected peak events over time, and the red dotted lines show which of the events satisfy such parameters as the time-distance between the peaks and their amplitude.

Event-based signal averaging

The signal averaging function around events allows for the creation of generalized activity characteristics. This helps identify trends, such as dynamics of channel activity related to specific events. For instance, it is possible to analyze the occurrence of other events, multi-unit activity (MUA), sinks, and sources in CSD, providing a more detailed understanding of processes in the analyzed events (see Figure 61).

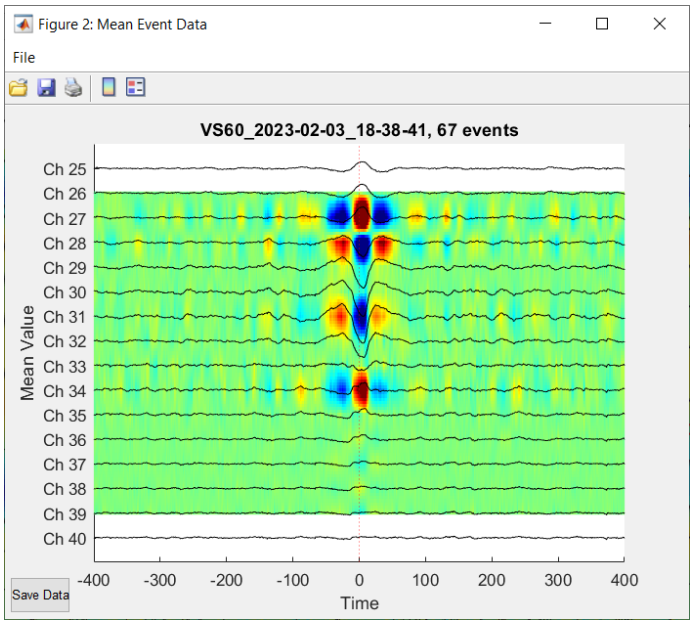

Figure 61. Event-based signal averaging showing activity dynamics with CSD.

Data loading and conversion

The software supports loading data in MATLAB format with custom extensions ZAV for electrophysiological data and EV for event data. The program allows conversion of raw electrophysiological files, such as NLX or DAT, into the ZAV format native to the software.

Easy Viewer provides robust tools for analyzing electrophysiological data, allowing researchers to tailor their workflow to specific research goals. This makes the program a versatile solution for handling datasets of varying volume and complexity.

3.3.2. Synapto Catcher: a software for analyzing microscopic images

The SynaptoCatcher software, developed by the author of this dissertation, was utilized for the analysis of microscopic images in this study. The program enabled precise data processing, object identification, and quantitative analysis, streamlining the workflow for image-based research. Key functionalities are outlined below.

Image preparation for analysis

SynaptoCatcher supports loading multi-layered image files, allowing users to specify the range of slices for analysis. Users can define a "target channel" for analysis and an "additional channel" for improved visualization if needed (see Figure 62).

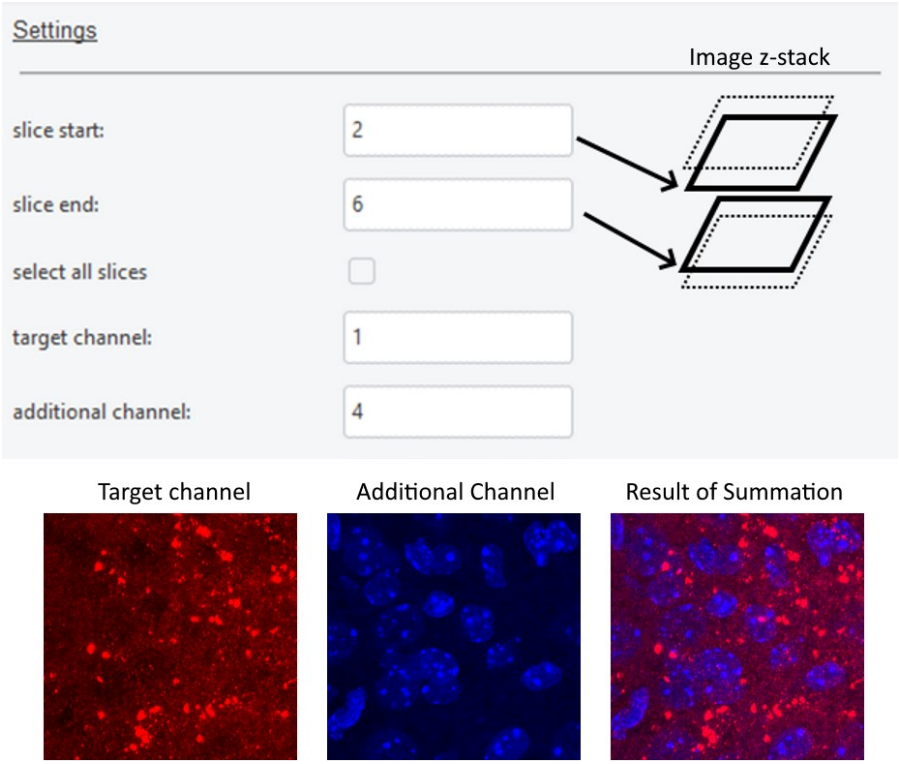

Figure 62. Image preparation and stacking settings in Synapto Catcher.
Data from the target channel is depicted in red, and data from an additional channel that is not processed, but may be needed for visualization, is depicted in blue.

Region of interest (ROI) selection

Users can manually select regions of interest (ROI) by marking and drawing specific areas within an image. These regions can be named and saved for further processing. Tools for deleting, modifying, or accepting selected ROIs provide flexibility and precision. This step ensures that only relevant areas of the image are analyzed (see Figure 63).

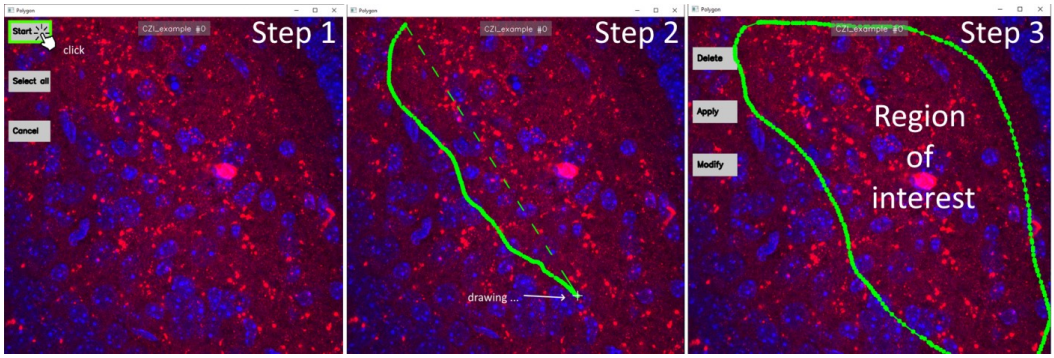

Figure 63. ROI selection and customization interface.

Image processing

The software includes powerful tools for filtering and binarization. Filtering removes background noise and allows users to specify the expected size of objects (e.g., spot radius). Binarization converts images into black-and-white representations, emphasizing the objects of interest. Various binarization methods, such as Otsu and Max entropy methods, can be selected. Additionally, users can define the range of object sizes (minimum and maximum) to include only relevant objects for further analysis (see Figure 64).

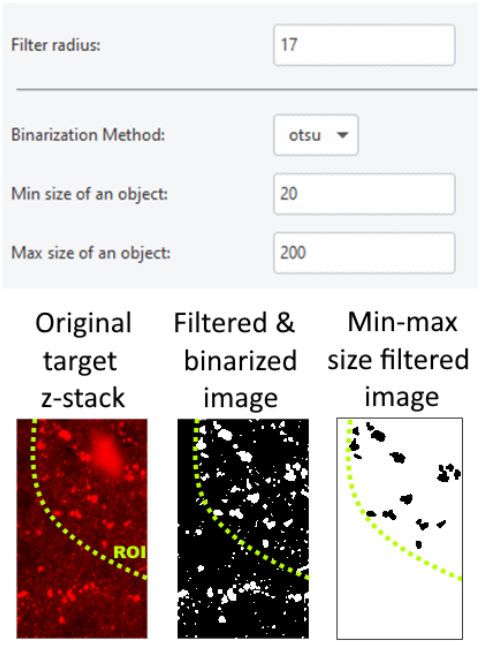

Figure 64. Filtering and binarization parameters.

Object identification and counting

Once ROIs are defined, the software applies filtering and binarization settings to count objects within these regions. Detected objects are quantified based on user-defined size constraints and binarization methods (see Figure 65).

filepath	Count	%Area	Binarization method	location	Postnatal_Age
\Experiment-05.czi	877	7,245	otsu	SP_CA1	11
\Experiment-06.czi	749	6,959	otsu	SP_CA1	11
\Experiment-30.czi	1101	11,036	otsu	SP_CA1	15
\Experiment-31.czi	992	10,995	otsu	SP_CA1	15
\Experiment-32.czi	1055	7,123	otsu	SP_CA3	15
Experiment-420.czi	311	4,62	otsu	SP_CA1	21
Experiment-421.czi	854	7,811	otsu	SP_CA3	21
Experiment-422.czi	749	5,932	otsu	SP_CA1	21

Figure 65. Object identification and counting results.

Result exploration

Processed results can be explored through a gallery view, where users can inspect preview images of intermediate steps and final outputs. Results, including object area measurements and ROI coordinates, are saved in organized folders containing both visual data and tabular summaries (see Figure 66).

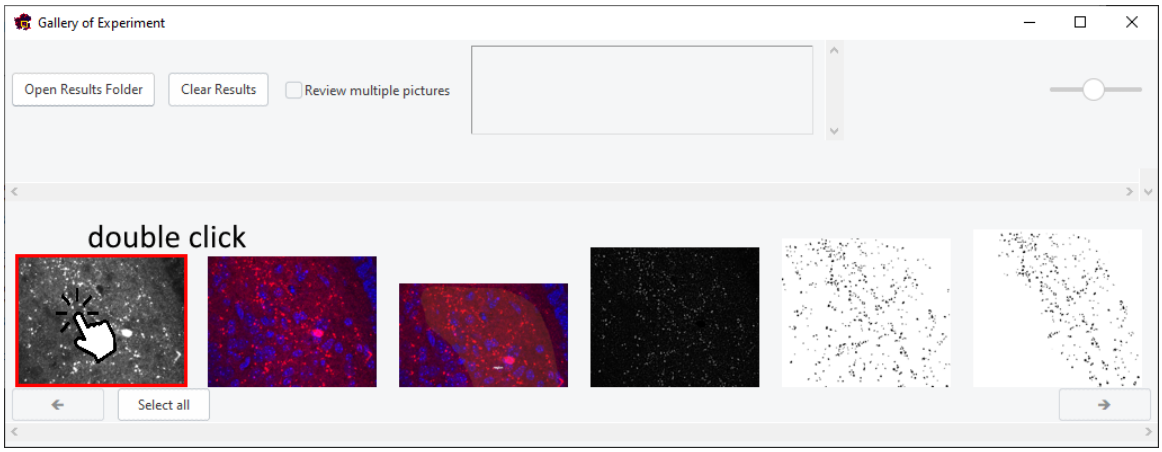

Figure 66. Results gallery.

SynaptoCatcher may significantly enhances the efficiency of analyzing microscopic images, providing a user-friendly interface and advanced processing tools. It is a valuable asset for researchers seeking precise quantification and visualization of image data.

4. Results

4.1. Article 1. Somatosensory-Evoked Early Sharp Waves in the Neonatal Rat Hippocampus

Azat Gainutdinov[1,†], Dmitrii Shipkov[2,†], Mikhail Sintsov[2], Lorenzo Fabrizi[2,3], Azat Nasretdinov[2], Roustem Khazipov[1,2,*] and Guzel Valeeva[2]

1. Institut de Neurobiologie de la Méditerranée (INMED U1249), Aix-Marseille University, 13273 Marseille, France; azat.gainutdinov@inserm.fr
2. Laboratory of Neurobiology, Kazan Federal University, 420008 Kazan, Russia; dmshipkov@gmail.com (D.S.); mikhail.yu.sintsov@gmail.com (M.S.); l.fabrizi@ucl.ac.uk (L.F.); azrnasretdinov@kpfu.ru (A.N.); gurvaleeva@kpfu.ru (G.V.)
3. Department of Neuroscience, Physiology and Pharmacology, University College London, London WC1E 6BT, UK

* Correspondence: roustem.khazipov@inserm.fr

† These authors contributed equally to this work.

ISSN 1422-0067, International Journal of Molecular Sciences 2023, 24, 8721
DOI: 10.3390/ijms24108721
Received: 13 April 2023
Revised: 5 May 2023
Accepted: 11 May 2023
Published: 13 May 2023

4.1.1. Abstract

The developing entorhinal–hippocampal system is embedded within a large-scale bottom-up network, where spontaneous myoclonic movements, presumably via somatosensory feedback, trigger hippocampal early sharp waves (eSPWs). The hypothesis, that somatosensory feedback links myoclonic movements with eSPWs, implies that direct somatosensory stimulation should also be capable of evoking eSPWs. In this study, we examined hippocampal responses to electrical stimulation of the somatosensory periphery in urethane-anesthetized, immobilized neonatal rat pups using silicone probe recordings. We found that somatosensory stimulation in ~33% of the trials evoked local field potential (LFP) and multiple unit activity (MUA) responses identical to spontaneous eSPWs. The somatosensory-evoked eSPWs were delayed from the stimulus, on average,

by 188 ms. Both spontaneous and somatosensory-evoked eSPWs (i) had similar amplitude of ~0.5 mV and half-duration of ~40 ms, (ii) had similar current-source density (CSD) profiles, with current sinks in CA1 strata radiatum, lacunosum-moleculare and DG molecular layer and (iii) were associated with MUA increase in CA1 and DG. Our results indicate that eSPWs can be triggered by direct somatosensory stimulations and support the hypothesis that sensory feedback from movements is involved in the association of eSPWs with myoclonic movements in neonatal rats.

Keywords: hippocampus; CA1; dentate gyrus; sharp wave; neonatal rat; somatosensory; sensory-evoked response; local field potentials; multiple unit activity; current-source density

4.1.2. Introduction

Early sharp waves (eSPWs) are the earliest organized activity pattern in the devel-oping hippocampus of neonatal rodents [1–6]. Electrophysiological traits of eSPWs are similar to those of adult SPWs, but their generative network mechanisms differ. While adult SPW-Rs are spontaneous top-down events, self-generated in the hippocampal cir-cuit [7], eSPWs are primarily bottom-up events involving the inputs from the entorhinal cortex (EC). These inputs are activated during myoclonic movements (startles and twitches) characteristic of active sleep during the neonatal period in rodents [3,6,8–10]. Yet, network mechanisms linking eSPWs with myoclonic movements remain largely unknown. The current hypothesis involves somatosensory (proprioceptive and tactile) feedback gener-ated by myoclonic movements [11,12], which trigger activity bursts in the somatosensory pathways [13–20]) that are further conveyed via the EC to the hippocampus [3–6,9,21]. The hypothesis that somatosensory feedback binds myoclonic movements with eSPWs implies that direct somatosensory stimulation should also be capable of evoking eSPWs.

The hippocampus is a sensory hub that integrates sensory inputs of all modalities to enable its functions in spatial navigation, learning and memory [22]. In adults, somatosensory, auditory and visual stimuli evoke local field potential (LFP) responses in the hippocampus and modulate hippocampal neuron firing [23–28]. The current-source density (CSD) profile of somatosensory-evoked LFP responses reveals activation of temporoammonic and per-forant pathways with characteristic sinks in the CA1 stratum lacunosum-moleculare and molecular layer of dentate gyrus, respectively [23,24]. These responses are also associated with the activation of granular cells in the dentate gyrus (DG) and variable but predomi-nantly inhibitory effects on CA1 pyramidal neurons [23]. However, somatosensory-evoked responses in the hippocampus of neonatal rats remain largely unexplored.

In the present study, we examined the responses evoked by somatosensory stimulation in the hippocampus of neonatal rat pups (P5–P6) using silicone probe recordings along the CA1–DG axis. Experiments were conducted under urethane anesthesia to suppress movements. We found that in neonatal rats, somatosensory stimulation evoked ample hippocampal responses with CSD profiles suggesting involvement of temporoammonic and perforant inputs from the EC, as well as Schaffer collateral input from CA3, and global activation of CA1 and DG neurons. The electrographic portrait of somatosensory-evoked hippocampal responses matched that of spontaneous eSPWs. These findings support the hypothesis that sensory feedback from

movements is involved in eSPW binding to myoclonic movements in neonatal rats and are compatible with delayed development of inhibition in the EC–hippocampal circuit.

4.1.3. Results

We explored somatosensory-evoked responses using 16-channel silicone probe record-ings of local field potential (LFP) and multiple unit activity (MUA) from the dorsal hip-pocampus of P5-P6 Wistar rat pups, in which eSPWs represent the earliest and most prominent hippocampal activity pattern [2, 5, 6, 29] (Figure 67A). The location of the recording sites was identified during post hoc analysis of the DiI electrode tracks in coronal brain sections (Figure 67B). Somatosensory responses were evoked by subcutaneous electrical stimulation of the contralateral whisker pad. Body movements were completely suppressed by urethane to isolate the "direct" somatosensory response uncontaminated by possible feedback from movements (Figure 67C). As illustrated by the example recording in Figure 67C (see also Figure 67D), the whisker pad stimulation evoked hippocampal LFP responses with a maximal negativity in CA1 stratum lacunosum-moleculare and polarity reversal near CA1 pyramidal cell layer/proximal stratum radiatum, as well as increased firing of CA1 and DG units.

These somatosensory-evoked responses were almost identical to spontaneous eSPWs in their spatiotemporal characteristics (Figure 68) and MUA modulation (see below) and therefore will be referred to hereafter as somatosensory-evoked eSPWs, or evoked eSPWs. The somatosensory-evoked eSPW peak was delayed from the stimulus, on average, by [median (first quartile–third quartile)] 188 (178–211) ms (n = 9 rats; Figure 68A,B), with a delay jitter of 25 (20–32) ms. Spontaneous eSPWs occurred with an average frequency of 0.019 (0.014–0.029) s−1(n = 9 rats), and the probability of eSPW generation calculated within 500 ms time window before and after the stimulus reached 1.7 (0.8–2.6)% and 32.7 (21.2–51.7)%, respectively (n = 9 rats; p = 0.004; Figure 68A,C). Somatosensory-evoked eSPWs had an average amplitude of 573 (455–601) μV and did not differ significantly from the spontaneous eSPW amplitude of 497 (440–650) μV (n = 9 rats; p = 1; Figure 68E,F). Spontaneous and evoked eSPWs also had similar half-widths, reaching 41 (36–48) ms and 43 (39–52) ms, respectively (n = 9 rats; p = 0.098; Figure 68D).

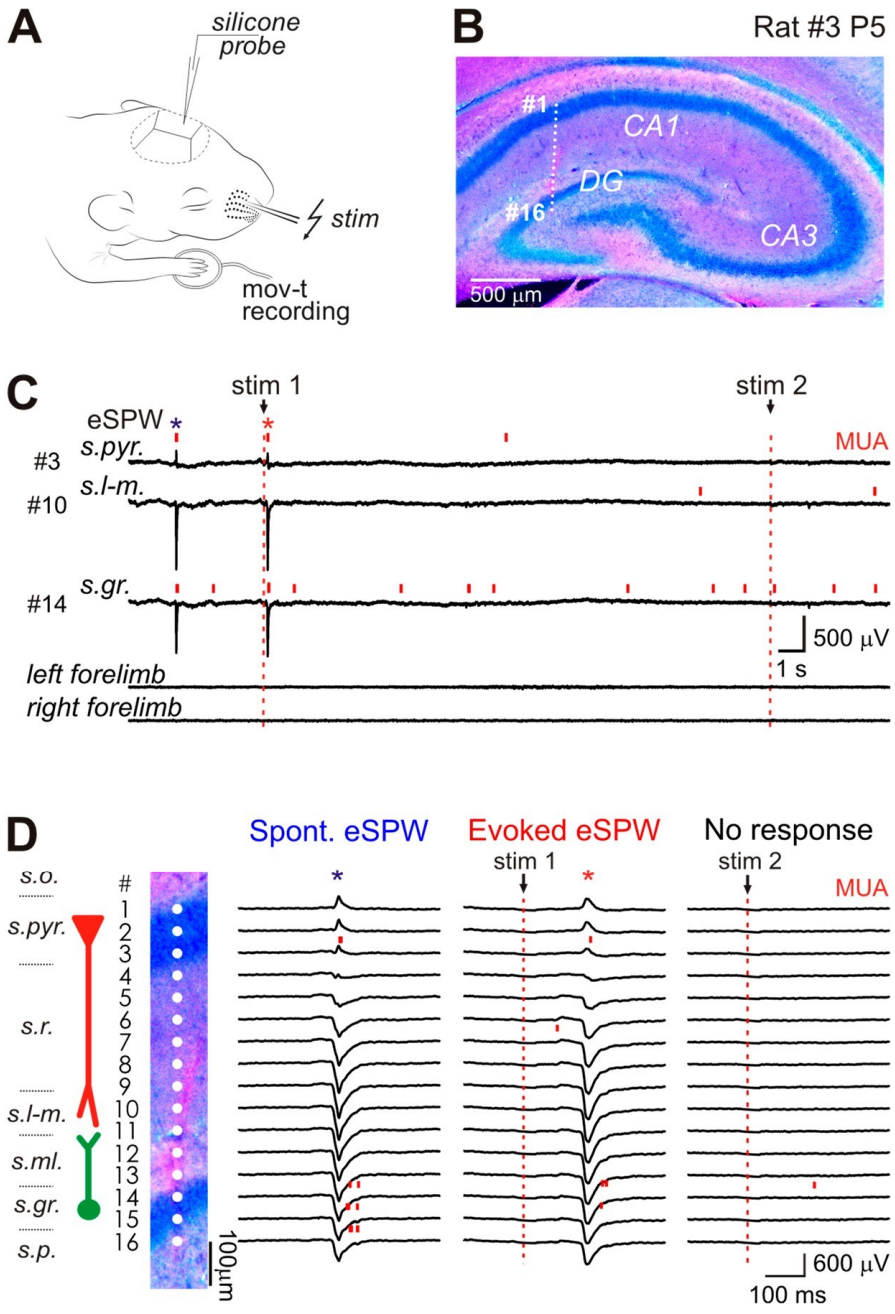

Figure 67. Spontaneous early sharp waves (eSPWs) and hippocampal responses evoked by electrical stimulation of skin in neonatal rat pup.

(**A**), Experimental setup represents silicone probe recording from left hippocampus of P5–P6 (P—postnatal day) rat pups during subcutaneous electrical stimulation of the right whisker pad. (**B**), Post hoc microphotograph of 100 µm-thick coronal hippocampal slice (cresyl violet staining) overlaid with recording electrodes of 16-channel silicone probe. (**C**), Hippocampal activity recorded from P5 rat on the probe sites shown in panels B and D. Spontaneous eSPWs and stimulus-evoked hippocampal responses are marked by blue and red asterisks (*), respectively. Simultaneous limb movement recordings from two piezo detectors are shown below. (**D**), The reconstruction of recoding electrode locations across hippocampal layers (s.o., CA1 str. oriens; s.pyr., str. pyramidale; s.r., str. radiatum; s.l-m., str. lacunosum-moleculare; s.ml., DG str. moleculae; s.gr., DG str. granulosum; s.p., DG polymorphic cell layer) and examples of individual spontaneous hippocampal eSPW (left), individual hippocampal response evoked by electrical stimulus (middle) and the stimulus evoking no response in the hippocampus (right). Red bars show multiple unit activity (MUA). The vertical dashed lines correspond to stimulus time.

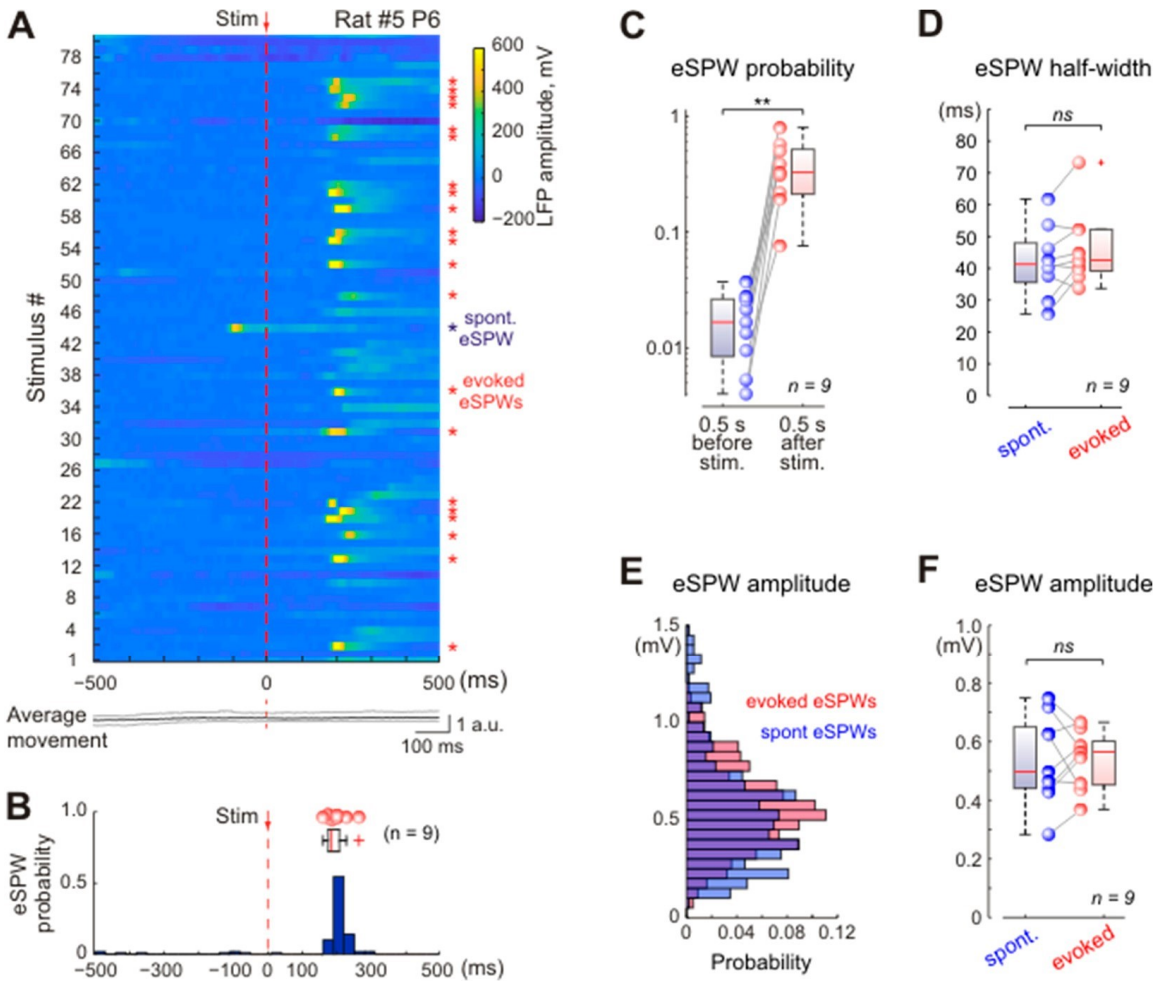

Figure 68. Somatosensory-evoked hippocampal eSPW response properties.

(A), Stimulus-triggered raster plot of hippocampal local field potential (LFP) responses evoked by the first 80 stimuli in a P6 rat. The stimuli that evoked eSPW responses are marked by red asterisks (*) on the right, blue asterisk indicates a spontaneous eSPW. Below, corresponding movement trace averaged over three piezo-channels (black) with a 25–75% interquartile range (gray). Dashed red line shows the stimulus time (0 ms). (B), PSTH of all eSPW responses recorded from the rat shown in (A). A boxplot above the histogram shows group data on eSPW response peak time in nine P5-P6 rats. Circles—median peak time values in individual animals. Outliers are shown by red crosses. (C–F), Group data on probability (C), half-width (D) and amplitude (E,F) of spontaneous eSPWs and evoked eSPW responses in nine P5-P6 rats. Circles show corresponding median values from individual animals. **, p-value < 0.01; ns, not significant.

The current-source density analysis also revealed CSD profiles of somatosensoryevoked eSPWs matching those of spontaneous eSPWs (Figure 69A). For a detailed description of eSPW CSD profiles, we selected six of the nine recorded animals where the probe sites completely covered the CA1 str. oriens—DG str. granulosum distance. Sink 1 in CA1 str. radiatum, reflecting the activation of CA3 ⇒ CA1 Schaffer collateral synapses, was located at an average depth of 48 (0–75) μm from the CA1 pyramidal cell layer during both sensory-evoked and spontaneous eSPWs (n = 6 rats; p = 1.0; Figure 69A,B). Another major current Sink 2, previously identified as a result of EC input activation [3, 6], was located within str. lacunosum-moleculare, 241 (225–251) μm below the CA1 pyramidal cell layer during both sensory-evoked and spontaneous eSPWs

(n = 6 rats; p = 1.0; Figure 69A,B). During both types of eSPWs, we also observed a third current sink localized in the external two-thirds of the DG str. moleculare (Sink 3). The average distance of Sink 3 from the hippocampal fissure was 50 (35–77) μm both for sensory-evoked and spontaneous eSPWs (n = 5 rats; p = 1.0; Figure 69A,B). Figure 69B represents the relative location of all three current sinks normalized to CA1 pyramidal cell layer—fissure distance in six individual animals.

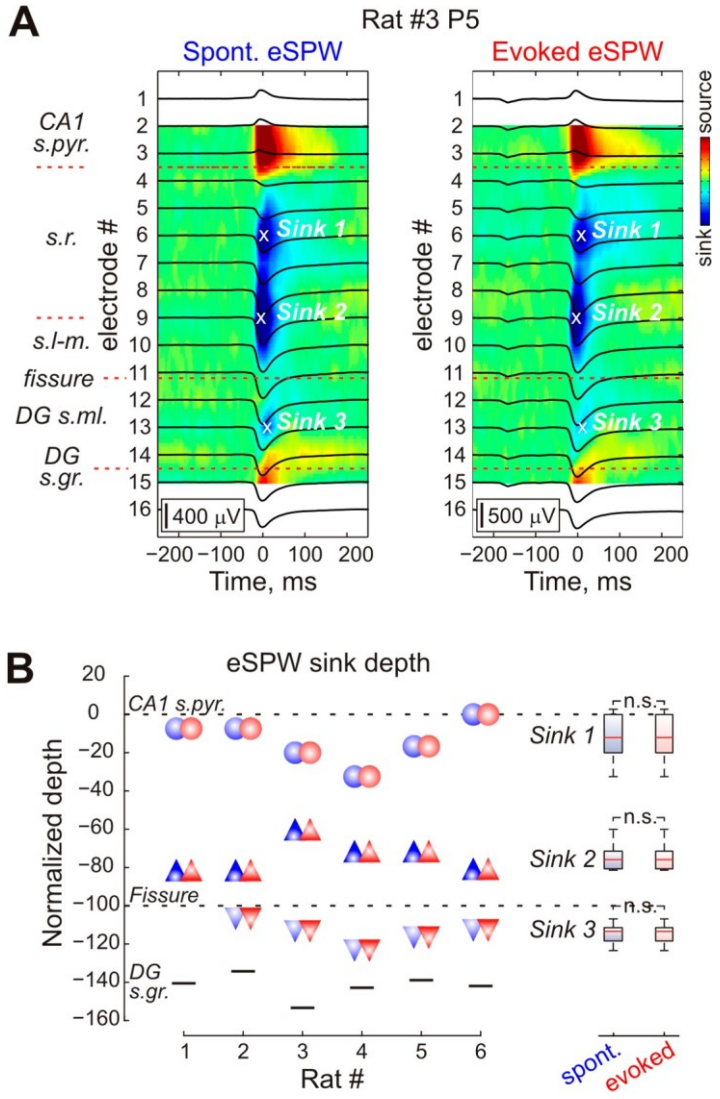

Figure 69. Current-source density (CSD) profile of spontaneous and stimulus-evoked eSPWs.

(**A**), Average LFP traces recorded in P5 rat during spontaneous and stimulus-evoked eSPWs overlaid on corresponding CSD maps. Hippocampal layer borders are shown on the left (CA1 s.pyr.—str. pyramidale, s.r.—str. radiatum, s.l-m.—str. lacunosum-moleculare, DG s.ml.—str. moleculare, DG s.gr.—str. granulosum). (**B**), Group data on the location of three main current sinks (Sink 1—circles, Sink 2—triangles, Sink 3—inverted triangles) in CSD profiles of spontaneous (blue) and stimulusevoked (red) eSPWs. Sink depths are normalized to CA1 s.pyr./s.r.–fissure distance. Boxplots on the right represent statistical data on sink depths. n.s.—not significant.

The comparison of current sink amplitudes revealed that Sink 2 was the most prominent of all three sinks observed during both spontaneous and sensory-evoked eSPWs. The magnitude of Sinks 1 and 3 reached 0.39 (0.29–0.48) and 0.29 (0.24–0.48) of

Sink 2 for spontaneous eSPWs and 0.42 (0.31–0.48) and 0.32 (0.21–0.50) of Sink 2 for sensory-evoked eSPWs, respectively (n = 6 rats; Figure 70).

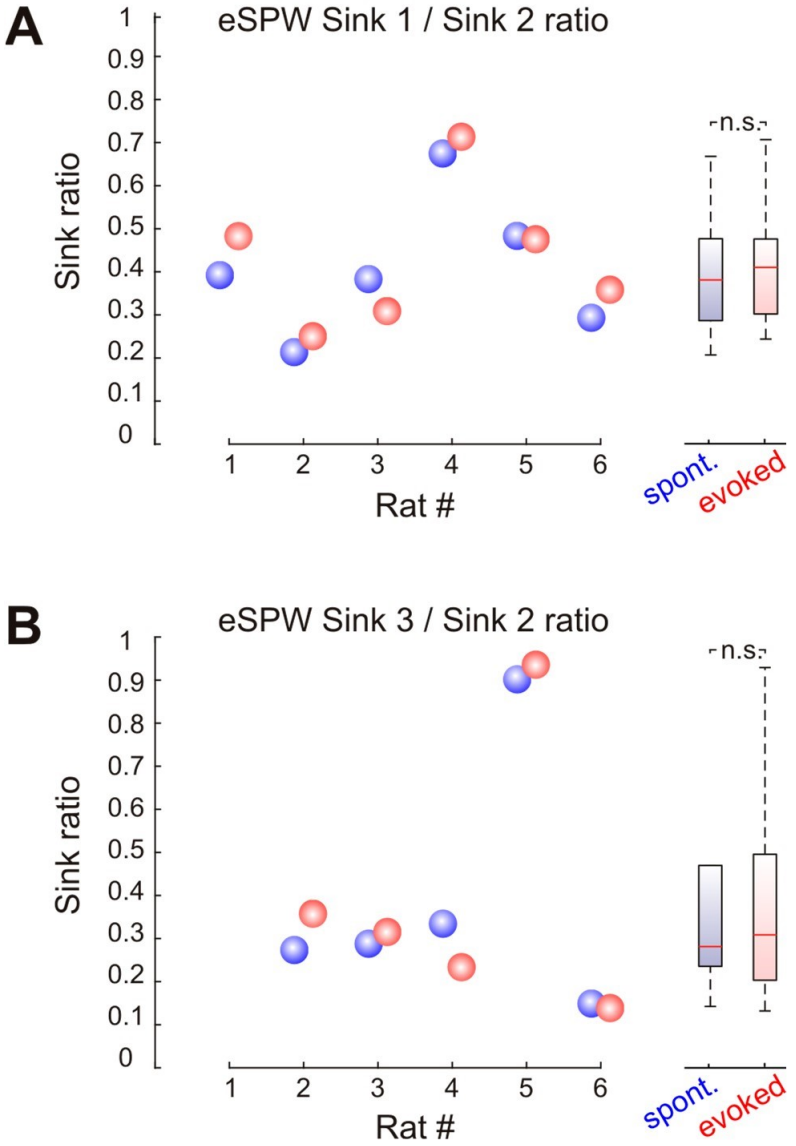

Figure 70. The relative magnitude of spontaneous and stimulus-evoked eSPWs.
Group data on Sink 1/Sink 2 (**A**) and Sink 3/Sink 2 (**B**) amplitude ratio. Boxplots on the right show statistical data for spontaneous (blue) and somatosensory-evoked (red) eSPWs. Circles show median sink ratio values for spontaneous (blue) and stimulus-evoked (red) eSPWs in six individual P5–P6 rats. n.s.—not significant.

We also found that Sink 2 occurred earlier than Sink 1 and Sink 3 (Figure 71). The current sink times were defined as the time of sink peak amplitude. During spontaneous eSPWs, Sink 1 and Sink 3 were delayed by 2.0 (1.0–7.0) ms and 17.0 (9.5–40.3) ms in relation to the negativity peak of eSPWs, while Sink 2 appeared 3.5 (3.0–4.0) ms earlier than the eSPW peak (n = 6 rats; Figure 71A). The current sink times of spontaneous eSPWs were significantly different from each other, as shown by the p-value map in Figure 71B. The temporal order of the main current sinks was identical for sensory-evoked eSPWs

(n = 6 rats; Figure 71A). Both Sink 1 and Sink 3 of sensory-evoked eSPWs were observed later than eSPW peak time with delay values reaching 8.0 (0.0–9.0) ms and 12.0 (6.8–43.3) ms, respectively (Figure 71A,B). At the same time, Sink 2 preceded eSPW peak by 4.0 (2.0–5.0) ms (n = 6 rats; Figure 71A,B). Although Sinks 1 and 3 were delayed from Sink 2, their timing was not significantly different from each other (Figure 71B). Taken together, the similarities in CSD profiles described above suggest the common network mechanisms underlying spontaneous and somatosensory-evoked eSPW generation.

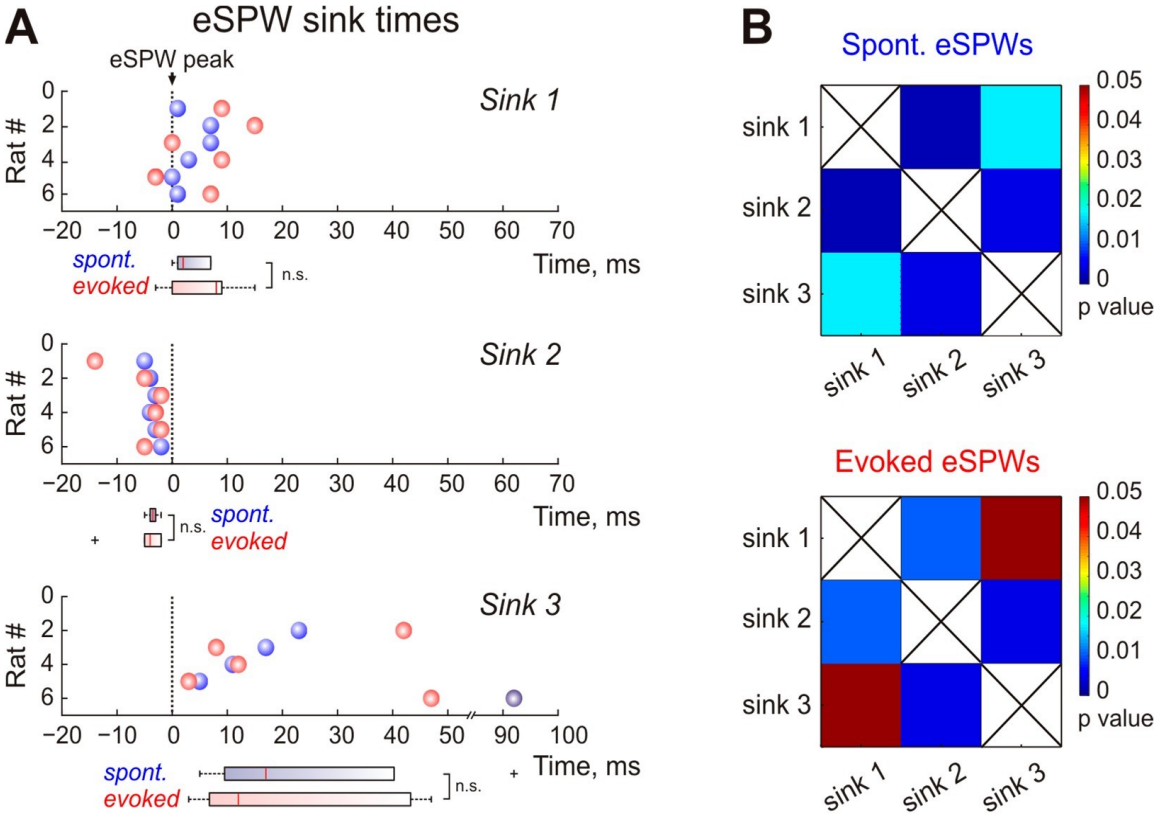

Figure 71. Time relations between three main current sink observed during spontaneous and stimulusevoked eSPWs.

(**A**), Group data on Sink 1, Sink 2 and Sink 3 times of spontaneous (blue circles) and stimulus-evoked (red circles) eSPWs in relation to eSPW peak (t = 0 ms). Corresponding boxplots are shown below each plot. n.s.—not significant. (**B**), p-value maps for current sink times of spontaneous (**top**) and stimulus-evoked (**bottom**) eSPWs.

The eSPWs generated in response to stimulation were associated with an increase in MUA in CA1 pyramidal cell layer and DG granular layer, also characteristic of spontaneous eSPWs (Figure 72). In four of the five recorded rat pups, CA1 pyramidal cell neurons fired before DG granular layer neurons during eSPWs. The averaged MUA z-score peak time was observed, on average, at 0 (−5–0) ms in relation to the eSPW peak in CA1 pyramidal cell layer and 30 (20–55) ms after the eSPW peak in the DG granular layer during spontaneous eSPWs (n = 4 rats; p = 0.029; Figure 72C). During sensory-evoked eSPWs, MUA z-score peaked at −5 (−10–5) ms before the eSPW peak in CA1 pyramidal layer and 45 (25–65) ms after the eSPW peak in DG granular layer (n = 4 rats; p = 0.029; Figure 72C). In one animal, MUA peak times coincided for the pyramidal and granular layers

during spontaneous eSPWs, and the granular layer MUA peak appeared earlier than peak neuronal firing in pyramidal cell layer.

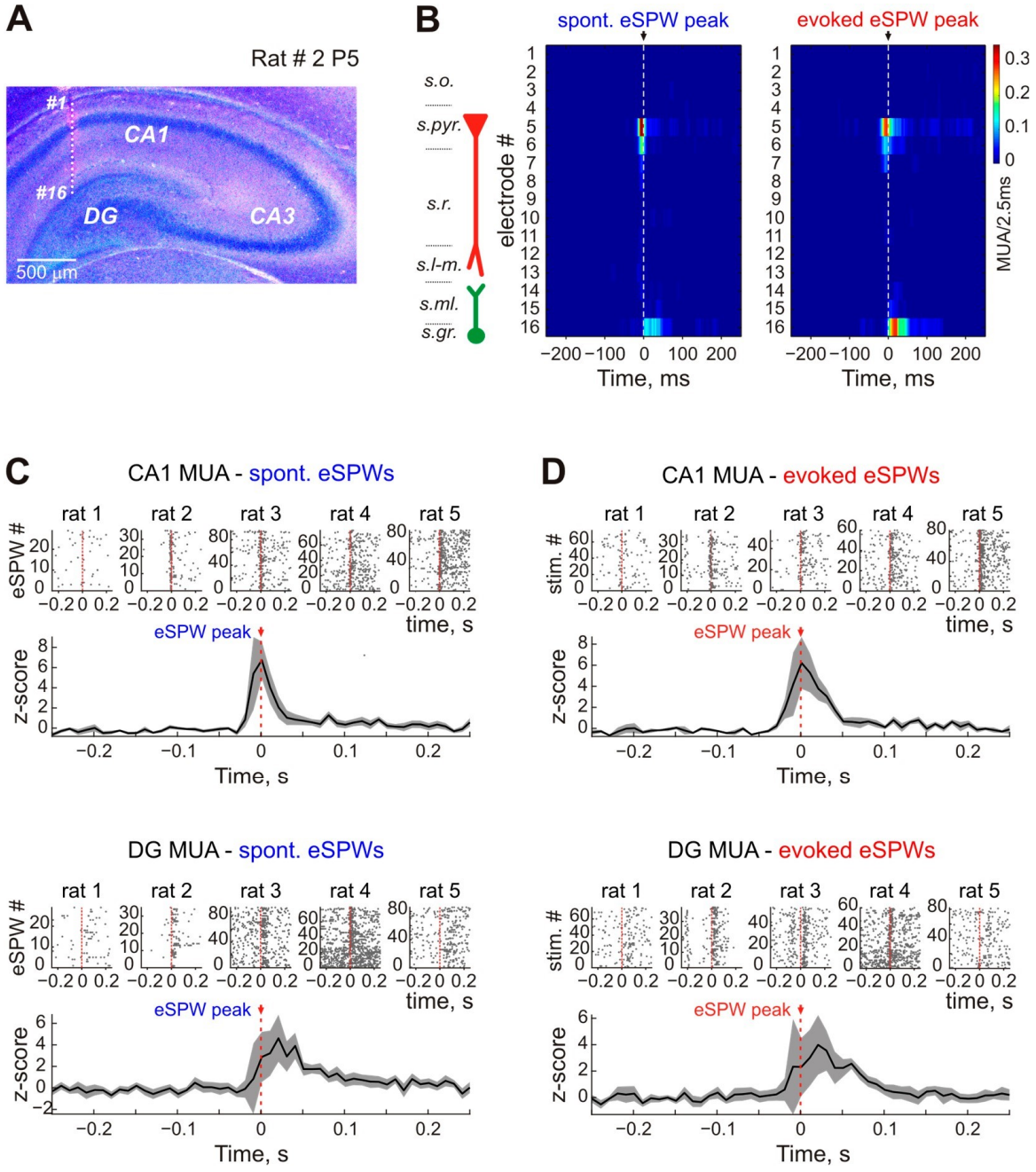

Figure 72. Multiple unit activity (MUA) recorded in CA1 pyramidal cell layer and DG granular cell layer during spontaneous and stimulus-evoked eSPW.

(**A**), Post hoc reconstruction of 16 recording electrode locations across the hippocampal layers of a P5 rat. (**B**), MUA density plots for spontaneous eSPWs and stimulus-evoked eSPW responses. Recording site numbers correspond to those shown in panel A. Hippocampal layer borders are shown on the left—*s.o.*, CA1 str. oriens; *s.pyr.*, str. pyramidale; *s.r.*, str. radiatum; *s.l-m.*, str. lacunosum-moleculare; *s.ml.*, DG str. moleculare; *s.gr.*, DG str. granulosum. (**C**,**D**), Raster plots and average PETHs for MUA detected in CA1 s. pyr. (**top**) and DG s. gr. (**bottom**) during spontaneous eSPWs (**C**) and stimulus-evoked eSPW responses (**D**).

4.1.4. Discussion

In the present study, we explored somatosensory-evoked responses in the hippocampus of neonatal rats after suppression of motor startle responses under urethane anesthesia. We found that somatosensory stimulation triggers ample hippocampal responses with spatiotemporal characteristics identical to spontaneous eSPWs, including CSD profiles, suggesting involvement of temporoammonic and perforant inputs from EC and Schaffer collateral input from CA3 as well as global activation of CA1 and DG neurons. These findings support the hypothesis that sensory feedback from movements is involved in eSPW binding to myoclonic movements in neonatal rats. The results of our study also highlight an important developmental difference in somatosensory-evoked hippocampal responses, likely reflecting the delayed development of inhibitory hippocampal circuits.

Previous studies hypothesized that binding of eSPWs with myoclonic movements involves reafferentation by sensory (tactile and proprioceptive) feedback activated during spontaneous myoclonic movements, which occur in the neonatal rodents during active sleep [1,4,6,21]. Neonatal myoclonic movements have been previously shown to evoke bottom-up neuronal activation along the somatosensory pathways, including the dorsal layers of the spinal cord, relay thalamus, primary somatosensory cortex and hippocampus [11,13,15,21,30–33]. However, whether somatosensory signals can reach the hippocampus remained hypothetical. In the present study, we found that direct somatosensory stimulation reliably evoked hippocampal eSPWs even after suppression of motor startle responses under urethane anesthesia. These findings directly indicate that somatosensory signals indeed can reach the neonatal hippocampus, thus supporting the network model of eSPWs in which sensory feedback from movements triggers hippocampal eSPWs. Importantly, sensory input is not an obligatory condition for the occurrence of eSPWs. In fact, eSPWs may arise spontaneously without any accompanying movements in behaving pups [6], as well as during quiet sleep-like state in immobilized pups under urethane anesthesia (Ref. [2] and the present study). Moreover, eSPWs become less frequent and dissociate from myoclonic movements but persist in the "cerveau isole" preparation following a supracollicular transection that severs external inputs [8]. Hence, eSPWs are events that are generated internally, and sensory input only serves as a trigger for their occurrence.

CSD analysis revealed similarities in the generative mechanisms of spontaneous and somatosensory-evoked eSPWs, including an involvement of extrinsic (from EC to CA1 and DG) and intrahippocampal (from CA3 to CA1) inputs in eSPW generation. While eSPWs' Sink 1 in CA1 *str. radiatum* (presumably generated by CA3–CA1 Schaffer collateral synapses) was consistent with previous studies [3, 6], the previously described eSPWs' Sink 2 near the fissure was actually composed of two sinks clearly separated by the hippocampal fissure: Sink 2 in CA1 *str. lacunosum-moleculare* (presumably generated by EC L3 ⇒ CA1 synapses on distal dendrites of CA1 pyramidal cells) and Sink 3 in DG *str. moleculare* (presumably generated by EC L2 ⇒ DG synapses on dendrites of DG granular cells). These findings align with co-activation of EC L2 and L3 neurons during population

bursts, which are generated in EC following myoclonic movements and precede hippocampal eSPWs [6, 34]. Additionally, in this study, DG Sink 3 was delayed from Sink 2 in CA1 *str. lacunosum-moleculare*, along with delayed activation of DG units from CA1 units, which differs from the more synchronous DG and CA1 neuronal discharge during eSPWs reported previously [6]. This suggests that EC layer 2 discharge is delayed from L3 during EC population bursts driving eSPWs, possibly due to the use of urethane in the present study. The delayed activation of the perforant pathway from the temporoammonic pathway may also explain delayed discharge of DG-driven CA3 neurons, as reflected by the delayed CA1 *str. radiatum* Sink 1 from str. *lacunosum-moleculare* Sink 2. Regardless of these differences, there was a good correspondence in CSD profiles and neuronal activation in CA1 and DG during both spontaneous and sensory-evoked eSPWs.

Somatosensory-evoked eSPWs described in the present study share many common features with somatosensory-evoked hippocampal responses in adult animals but also display important developmental differences. In adults, sensory stimulation in different modalities evokes LFP responses and modulates neuronal activity both in the hippocampus and DG [23–28]. The most prominent sinks of sensory-evoked responses are located in DG *str. moleculare* along with a less consistent sink in CA1 *str. lacunosum-moleculare*, which correspond to Sinks 3 and 2 of the sensory-evoked eSPWs of the present study, respectively [23, 24]. This suggests that sensory-evoked responses involve activation of EC layers 2 and 3 both in neonates and adults. However, sensory responses in adults lack the sink in CA1 *str. radiatum*, which is characteristic of eSPWs in neonates, suggesting that CA3 ⇒ CA1 Schaffer collateral synapses are not activated during sensory responses in adults. This is in line with the global inhibition exerted by perforant input on CA3 neurons [35]. Additionally, neuronal activation during sensory responses is observed in adults as well as in neonates in DG [23, 24]. Yet, CA1 units show variable change in firing with predominantly inhibitory response to sensory stimuli, which is associated with GABAergic hyperpolarization in the majority of CA1 pyramidal neurons [23]. The mechanisms underlying developmental transition of somatosensory-evoked responses from eSPWs, which are generated by feedforward excitation in entorhinal–hippocampal and intrahippocampal circuits, to more sparse and variable responses in adults remain unknown. A likely candidate is the delayed development of hippocampal inhibitory circuits [10, 36–42], which may explain the lack of CA3 activation in adults as a result of feedforward CA3 inhibition by inputs from DG and inhibition of the majority of CA1 units during sensory-evoked response.

In conclusion, results of the present study support the hypothesis that somatosensory feedback is involved in binding hippocampal eSPWs with myoclonic movements in neonatal rats. By providing sequential activation of all major synaptic pathways and

"causality" in the timing of activation of pre- and postsynaptic elements within the largescale bottom-up circuit processing somatosensory information, such mode of function, supported by spontaneous movements, may serve for the activity-dependent formation of these circuits [1,43–48].

4.1.5. Materials and Methods

Wistar rats of either sex from postnatal days (P) 5–6 were used. Preparation of the animals for recordings was performed under isoflurane anesthesia. Recordings were performed from head-restrained urethane-anesthetized rats (1.3–1.5 g/kg). A metal ring was fixed to the skull with a self-curing acrylic denture repair material (Meliodent RR, Kulzer, GmbH, Hanau, Germany) and via ball-joint to a magnetic stand. Animals were surrounded by a cotton nest and heated via a thermal pad (35–37 °C) throughout the recording session.

Extracellular recordings of local field potentials (LFPs) and multiple unit activity

(MUA) were performed along the CA1–dentate gyrus axis of left dorsal hippocampus using a 16-site linear silicon probes with 50 μm separation distance between the electrodes (NeuroNexus, Ann Arbor, MI, USA). DiI-coated silicone probes were placed using stereotaxic coordinates [49]. A chlorided silver wire inserted into occipital or frontal cortex served as a ground electrode. Signals from extracellular recordings were amplified and filtered (×10,000; 0.15–4 kHz) using a Digital Lynx SX amplifier (Neuralynx, Bozeman, MT, USA) and digitized at 32 kHz. One recording session lasted from 30 min to an hour. Somatosensory stimulation was applied to the right whiskerpad, forelimb or hindlimb via a pair of stainless-steel subcutaneous needle electrodes. Square current pulses of 4–7 mA (50 μs duration) were generated by a Master-8 stimulator (A.M.P.I., Jerusalem, Israel) with a 10–20 s interpulse interval. Body movement recordings were performed using piezoelectric sensors attached to both forelimbs and a hindlimb.

After recordings, the animals were deeply anesthetized with urethane (3 g/kg, intraperitoneally). The brains were removed and left for fixation in 4% paraformaldehyde and 1% glutaraldehyde (Sigma-Aldrich, Steinheim, Germany) solution for a few days.

Next, 100 μm-thick coronal slices were cut using a Vibratome (Thermo Fisher Scientific, Waltham, MA, USA). Probe positions were identified from the DiI tracks overlaid on the microphotographs of hippocampal sections after cresyl violet staining. The recording site locations was verified by the highest MUA rate in CA1 str. pyramidale and LFP polarity reversion observed during eSPWs across the CA1 str. pyramidale/str. radiatum border.

Electrophysiological data processing and analysis were performed as described previously [6, 15, 30]. In brief, wideband recordings were preprocessed using custom-written functions in MATLAB (MathWorks, Natick, MA, USA). eSPWs were detected semi-automatically from down-sampled (1000 Hz), bandpass filtered (1–100 Hz, Chebyshev Type 2 Filter) LFP signals. First, the filtered LFP signal from the channel located in CA1 pyramidal cell layer (positive LFP signal during eSPWs) was subtracted from the LFP trace recorded from the channel in *str. lacunosum-moleculare* (the most negative LFP signal during eSPWs). In the resulting trace, all events reaching an amplitude greater than 3 standard deviations were considered as putative eSPWs. Afterwards, LFP segments of the original 16-channel recording from −1 s to 1 around the putative eSPW were visually inspected to select eSPWs. eSPW amplitude and half-width was estimated using the trace

resulting from LFP subtraction between channels located in *str. lacunosum-moleculare* and *str. pyramidale*.

To eliminate volume conductance and localize synaptic currents, CSD analysis across depth was performed on LFP traces normalized to the maximum amplitude signal across all channels and averaged across events. CSD was computed for each recording site according to a differential scheme for second derivative and smoothed with a triangular kernel of length 3 [50]. For MUA analysis, we considered five animals showing well-detectable and stable neuronal firing in pyramidal and granular layers throughout the length of recording session. For MUA detection, raw data were filtered using a 200–1000 Hz bandpass filter and spikes were detected as negative events exceeding 1.8–3 standard deviations (STD) of the filtered signal. STD was calculated individually for each of 16 recording channels. Normalized MUA z-scores were calculated as z-score = $(x-\mu)/\sigma$, where x—MUA PETH value, μ—mean value and σ—standard deviation.

Statistical analysis was performed using the MATLAB Statistics toolbox. Statistical comparisons were carried out using paired-sample Wilcoxon signed-rank and Mann–Whitney tests. A *p*-value of less than 0.05 was considered significant. Group data are presented as median (first quartile–third quartile).

Author Contributions: Conceptualization, R.K. and G.V.; methodology, R.K., G.V., M.S. and L.F.; software, M.S., A.G. and A.N.; validation, G.V. and R.K.; formal analysis, A.G., M.S., A.N, D.S., G.V. and R.K.; investigation, G.V., D.S., M.S. and L.F.; resources, G.V. and R.K.; data curation, A.G. and G.V.; writing—original draft preparation, G.V. and R.K.; writing—review and editing, G.V., R.K., A.G., A.N, D.S., L.F. and M.S.; visualization, A.G. and G.V.; supervision, G.V. and R.K.; project administration, G.V.; funding acquisition, G.V. All authors have read and agreed to the published version of the manuscript.

Funding: This research was funded by the Russian Science Foundation, grant number 21-75-10033.

Institutional Review Board Statement: The study was conducted in accordance with the Declaration of Helsinki and approved by the Ethics Committee of Kazan Federal University (#24/22.09.2020).

Data Availability Statement: Original and processed data and signal processing and analysis routines are available on request from the authors.

Conflicts of Interest: The authors declare no conflict of interest.

4.1.6. References

1. Cossart, R.; Khazipov, R. How development sculpts hippocampal circuits and function. *Physiol. Rev.* **2022**, *102*, 343–378. https://doi.org/10.1152/physrev.00044.2020

2. Leinekugel, X.; Khazipov, R.; Cannon, R.; Hirase, H.; Ben Ari, Y.; Buzsaki, G. Correlated bursts of activity in the neonatal hippocampus in vivo. *Science* **2002**, *296*, 2049–2052. https://doi.org/10.1126/science.1071111

3. Marguet, S.L.; Le-Schulte, V.T.; Merseburg, A.; Neu, A.; Eichler, R.; Jakovcevski, I.; Ivanov, A.; Hanganu-Opatz, I.L.; Bernard, C.; Morellini, F.; et al., Treatment during a vulnerable developmental period rescues a genetic epilepsy. *Nat. Med.* **2015**, *21*, 1436–1444. https://doi.org/10.1038/nm.3987

4. Mohns, E.J.; Blumberg, M.S. Synchronous bursts of neuronal activity in the developing hippocampus: Modulation by active sleep and association with emerging gamma and theta rhythms. *J. Neurosci.* **2008**, *28*, 10134–10144. https://doi.org/10.1523/JNEUROSCI.1967-08.2008

5. Mohns, E.J.; Karlsson, K.A.; Blumberg, M.S. Developmental emergence of transient and persistent hippocampal events and oscillations and their association with infant seizure susceptibility. *Eur. J. Neurosci.* **2007**, *26*, 2719–2730. https://doi.org/10.1111/j.1460-9568.2007.05928.x

6. Valeeva, G.; Janackova, S.; Nasretdinov, A.; Rychkova, V.; Makarov, R.; Holmes, G.L.; Khazipov, R.; Lenck-Santini, P.P. Emergence of Coordinated Activity in the Developing Entorhinal-Hippocampal Network. *Cereb. Cortex* **2019**, *29*, 906–920. https://doi.org/10.1093/cercor/bhy309

7. Buzsaki, G. Hippocampal sharp wave-ripple: A cognitive biomarker for episodic memory and planning. *Hippocampus* **2015**, *25*, 1073–1188. https://doi.org/10.1002/hipo.22488

8. Karlsson, K.A.; Mohns, E.J.; di Prisco, G.V.; Blumberg, M.S. On the co-occurrence of startles and hippocampal sharp waves in newborn rats. *Hippocampus* **2006**, *16*, 959–965. https://doi.org/10.1002/hipo.20224

9. Leprince, E.; Dard, R.F.; Mortet, S.; Filippi, C.; Giorgi-Kurz, M.; Bourboulou, R.; Lenck-Santini, P.P.; Picardo, M.A.; Bocchio, M.; Baude, A.; et al., Extrinsic control of the early postnatal CA1 hippocampal circuits. *Neuron* **2023**, *111*, 888–902.e8. https://doi.org/10.1016/j.neuron.2022.12.013

10. Dard, R.F.; Leprince, E.; Denis, J.; Rao Balappa, S.; Suchkov, D.; Boyce, R.; Lopez, C.; Giorgi-Kurz, M.; Szwagier, T.; Dumont, T.; et al., The rapid developmental rise of somatic inhibition disengages hippocampal dynamics from self-motion. *eLife* **2022**, *11*, e78116. https://doi.org/10.7554/eLife.78116

11. Inacio, A.R.; Nasretdinov, A.; Lebedeva, J.; Khazipov, R. Sensory feedback synchronizes motor and sensory neuronal networks in the neonatal rat spinal cord. *Nat. Commun.* **2016**, *7*, 13060. https://doi.org/10.1038/ncomms13060

12. Petersson, P.; Waldenstrom, A.; Fahraeus, C.; Schouenborg, J. Spontaneous muscle twitches during sleep guide spinal selforganization. *Nature* **2003**, *424*, 72–75. https://doi.org/10.1038/nature01719

13. Akhmetshina, D.; Nasretdinov, A.; Zakharov, A.; Valeeva, G.; Khazipov, R. The Nature of the Sensory Input to the Neonatal Rat Barrel Cortex. *J. Neurosci.* **2016**, *36*, 9922–9932. https://doi.org/10.1523/JNEUROSCI.1781-16.2016

14. Dooley, J.C.; Glanz, R.M.; Sokoloff, G.; Blumberg, M.S. Self-Generated Whisker Movements Drive State-Dependent Sensory Input to Developing Barrel Cortex. *Curr. Biol.* **2020**, *30*, 2404–2410. https://doi.org/10.1016/j.cub.2020.04.045

15. Khazipov, R.; Sirota, A.; Leinekugel, X.; Holmes, G.L.; Ben Ari, Y.; Buzsaki, G. Early motor activity drives spindle bursts in the developing somatosensory cortex. *Nature* **2004**, *432*, 758–761. https://doi.org/10.1038/nature03132

16. McVea, D.A.; Mohajerani, M.H.; Murphy, T.H. Voltage-sensitive dye imaging reveals dynamic spatiotemporal properties of cortical activity after spontaneous muscle twitches in the newborn rat. *J. Neurosci.* **2012**, *32*, 10982–10994. https://doi.org/10.1523/JNEUROSCI.1322-12.2012

17. Colonnese, M.T.; Kaminska, A.; Minlebaev, M.; Milh, M.; Bloem, B.; Lescure, S.; Moriette, G.; Chiron, C.; Ben-Ari, Y.; Khazipov, R. A conserved switch in sensory processing prepares developing neocortex for vision. *Neuron* **2010**, *67*, 480–498. https://doi.org/10.1016/j.neuron.2010.07.015

18. Khazipov, R.; Milh, M. Early patterns of activity in the developing cortex: Focus on the sensorimotor system. *Semin. Cell Dev. Biol.* **2018**, *76*, 120–129. https://doi.org/10.1016/j.semcdb.2017.09.014

19. Khazipov, R.; Luhmann, H.J. Early patterns of electrical activity in the developing cerebral cortex of humans and rodents. *Trends Neurosci.* **2006**, *29*, 414–418. https://doi.org/10.1016/j.tins.2006.05.007

20. Luhmann, H.J.; Khazipov, R. Neuronal activity patterns in the developing barrel cortex. *Neuroscience* **2018**, *368*, 256–267. https://doi.org/10.1016/j.neuroscience.2017.05.025

21. Mohns, E.J.; Blumberg, M.S. Neocortical activation of the hippocampus during sleep in infant rats. *J. Neurosci.* **2010**, *30*, 3438–3449. https://doi.org/10.1523/JNEUROSCI.4832-09.2010

22. Buzsaki, G.; Moser, E.I. Memory, navigation and theta rhythm in the hippocampal-entorhinal system. *Nat. Neurosci.* **2013**, *16*, 130–138. https://doi.org/10.1038/nn.3304

23. Bellistri, E.; Aguilar, J.; Brotons-Mas, J.R.; Foffani, G.; de la Prida, L.M. Basic properties of somatosensory-evoked responses in the dorsal hippocampus of the rat. *J. Physiol.* **2013**, *591*, 2667–2686. https://doi.org/10.1113/jphysiol.2013.251892

24. Brankack, J.; Buzsaki, G. Hippocampal responses evoked by tooth pulp and acoustic stimulation: Depth profiles and effect of behavior. *Brain Res.* **1986**, *378*, 303–314. https://doi.org/10.1016/0006-8993(86)90933-9

25. Deadwyler, S.A.; West, M.O.; Robinson, J.H. Entorhinal and septal inputs differentially control sensory-evoked responses in the rat dentate gyrus. *Science* **1981**, *211*, 1181–1183. https://doi.org/10.1126/science.7466392

26. O'Keefe, J.; Krupic, J. Do hippocampal pyramidal cells respond to nonspatial stimuli? *Physiol. Rev.* **2021**, *101*, 1427–1456. https://doi.org/10.1152/physrev.00014.2020

27. Pereira, A.; Ribeiro, S.; Wiest, M.; Moore, L.C.; Pantoja, J.; Lin, S.C.; Nicolelis, M.A. Processing of tactile information by the hippocampus. *Proc. Natl. Acad. Sci. USA* **2007**, *104*, 18286–18291. https://doi.org/10.1073/pnas.0708611104

28. Vinogradova, O.S. Hippocampus as comparator: Role of the two input and two output systems of the hippocampus in selection and registration of information. *Hippocampus* **2001**, *11*, 578–598. https://doi.org/10.1002/hipo.1073

29. Valeeva, G.; Nasretdinov, A.; Rychkova, V.; Khazipov, R. Bilateral Synchronization of Hippocampal Early Sharp Waves in Neonatal Rats. *Front. Cell. Neurosci.* **2019**, *13*, 29. https://doi.org/10.3389/fncel.2019.00029

30. Minlebaev, M.; Colonnese, M.; Tsintsadze, T.; Sirota, A.; Khazipov, R. Early gamma oscillations synchronize developing thalamus and cortex. *Science* **2011**, *334*, 226–229. https://doi.org/10.1126/science.1210574

31. Tiriac, A.; Uitermarkt, B.D.; Fanning, A.S.; Sokoloff, G.; Blumberg, M.S. Rapid whisker movements in sleeping newborn rats. *Curr. Biol.* **2012**, *22*, 2075–2080. https://doi.org/10.1016/j.cub.2012.09.009

32. Yang, J.W.; An, S.; Sun, J.J.; Reyes-Puerta, V.; Kindler, J.; Berger, T.; Kilb, W.; Luhmann, H.J. Thalamic Network Oscillations Synchronize Ontogenetic Columns in the Newborn Rat Barrel Cortex. *Cereb. Cortex* **2013**, *23*, 1299–1316. https://doi.org/10.1093/cercor/bhs103

33. Yang, J.W.; Hanganu-Opatz, I.L.; Sun, J.J.; Luhmann, H.J. Three patterns of oscillatory activity differentially synchronize developing neocortical networks in vivo. *J. Neurosci.* **2009**, *29*, 9011–9025. https://doi.org/10.1523/JNEUROSCI.5646-08.2009

34. Unichenko, P.; Yang, J.W.; Luhmann, H.J.; Kirischuk, S. Glutamatergic system controls synchronization of spontaneous neuronal activity in the murine neonatal entorhinal cortex. *Pflug. Arch.* **2015**, *467*, 1565–1575. https://doi.org/10.1007/s00424-014-1600-5

35. Bragin, A.; Jando, G.; Nadasdy, Z.; van Landeghem, M.; Buzsaki, G. Dentate EEG spikes and associated interneuronal population bursts in the hippocampal hilar region of the rat. *J. Neurophysiol.* **1995**, *73*, 1691–1705. https://doi.org/10.1152/jn.1995.73.4.1691

36. Doischer, D.; Hosp, J.A.; Yanagawa, Y.; Obata, K.; Jonas, P.; Vida, I.; Bartos, M. Postnatal differentiation of basket cells from slow to fast signaling devices. *J. Neurosci.* **2008**, *28*, 12956–12968. https://doi.org/10.1523/JNEUROSCI.2890-08.2008

37. Khazipov, R.; Minlebaev, M.; Valeeva, G. Early gamma oscillations. *Neuroscience* **2013**, *250*, 240–252. https://doi.org/10.1016/j.neuroscience.2013.07.019

38. Le, M.C.; Monyer, H. GABAergic interneurons shape the functional maturation of the cortex. *Neuron* **2013**, *77*, 388–405. https://doi.org/10.1016/j.neuron.2013.01.011

39. Pelkey, K.A.; Chittajallu, R.; Craig, M.T.; Tricoire, L.; Wester, J.C.; McBain, C.J. Hippocampal GABAergic Inhibitory Interneurons. *Physiol. Rev.* **2017**, *97*, 1619–1747. https://doi.org/10.1152/physrev.00007.2017

40. Ben Ari, Y.; Gaiarsa, J.L.; Tyzio, R.; Khazipov, R. GABA: A Pioneer Transmitter That Excites Immature Neurons and Generates Primitive Oscillations. *Physiol. Rev.* **2007**, *87*, 1215–1284. https://doi.org/10.1152/physrev.00017.2006

41. Murata, Y.; Colonnese, M.T. GABAergic interneurons excite neonatal hippocampus in vivo. *Sci. Adv.* **2020**, *6*, eaba1430. https://doi.org/10.1126/sciadv.aba1430

42. Graf, J.; Zhang, C.; Marguet, S.L.; Herrmann, T.; Flossmann, T.; Hinsch, R.; Rahmati, V.; Guenther, M.; Frahm, C.; Urbach, A.; et al., A limited role of NKCC1 in telencephalic glutamatergic neurons for developing hippocampal network dynamics and behavior. *Proc. Natl. Acad. Sci. USA* **2021**, *118*, e2014784118. https://doi.org/10.1073/pnas.2014784118

43. Donato, F.; Jacobsen, R.I.; Moser, M.B.; Moser, E.I. Stellate cells drive maturation of the entorhinal-hippocampal circuit. *Science* **2017**, *355*, eaai8178. https://doi.org/10.1126/science.aai8178

44. Kasyanov, A.M.; Safiulina, V.F.; Voronin, L.L.; Cherubini, E. GABA-mediated giant depolarizing potentials as coincidence detectors for enhancing synaptic efficacy in the developing hippocampus. *Proc. Natl. Acad. Sci. USA* **2004**, *101*, 3967–3972. https://doi.org/10.1073/pnas.0305974101

45. Durand, G.M.; Kovalchuk, Y.; Konnerth, A. Long-term potentiation and functional synapse induction in developing hippocampus. *Nature* **1996**, *381*, 71–75. https://doi.org/10.1038/381071a0

46. Groc, L.; Petanjek, Z.; Gustafsson, B.; Ben Ari, Y.; Hanse, E.; Khazipov, R. In vivo blockade of neural activity alters dendritic development of neonatal CA1 pyramidal cells. *Eur. J. Neurosci.* **2002**, *16*, 1931–1938. https://doi.org/10.1046/j.1460-9568.2002.02264.x

47. Ben-Ari, Y.; Khazipov, R.; Leinekugel, X.; Caillard, O.; Gaïarsa, J.-L. $GABA_A$, NMDA and AMPA receptors: A developmentally regulated 'ménage a trois'. *Trends Neurosci.* **1997**, *20*, 523–529. https://doi.org/10.1016/S0166-2236(97)01147-8

48. Leinekugel, X.; Medina, I.; Khalilov, I.; Ben-Ari, Y.; Khazipov, R. Ca^{2+} oscillations mediated by the synergistic excitatory actions of $GABA_A$ and NMDA receptors in the neonatal hippocampus. *Neuron* **1997**, *18*, 243–255. https://doi.org/10.1016/S0896-6273(00)80265-2

49. Khazipov, R.; Zaynutdinova, D.; Ogievetsky, E.; Valeeva, G.; Mitrukhina, O.; Manent, J.B.; Represa, A. Atlas of the Postnatal Rat Brain in Stereotaxic Coordinates. *Front. Neuroanat.* **2015**, *9*, 161. https://doi.org/10.3389/fnana.2015.00161

50. Freeman, J.A.; Nicholson, C. Experimental optimization of current source-density technique for anuran cerebellum. *J. Neurophysiol.* **1975**, *38*, 369–382. https://doi.org/10.1152/jn.1975.38.2.369

Disclaimer/Publisher's Note: The statements, opinions and data contained in all publications are solely those of the individual author(s) and contributor(s) and not of MDPI and/or the editor(s). MDPI and/or the editor(s) disclaim responsibility for any injury to people or property resulting from any ideas, methods, instructions or products referred to in the content.

4.2. Article 2. (in preparation) Temporal Window of Integration during Early Sharp Waves in the CA1 hippocampus of neonatal rats

Daria VINOKUROVA [a], Azat GAINUTDINOV [b], Dmitrii SHIPKOV [a], Guzel VALEEVA [a], Roustem KHAZIPOV [a,b*]

[a] Laboratory of Neurobiology, Institute of Fundamental Medicine and Biology, Kazan Federal University, Kazan, 420015 Russia

[b] Aix-Marseille University, INMED, INSERM, Marseille, 13273 France

*** Correspondence:** Roustem Khazipov roustem.khazipov@inserm.fr

ORCID ID: 0000-0002-6763-2841

Running Title: *Synaptic Correlates of the Early Sharp Waves*

4.2.1. Abstract

Early Sharp Waves (eSPWs) are the major pattern of neuronal network activity, primarily driven by excitatory inputs from the entorhinal cortex, in the developing hippocampus of neonatal rodents *in vivo*. While eSPWs are associated with an activation of excitatory and inhibitory postsynaptic currents in CA1 pyramidal cells, relative dynamics of glutamatergic and GABAergic postsynaptic conductances during eSPWs remains largely unknown. Here, addressed this question using concomitant patch-clamp and local field potential recordings (LFP) from CA1 hippocampus of the postnatal day P3 to P7 neonatal rats in vivo. We show that: (i) the time course of glutamatergic conductance activated during eSPWs matches the time course of the negative trough of field eSPWs; (ii) glutamatergic and GABAergic conductances activated during eSPWs are comparable in size, and that (iii) GABAergic currents are delayed from glutamatergic currents by tens of milliseconds during eSPWs, and that this delay decreases during the first postnatal week. Our findings indicate that eSPWs are primarily driven by glutamatergic inputs, and that delayed recruitment of inhibition enables large temporal integration window for summation of glutamatergic inputs during eSPWs in the neonatal CA1 hippocampus.

Keywords: hippocampus, sharp wave, neonatal rat, patch-clamp, excitatory postsynaptic currents, inhibitory postsynaptic currents

4.2.2. Introduction

In the immature hippocampus, a key brain structure involved in learning and memory, neuronal network activity exhibits discontinuous temporal organization, with most neuronal activity synchronized in intermittent bursts (Cossart and Khazipov, 2022).

Initial studies in hippocampal slices from neonatal rodents and primates emphasized early development of GABAergic synapses on CA1 pyramidal cells, prior to formation of glutamatergic synapses (Tyzio et al., 1999; Khazipov et al., 2001). Together with depolarizing and excitatory actions of GABA, which GABA exerts in neonatal slices in vitro, and the pivotal roles of depolarizing GABA in the generation of the hippocampal network discharges during neonatal period, so-called Giant Depolarizing Potentials (GDPs), during which GABAergic conductance dominates over and preceeds glutamatergic conductance (Ben-Ari et al., 1989; Khalilov et al., 2015), this has led to the hypothesis that GABA is the primary excitatory neurotransmitter driving primitive forms of the network activity in the neonatal hippocampus (Ben-Ari et al., 2007).

Subsequent studies also revealed discontinuous temporal organization of activity in the neonatal rodent hippocampus in vivo, with intermittent bursts of activity organized in early sharp waves (eSPWs) (Leinekugel et al., 2002; Karlsson et al., 2006; Marguet et al., 2015; Valeeva and Janackova et al., 2019; Graf et al., 2021; Cossart and Khazipov, 2022; Pochinok et al., 2024). While eSPWs in vivo and GDPs in vitro were initially thought to be homologous patterns, recent studies have challenged this hypothesis by demonstrating the primary role of extrinsic excitatory inputs from the entorhinal cortex (EC) in generation of eSPWs in vivo (Marguet et al., 2015; Valeeva and Janackova et al., 2019; Gainutdinov et al., 2023; Graf et al., 2024; Juzekaeva et al., 2024). Also, several lines of evidence indicated limited roles for excitatory actions of GABA in the neonatal rodent neocortex and hippocampus in vivo (Minlebaev et al., 2007; Kirmse et al., 2015; Valeeva et al., 2016; Graf et al., 2021 but see also Murata and Colonnese, 2020). Recent studies using biphoton calcium imaging have also demonstrated delayed development of perisomatic inhibition after P9-10, which allows global burst activation of CA1 neurons following mycoclonic movements, known to trigger eSPWs in the hippocampus of neonatal rodents during the first postnatal week (Karlsson et al., 2006; Valeeva and Janackova et al., 2019; Dard et al., 2022). Lack of inhibition has also been suggested as a cause of a lack of ripple oscillations during eSPWs in the neonatal rodents (Pochinok et al., 2024). On the other hand, previous studies revealed co-activation of glutamatergic and GABAergic synaptic currents in CA1 pyramidal neurons during eSPWs (Leinekugel et al., 2002). In the present study, we addressed the precise dynamics of excitatory and inhibitory conductances during eSPWs in the neonatal rat CA1 hippocampus and found that glutamatergic conductance is the primary generator of the field eSPWs, and that GABAergic conductance, also activated during eSPWs, is delayed from glutamatergic conductance by tens of milliseconds. We propose that glutamatergic drive to CA1 pyramidal cells is the main generator of eSPWs, and that delayed activation of inhibition, together with a lack of perisomatic, most powerful form of inhibition, enable temporal integration of excitatory inputs and support global burst activation during eSPWs in the neonatal CA1 hippocampus.

4.2.3. Materials and Methods

The animal experiments were carried out in compliance with the ARRIVE guidelines. Animal care and procedures were in accordance with EU Directive 2010/63/EU for animal experiments, and all animal-use protocols were approved by the Local Ethical Committee of Kazan Federal University (#24/22.09.2020).

Wistar rats of both sexes from postnatal days (P) 3-7 were used. For recordings in vivo, preparation of the animals for head-restrained recordings was performed under isoflurane (1.5-2.5%) anesthesia as described previously (Valeeva and Janackova et al., 2019, Khazipov and Holmes, 2003). A metal ring was fixed to the skull by dental cement and to a magnetic stand to restrain the animal head movements, and the animal was placed to the recording rig at a thermal pad (37°C, Warner Instr., USA). 16-channel linear silicon probes with 50 μm separation distance between the electrodes (NeuroNexus, USA) were placed at - 2.1 mm posterior and 1.35 mm lateral from bregma at a depth of 2300–2600 m to record extracellular local field potentials (LFP) and multiple unit activity (MUA) from the dorsal CA1 hippocampus (Figure 74). An Ag/AgCl2 wire was placed in the neocortex to serve as a ground electrode. Electrodes for patch clamp recordings were prepared from borosilicate glass with resistance of 4-7 MOhm when filled with the pipette solution containing Cs-Gluconate 135, MgCl2 2, CaCl2 2, EGTA 1, and HEPES 10 (pH 7.26). Whole-cell recordings were performed using Axapatch-200B amplifier (Molecular Devices, CA, USA) in voltage clamp mode at different holding potentials to enable voltage separation of EPSCs and IPSCs as described previously (Leinekugel et al., 1997; Khalilov et al., 2015). Signals from extracellular and patch-clamp recordings were digitized using using Digital Lynx SX amplifier (Neuralynx, USA; 10,000X; 0.15 Hz – 9 kHz; at 16-32 kHz). From one to two hours of spontaneous activity were recorded from each animal.

After recordings in vivo, the rats were anaesthetized with isoflurane (5%), the brains were removed and fixed in 4% paraformaldehyde and 1% glutaraldehyde during 2 days. 100 μm-thick coronal slices were prepared using Vibratome (Thermo Fisher Scientific, USA), and electrode positions were identified from the DiI tracks overlaid on cresyl violet stained slices.

The electrophysiological data was processed and analyzed in the following way. To standardize the temporal resolution across all recordings, the original signals were resampled to a target sampling frequency of 1000 Hz. Data smoothing was performed using a 20 ms moving average filter to reduce high-frequency noise. Baseline subtraction was applied, defined as the median value of the signal in the interval from -1000 ms to -500 ms before the peak negativity of eSPWs. The data were normalized by dividing each signal by its maximum value. Peak detection was conducted using automatic function to identify the maximum peak amplitude and its corresponding time point. The half-peak value was calculated as 50% of the maximum peak amplitude. The time at which the signal reached the half-peak value during the rising phase (half-rise time: T1/2) was calculated by finding the points closest to the half-peak value before the peak. Statistical analyses were performed to compare electrophysiological parameters between

AMPAergic and GABAergic responses. Non-parametric tests, such as the Mann-Whitney U test, were employed to assess differences between groups due to the potential non-normal distribution of the data. Linear regression models were fitted to explore relationships between variables, and Pearson correlation coefficients were calculated to quantify the strength and direction of linear associations. All statistical data in the text are presented as: Mean value (± standard error). All statistical analyses and visualizations were performed using MATLAB, utilizing built-in functions and custom scripts.

4.2.4. Results

In the present study, we aimed to characterize dynamics of excitation and inhibition in CA1 pyramidal cells during eSPWs in the neonatal rat hippocampus. For this purpose, we performed concomitant whole-cell recordings from CA1 pyramidal cells and recordings of LFPs in the CA1 region of head restrained, anaesthetized rats during postnatal days [P] 3-7. Whole cell recordings were performed using low intracellular chloride (4.2 mM, EGABA ~ -70 mV) solution to enable voltage separation of excitatory and inhibitory synaptic currents. Glutamatergic excitatory postsynaptic currents (EPSCs) were recorded at the reversal potentials of GABAergic currents (-70 mV), whereas GABAergic inhibitory postsynaptic currents (IPSCs) were recorded at the reversal potentials of glutamatergic currents (0 mV). LFP recordings were performed simultaneously at different depths of CA1 using multisite silicon probes (Figure 74). Consistent with previous studies, the activity in CA1 hippocampus of urethane-anaesthetized rat pups was characterized by highly discontinuous temporal organization with activity organized in intermittent eSPWs separated by periods of electrical silence (Leinekugel et al., 2002). eSPWs could be also evoked by somatosensory stimulation as shown previously (Gainutdinov et al., 2023). Example recordings of eSPWs in the CA1 PCL and the SLM, and concomitant whole cell recordings from a CA1 pyramidal cell at -70 mV and 0 mV from a P3 rat are shown in Figure 74. eSPWs were associated with a positive LFP wave in PCL and a strong negativity in SLM. At cellular level, eSPWs were associated with bursts of collective EPSCs and IPSCs, with very few synaptic activities occurring during the periods between eSPWs. As illustrated by typical eSPW example on expanded time scale, EPSCs bursts occurred earlier than IPSCs bursts, with the EPSCs' burst onset typically located before the eSPW's peak, whereas IPSCs' burst onset typically located shortly after the eSPW's peak (Figure 75). The delay of IPSCs' bursts from EPSCs' burst during eSPWs was also evident on average eSPWs referenced to the peak negativity of eSPWs' troughs in SLM (time = 0, green triangle). To estimate the timing of the EPSCs and IPSCs burst onsets, we calculated their half-rise time (T1/2) and then plotted T1/2 against relatively eSPWs peak time (Figure 76). At the population level, the half-rise of EPSCs bursts preceded eSPWs peak by -21.07 (± 20.39) ms, whereas the half-rise of IPSCs bursts followed the eSPWs peak by 17.55 (± 10.15) ms (n=10 cells, P3-7). The delay between IPCSs from EPSCs burst half-rise times was of 38.62 (± 20.31) ms. Interestingly, this delay of inhibition from excitation during eSPWs decreased with age (Figure 77; R= -0.73, p = 0.02; n=10 cells, P3-7).

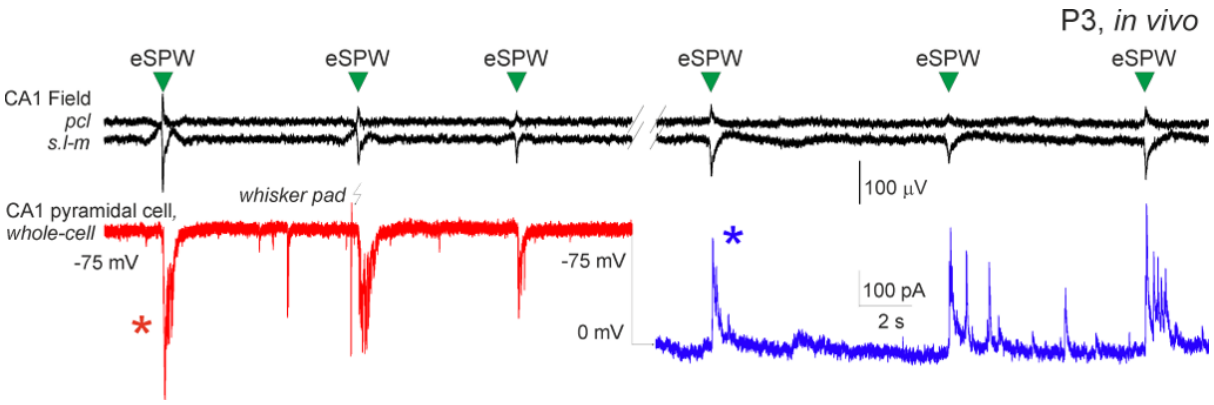

Figure 73. Synaptic correlates of eSPWs.

Concomitant recordings of LFP in CA1 PCL and sl-m (top black traces) and whole-cell recordings of EPSCs (red traces) and IPSCs (blue traces) from a P3 rat. Green triangles indicate eSPWs.

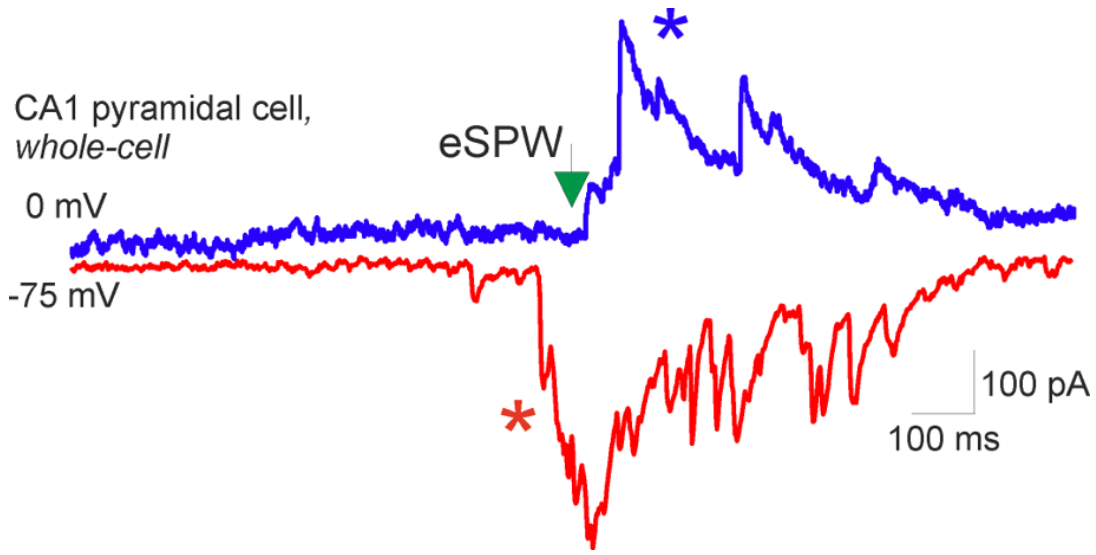

Figure 74. Examples of IPSC and EPSC bursts in a CA1 pyramidal cell during eSPWs.

Traces represent examples marked with asterisks (*) on Figure 73 and aligned to eSPW peak negativity in sl-m (green arrowhead).

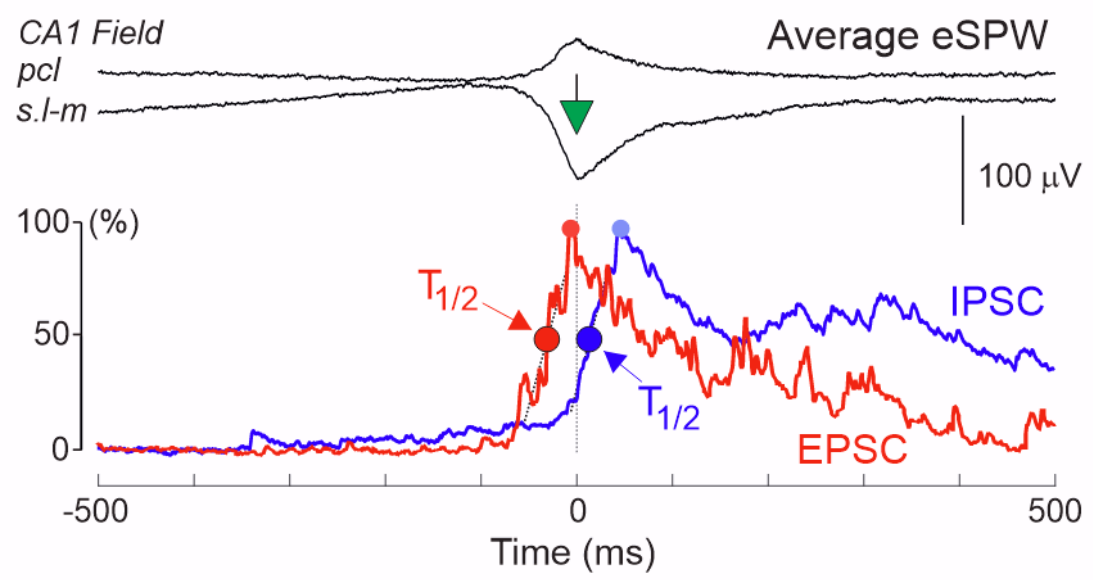

Figure 75. Averaged EPSC and IPSC components of eSPWs.

Normalized EPSC (red) and IPSC (blue) components of eSPWs are averaged with a reference to the peak negativity of eSPWs pek negativity in sl-m (green triangle, eSPW time = 0). T1/2 indicates the half-rise. Data from a P3 rat.

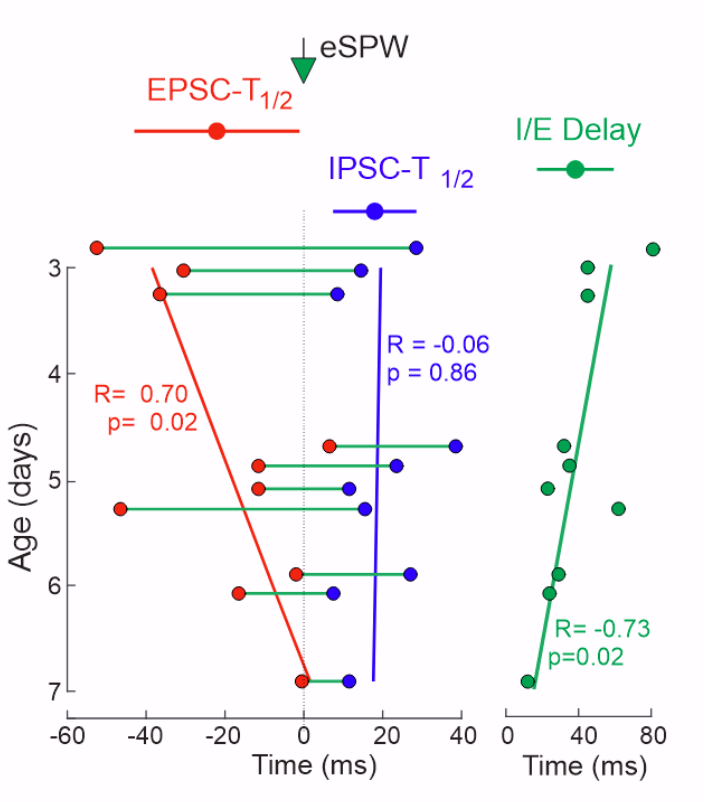

Figure 76. Age-dependence of the EPSC and IPSC components half-rise times.

Left, Green lines connect T1/2 values of EPSC and GABA components in one cell. Values of T1/2 are referenced to eSPW time. Right, corresponding delays of IPSC from EPSC component half-rise times (I-E delay). Colored lines show linear regression, R – coefficient of correlation, p – probability value for the age dependence. Above, mean ± standard error for entire group.

Discussion

The main findings of the present study are that in the neonatal rat CA1 hippocampus, eSPWs are primarily driven by glutamatergic inputs, and that activation of GABAergic inputs is delayed from glutamatergic inputs by tens of milliseconds. We suggest that delayed recruitment of inhibition enables large temporal integration window for integration of excitatory inputs during eSPWs in the neonatal CA1 hippocampus.

We found that glutamatergic synaptic input plays dominant role in eSPWs generation, as evidenced by close match between the EPSC component of eSPWs and eSPWs' LFP waveform. This is in keeping with the pivotal role of excitatory inputs from EC in generation of eSPWs, and a contribution of CA3 inputs with a similar time course to eSPWs (Marguet et al., 2015; Valeeva and Janackova et al., 2019; Gainutdinov et al., 2023; Graf et al., 2024; Juzekaeva et al., 2024). Importantly, the inhibitory component of eSPWs was delayed and typically occurred after the eSPWs peak, suggesting that inhibitory currents play limited role in generating the initial part of eSPWs, but could participate in their termination. Of note, while the magnitude of inhibitory conductance was found to be nearly twice of excitatory conductance, driving force acting on currents through GABA(A) receptors is much smaller than the driving force acting on currents through glutamate receptors (Khalilov et al., 2015). Synaptic correlates of eSPWs described in the present study differ significantly from GDPs both in relative contribution and dynamics of glutamatergic and GABAergic conductances. During GDPs in the hippocampal slices in vitro, GABAergic conductance precedes glutamatergic conductance, and exceeds it by ~30 fold (Khazipov et al., 1997; Leinekugel et al., 1997; Bolea et al., 1999; Lamsa et al., 2000; Mohajerani and Cherubini, 2005; Cherubini et al., 2011; Khalilov et al., 2014; Khalilov et al., 2015). Taken together with the primary involvement of EC input in eSPWs genesis in vivo (while EC input is absent in hippocampal slices in vitro) (Marguet et al., 2015; Valeeva and Janackova et al., 2019; Gainutdinov et al., 2023; Graf et al., 2024; Juzekaeva et al., 2024) and difference in GABA actions on neonatal cortical neurons in these preparations (inhibitory in vivo and mainly excitatory in vitro (Ben-Ari et al., 1989; Minlebaev et al., 2007; Kirmse et al., 2015; Valeeva et al., 2016; Graf et al., 2021) (>P2 in a study Murata and Colonnese, 2020), our results support the idea that eSPWs and GDPs are mechanistically different activity patterns.

Our observations are in line with delayed development of perisomatic inhibition in CA1 hippocampus (Dard et al., 2022; Pochinok et al., 2024), as has also been shown in dentate dyrus (Doischer et al., 2008; Frolova et al., 2023) and neocortex (Daw et al., 2007; Minlebaev et al., 2011), raising a hypothesis that inhibitory currents activated during eSPWs involve dendritic-projecting synapses. In keeping with the pivotal role of perisomatic feedforward inhibition in setting the narrow (few milliseconds long in adults) time window of integration of excitatory inputs (Pouille and Scanziani, 2001), delayed inhibition in the neoanates may enable large (tens of milliseconds long) time window for summation of excitatory inputs to drive global neuronal excitation during eSPWs (Leinekugel et al., 2002; Marguet et al., 2015; Valeeva and Janackova et al., 2019;

Dard et al., 2022), and support plasticity in the developing entorhinal-hippocampal network (Donato et al., 2017).

4.2.5. Author Contributions

RK conceptualized and drafted the manuscript. DV, DS, GV performed the experiments. AG, DV, DS, GV analyzed data. All authors revised the manuscript and interpreted the data.

4.2.6. Funding sources

This research was supported by ANR (grant "HIPPODEV") and RSF (grant #21-75-10033).

4.2.7. Conflict of Interest

The authors declare that the research was conducted in the absence of any commercial or financial relationships that could be construed as a potential conflict of interest.

4.2.8. Data Availability Statement

The datasets generated and analyzed in this study are available on reasonable request from the authors.

4.2.9. References

- Ben-Ari Y, Cherubini E, Corradetti R, Gaïarsa J-L. 1989. Giant synaptic potentials in immature rat CA3 hippocampal neurones. J Physiol (Lond). 416:303-325.
- Ben Ari Y, Gaiarsa JL, Tyzio R, Khazipov R. 2007. GABA: A Pioneer Transmitter That Excites Immature Neurons and Generates Primitive Oscillations. Physiol Rev. 87:1215-1284.
- Bolea S, Avignone E, Berretta N, Sanchez-Andres JV, Cherubini E. 1999. Glutamate controls the induction of GABA-mediated giant depolarizing potentials through AMPA receptors in neonatal rat hippocampal slices [In Process Citation]. J Neurophysiol. 81:2095-2102.
- Cherubini E, Griguoli M, Safiulina V, Lagostena L. 2011. The depolarizing action of GABA controls early network activity in the developing hippocampus. Mol Neurobiol. 43:97-106.
- Cossart R, Khazipov R. 2022. How development sculpts hippocampal circuits and function. Physiol Rev. 102:343-378.
- Dard RF, Leprince E, Denis J, Rao BS, Suchkov D, Boyce R, Lopez C, Giorgi-Kurz M, Szwagier T, Dumont T, Rouault H, Minlebaev M, Baude A, Cossart R, Picardo MA. 2022. The rapid developmental rise of somatic inhibition disengages hippocampal dynamics from self-motion. Elife. 11.

- Daw MI, Ashby MC, Isaac JT. 2007. Coordinated developmental recruitment of latent fast spiking interneurons in layer IV barrel cortex. Nat Neurosci. 10:453-461.
- Doischer D, Hosp JA, Yanagawa Y, Obata K, Jonas P, Vida I, Bartos M. 2008. Postnatal differentiation of basket cells from slow to fast signaling devices. J Neurosci. 28:12956-12968.
- Donato F, Jacobsen RI, Moser MB, Moser EI. 2017. Stellate cells drive maturation of the entorhinal-hippocampal circuit. Science. 355.
- Frolova A, Gainutdinov A, Juzekaeva E, Safeeva L, Valeeva G, Khazipov R. 2023. Development of GABAergic Inhibition Associated with Entorhinal Input in Granular Cells of the Dentate Gyrus. J Evol Biochem Physiol. 59:2390-2398.
- Gainutdinov A, Shipkov D, Sintsov M, Fabrizi L, Nasretdinov A, Khazipov R, Valeeva G. 2023. Somatosensory-Evoked Early Sharp Waves in the Neonatal Rat Hippocampus. Int J Mol Sci. 24.
- Graf J, Samiee A, Flossmann T, Holthoff K, Kirmse K. 2024. Chemogenetic silencing reveals presynaptic G(i/o) protein-mediated inhibition of developing hippocampal synchrony in vivo. iScience. 27:110997.
- Graf J, Zhang CQ, Marguet SL, Herrmann T, Flossmann T, Hinsch R, Rahmati V, Guenther M, Frahm C, Urbach A, Neves RM, Witte OW, Kiebel SJ, Isbrandt D, Hubner CA, Holthoff K, Kirmse K. 2021. A limited role of NKCC1 in telencephalic glutamatergic neurons for developing hippocampal network dynamics and behavior. Proceedings of the National Academy of Sciences of the United States of America. 118:11.
- Juzekaeva E, Nasretdinov A, Mukhtarov M, Shipkov D, Valeeva G, Khazipov R. 2024. Comparison of extracellular Giant depolarizing potentials in vitro and early sharp waves in vivo in the CA1 hippocampus of neonatal rats. Biochem Biophys Res Commun. 735:150823.
- Karlsson KA, Mohns EJ, di Prisco GV, Blumberg MS. 2006. On the co-occurrence of startles and hippocampal sharp waves in newborn rats. Hippocampus. 16:959-965.
- Khalilov I, Leinekugel X, Mukhtarov M, Khazipov R. 2014. Intracellular Blockade of Gaba(A) Receptors in the Rat Hippocampal Neurons. Biologicheskie Membrany. 31:25-32.
- Khalilov I, Minlebaev M, Mukhtarov M, Khazipov R. 2015. Dynamic Changes from Depolarizing to Hyperpolarizing GABAergic Actions during Giant Depolarizing Potentials in the Neonatal Rat Hippocampus. J Neurosci. 35:12635-12642.
- Khazipov R, Esclapez M, Caillard O, Bernard C, Khalilov I, Tyzio R, Hirsch J, Dzhala V, Berger B, Ben-Ari Y. 2001. Early development of neuronal activity in the primate hippocampus in utero. Journal of Neuroscience. 21:9770-9781.
- Khazipov R, Holmes GL. 2003. Synchronization of kainate-induced epileptic activity via GABAergic inhibition in the superfused rat hippocampus in vivo. J Neurosci. 23:5337-5341.

- Khazipov R, Leinekugel X, Khalilov I, Gaïarsa J-L, Ben-Ari Y. 1997. Synchronization of GABAergic interneuronal network in CA3 subfield of neonatal rat hippocampal slices. J Physiol (Lond). 498:763-772.
- Kirmse K, Kummer M, Kovalchuk Y, Witte OW, Garaschuk O, Holthoff K. 2015. GABA depolarizes immature neurons and inhibits network activity in the neonatal neocortex in vivo. Nat Commun. 6:7750.
- Lamsa K, Palva JM, Ruusuvuori E, Kaila K, Taira T. 2000. Synaptic GABA(A) activation inhibits AMPA-kainate receptor-mediated bursting in the newborn (P0-P2) rat hippocampus. J Neurophysiol. 83:359-366.
- Leinekugel X, Khazipov R, Cannon R, Hirase H, Ben Ari Y, Buzsaki G. 2002. Correlated bursts of activity in the neonatal hippocampus in vivo. Science. 296:2049-2052.
- Leinekugel X, Medina I, Khalilov I, Ben-Ari Y, Khazipov R. 1997. Ca2+ oscillations mediated by the synergistic excitatory actions of GABAA and NMDA receptors in the neonatal hippocampus. Neuron. 18:243-255.
- Marguet SL, Le-Schulte VT, Merseburg A, Neu A, Eichler R, Jakovcevski I, Ivanov A, Hanganu-Opatz IL, Bernard C, Morellini F, Isbrandt D. 2015. Treatment during a vulnerable developmental period rescues a genetic epilepsy. Nat Med. 21:1436-1444.
- Minlebaev M, Ben-Ari Y, Khazipov R. 2007. Network mechanisms of spindle-burst oscillations in the neonatal rat barrel cortex in vivo. Journal of Neurophysiology. 97:692-700.
- Minlebaev M, Colonnese M, Tsintsadze T, Sirota A, Khazipov R. 2011. Early gamma oscillations synchronize developing thalamus and cortex. Science. 334:226-229.
- Mohajerani MH, Cherubini E. 2005. Spontaneous recurrent network activity in organotypic rat hippocampal slices. Eur J Neurosci. 22:107-118.
- Murata Y, Colonnese MT. 2020. GABAergic interneurons excite neonatal hippocampus in vivo. Sci Adv. 6:eaba1430.
- Pochinok I, Stober TM, Triesch J, Chini M, Hanganu-Opatz IL. 2024. A developmental increase of inhibition promotes the emergence of hippocampal ripples. Nat Commun. 15:738.
- Pouille F, Scanziani M. 2001. Enforcement of temporal fidelity in pyramidal cells by somatic feed-forward inhibition. Science. 293:1159-1163.
- Shipkov D, Nasretdinov A, Khazipov R, Valeeva G. 2024. Synchronous excitation in the superficial and deep layers of the medial entorhinal cortex precedes early sharp waves in the neonatal rat hippocampus. Front Cell Neurosci. 18:1403073.
- Tyzio R, Represa A, Jorquera I, Ben-Ari Y, Gozlan H, Aniksztejn L. 1999. The establishment of GABAergic and glutamatergic synapses on CA1 pyramidal neurons is sequential and correlates with the development of the apical dendrite. J Neurosci. 19:10372-10382.

- Valeeva G, Janackova S, Nasretdinov A, Rychkova V, Makarov R, Holmes GL, Khazipov R, Lenck-Santini PP. 2019. Emergence of Coordinated Activity in the Developing Entorhinal-Hippocampal Network. Cereb Cortex. 29:906-920.
- Valeeva G, Tressard T, Mukhtarov M, Baude A, Khazipov R. 2016. An Optogenetic Approach for Investigation of Excitatory and Inhibitory Network GABA Actions in Mice Expressing Channelrhodopsin-2 in GABAergic Neurons. J Neurosci. 36:5961-5973.

4.3. Article 3. Development of GABAergic Inhibition Associated with Entorhinal Input in Granular Cells of the Dentate Gyrus

A. Frolova[a], A. Gainutdinov[b], E. Juzekaeva[a], L. Safeeva[a], G. Valeeva[a], and R. Khazipov[a,b,*]
[a]Laboratory of Neurobiology, Kazan Federal University, Kazan, Russia
[b]INMED-INSERM, AixMarseille University, Marseille, France *e-mail: roustem.khazipov@inserm.fr

ISSN 00220930, Journal of Evolutionary Biochemistry and Physiology, 2023, Vol. 59, No. 6, pp. 2390–2398. © Pleiades Publishing, Ltd., 2023. EXPERIMENTAL PAPERS
DOI: 10.1134/S002209302306039X
Received: November 29, 2023;
Revised: December 4, 2023;
Accepted: December 6, 2023
Published: January 9, 2024

4.3.1. Abstract

Granule cells (GC) in the dentate gyrus receive main excitatory input from the entorhinal cortex (EC) via the perforant pathway (PP). In adults, this excitatory input is rapidly curtailed by feedforward inhibition, creating a short temporal window for integration of excitatory inputs. However, the delayed maturation and integration of interneurons into the circuitry involved in feedforward inhibition suggests a developmental delay in the inhibition associated with EC input to GCs. Here, we explored developmental changes in inhibition associated with EC input to the GCs using wholecell recordings in postnatal days P2 to P62 mouse hippocampal slices. PP evoked excitatory and inhibitory postsynaptic currents (EPSCs and IPSCs) in the GCs were voltageseparated using a lowchloride pipette solution. Shortlatency EPSCs could be evoked in granule cells from P2, and their delay remained stable during development. In contrast, the delay of IPSCs was highly dependent on age. In the first postnatal week, IPSC delays reached tens of milliseconds and showed high variability across trials. IPSC delays gradually decreased with age to reach adult values by the end of the first postnatal month. The temporal integration window, assessed as a time difference between EPSC and IPSC delays, decreased during the postnatal period. Thus, GABAergic inhibition associated with EC input to GCs undergoes significant changes during postnatal development and enables a large integration window for excitatory EC inputs to GCs during the neonatal period.

Keywords: dentate gyrus, inhibition, inhibitory postsynaptic currents, excitatory postsynaptic currents, entorhinal cortex, neonate

4.3.2. Graphical abstract

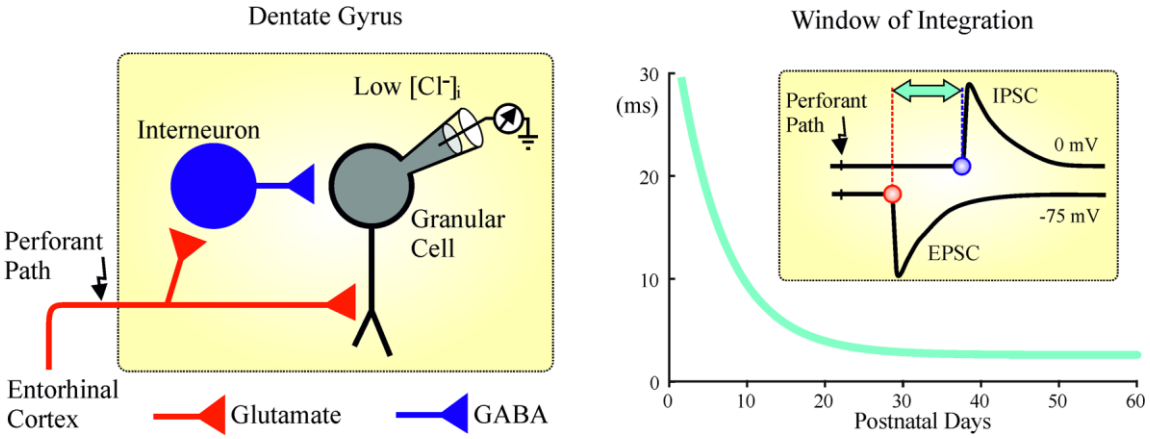

We investigated postnatal developmental changes in the integration window, defined as the delay between excitatory and inhibitory postsynaptic currents evoked by stimulation of the perforant pathway from entorhinal cortex to granular cells of the dentate gyrus. The integration window appears to be long during the neonatal period.

4.3.3. Introduction

Entorhinal cortex (EC), the main source of cortical input to hippocampus, provides an activitydependent instructive signal that drives maturation sequentially and unidirectionally through the intrinsic circuits of the entorhinal–hippocam pal network during the postnatal period [1, 2]. Dentate gyrus, the first relay in the canonical tri synaptic hippocampal circuit [3–6], starts receiv ing cortical input, conveyed through the perforant path (PP), from the EC layer 2 neurons before P3—P4 [7–10]. During the first postnatal week, the input from EC drives robust neuronal activa tion in dentate gyrus with nearly 70% participa tion rate during early sharp waves (eSPWs), the first organized activity pattern in the EChippo campal network [11–16]. However, how develop ing dentate gyrus network processes the inputs originated from EC remains poorly understood.

In adults, EC inputs innervate both the princi pal cells of the DG (GCs) and local interneurons, and monosynaptic excitatory EC input to GCs is rapidly curtailed by inhibition [17, 18]. The delay between excitatory and inhibitory postsynaptic currents (EPSCs and IPSCs), which sets the tem poral window for integration of excitatory inputs, is only few milliseconds long [19]. Because excitation of GCs requires summation of multiple EC inputs, such short window for integration contributes to sparse activation of GCs [20]. GCs start receiving GABAergic inputs from birth, as evi denced by presence of spontaneous IPSCs, often organized in hippocampal CA3—driven giant depolarizing potentials (GDPs) in GCs during the first postnatal week [21–23]. The onset of inhibi tion associated with EC input is less well under stood. Complex synaptic responses to electrical stimulation in the molecular layer of dentate gyrus were reported in GCs starting from P8 [24, 25]. These responses comprised shortlatency mono synaptic EPSCs and IPSCs evoked by stimulation of PP axons and local interneurons, respectively, and

late polysynaptic IPSCs presumably associ ated with activation of the feedforward and back ward inhibitory circuits, whose latency decreased with maturation of GCs over P8–P32 [24]. Con sistent with these observations, PP stimulation evoked robust activation of GCs at P12 but only sparse activation of GCs at P22 and P60, and this developmental sparsification of responses, accompanied by increased temporal precision of activation, were primarily mediated by changes in local circuit inhibition because GABA(A) antago nists normalized developmental differences [26]. These developmental changes are paralleled with a progressive development of perisomaticpro jecting PV interneurons, which are primarily involved in the fast feedforward inhibition [27, 28], over P6–P25 period, which involves maturation of their fast spiking properties and integration into the dentate circuit [29]. Here, we provide further evidence to this hypothesis by showing that delays of IPSC evoked in GCs by stimulation of the EC inputs, and the duration of the temporal integration window are extremely long and vari able, attaining values of tens of milliseconds during the first postnatal week, and that IPSC delays and temporal integration window progres sively reduce upon maturation, attaining adult values only by the end of the first postnatal month.

4.3.4. Materials and methods

The animal experiments were carried out in compliance with the ARRIVE guidelines. C57BL/6 mice of both sexes aged from postnatal days (P)2 to 62 were used. Animals were decapitated under isoflurane anesthesia (5%), the brain was rapidly removed and placed in ice-cold (2–5°C) oxygenated (95% O_2–5% CO_2) artificial cerebrospinal fluid (ACSF) of the following composition (in mM): NaCl 126, KCl 3.5, $CaCl_2$ 2, $MgCl_2$ 1.3, $NaHCO_3$ 25, NaH_2PO_4 1.2, and glucose 11 (pH 7.4). Three hundred fifty μm thick horizontal slices were cut using a PELCO easiSlicer vibratome (Ted Pella, Inc., Redding, CA, USA). Ventral slices containing hippocampal formation were kept in oxygenated ACSF at room temperature (20–22°C) for at least 1 hour before use.

For recordings, slices were placed into a submerged chamber and superfused with oxygenated ACSF at 30–32°C at a flow rate of 10 mL/min. Individual DG granular cells were identified using a vertical microscope (BX51 WI; Olympus, Japan) at 40× magnification using infrared differential interference contrast microscopy (IRDIC). Whole-cell recordings were performed in voltage-clamp mode using electrodes prepared from borosilicate glass with resistance of 4–7 MΩ when filled with the pipette solution of the following composition (in mM): CsGluconate 135, $MgCl_2$ 2, $CaCl_2$ 2, EGTA 1, and HEPES 10 (pH 7.26). E_m values obtained during whole-cell recordings were corrected for the liquid junction potential of 16 mV. Patch-clamp recordings were performed using a MultiClamp 700B (Molecular Devices, USA) amplifier. Recordings were digitized at 10 kHz using a Digidata 1440A interface (Molecular Devices, USA).

For PP stimulation, a bipolar tungsten electrode (Microelectrodes Ltd., UK) was placed adjacent to the hippocampal fissure in the CA_1 stratum lacunosum-moleculare, subiculum, or presubiculum, and two consecutive 50 μs long, ±10–40 mV square pulses were delivered at 10–20 s interstimulus intervals using a Master-8 stimulator (Ampi,

Jerusalem, Israel). Stimulus intensity was set at levels to reliably evoke EPSCs. Notably, stimulus intensity did not show any significant age dependence. Ten to thirty EPSCs were recorded at the IPSC reversal potential (about –75 mV), and then ten to thirty IPSCs were recorded at the EPSC reversal potential (about 0 mV). If the stimulation did not induce EPSCs, recording was stopped, and these cells were excluded from the analysis. Cells with monosynaptic IPSCs occurring within a time window <2 ms from EPSCs, and cells without IPSCs within <100 ms after the stimulus were also excluded from the analysis.

Data were analyzed using Clampfit (Molecular Devices, USA) and custom-written Matlab procedures (MathWorks, Inc., Natick, MA, USA). Preprocessing and preliminary analysis were conducted with the ExpressAnalysis and Eview tools (https://github.com/AndreyZakharovExp). PP-evoked IPSC and EPSC were detected using ExpressAnalysis, visually confirmed in Eview to discard artifacts, and precise onsets were identified as extremums of the second derivative during the rise phase within a 25 ms time window. Statistical analysis was performed using MATLAB routines. For each cell, delays of EPSC and IPSC onsets were analyzed to determine median values and their time jitter assessed by Q_1–Q_3 interquartile range, and temporal integration window, calculated as the difference between the median values of IPSC and EPSC onset delays. Data from individual cells were further analyzed in three age groups: P2-7 (first postnatal week), P8-14 (second postnatal week), and P27-62 (young adult) (n = 15 cells in each age group) and compared using the Mann–Whitney–Wilcoxon nonparametric test for unpaired groups. Age-dependence was also assessed through a regression analysis based on an exponential function providing the regression coefficients (R and p-value). The level of significance was kept at $p < 0.05$.

4.3.5. Results

We used wholecell patchclamp recordings from GCs of the dentate gyrus to explore the developmental changes in the dynamics of inhibi tion associated with the activation of the PP from EC to dentate gyrus. In this aim, lowchloride containing wholecell pipette solution was used for the voltage separation of EPSCs and IPSCs, which were recorded at membrane potentials of –75 mV and 0 mV, respectively. In total, 45 GCs were recorded in dentate gyrus of horizontal hip pocampal slices obtained from 21 mice aged from P2 to P62. Typical synaptic responses evoked by PP stimulation in GCs at different ages (P4, P14 and P60) are shown in Figure 77. At all ages, PP evoked response was characterized by a sequence of short latency EPSCs followed by IPSCs. During the first postnatal week, PP stimulation also evoked network afterdischarges lasting for several hundreds of milliseconds, reminiscent of giant depolarizing potentials (GDPs) (Figure 77a). These afterdischarges were absent in older ani mals (Figure 77c, 1e). For each neuron, EPSC and IPSC onsets after the PP stimulus were detected in each trial and their median values and Q1–Q3 interquartile range, as a metrics of jitter, were cal culated for the further population analysis. As evi denced by examples presented on Figure 77, delay of the PPevoked EPSCs did not significantly differ, whereas IPSC delays after the PP stimulus short ened with age from tens of milliseconds at P4 (Figure 77b) to few milliseconds at

P60 (Figure 77f), and with intermediate value of ~10 ms attained at P14 (Figure 77d), along with a developmental decrease in the time jitter of IPSC delays.

The developmental changes in the timing of the PPevoked EPSC and IPSC delays were further analyzed at the group level. As illustrated by the Figure 78a, the EPSC delays were of [median (Q1–Q3)]: 3.9 (3.0–5.0) ms (n = 45 cells) and although there was a developmental trend towards shorten ing, they did not show any significant change during postnatal maturation ($R2 = 0.06$, $p > 0.05$). In contrast, delays of IPSCs from the PP stimulus in GCs where long and highly variable during the first postnatal week, and they progressively decreased with age ($R2 = 0.53$, $p < 0.001$). For sta tistical comparisons, we divided animals in three age groups: P2-7 (first postnatal week, n = 15 cells), P8-14 (second postnatal week, n = 15 cells) and P27-62 (young adult, n = 15 cells). In the latter group, data from P27-33 and P60-62 mice were not significantly different and therefore were pooled together. IPSC delays attained 19.5 (11.9–23.2) ms at P2-7, and decreased to 10.0 (8.4–12.6) ms at P8-14 ($p < 0.005$), and to 5.6 (4.7–7.0) ms at P27-62 ($p< 0.001$) (Figure 78a). Along with a developmental reduction in IPSC delays, we also observed a reduction in their trial—to trial variability, assessed as a Q1—Q3 interquartile range of the response onset in each individual neuron, with a reduction from 2.9 (1.9–5.7) ms at P27 to 1.2 (0.6–1.5) ms at P8-14 ($p < 0.01$), and to 0.6 (0.3–0.9) ms at P27-62 ($p < 0.001$(Figure 78b; $R2 = 0.22$, $p < 0.01$). In keeping with the developmental reduction in IPSC delays, the duration of the temporal integration window, calculated as a difference between median values of IPSC and EPSC delays, also showed a develop mental decrease ($R2 = 0.53$, $p < 0.0001$), with a reduction from 12.9 (7.9–20.7) ms at P2-7 to 6.0 (4.8–7.5) ms at P8-14 ($p < 0.001$), and to 2.6 (1.5–3.4) ms at P27-62 ($p < 0.0001$) (Figure 78c).

4.3.6. Discussion

In the present study, we aimed to characterize the postnatal changes in the dynamics of inhibi tion associated with EC input to GCs. Our main finding is that during the first postnatal week, delays of IPSC evoked by stimulation of the EC inputs are extremely long and variable, attaining values of tens of milliseconds, and that IPSC latencies gradually decrease along with the inte gration window and reach adult values by the end of the first postnatal month.

Our findings on the delayed maturation of inhi bition within the ECDG circuit are in agreement with previous findings [7–10, 24–26, 29]. Because the temporal integration window is primarily determined by feedforward inhibition provided by the perisomatic projecting PVinterneurons, delayed maturation of their fastspiking properties and their delayed developmental recruitment into the dentate circuitry [29] likely explains long and variable IPSC delays in the neonatal GCs observed in the present study. Interestingly, simi lar delayed development of feedforward inhibition also characterizes development of thalamocorti cal circuit, in which IPSCs are either absent or strongly delayed from EPSCs in barrel cortex during responses evoked by activation of thalamic inputs [30, 31]. Together, these findings raise a hypothesis that delayed development of the feed forward inhibition is a general developmental phenomenon [2, 32], and in the future studies it

would be interesting to verify this hypothesis in other networks including development of inhibi tion associated with EC and CA3 inputs to CA1 hippocampus.

Present findings are important for understand ing the ontogenesis of DG functions. Indeed, delayed recruitment of inhibition to the PP evoked responses in GCs is consistent robust neu ronal activation in dentate gyrus with nearly 70% participation rate during ECdriven eSPWs during the first postnatal week [11–16], and developmental switch from robust to sparse acti vation of GCs in response to PPstimulation during the first postnatal month [26]. The wide temporal window of integration likely contributes to the summation of inputs organized into EC population bursts driving robust DG activation during eSPWs, and thus an integrative mode of function in the developing ECdentate circuitry. Progressive reduction in IPSC delay with age, which attains adult values by the end of the first postnatal month, likely supports a developmental switch from integrative mode to sparse coding, and emergence of the "gating" function of dentate in the entorhinal-hippocampal circuit.

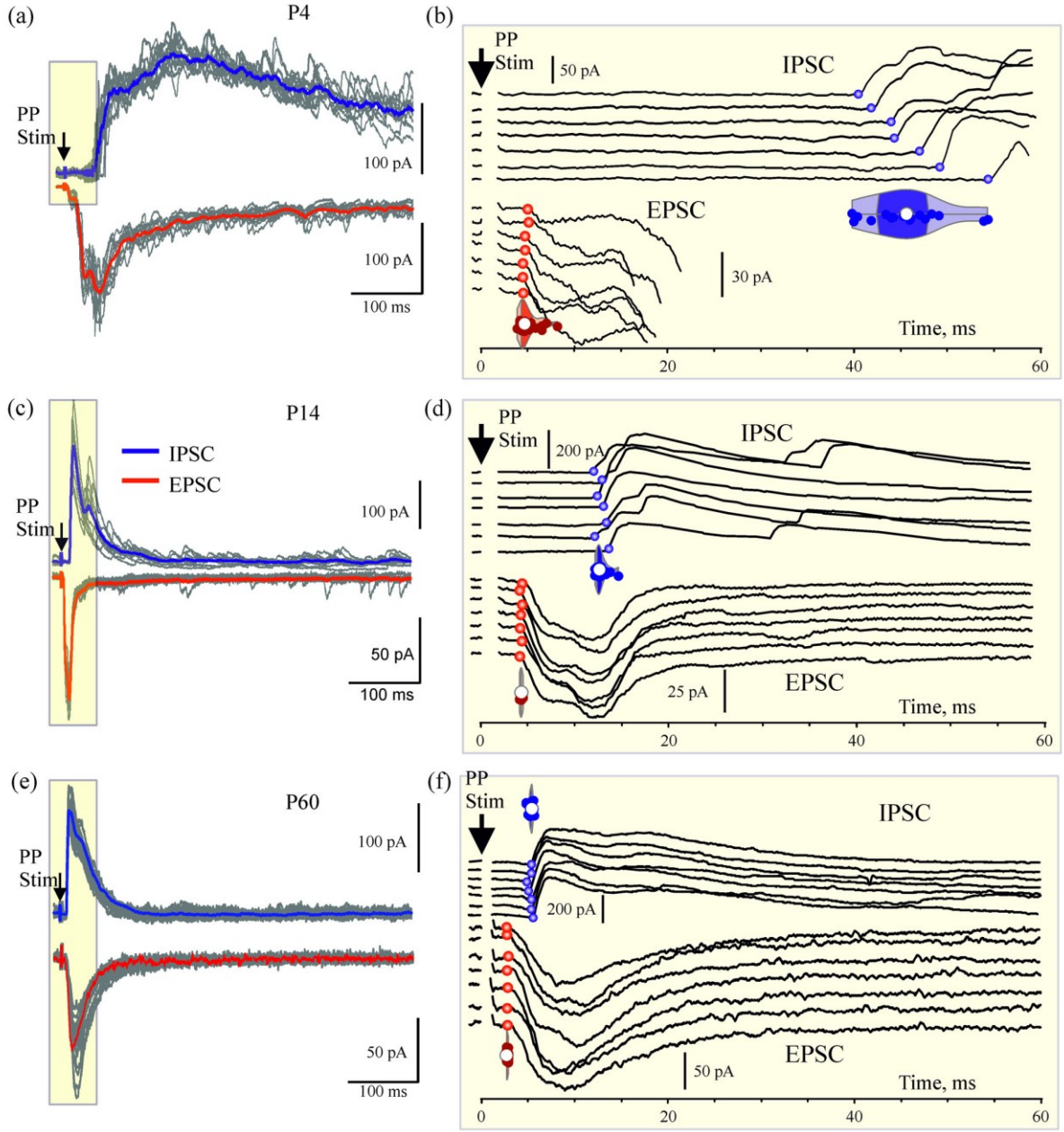

Figure 77. Perforant path stimulationevoked EPSCs and IPSCs in GCs at different postnatal ages.

(a) Example traces of PP evoked IPSCs and EPSCs in a GC from the postnatal day P4 mouse dentate gyrus. IPSCs were recorded at holding potential of 0 mV, which is a reversal potential of EPSCs, and EPSCs, vice versa, were recorded at holding potential of –75 mV, which is a reversal potential of IPSCs. Ten individual responses (grey traces) are superimposed, overlaid by average IPSC (blue trace) and average EPSC (red trace). (b) Early response fragments outlined in yellow box on panel (a) are shown at expanded time scale. Seven randomly selected individual IPSCs (top traces) and EPSCs (bottom traces), circles indicate PSC onset. Violin plots show the probability density distribution of the delays of PSCs onsets from the PP stimulus. Hereafter, violin histograms are smoothed by a kernel density estimator, white dot indicates median, dark area indicates Q1–Q3 interquartile range, each dark dot corresponds to an individual PSC. (c–d) and (e–f) show similar examples of IPSC and EPSC recordings from GCs in P14 (c–d) and P60 (e–f) mice.

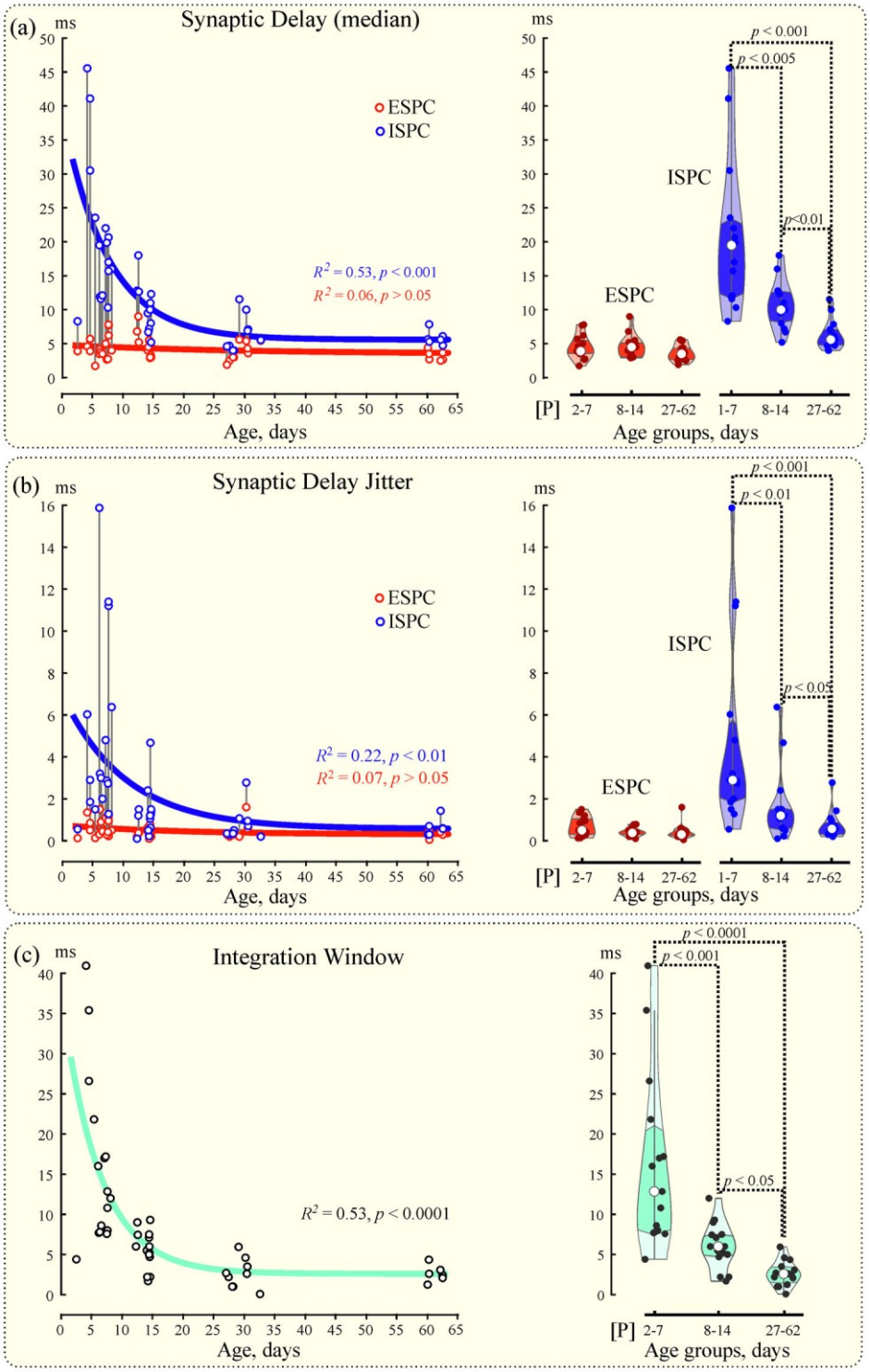

Figure 78. Agedependence of the PPevoked EPSCs and IPCSs delays in GCs.

(a) EPSCs and IPSCs delay medians in GCs as a function of animal age. Each dot corresponds to the median value in an individual GC. Right violin plots show the probability density distribution of the delays of EPSC and IPSC onsets from the PP stimulus in GCs pooled in three age groups: P2-7, P8-14 and P27-62. EPSC delays were not significantly different between the three age groups. (b, c) Similar group data analysis for the time jitter of the PPevoked IPSCs and EPSCs delays, presented as a Q1–Q3 interquartile range (b), and for the tem poral integration window, calculated as a delay of the PPevoked IPSCs from EPSCs (c). (a–c): Pooled data from 45 granular cells (n = 15 cells in each age group).

4.3.7. Authors' contribution

Conceptualization: RK, GV. Investigation and data analysis: AF, EJ, LS, AG. Supervision: RK, GV. Writing original draft: RK. Writing review and editing: AF, AG, LS, EJ, GV, RK. All authors have read and agreed to the published version of the manuscript.

4.3.8. Funding

This research was supported by the Russian Science Foundation (grant no. 217510033) and was performed in the frame of the "Priority 2030" research program at Kazan Federal University.

4.3.1. Ethics approval and consent to participate

All procedures performed with the involvement of animals complied with ethical standards approved by legal acts of the Russian Federation, the principles of the Basel Declaration, and rec ommendations of the Directive 2010/63/EU for animal experiments and all animal use protocols were approved by the French National Institute of Health and Medical Research (APAFIS #16992 2020070612319346 v2) and Local Ethical Com mittee of Kazan Federal University (#24/ 22.09.2020).

4.3.1. Conflict of interest

The authors declare that they have no conflict of interest.

4.3.2. References

1. Donato F, Jacobsen RI, Moser MB, Moser EI (2017) Stellate cells drive maturation of the entorhinal hippocampal circuit. Science 355(6330): 8178. https://doi.org/10.1126/science.aai8178

2. Cossart R, Khazipov R (2022) How development sculpts hippocampal circuits and function. Physiol Rev 102(1): 343–378. https://doi.org/10.1152/physrev.00044.2020

3. Treves A, Tashiro A, Witter MP, Moser EI (2008) What is the mammalian dentate gyrus good for? Neuroscience 154(4): 1155–1172. https://doi.org/10.1016/j.neuroscience.2008.04.073

4. Amaral DG, Scharfman HE, Lavenex P (2007) The dentate gyrus: fundamental neuroanatomical organization (dentate gyrus for dummies). Prog Brain Res 163: 3–22. https://doi.org/10.1016/s0079-6123(07)63001-5

5. Borzello M, Ramirez S, Treves A, Lee I, Scharfman H, Stark C, Knierim JJ, Rangel LM (2023) Assessments of dentate gyrus function: discoveries and debates. Nat Rev Neurosci 24(8): 502–517. https://doi.org/10.1038/s41583-023-00710-z

6. Scharfman HE, Witter M (2007) The dentate gyrus—A comprehensive guide to structure, function, and clinical implications—Preface. Dentate Gyrus: A Comprehensive Guide to Structure, Function, and Clinical Implications. Progress in

Brain Research 163: Ix–Xiii. ISBN10: 0444530150 https://www.researchgate.net/publication/278251777_The_dentate_gyrus_-_A_comprehensive_guide_to_structure_function_and_clinical_implications_-_Preface

7. Fricke, R., and Cowan, W. M. (1977). An autoradiographic study of the development of the entorhinal and commissural afferents to the dentate gyrus of the Rat. In Journal of Comparative Neurology (Vol. 173, Issue 2, pp. 231–250). Wiley. https://doi.org/10.1002/cne.901730203

8. Loy, R., Lynch, G., and Cotman, C. W. (1977). Development of afferent lamination in the fascia dentata of the rat. In Brain Research (Vol. 121, Issue 2, pp. 229–243). Elsevier BV. https://doi.org/10.1016/0006-8993(77)90149-4

9. Ye, G., Yi, S., Gamkrelidze, G., Pasternak, J. F., and Trommer, B. L. (2005). AMPA and NMDA receptor-mediated currents in developing dentate gyrus granule cells. In Developmental Brain Research (Vol. 155, Issue 1, pp. 26–32). Elsevier BV. https://doi.org/10.1016/j.devbrainres.2004.12.002

10. Ye, G., Song Liu, X., Pasternak, J. F., and Trommer, B. L. (2000). Maturation of glutamatergic neurotransmission in dentate gyrus granule cells. In Developmental Brain Research (Vol. 124, Issues 1–2, pp. 33–42). Elsevier BV. https://doi.org/10.1016/s0165-3806(00)00103-6

11. Valeeva, G., Janackova, S., Nasretdinov, A., Rychkova, V., Makarov, R., Holmes, G. L., Khazipov, R., and Lenck-Santini, P.-P. (2018). Emergence of Coordinated Activity in the Developing Entorhinal–Hippocampal Network. In Cerebral Cortex (Vol. 29, Issue 2, pp. 906–920). Oxford University Press (OUP). https://doi.org/10.1093/cercor/bhy309

12. Karlsson, K. Æ., Mohns, E. J., di Prisco, G. V., and Blumberg, M. S. (2006). On the co-occurrence of startles and hippocampal sharp waves in newborn rats. In Hippocampus (Vol. 16, Issue 11, pp. 959–965). Wiley. https://doi.org/10.1002/hipo.20224

13. Mohns, E. J., and Blumberg, M. S. (2008). Synchronous Bursts of Neuronal Activity in the Developing Hippocampus: Modulation by Active Sleep and Association with Emerging Gamma and Theta Rhythms. In The Journal of Neuroscience (Vol. 28, Issue 40, pp. 10134–10144). Society for Neuroscience. https://doi.org/10.1523/jneurosci.1967-08.2008

14. Leinekugel, X., Khazipov, R., Cannon, R., Hirase, H., Ben-Ari, Y., and Buzsáki, G. (2002). Correlated Bursts of Activity in the Neonatal Hippocampus in Vivo. In Science (Vol. 296, Issue 5575, pp. 2049–2052). American Association for the Advancement of Science (AAAS). https://doi.org/10.1126/science.1071111

15. Marguet, S. L., Le-Schulte, V. T. Q., Merseburg, A., Neu, A., Eichler, R., Jakovcevski, I., Ivanov, A., Hanganu-Opatz, I. L., Bernard, C., Morellini, F., and Isbrandt, D. (2015). Treatment during a vulnerable developmental period rescues a genetic epilepsy. In Nature Medicine (Vol. 21, Issue 12, pp. 1436–1444). Springer Science and Business Media LLC. https://doi.org/10.1038/nm.3987

16. Gainutdinov, A., Shipkov, D., Sintsov, M., Fabrizi, L., Nasretdinov, A., Khazipov, R., and Valeeva, G. (2023). Somatosensory-Evoked Early Sharp Waves in the Neonatal Rat Hippocampus. In International Journal of Molecular Sciences (Vol. 24, Issue 10, p. 8721). MDPI AG. https://doi.org/10.3390/ijms24108721

17. Hu, H., Gan, J., and Jonas, P. (2014). Fast-spiking, parvalbumin + GABAergic interneurons: From cellular design to microcircuit function. In Science (Vol. 345, Issue 6196). American Association for the Advancement of Science (AAAS). https://doi.org/10.1126/science.1255263

18. Scharfman, H. (1991). Dentate hilar cells with dendrites in the molecular layer have lower thresholds for synaptic activation by perforant path than granule cells. In The Journal of Neuroscience (Vol. 11, Issue 6, pp. 1660–1673). Society for Neuroscience. https://doi.org/10.1523/jneurosci.11-06-01660.1991

19. Ewell, L. A., and Jones, M. V. (2010). Frequency-Tuned Distribution of Inhibition in the Dentate Gyrus. In The Journal of Neuroscience (Vol. 30, Issue 38, pp. 12597–12607). Society for Neuroscience. https://doi.org/10.1523/jneurosci.1854-10.2010

20. Leutgeb, J. K., Leutgeb, S., Moser, M.-B., and Moser, E. I. (2007). Pattern Separation in the Dentate Gyrus and CA3 of the Hippocampus. In Science (Vol. 315, Issue 5814, pp. 961–966). American Association for the Advancement of Science (AAAS). https://doi.org/10.1126/science.1135801

21. Hollrigel, G. S., and Soltesz, I. (1997). Slow Kinetics of Miniature IPSCs during Early Postnatal Development in Granule Cells of the Dentate Gyrus. In The Journal of Neuroscience (Vol. 17, Issue 13, pp. 5119–5128). Society for Neuroscience. https://doi.org/10.1523/jneurosci.17-13-05119.1997

22. Hollrigel, G. S., Ross, S. T., and Soltesz, I. (1998). Temporal Patterns and Depolarizing Actions of Spontaneous GABAA Receptor Activation in Granule Cells of the Early Postnatal Dentate Gyrus. In Journal of Neurophysiology (Vol. 80, Issue 5, pp. 2340–2351). American Physiological Society. https://doi.org/10.1152/jn.1998.80.5.2340

23. De La Prida, L. M., Bolea, and Sanchez-Andres. (1998). Origin of the synchronized network activity in the rabbit developing hippocampus. In European Journal of Neuroscience (Vol. 10, Issue 3, pp. 899–906). Wiley. https://doi.org/10.1046/j.1460-9568.1998.00097.x

24. Liu, Y. B., Lio, P. A., Pasternak, J. F., and Trommer, B. L. (1996). Developmental changes in membrane properties and postsynaptic currents of granule cells in rat dentate gyrus. In Journal of Neurophysiology (Vol. 76, Issue 2, pp. 1074–1088). American Physiological Society. https://doi.org/10.1152/jn.1996.76.2.1074

25. Liu, Y. B., Ye, G.-L., Liu, X.-S., Pasternak, J. F., and Trommer, B. L. (1998). GABAA Currents in Immature Dentate Gyrus Granule Cells. In Journal of Neurophysiology (Vol. 80, Issue 5, pp. 2255–2267). American Physiological Society. https://doi.org/10.1152/jn.1998.80.5.2255

26. Yu, E. P., Dengler, C. G., Frausto, S. F., Putt, M. E., Yue, C., Takano, H., and Coulter, D. A. (2013). Protracted Postnatal Development of Sparse, Specific Dentate Granule Cell Activation in the Mouse Hippocampus. In The Journal of Neuroscience (Vol. 33, Issue

7, pp. 2947–2960). Society for Neuroscience. https://doi.org/10.1523/jneurosci.1868-12.2013

27. Pouille, F., and Scanziani, M. (2001). Enforcement of Temporal Fidelity in Pyramidal Cells by Somatic Feed-Forward Inhibition. In Science (Vol. 293, Issue 5532, pp. 1159–1163). American Association for the Advancement of Science (AAAS). https://doi.org/10.1126/science.1060342

28. Galarreta, M., and Hestrin, S. (2001). Spike Transmission and Synchrony Detection in Networks of GABAergic Interneurons. In Science (Vol. 292, Issue 5525, pp. 2295–2299). American Association for the Advancement of Science (AAAS). https://doi.org/10.1126/science.1061395

29. Doischer, D., Aurel Hosp, J., Yanagawa, Y., Obata, K., Jonas, P., Vida, I., and Bartos, M. (2008). Postnatal Differentiation of Basket Cells from Slow to Fast Signaling Devices. In The Journal of Neuroscience (Vol. 28, Issue 48, pp. 12956–12968). Society for Neuroscience. https://doi.org/10.1523/jneurosci.2890-08.2008

30. Daw, M. I., Ashby, M. C., and Isaac, J. T. R. (2007). Coordinated developmental recruitment of latent fast spiking interneurons in layer IV barrel cortex. In Nature Neuroscience (Vol. 10, Issue 4, pp. 453–461). Springer Science and Business Media LLC. https://doi.org/10.1038/nn1866

31. Minlebaev, M., Colonnese, M., Tsintsadze, T., Sirota, A., and Khazipov, R. (2011). Early Gamma Oscillations Synchronize Developing Thalamus and Cortex. In Science (Vol. 334, Issue 6053, pp. 226–229). American Association for the Advancement of Science (AAAS). https://doi.org/10.1126/science.1210574

32. Khazipov, R., Minlebaev, M., and Valeeva, G. (2013). Early gamma oscillations. In Neuroscience (Vol. 250, pp. 240–252). Elsevier BV. https://doi.org/10.1016/j.neuroscience.2013.07.019

4.4. Article 4. (in preparation) Development of inhibition associated with the Entorhinal Cortex input in the CA1 hippocampus of neonatal rats

Ilgam KHALILOV [a], Azat GAINUTDINOV [a], Roustem KHAZIPOV [a,b*]

[a] Aix-Marseille University, INMED, INSERM, Marseille, 13273 France

[b] Laboratory of Neurobiology, Institute of Fundamental Medicine and Biology, Kazan Federal University, Kazan, 420015 Russia

*** Correspondence:** Roustem Khazipov roustem.khazipov@inserm.fr

ORCID ID: 0000-0002-6763-2841

4.4.1. Abstract

In the neonatal hippocampus, GABAergic inputs are first formed on CA1 pyramidal cells (CA1 PCs) before the emergence of glutamatergic inputs. However, little is known about the development of GABAergic input associated with the temporoammonic (TA) pathway, which carries information from the entorhinal cortex (EC) to the CA1 hippocampus and which is the main driver of neonatal hippocampal activity *in vivo*. Here, we investigated developmental changes in GABAergic synaptic inputs associated with EC input to CA1 PCs using whole-cell recordings in the intact hippocampus *in vitro* from postnatal days P1 to P11 mice. Angular band - evoked excitatory and inhibitory postsynaptic currents (ecEPSCs and ecIPSCs) were voltage-isolated using a low-chloride pipette solution. Short-latency ecEPSCs could be evoked in CA1 PCs from P1, and their latency remained stable during development. In contrast, ecIPSCs were either absent or showed a high degree of failure during the first postnatal week. Furthermore, ecIPSC delays were long, from tens to hundreds of milliseconds, and showed high variability across trials in the first postnatal days. ecIPSC delays and their time jitter progressively decreased during the postnatal period. The temporal integration window, assessed as the time difference between ecEPSC and ecIPSC delays, decreased during the postnatal period and reached ~5 ms at P10. Thus, the development of GABAergic inhibition associated with EC input to CA1 PCs is delayed, allowing a large integration window for excitatory EC inputs to CA1 PCs during the first postnatal week. These findings suggest that the activation of GABAergic circuits associated with inputs from the entorhinal cortex is delayed in development.

Keywords: hippocampus, temporoammonic, neonatal rat, patch-clamp, excitatory postsynaptic currents, inhibitory postsynaptic currents

4.4.2. Introduction

Temporoammonic (TA) input to the CA1 region of the hippocampus provides critical excitatory drive, linking the entorhinal cortex to the hippocampus and playing a key role in memory formation and spatial navigation (Amaral and Lavenex, 2007). Unlike the trisynaptic perforant pathway, which relays information through the dentate gyrus and CA3, the TA path offers a direct entorhinal-to-CA1 connection, primarily targeting axons of L3 EC neurons on the distal apical dendrites of CA1 pyramidal neurons in the stratum lacunosum-moleculare (sl-m) (van Strien et al., 2009; Spruston, 2008). This input is modulated by feedforward inhibition mediated by diverse GABAergic interneurons, notably by fast spiking parbalbumin perisomatic basket cells which provide rapid and powerful somatic inhibition and establish a precise temporal integration window (Freund and Katona, 2007; Pouille and Scanziani, 2001; Klausberger and Somogyi, 2008). TA input to CA1 is also balanced by inhibitory oriens-lacunosum moleculare interneurons which selectively inhibit distal dendrites, regulating the timing and strength of perforant path input (Losonczy et al., 2002), bistratified cells that further refine synaptic integration by targeting proximal dendrites, influencing the balance between local and distal excitatory inputs (Klausberger et al., 2004). Together, these inhibitory mechanisms synchronize activity across the CA1 network to support sparse coding and ensure that only temporally precise inputs drive pyramidal cell firing (Pouille and Scanziani, 2001; Klausberger and Somogyi, 2008; Buzsaki, 2006).

During development, in rodents, entorhinal TA axons arrive to CA1 sl-m already and establish excitatory synapses on CA1 pyramidal cells, whose apical dendrites attend sl-m, already at birth (Tyzio et al., 1999; Super, 1994). TA input is instrumental in genesis of the early sharp waves (eSPWs), the main activity pattern in rodent hippocampus during the neonatal period (Leinekugel et al., 2002; Cossart and Khazipov, 2022; Valeeva and Janackova et al., 2019; Mohns et al., 2007;Mohns et al., 2008;Marguet, et al., 2015;Gainutdinov et al., 2023;Juzekaeva et al., 2024;Pochinok et al., 2024). Unlike in adults, activation of entorhinal input provided by bursts in superficial layers of EC, which are in turn triggered by sensory feedback from neonatal movements, is associated with global and long-lasting excitation in CA1 network during eSPWs suggesting that TA excitatory inputs are poorly balanced by inhibition in the neonatal hippocampus (Valeeva and Janackova et al., 2019; Dard et al., 2022). Along with these observations, pair-pulse inhibition of population spikes in response to repetitive afferent stimulation, that is a test for the feedforward inhibition, was found to be absent in CA1 hippocampus of neonatal rodents (Harris and Teyler, 1983; Michelson et al., 1989). Importantly, biphoton imaging of presynaptic terminals of interneurons in pyramidal cell layer revealed nearly silence of perisomatic inhibition in neonatal mouse hippocampus following neonatal movements (Dard et al., 2022), that is keeping with very few perisomatic GABAergic synapses during immunochemiscal staining for their markers (GAD, synapsin, synaptotagmin-2) as well as during electron microscopy during the first postnatal week (Schwartzkroin et al., 1981;Tyzio et al., 1999;Dard et al., 2022). Altogether, these observations raise a hypothesis that feedforward inhibition associated with the TA input maybe delayed in

development. In the present study, we directly addressed this question by examining the synaptic responses evoked in CA1 pyramidal cells by TA input stimulation in the intact hippocampus in vitro preparation.

4.4.3. Materials and Methods

The animal experiments were carried out in compliance with the ARRIVE guidelines. Animal care and procedures were in accordance with EU Directive 2010/63/EU for animal experiments, and all animal-use protocols were approved by the INSERM Ethical Committee (APAFIS #16992-2020070612319346 v2)). C57BL/33 mice of both sexes aged from postnatal days [P] 1 to 11 were used. Animals were decapitated under isoflurane anesthesia (5%), and the brain was rapidly removed and placed in ice-cold (2–5°C) oxygenated (95% O2–5% CO2) artificial cerebrospinal fluid (ACSF) of the following composition (in mM): NaCl 126, KCl 3.5, CaCl2 2, MgCl2 1.3, NaHCO3 25, NaH2PO4 1.2 and glucose 11 (pH 7.4). Intact hippocampal preparations were prepared as described previously (Khalilov et al., 1997) and were kept in oxygenated ACSF at room temperature (20–22°C) for at least 1 hour before use. For recordings, hippocampi were placed into a submerged chamber and superfused with oxygenated ACSF at 30-32oC at a flow rate of 10 ml/min. Extracellular local field potential (LFP) recordings were conducted using electrodes made from tungsten wire (diameter: 50 μm, California Fine Wire, Grover Beach, CA, USA). LFP and patch-clamp were amplified using DAM–8A amplifier (×1000, bandwidth 0.1 Hz – 3 kHz). Electrodes for patch clamp recordings were prepared from borosilicate glass with resistance of 4-7 MOhm when filled with the pipette solution containing Cs-Gluconate 135, MgCl2 2, CaCl2 2, EGTA 1, and HEPES 10 (pH 7.26). Whole-cell recordings were performed using Axapatch-200B amplifier (Molecular Devices, CA, USA) in voltage clamp mode at different holding potentials to enable voltage separation of EPSCs and IPSCs as described previously (Leinekugel et al., 1997; Khalilov et al., 2015). LFP and patch-clamp signals were digitized using Digidata 1440A interface (Molecular Devices, CA, USA) at a sampling rate of 10 kHz and stored in the PC memory for analysis. Electrical stimulations were performed with a bipolar tungsten electrode (10–20 V, 40 μs duration, 10 s interstimulus interval) placed in the angular bundle (AB). Stimulus intensity was set at minimal level to reliably evoke EPSCs in more than 80% of trials. From 15 to 50 EPSCs were recorded from each cell at the reversal potential of IPSCs (-70 mV), then holding potential was set at the reversal of EPSCs (0 mV) and similar number of IPSCs were recorded without changing stimulus intensity.

Each trace of the angular band-evoked excitatory and inhibitory postsynaptic currents (EPSCs and IPSCs) was initially reviewed manually. The experimenter determined the time and presence of the response onset within a window from T = 0 to T = 500 ms after stimulation began. The recorded data on response timing and presence were organized into tables separately for each type of current (EPSCs or IPSCs) for each cell of the animal. Using MATLAB, data from these tables were extracted for further analysis. The analysis

focused on calculating the median onset times, the variability in onset times (jitter), and the differences between median onset times for each type of current in each animal's cells. The results were grouped and displayed based on cell age (Figure 81A) and also categorized into four age groups (Figure 80D, E, Figure 81B, C, D): P1-3 (n = 21 cells), P4-5 (n = 25 cells), P6-8 (n = 20 cells), and P9-11 (n = 7 cells). Comparisons among groups were performed using a two-sided Wilcoxon rank-sum nonparametric test. All statistical data in the text are presented as: Median value (Q1 – Q3).

4.4.4. Results

In the present study, we aimed to characterize the dynamics of excitation and inhibition in CA1 pyramidal cells during responses evoked by stimulation of TA input from EC. For this purpose, we stimulated AB, where axons of TA pathway from EC to CA1 hippocampus are located (Figure 79A). Example traces of LFP responses evoked by AB stimulation at different depth of CA1 subfield are shown on Figure 79B. AB-evoked responses were characterized by sequential electrographic elements, starting with an afferent volley, followed by biphasic negative wave with maximal amplitude close to the hippocampal fissure and to sequential sinks in sl-m (Figure 79B). Application of the ionotropic glutamate receptor blockers CNQX (10 mkM) and APV (50 mkM) did not affect the afferent volley, but suppressed the short latency biphasic component of the response suggesting that it involves monosynaptic EC input and activation of AMPA and NMDA receptors in CA1 pyramidal neurons (Fig, 1 B, right panel). We further performed whole-cell recordings from CA1 pyramidal cells using low chloride pipette solution to voltage-separate EPSCs and IPSCs as shown on scheme (Figure 79C). In these experiments, CA1 pyramidal cells membrane potential was first hold at the reversal potential of IPSCs (circa -70 mV), and AB stimulus intensity was set to reliably evoke short latency monosynaptic EPSCs (from 15 to 50 EPSCs per cell). Then holding potential was set at the reversal of EPSCs (0 mV) and similar number of trials were recorded without changing stimulus parameters. Example responses to AB stimulation in a P3 CA1 pyramidal cell are shown on Figure 79D. AB evoked short-latency EPSCs (Figure 79D, left), as well as all ongoing synaptic activity recorded at the IPSCs' reversal potential was blocked by CNQX (10 mkM) and APV (50 mkM) (of note, at -70 mV EPSCs are primarily mediated by AMPA receptors, whereas NMDA receptors are blocked by magnesium). AB-evoked EPSCs were almost fully reversed at the holding potential of 0 mV, and longer latency AB-evoked IPSCs were revealed (Figure 79D, right panels). During recordings of IPSCs, we maintained membrane potential close to reversal of EPSCs, so that CNQX+APV – sensitive short latency EPSCs remained slightly negative to avoid a confound with IPSCs. Importantly, the AB-evoked (but not spontaneous) IPSCs were also fully suppressed by CNQX+APV indicating that they involve an intermediate stage of glutamatergic activation of interneurons, which are at the origin of IPSCs recorded from pyramidal cells as shown on the Figure 79C (of note, in addition to the feedforward circuit shown on Figure 79C, activation of interneurons can also occur through a backward circuit which is not shown

in the figure). Hereafter, the AB-evoked excitatory and inhibitory postsynaptic currents in CA1 pyramidal cells will be referred to as EC driven ecEPSCs and ecIPSCs, respectively.

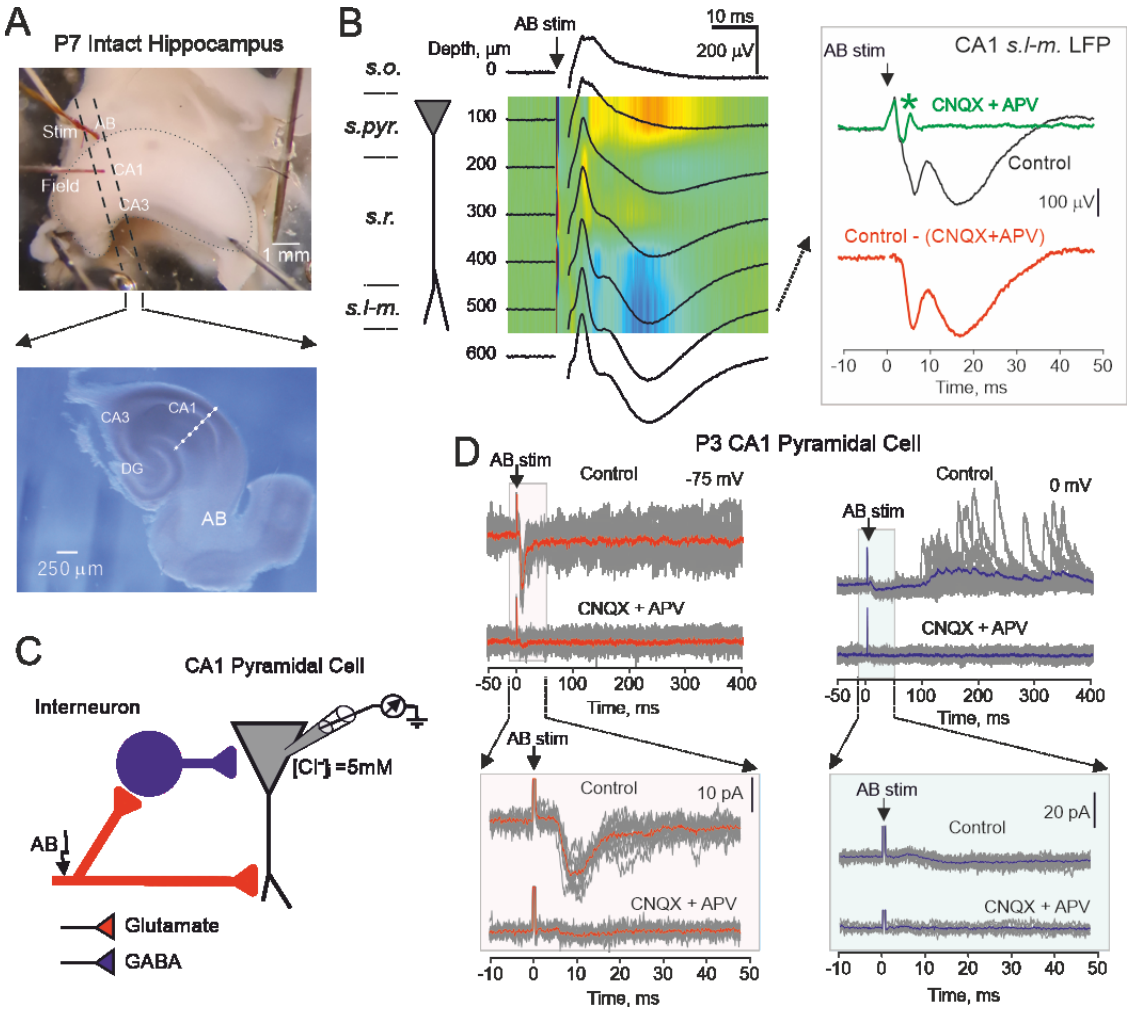

Figure 79 Angular bandle – evoked responses in the CA1 area of the neonatal rat intact hippocampus in vitro.

(A) Top, microphotograph of the intact hippocampus in vitro prepared from a P7 rat. Electrode for local field potential recordings (LFP, Field) is placed in CA1 hippocampus along CA1-dentate dentate gyrus (DG) axis, while another bipolar electrode (Stim) is placed in angular bandle (AB) to stimulate inputs from entorhinal cortex. Bottom, recording sites (white dots) at different depth of CA1 in a hippocampal slice cut from the intact hippocampus as indicated by dashed lines above. (B) Left, AB-evoked LFP responses at different depth in CA1 (s.o. – stratum oriens, s.pyr. – stratum pyramidale, s.r. – stratum radiatum, s.l-m. – stratum lacunosum-oleculare), overlaid on a current-source density map, with a notable sink in s.l-m. Right, effect of combined application of the ionotropic glutamate receptor antagonists CNQX and APV on the AB-evoked LF responses in CA1 s.l-m. (control - black trace, CNQX+APV – green trace; CNQX+APV – persistent afferent volley is marked by a green asterisk). Red trace below shows a result of subtraction of the response obtained in the presence of CNQX+APV from the control response. (C) Scheme of whole-cell recordings with low-chloride pipette solution for a voltage-separation of the glutamatergic and GABAergic components of the AB-evoked responses in CA1 pyramidal cells. Electrical stimulation of inputs from entorhinal cortex (EC) located in AB elicits monosynaptic EC-driven excitatory postsynaptic currents (ecEPSC) and two-synaptic inhibitory postsynaptic currents (ecIPSCs) in a CA1 pyramidal cell. (D) Left, example AB-evoked ecEPSCs (ten individual grey traces are superimposed, red trace shows average) recorded in a P3 CA1 pyramidal cell at the reversal potential of IPSCs (-75 mV) in control conditions (top) and after addition of CNQX+APV (below). Bottom plot shows the early part of the AB-evoked responses outlined in pink box on expanded time scale. Note short-latency ecEPSCs fully suppressed by CNQX+APV. Right, similar recordings of the AB-evoked ecIPSCs from the same neuron, with the

same stimulus intensity, at EPSCs reversal potential (0 mV). Note that ecIPSCs occur at long (>100 ms) and variable delays after the AB stimulus, and that they are also suppressed by application of CNQX+APV, indicating that generation of ecIPSCs involves glutamatergic interneuron activation as shown on panel C.

Example trials and average ecEPSCs and ecIPSCs from CA1 pyramidal cells recorded from P1, P2 and P7 rats are presented on Figure 80A,B and C, respectively. Since in our experimental setting the stimulus was set to reliably evoke ecEPSCs, there was little of ecEPSC failures at all ages (Figure 80A-CandD). In contrast, ecIPSC failures occurred more often in age-dependent manner (Figure 80A-CandD). In the most extreme cases, none of AB stimulations evoked ecIPSC through the entire recording session as illustrated by example recordings from such ecIPSC-lacking cell on Figure 80A. ecIPSC-lacking cells represented about one third of all cells during the first postnatal week (n=16 of 65 cells between P1-P7), but they were never observed at postnatal ages >P7 (none of 8 cells between P8-P11) (Figure 80E). Of note, all ecIPSC-lacking cells displayed spontaneous IPSCs (note spontaneous IPSC marked by asterisk on Figure 79A). Second category of cells during the first postnatal week was represented by significant number of failures, with ecIPSCs, if present, occurring at long and variable delays after the AB stimulus (Figure 79B, cell at P2). The number of cells with high ecIPSC failure rate was observed during the first postnatal week (Figure 80D), whereas AB stimulation reliably evoked both ecEPSCs and ecIPSCs in all trials in older animals (Figure 80D). These data suggest that inhibition associated with EC input is weak and variable during the first postnatal week.

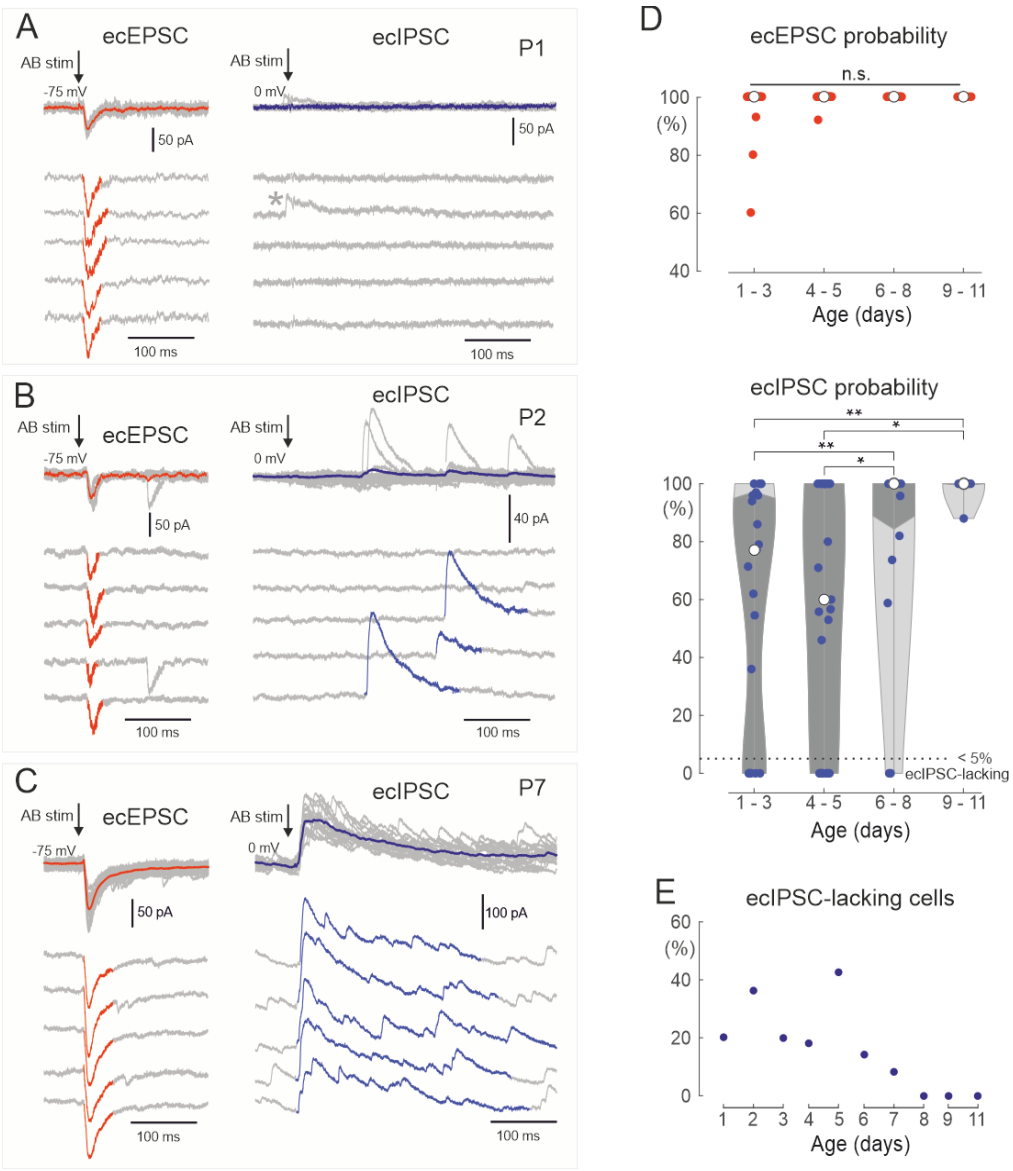

Figure 80 High incidence of ecIPSCs failure in neonatal CA1 pyramidal cells.

(A-C) Three main phenotypes with different levels of ecIPSC failure rate. (A) An ecIPSC – lacking neuron. Top, example AB-evoked ecEPSCs (left, red – average, grey – individual traces) and ecIPSCs (right, blue - average) in a P1 CA1 pyramidal cell. Below, five examples of individual responses. Note absence of ecIPSCs in a 400 ms time window after AB stimulus in contrast to high-fidelity ecEPSCs, but also presence of spontaneous IPSCs (grey asterisk). (B) Neuron with high ecIPSC failure rate, P2. Also note long and variable ecIPSC delays. (C) Neuron with high fidelity and short latency ecIPSCs, P7. (D) Violin plots of group data for age-dependence of ecEPSC (top) and ecIPSC (bottom) probability in response to AB stimulation. Each dot corresponds to individual CA1 pyramidal cell. White circle shows median, dark grey area shows Q1 – Q3, light grey area shows 5 - 95% range. For the ecIPSC plot, note a subgroup of ecIPSC – lacking cells with a probability threshold set at 5%. (E) Age-dependence of a probability for ecIPSC – lacking cell. Below, total studied cell number per postnatal day. *, p value < 0.05; **, p value < 0.01; n.s., non-significant (Mann–Whitney–Wilcoxon nonparametric test for unpaired groups). See Table S1 for numerical data on descriptive and comparative statistics.

We next examined the dynamics of the AB-evoked excitatory and inhibitory responses. Raster plot of the ecEPSC and ecIPSC onsets in all trials from all CA1 pyramidal cells within the age group from P1 to P11 (n=73 cells) is shown on Figure 81A. It is noticeable that ecEPCSs reliably occurred at short (~8 ms) and constant delays that did not show

any age-dependence (Figure 81A, B). In contrast, ecIPSC, if present, were strongly delayed from the stimulus and their delay was highly variable during the first postnatal week (Figure 81B, note semilogarithmic time scale on ecIPSC age-dependence plot). At P1-P3, the ecIPSC delay was of 133 (54 – 200) ms (n=21 cells, P1 - P3), and it progressively reduced during the postnatal period to attain 13.7 (13.24 – 15.28) ms (n=7 cells) by P9 – P11) (Figure 81B). Along with the reduction in delay values, we also observed a developmental decrease in ecIPSC delay jitter from 51 (20 – 86) ms (n=21) during the first postnatal days to ~ 1 ms by the end of the first postnatal week, whereas ecEPSC delay jitter was already small (~ 0.2 ms) after birth and remained constant during the postnatal period (Figure 81D). Finally, we calculated the temporal integration window defined as a delay of inhibition from excitation (ecIPSC – ecEPSC delay) and found that it attains 127 (46 – 190) ms at P1 – P3 (n=21), and that it progressively shortens during postnatal period to attain 4.6 (4.0 – 5.7) ms by P9-P11 (n=7) (Figure 81C).

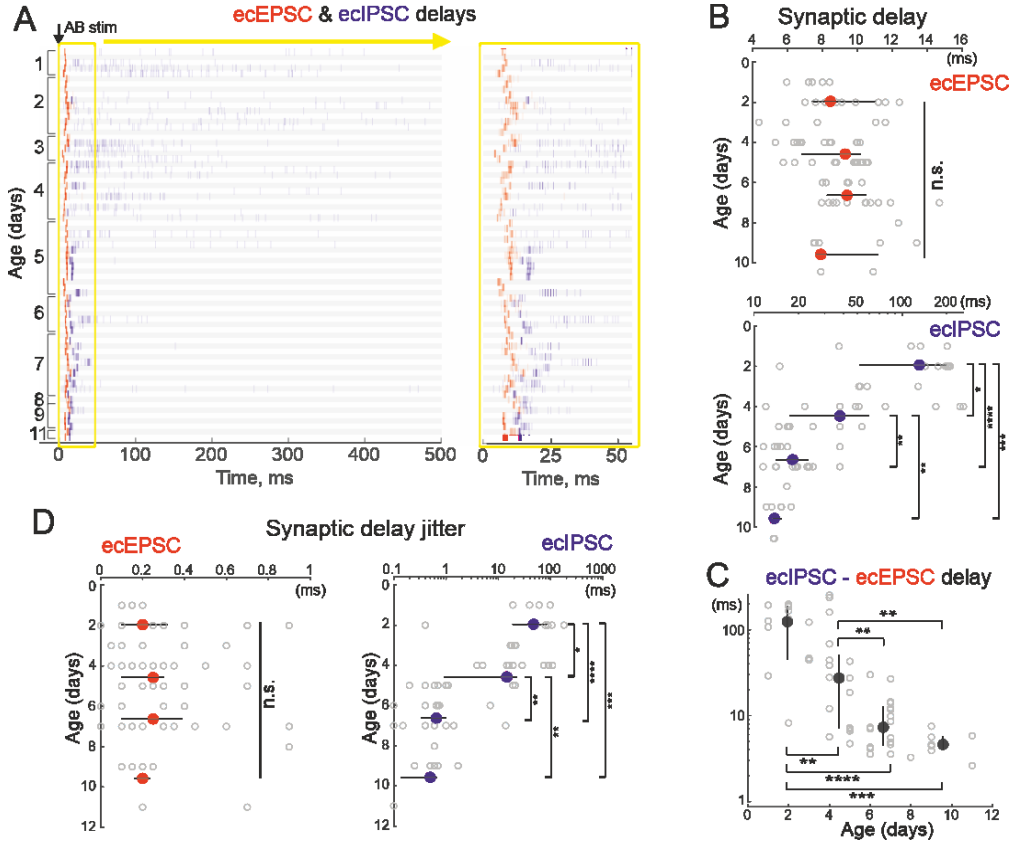

Figure 81. Long and variable ecIPSC delays in neonatal CA1 hippocampus.

(A) Raster plot of ecEPSC (red bars) and ecIPSC (blue bars) onsets in CA1 pyramidal cells. Neurons are ranged top-down according to the animal age, each row corresponds to an individual neuron and shows results for 10-25 EPSCs and IPSCs for each neuron. Early part of the response outlined in yellow box is shown on right at expanded time scale. (B-D) Age-dependence of B: ecEPSC and ecIPSC delays from AB stimulus; C: delay of ecIPSCs from ecEPSCs and D: ecEPSC and ecIPSC delay jitter. Each open circle shows average delay value for one cell, colored circles and horizontal bars show median and Q1 – Q3 range in age groups P1-3, P4-5, P6-7 and P8-11. *, p value < 0.05; **, p value < 0.01; ***, p value < 0.001; ****, p value < 0.0001; n.s., non-significant (Mann–Whitney–Wilcoxon nonparametric test for unpaired groups). See Table S1 for numerical data on descriptive and comparative statistics.

Discussion

The main finding of the present study is that feedforward inhibition associated with the TA input from EC is either absent or strongly delayed that enables large temporal integration window in the neonatal rat CA1 hippocampus.

Our findings on the delayed development of GABAergic responses in CA1 pyramidal cells are in apparent contradiction with the results of previous studies which presented evidence that GABAergic synapses are first formed on CA1 pyramidal cells, prior to establishment of glutamatergic synapses (Tyzio et al., 1999; Khazipov et al., 2001). Here, we found that significant proportion (nearly one third) of CA1 pyramidal cells during the first postnatal week displayed glutamatergic ecEPSCs but lacked ecIPSCs. However, even ecIPSC-lacking neurons displayed spontaneous IPSCs indicating that there is no contradiction with the previous studies, and that lack of inhibition in these immature ecIPSC-lacking neurons is specific for the inhibition associated with the TA pathway. In addition to the presence of ecIPSC-lacking neurons, we also found that the delays of ecIPSCs, if present, were long, in the range of tens or hundreds of milliseconds, and variable from trial-to-trial during the first postnatal week. These observations are in keeping with similar observations made in dentate gyrus (Frolova et al., 2023) and neocortex (Daw et al., 2007; Minlebaev et al., 2011). The ecIPSC delays, as well as the duration of the temporal integration window. progressively became shorter and less variable durinng the postnatal period to achieve adult-like values of few milliseconds by ~P10. Because the duration of the integration window is primarily determined by activation of the feedforward fast spiking perisomatic parvalbumin-containing interneurons (Pouille and Scanziani, 2001; Hu et al., 2014), our results suggest that development of the feedforward inhibition within the entorhinal-hippocampal TA pathway poorly operates during the first postnatal week. This is in keeping with a lack of perisomatic inhibition in CA1 hippocampus as evidenced by the lack of St2 staining of terminals of the fast spiking parvalbumin interneurons in CA1 pyramidal cell layer, as well as absence of calcium transients in perisomatic rings of GABAergic terminals following movements before P9-10 (Dard et al., 2022), as well as lack of high frequency ripple-oscillations, which are supported by perisomatic fast spiking interneurons (Buzsaki, 2015), in rodents before P10 (Leinekugel et al., 2002; Buhl and Buzsaki, 2005; Pochinok et al., 2024). The mechanisms of delayed development of perisomatic inhibition in CA1 hippocampus remain open question for the future studies, but these may involve protracted development of fast-spiking properties of parvalbumin interneurons, development of their feedforward excitatory inputs, as well as formation and maturation of perisomatic synapses between these interneurons and target CA1 pyramidal cells (Daw et al., 2007; Doischer et al., 2008; Khazipov et al., 2013).

Delayed development of inhibition associated with the TA input from EC to CA1 hippocampus may have strong impact on the functional organization of activity in the entorhinal-hippocampal circuit during development. During the first postnatal week, most of hippocampal activity is organized in a characteristic network activity pattern of eSPWs (Leinekugel et al., 2002; Karlsson et al., 2006; Marguet et al., 2015; Valeeva and Janackova et al., 2019; Graf et al., 2021; Cossart and Khazipov, 2022; Pochinok et al.,

2024), which are primarily driven by excitatory inputs from the EC (Marguet et al., 2015; Valeeva and Janackova et al., 2019; Gainutdinov et al., 2023; Graf et al., 2024; Juzekaeva et al., 2024). This EC input includes bursts of neurons in L3 of EC, which directly project, via TA pathway, to CA1 pyramidal cells and generate prominent current sink of eSPWs in sl-m (Marguet et al., 2015; Valeeva and Janackova et al., 2019; Gainutdinov et al., 2023; Graf et al., 2024; Juzekaeva et al., 2024; Shipkov et al., 2024). eSPWs are often preceded by myoclonic movements and are associated with a global burst activation of CA1 pyramidal cells following movements (Karlsson et al., 2006; Valeeva and Janackova et al., 2019; Dard et al., 2022). Defecits in the inhibition associated with the TA input to CA1 including lack of inhibition in ecIPSC – lacking neurons and delayed from excitatory currents ecIPSCs likely enable large temporal widow of integration of EC inputs and support global bursting of CA1 pyramidal cells during eSPWs in the neonatal CA1 hippocampus, and plasticity in the developing entorhinal-hippocampal network (Donato et al., 2017).

Author Contributions

RK conceptualized and drafted the manuscript. IK performed the experiments. AG, IK analyzed data. All authors revised the manuscript and interpreted the data.

4.4.5. Funding sources

This research was supported by ANR (grant “HIPPODEV”) and RSF (grant #21-75-10033).

4.4.6. Conflict of Interest

The authors declare that the research was conducted in the absence of any commercial or financial relationships that could be construed as a potential conflict of interest.

4.4.7. Data Availability Statement

The datasets generated and analyzed in this study are available on reasonable request from the authors.

4.4.8. References

- Pochinok I, Stöber T, Triesch J, Chini M, Hanganu-Opatz I (2024) A developmental increase of inhibition promotes the emergence of hippocampal ripples. Nature Communications. 15(1). https://doi.org/10.1038/s41467-024-44983-z
- Daw M, Ashby M, Isaac J (2007) Coordinated developmental recruitment of latent fast spiking interneurons in layer IV barrel cortex. Nature Neuroscience. 10(4). 453-461. https://doi.org/10.1038/nn1866
- Buzsaki G (2006) Rhythms of the Brain. DOI: https://doi.org/10.1093/acprof:oso/9780195301069.001.0001
- Tyzio R, Represa A, Jorquera I, Ben-Ari Y, Gozlan H, Aniksztejn L (1999) The Establishment of GABAergic and Glutamatergic Synapses on CA1 Pyramidal Neurons is

Sequential and Correlates with the Development of the Apical Dendrite. The Journal of Neuroscience. 19(23). 10372-10382. https://doi.org/10.1523/jneurosci.19-23-10372.1999

- Cossart R, Khazipov R (2022) How development sculpts hippocampal circuits and function. Physiological Reviews. 102(1). 343-378. https://doi.org/10.1152/physrev.00044.2020
- Minlebaev M, Colonnese M, Tsintsadze T, Sirota A, Khazipov R (2011) Early Gamma Oscillations Synchronize Developing Thalamus and Cortex. Science. 334(6053). 226-229. https://doi.org/10.1126/science.1210574
- Freund T, Katona I (2007) Perisomatic Inhibition. Neuron. 56(1). 33-42. https://doi.org/10.1016/j.neuron.2007.09.012
- Juzekaeva E, Nasretdinov A, Mukhtarov M, Shipkov D, Valeeva G, Khazipov R (2024) Comparison of extracellular Giant depolarizing potentials in vitro and early sharp waves in vivo in the CA1 hippocampus of neonatal rats. Biochemical and Biophysical Research Communications. 735. 150823. https://doi.org/10.1016/j.bbrc.2024.150823
- Karlsson K, Mohns E, di Prisco G, Blumberg M (2006) On the co-occurrence of startles and hippocampal sharp waves in newborn rats. Hippocampus. 16(11). 959-965. https://doi.org/10.1002/hipo.20224
- Mohns E, Blumberg M (2008) Synchronous Bursts of Neuronal Activity in the Developing Hippocampus: Modulation by Active Sleep and Association with Emerging Gamma and Theta Rhythms. The Journal of Neuroscience. 28(40). 10134-10144. https://doi.org/10.1523/jneurosci.1967-08.2008
- Andersen, Per, and others (eds) (New York, 2006; online edn, Oxford Academic, 1 May 2009) *The Hippocampus Book*, Oxford Neuroscience Series, https://doi.org/10.1093/acprof:oso/9780195100273.001.0001
- Khazipov R, Minlebaev M, Valeeva G (2013) Early gamma oscillations. Neuroscience. 250. 240-252. HTTPS://DOI.ORG/10.1016/j.neuroscience.2013.07.019
- Pouille F, Scanziani M (2001) Enforcement of Temporal Fidelity in Pyramidal Cells by Somatic Feed-Forward Inhibition. Science. 293(5532). 1159-1163. https://doi.org/10.1126/science.1060342
- Shipkov D, Nasretdinov A, Khazipov R, Valeeva G (2024) Synchronous excitation in the superficial and deep layers of the medial entorhinal cortex precedes early sharp waves in the neonatal rat hippocampus. Frontiers in Cellular Neuroscience. 18. https://doi.org/10.3389/fncel.2024.1403073
- Klausberger T, Somogyi P (2008) Neuronal Diversity and Temporal Dynamics: The Unity of Hippocampal Circuit Operations. Science. 321(5885). 53-57. https://doi.org/10.1126/science.1149381
- Doischer D, Aurel Hosp J, Yanagawa Y, Obata K, Jonas P, Vida I, Bartos M (2008) Postnatal Differentiation of Basket Cells from Slow to Fast Signaling Devices. The Journal of Neuroscience. 28(48). 12956-12968. https://doi.org/10.1523/jneurosci.2890-08.2008
- Gainutdinov A, Juzekaeva E, Mukhtarov M, Khazipov R (2023) Anoxic spreading depolarization in the neonatal rat cortex in vitro. Frontiers in Cellular Neuroscience. 17. https://doi.org/10.3389/fncel.2023.1106268

- van Strien N, Cappaert N, Witter M (2009) The anatomy of memory: an interactive overview of the parahippocampal–hippocampal network. Nature Reviews Neuroscience. 10(4). 272-282. https://doi.org/10.1038/nrn2614
- Leinekugel X, Medina I, Khalilov I, Ben-Ari Y, Khazipov R (1997) Ca2+ Oscillations Mediated by the Synergistic Excitatory Actions of GABAA and NMDA Receptors in the Neonatal Hippocampus. Neuron. 18(2). 243-255. https://doi.org/10.1016/s0896-6273(00)80265-2
- Valeeva G, Janackova S, Nasretdinov A, Rychkova V, Makarov R, Holmes G, Khazipov R, Lenck-Santini P (2018) Emergence of Coordinated Activity in the Developing Entorhinal–Hippocampal Network. Cerebral Cortex. 29(2). 906-920. https://doi.org/10.1093/cercor/bhy309
- Mohns E, Karlsson K, Blumberg M (2007) Developmental emergence of transient and persistent hippocampal events and oscillations and their association with infant seizure susceptibility. European Journal of Neuroscience. 26(10). 2719-2730. https://doi.org/10.1111/j.1460-9568.2007.05928.x
- Dard R, Leprince E, Denis J, Rao Balappa S, Suchkov D, Boyce R, Lopez C, Giorgi-Kurz M, Szwagier T, Dumont T, Rouault H, Minlebaev M, Baude A, Cossart R, Picardo M (2022) The rapid developmental rise of somatic inhibition disengages hippocampal dynamics from self-motion. eLife. 11. https://doi.org/10.7554/elife.78116
- Frolova A, Gainutdinov A, Juzekaeva E, Safeeva L, Valeeva G, Khazipov R (2023) Development of GABAergic Inhibition Associated with Entorhinal Input in Granular Cells of the Dentate Gyrus. Journal of Evolutionary Biochemistry and Physiology. 59(6). 2390-2398. https://doi.org/10.1134/s002209302306039x
- Super M (1994) Human Embryology. Postgraduate Medical Journal. 70(823). 387-387. https://doi.org/10.1136/pgmj.70.823.387-a
- Graf J, Zhang C, Marguet S, Herrmann T, Flossmann T, Hinsch R, Rahmati V, Guenther M, Frahm C, Urbach A, Neves R, Witte O, Kiebel S, Isbrandt D, Hübner C, Holthoff K, Kirmse K (2021) A limited role of NKCC1 in telencephalic glutamatergic neurons for developing hippocampal network dynamics and behavior. Proceedings of the National Academy of Sciences. 118(14). https://doi.org/10.1073/pnas.2014784118
- Khalilov I, Esclapez M, Medina I, Aggoun D, Lamsa K, Leinekugel X, Khazipov R, Ben-Ari Y (1997) A Novel In Vitro Preparation: the Intact Hippocampal Formation. Neuron. 19(4). 743-749. https://doi.org/10.1016/s0896-6273(00)80956-3
- Spruston N (2008) Pyramidal neurons: dendritic structure and synaptic integration. Nature Reviews Neuroscience. 9(3). 206-221. https://doi.org/10.1038/nrn2286
- Marguet S, Le-Schulte V, Merseburg A, Neu A, Eichler R, Jakovcevski I, Ivanov A, Hanganu-Opatz I, Bernard C, Morellini F, Isbrandt D (2015) Treatment during a vulnerable developmental period rescues a genetic epilepsy. Nature Medicine. 21(12). 1436-1444. https://doi.org/10.1038/nm.3987
- Khalilov I, Minlebaev M, Mukhtarov M, Khazipov R (2015) Dynamic Changes from Depolarizing to Hyperpolarizing GABAergic Actions during Giant Depolarizing Potentials in the Neonatal Rat Hippocampus. The Journal of Neuroscience. 35(37). 12635-12642. https://doi.org/10.1523/jneurosci.1922-15.2015

- Hu H, Gan J, Jonas P (2014) Fast-spiking, parvalbumin + GABAergic interneurons: From cellular design to microcircuit function. Science. 345(6196). https://doi.org/10.1126/science.1255263
- Dzhala V, Khalilov I, Ben-Ari Y, Khazipov R (2001) Neuronal mechanisms of the anoxia-induced network oscillations in the rat hippocampus in vitro. The Journal of Physiology. 536(2). 521-531. https://doi.org/10.1111/j.1469-7793.2001.0521c.xd
- Losonczy A, Zhang L, Shigemoto R, Somogyi P, Nusser Z (2002) Cell type dependence and variability in the short-term plasticity of EPSCs in identified mouse hippocampal interneurones. The Journal of Physiology. 542(1). 193-210. https://doi.org/10.1113/jphysiol.2002.020024
- Leinekugel X, Khazipov R, Cannon R, Hirase H, Ben-Ari Y, Buzsáki G (2002) Correlated Bursts of Activity in the Neonatal Hippocampus in Vivo. Science. 296(5575). 2049-2052. https://doi.org/10.1126/science.1071111
- Klausberger T, Márton L, Baude A, Roberts J, Magill P, Somogyi P (2003) Spike timing of dendrite-targeting bistratified cells during hippocampal network oscillations in vivo. Nature Neuroscience. 7(1). 41-47. https://doi.org/10.1038/nn1159

4.5. Article 5. (in preparation) Distribution of synapses along the radial axis of the CA1 hippocampus

Azat GAINUTDINOV, Rin KIKUCHI, Marie Giorgi-KURZ, Robin F DARD, Michel A PICARDO, Rosa COSSART, Roustem KHAZIPOV, Agnès BAUDE

Aix-Marseille University, INMED, INSERM, Marseille, 13273 France

4.5.1. Abstract

The developmental organization of synaptic connections within the hippocampal CA1 region plays a crucial role in shaping neural circuits that underpin cognitive functions. Here, we investigated the distribution and maturation of inhibitory synapses marked by synaptotagmin-2 (Syt-2) expression (a proxy for future parvalbumin-expressing axon terminals) along the radial axis of the CA1 in postnatal mice. Using immunocytological techniques and confocal microscopy, we analyzed Syt-2 expression within the stratum oriens (SO), stratum pyramidale (SP), and stratum radiatum (SR) of CA1 hippocampus area across postnatal period (P5, P11, P15, P21). Our results demonstrate a developmental increase in Syt-2 expressing axon terminals density within SP, peaking at P15, followed by a slight reduction at P21. In contrast, SO exhibited high axon terminals density early at P5, with moderate changes throughout development, suggesting a distinct maturation timeline compared to SP. The SR showed minimal variation in axon terminals density across the studied ages. These findings suggest a sequential maturation pattern, where dendritic inhibition by interneurons precedes the establishment of perisomatic inhibitory synapses. We propose that this developmental trajectory reflects a critical transition in GABAergic regulation, potentially underlying the evolving functional properties of CA1 pyramidal neurons. Our study provides new insights into the spatial and temporal dynamics of inhibitory innervation development, with implications for understanding the mechanisms of hippocampal maturation and synaptic plasticity.

4.5.2. Introduction

The hippocampus is a critical brain structure involved in learning and memory, playing a central role in processing and storing information (Dhikav and Anand, 2012). Within the hippocampal formation, the CA1 region serves as a key integrative hub, receiving and refining input from other regions to produce well-coordinated output (Barrientos and Tiznado, 2016). The proper functioning of the CA1 area relies heavily on a precise balance between excitatory and inhibitory signals, with local GABAergic interneurons providing essential inhibitory control (Hernández-Frausto et al., 2023; Pelkey et al., 2017). These interneurons, by forming synaptic connections at strategic locations on pyramidal cells, regulate excitability and maintain network stability (Pelkey et al., 2017).

During postnatal development, the organization of synaptic connections within the hippocampus undergoes significant changes. The maturation of inhibitory circuits is particularly important, as it influences the timing and strength of network activity patterns that are critical for cognitive function (Hernández-Frausto et al., 2023; Pelkey et al., 2017). Previous research has shown a general increase in the density of GABAergic axon terminals (Dard et al., 2022) within the stratum pyramidale of CA1 through postnatal ages. However how these terminals are distributed across different layers of the CA1 region and how this distribution evolves over time remain to be analyzed. GABAergic axon terminals distribution along the radial axis—from the stratum oriens (SO) and stratum pyramidale (SP) to the stratum radiatum (SR)—may have important implications for the functional maturation of CA1 circuits (Hernández-Frausto et al., 2023).

We have focused our analysis on parvalbumin expressing interneurons that regroup three major interneuron sub-populations: the basket cells, the axo-axonic cells, and the bi-stratified cells at the origin of perisomatic innervation, initial segment, and dendrite innervation of pyramidal cells, respectively (Pelkey et al., 2017; Harris et al., 2018). Specifically in this study, we aim to investigate the developmental changes in the distribution of parvalbumin-positive inhibitory axon terminals along the radial axis of the CA1 region in postnatal rodents. As parvalbumin is expressed after the second post-natal week, we used synaptotagmin2 (Syt2), a reliable marker for parvalbumin-positive inhibitory boutons in cortical areas (Sommeijer and Levelt, 2012). In addition, Syt-2 appears to be specific to fast-spiking parvalbumin basket cells (Sommeijer and Levelt, 2012; Harris et al., 2018). Using immunohistochemical techniques and high-resolution confocal microscopy, we analyze axon terminal density patterns in the SO, SP, and SR layers across key postnatal ages. By understanding how inhibitory axon terminals are distributed and how this distribution shifts over time, we can gain insights into the maturation of hippocampal circuits and the mechanisms underlying developmental changes in network function (Hernández-Frausto et al., 2023). This research may also provide valuable clues about the origins of neurodevelopmental disorders characterized by disrupted inhibitory signaling (Masurkar, 2018).

4.5.3. Materials and methods

4.5.3.1. Histological processing

Pups were deeply anesthetized with a mix of Domitor and Zoletil (0.9 and 60 mg/kg, respectively), then transcardially perfused with 4% paraformaldehyde (PFA) in 0.1 M phosphate-buffered saline (PBS) (PBS tablets, 18912-014, Life Technologies). For perisomatic innervation analysis, brains were post-fixed overnight at 4°C in 4% PFA in 0.1 M PBS, washed in PBS, cryo-protected in 30% sucrose in PBS, before liquid nitrogen freezing. Brains were then sectioned using a cryostat (CM 3050S, Leica) into 50-µm-thick slices collected on slides. Sections were stored at –20°C until further usage. Immunocytochemistry was processed as described previously (Bocchio et al., 2020).

Briefly, sections were blocked with PBS-Triton (PBST) 0.3 and 10% normal donkey serum (NDS), and incubated with the following primary antibody, mouse anti- Syt-2 (1:100; Developmental Studies Hybridoma Bank, AB_2315626) diluted in PBST with 1% NDS overnight at room temperature. After several washes, the following secondary antibody was used: donkey anti-mouse Alexa 647 (1:500, Thermo Fisher, A31571). After Hoechst counter-staining, slices were mounted in Fluoromount. Epifluorescence images were obtained with a Zeiss AxioImager Z2 microscope coupled to a camera (Zeiss AxioCam MR3) with an HBO lamp associated with 470/40 and 605/70 filter cubes. Confocal images were acquired with a Zeiss LSM-800 system equipped with a tunable laser providing excitation range from 405 to 670 nm. For quantifying Syt-2, 11-µm-thick stacks were taken (z = 1 µm, pixel size = 0,156 µm) with the confocal microscope using a Plan-Achromat ×40/1.4 oil DIC objective.

4.5.3.2. Data analysis

For the analysis we had the following number of pups and the average number of slices per pup for each postnatal age. For the locations SO and SR at postnatal age P5, there were 3 pups and an average of 10 slices per pup. At P11, there were 5 pups and an average of 9 slices per pup. At P15, there were 4 pups and an average of 7 slices per pup. At P21, there were 6 pups and an average of 8 slices per pup. At 4 months, there were 2 pups and an average of 8 slices per pup. For the location SP at postnatal age P5, there were 4 pups and an average of 12 slices per pup. At P11, there were 6 pups and an average of 11 slices per pup. At P15, there were 5 pups and an average of 9 slices per pup. At P21, there were 7 pups and an average of 10 slices per pup. At 4 months, there were 3 pups and an average of 9 slices per pup.

Confocal images of Syt-2 immunostaining were analyzed using a custom Python program named SynaptoCatcher. The following is a description of the program. A max-intensity projection of the z-stack images of the top 6 µm from the slice surface was performed first. The user selects a region of interest (ROI) for three regions (SO, SP, SR) using polygonal shapes. The obtained images were denoised by subtracting the background. The background image was generated using the OpenCV library's median Blur function, which applies a median filter with a radius of 50 pixels, corresponding to 7.8 µm. This radius defines the size of the neighborhood used to calculate the median, effectively reducing noise while preserving edges. After background subtraction, the images underwent Otsu's thresholding for binarization. Otsu's method works by automatically finding the threshold value that minimizes the intra-class variance of the pixel intensities, separating the foreground from the background.

Objects from the resulting binary image were filtered by size, retaining only those with an area between 0.49 and 4.9 μm^2, ensuring that only objects of axon terminal size remained. These retained objects were considered covered by positive Syt-2 labeling. The relative area within each ROI was then calculated based on the remaining objects. The relative area was determined as the area occupied by objects covered by positive Syt-2 labeling, divided by the area of the selected region.

4.5.3.3. Statistical Analysis and Data Visualization

Groups were compared using the non-parametric Kruskal-Wallis test. Statistical significance of the differences is indicated by stars: `****` — $p \leq 0.0001$; `***` — $p \leq 0.001$; `**` — $p \leq 0.01$; `*` — $p \leq 0.05$; `ns` (not significant) — $p > 0.05$. The white horizontal line on the boxplot represents the median. The rectangular area (the box) corresponds to the 25th and 75th percentiles (interquartile range). The ends of the vertical lines ("whiskers") indicate the 5th and 95th percentiles, showing the range of the data excluding extreme values.

4.5.4. Results

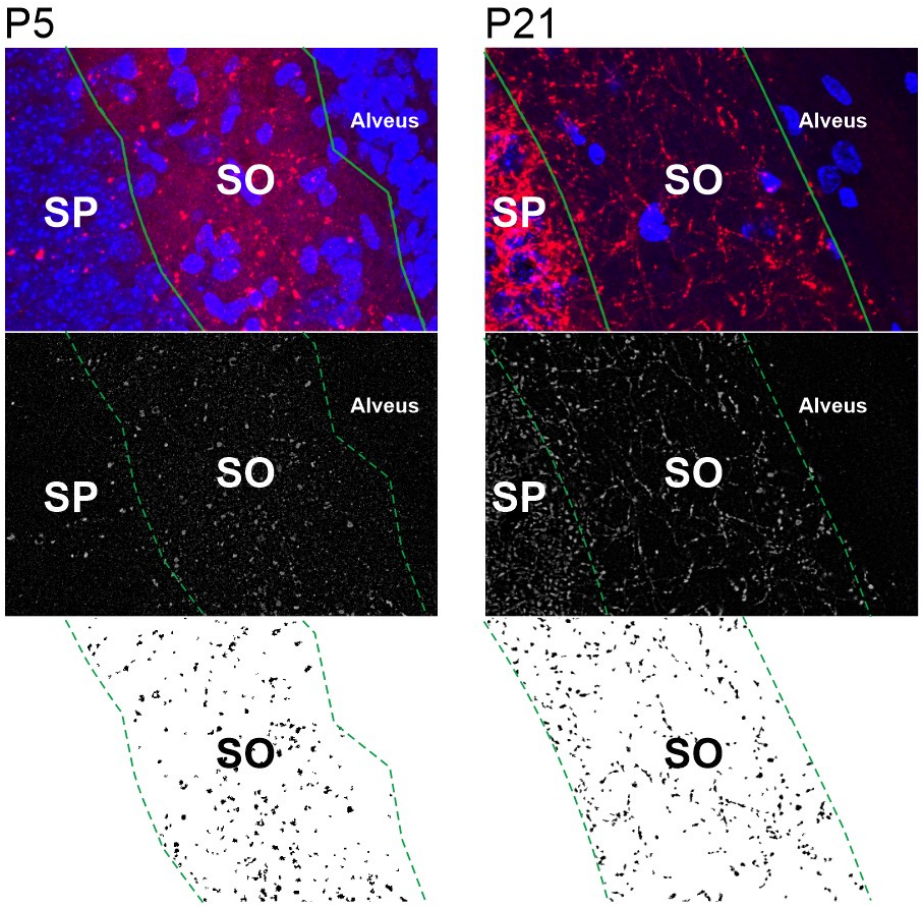

Figure 82. Image processing example: filtering and binarization of synaptotagmin-2 (Syt-2) staining within the stratum oriens (SO) at two developmental ages (P5 and P21).

The top panels show raw z-stack images of Syt-2 staining (red) marking Syt-2-positive axon terminals, with nuclei counterstained by **Hoechst** (blue). Middle panels represent filtered Syt-2 signal after noise reduction to isolate axon terminal structures. Bottom panels display binary masks generated from the processed Syt-2 signal, where objects are selected based on size and identified as putative axon terminals. In the bottom panel, only the terminals in the SO region selected for this analysis can be seen, since the other regions are ignored after the mask is applied. The structural changes observed between P5 and P21 highlight the developmental refinement of axonal terminals in the SO region, with the boundaries of stratum pyramidale (SP), SO, and alveus outlined in green.

Previous findings (Dard et al., 2022) indicated that the relative number of Syt-2 positive axon terminals in the pyramidal layer of the CA region increases with age. We

performed similar image analysis (See Figure 83). In keeping with the findings reported by Dard and colleagues, we found few Syt-2 expression within the CA1 pyramidal cell layer at P5, and strong increase at P11 and P15 (See Figure 84). However, a slight decline in synaptic area is seen at P21, showing a putative period of axon terminal pruning or stabilization as the network matures.

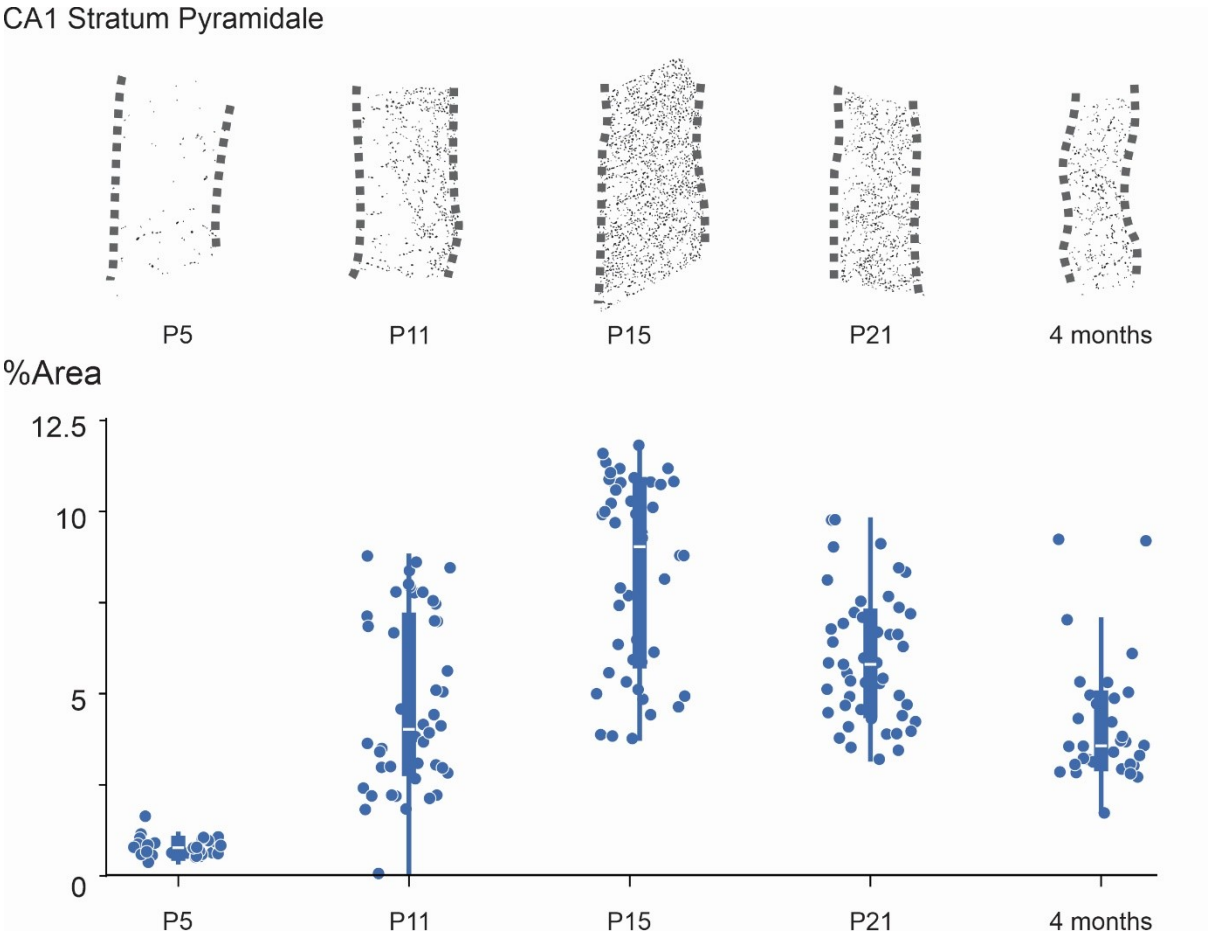

Figure 83. Syt-2 staining within Stratum Pyramidale.

Top - examples of filtered and binarized image of Syt-2 staining within SP across different postnatal ages (P5, P11, P15, P21 and adult-4 months). Bottom - Boxplots showing the distribution of axon terminal density (%Area) at different postnatal ages. There is a significant increase in density from day 5 to day 11, which continues to rise until day 15 before decreasing slightly by day 21 and later. For additional information, refer to the Data analysis and the Statistical Analysis and Data Visualization sections in Materials and Methods.

In contrast to pyramidal cell layer, we found high Syt-2 levels in the stratum oriens of CA1 already at P5 (See Figure 84). This was followed by moderate increase at P11 and P15, then a decline in older animals. This suggests a distinct developmental trajectory in SO compared to SP.

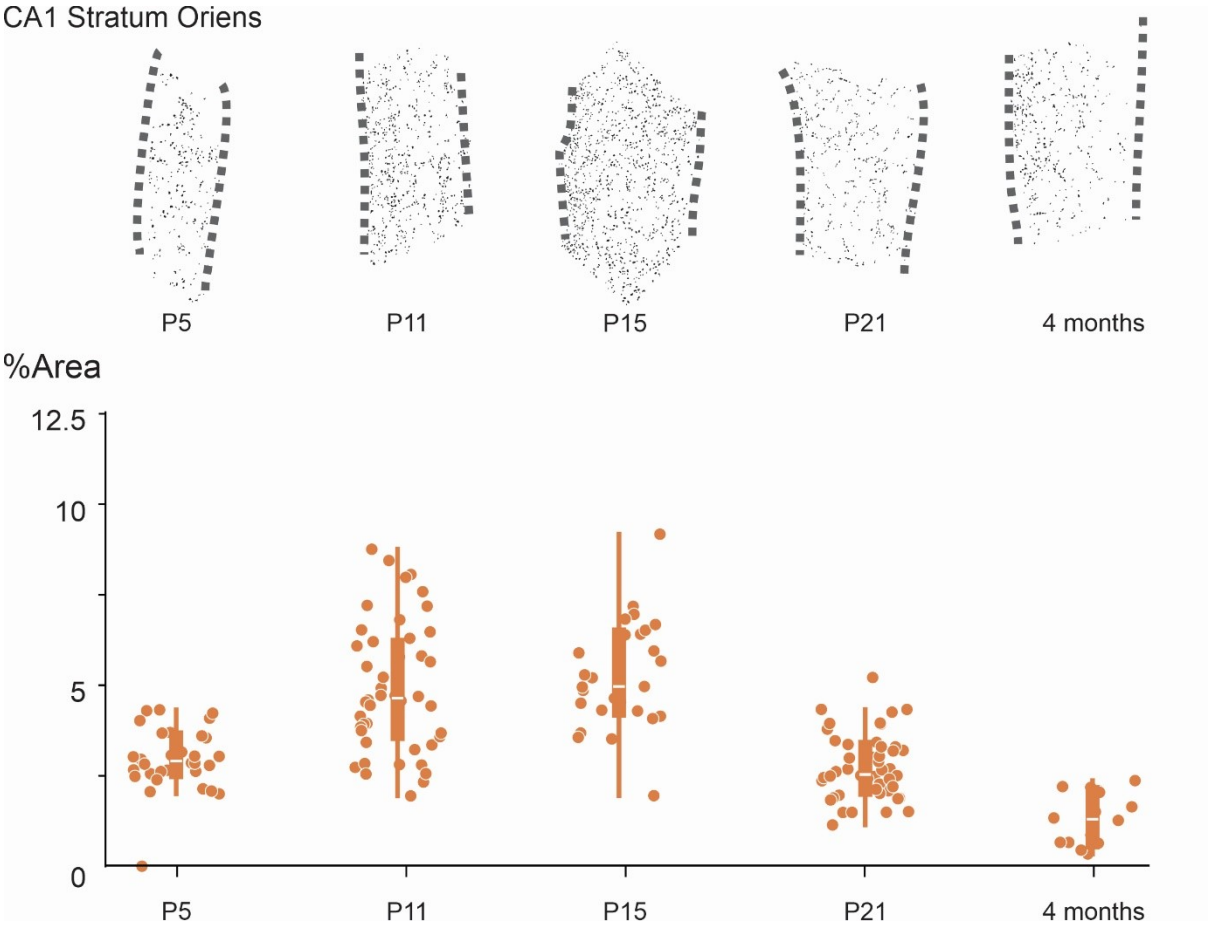

Figure 84. Syt-2 staining within Stratum Oriens.

Top - examples of filtered and binarized image of Syt-2 staining within SO across different postnatal ages (P5, P11, P15, P21 and adult-4 months). Bottom - Boxplots showing the distribution of axon terminal density (%Area) at different postnatal ages. There is a noticeable increase in synaptic density at postnatal day 11 compared to day 5, but this is not sustained at day 15. When comparing P15 and older ages (P21, 4 months), a significant reduction in synapse density was found. For additional information, refer to the Data analysis and the Statistical Analysis and Data Visualization sections in Materials and Methods.

In the stratum radiatum of CA1 (See Figure 85) Syt-2 expression remains relatively low and consistent across postnatal development from P5 to 4 months.

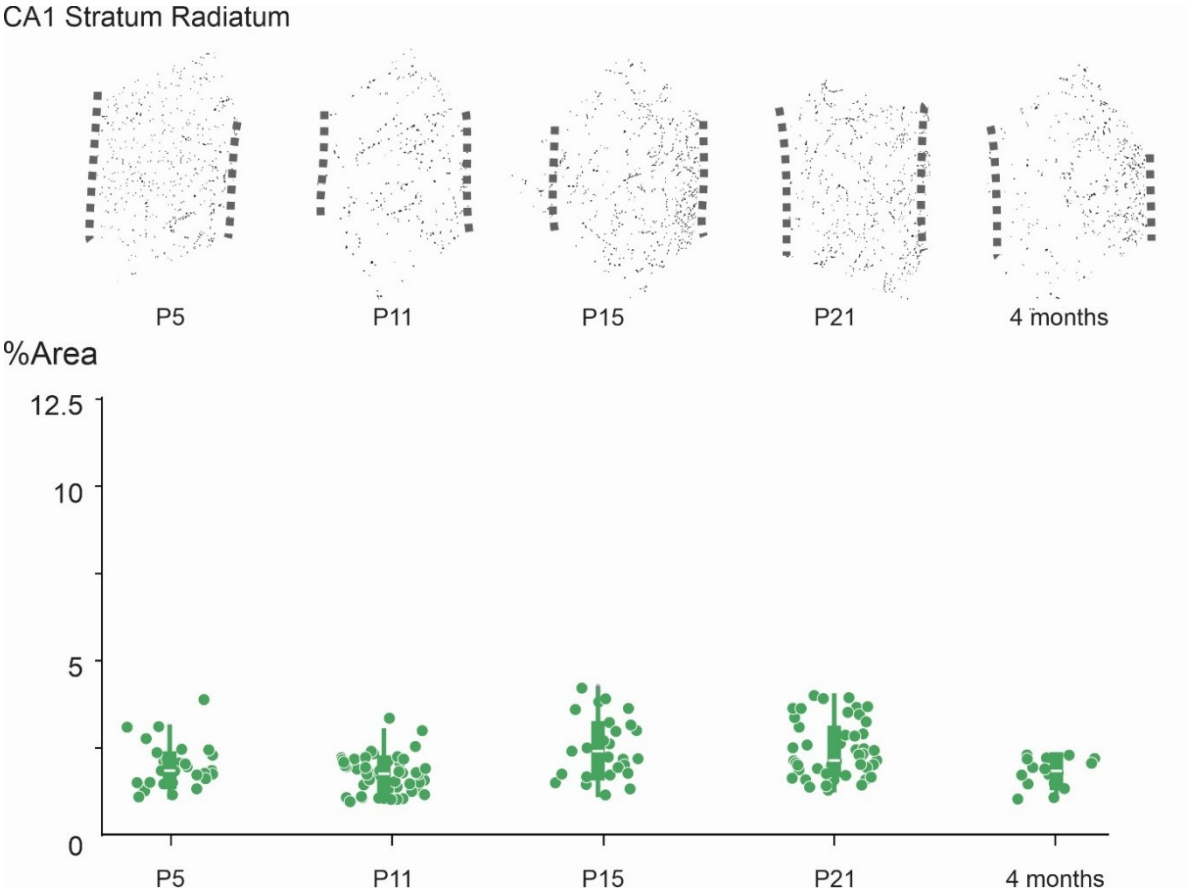

Figure 85. Syt-2 staining within Stratum Radiatum.

Top - examples of filtered and binarized image of Syt-2 staining within SO across different postnatal ages (P5, P11, P15, P21 and adult-4 months). Bottom - Boxplots showing the distribution of axon terminal density (%Area) at different postnatal ages. There is no significant change in axon terminal density at postnatal day 11 compared to day 5, but a notable increase is observed at day 15, indicating some growth but not as pronounced as in the SP layer. For additional information, refer to the Data analysis and the Statistical Analysis and Data Visualization sections in Materials and Methods.

The most important observation was the comparison of the density of Syt-2 expressing axon terminals between different layers within the first week. The bar graph on the Figure 86 shows that Syt-2 is expressed significantly more in SO compared to the other layers. The SP has the lowest expression at this early stage.

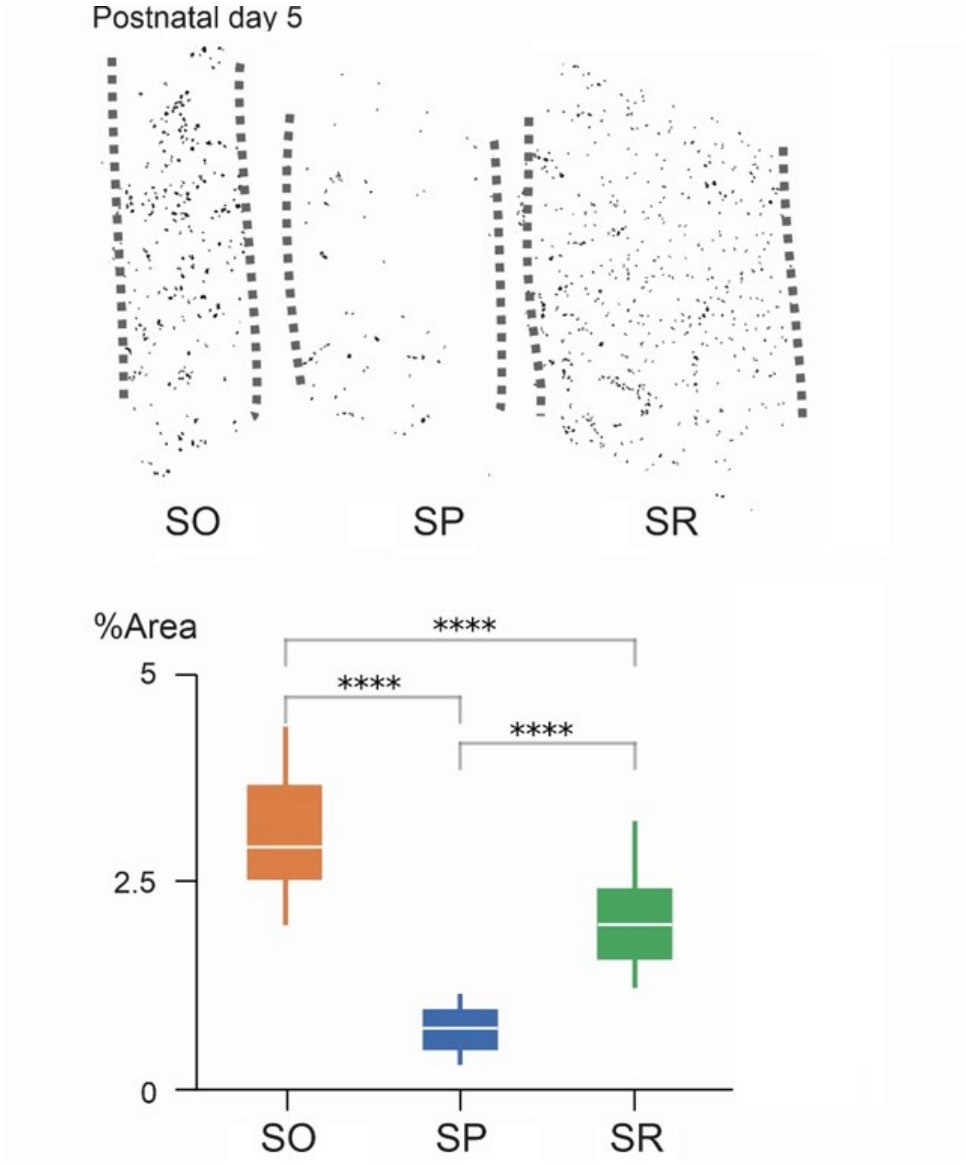

Figure 86. Syt-2 axon terminal density (%Area) within SP (stratum pyramidale), SO (stratum oriens) and SR (stratum radiatum) at postnatal day 5.

Synaptic density is lowest in SP and higher in SO and SR, with SO having the highest density. Statistical significance indicated by asterisks For additional information, refer to the Data analysis and the Statistical Analysis and Data Visualization sections in Materials and Methods.

Figure 87 provides a comprehensive view of how axon terminal density changed with age across different regions. In addition to the previously noted dominance of axon terminal density in SO over SP and SR at P5, we can observe how the values for SP and SO initially equalized at P11, and then at P15, Syt-2 became more abundant in SP than in SO. This transition after P11 persists into adulthood.

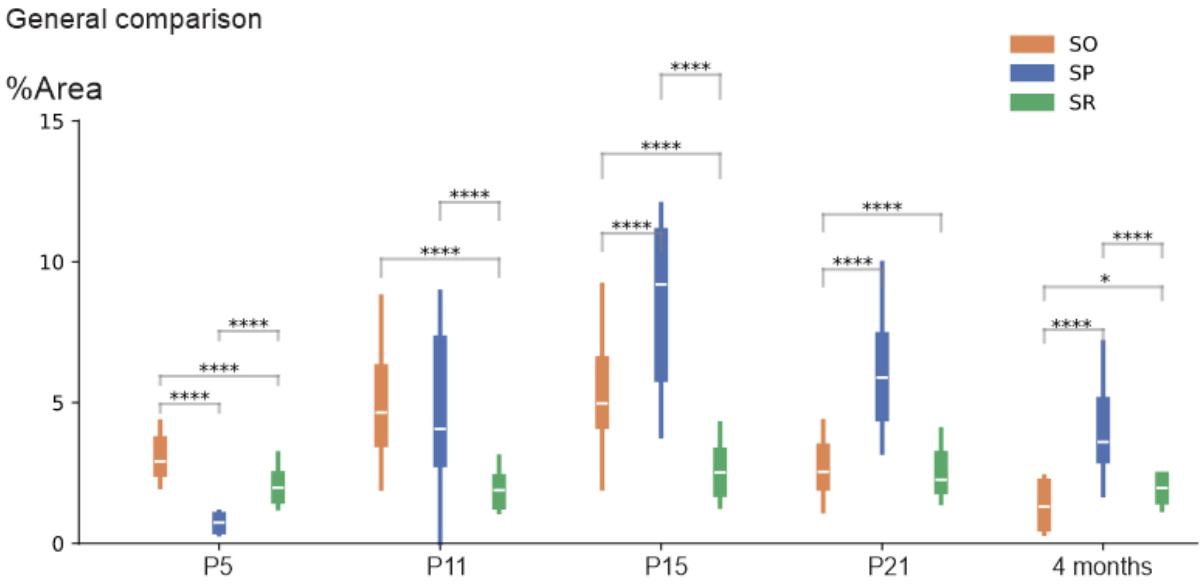

Figure 87. Axon terminal density (%Area) in hippocampal CA1 sublayers during postnatal development (P5, P11, P15, P21 and adult).

Statistical significance indicated by asterisks. At P5, synaptic density is lowest in SP and higher in SO and SR, with SO having the highest density. By P11, SP density increases significantly, surpassing SO and SR. At P15, SP maintains the highest density, with SO and SR showing lower and more comparable densities. By P21, SP remains the highest, but overall each areas SP, SO and SR slightly decreases. For additional information, refer to the Data analysis and the Statistical Analysis and Data Visualization sections in Materials and Methods.

This observation of axon terminal density across multiple ages and CA1 sublayers leads us to the following hypothesis - fast-spiking PV-basket interneurons first form transient synapses on the dendrites of CA1 pyramidal cells, with a preference for basal dendrites, before establishing perisomatic synapses (See Figure 88). This developmental pattern suggests a sequential maturation of inhibitory synapses, where dendritic inhibition precedes the more mature perisomatic inhibition, which plays a key role in regulating pyramidal cell output.

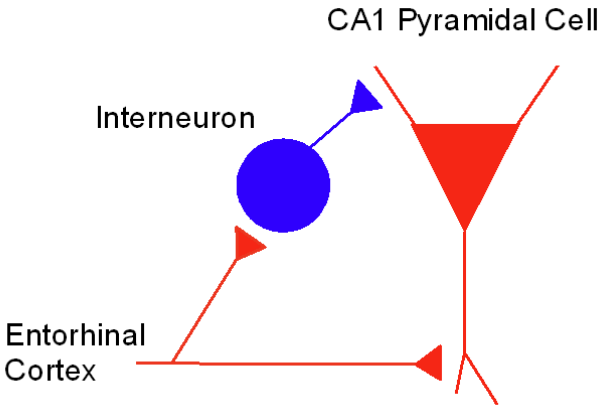

Figure 88. Hypothetical scheme of connections at early postnatal age (P5).

In this diagram, during the first week of development, future fast-spiking parvalbumin basket cells would first establish synapses on the on the basal dendrites of CA1 pyramidal cell before perisomatic ones. Thus, the distribution of future parvalbuminergic axon terminals detected through Syt-2 staining suggests that there is no full-fledged perisomatic inhibition in the first week of development.

4.5.5. Discussion

Our findings reveal a sequential maturation of inhibitory synapses in the hippocampal CA1 region, shedding light on the developmental progression of Syt-2 -positive axon terminals along the radial axis. The observed changes served as the basis for us to put forward the hypothesis that fast-spiking parvalbumin basket cells first establish synaptic connections on the dendrites of CA1 pyramidal cells, preferentially targeting basal dendrites, before forming perisomatic synapses. This developmental sequence likely reflects a strategic shift in the regulation of neuronal excitability. Another hypothesis would be that inhibitory synapses in early ages operate differently than adult synapses (Cohen et al., 2000).

4.5.6. Sequential maturation and functional implications

The increase in axon terminal density within the stratum pyramidale (SP) from P5 to P15, followed by a slight decline at P21, suggests that the maturation of perisomatic innervation (Dard et al., 2022; Hijazi et al., 2023) coincides with a critical window of hippocampal development. This timeline may correspond to key functional transitions, such as the emergence of mature network oscillations and improved spatial memory encoding. In contrast, the high synaptic density observed in the stratum oriens (SO) at P5 and its subsequent moderate fluctuation suggests an early and persistent role for dendritic inhibition. This pattern suggests that basal dendritic inhibition would be crucial during the initial phases of postnatal development, potentially facilitating proper dendritic integration of excitatory inputs (Muller and Remy, 2014).

4.5.7. Developmental differences among layers

The distinct axon terminal density trajectories observed in SO, SP, and the stratum radiatum (SR) underscores the complexity of inhibitory circuit maturation. The relatively stable axon terminal density in SR suggests that this region does not undergo the same developmental shifts as SP and SO, possibly indicating that dendritic synapses in SR are established early. Thus, SR located inhibition remains unchanged to support stable input integration. In contrast, the pronounced increase and subsequent reduction in SP and SO may highlight a dynamic restructuring of perisomatic inhibitory circuits, suggesting a maturation process that would optimize inhibitory control over pyramidal cell output (Cohen et al., 2000).

4.5.8. Comparison with previous studies

Our results align with findings by Dard et al., 2022, who reported an age-related increase in axon terminal density in the pyramidal cell layer of the CA1 region. We extend these observations by demonstrating that the increase is not uniform across all layers and that a developmental decline occurs around P15. This suggests a more nuanced

developmental trajectory, where early overproduction of synapses is followed by pruning or stabilization as the network matures (Cohen et al., 2000). These results also resonate with other studies that emphasize the importance of synaptic reorganization during critical periods of hippocampal development (Hijazi et al., 2023).

4.5.9. Mechanistic insights and future directions

The mechanisms underlying the observed sequential maturation remain an area of active investigation. One possibility is that activity-dependent synaptic plasticity, influenced by sensory experience or network activity, drives the establishment and refinement of inhibitory synapses. The role of signaling pathways, such as NT-3-TrkC or neuroligin-neurexin interactions (Tsetsenis et al., 2014), should be explored to determine their contributions to synaptic maturation. Future studies could use genetic models or optogenetic tools to manipulate specific interneuron populations and examine the impact on synaptic distribution and hippocampal function (Hijazi et al., 2023).

4.5.10. Limitations and considerations

While our study provides valuable insights into the developmental distribution of axon terminal distribution allowing us to make assumptions about synaptic development, there are several limitations to consider. The resolution of our imaging techniques, while suitable for detecting Syt-2-positive axon terminals, may not capture finer synaptic details. Additionally, the use of rodent models, though informative, raises questions about the generalizability of these findings to other species, including humans. Further research should aim to characterize the functional properties of synapses in different hippocampal layers and explore the impact of environmental or genetic factors on inhibitory synapse development (Ekins et al., 2020).

4.5.11. Conclusion

In conclusion, our study highlights the importance of a well-orchestrated developmental program in the maturation of inhibitory circuits within the CA1 region. The transition from dendritic to perisomatic inhibition represents a crucial step in the establishment of mature hippocampal function. Understanding these processes is crucial for elucidating the mechanisms underlying cognitive development and will provide insights into neurodevelopmental disorders where inhibitory circuit maturation could be disrupted.

4.5.12. Author contributions

RK, AB, MP, RC conceptualized and drafted the manuscript. AB, RK, MK performed the histological preparation of the slices. AG, RD analyzed data. All authors revised the manuscript and interpreted the data.

4.5.13. Funding sources

This research was supported by ANR (grant “HIPPODEV”) and RSF (grant #21-75-10033).

4.5.14. Conflict of interest

The authors declare that the research was conducted in the absence of any commercial or financial relationships that could be construed as a potential conflict of interest.

4.5.15. Data availability statement

The datasets generated and analyzed in this study are available on reasonable request from the authors.

4.5.16. References

- Ekins T, Mahadevan V, Zhang Y, D'Amour J, Akgül G, Petros T, McBain C (2020) Emergence of non-canonical parvalbumin-containing interneurons in hippocampus of a murine model of type I lissencephaly. eLife. 9. https://doi.org/10.7554/elife.62373
- Pelkey K, Chittajallu R, Craig M, Tricoire L, Wester J, McBain C (2017) Hippocampal GABAergic Inhibitory Interneurons. Physiological Reviews. 97(4). 1619-1747. https://doi.org/10.1152/physrev.00007.2017
- Cohen A, Lin D, Coulter D (2000) Protracted Postnatal Development of Inhibitory Synaptic Transmission in Rat Hippocampal Area CA1 Neurons. Journal of Neurophysiology. 84(5). 2465-2476. https://doi.org/10.1152/jn.2000.84.5.2465
- Megías M, Emri Z, Freund T, Gulyás A (2001) Total number and distribution of inhibitory and excitatory synapses on hippocampal CA1 pyramidal cells. Neuroscience. 102(3). 527-540. https://doi.org/10.1016/s0306-4522(00)00496-6
- Harris K, Hochgerner H, Skene N, Magno L, Katona L, Bengtsson Gonzales C, Somogyi P, Kessaris N, Linnarsson S, Hjerling-Leffler J (2018) Classes and continua of hippocampal CA1 inhibitory neurons revealed by single-cell transcriptomics. PLOS Biology. 16(6). e2006387. https://doi.org/10.1371/journal.pbio.2006387
- MÃ¼ller C, Remy S (2014) Dendritic inhibition mediated by O-LM and bistratified interneurons in the hippocampus. Frontiers in Synaptic Neuroscience. 6. https://doi.org/10.3389/fnsyn.2014.00023
- Hernández-Frausto M, Bilash O, Masurkar A, Basu J (2023) Local and long-range GABAergic circuits in hippocampal area CA1 and their link to Alzheimer’s disease. Frontiers in Neural Circuits. 17. https://doi.org/10.3389/fncir.2023.1223891
- Masurkar A (2018) Towards a Circuit-Level Understanding of Hippocampal CA1 Dysfunction in Alzheimer's Disease Across Anatomical Axes. Journal of Alzheimer’s Disease and Parkinsonism. 08(01). https://doi.org/10.4172/2161-0460.1000412

- Tsetsenis T, Boucard A, Araç D, Brunger A, Südhof T (2014) Direct Visualization of Trans-Synaptic Neurexin–Neuroligin Interactions during Synapse Formation. The Journal of Neuroscience. 34(45). 15083-15096. https://doi.org/10.1523/jneurosci.0348-14.2014
- Sommeijer J, Levelt C (2012) Synaptotagmin-2 Is a Reliable Marker for Parvalbumin Positive Inhibitory Boutons in the Mouse Visual Cortex. PLoS ONE. 7(4). e35323. https://doi.org/10.1371/journal.pone.0035323
- Han K, Woo D, Kim S, Choii G, Jeon S, Won S, Kim H, Heo W, Um J, Ko J (2016) Neurotrophin-3 Regulates Synapse Development by Modulating TrkC-PTPσ Synaptic Adhesion and Intracellular Signaling Pathways. The Journal of Neuroscience. 36(17). 4816-4831. https://doi.org/10.1523/jneurosci.4024-15.2016
- Dhikav V, Anand K (2012) Hippocampus in health and disease: An overview. Annals of Indian Academy of Neurology. 15(4). 239. https://doi.org/10.4103/0972-2327.104323
- Barrientos S, Tiznado V (2016) Hippocampal CA1 Subregion as a Context Decoder. The Journal of Neuroscience. 36(25). 6602-6604. https://doi.org/10.1523/jneurosci.1107-16.2016
- Dard R, Leprince E, Denis J, Rao Balappa S, Suchkov D, Boyce R, Lopez C, Giorgi-Kurz M, Szwagier T, Dumont T, Rouault H, Minlebaev M, Baude A, Cossart R, Picardo M (2022) The rapid developmental rise of somatic inhibition disengages hippocampal dynamics from self-motion. eLife. 11. https://doi.org/10.7554/elife.78116
- Hijazi S, Smit A, van Kesteren R (2023) Fast-spiking parvalbumin-positive interneurons in brain physiology and Alzheimer's disease. Molecular Psychiatry. 28(12). 4954-4967. https://doi.org/10.1038/s41380-023-02168-y

5. Discussion

Our work provides significant insights into the mechanisms underlying the generation of Early Sharp Waves (eSPWs) in the neonatal rodent hippocampus, integrating key aspects of sensory activation, age-dependent changes in inhibition, and the spatial organization of synapses made by fast spiking interneurons on pyramidal cells. These findings are crucial for understanding how early activity shapes neural circuits, laying the groundwork for further brain maturation.

5.1. The role of sensory signals in generating eSPW

Our first major finding highlights that sensory stimulation can evoke eSPWs, underscoring the importance of sensory inputs in early hippocampal development. This supports the findings (Karlsson et al., 2006, Valeeva and Janackova et al., 2019, Dard et al., 2022), which demonstrated a link between myoclonic movements and hippocampal activity. However, we extended these findings by demonstrating that evoked sensory stimulation triggers eSPWs even when motor activity is suppressed. This discovery emphasizes the critical role of ascending sensory signals in activating the neonatal hippocampus and shaping its networks (Karlsson et al., 2006; Valeeva and Janackova et al., 2019, Dard et al., 2022).

Important finding of this work is that we were able to separate, using high density recordings and signal reconstruction with a spatial reference to the fissure, the two sinks (sink 2 in CA1 SLM and sink 3 in DG ml) which are presumably generated by inputs from MEC L3 and L2, respectively. Previously, these two sinks were primarily described as single CA1 SLM sink or sink “near the fissure”. These findings are along with the observations on synchronous activation of MEC L2 and L3 neurons during MEC population bursts driving hippocampal eSPWs.

Interestingly, sensory-evoked dentate spikes- 2 (DS2) share some similarity with the neonatal eSPWs including the pivotal role of MEC inputs to DG, and that both eSPWs and DS2 can be evoked by sensory stimulation (Farrell et al., 2024). This raises hypothesis that eSPWs are developmental precursors of DS2, with a difference that EC activation during eSPWs involves co-activation of L2 and L3 (Shipkov et al., 2024), whereas EC activation during DS2 involves activation of L2, but not L3 neurons, according to DS2 depth profile. In future studies it would be of interest to test this hypothesis by exploring EC L2 and L3 activation during DS2 in adult animals.

While our results on sensory-evoked eSPWs are supporting the hypothesis of sensory feedback linking neonatal movements and hippocampal eSPWs, alternative explanations remain including a non-canonical circuit involved in hippocampal activation during

sensory-evoked startles, as described in adults (Zhang et al., 2018). Therefore, further research is needed to identify the involvement of classical sensory feedback pathways to hippocampus and non-canonical pathway involving brainstem – medial septum – EC in linking neonatal movements with eSPWs. Perhaps, the most compelling evidence could be provided by exploring the effect of silencing the S1 cortex, as well as the effects of activation and silencing medial septum on movement-related and sensory evoked eSPWs.

Our results align with theories suggesting that early patterns of activity, such as eSPWs, are involved in the initial programming of neural circuits (Khazipov et al., 2004). Previous studies have noted that early infant movements often coincide with hippocampal events, linking motor and sensory systems to neural activity (Khazipov et al., 2004; Karlsson et al., 2006; Cossart and Khazipov, 2022). Our study is the first to demonstrate that sensory stimulation alone (without causing a movement) is sufficient to generate these patterns in hippocampus, emphasizing the role of the external sensory environment in early brain development. Our findings align with those of Donato et al., 2017 who demonstrated that excitatory signals originating outside the hippocampus, specifically from stellate cells in MEC-L2, sequentially and unidirectionally drive the maturation of the entorhinal-hippocampal network (MEC-L2 → CA3 → CA1 → DG). Similarly, in our case, the induced activation of eSPWs was also triggered by inputs from outside the hippocampus, yet adding to this model importance of the direcr temporo-ammonic pathway (MEC-L3 → CA1) during the early neonatal period.

5.2. Age-dependent changes in inhibitory activity

Another key aspect of our study is understanding how excitatory and inhibitory signals in the hippocampus change with age. We found that inhibitory postsynaptic currents (IPSCs) are delayed from EPSCs both during eSPWs in vivo, and EC-evoked responses in vitro, during the early postnatal days, creating a significant window for the integration of excitatory inputs. This finding supports evidence that GABAergic inhibitory activity matures slowly in early life (Cohen et al., 2000). Our work adds nuance by showing that the delay in inhibitory signaling is particularly pronounced for inputs associated with the entorhinal cortex, which has been underexplored until now.

5.3. Mechanisms behind delayed GABA in neonates

The delay in inhibitory GABA activity in newborns may arise due to various developmental factors, including the immaturity of perisomatic inhibitory neurons, the weakness of excitatory cortical (EC) inputs to interneurons, and the limited functional connectivity between interneurons and their target neurons during early postnatal development. To understand the mechanisms underlying this delayed GABA activity in

neonates, a comparison of the properties of immature and mature fast-spiking interneurons (FS INs) should provide valuable insights. One significant aspect involves the developmental differences in ion channel expression. Mature neurons express Nav1.1 sodium channels, facilitating the rapid generation of short action potentials and enabling high-frequency firing without accommodation. In contrast, developing neurons predominantly express NaV1.3 channels during embryonic life, with a postnatal decline as NaV1.1 and NaV1.2 channels become predominant, and NaV1.1 expression becomes detectable only after postnatal day 7 (Gordon et al., 1987; Beckh et al., 1989).

Further contributing to this delay, insufficient axonal myelination during early developmental stages impedes the rapid propagation of action potentials (Hijazi et al., 2023; Benamer et al., 2020). Additionally, the abundance of GABAergic vesicles in the neocortex of newborn mice is relatively low, with a gradual increase in the expression of GABAergic synaptic markers, reaching a plateau by the end of the second postnatal week (Minelli et al., 2003). The synthesis of GABA itself also plays a crucial role in synapse development. During normal development, the activity of glutamic acid decarboxylase 67 (GAD67), the primary enzyme responsible for GABA synthesis in cortical interneurons, increases. When GAD67 is knocked down, severe deficits in axonal branching are observed, along with reduced formation and size of perisomatic synapses on cortical pyramidal neurons (Chattopadhyaya et al., 2007; Wu et al., 2012).

Another factor lies in the expression of GABA receptors on postsynaptic neurons, which is lower during early developmental stages compared to adults, thereby limiting inhibitory transmission (Behuet et al., 2019). This limitation is gradually alleviated as the connectivity rate between interneurons and pyramidal cells increases, with a demonstrated likelihood of connections rising from 4–20% in neonates to 16–35% in juveniles (Wester and McBain, 2016). Lastly, the synchronization of interneuron activity is less effective during early development due to the reduced number and functionality of gap junctions among interneurons, a factor that significantly enhances in adulthood (Belousov, 2011). These interconnected developmental processes likely collectively contribute to the delayed inhibitory GABA activity observed in newborns.

Thus, as shown by developmental studies in the hippocampus and other brain regions, these factors collectively contribute to delayed development. Remaining key questions for CA1 hippocampus include characterizing EC inputs to FS INs (weak/slow in neonates?), fast firing (does it develop late?), and the connectivity rate with PCs (low?). Addressing these questions requires direct recordings from FS INs and from pairs of connected FS INs and CA1 PCs, as done in studies by Daw et al., 2007 and Doischer et al., 2008.

5.4. Absence of GABA-silent cells in in vivo CA1

In Article 4, GABA-silent cells were observed in in vitro CA1 during the first postnatal week — these cells did not respond to GABAergic stimulation with a GABA current,

although an AMPA current was present. However, such GABA-silent cells were not detected in in vivo CA1 conditions in Article 2.

One possible explanation for the differences between in vivo and in vitro conditions could be the differences in the microenvironment and the level of excitatory input interneurons are exposed to. In in vivo conditions, the tissue preserves natural connections and interactions between neurons, including the influence of neuromodulators, glial cell activity, and constant sensory stimuli, all of which can sustain normal activity of interneurons. In in vitro conditions, these connections and stimuli are limited or absent, potentially altering cell behavior. In our in vitro study (Article 4) we used nearly minimal, single electroshock to evoke monosynaptic EPSCs, whereas in vivo the natural input from EC during eSPWs was not experimentally controlled and could be more ample and organized in a series of repetitive spikes in multiple inputs to efficiently drive interneurons, yet at longer delays.

5.5. Absence of GABA-silent cells in the dentate gyrus

However, in Article 3, which also studied the DG under in vitro conditions, no GABA-silent cells were observed either. A possible explanation may lie in the differences between the two hippocampal regions — CA1 and DG — in their functional organization and maturation. However, it is not possible to definitively state that dentate gyrus (DG) neurons have stronger or more stable connections with interneurons or that they establish connections earlier compared to CA1. Otherwise, this could explain the absence of GABA-silent cells in our study presented in Article 3. Unfortunately, we cannot provide a definitive answer to this question at this time.

5.6. Timing differences in GABA and glutamate synapse formation

In the article by Tyzio and colleagues (Tyzio et al., 1999), it has been hypothesized that GABA synapses are formed earlier than glutamatergic ones. This was supported with evidence of three types of CA1 pyramidal cells at birth in response to stimulation: silent, GABA-only, and GABA + glutamatergic cells. However, in our study (Article 4), using in vitro stimulation of the angular bundle, we did not observe ecGABA-only cells during the first postnatal week. Instead, we found ecGABA-silent cells, which displayed only ecEPSCs.

The differences between our results and those of Tyzio et al., may be due to methodological differences, especially in the location of stimulation. Tyzio et al. directly stimulated the area near the apical dendrites of pyramidal cells, directly activating all types of inputs, including both GABAergic and glutamatergic. In our case, stimulation of

the angular bundle mainly activated EC pathways projecting to pyramidal cells and interneurons, but not directly interneurons.

Interestingly, in the study (Tyzio et al., 1999) EPSCs could only be observed in P0 CA1 pyramidal cells whose apical dendrites reached SLM, that provides additional evidence to the hypothesis that EC inputs are the main early excitatory drivers in neonatal CA1 hippocampus.

5.7. Delayed feedforward GABAergic transmission in neonatal DG, CA1, and neocortex: Evidence for a universal developmental principle

The delay in the development of inhibitory feedforward GABAergic transmission observed in neonatal DG and CA1 (Articles 2–4) reflects similar patterns noted in the neocortex (Minlebaev et al., 2011; Daw et al., 2007). These parallels across different brain regions may indicate a common principle: delayed maturation of inhibitory feedforward transmission creates optimal conditions for the formation of neural networks.

A similar mechanism has been described in the visual cortex, where researchers demonstrated that the maturation of GABAergic transmission plays a key role in defining critical periods of plasticity (Hensch et al., 1998; Sale et al., 2010). The slow development of inhibitory synapses allows sensory experience to shape neural networks during these periods (Morales et al., 2002). Findings from studies on mice with early BDNF expression show that accelerated maturation of inhibitory GABAergic interneurons leads to a premature closure of the critical period for monocular deprivation effects (Hanover et al., 1999; Huang et al., 1999).

As GABAergic transmission matures, the temporal window for integration narrows, improving the precision and reliability of neural communication. This aligns with the needs of the developing brain, where initial high plasticity gradually gives way to stable and accurate neural connections. Thus, the delayed development of inhibitory feedforward transmission may represent an evolutionarily conserved mechanism that ensures a balance between plasticity and stability in neural networks during critical developmental periods. Our findings indicate that this delay contributes to the high excitability of the hippocampus during early development, promoting plasticity and the formation of functional connections. By the end of the first postnatal week, inhibitory mechanisms become more precise, leading to a more organized and stable network state (Cohen et al., 2000).

5.8. Spatial organization of synapses and maturation of inhibition

An important part of our research examined the distribution of inhibitory synapses made by PV interneurons along the radial axis of CA1. We demonstrated that PV-inhibition primarily targets the dendrites of pyramidal neurons in the stratum oriens (SO) at early developmental stages. In contrast, synaptic density in the stratum pyramidale (SP) peaks at P15 and then slightly decreases, suggesting synaptic pruning or stabilization (Dard et al., 2022). This observation led us to hypothesize that dendritic inhibition by PV interneurons precedes the establishment of mature perisomatic PV inhibition. Future research should verify this hypothesis, using techniques to map the functional cartography of synapses made by PV interneurons.

5.9. Study limitations

The effects of anesthesia and artificial stimulation on signal characteristics must be considered when interpreting our results from Articles 1 and 2. Our experiments described in Articles 3, 4, 5 were conducted in vitro, which may not fully capture the complexity of in vivo neuronal interactions. While this approach allows for isolating and studying specific mechanisms, it also imposes limitations on the generalizability of the findings to real biological contexts. Furthermore, the use of rodent models requires caution when extrapolating to human brain development, given the potential differences in maturation rates and mechanisms.

5.10. Conclusions

Based on the conducted research, the following conclusions are drawn, addressing the key research questions:

1. **The possibility of triggering eSPWs through direct somatosensory stimulation**: The experiments demonstrated that direct somatosensory stimulation, such as whisker pad electrical stimulation, can effectively evoke early sharp waves (eSPWs) in the hippocampus of neonatal rats. These evoked events exhibit characteristics similar to spontaneous eSPWs, confirming the role of external sensory inputs in activating and modulating the hippocampal network during early development (Article 1).

2. **Dynamics of synaptic response changes (IPSCs and EPSCs)**: The analysis of synaptic currents revealed that during early postnatal stages, excitatory postsynaptic currents (EPSCs) dominate over inhibitory postsynaptic currents (IPSCs), owing to the delayed maturation of GABAergic inhibition. This temporal mismatch creates a broad window for signal integration in the early state of hippocampal development (Articles 2, 3, 4).

3. **Developmental distribution of PV interneuron terminals in the hippocampus**: The study found that the distribution of fast spiking parvalbumin interneuron

inhibitory synaptic terminals follows a sequential developmental trajectory. The results suggest that dendritic synapses form earlier than perisomatic synapses (Article 5).

6. Copyright permissions for figures

- **Figure 1.** Schematic drawing of the hippocampal formation. Kiernan, J. A. (2012). Anatomy of the Temporal Lobe. In Epilepsy Research and Treatment (Vol. 2012, pp. 1–12). Hindawi Limited. ***Licensed under CC BY 4.0.***

- **Figure 2.** Cross-sectional diagram of the entorhinal cortex (EC). van Strien, N. M., Cappaert, N. L. M., & Witter, M. P. (2009). The anatomy of memory: an interactive overview of the parahippocampal–hippocampal network. In Nature Reviews Neuroscience (Vol. 10, Issue 4, pp. 272–282). Springer Science and Business Media LLC. ***Reprinted with permission from Springer Nature, License Number 5934400442270***

- **Figure 3.** Topographic organization of downstream pathways from EC. Neves, G., Cooke, S. F., & Bliss, T. V. P. (2008). Synaptic plasticity, memory and the hippocampus: a neural network approach to causality. In Nature Reviews Neuroscience (Vol. 9, Issue 1, pp. 65–75). Springer Science and Business Media LLC. ***Reprinted with permission from Springer Nature, License Number 5934271113465.***

- **Figure 4.** Ventral hippocampal commissure. ***Created by the author using Siibra Explorer.***

- **Figure 5.** Commissural path. ***Inspired by Janáčková S.***, "Functional maturation of postnatal hippocampus in rodents: electrophysiological approach", PhD Dissertation, Université Paris Descartes, 2013.

- **Figure 6.** Trisynaptic loop. ***Inspired by Janáčková S.***, "Functional maturation of postnatal hippocampus in rodents: electrophysiological approach", PhD Dissertation, Université Paris Descartes, 2013.

- **Figure 7.** Hippocampal connections. ***Inspired by Janáčková S.***, "Functional maturation of postnatal hippocampus in rodents: electrophysiological approach", PhD Dissertation, Université Paris Descartes, 2013.

- **Figure 8.** Feedback excitation and inhibition of dentate gyrus. ***Inspired by Janáčková S.***, "Functional maturation of postnatal hippocampus in rodents: electrophysiological approach", PhD Dissertation, Université Paris Descartes, 2013.

- **Figure 9.** Feedforward excitation and inhibition of dentate gyrus. ***Inspired by Janáčková S.***, "Functional maturation of postnatal hippocampus in rodents: electrophysiological approach", PhD Dissertation, Université Paris Descartes, 2013.

- **Figure 10.** Morphology of hippocampal principal cells. Vida, I., Degro, C.E., Booker, S.A., 2018. Morphology of Hippocampal Neurons, in: Cutsuridis, V., Graham, B.P., Cobb, S., Vida, I. (Eds.), Hippocampal Microcircuits, Springer Series in Computational Neuroscience. Springer International Publishing, Cham, pp. 29–90. ***Reprinted with permission from Springer Nature, License Number 5933800478149.***

- **Figure 11.** Summary of all described IN subtypes in hippocampal subfield CA. Booker S, Vida I (2018) Morphological diversity and connectivity of hippocampal interneurons. Cell and Tissue Research. 373(3). 619-641. ***Licensed under CC BY 4.0.***

- **Figure 12.** IN subtypes of the dentate gyrus. Booker S, Vida I (2018) Morphological diversity and connectivity of hippocampal interneurons. Cell and Tissue Research. 373(3). 619-641. ***Licensed under CC BY 4.0.***

- **Figure 13.** Mouse Hippocampus Development. Urbán, N., Guillemot, F., 2014. Neurogenesis in the embryonic and adult brain: same regulators, different roles. Frontiers in Cellular Neuroscience 8. ***Licensed under CC BY 4.0.***

- **Figure 14.** The axes of the mouse hippocampus and its characteristic PCs. Cembrowski, M. S., & Spruston, N. (2019). Heterogeneity within classical cell types is the rule: lessons from hippocampal pyramidal neurons. In Nature Reviews Neuroscience (Vol. 20, Issue 4, pp. 193–204). Springer Science and Business Media LLC. ***Reprinted with permission from Springer Nature, License Number 5933800901240.***

- **Figure 15.** CA1 pyramidal neurons. Cossart R, Khazipov R (2022) How development sculpts hippocampal circuits and function. Physiological Reviews. 102(1). 343-378. ***Reprinted with permission from the American Physiological Society, License Number 1558859-1.***

- **Figure 16.** Timetable of neurogenesis. ***Visualised data from Bayer et al., 1993.***

- **Figure 17.** Sharp wave in adult animal. Cossart R, Khazipov R (2022) How development sculpts hippocampal circuits and function. Physiological Reviews. 102(1). 343-378. ***Reprinted with permission from the American Physiological Society, License Number 1558859-1.***

- **Figure 18.** Response to ventral hippocampal commissure stimulation. Brankačk J, Stewart M, E. Fox S (1993) Current source density analysis of the hippocampal theta rhythm: associated sustained potentials and candidate synaptic generators. Brain Research. 615(2). 310-327. ***Reprinted with permission from Elsevier, License Number 5933811033358.***

- **Figure 19.** Response to perforant path stimulation. Brankačk J, Stewart M, E. Fox S (1993) Current source density analysis of the hippocampal theta rhythm: associated

sustained potentials and candidate synaptic generators. Brain Research. 615(2). 310-327. ***Reprinted with permission from Elsevier, License Number 5933811033358.***

- **Figure 20.** Example of sharp wave in adult rat with superimposed ripple. Buhl D, Buzsaki G (2005) Developmental emergence of hippocampal fast-field "ripple" oscillations in the behaving rat pups. Neuroscience. 134(4). 1423-1430. ***Reprinted with permission from Elsevier, License 5933830407486.***

- **Figure 21.** Ripple oscillations in rat pups do not appear until after the second week of life. Buhl D, Buzsaki G (2005) Developmental emergence of hippocampal fast-field "ripple" oscillations in the behaving rat pups. Neuroscience. 134(4). 1423-1430. ***Reprinted with permission from Elsevier, License 5933830407486.***

- **Figure 22.** Ripple oscillations in mice hippocampus do not appear until postnatal day 10. Pochinok I, Stöber T, Triesch J, Chini M, Hanganu-Opatz I (2024) A developmental increase of inhibition promotes the emergence of hippocampal ripples. Nature Communications. 15(1). ***Licensed under CC BY 4.0.***

- **Figure 23.** Example of dentate spikes type 1 and 2. Farrell J, Hwaun E, Dudok B, Soltesz I (2024) Neural and behavioural state switching during hippocampal dentate spikes. Nature. 628(8008). 590-595. ***Licensed under CC BY 4.0.***

- **Figure 24.** Hippocampal bursts in freely moving rat pups (P4 to P6). Leinekugel X, Khazipov R, Cannon R, Hirase H, Ben-Ari Y, Buzsáki G (2002) Correlated Bursts of Activity in the Neonatal Hippocampus in Vivo. Science. 296(5575). 2049-2052. ***Reprinted with permission from AAAS.***

- **Figure 25.** Recording of SPWs preceded by startles in a head-fixed P2 rat. Karlsson K, Mohns E, di Prisco G, Blumberg M (2006) On the co-occurrence of startles and hippocampal sharp waves in newborn rats. Hippocampus. 16(11). 959-965. ***Reprinted with permission from John Wiley & Sons, License Number 1558855-1.***

- **Figure 26.** Activity bursts in MEC layer 3 precede eSPWs in neonatal rats. Valeeva G, Janackova S, Nasretdinov A, Rychkova V, Makarov R, Holmes G, Khazipov R, Lenck-Santini P (2018) Emergence of Coordinated Activity in the Developing Entorhinal–Hippocampal Network. Cerebral Cortex. 29(2). 906-920. ***Licensed under CC BY-NC 4.0.***

- **Figure 27.** Single unit activity in hippocampus and MEC L3 in relation to eSPWs. Valeeva G, Janackova S, Nasretdinov A, Rychkova V, Makarov R, Holmes G, Khazipov R, Lenck-Santini P (2018) Emergence of Coordinated Activity in the Developing Entorhinal–Hippocampal Network. Cerebral Cortex. 29(2). 906-920. ***Licensed under CC BY-NC 4.0.***

- **Figure 28.** Single unit firing properties with regards to eSPWs. Valeeva G, Janackova S, Nasretdinov A, Rychkova V, Makarov R, Holmes G, Khazipov R, Lenck-Santini P (2018) Emergence of Coordinated Activity in the Developing Entorhinal–Hippocampal Network. Cerebral Cortex. 29(2). 906-920. ***Licensed under CC BY-NC 4.0.***

- **Figure 29.** Comparison of eSPWs with adult SPWs. Cossart R, Khazipov R (2022) How development sculpts hippocampal circuits and function. Physiological Reviews. 102(1). 343-378. ***Reprinted with permission from the American Physiological Society, License Number 1558859-1.***

- **Figure 30.** Unitary discharges and evoked potentials in response to tooth pulp (TP) and acoustic (click) stimulations. Brankačk J, Buzsaki G (1986) Hippocampal responses evoked by tooth pulp and acoustic stimulation: Depth profiles and effect of behavior. Brain Research. 378(2). 303-314. ***Reprinted with permission from Elsevier, License Number 5933811353416.***

- **Figure 31.** Hippocampal responses to somatosensory stimulation in the urethane-anaesthetized rat Bellistri E, Aguilar J, Brotons-Mas J, Foffani G, de la Prida L (2013) Basic properties of somatosensory-evoked responses in the dorsal hippocampus of the rat. The Journal of Physiology. 591(10). 2667-2686. ***Reprinted with permission from John Wiley & Sons, License Number 1558856-1.***

- **Figure 32.** Hippocampal MUA responses to somatosensory stimulation Bellistri E, Aguilar J, Brotons-Mas J, Foffani G, de la Prida L (2013) Basic properties of somatosensory-evoked responses in the dorsal hippocampus of the rat. The Journal of Physiology. 591(10). 2667-2686. ***Reprinted with permission from John Wiley & Sons, License Number 1558856-1.***

- **Figure 33.** Feedforward inhibition (FFI). Fröhlich, F. (2016). Microcircuits of the Neocortex. In Network Neuroscience (pp. 85–95). Elsevier. ***Reprinted with permission from Elsevier, License Number 5934410299811***

- **Figure 34.** Coincidence detection in PCs is abolished by GABAAR antagonists. Pouille F, Scanziani M (2001) Enforcement of Temporal Fidelity in Pyramidal Cells by Somatic Feed-Forward Inhibition. Science. 293(5532). 1159-1163. ***Reprinted with permission from AAAS.***

- **Figure 35.** Feed-forward inhibitory inputs selectively impinge on the soma of PCs. Pouille F, Scanziani M (2001) Enforcement of Temporal Fidelity in Pyramidal Cells by Somatic Feed-Forward Inhibition. Science. 293(5532). 1159-1163. ***Reprinted with permission from AAAS.***

- **Figure 36.** Synaptic mechanisms of early gamma oscillations. Minlebaev M, Colonnese M, Tsintsadze T, Sirota A, Khazipov R (2011) Early Gamma Oscillations Synchronize

Developing Thalamus and Cortex. Science. 334(6053). 226-229. ***Reprinted with permission from AAAS.***

- **Figure 37.** Developmental increase in GABAA receptor-mediated transmission in response to thalamocortical input. Daw M, Ashby M, Isaac J (2007) Coordinated developmental recruitment of latent fast spiking interneurons in layer IV barrel cortex. Nature Neuroscience. 10(4). 453-461. ***Reprinted with permission from Springer Nature, License Number 1558858-1.***

- **Figure 38.** Age-related increase in thalamic input to fast-spiking (FS) interneurons compared to stellate cells (SC). Daw M, Ashby M, Isaac J (2007) Coordinated developmental recruitment of latent fast spiking interneurons in layer IV barrel cortex. Nature Neuroscience. 10(4). 453-461. ***Reprinted with permission from Springer Nature, License Number 1558858-1.***

- **Figure 39.** Development of connection probability and strength between fast-spiking (FS) interneurons and stellate cells (SC) across early postnatal days. Daw M, Ashby M, Isaac J (2007) Coordinated developmental recruitment of latent fast spiking interneurons in layer IV barrel cortex. Nature Neuroscience. 10(4). 453-461. ***Reprinted with permission from Springer Nature, License Number 1558858-1.***

- **Figure 40.** Developmental changes in BC signaling. Doischer D, Aurel Hosp J, Yanagawa Y, Obata K, Jonas P, Vida I, Bartos M (2008) Postnatal Differentiation of Basket Cells from Slow to Fast Signaling Devices. The Journal of Neuroscience. 28(48). 12956-12968. ***Licensed under CC BY-NC-SA 4.0.***

- **Figure 41.** Developmental changes in IPSCs at BC synapses in the dentate gyrus. Doischer D, Aurel Hosp J, Yanagawa Y, Obata K, Jonas P, Vida I, Bartos M (2008) Postnatal Differentiation of Basket Cells from Slow to Fast Signaling Devices. The Journal of Neuroscience. 28(48). 12956-12968. ***Licensed under CC BY-NC-SA 4.0.***

- **Figure 42.** CA1 dynamics and movement during early postnatal development. Dard R, Leprince E, Denis J, Rao Balappa S, Suchkov D, Boyce R, Lopez C, Giorgi-Kurz M, Szwagier T, Dumont T, Rouault H, Minlebaev M, Baude A, Cossart R, Picardo M (2022) The rapid developmental rise of somatic inhibition disengages hippocampal dynamics from self-motion. eLife. 11. ***Licensed under CC BY 4.0.***

- **Figure 43.** Recruitment of CA1 glutamatergic and GABAergic neurons. Dard R, Leprince E, Denis J, Rao Balappa S, Suchkov D, Boyce R, Lopez C, Giorgi-Kurz M, Szwagier T, Dumont T, Rouault H, Minlebaev M, Baude A, Cossart R, Picardo M (2022) The rapid developmental rise of somatic inhibition disengages hippocampal dynamics from self-motion. eLife. 11. ***Licensed under CC BY 4.0.***

- **Figure 44.** Development of perisomatic GABAergic innervation in CA1 region. Dard R, Leprince E, Denis J, Rao Balappa S, Suchkov D, Boyce R, Lopez C, Giorgi-Kurz M,

Szwagier T, Dumont T, Rouault H, Minlebaev M, Baude A, Cossart R, Picardo M (2022) The rapid developmental rise of somatic inhibition disengages hippocampal dynamics from self-motion. eLife. 11. ***Licensed under CC BY 4.0.***

- **Figure 45.** Sketch of a model illustrating the generation of LFP from a population of identical neurons. Einevoll, Gaute & Lindén, Henrik & Tetzlaff, Tom & Łęski, Szymon & Pettersen, Klas. (2013). Local Field Potentials: Biophysical Origin and Analysis. ***Reprinted with permission from CRC Press, License Number 1558948-1.***

- **Figure 46.** Examples of commonly used single unit and LFP recording devices. Pashaie, R., Anikeeva, P., Jin Hyung Lee, Prakash, R., Yizhar, O., Prigge, M., Chander, D., Richner, T. J., & Williams, J. (2014). Optogenetic Brain Interfaces. In IEEE Reviews in Biomedical Engineering (Vol. 7, pp. 3–30). Institute of Electrical and Electronics Engineers (IEEE). ***Reprinted with permission from IEEE.***

- **Figure 47.** An example of a silicon probe inserted into the principal barrel of a P6 rat. Sintsov M, Suchkov D, Khazipov R, Minlebaev M (2017) Developmental Changes in Sensory-Evoked Optical Intrinsic Signals in the Rat Barrel Cortex. Frontiers in Cellular Neuroscience. 11. ***Licensed under CC BY 4.0.***

- **Figure 48.** Example of CSD profiles derived from spatially resolved LFP recordings. Valeeva G, Janackova S, Nasretdinov A, Rychkova V, Makarov R, Holmes G, Khazipov R, Lenck-Santini P (2018) Emergence of Coordinated Activity in the Developing Entorhinal–Hippocampal Network. Cerebral Cortex. 29(2). 906-920. ***Licensed under CC BY-NC 4.0.***

- **Figure 49.** Example of MUA extraction from the high-frequency components of extracellular data. Quairiaux, C., Megevand, P., Kiss, J. Z., & Michel, C. M. (2011). Functional Development of Large-Scale Sensorimotor Cortical Networks in the Brain. In Journal of Neuroscience (Vol. 31, Issue 26, pp. 9574–9584). Society for Neuroscience. ***Licensed under CC BY-NC-SA 4.0.***

- **Figure 50.** Patch-clamp procedure and configurations. Annecchino, L. A., & Schultz, S. R. (2018). Progress in automating patch clamp cellular physiology. In Brain and Neuroscience Advances (Vol. 2). SAGE Publications. ***Licensed under CC BY 4.0.***

- **Figure 51.** Example of patch-clamp in whole-cell current-clamp configuration. Vazetdinova A, Valiullina-Rakhmatullina F, Rozov A, Evstifeev A, Khazipov R, Nasretdinov A (2022) On the accuracy of cell-attached current-clamp recordings from cortical neurons. Frontiers in Molecular Neuroscience. 15. ***Licensed under CC BY 4.0.***

- **Figure 52.** Example of collecting information about synaptic currents using the low chloride concentration method. Khalilov I, Minlebaev M, Mukhtarov M, Khazipov R (2015) Dynamic Changes from Depolarizing to Hyperpolarizing GABAergic Actions

during Giant Depolarizing Potentials in the Neonatal Rat Hippocampus. The Journal of Neuroscience. 35(37). 12635-12642. ***Licensed under CC BY-NC-SA 4.0.***

- **Figure 53.** Synaptic vesicle fusion. Chapman, E. R. (2002). Synaptotagmin: A Ca2+ sensor that triggers exocytosis? In Nature Reviews Molecular Cell Biology (Vol. 3, Issue 7, pp. 498–508). Springer Science and Business Media LLC. ***Reprinted with permission from Springer Nature, License Number 5933801270718.***

- **Figure 54.** The principle of antibody-based immunocytochemistry. Rohilla, S., Krämer, B., Koberling, F., Gregor, I., & Hocke, A. C. (2020). Multi-target immunofluorescence by separation of antibody cross-labelling via spectral-FLIM-FRET. In Scientific Reports (Vol. 10, Issue 1). Springer Science and Business Media LLC. ***Licensed under CC BY 4.0.***

- **Figure 55.** The working principle of a confocal microscope. Debarnot, V., Kahn, J., & Weiss, P. (2019). Multiview Attenuation Estimation and Correction. In Journal of Mathematical Imaging and Vision (Vol. 61, Issue 6, pp. 780–797). Springer Science and Business Media LLC. ***Reprinted with permission from Springer Nature, License Number 5933810259057.***

- **Figure 56.** Example of a confocal image with fluorophore markers. Sommeijer, J.-P., & Levelt, C. N. (2012). Synaptotagmin-2 Is a Reliable Marker for Parvalbumin Positive Inhibitory Boutons in the Mouse Visual Cortex. In M. A. Fox (Ed.), PLoS ONE (Vol. 7, Issue 4, p. e35323). Public Library of Science (PLoS). ***Licensed under CC BY 4.0.***

- **Figure 57.** Validation of the overlap between immunohistochemical and genetic methods for localizing PV+ interneurons. Hu H, Gan J, Jonas P (2014) Fast-spiking, parvalbumin + GABAergic interneurons: From cellular design to microcircuit function. Science. 345(6196). ***Reprinted with permission from AAAS.***

- **Figures** from **58** to **88** were ***created by the author***.

7. References

- Ackman J, Burbridge T, Crair M (2012) Retinal waves coordinate patterned activity throughout the developing visual system. Nature. 490(7419). 219-225. https://doi.org/10.1038/nature11529
- Ahlbeck J, Song L, Chini M, Bitzenhofer S, Hanganu-Opatz I (2018) Glutamatergic drive along the septo-temporal axis of hippocampus boosts prelimbic oscillations in the neonatal mouse. eLife. 7. https://doi.org/10.7554/eLife.33158
- Akhmetshina D, Nasretdinov A, Zakharov A, Valeeva G, Khazipov R (2016) The Nature of the Sensory Input to the Neonatal Rat Barrel Cortex. The Journal of Neuroscience. 36(38). 9922-9932. https://doi.org/10.1523/jneurosci.1781-16.2016
- Allene C, Picardo M, Becq H, Miyoshi G, Fishell G, Cossart R (2012) Dynamic Changes in Interneuron Morphophysiological Properties Mark the Maturation of Hippocampal Network Activity. The Journal of Neuroscience. 32(19). 6688-6698. https://doi.org/10.1523/jneurosci.0081-12.2012
- Altman J, Bayer S (1990) Migration and distribution of two populations of hippocampal granule cell precursors during the perinatal and postnatal periods. Journal of Comparative Neurology. 301(3). 365-381. https://doi.org/10.1002/cne.903010304
- Amaral D (1978) A golgi study of cell types in the hilar region of the hippocampus in the rat. Journal of Comparative Neurology. 182(5). 851-914. https://doi.org/10.1002/cne.901820508
- Amaral D, Kurz J (1985) An analysis of the origins of the cholinergic and noncholinergic septal projections to the hippocampal formation of the rat. Journal of Comparative Neurology. 240(1). 37-59. https://doi.org/10.1002/cne.902400104
- Amaral DG, Scharfman HE, Lavenex P (2007) The dentate gyrus: fundamental neuroanatomical organization (dentate gyrus for dummies). Prog Brain Res 163: 3–22. https://doi.org/10.1016/s00796123(07)630015
- Andersen P, Holmqvist B, Voorhoeve P (1966) Entorhinal Activation of Dentate Granule Cells. Acta Physiologica Scandinavica. 66(4). 448-460. https://doi.org/10.1111/j.1748-1716.1966.tb03223.x
- Andersen, P., Morris, R., Amaral, D., Bliss, T., & O'Keefe, J. (Eds.). (2006). The Hippocampus Book. Oxford University Press. https://doi.org/10.1093/acprof:oso/9780195100273.001.0001
- Annecchino, L. A., & Schultz, S. R. (2018). Progress in automating patch clamp cellular physiology. In Brain and Neuroscience Advances (Vol. 2). SAGE Publications. https://doi.org/10.1177/2398212818776561

- Ari Y, Cherubini E, Aniksztejn L, Roisin M, Charriaut-Marlangue C (1989) Mechanism of Induction of Long Term Potentiation by the Mast Cell Degranulating Peptide. Pharmacopsychiatry. 22(S 2). 107-110. https://doi.org/10.1055/s-2007-1014628

- Babola T, Li S, Gribizis A, Lee B, Issa J, Wang H, Crair M, Bergles D (2018) Homeostatic Control of Spontaneous Activity in the Developing Auditory System. Neuron. 99(3). 511-524.e5. https://doi.org/10.1016/j.neuron.2018.07.004

- Barrientos S, Tiznado V (2016) Hippocampal CA1 Subregion as a Context Decoder. The Journal of Neuroscience. 36(25). 6602-6604. https://doi.org/10.1523/jneurosci.1107-16.2016

- Bayer S (1980) Development of the hippocampal region in the rat II. Morphogenesis during embryonic and early postnatal life. Journal of Comparative Neurology. 190(1). 115-134. https://doi.org/10.1002/cne.901900108

- Bayer, S.A., Altman, J., Russo, R.J., Zhang, X., 1993. Timetables of neurogenesis in the human brain based on experimentally determined patterns in the rat. Neurotoxicology 14, 83–144. https://pubmed.ncbi.nlm.nih.gov/8361683/

- Beckh, S., Noda, M., Lübbert, H., & Numa, S. (1989). Differential regulation of three sodium channel messenger RNAs in the rat central nervous system during development. In The EMBO Journal (Vol. 8, Issue 12, pp. 3611–3616). Springer Science and Business Media LLC. https://doi.org/10.1002/j.1460-2075.1989.tb08534.x

- Behuet, S., Cremer, J. N., Cremer, M., Palomero-Gallagher, N., Zilles, K., & Amunts, K. (2019). Developmental Changes of Glutamate and GABA Receptor Densities in Wistar Rats. In Frontiers in Neuroanatomy (Vol. 13). Frontiers Media SA. https://doi.org/10.3389/fnana.2019.00100

- Bellistri E, Aguilar J, Brotons-Mas J, Foffani G, de la Prida L (2013) Basic properties of somatosensory-evoked responses in the dorsal hippocampus of the rat. The Journal of Physiology. 591(10). 2667-2686. https://doi.org/10.1113/jphysiol.2013.251892

- Belousov A. B. (2011). The regulation and role of neuronal gap junctions during development. Communicative & integrative biology, 4(5), 579–581. https://doi.org/10.4161/cib.4.5.16380

- Ben-Ari Y, Gaiarsa J, Tyzio R, Khazipov R (2007) GABA: A Pioneer Transmitter That Excites Immature Neurons and Generates Primitive Oscillations. Physiological Reviews. 87(4). 1215-1284. https://doi.org/10.1152/physrev.00017.2006

- Benamer, N., Vidal, M., Balia, M., & Angulo, M. C. (2020). Myelination of parvalbumin interneurons shapes the function of cortical sensory inhibitory circuits. In Nature Communications (Vol. 11, Issue 1). Springer Science and Business Media LLC. https://doi.org/10.1038/s41467-020-18984-7

- Blackstad T (1956) Commissural connections of the hippocampal region in the rat, with special reference to their mode of termination. Journal of Comparative Neurology. 105(3). 417-537. https://doi.org/10.1002/cne.901050305

- Bocchio, M., Gouny, C., Angulo-Garcia, D., Toulat, T., Tressard, T., Quiroli, E., Baude, A., & Cossart, R. (2020). Hippocampal hub neurons maintain distinct connectivity throughout their lifetime. In Nature Communications (Vol. 11, Issue 1). Springer Science and Business Media LLC. https://doi.org/10.1038/s41467-020-18432-6

- Bocian R, Kowalczyk T (2012) Gap junction involvement in hippocampal theta rhythm generation. Postępy Higieny i Medycyny Doświadczalnej. 66. 702-713. https://doi.org/10.5604/17322693.1014656

- Bolea S, Avignone E, Berretta N, Sanchez-Andres J, Cherubini E (1999) Glutamate Controls the Induction of GABA-Mediated Giant Depolarizing Potentials Through AMPA Receptors in Neonatal Rat Hippocampal Slices. Journal of Neurophysiology. 81(5). 2095-2102. https://doi.org/10.1152/jn.1999.81.5.2095

- Booker S, Vida I (2018) Morphological diversity and connectivity of hippocampal interneurons. Cell and Tissue Research. 373(3). 619-641. https://doi.org/10.1007/s00441-018-2882-2

- Bragin A, Engel J, Staba R (2010) High-frequency oscillations in epileptic brain. Current Opinion in Neurology. 23(2). 151-156. https://doi.org/10.1097/WCO.0b013e3283373ac8

- Bragin A, Engel J, Wilson C, Vizentin E, Mathern G (1999) Electrophysiologic Analysis of a Chronic Seizure Model After Unilateral Hippocampal KA Injection. Epilepsia. 40(9). 1210-1221. https://doi.org/10.1111/j.1528-1157.1999.tb00849.x

- Bragin A, Jando G, Nadasdy Z, van Landeghem M, Buzsaki G (1995) Dentate EEG spikes and associated interneuronal population bursts in the hippocampal hilar region of the rat. Journal of Neurophysiology. 73(4). 1691-1705. https://doi.org/10.1152/jn.1995.73.4.1691

- Bragin A, Penttonen M, Buzsaki G (1997) Termination of Epileptic Afterdischarge in the Hippocampus. The Journal of Neuroscience. 17(7). 2567-2579. https://doi.org/10.1523/jneurosci.17-07-02567.1997

- Bragin A, Wilson C, Engel J (2003) Spatial Stability over Time of Brain Areas Generating Fast Ripples in the Epileptic Rat. Epilepsia. 44(9). 1233-1237. https://doi.org/10.1046/j.1528-1157.2003.18503.x

- Brankačk J, Buzsaki G (1986) Hippocampal responses evoked by tooth pulp and acoustic stimulation: Depth profiles and effect of behavior. Brain Research. 378(2). 303-314. https://doi.org/10.1016/0006-8993(86)90933-9

- Brankačk J, Stewart M, E. Fox S (1993) Current source density analysis of the hippocampal theta rhythm: associated sustained potentials and candidate synaptic generators. Brain Research. 615(2). 310-327. https://doi.org/10.1016/0006-8993(93)90043-m

- Brockmann M, Pöschel B, Cichon N, Hanganu-Opatz I (2011) Coupled Oscillations Mediate Directed Interactions between Prefrontal Cortex and Hippocampus of the

Neonatal Rat. Neuron. 71(2). 332-347. https://doi.org/10.1016/j.neuron.2011.05.041

- Brunel N, Wang X (2003) What Determines the Frequency of Fast Network Oscillations With Irregular Neural Discharges? I. Synaptic Dynamics and Excitation-Inhibition Balance. Journal of Neurophysiology. 90(1). 415-430. https://doi.org/10.1152/jn.01095.2002

- Buhl D, Buzsaki G (2005) Developmental emergence of hippocampal fast-field "ripple" oscillations in the behaving rat pups. Neuroscience. 134(4). 1423-1430. https://doi.org/10.1016/j.neuroscience.2005.05.030

- Buhl D, Harris K, Hormuzdi S, Monyer H, Buzsaki G (2003) Selective Impairment of Hippocampal Gamma Oscillations in Connexin-36 Knock-Out MouseIn Vivo. The Journal of Neuroscience. 23(3). 1013-1018. https://doi.org/10.1523/jneurosci.23-03-01013.2003

- Buzsaki G (1986) Hippocampal sharp waves: Their origin and significance. Brain Research. 398(2). 242-252. https://doi.org/10.1016/0006-8993(86)91483-6

- Buzsaki G (2002) Homeostatic Maintenance of Neuronal Excitability by Burst Discharges In Vivo. Cerebral Cortex. 12(9). 893-899. https://doi.org/10.1093/cercor/12.9.893

- Buzsaki G (2006) Rhythms of the Brain. https://doi.org/10.1093/acprof:oso/9780195301069.001.0001

- Buzsaki G (2015) Hippocampal sharp wave-ripple: A cognitive biomarker for episodic memory and planning. Hippocampus. 25(10). 1073-1188. https://doi.org/10.1002/hipo.22488

- Buzsaki G, Buhl D, Harris K, Csicsvari J, Czéh B, Morozov A (2003) Hippocampal network patterns of activity in the mouse. Neuroscience. 116(1). 201-211. https://doi.org/10.1016/s0306-4522(02)00669-3

- Buzsaki G, Horváth Z, Urioste R, Hetke J, Wise K (1992) High-frequency network oscillation in the hippocampus. Science. 256(5059). 1025-1027. https://doi.org/10.1126/science.1589772

- Buzsaki G, Lai-Wo S. L, Vanderwolf C (1983) Cellular bases of hippocampal EEG in the behaving rat. Brain Research Reviews. 6(2). 139-171. https://doi.org/10.1016/0165-0173(83)90037-1

- Bédard C, Destexhe A (2011) Generalized theory for current-source-density analysis in brain tissue. Physical Review E. 84(4). https://doi.org/10.1103/physreve.84.041909

- Cash S, Dan Y, Poo M, Zucker R (1996) Postsynaptic Elevation of Calcium Induces Persistent Depression of Developing Neuromuscular Synapses. Neuron. 16(4). 745-754. https://doi.org/10.1016/s0896-6273(00)80095-1

- Cembrowski, M. S., & Spruston, N. (2019). Heterogeneity within classical cell types is the rule: lessons from hippocampal pyramidal neurons. In Nature Reviews Neuroscience (Vol. 20, Issue 4, pp. 193–204). Springer Science and Business Media LLC. https://doi.org/10.1038/s41583-019-0125-5

- Chapman, E. R. (2002). Synaptotagmin: A Ca2+ sensor that triggers exocytosis? In Nature Reviews Molecular Cell Biology (Vol. 3, Issue 7, pp. 498–508). Springer Science and Business Media LLC. https://doi.org/10.1038/nrm855

- Chattopadhyaya, B., Di Cristo, G., Wu, C. Z., Knott, G., Kuhlman, S., Fu, Y., Palmiter, R. D., & Huang, Z. J. (2007). GAD67-Mediated GABA Synthesis and Signaling Regulate Inhibitory Synaptic Innervation in the Visual Cortex. In Neuron (Vol. 54, Issue 6, pp. 889–903). Elsevier BV. https://doi.org/10.1016/j.neuron.2007.05.015

- Chen K, Baram T, Soltesz I (1999) Febrile seizures in the developing brain result in persistent modification of neuronal excitability in limbic circuits. Nature Medicine. 5(8). 888-894. https://doi.org/10.1038/11330

- Cherubini E, Griguoli M, Safiulina V, Lagostena L (2010) The Depolarizing Action of GABA Controls Early Network Activity in the Developing Hippocampus. Molecular Neurobiology. 43(2). 97-106. https://doi.org/10.1007/s12035-010-8147-z

- Cherubini E, Rovira C, Gaiarsa J, Corradetti R, Ari Y (1990) GABA mediated excitation in immature rat CA3 hippocampal neurons. International Journal of Developmental Neuroscience. 8(4). 481-490. https://doi.org/10.1016/0736-5748(90)90080-l

- Chrobak J, Buzsaki G (1994) Selective activation of deep layer (V-VI) retrohippocampal cortical neurons during hippocampal sharp waves in the behaving rat. The Journal of Neuroscience. 14(10). 6160-6170. https://doi.org/10.1523/jneurosci.14-10-06160.1994

- Chrobak J, Buzsaki G (1996) High-Frequency Oscillations in the Output Networks of the Hippocampal–Entorhinal Axis of the Freely Behaving Rat. The Journal of Neuroscience. 16(9). 3056-3066. https://doi.org/10.1523/jneurosci.16-09-03056.1996

- Cohen A, Lin D, Coulter D (2000) Protracted Postnatal Development of Inhibitory Synaptic Transmission in Rat Hippocampal Area CA1 Neurons. Journal of Neurophysiology. 84(5). 2465-2476. https://doi.org/10.1152/jn.2000.84.5.2465

- Colgin L, Jia Y, Sabatier J, Lynch G (2005) Blockade of NMDA receptors enhances spontaneous sharp waves in rat hippocampal slices. Neuroscience Letters. 385(1). 46-51. https://doi.org/10.1016/j.neulet.2005.05.005

- Colgin L, Moser E (2010) Gamma Oscillations in the Hippocampus. Physiology. 25(5). 319-329. https://doi.org/10.1152/physiol.00021.2010

- Colonnese M, Khazipov R (2010) “Slow Activity Transients” in Infant Rat Visual Cortex:A Spreading Synchronous Oscillation Patterned by Retinal Waves. The Journal of Neuroscience. 30(12). 4325-4337. https://doi.org/10.1523/jneurosci.4995-09.2010

- Cossart R, Khazipov R (2022) How development sculpts hippocampal circuits and function. Physiological Reviews. 102(1). 343-378. https://doi.org/10.1152/physrev.00044.2020

- Crépel V, Aronov D, Jorquera I, Represa A, Ben-Ari Y, Cossart R (2007) A Parturition-Associated Nonsynaptic Coherent Activity Pattern in the Developing Hippocampus. Neuron. 54(1). 105-120. https://doi.org/10.1016/j.neuron.2007.03.007

- Csicsvari J, Henze D, Jamieson B, Harris K, Sirota A, Barthó P, Wise K, Buzsaki G (2003) Massively Parallel Recording of Unit and Local Field Potentials With Silicon-Based Electrodes. Journal of Neurophysiology. 90(2). 1314-1323. https://doi.org/10.1152/jn.00116.2003

- Csicsvari J, Hirase H, Mamiya A, Buzsaki G (2000) Ensemble Patterns of Hippocampal CA3-CA1 Neurons during Sharp Wave–Associated Population Events. Neuron. 28(2). 585-594. https://doi.org/10.1016/s0896-6273(00)00135-5

- Danglot L, Triller A, Marty S (2006) The development of hippocampal interneurons in rodents. Hippocampus. 16(12). 1032-1060. https://doi.org/10.1002/hipo.20225

- Dard R, Leprince E, Denis J, Rao Balappa S, Suchkov D, Boyce R, Lopez C, Giorgi-Kurz M, Szwagier T, Dumont T, Rouault H, Minlebaev M, Baude A, Cossart R, Picardo M (2022) The rapid developmental rise of somatic inhibition disengages hippocampal dynamics from self-motion. eLife. 11. https://doi.org/10.7554/eLife.78116

- Daw M, Ashby M, Isaac J (2007) Coordinated developmental recruitment of latent fast spiking interneurons in layer IV barrel cortex. Nature Neuroscience. 10(4). 453-461. https://doi.org/10.1038/nn1866

- Daw M, Bannister N, Isaac J (2006) Rapid, Activity-Dependent Plasticity in Timing Precision in Neonatal Barrel Cortex. The Journal of Neuroscience. 26(16). 4178-4187. https://doi.org/10.1523/JNEUROSCI.0150-06.2006

- Deadwyler S, West M, Robinson J (1981) Entorhinal and Septal Inputs Differentially Control Sensory-Evoked Responses in the Rat Dentate Gyrus. Science. 211(4487). 1181-1183. https://doi.org/10.1126/science.7466392

- Debarnot, V., Kahn, J., & Weiss, P. (2019). Multiview Attenuation Estimation and Correction. In Journal of Mathematical Imaging and Vision (Vol. 61, Issue 6, pp. 780–797). Springer Science and Business Media LLC. https://doi.org/10.1007/s10851-019-00871-6

- Deguchi Y, Donato F, Galimberti I, Cabuy E, Caroni P (2011) Temporally matched subpopulations of selectively interconnected principal neurons in the hippocampus. Nature Neuroscience. 14(4). 495-504. https://doi.org/10.1038/nn.2768

- Del Rio-Bermudez, C., Kim, J., Sokoloff, G., & Blumberg, M. S. (2017). Theta Oscillations during Active Sleep Synchronize the Developing Rubro-Hippocampal Sensorimotor Network. In Current Biology (Vol. 27, Issue 10, pp. 1413-1424.e4). Elsevier BV. https://doi.org/10.1016/j.cub.2017.03.077

- Deller T, Nitsch R, Frotscher M (1995) Phaseolus vulgaris –leucoagglutinin tracing of commissural fibers to the rat dentate gyrus: Evidence for a previously unknown commissural projection to the outer molecular layer. Journal of Comparative Neurology. 352(1). 55-68. https://doi.org/10.1002/cne.903520105

- Dhikav V, Anand K (2012) Hippocampus in health and disease: An overview. Annals of Indian Academy of Neurology. 15(4). 239. https://doi.org/10.4103/0972-2327.104323

- Doischer D, Aurel Hosp J, Yanagawa Y, Obata K, Jonas P, Vida I, Bartos M (2008) Postnatal Differentiation of Basket Cells from Slow to Fast Signaling Devices. The Journal of Neuroscience. 28(48). 12956-12968. https://doi.org/10.1523/JNEUROSCI.2890-08.2008

- Donato F, Jacobsen R, Moser M, Moser E (2017) Stellate cells drive maturation of the entorhinal-hippocampal circuit. Science. 355(6330). https://doi.org/10.1126/science.aai8178

- Dooley J, Glanz R, Sokoloff G, Blumberg M (2020) Self-generated whisker movements drive state-dependent sensory input to developing barrel cortex. https://doi.org/10.1101/2020.01.21.914259

- Dragoi, G., & Tonegawa, S. (2010). Preplay of future place cell sequences by hippocampal cellular assemblies. In Nature (Vol. 469, Issue 7330, pp. 397–401). Springer Science and Business Media LLC. https://doi.org/10.1038/nature09633

- Draguhn A, Traub R, Schmitz D, Jefferys J (1998) Electrical coupling underlies high-frequency oscillations in the hippocampus in vitro. Nature. 394(6689). 189-192. https://doi.org/10.1038/28184

- Dupuy S, Houser C (1996) Prominent Expression of Two Forms of Glutamate Decarboxylase in the Embryonic and Early Postnatal Rat Hippocampal Formation. The Journal of Neuroscience. 16(21). 6919-6932. https://doi.org/10.1523/jneurosci.16-21-06919.1996

- Durand G, Konnerth A (1996) Long-term potentiation as a mechanism of functional synapse induction in the developing hippocampus. Journal of Physiology-Paris. 90(5-6). 313-315. https://doi.org/10.1016/s0928-4257(97)87905-3

- Dvorak D, Chung A, Park E, Fenton A (2021) Dentate spikes and external control of hippocampal function. Cell Reports. 36(5). 109497. https://doi.org/10.1016/j.celrep.2021.109497

- Einevoll, Gaute & Lindén, Henrik & Tetzlaff, Tom & Łęski, Szymon & Pettersen, Klas. (2013). Local Field Potentials: Biophysical Origin and Analysis. https://www.researchgate.net/publication/281869785_Local_Field_Potentials_Biophysical_Origin_and_Analysis

- Ekins T, Mahadevan V, Zhang Y, D'Amour J, Akgül G, Petros T, McBain C (2020) Emergence of non-canonical parvalbumin-containing interneurons in hippocampus

of a murine model of type I lissencephaly. eLife. 9. https://doi.org/10.7554/eLife.62373

- El-Falougy H, Benuska J. History, anatomical nomenclature, comparative anatomy and functions of the hippocampal formation. Bratisl Lek Listy. 2006;107(4):103-6. PMID: 16796134. https://pubmed.ncbi.nlm.nih.gov/16796134/

- Ellender T, Nissen W, Colgin L, Mann E, Paulsen O (2010) Priming of Hippocampal Population Bursts by Individual Perisomatic-Targeting Interneurons. The Journal of Neuroscience. 30(17). 5979-5991. https://doi.org/10.1523/jneurosci.3962-09.2010

- Ellender TJ, Paulsen O. (2010) The many tunes of perisomatic targeting interneurons in the hippocampal network. Frontiers in Cellular Neuroscience. https://doi.org/10.3389/fncel.2010.00026

- Farooq, U., & Dragoi, G. (2019). Emergence of preconfigured and plastic time-compressed sequences in early postnatal development. In Science (Vol. 363, Issue 6423, pp. 168–173). American Association for the Advancement of Science (AAAS). https://doi.org/10.1126/science.aav0502

- Farrell J, Hwaun E, Dudok B, Soltesz I (2024) Neural and behavioural state switching during hippocampal dentate spikes. Nature. 628(8008). 590-595. https://doi.org/10.1038/s41586-024-07192-8

- Fisahn A, Pike F, Buhl E, Paulsen O (1998) Cholinergic induction of network oscillations at 40 Hz in the hippocampus in vitro. Nature. 394(6689). 186-189. https://doi.org/10.1038/28179

- Freemon F, Walter R (1970) Electrical activity of human limbic system during sleep. Comprehensive Psychiatry. 11(6). 544-551. https://doi.org/10.1016/0010-440x(70)90017-9

- Freund T, Katona I (2007) Perisomatic Inhibition. Neuron. 56(1). 33-42. https://doi.org/10.1016/j.neuron.2007.09.012

- Freund, T. F., & Buzsáki, G. (1998). Interneurons of the hippocampus. In Hippocampus (Vol. 6, Issue 4, pp. 347–470). Wiley. https://doi.org/10.1002/(sici)1098-1063(1996)6:4<347::aid-hipo1>3.0.co;2-i

- Fricke R, Cowan W (1978) An autoradiographic study of the commissural and ipsilateral hippocampo-dentate projections in the adult rat. Journal of Comparative Neurology. 181(2). 253-269. https://doi.org/10.1002/cne.901810204

- Frolova A, Gainutdinov A, Juzekaeva E, Safeeva L, Valeeva G, Khazipov R (2023) Development of GABAergic Inhibition Associated with Entorhinal Input in Granular Cells of the Dentate Gyrus. Journal of Evolutionary Biochemistry and Physiology. 59(6). 2390-2398. https://doi.org/10.1134/s002209302306039x

- Frotscher M, Zafirov S, Heimrich B (1995) Development of identified neuronal types and of specific synaptic connections in slice cultures of rat hippocampus. Progress in Neurobiology. 45(2). 143-164. https://doi.org/10.1016/0301-0082(94)00040-o

- Fröhlich, F. (2016). Microcircuits of the Neocortex. In Network Neuroscience (pp. 85–95). Elsevier. https://doi.org/10.1016/b978-0-12-801560-5.00007-0

- Gainutdinov A, Juzekaeva E, Mukhtarov M, Khazipov R (2023) Anoxic spreading depolarization in the neonatal rat cortex in vitro. Frontiers in Cellular Neuroscience. 17. https://doi.org/10.3389/fncel.2023.1106268

- Garaschuk O, Hanse E, Konnerth A (1998) Developmental profile and synaptic origin of early network oscillations in the CA1 region of rat neonatal hippocampus. The Journal of Physiology. 507(1). 219-236. https://doi.org/10.1111/j.1469-7793.1998.219bu.x

- Gebhardt C, Del Turco D, Drakew A, Tielsch A, Herz J, Frotscher M, Deller T (2002) Abnormal positioning of granule cells alters afferent fiber distribution in the mouse fascia dentata: Morphologic evidence from reeler, apolipoprotein E receptor 2-, and very low density lipoprotein receptor knockout mice. Journal of Comparative Neurology. 445(3). 278-292. https://doi.org/10.1002/cne.10172

- Gilbert, S. F., & Singer, S. R. (2010). Developmental biology (9th revised ed.). Sunderland, MA: Palgrave.

- Gordon, D., Merrick, D., Auld, V., Dunn, R., Goldin, A. L., Davidson, N., & Catterall, W. A. (1987). Tissue-specific expression of the RI and RII sodium channel subtypes. In Proceedings of the National Academy of Sciences (Vol. 84, Issue 23, pp. 8682–8686). Proceedings of the National Academy of Sciences. https://doi.org/10.1073/pnas.84.23.8682

- Graf J, Zhang C, Marguet S, Herrmann T, Flossmann T, Hinsch R, Rahmati V, Guenther M, Frahm C, Urbach A, Neves R, Witte O, Kiebel S, Isbrandt D, Hübner C, Holthoff K, Kirmse K (2021) A limited role of NKCC1 in telencephalic glutamatergic neurons for developing hippocampal network dynamics and behavior. Proceedings of the National Academy of Sciences. 118(14). https://doi.org/10.1073/pnas.2014784118

- Graf, J., Samiee, A., Flossmann, T., Holthoff, K., & Kirmse, K. (2024). Chemogenetic silencing reveals presynaptic Gi/o protein-mediated inhibition of developing hippocampal synchrony in vivo. In iScience (Vol. 27, Issue 10, p. 110997). Elsevier BV. https://doi.org/10.1016/j.isci.2024.110997

- Gray, C. M., Maldonado, P. E., Wilson, M., & McNaughton, B. (1995). Tetrodes markedly improve the reliability and yield of multiple single-unit isolation from multi-unit recordings in cat striate cortex. In Journal of Neuroscience Methods (Vol. 63, Issues 1–2, pp. 43–54). Elsevier BV. https://doi.org/10.1016/0165-0270(95)00085-2

- Gulyás, A. I., Megías, M., Emri, Z., & Freund, T. F. (1999). Total Number and Ratio of Excitatory and Inhibitory Synapses Converging onto Single Interneurons of Different Types in the CA1 Area of the Rat Hippocampus. In The Journal of Neuroscience (Vol. 19, Issue 22, pp. 10082–10097). Society for Neuroscience. https://doi.org/10.1523/jneurosci.19-22-10082.1999

- Hafting, T., Fyhn, M., Molden, S., Moser, M. B., & Moser, E. I. (2005). Microstructure of a spatial map in the entorhinal cortex. Nature, 436(7052), 801–806. https://doi.org/10.1038/nature03721

- Hanganu I, Ben-Ari Y, Khazipov R (2006) Retinal Waves Trigger Spindle Bursts in the Neonatal Rat Visual Cortex. Journal of Neuroscience. 26(25). 6728-6736. https://doi.org/10.1523/jneurosci.0752-06.2006

- Hanover, t J. L., Huang, Z. J., Tonegawa, S., & Stryker, M. P. (1999). t Brain-Derived Neurotrophic Factor Overexpression Induces Precocious Critical Period in Mouse Visual Cortex. In The Journal of Neuroscience (Vol. 19, Issue 22, pp. RC40–RC40). Society for Neuroscience. https://doi.org/10.1523/jneurosci.19-22-j0003.1999

- Harris K, Hochgerner H, Skene N, Magno L, Katona L, Bengtsson Gonzales C, Somogyi P, Kessaris N, Linnarsson S, Hjerling-Leffler J (2018) Classes and continua of hippocampal CA1 inhibitory neurons revealed by single-cell transcriptomics. PLOS Biology. 16(6). e2006387. https://doi.org/10.1371/journal.pbio.2006387

- Harris K, Teyler T (1983) Evidence for late development of inhibition in area CA1 of the rat hippocampus. Brain Research. 268(2). 339-343. https://doi.org/10.1016/0006-8993(83)90500-0

- Hartung H, Cichon N, De Feo V, Riemann S, Schildt S, Lindemann C, Mulert C, Gogos J, Hanganu-Opatz I (2016) From Shortage to Surge: A Developmental Switch in Hippocampal–Prefrontal Coupling in a Gene–Environment Model of Neuropsychiatric Disorders. Cerebral Cortex. 26(11). 4265-4281. https://doi.org/10.1093/cercor/bhw274

- Hensch T, Gordon J, Brandon E, McKnight G, Idzerda R, Stryker M (1998) Comparison of PlasticityIn VivoandIn Vitroin the Developing Visual Cortex of Normal and Protein Kinase A RIβ-Deficient Mice. The Journal of Neuroscience. 18(6). 2108-2117. https://doi.org/10.1523/jneurosci.18-06-02108.1998

- Hernández-Frausto M, Bilash O, Masurkar A, Basu J (2023) Local and long-range GABAergic circuits in hippocampal area CA1 and their link to Alzheimer's disease. Frontiers in Neural Circuits. 17. https://doi.org/10.3389/fncir.2023.1223891

- Hijazi, S., Pascual-García, M., Nabawi, Y., & Kushner, S. A. (2023). A critical period for prefrontal cortex PV interneuron myelination and maturation. Cold Spring Harbor Laboratory. https://doi.org/10.1101/2023.08.15.553393

- Hu C, Ahmed M, Melia T, Söllner T, Mayer T, Rothman J (2003) Fusion of Cells by Flipped SNAREs. Science. 300(5626). 1745-1749. https://doi.org/10.1126/science.1084909

- Hu H, Gan J, Jonas P (2014) Fast-spiking, parvalbumin + GABAergic interneurons: From cellular design to microcircuit function. Science. 345(6196). https://doi.org/10.1126/science.1255263

- Huang Z, Kirkwood A, Pizzorusso T, Porciatti V, Morales B, Bear M, Maffei L, Tonegawa S (1999) BDNF Regulates the Maturation of Inhibition and the Critical Period of

Plasticity in Mouse Visual Cortex. Cell. 98(6). 739-755. https://doi.org/10.1016/s0092-8674(00)81509-3

- Hájos N, Kathuria S, Dinh T, Piomelli D, Freund T (2004) Endocannabinoid transport tightly controls 2-arachidonoyl glycerol actions in the hippocampus: effects of low temperature and the transport inhibitor AM404. European Journal of Neuroscience. 19(11). 2991-2996. https://doi.org/10.1111/j.0953-816x.2004.03433.x

- Inácio A, Nasretdinov A, Lebedeva J, Khazipov R (2016) Sensory feedback synchronizes motor and sensory neuronal networks in the neonatal rat spinal cord. Nature Communications. 7(1). https://doi.org/10.1038/ncomms13060

- Janáčková S. (2013) Functional maturation of postnatal hippocampus in rodents: electrophysiological approach. PhD Dissertation. Université Paris Descartes. https://theses.fr/2013pa05t050

- Jensen O, Colgin L (2007) Cross-frequency coupling between neuronal oscillations. Trends in Cognitive Sciences. 11(7). 267-269. https://doi.org/10.1016/j.tics.2007.05.003

- Ji, D., & Wilson, M. A. (2006). Coordinated memory replay in the visual cortex and hippocampus during sleep. In Nature Neuroscience (Vol. 10, Issue 1, pp. 100–107). Springer Science and Business Media LLC. https://doi.org/10.1038/nn1825

- Juergens, E., Guettler, A., & Eckhorn, R. (1999). Visual stimulation elicits locked and induced gamma oscillations in monkey intracortical- and EEG-potentials, but not in human EEG. In Experimental Brain Research (Vol. 129, Issue 2, pp. 247–259). Springer Science and Business Media LLC. https://doi.org/10.1007/s002210050895

- Juzekaeva, E., Nasretdinov, A., Mukhtarov, M., Shipkov, D., Valeeva, G., & Khazipov, R. (2024). Comparison of extracellular Giant depolarizing potentials in vitro and early sharp waves in vivo in the CA1 hippocampus of neonatal rats. In Biochemical and Biophysical Research Communications (Vol. 735, p. 150823). Elsevier BV. https://doi.org/10.1016/j.bbrc.2024.150823

- Kahle K, Staley K, Nahed B, Gamba G, Hebert S, Lifton R, Mount D (2008) Roles of the cation–chloride cotransporters in neurological disease. Nature Clinical Practice Neurology. 4(9). 490-503. https://doi.org/10.1038/ncpneuro0883

- Karlsson K, Mohns E, di Prisco G, Blumberg M (2006) On the co-occurrence of startles and hippocampal sharp waves in newborn rats. Hippocampus. 16(11). 959-965. https://doi.org/10.1002/hipo.20224

- Khalilov I, Esclapez M, Medina I, Aggoun D, Lamsa K, Leinekugel X, Khazipov R, Ben-Ari Y (1997) A Novel In Vitro Preparation: the Intact Hippocampal Formation. Neuron. 19(4). 743-749. https://doi.org/10.1016/s0896-6273(00)80956-3

- Khalilov I, Le Van Quyen M, Gozlan H, Ben-Ari Y (2005) Epileptogenic Actions of GABA and Fast Oscillations in the Developing Hippocampus. Neuron. 48(5). 787-796. https://doi.org/10.1016/j.neuron.2005.09.026

- Khalilov I, Leinekugel X, Mukhtarov M, Khazipov R (2014) Intracellular blockade of GABAA receptors in the rat hippocampal neurons. Biochemistry (Moscow) Supplement Series A: Membrane and Cell Biology. 8(2). 162-168. https://doi.org/10.1134/s1990747814010061

- Khalilov I, Minlebaev M, Mukhtarov M, Khazipov R (2015) Dynamic Changes from Depolarizing to Hyperpolarizing GABAergic Actions during Giant Depolarizing Potentials in the Neonatal Rat Hippocampus. The Journal of Neuroscience. 35(37). 12635-12642. https://doi.org/10.1523/JNEUROSCI.1922-15.2015

- Khazipov R, Esclapez M, Caillard O, Bernard C, Khalilov I, Tyzio R, Hirsch J, Dzhala V, Berger B, Ben-Ari Y (2001) Early Development of Neuronal Activity in the Primate HippocampusIn Utero. The Journal of Neuroscience. 21(24). 9770-9781. https://doi.org/10.1523/jneurosci.21-24-09770.2001

- Khazipov R, Holmes G (2003) Synchronization of Kainate-Induced Epileptic Activity via GABAergic Inhibition in the Superfused Rat HippocampusIn Vivo. The Journal of Neuroscience. 23(12). 5337-5341. https://doi.org/10.1523/jneurosci.23-12-05337.2003

- Khazipov R, Khalilov I, Tyzio R, Morozova E, Ben-Ari Y, Holmes G (2004) Developmental changes in GABAergic actions and seizure susceptibility in the rat hippocampus. European Journal of Neuroscience. 19(3). 590-600. https://doi.org/10.1111/j.0953-816x.2003.03152.x

- Khazipov R, Leinekugel X, Khalilov I, Gaiarsa J, Ben-Ari Y (1997) Synchronization of GABAergic interneuronal network in CA3 subfield of neonatal rat hippocampal slices. The Journal of Physiology. 498(3). 763-772. https://doi.org/10.1113/jphysiol.1997.sp021900

- Khazipov R, Minlebaev M, Valeeva G (2013) Early gamma oscillations. Neuroscience. 250. 240-252. https://doi.org/10.1016/j.neuroscience.2013.07.019

- Kiernan, J. A. (2012). Anatomy of the Temporal Lobe. In Epilepsy Research and Treatment (Vol. 2012, pp. 1–12). Hindawi Limited. https://doi.org/10.1155/2012/176157

- Kirmse K, Kummer M, Kovalchuk Y, Witte O, Garaschuk O, Holthoff K (2015) GABA depolarizes immature neurons and inhibits network activity in the neonatal neocortex in vivo. Nature Communications. 6(1). https://doi.org/10.1038/ncomms8750

- Klausberger T, Somogyi P (2008) Neuronal Diversity and Temporal Dynamics: The Unity of Hippocampal Circuit Operations. Science. 321(5885). 53-57. https://doi.org/10.1126/science.1149381

- Klausberger, T., Márton, L. F., Baude, A., Roberts, J. D. B., Magill, P. J., & Somogyi, P. (2003). Spike timing of dendrite-targeting bistratified cells during hippocampal network oscillations in vivo. In Nature Neuroscience (Vol. 7, Issue 1, pp. 41–47). Springer Science and Business Media LLC. https://doi.org/10.1038/nn1159

- Kneisler T, Dingledine R (1995) Spontaneous and synaptic input from granule cells and the perforant path to dentate basket cells in the rat hippocampus. Hippocampus. 5(3). 151-164. https://doi.org/10.1002/hipo.450050302

- Kranig S, Duhme N, Waldeck C, Draguhn A, Reichinnek S, Both M (2013) Different functions of hyperpolarization-activated cation channels for hippocampal sharp waves and ripples in vitro. Neuroscience. 228. 325-333. https://doi.org/10.1016/j.neuroscience.2012.10.050

- Lahtinen H, Palva J, Sumanen S, Voipio J, Kaila K, Taira T (2002) Postnatal Development of Rat Hippocampal Gamma Rhythm In Vivo. Journal of Neurophysiology. 88(3). 1469-1474. https://doi.org/10.1152/jn.2002.88.3.1469

- Lamsa K, Palva J, Ruusuvuori E, Kaila K, Taira T (2000) Synaptic GABAA Activation Inhibits AMPA-Kainate Receptor–Mediated Bursting in the Newborn (P0–P2) Rat Hippocampus. Journal of Neurophysiology. 83(1). 359-366. https://doi.org/10.1152/jn.2000.83.1.359

- Langston W, Pope N, Jonas P, Nikitic C, Field M, Dowell B, Shillabeer N, Swarbrick R, Brown A (2010) Contaminants in fine sediments and their consequences for biota of the Severn Estuary. Marine Pollution Bulletin. 61(1-3). 68-82. https://doi.org/10.1016/j.marpolbul.2009.12.014

- Le Van Quyen M, Khalilov I, Ben-Ari Y (2006) The dark side of high-frequency oscillations in the developing brain. Trends in Neurosciences. 29(7). 419-427. https://doi.org/10.1016/j.tins.2006.06.001

- Leblanc M, Bland B (1979) Developmental aspects of hippocampal electrical activity and motor behavior in the rat. Experimental Neurology. 66(2). 220-237. https://doi.org/10.1016/0014-4886(79)90076-1

- Legatt, A. D., Arezzo, J., & Vaughan, H. G., Jr. (1980). Averaged multiple unit activity as an estimate of phasic changes in local neuronal activity: effects of volume-conducted potentials. In Journal of Neuroscience Methods (Vol. 2, Issue 2, pp. 203–217). Elsevier BV. https://doi.org/10.1016/0165-0270(80)90061-8

- Leinekugel X, Khazipov R, Cannon R, Hirase H, Ben-Ari Y, Buzsáki G (2002) Correlated Bursts of Activity in the Neonatal Hippocampus in Vivo. Science. 296(5575). 2049-2052. https://doi.org/10.1126/science.1071111

- Leinekugel X, Medina I, Khalilov I, Ben-Ari Y, Khazipov R (1997) Ca2+ Oscillations Mediated by the Synergistic Excitatory Actions of GABAA and NMDA Receptors in the Neonatal Hippocampus. Neuron. 18(2). 243-255. https://doi.org/10.1016/S0896-6273(00)80265-2

- Leinekugel X, Tseeb V, Ben-Ari Y, Bregestovski P (1995) Synaptic GABAA activation induces Ca2+ rise in pyramidal cells and interneurons from rat neonatal hippocampal slices. The Journal of Physiology. 487(2). 319-329. https://doi.org/10.1113/jphysiol.1995.sp020882

- Leung L (1992) Fast (beta) rhythms in the hippocampus: A review. Hippocampus. 2(2). 93-98. https://doi.org/10.1002/hipo.450020202

- Li Y, Stam F, Aimone J, Goulding M, Callaway E, Gage F (2013) Molecular layer perforant path-associated cells contribute to feed-forward inhibition in the adult dentate gyrus. Proceedings of the National Academy of Sciences. 110(22). 9106-9111. https://doi.org/10.1073/pnas.1306912110

- Lisman J, Idiart M (1995) Storage of 7 ± 2 Short-Term Memories in Oscillatory Subcycles. Science. 267(5203). 1512-1515. https://doi.org/10.1126/science.7878473

- Losonczy A, Zhang L, Shigemoto R, Somogyi P, Nusser Z (2002) Cell type dependence and variability in the short-term plasticity of EPSCs in identified mouse hippocampal interneurones. The Journal of Physiology. 542(1). 193-210. https://doi.org/10.1113/jphysiol.2002.020024

- Manent J, Jorquera I, Ben-Ari Y, Aniksztejn L, Represa A (2006) Glutamate Acting on AMPA But Not NMDA Receptors Modulates the Migration of Hippocampal Interneurons. The Journal of Neuroscience. 26(22). 5901-5909. https://doi.org/10.1523/jneurosci.1033-06.2006

- Marguet S, Le-Schulte V, Merseburg A, Neu A, Eichler R, Jakovcevski I, Ivanov A, Hanganu-Opatz I, Bernard C, Morellini F, Isbrandt D (2015) Treatment during a vulnerable developmental period rescues a genetic epilepsy. Nature Medicine. 21(12). 1436-1444. https://doi.org/10.1038/nm.3987

- Marty and Neher, 1983: Tight-seal whole-cell recording. B. Sakmann & E. Neher, Single-Channel Recording (стр. 107–122). Springer. https://doi.org/10.1007/978-1-4615-7858-1_7

- Masurkar A (2018) Towards a Circuit-Level Understanding of Hippocampal CA1 Dysfunction in Alzheimer's Disease Across Anatomical Axes. Journal of Alzheimer’s Disease andamp; Parkinsonism. 08(01). https://doi.org/10.4172/2161-0460.1000412

- McBain C, DiChiara T, Kauer J (1994) Activation of metabotropic glutamate receptors differentially affects two classes of hippocampal interneurons and potentiates excitatory synaptic transmission. The Journal of Neuroscience. 14(7). 4433-4445. https://doi.org/10.1523/jneurosci.14-07-04433.1994

- McVea D, Mohajerani M, Murphy T (2012) Voltage-Sensitive Dye Imaging Reveals Dynamic Spatiotemporal Properties of Cortical Activity after Spontaneous Muscle Twitches in the Newborn Rat. The Journal of Neuroscience. 32(32). 10982-10994. https://doi.org/10.1523/jneurosci.1322-12.2012

- Michelson H, Kapur J, Lothman E (1989) Reduction of paired pulse inhibition in the CA1 region of the hippocampus by pilocarpine in naive and in amygdala-kindled rats. Experimental Neurology. 104(3). 264-271. https://doi.org/10.1016/0014-4886(89)90039-3

- Miles R, Poncer J (1993) Metabotropic glutamate receptors mediate a post-tetanic excitation of guinea-pig hippocampal inhibitory neurones. The Journal of Physiology. 463(1). 461-473. https://doi.org/10.1113/jphysiol.1993.sp019605
- Miles R, Tóth K, Gulyás A, Hájos N, Freund T (1996) Differences between Somatic and Dendritic Inhibition in the Hippocampus. Neuron. 16(4). 815-823. https://doi.org/10.1016/s0896-6273(00)80101-4
- Minelli, A., Alonso-Nanclares, L., Edwards, R. H., DeFelipe, J., & Conti, F. (2003). Postnatal development of the vesicular gaba transporter in rat cerebral cortex. In Neuroscience (Vol. 117, Issue 2, pp. 337–346). Elsevier BV. https://doi.org/10.1016/s0306-4522(02)00864-3
- Minlebaev M, Ben-Ari Y, Khazipov R (2007) Network Mechanisms of Spindle-Burst Oscillations in the Neonatal Rat Barrel Cortex In Vivo. Journal of Neurophysiology. 97(1). 692-700. https://doi.org/10.1152/jn.00759.2006
- Minlebaev M, Colonnese M, Tsintsadze T, Sirota A, Khazipov R (2011) Early Gamma Oscillations Synchronize Developing Thalamus and Cortex. Science. 334(6053). 226-229. https://doi.org/10.1126/science.1210574
- Mishra P, Narayanan R (2020) Heterogeneities in intrinsic excitability and frequency-dependent response properties of granule cells across the blades of the rat dentate gyrus. Journal of Neurophysiology. 123(2). 755-772. https://doi.org/10.1152/jn.00443.2019
- Mohajerani M, Cherubini E (2005) Spontaneous recurrent network activity in organotypic rat hippocampal slices. European Journal of Neuroscience. 22(1). 107-118. https://doi.org/10.1111/j.1460-9568.2005.04198.x
- Mohns E, Blumberg M (2008) Synchronous Bursts of Neuronal Activity in the Developing Hippocampus: Modulation by Active Sleep and Association with Emerging Gamma and Theta Rhythms. The Journal of Neuroscience. 28(40). 10134-10144. https://doi.org/10.1523/jneurosci.1967-08.2008
- Mohns E, Blumberg M (2010) Neocortical Activation of the Hippocampus during Sleep in Infant Rats. The Journal of Neuroscience. 30(9). 3438-3449. https://doi.org/10.1523/jneurosci.4832-09.2010
- Mohns E, Karlsson K, Blumberg M (2007) Developmental emergence of transient and persistent hippocampal events and oscillations and their association with infant seizure susceptibility. European Journal of Neuroscience. 26(10). 2719-2730. https://doi.org/10.1111/j.1460-9568.2007.05928.x
- Morales B, Choi S, Kirkwood A (2002) Dark Rearing Alters the Development of GABAergic Transmission in Visual Cortex. The Journal of Neuroscience. 22(18). 8084-8090. https://doi.org/10.1523/jneurosci.22-18-08084.2002
- Muessig, L., Lasek, M., Varsavsky, I., Cacucci, F., & Wills, T. J. (2019). Coordinated Emergence of Hippocampal Replay and Theta Sequences during Post-natal

Development. In Current Biology (Vol. 29, Issue 5, pp. 834-840.e4). Elsevier BV. https://doi.org/10.1016/j.cub.2019.01.005

- Muller, C., & Remy, S. (2014). Dendritic inhibition mediated by O-LM and bistratified interneurons in the hippocampus. In Frontiers in Synaptic Neuroscience (Vol. 6). Frontiers Media SA. https://doi.org/10.3389/fnsyn.2014.00023

- Murata Y, Colonnese M (2020) GABAergic interneurons excite neonatal hippocampus in vivo. Science Advances. 6(24). https://doi.org/10.1126/sciadv.aba1430

- Neher E, Sakmann B (1976) Noise analysis of drug induced voltage clamp currents in denervated frog muscle fibres. The Journal of Physiology. 258(3). 705-729. https://doi.org/10.1113/jphysiol.1976.sp011442

- Neves, G., Cooke, S. F., & Bliss, T. V. P. (2008). Synaptic plasticity, memory and the hippocampus: a neural network approach to causality. In Nature Reviews Neuroscience (Vol. 9, Issue 1, pp. 65–75). Springer Science and Business Media LLC. https://doi.org/10.1038/nrn2303

- Nicholson C, Freeman J (1975) Theory of current source-density analysis and determination of conductivity tensor for anuran cerebellum. Journal of Neurophysiology. 38(2). 356-368. https://doi.org/10.1152/jn.1975.38.2.356

- O'Keefe J, Krupic J (2021) Do hippocampal pyramidal cells respond to nonspatial stimuli? Physiological Reviews. 101(3). 1427-1456. https://doi.org/10.1152/physrev.00014.2020

- O'Keefe, J., & Dostrovsky, J. (1971). The hippocampus as a spatial map. Preliminary evidence from unit activity in the freely-moving rat. In Brain Research (Vol. 34, Issue 1, pp. 171–175). Elsevier BV. https://doi.org/10.1016/0006-8993(71)90358-1

- PING (2008) Petilla terminology: nomenclature of features of GABAergic interneurons of the cerebral cortex. Nature Reviews Neuroscience. 9(7). 557-568. https://doi.org/10.1038/nrn2402

- Pang Z, Melicoff E, Padgett D, Liu Y, Teich A, Dickey B, Lin W, Adachi R, Südhof T (2006) Synaptotagmin-2 Is Essential for Survival and Contributes to Ca2+Triggering of Neurotransmitter Release in Central and Neuromuscular Synapses. The Journal of Neuroscience. 26(52). 13493-13504. https://doi.org/10.1523/JNEUROSCI.3519-06.2006

- Pashaie, R., Anikeeva, P., Jin Hyung Lee, Prakash, R., Yizhar, O., Prigge, M., Chander, D., Richner, T. J., & Williams, J. (2014). Optogenetic Brain Interfaces. In IEEE Reviews in Biomedical Engineering (Vol. 7, pp. 3–30). Institute of Electrical and Electronics Engineers (IEEE). https://doi.org/10.1109/rbme.2013.2294796

- Patel J, Schomburg E, Berényi A, Fujisawa S, Buzsaki G (2013) Local Generation and Propagation of Ripples along the Septotemporal Axis of the Hippocampus. The Journal of Neuroscience. 33(43). 17029-17041. https://doi.org/10.1523/JNEUROSCI.2036-13.2013

- Pelkey K, Chittajallu R, Craig M, Tricoire L, Wester J, McBain C (2017) Hippocampal GABAergic Inhibitory Interneurons. Physiological Reviews. 97(4). 1619-1747. https://doi.org/10.1152/physrev.00007.2017

- Penttonen M, Kamondi A, Sik A, Acsády L, Buzsaki G (1997) Feed-forward and feed-back activation of the dentate gyrus in vivo during dentate spikes and sharp wave bursts. Hippocampus. 7(4). 437-450. https://doi.org/10.1002/(SICI)1098-1063(1997)7:4<437::AID-HIPO9>3.0.CO;2-F

- Pereira A, Ribeiro S, Wiest M, Moore L, Pantoja J, Lin S, Nicolelis M (2007) Processing of tactile information by the hippocampus. Proceedings of the National Academy of Sciences. 104(46). 18286-18291. https://doi.org/10.1073/pnas.0708611104

- Petersson P, Waldenström A, Fåhraeus C, Schouenborg J (2003) Spontaneous muscle twitches during sleep guide spinal self-organization. Nature. 424(6944). 72-75. https://doi.org/10.1038/nature01719

- Pleasure S, Anderson S, Hevner R, Bagri A, Marin O, Lowenstein D, Rubenstein J (2000) Cell Migration from the Ganglionic Eminences Is Required for the Development of Hippocampal GABAergic Interneurons. Neuron. 28(3). 727-740. https://doi.org/10.1016/s0896-6273(00)00149-5

- Pochinok I, Stöber T, Triesch J, Chini M, Hanganu-Opatz I (2024) A developmental increase of inhibition promotes the emergence of hippocampal ripples. Nature Communications. 15(1). https://doi.org/10.1038/s41467-024-44983-z

- Poncer J, Shinozaki H, Miles R (1995) Dual modulation of synaptic inhibition by distinct metabotropic glutamate receptors in the rat hippocampus. The Journal of Physiology. 485(1). 121-134. https://doi.org/10.1113/jphysiol.1995.sp020717

- Pouille F, Scanziani M (2001) Enforcement of Temporal Fidelity in Pyramidal Cells by Somatic Feed-Forward Inhibition. Science. 293(5532). 1159-1163. https://doi.org/10.1126/science.1060342

- Quairiaux, C., Megevand, P., Kiss, J. Z., & Michel, C. M. (2011). Functional Development of Large-Scale Sensorimotor Cortical Networks in the Brain. In Journal of Neuroscience (Vol. 31, Issue 26, pp. 9574–9584). Society for Neuroscience. https://doi.org/10.1523/jneurosci.5995-10.2011

- Rivera C, Voipio J, Thomas-Crusells J, Li H, Emri Z, Sipilä S, Payne J, Minichiello L, Saarma M, Kaila K (2004) Mechanism of Activity-Dependent Downregulation of the Neuron-Specific K-Cl Cotransporter KCC2. The Journal of Neuroscience. 24(19). 4683-4691. https://doi.org/10.1523/jneurosci.5265-03.2004

- Rohilla, S., Krämer, B., Koberling, F., Gregor, I., & Hocke, A. C. (2020). Multi-target immunofluorescence by separation of antibody cross-labelling via spectral-FLIM-FRET. In Scientific Reports (Vol. 10, Issue 1). Springer Science and Business Media LLC. https://doi.org/10.1038/s41598-020-60877-8

- Rozenberg F, Robain O, Jardin L, Ben-Ari Y (1989) Distribution of GABAergic neurons in late fetal and early postnatal rat hippocampus. Developmental Brain Research. 50(2). 177-187. https://doi.org/10.1016/0165-3806(89)90193-4
- Sah P, Hestrin S, Nicoll R (1990) Properties of excitatory postsynaptic currents recorded in vitro from rat hippocampal interneurones. The Journal of Physiology. 430(1). 605-616. https://doi.org/10.1113/jphysiol.1990.sp018310
- Sakmann and Neher, 1984: Patch clamp techniques for studying ionic channels in excitable membranes. Annual Review of Physiology, 46, 455–472. https://doi.org/10.1146/annurev.ph.46.030184.002323
- Sale. (2010). GABAergic inhibition in visual cortical plasticity. In Frontiers in Cellular Neuroscience. Frontiers Media SA. https://doi.org/10.3389/fncel.2010.00010
- Scharfman H (1993) Activation of dentate hilar neurons by stimulation of the fimbria in rat hippocampal slices. Neuroscience Letters. 156(1-2). 61-66. https://doi.org/10.1016/0304-3940(93)90440-v
- Scharfman H (1994) EPSPs of dentate gyrus granule cells during epileptiform bursts of dentate hilar "mossy" cells and area CA3 pyramidal cells in disinhibited rat hippocampal slices. The Journal of Neuroscience. 14(10). 6041-6057. https://doi.org/10.1523/JNEUROSCI.14-10-06041.1994
- Scharfman H (1995) Electrophysiological diversity of pyramidal-shaped neurons at the granule cell layer/hilus border of the rat dentate gyrus recorded in vitro. Hippocampus. 5(4). 287-305. https://doi.org/10.1002/hipo.450050403
- Schmitz D, Schuchmann S, Fisahn A, Draguhn A, Buhl E, Petrasch-Parwez E, Dermietzel R, Heinemann U, Traub R (2001) Axo-Axonal Coupling. Neuron. 31(5). 831-840. https://doi.org/10.1016/s0896-6273(01)00410-x
- Schwartzkroin P, Kunkel D, Mathers L (1981) Development of rabbit hippocampus: Anatomy. Developmental Brain Research. 2(4). 453-468. https://doi.org/10.1016/0165-3806(81)90016-x
- Scott, R. C., Richard, G. R., Holmes, G. L., & Lenck-Santini, P. (2011). Maturational dynamics of hippocampal place cells in immature rats. In Hippocampus (Vol. 21, Issue 4, pp. 347–353). Wiley. https://doi.org/10.1002/hipo.20789
- Senior T, Huxter J, Allen K, O'Neill J, Csicsvari J (2008) Gamma Oscillatory Firing Reveals Distinct Populations of Pyramidal Cells in the CA1 Region of the Hippocampus. The Journal of Neuroscience. 28(9). 2274-2286. https://doi.org/10.1523/JNEUROSCI.4669-07.2008
- Shipkov D, Nasretdinov A, Khazipov R, Valeeva G (2024) Synchronous excitation in the superficial and deep layers of the medial entorhinal cortex precedes early sharp waves in the neonatal rat hippocampus. Frontiers in Cellular Neuroscience. 18. https://doi.org/10.3389/fncel.2024.1403073
- Sigworth and Neher, 1980: Single Na+ channel currents observed in cultured rat muscle cells. Nature, 287(5781), 447–449. HTTPS://DOI.ORG/10.1038/287447a0

- Sintsov M, Suchkov D, Khazipov R, Minlebaev M (2017) Developmental Changes in Sensory-Evoked Optical Intrinsic Signals in the Rat Barrel Cortex. Frontiers in Cellular Neuroscience. 11. https://doi.org/10.3389/fncel.2017.00392

- Sipilä S, Huttu K, Voipio J, Kaila K (2006) Intrinsic bursting of immature CA3 pyramidal neurons and consequent giant depolarizing potentials are driven by a persistent Na+ current and terminated by a slow Ca2+-activated K+ current. European Journal of Neuroscience. 23(9). 2330-2338. https://doi.org/10.1111/j.1460-9568.2006.04757.x

- Soltesz I, Jones R (1995) The direct perforant path input to CA1: Excitatory or inhibitory? Hippocampus. 5(2). 101-103. https://doi.org/10.1002/hipo.450050202

- Sommeijer, J.-P., & Levelt, C. N. (2012). Synaptotagmin-2 Is a Reliable Marker for Parvalbumin Positive Inhibitory Boutons in the Mouse Visual Cortex. In M. A. Fox (Ed.), PLoS ONE (Vol. 7, Issue 4, p. e35323). Public Library of Science (PLoS). https://doi.org/10.1371/journal.pone.0035323

- Spruston, N. (2008). Pyramidal neurons: dendritic structure and synaptic integration. In Nature Reviews Neuroscience (Vol. 9, Issue 3, pp. 206–221). Springer Science and Business Media LLC. https://doi.org/10.1038/nrn2286

- Staba R, Wilson C, Bragin A, Fried I, Engel J (2002) Quantitative Analysis of High-Frequency Oscillations (80–500 Hz) Recorded in Human Epileptic Hippocampus and Entorhinal Cortex. Journal of Neurophysiology. 88(4). 1743-1752. https://doi.org/10.1152/jn.2002.88.4.1743

- Stumpf C (1965) The fast component in the electrical activity of rabbit's hippocampus. Electroencephalography and Clinical Neurophysiology. 18(5). 477-486. https://doi.org/10.1016/0013-4694(65)90128-8

- Super M (1994) Human Embryology. Postgraduate Medical Journal. 70(823). 387-387. https://doi.org/10.1136/pgmj.70.823.387-a

- Supèr H, Martínez A, Del Río J, Soriano E (1998) Involvement of Distinct Pioneer Neurons in the Formation of Layer-Specific Connections in the Hippocampus. The Journal of Neuroscience. 18(12). 4616-4626. https://doi.org/10.1523/jneurosci.18-12-04616.1998

- Supèr H, Soriano E (1994) The organization of the embronic and early postnatal murine hippocampus. II. Development of entorhinal, commissural, and septal connections studied with the lipophilic tracer DiI. Journal of Comparative Neurology. 344(1). 101-120. https://doi.org/10.1002/cne.903440108

- Suzuki S, Smith G (1988) Spontaneous EEG spikes in the normal hippocampus II. Relations to synchronous burst discharges. Electroencephalography and Clinical Neurophysiology. 69(6). 532-540. https://doi.org/10.1016/0013-4694(88)90165-4

- Thermo Fisher Scientific. (n.d.). Alexa Fluor 647. Retrieved December 9, 2024, from https://www.thermofisher.com/order/catalog/product/A30107

- Towers S, LeBeau F, Gloveli T, Traub R, Whittington M, Buhl E (2002) Fast Network Oscillations in the Rat Dentate Gyrus In Vitro. Journal of Neurophysiology. 87(2). 1165-1168. https://doi.org/10.1152/jn.00495.2001

- Traub R, Draguhn A, Whittington M, Baldeweg T, Bibbig A, Buhl E, Schmitz D (2002) Axonal Gap Junctions Between Principal Neurons: A Novel Source of Network Oscillations, and Perhaps Epileptogenesis. Reviews in the Neurosciences. 13(1). 1-30. https://doi.org/10.1515/revneuro.2002.13.1.1

- Traub R, Jefferys J, Miles R, Whittington M, Tóth K (1994) A branching dendritic model of a rodent CA3 pyramidal neurone.. The Journal of Physiology. 481(1). 79-95. https://doi.org/10.1113/jphysiol.1994.sp020420

- Traub R, Whittington M, Stanford I, Jefferys J (1996) A mechanism for generation of long-range synchronous fast oscillations in the cortex. Nature. 383(6601). 621-624. https://doi.org/10.1038/383621a0

- Tricoire L, Pelkey K, Erkkila B, Jeffries B, Yuan X, McBain C (2011) A Blueprint for the Spatiotemporal Origins of Mouse Hippocampal Interneuron Diversity. Journal of Neuroscience. 31(30). 10948-10970. https://doi.org/10.1523/JNEUROSCI.0323-11.2011

- Tritsch N, Yi E, Gale J, Glowatzki E, Bergles D (2007) The origin of spontaneous activity in the developing auditory system. Nature. 450(7166). 50-55. https://doi.org/10.1038/nature06233

- Tsetsenis, T., Boucard, A. A., Araç, D., Brunger, A. T., & Südhof, T. C. (2014). Direct Visualization ofTrans-Synaptic Neurexin–Neuroligin Interactions during Synapse Formation. In The Journal of Neuroscience (Vol. 34, Issue 45, pp. 15083–15096). Society for Neuroscience. https://doi.org/10.1523/jneurosci.0348-14.2014

- Tsintsadze V, Minlebaev M, Suchkov D, Cunningham M, Khazipov R (2015) Ontogeny of kainate-induced gamma oscillations in the rat CA3 hippocampus in vitro. Frontiers in Cellular Neuroscience. 9. https://doi.org/10.3389/fncel.2015.00195

- Tyzio R, Represa A, Jorquera I, Ben-Ari Y, Gozlan H, Aniksztejn L (1999) The Establishment of GABAergic and Glutamatergic Synapses on CA1 Pyramidal Neurons is Sequential and Correlates with the Development of the Apical Dendrite. The Journal of Neuroscience. 19(23). 10372-10382. https://doi.org/10.1523/jneurosci.19-23-10372.1999

- Urbán, N., Guillemot, F., 2014. Neurogenesis in the embryonic and adult brain: same regulators, different roles. Frontiers in Cellular Neuroscience 8.

- Valeeva G, Janackova S, Nasretdinov A, Rychkova V, Makarov R, Holmes G, Khazipov R, Lenck-Santini P (2018) Emergence of Coordinated Activity in the Developing Entorhinal–Hippocampal Network. Cerebral Cortex. 29(2). 906-920. https://doi.org/10.1093/cercor/bhy309

- Valeeva G, Nasretdinov A, Rychkova V, Khazipov R (2019) Bilateral Synchronization of Hippocampal Early Sharp Waves in Neonatal Rats. Frontiers in Cellular Neuroscience. 13. https://doi.org/10.3389/fncel.2019.00029

- Valeeva G, Rychkova V, Vinokurova D, Nasretdinov A, Khazipov R (2020) Early Sharp Wave Synchronization along the Septo-Temporal Axis of the Neonatal Rat Hippocampus. Neuroscience and Behavioral Physiology. 50(9). 1195-1202. https://doi.org/10.1007/s11055-020-01021-x

- Valeeva G, Tressard T, Mukhtarov M, Baude A, Khazipov R (2016) An Optogenetic Approach for Investigation of Excitatory and Inhibitory Network GABA Actions in Mice Expressing Channelrhodopsin-2 in GABAergic Neurons. The Journal of Neuroscience. 36(22). 5961-5973. https://doi.org/10.1523/jneurosci.3482-15.2016

- Vandecasteele M, Varga V, Berényi A, Papp E, Barthó P, Venance L, Freund T, Buzsaki G (2014) Optogenetic activation of septal cholinergic neurons suppresses sharp wave ripples and enhances theta oscillations in the hippocampus. Proceedings of the National Academy of Sciences. 111(37). 13535-13540. https://doi.org/10.1073/pnas.1411233111

- Vanderwolf C (1969) Hippocampal electrical activity and voluntary movement in the rat. Electroencephalography and Clinical Neurophysiology. 26(4). 407-418. https://doi.org/10.1016/0013-4694(69)90092-3

- Vazetdinova A, Valiullina-Rakhmatullina F, Rozov A, Evstifeev A, Khazipov R, Nasretdinov A (2022) On the accuracy of cell-attached current-clamp recordings from cortical neurons. Frontiers in Molecular Neuroscience. 15. https://doi.org/10.3389/fnmol.2022.979479

- Vida, I., Degro, C.E., Booker, S.A., 2018. Morphology of Hippocampal Neurons, in: Cutsuridis, V., Graham, B.P., Cobb, S., Vida, I. (Eds.), Hippocampal Microcircuits, Springer Series in Computational Neuroscience. Springer International Publishing, Cham, pp. 29–90. https://doi.org/10.1007/978-3-319-99103-0_2

- Vinogradova O (2001) Hippocampus as comparator: Role of the two input and two output systems of the hippocampus in selection and registration of information. Hippocampus. 11(5). 578-598. https://doi.org/10.1002/hipo.1073

- Wang H, Lin C, Chong R, Zhang-Hooks Y, Agarwal A, Ellis-Davies G, Rock J, Bergles D (2015) Spontaneous Activity of Cochlear Hair Cells Triggered by Fluid Secretion Mechanism in Adjacent Support Cells. Cell. 163(6). 1348-1359. https://doi.org/10.1016/j.cell.2015.10.070

- Wester, J. C., & McBain, C. J. (2016). Interneurons Differentially Contribute to Spontaneous Network Activity in the Developing Hippocampus Dependent on Their Embryonic Lineage. In The Journal of Neuroscience (Vol. 36, Issue 9, pp. 2646–2662). Society for Neuroscience. https://doi.org/10.1523/jneurosci.4000-15.2016

- Whittington M, Doheny H, Traub R, LeBeau F, Buhl E (2001) Differential Expression of Synaptic and Nonsynaptic Mechanisms Underlying Stimulus-Induced Gamma

OscillationsIn Vitro. The Journal of Neuroscience. 21(5). 1727-1738. https://doi.org/10.1523/JNEUROSCI.21-05-01727.2001

- Whittington M, Traub R, Jefferys J (1995) Erosion of inhibition contributes to the progression of low magnesium bursts in rat hippocampal slices.. The Journal of Physiology. 486(3). 723-734. https://doi.org/10.1113/jphysiol.1995.sp020848

- Wills T, Barry C, Cacucci F (2012) The abrupt development of adult-like grid cell firing in the medial entorhinal cortex. Frontiers in Neural Circuits. 6. https://doi.org/10.3389/fncir.2012.00021

- Wu N, Zhang X, Murphy J, Chai J, Harris K, Buriak J (2011) Density Doubling of Block Copolymer Templated Features. Nano Letters. 12(1). 264-268. https://doi.org/10.1021/nl203488a

- Yamada J, Okabe A, Toyoda H, Kilb W, Luhmann H, Fukuda A (2004) Cl− uptake promoting depolarizing GABA actions in immature rat neocortical neurones is mediated by NKCC1. The Journal of Physiology. 557(3). 829-841. https://doi.org/10.1113/jphysiol.2004.062471

- Yang J, Hanganu-Opatz I, Sun J, Luhmann H (2009) Three Patterns of Oscillatory Activity Differentially Synchronize Developing Neocortical Networks In Vivo. Journal of Neuroscience. 29(28). 9011-9025. https://doi.org/10.1523/jneurosci.5646-08.2009

- Ylinen A, Soltész I, Bragin A, Penttonen M, Sik A, Buzsaki G (1995) Intracellular correlates of hippocampal theta rhythm in identified pyramidal cells, granule cells, and basket cells. Hippocampus. 5(1). 78-90. https://doi.org/10.1002/hipo.450050110

- Zhang F, Wang L, Boyden E, Deisseroth K (2006) Channelrhodopsin-2 and optical control of excitable cells. Nature Methods. 3(10). 785-792. https://doi.org/10.1038/nmeth936

- Zhang G, Sun W, Zingg B, Shen L, He J, Xiong Y, Tao H, Zhang L (2018) A Non-canonical Reticular-Limbic Central Auditory Pathway via Medial Septum Contributes to Fear Conditioning. Neuron. 97(2). 406-417.e4. https://doi.org/10.1016/j.neuron.2017.12.010

- Zhang J, Ackman J, Xu H, Crair M (2011) Visual map development depends on the temporal pattern of binocular activity in mice. Nature Neuroscience. 15(2). 298-307. https://doi.org/10.1038/nn.3007

- Zhao S, Förster E, Chai X, Frotscher M (2003) Different Signals Control Laminar Specificity of Commissural and Entorhinal Fibers to the Dentate Gyrus. The Journal of Neuroscience. 23(19). 7351-7357. https://doi.org/10.1523/JNEUROSCI.23-19-07351.2003

- Zsiros, V., & Maccaferri, G. (2005). Electrical coupling between interneurons with different excitable properties in the stratum lacunosum-moleculare of the juvenile CA1 rat hippocampus. The Journal of neuroscience : the official journal of the Society

for Neuroscience, 25(38), 8686–8695. https://doi.org/10.1523/JNEUROSCI.2810-05.2005

- van Groen, T., & Michael Wyss, J. (1990). Connections of the retrosplenial granular a cortex in the rat. In Journal of Comparative Neurology (Vol. 300, Issue 4, pp. 593–606). Wiley. https://doi.org/10.1002/cne.903000412

- van Strien, N. M., Cappaert, N. L. M., & Witter, M. P. (2009). The anatomy of memory: an interactive overview of the parahippocampal–hippocampal network. In Nature Reviews Neuroscience (Vol. 10, Issue 4, pp. 272–282). Springer Science and Business Media LLC. https://doi.org/10.1038/nrn2614

ANNEXES

The following publications, co-authored with Azat Gainutdinov, are included in this annex. They were previously published and are not related to the topic of the thesis.

- Juzekaeva, E., Nasretdinov, A., Gainutdinov, A., Sintsov, M., Mukhtarov, M., & Khazipov, R. (2017). Preferential Initiation and Spread of Anoxic Depolarization in Layer 4 of Rat Barrel Cortex. In Frontiers in Cellular Neuroscience (Vol. 11). Frontiers Media SA. https://doi.org/10.3389/fncel.2017.00390
- Juzekaeva, E., Gainutdinov, A., Mukhtarov, M., & Khazipov, R. (2018). Dynamics of the Hypoxia—Induced Tissue Edema in the Rat Barrel Cortex in vitro. In Frontiers in Cellular Neuroscience (Vol. 12). Frontiers Media SA. https://doi.org/10.3389/fncel.2018.00502
- Juzekaeva, E., Gainutdinov, A., Mukhtarov, M., & Khazipov, R. (2020). Reappraisal of anoxic spreading depolarization as a terminal event during oxygen–glucose deprivation in brain slices in vitro. In Scientific Reports (Vol. 10, Issue 1). Springer Science and Business Media LLC. https://doi.org/10.1038/s41598-020-75975-w

frontiers in Cellular Neuroscience

ORIGINAL RESEARCH
published: 15 December 2017
doi: 10.3389/fncel.2017.00390

Preferential Initiation and Spread of Anoxic Depolarization in Layer 4 of Rat Barrel Cortex

Elvira Juzekaeva[1], *Azat Nasretdinov*[1], *Azat Gainutdinov*[1], *Mikhail Sintsov*[1], *Marat Mukhtarov*[1] *and Roustem Khazipov*[1,2]*

[1] *Laboratory of Neurobiology, Kazan Federal University, Kazan, Russia,* [2] *INMED - Institut National de la Santé et de la Recherche Médicale, Aix-Marseille University, Marseille, France*

Anoxic depolarization (AD) is a hallmark of ischemic brain damage. AD is associated with a spreading wave of neuronal depolarization and an increase in light transmittance. However, initiation and spread of AD across the layers of the somatosensory cortex, which is one of the most frequently affected brain regions in ischemic stroke, remains largely unknown. Here, we explored the initiation and propagation of AD in slices of the rat barrel cortex using extracellular local field potential (LFP) recordings and optical intrinsic signal (OIS) recordings. We found that ischemia-like conditions induced by oxygen-glucose deprivation (OGD) evoked AD, which manifested as a large negative LFP shift and an increase in light transmittance. AD typically initiated in one or more barrels and further spread across the entire slice with a preferential propagation through L4. Elevated extracellular potassium concentration accelerated the AD onset without affecting proneness of L4 to AD. In live slices, barrels were most heavily labeled by the metabolic level marker 2,3,5-triphenyltetrazolium chloride, suggesting that the highest metabolic demand is in L4 when compared to the other layers. Thus, L4 is the layer of the barrel cortex most prone to AD, which may be due to the highest metabolic demand and cell density in this layer.

Keywords: ischemia, anoxic depolarization, spreading cortical depression, barrel cortex, barrel, optical intrinsic signals, silicone probes, electrophysiology

OPEN ACCESS

Edited by:
Andrea Nistri,
Scuola Internazionale Superiore di Studi Avanzati (SISSA), Italy

Reviewed by:
Claire Cheetham,
University of Pittsburgh, United States
Joshua C. Brumberg,
Queens College (CUNY), United States

***Correspondence:**
Roustem Khazipov
roustem.khazipov@inserm.fr

Received: *04 October 2017*
Accepted: *27 November 2017*
Published: *15 December 2017*

Citation:
Juzekaeva E, Nasretdinov A, Gainutdinov A, Sintsov M, Mukhtarov M and Khazipov R (2017) Preferential Initiation and Spread of Anoxic Depolarization in Layer 4 of Rat Barrel Cortex. Front. Cell. Neurosci. 11:390. doi: 10.3389/fncel.2017.00390

INTRODUCTION

The brain is highly metabolically active and particularly vulnerable to metabolic insults. During global or focal ischemia, the limited supply of oxygen and glucose causes a fall in ATP levels, arrest in sodium-potassium pump activity and depolarization of neurons in the metabolically deprived brain regions (Lipton, 1999; Somjen, 2001). Release of potassium and glutamate into the extracellular space accelerates depolarization of the adjacent neurons igniting an avalanche-like wave of collective Anoxic Depolarization (AD), which shares many common features with the spreading depression (SD) described by Leao (Leao, 1947; Nedergaard and Hansen, 1993; Somjen, 2001; Pietrobon and Moskowitz, 2014; Dreier and Reiffurth, 2015; Hartings et al., 2017). Near total collective neuronal depolarization during AD is associated with large DC shifts of the extracellular local field potential, and with an increase in tissue light transmittance as a result of cellular swelling (Aitken et al., 1999; Joshi and Andrew, 2001; Somjen, 2001). AD is an initiator of the ischemic damage and irreversible loss of activity in the ischemic core *in vivo* and oxygen-glucose deprivation

(OGD) induced injury in the submerged brain slices *in vitro* (Rader and Lanthorn, 1989; Tanaka et al., 1997; Joshi and Andrew, 2001) (for reviews, Martin et al., 1994; Lipton, 1999; Dreier, 2011). Factors that increase metabolic activity such as increased neuronal activity or elevated temperature accelerate AD onset and ischemic neuronal death, whereas reduction in metabolic demand is neuroprotective against ischemic damage (Dzhala et al., 2000; Joshi and Andrew, 2001; Tyzio et al., 2006).

Different neuronal populations and structures display different sensitivities to ischemia that may involve different metabolism in different cell types (Kawai et al., 1992; Lipton, 1999). In the hippocampus, CA1 pyramidal cells display the highest vulnerability to ischemia, which correlates with the preferential initiation and spread of AD in the CA1 region of the hippocampus (Aitken et al., 1998; Basarsky et al., 1998). The neocortex also displays heterogenous incidence and propagation of SD and AD between different cortical regions and layers (Bogdanov et al., 2016; Kaufmann et al., 2017). Previous studies using slices of non-identified neocortical areas revealed AD and SD "tropism" for the superficial layers 2/3 (Basarsky et al., 1998; Joshi and Andrew, 2001; Kaufmann et al., 2017). The somatosensory cortex and particularly its whisker-related barrel region are highly sensitive to ischemia (Lin et al., 1990), and SD and AD preferentially arise in and propagate through the whisker barrel region of the parietal sensory cortex (Bogdanov et al., 2016; Kaufmann et al., 2017). However, the initiation and spread of AD across the layers of the somatosensory cortex remain largely unknown.

Here, we addressed initiation and propagation of AD induced by OGD to mimic ischemia-like conditions in slices of the rat barrel cortex. We found that AD was specifically initiated in L4 barrels and its initial front preferentially propagated along layer 4. Preferential initiation and spread of AD in L4 correlated with the most intense L4 staining with TTC, a histological metabolic activity marker. We propose that sensitivity to metabolic insult is non-uniform across layers of the barrel cortex: it is highest in L4 barrels, where AD is preferentially initiated, that may involve the highest metabolic demand and cell density in this layer.

MATERIALS AND METHODS

Ethical Approval

All animal-use protocols followed the guidelines of the French National Institute of Health and Medical Research (INSERM, protocol N007.08.01) and the Kazan Federal University on the use of laboratory animals (ethical approval by the Institutional Animal Care and Use Committee of Kazan State Medical University N9-2013).

Brain Slice Preparation

Wistar rats (16–23 days old) of either sex were used. Animals were decapitated under isoflurane anesthesia (5%), the brain was rapidly removed and placed in ice-cold (2–5°C) slicing solution (modified from Dugué et al., 2005) of the following composition (in mM): K-Gluconate 140, Na-Gluconate 15, NaCl 4, EGTA 0.2, D-AP5 50 μM and HEPES 10 (pH 7.4). Four hundred μm thick thalamocortical slices were cut using a PELCO easiSlicer® vibratome (Ted Pella, Inc., Redding, CA, USA). Slices containing the barrel cortex were selected by anatomical coordinates (Khazipov et al., 2015) and the presence of barrel structures in L4 (**Figure 1B**). Slices were first kept in oxygenated (95% O_2-5% CO_2) artificial cerebrospinal fluid (ACSF) of the following composition (in mM): NaCl 126, KCl 3.5, $CaCl_2$ 2, $MgCl_2$ 1.3, $NaHCO_3$ 25, NaH_2PO_4 1.2 and glucose 11 (pH 7.4) for 30 min at 32°C and then at room temperature (20–22°C) for at least 1 h before use. For recordings, slices were placed into a submerged chamber and superfused with oxygenated ACSF at 30–32°C at a flow rate of 10 ml/min. Oxygen/glucose deprivation (OGD) was induced by superfusion with ACSF in which N_2 replaced O_2 and sucrose replaced glucose at equimolar concentration.

Electrophysiological Recordings

Extracellular recordings of the local field potentials (LFP) were performed in the barrel cortex using single or 16-site electrodes. Single site glass pipette electrodes were pulled from borosilicate glass capillaries (BF150-86-10, Sutter Instrument, Novato, CA, USA) and had resistances of 2–3 MΩ when filled with ACSF. Electrodes were connected via chlorided silver wire to the headstage of a MultiClamp700B patch-clamp amplifier (Axon Instruments, Union City, CA, USA). Recordings were performed in voltage-clamp mode and currents were inverted and voltage calibrated using 5 mV steps. 16-channel recordings were performed using Menendez-de La Prida style 16 shank silicone probes with a separation distance of 100 μm between electrodes (NeuroNexus, Ann Arbor, MI, USA). The signals from extracellular recordings using silicone probes were amplified and filtered (1,000×; 0–9 kHz) using a Digital Lynx SX amplifier (Neuralynx, Inc., Bozeman, MT, USA), digitized at 32 kHz and saved on a PC for *post-hoc* analysis. Stimulating bipolar electrodes were placed in the white matter or L6 above the recorded cortical column. Voltage pulses (10–50 V, 50 μs duration, 0.1 Hz) were applied to evoke LFP responses of 100–300 μV in L4.

Optical Intrinsic Signal Recordings

Optical intrinsic signal (OIS) recordings were performed using slice transillumination as described in Aitken et al. (1999). The slice was illuminated by a halogen lamp with a 775 nm bandpass filter and visualized using a BX51WI upright microscope equipped with a 4×/0.10 Plan N objective (Olympus, Tokyo, Japan). Images were acquired using a QIClick-R-F-M-12 CCD camera (QImaging, Surrey, BC, Canada) usually at 174 × 130 pixel resolution and 5 frames/s acquisition rate. In some experiments a higher resolution of 348 × 260 or 696 × 520 was used.

TTC-Staining

Brain slices were stained with 1% TTC (2,3,5-triphenyltetrazolium chloride) in phosphate-buffered solution (PBS) for 2–3 min at 38°C. Then slices were rinsed in PBS (for 1 min, 3 times). Microphotographs of TTC-stained slices were

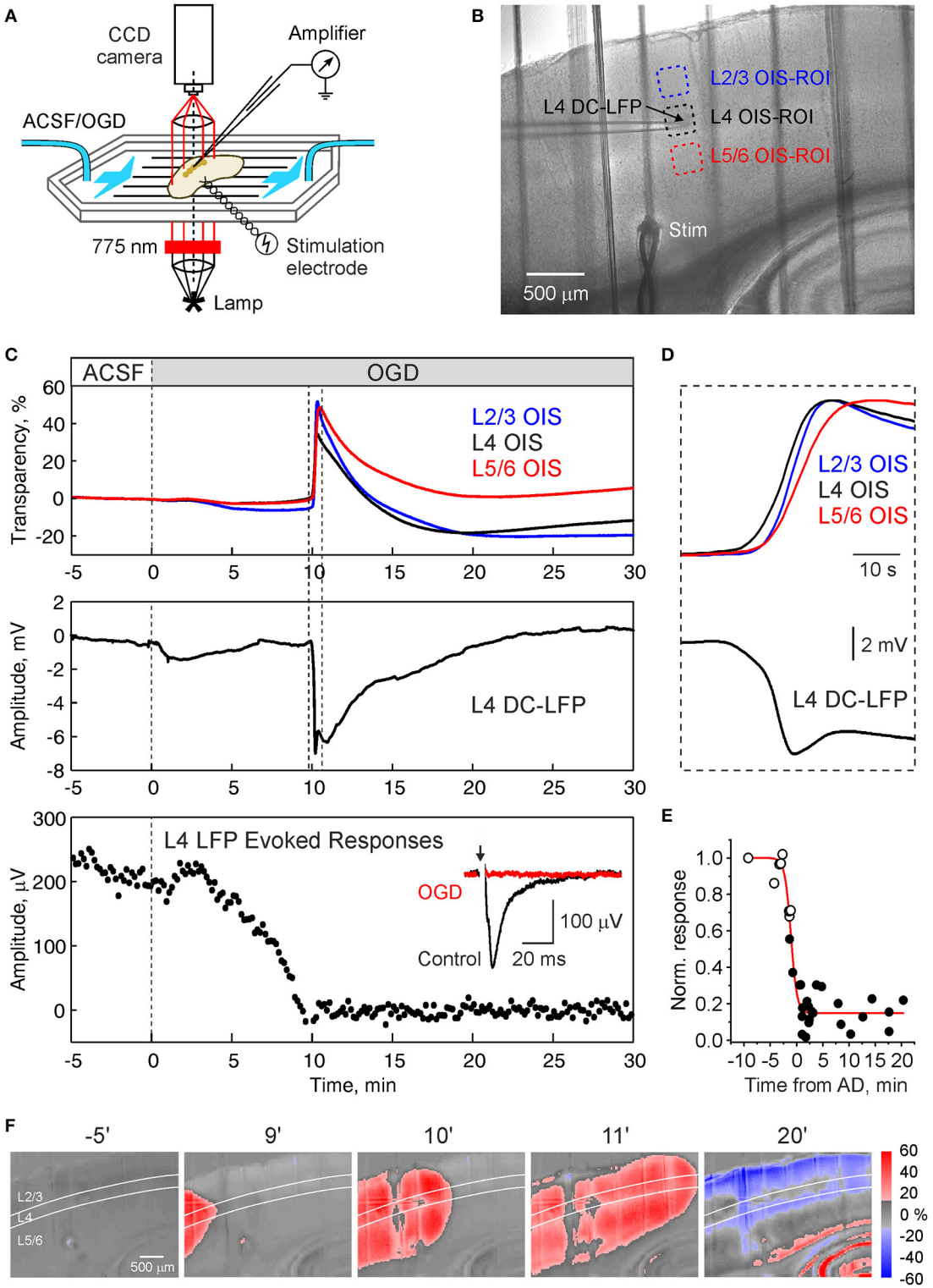

FIGURE 1 | Oxygen-glucose deprivation induced anoxic depololarization in barrel cortex. **(A)** Scheme of the experimental setup. Submerged cortical slices is exposed to the ACSF in which oxygen is replaced by nitrogen and glucose is replaced by sucrose (oxygen-glucose deprivation, OGD) to mimic ischemic conditions. Local field potential (LFP) recordings and optical intrinsic signal (OIS) imaging in transmittance mode is performed to record anoxic depolarization (AD). **(B)** Microphotograph of the cortical slice. LFP is recorded from a cortical barrel, regions of interest (ROIs) in the supragranular, granular, and infragranular layers of are indicated by color boxes.

(Continued)

FIGURE 1 | (C) Traces of OIS from the ROIs as indicated on panel **(B)** (top), DC-LFP recordings from L4 and the amplitude of the responses in L4 evoked by stimulation of the white matter during superfusion with OGD solution. **(D)** Initial phase of AD outlined on panel **(C)** on expanded time scale. Note that onset of OIS-AD in L4 precedes the OIS in supra- and infragranular layers. Inset shows average white matter-evoked LFP response in L4 before (black) and after (red) OGD. **(E)** Dependence of the L4 evoked response recovery on the delay of reperfusion with normal ACSF from AD. Each point indicates the scalar integral of the response 15–30 min after reperfusion with oxygenated ACSF normalized to the control values. Black and open circles indicate OGD episodes with and without AD, respectively. The time values for the open circles were deduced from AD values in the experiments with repetitive OGD episodes, where each next OGD increased in duration until the AD was evoked. Red line indicates Boltzmann fit. **(F)** Snapshots of OIS at different time points after superfusion with OGD-solution. Note that the AD front preferentially propagates along L4.

obtained using a SZX16 wide zoom stereo microscope equipped with a SDF PLAPO 1 × PF objective and SZX2-ILLT LED transmitted light illumination base (Olympus, Tokyo, Japan). Images were acquired at 0.7×-1× magnification using a XC50 CCD camera (Olympus, Tokyo, Japan) at 2,576 × 1,932 pixel resolution.

Data Analysis

Data were analyzed using custom-written procedures in Matlab (MathWorks, Inc., Natick, MA, USA). OIS was calculated using the first-frame subtraction approach: $OIS(t) = (I(t) - I_0)/I_0$, where I(t) – pixel intensity at the moment t, I_0 – time-averaged pixel intensity in the preconditioned baseline period (100 s). Resulting frames were filtered with a 10 × 10 median filter. Regions of interest (ROI) were selected as square areas near recording sites. OIS traces were calculated as the average OIS signal within selected ROIs.

LFP signals were downsampled to 1 kHz. Continuous running line fit was removed using local linear regression in 300 s windows with a 10 s overlap [*locdetrend* function from the Chronux toolbox (http://chronux.org/)]. Amplitude of the LFP evoked response was calculated as a negative peak value of the LFP in the 100 ms after the stimulus relative to baseline level (average of the LFP in the 10 ms before the stimulus).

Data were smoothed by the 1,000-point moving average filter and the first derivatives were calculated. Local negative peak time of the first LFP derivative was calculated within the 20 s window preceding the negative AD peak. The value of the LFP at this time was taken as 100% and the previous time corresponding to 30% considered as AD onset. Velocity of vertical AD propagation was calculated from onset values as a distance between neighboring recording sites (100 μm) divided by AD onset delays between corresponding channels. The baseline level was calculated for each recording site as the mean value of the LFP in the −20 to −10 s time window preceding AD onset. AD amplitude was calculated as the maximal negative LFP peak from the baseline. Data from different slices were aligned by L4 and average amplitude and onset depth profiles were calculated. Depth profiles of amplitude were smoothed by the 2-point moving average filter. OIS onsets and amplitudes were calculated in same manner.

Microphotographs of TTC-stained slices were analyzed as follows. Pixel intensities were calculated along the barrel cortex and along the perpendicular direction intersecting the barrel and averaged in a 100 μm wide bar. Intensity was converted to a percentage (intensity value of each pixel divided by maximal intensity). Staining efficiency (opacity) was calculated as the value inverse to the calculated intensity.

Statistical Analysis

Statistical analysis was based on the nonparametric Wilcoxon (paired samples) or Mann-Whitney (independent samples) signed rank sum test with the significance level set at $p < 0.05$. Results are given as means ± SEM.

RESULTS

Electrophysiological and Optical Intrinsic Signals during Anoxic Depolarization

In the present study, we explored spatial-temporal dynamics of the OGD-induced AD in slices of the barrel cortex using extracellular recordings of LFP, and OIS recordings (**Figures 1A,B**). AD was initiated within 6–13 min (9.5 ± 0.5 min; $n = 17$ slices from 8 rats) and manifested as a sharp increase of light transparency attaining 29.2 ± 3.0% dI/I and negative LFP shift of 8.9 ± 0.6 mV in L4 ($n = 17$; **Figure 1C**). LFP signals were typically biphasic with an initial sharp negative transient followed by a secondary negative wave. The increase in OIS during AD started in L4 and further spread to L2/3 and L5/6 (**Figure 1D**). The responses evoked in L4 by stimulation of the white matter or L6, progressively decreased during OGD and were completely and irreversibly abolished during and after AD (**Figure 1C**), while the evoked responses could recover following shorter OGD episodes without AD (**Figure 1E**) that is in keeping with the results of previous studies (Rader and Lanthorn, 1989; Tanaka et al., 1997; Joshi and Andrew, 2001). In the experiment illustrated in **Figure 1**, OIS recordings revealed that AD unilaterally propagated through the slice with the leading front in L4 and delayed fronts in the supra- and infragranular layers (**Figure 1F**). The increase in light transmittance was followed by a decrease in light transmittance probably reflecting cellular swelling followed by dendritic beading (Aitken et al., 1999; Joshi and Andrew, 2001; Somjen, 2001). After AD in the barrel cortex, AD was also observed in the hippocampus and striatum after a several minute delay (**Figure 1F**).

Vertical AD Propagation in a Cortical Barrel Column

We also performed simultaneous OIS and multisite LFP recordings from a cortical barrel column using 16-shank silicone probes (**Figures 2A,B**). In keeping with the results described above, AD was initiated in L4 and spread to L2/3 and L5/6

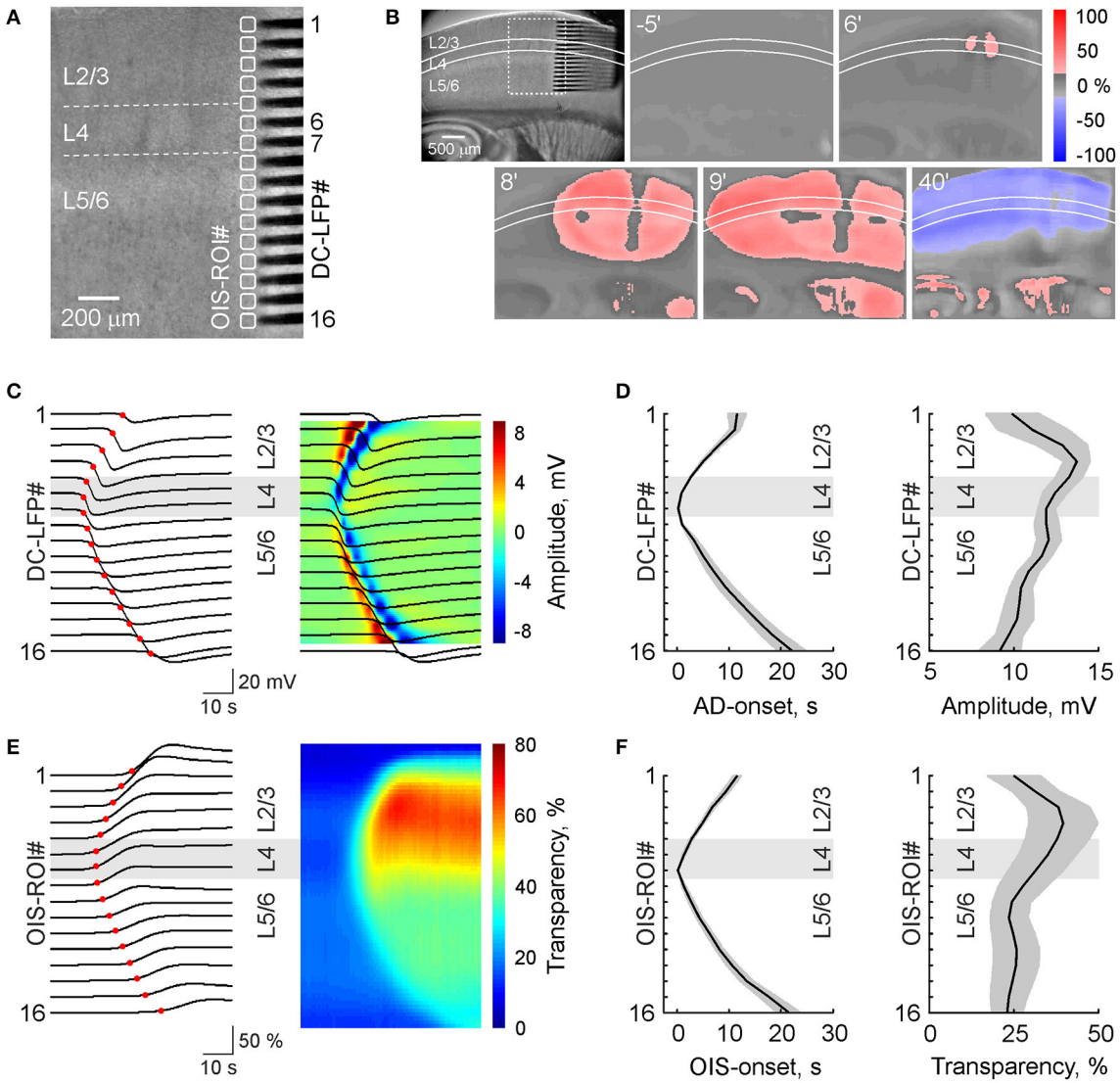

FIGURE 2 | Spread of anoxic depolarization within a cortical barrel column. **(A)** IR-DIC microphotograph of a slice of the barrel cortex with a 16-shank silicone probe (100 µm electrode separation distance) vertically placed to record DC-coupled LFP from all layers of a cortical barrel column. Corresponding OIS-ROIs are outlined by white boxes. **(B)** Microphotograph of the brain slice shown on panel **(A)** on a reduced scale (left) and snapshots of OIS at different time points after OGD induction. **(C)** Corresponding DC-LFP traces (black) during AD propagation at different depths of the cortical column with the AD onsets marked at each channel with a red circle (left) and the same DC-LFP traces overlaid on the color-coded current-source density map (right). **(D)** Group data on OGD-induced AD onsets and AD amplitudes as a function of cortical depth (mean ± *SE*, $n = 7$). **(E)** Concomitant OIS recordings of AD (left) and color-coded transparency map calculated from OIS traces (right) in the ROIs indicated on panel **(A)**. Red circles indicate the OIS-AD onset. **(F)** Group data on the onsets and amplitudes of OIS associated with OGD-induced AD as a function of cortical depth (mean ± *SE*, $n = 7$). Note that AD first occurs in L4 and further spreads to L2/3 and L5/6 and that AD amplitude is maximal in L2/3.

with a velocity of 4.0 ± 0.1 mm/min ($n = 7$ slices from 4 rats). The maximal amplitude of negative LFP shift during AD was observed in the superficial layers (13.8 ± 0.8 mV at a depth of 400 µm from the cortical surface; $n = 7$; **Figures 2C,D**). In L4 and L5/L6 the amplitude of AD was 12.0 ± 0.6 and 10.7 ± 0.7 mV, respectively ($n = 7$). The OIS profile of AD was remarkably similar to that of the electrophysiological response including an initial onset in L4 and vertical delays in the supra- and infragranular layers, the speed of vertical propagation, and a maximal amplitude of light transmittance increase of 38.5 ± 10.3% ($n = 7$) attained in L2/3 and smaller change in deeper layers (**Figures 2E,F**).

Patterns of AD Initiation and Propagation

OIS imaging revealed variability of the AD initiation and propagation patterns, which could be classified in four main groups (**Figure 3** and **Videos 1–4**):

1. *Single-barrel AD initiation* (**Figure 3A**; **Video 1**). AD emerges in one barrel within the imaging window and spreads

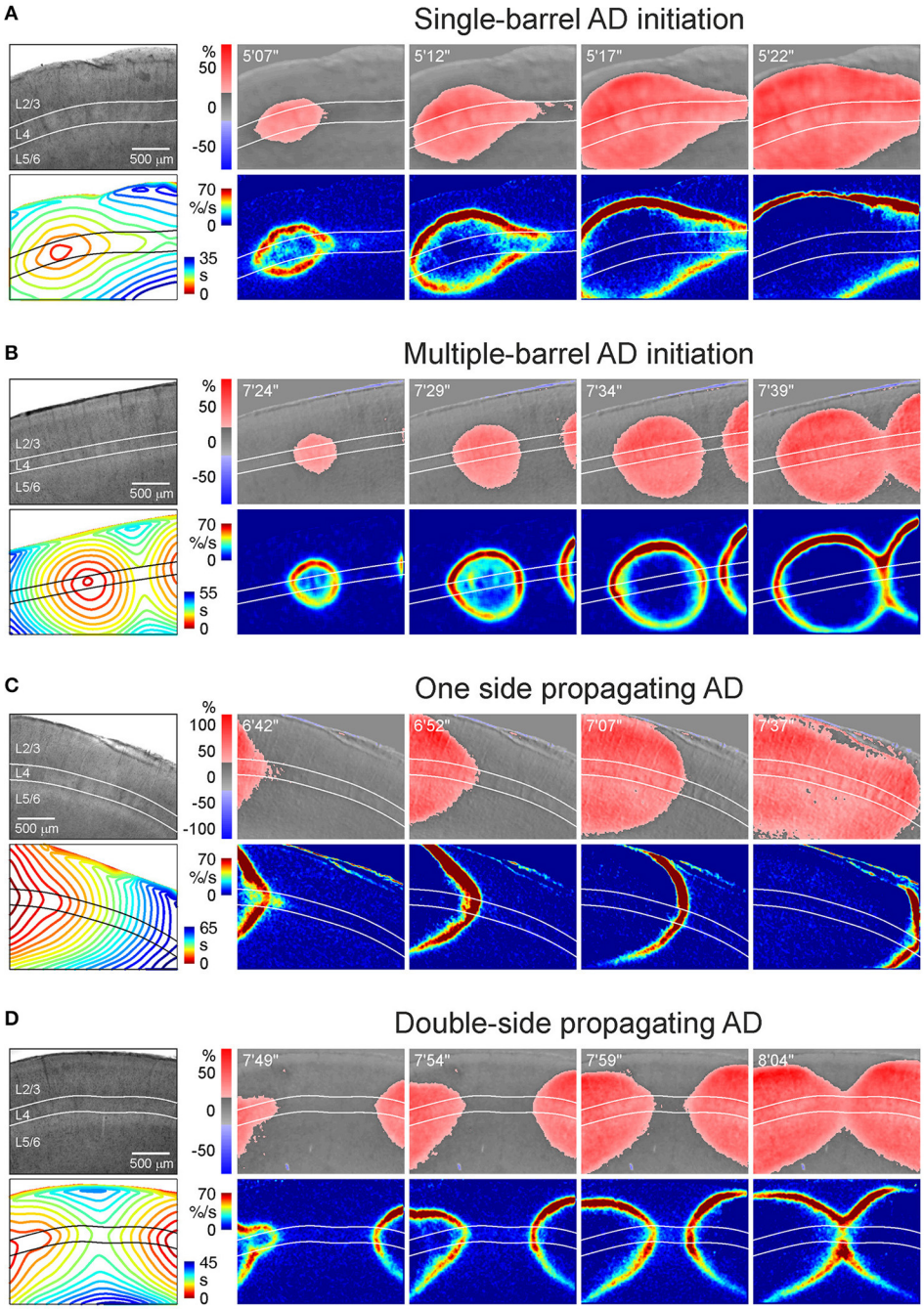

FIGURE 3 | Various patterns of AD initiation and propagation in barrel cortex. **(A)** Microphotograph of a barrel cortex slice in DIC-IR (left) and OIS snapshots at different time points after OGD induction. Below, the corresponding AD fronts are presented as the OIS first derivative. Bottom left panel shows time color coded AD front contours plotted at 3 s intervals. Note that AD is initiated in one barrel and further propagates preferentially through L4. **(B)** Similar example of AD which is initiated in a barrel located in the middle of the imaging window and which collides with another AD wave arriving from another locus on the right of the imaging window. **(C)** Example of AD propagating preferentially through layer 4 from the left side of the imaging window. **(D)** Example of AD propagating from the left and right sides and colliding in the middle of the imaging window in L4.

concentrically. The AD spread is often anisotropic with a preferential horizontal propagation along L4 forming a characteristic "bird head" OIS image. This pattern was observed in 11 of 30 slices.

2. *Multiple-barrel AD initiation* (**Figure 3B**; **Video 2**). AD emerges in two (or more) barrels within the imaging window. AD fronts move concentrically and collide first in L4 and then in the superficial and deep layers ($n = 6$ of 30 slices).

3. *One side propagating AD* (**Figure 3C**; **Video 3**). AD originates on one side of slice but outside of the imaging window and spreads through the slice with a preference to L4 ($n = 8$ of 30 slices).
4. *Double-side propagating AD* (**Figure 3D**; **Video 4**). AD emerges on two sides of slice outside of the imaging window. Two AD waves move toward each other with a preference to the L4 and collide similarly to the multi-barrel initiation pattern ($n = 5$ of 30 slices).

These results indicate that despite variety in the site of OGD-induced AD initiation in a slice, preference of AD to L4 is a hallmark of all initiation and propagation AD patterns. The rate of AD propagation along L4 was 1.7 ± 0.1 mm/min ($n = 18$ slices from 8 rats) which is consistent with the rate of AD and SD propagation in slices and in the intact brain *in vivo* (Nedergaard, 1996; Basarsky et al., 1998; Joshi and Andrew, 2001). In the cases of single-barrel AD initiation the rate of medial AD propagation along L4 was of 1.8 ± 0.1 mm/min that was not different from the rate of lateral AD propagation of 1.7 ± 0.1 mm/min ($n = 11$ slices from 4 rats, $p = 0.76$).

We next addressed a question of whether AD in L4 is a necessary condition for emergence of AD in the supragranular and infragranular layers. In this aim, we explored OGD-induced AD after surgical cuts made above, below and through the L4 (**Figure 4** and **Videos 5**–**7**). We found that AD efficiently invaded supragranular and infragranular layers even after disconnection from L4, with an AD front moving horizontally around the cuts thus indicating that both superficial and deep layers are capable of generating AD independently from L4. We further calculated the time difference between AD in the surface and deep layers

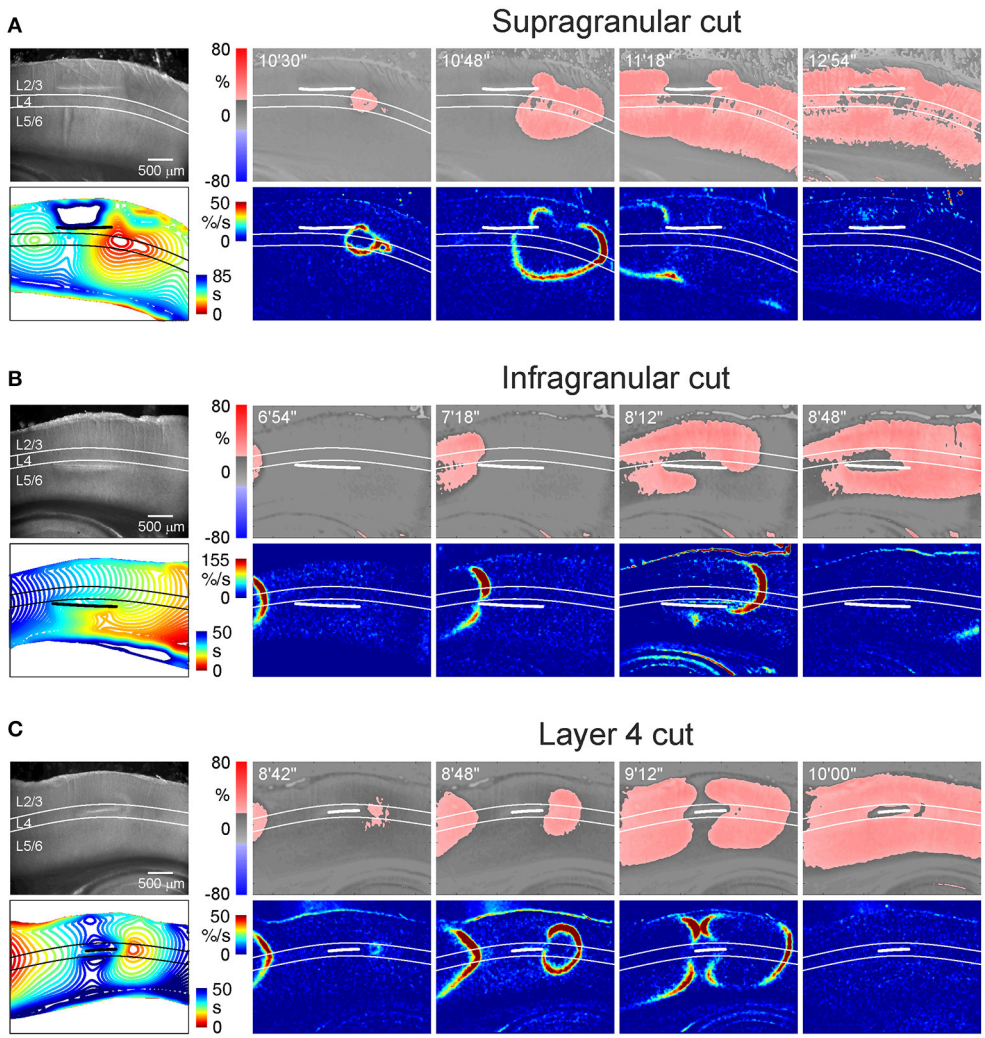

FIGURE 4 | AD propagation after surgical cut above, below and through L4. **(A–C)** Example microphotographs of the barrel cortex slices in DIC-IR (left) with the cuts made above **(A)**, below **(B)**, and through **(C)** the layer 4 and OIS snapshots at different time points after OGD induction. Below, the corresponding AD fronts are presented as the OIS first derivative. Bottom left panel shows time color coded SD front contours plotted at 3 s intervals. Note that AD waves invade supragranular and infragranular layers in all cases but AD emerges earlier if connection with L4 is preserved. AD propagation to L2/3 above the cut on panel **(A)** was too slow and is truncated on the contour map. See **Video 5** for the entire AD wave in this experiment.

at the areas vertically aligned to the middle of the cut. When the cut was made above L4, AD arrived to L2/3 88 ± 19 s later than to L5/6 ($n = 4$). When the cut was made below L4, AD in L2/3 emerged 49 ± 6 s earlier than in L5/6 ($n = 5$). Thus, AD was generated earlier in the layers maintaining connection with L4 than AD in the layers disconnected from L4. With the cut made through L4, the time delay between AD in L2/3 and L5/6 reduced to 12 ± 4 s ($n = 4$). Together, these results indicate that AD in L4 is not a necessary condition for AD in the surface and deep layers, where AD can propagate horizontally. However, vertical AD vector originating from L4 accelerates AD in the supragranular and infragranular layers maintaining their connection with L4.

Elevated Extracellular Potassium Concentration Accelerates the AD Onset

Hyperactivity compromises the metabolic state of the tissue under OGD-conditions and accelerates the AD onset in hippocampus (Dzhala et al., 2000). With the aim of exploring the effect of increased activity on the OGD-induced AD in the barrel cortex, we elevated extracellular potassium concentration in ACSF from 3.5 to 8.5 mM. The high-potassium solution itself induced a slight increase in light transmittance and a negative shift in the LFP baseline in L4 (**Figure 5A**). Further superfusion with high-potassium/OGD solution evoked AD with a delay of 5.9 ± 0.4 min ($n = 13$ slices from 5 rats), that was almost two-fold quicker ($p < 0.001$) than AD evoked by OGD in normal potassium conditions (9.5 ± 0.5 min; $n = 17$ slices from 8 rats) (**Figure 5C**). In the high-potassium/OGD solution the negative LFP shift of 8.5 ± 0.6 mV ($n = 13$) in L4 was similar to those in normal potassium conditions ($p > 0.05$) while the increase in light transparency of 19.8 ± 1.0% dI/I ($n = 13$) was less than in normal conditions ($p < 0.05$), due to the progressive increase of dI/I before AD which occurs in elevated potassium conditions (**Figure 5A**). OIS imaging revealed that preference of AD initiation and propagation in L4 was maintained under conditions of elevated potassium (**Figure 5B**).

Highest Metabolic Activity in L4

Preferential initiation and propagation of AD in the barrels may involve the higher metabolic demand of barrels and therefore their higher vulnerability to metabolic deprivation. We explored this hypothesis using 2,3,5-triphenyltetrazolium chloride (TTC) staining of live slices of the barrel cortex. As shown on **Figures 6A,D**, TTC most intensively stained L4. Quantification

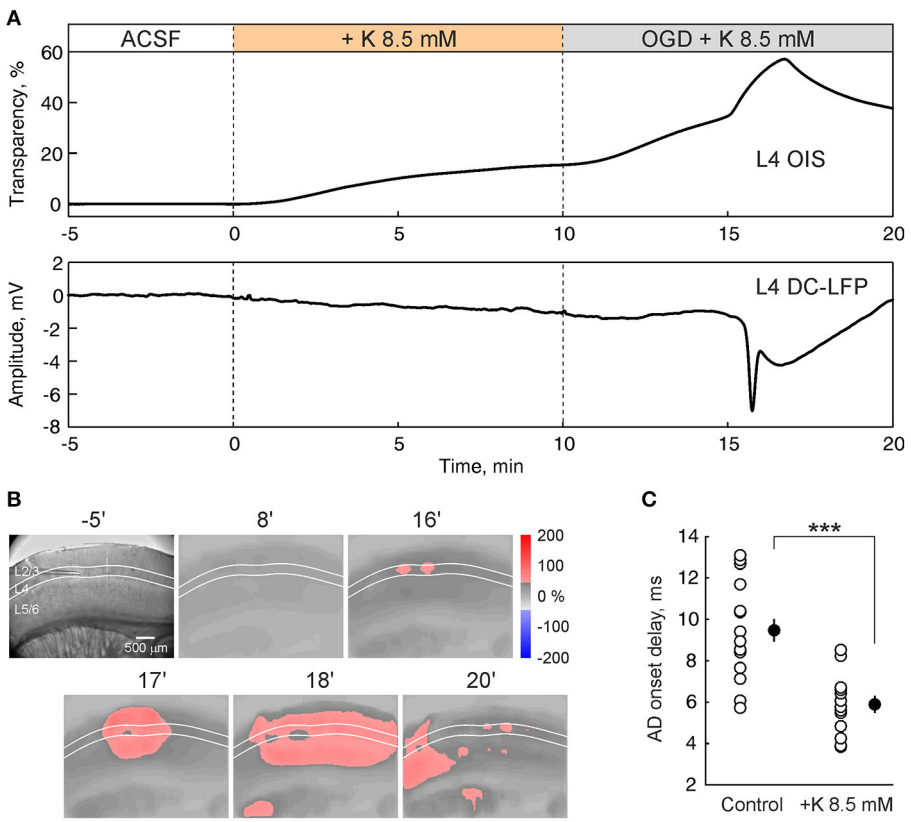

FIGURE 5 | Elevation of extracellular potassium accelerates the onset of anoxic depolarization. **(A)** OIS from L4 (top trace) and nearby L4 DC-coupled LFP (bottom trace) during superfusion with ACSF with elevated (from 3.5 to 8.5 mM) potassium concentration and after OGD induction. **(B)** Corresponding microphotograph (left) and OIS snapshots at different time points after OGD induction. **(C)** Group data on AD onsets in control ACSF ($n = 17$) and in the ACSF with potassium concentration elevated to 8.5 mM ($n = 13$). Each white circle corresponds to one slice and black circles show the mean ± SE. Note that AD onset is accelerated almost two-fold after elevation of extracellular potassium concentration. ***$p < 0.001$.

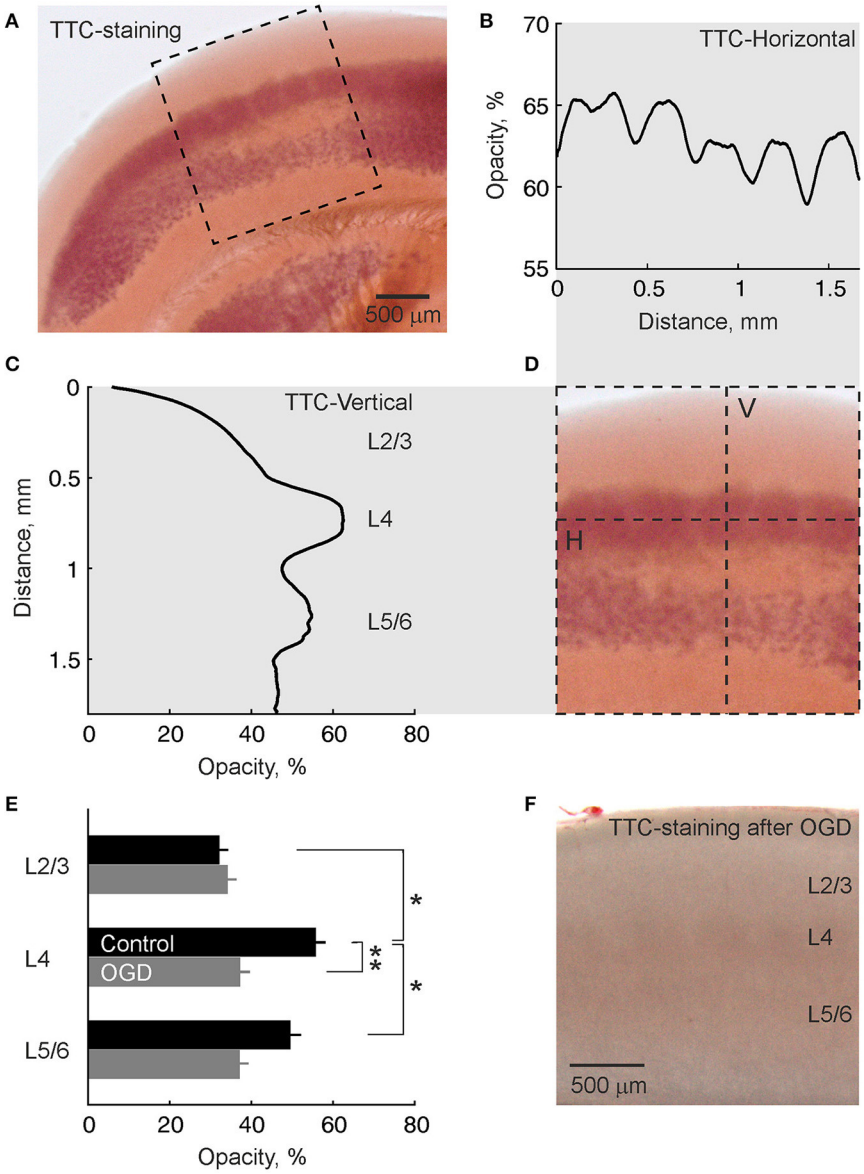

FIGURE 6 | TTC-staining of a live slice of the barrel cortex shows highest metabolic activity in L4. **(A)** Microphotograph of a slice of barrel cortex stained with TTC. **(B–D)** Intensity of TTC-staining within a region outlined by dashed box on panel **(A)** in **(B)** horizontal projection along the L4 (indicated by H-line on panel **D**) and **(C)** vertical projection across cortical layers of a barrel column (indicated by V-line on panel **D**). Note the horizontal barrel staining pattern and maximal staining of L4 in vertical projection. **(E)** Group data on the intensity of TTC-staining of different cortical layers in control slices ($n = 7$) and slices after OGD exposure ($n = 9$). *$p < 0.05$; **$p < 0.01$. **(F)** Microphotograph of a TTC-stained slice of barrel cortex after OGD exposure. Note weak non-specific staining compared with the live slice.

of TTC-staining along the horizontal projection in L4 revealed peaks in TTC-staining corresponding to neighboring barrels (**Figure 6B**). In the vertical projection across cortical depth, TTC staining peaked at the L4 depth (**Figure 6C**). A second, less intense peak was found ~0.5 mm deeper at the L5B/L6A border (**Figure 6C**). Cross-layer comparisons revealed significantly higher TTC-staining of L4 compared to L2/3 ($p < 0.05$) and L5/6 ($p < 0.05$) ($n = 7$ slices from 4 rats; **Figure 6E**). Slices that had been exposed to OGD for 30 min and reperfused with normal ACSF for 2 h displayed only weak non-specific staining (**Figure 6F**). TTC-staining of L4 in OGD-exposed slices revealed no difference with L2/3 ($p > 0.05$) and L5/6 ($p > 0.05$) staining and was significantly lower compared to control slices ($p < 0.01$; $n = 9$ slices from 4 rats) (**Figure 6E**).

DISCUSSION

The principal conclusion emerging from the present study is that different layers of the barrel cortex differ in their propensity to AD and that L4 is the most prone to AD. This conclusion is

supported by electrophysiological recordings and OIS imaging indicating that OGD-induced AD is preferentially initiated in, and preferentially spreads through L4. We also found that enhanced L4 susceptibility to OGD correlates with the highest metabolic activity, in L4, revealed with TTC staining of live slices.

Anisotropy is a characteristic feature of the heterogeneous incidence and horizontal spread of cortical SD *in vivo* (Kaufmann et al., 2017). Previous studies in non-identified neocortical areas revealed anisotropy of AD and SD across cortical layers with a "tropism" to the superficial layers 2/3 (Basarsky et al., 1998; Joshi and Andrew, 2001; Kaufmann et al., 2017). However, our findings indicate that in the barrel cortex, which contains large barrels and the thickest L4 of all the cortical regions, AD is initiated and preferentially propagates via L4. Onset and preferential propagation of AD in L4 was evidenced by the earliest onset of the negative LFP DC shift and the earliest increase in optical transparency in barrels during the OGD-induced AD. Multisite LFP recordings and simultaneous OIS imaging revealed vertical spread of AD from the L4 to the superficial and deep layers within a column. OIS recordings also enabled us to assess two-dimensional spatial-temporal AD dynamics in the barrel cortex slices revealing a variety of AD initiation and propagation patterns, yet with a common delimiter of the highest proneness of L4 to AD. While AD primarily originated in L4 in the barrel cortex, L4 appeared to be not necessary for the emergence of AD in the supragranular and infragranular layers, however. Indeed, our experiments with surgical cuts above, below and through the L4 revealed that AD may propagate through these layers horizontally around the cuts, although at lower speed. This indicates that supra- and infragranular layers are capable of generating AD independently from the L4. Yet, early ignition of AD in L4 is important for driving AD in the supra- and infragranular layers in the intact slice.

Various factors have been suggested to explain anisotropy of SD and AD (Herreras and Somjen, 1993; Somjen, 2001; Canals et al., 2005; Kaufmann et al., 2017). High neuronal density in L2/3 has been hypothesized to promote a mutual promotion of depolarization and potassium release and accumulation, making these layers more prone to AD (Joshi and Andrew, 2001). In the barrel cortex, the highest neuronal density is observed in L4, where it attains 124 thousand neurons/mm^3 compared to 102 and 86 thousand neurons/mm^3 in L3 and L2, respectively (Meyer et al., 2010). Thus, our findings of the preferential initiation and spread of AD in L4 of the barrel cortex are consistent with the "neuronal density" hypothesis. Interestingly, SD and AD preferentially arise in and propagate through the whisker barrel region of parietal sensory cortex *in vivo* (Bogdanov et al., 2016; Kaufmann et al., 2017). Because the barrel cortex contains large barrels and the thickest L4 of all the somatosensory cortical regions, the elevated proneness of L4 to AD as revealed in the present study may also explain high proneness of the barrel cortex to AD.

Our observations of heterogeneous TTC-staining in different cortical layers with the maximum in L4 suggest that elevated metabolic demand could also be a factor contributing to the particular susceptibility of this layer to AD. TTC staining intensity is determined by the metabolic activity of mitochondrial dehydrogenases, which enzymatically convert colorless TTC to red formazan (Goldlust et al., 1996). The elevated L4 metabolic activity revealed with TTC-staining is consistent with the highest density of a mitochondrial enzyme cytochrome oxydase and elevated number of mitochondria in L4 of the barrel cortex where they reside mainly in dendrites and axonal terminals (Wong-Riley and Welt, 1980). Considerable evidence indicates that elevation of metabolic debt strongly aggravates ischemic insults. Indeed, various factors increasing the metabolism such as an increase in neuronal activity caused by adenosine A1 receptor antagonists, blockers of GABA(A) receptors and potassium channels (Dzhala et al., 2000), elevation of extracellular potassium as in the present study or elevated temperature (Joshi and Andrew, 2001) strongly accelerate the AD onset. Thus, due to elevated metabolic activity, L4 neurons are most likely to quickly lose ATP, depolarize and ignite AD in metabolically-compromised conditions. The question then arises: why the metabolic activity is highest in L4 barrels? Although the underlying mechanisms are unknown, it could be suggested that it involves a particular cytoarchitectonic and synaptic barrel organization. Indeed, densely packed excitatory and inhibitory neurons form a highly interconnected network in L4 barrels (Feldmeyer et al., 1999; Lefort et al., 2009; Valiullina et al., 2016) that may impose a higher metabolic charge to equilibrate the ionic disturbances caused by the activity in this layer.

Thus, in the present study we have shown that different cortical layers differ in their sensitivity to metabolic insult with L4 being the most prone to AD initiation and preferential propagation. Elevated ongoing metabolic demand of L4 could be a factor contributing to this enhanced sensitivity of L4 to OGD. Our findings also support rationale of the strategies aimed to reduce the metabolic demand as an approach to alleviate ischemic brain damage.

AUTHOR CONTRIBUTIONS

RK conceived the project. EJ and MM performed the experiments. AN, MM, EJ, AG, and MS analyzed the data. RK wrote the paper.

ACKNOWLEDGMENTS

This work was supported by RSF (17-15-01271) and performed in the framework of the Program of Competitive Growth of Kazan Federal University. We thank D. Suchkov for providing the code for the OIS acquisition.

SUPPLEMENTARY MATERIAL

The Supplementary Material for this article can be found online at: https://www.frontiersin.org/articles/10.3389/fncel.2017.00390/full#supplementary-material

Video 1 | Single-barrel AD initiation pattern (related to **Figure 3A**). Left, OIS and right, AD front. 5× playback speed.

Video 2 | Multiple-barrel AD initiation (related to **Figure 3B**). Left, OIS and right, AD front. 5× playback speed.

Video 3 | One side propagating AD (related to **Figure 3C**). Left, OIS and right, AD front. 5× playback speed.

Video 4 | Double-side propagating AD (related to **Figure 3D**). Left, OIS and right, AD front. 5× playback speed.

Video 5 | AD propagation in a slice with a cut above L4 (related to **Figure 4A**). Left, OIS and right, AD front. 5× playback speed.

Video 6 | AD propagation in a slice with a cut below L4 (related to **Figure 4B**). Left, OIS and right, AD front. 5× playback speed.

Video 7 | AD propagation in a slice with a cut through L4 (related to **Figure 4C**). Left, OIS and right, AD front. 5× playback speed.

REFERENCES

Aitken, P. G., Fayuk, D., Somjen, G. G., and Turner, D. A. (1999). Use of intrinsic optical signals to monitor physiological changes in brain tissue slices. *Methods* 18, 91–103. doi: 10.1006/meth.1999.0762

Aitken, P. G., Tombaugh, G. C., Turner, D. A., and Somjen, G. G. (1998). Similar propagation of SD and hypoxic SD-like depolarization in rat hippocampus recorded optically and electrically. *J. Neurophysiol.* 80, 1514–1521.

Basarsky, T. A., Duffy, S. N., Andrew, R. D., and MacVicar, B. A. (1998). Imaging spreading depression and associated intracellular calcium waves in brain slices. *J. Neurosci.* 18, 7189–7199.

Bogdanov, V. B., Middleton, N. A., Theriot, J. J., Parker, P. D., Abdullah, O. M., Ju, Y. S., et al. (2016). Susceptibility of primary sensory cortex to spreading depolarizations. *J. Neurosci.* 36, 4733–4743. doi: 10.1523/JNEUROSCI.3694-15.2016

Canals, S., Makarova, I., López-Aguado, L., Largo, C., Ibarz, J. M., and Herreras, O. (2005). Longitudinal depolarization gradients along the somatodendritic axis of CA1 pyramidal cells: a novel feature of spreading depression. *J. Neurophysiol.* 94, 943–951. doi: 10.1152/jn.01145.2004

Dreier, J. P. (2011). The role of spreading depression, spreading depolarization and spreading ischemia in neurological disease. *Nat. Med.* 17, 439–447. doi: 10.1038/nm.2333

Dreier, J. P., and Reiffurth, C. (2015). The stroke-migraine depolarization continuum. *Neuron* 86, 902–922. doi: 10.1016/j.neuron.2015.04.004

Dugué, G. P., Dumoulin, A., Triller, A., and Dieudonné, S. (2005). Target-dependent use of co-released inhibitory transmitters at central synapses. *J. Neurosci.* 25, 6490–6498. doi: 10.1523/JNEUROSCI.1500-05.2005

Dzhala, V., Ben-Ari, Y., and Khazipov, R. (2000). Seizures accelerate anoxia-induced neuronal death in the neonatal rat hippocampus. *Ann. Neurol.* 48, 632–640.

Feldmeyer, D., Egger, V., Lubke, J., and Sakmann, B. (1999). Reliable synaptic connections between pairs of excitatory layer 4 neurones within a single 'barrel' of developing rat somatosensory cortex. *J. Physiol.* 521(Pt 1), 169–190. doi: 10.1111/j.1469-7793.1999.00169.x

Goldlust, E. J., Paczynski, R. P., He, Y. Y., Hsu, C. Y., and Goldberg, M. P. (1996). Automated measurement of infarct size with scanned images of triphenyltetrazolium chloride-stained rat brains. *Stroke* 27, 1657–1662. doi: 10.1161/01.STR.27.9.1657

Hartings, J. A., Shuttleworth, C. W., Kirov, S. A., Ayata, C., Hinzman, J. M., Foreman, B., et al. (2017). The continuum of spreading depolarizations in acute cortical lesion development: examining Leao's legacy. *J. Cereb. Blood Flow Metab.* 37, 1571–1594. doi: 10.1177/0271678X16654495

Herreras, O., and Somjen, G. G. (1993). Propagation of spreading depression among dendrites and somata of the same cell population. *Brain Res.* 610, 276–282. doi: 10.1016/0006-8993(93)91411-K

Joshi, I., and Andrew, R. D. (2001). Imaging anoxic depolarization during ischemia-like conditions in the mouse hemi-brain slice. *J. Neurophysiol.* 85, 414–424. doi: 10.1152/jn.2001.85.1.414

Kaufmann, D., Theriot, J. J., Zyuzin, J., Service, C. A., Chang, J. C., Tang, Y. T., et al. (2017). Heterogeneous incidence and propagation of spreading depolarizations. *J. Cereb. Blood Flow Metab.* 37, 1748–1762. doi: 10.1177/0271678X16659496

Kawai, K., Nitecka, L., Ruetzler, C. A., Nagashima, G., Joó, F., Mies, G., et al. (1992). Global cerebral ischemia associated with cardiac arrest in the rat: I. Dynamics of early neuronal changes. *J. Cereb. Blood Flow Metab.* 12, 238–249. doi: 10.1038/jcbfm.1992.34

Khazipov, R., Zaynutdinova, D., Ogievetsky, E., Valeeva, G., Mitrukhina, O., Manent, J. B., et al. (2015). Atlas of the postnatal rat brain in stereotaxic coordinates. *Front. Neuroanat.* 9:161. doi: 10.3389/fnana.2015.00161

Leao, A. A. (1947). Further observations on the spreading depression of activity in the cerebral cortex. *J. Neurophysiol.* 10, 409–414.

Lefort, S., Tomm, C., Floyd Sarria, J. C., and Petersen, C. C. (2009). The excitatory neuronal network of the C2 barrel column in mouse primary somatosensory cortex. *Neuron* 61, 301–316. doi: 10.1016/j.neuron.2008.12.020

Lin, C. S., Polsky, K., Nadler, J. V., and Crain, B. J. (1990). Selective neocortical and thalamic cell death in the gerbil after transient ischemia. *Neuroscience* 35, 289–299. doi: 10.1016/0306-4522(90)90083-G

Lipton, P. (1999). Ischemic cell death in brain neurons. *Physiol. Rev.* 79, 1431–1568.

Martin, R. L., Lloyd, H. G., and Cowan, A. I. (1994). The early events of oxygen and glucose deprivation: setting the scene for neuronal death? *Trends Neurosci.* 17, 251–257. doi: 10.1016/0166-2236(94)90008-6

Meyer, H. S., Wimmer, V. C., Oberlaender, M., de Kock, C. P., Sakmann, B., and Helmstaedter, M. (2010). Number and laminar distribution of neurons in a thalamocortical projection column of rat vibrissal cortex. *Cereb Cortex.* 20, 2277–2286. doi: 10.1093/cercor/bhq067

Nedergaard, M. (1996). Spreading depression as a contributor to ischemic brain damage. *Cell. Mol. Mech. Ischem. Brain Damage* 71, 75–84.

Nedergaard, M., and Hansen, A. J. (1993). Characterization of cortical depolarizations evoked in focal cerebral ischemia. *J. Cereb. Blood Flow Metab.* 13, 568–574. doi: 10.1038/jcbfm.1993.74

Pietrobon, D., and Moskowitz, M. A. (2014). Chaos and commotion in the wake of cortical spreading depression and spreading depolarizations. *Nat. Rev. Neurosci.* 15, 379–393. doi: 10.1038/nrn3770

Rader, R. K., and Lanthorn, T. H. (1989). Experimental ischemia induces a persistent depolarization blocked by decreased calcium and NMDA antagonists. *Neurosci. Lett.* 99, 125–130. doi: 10.1016/0304-3940(89)90276-0

Somjen, G. G. (2001). Mechanisms of spreading depression and hypoxic spreading depression-like depolarization. *Physiol. Rev.* 81, 1065–1096. doi: 10.1152/physrev.2001.81.3.1065

Tanaka, E., Yamamoto, S., Kudo, Y., Mihara, S., and Higashi, H. (1997). Mechanisms underlying the rapid depolarization produced by deprivation of oxygen and glucose in rat hippocampal CA1 neurons *in vitro*. *J. Neurophysiol.* 78, 891–902.

Tyzio, R., Cossart, R., Khalilov, I., Minlebaev, M., Hübner, C. A., Represa, A., et al. (2006). Maternal oxytocin triggers a transient inhibitory switch in GABA signaling in the fetal brain during delivery. *Science* 314, 1788–1792. doi: 10.1126/science.1133212

Valiullina, F., Akhmetshina, D., Nasretdinov, A., Mukhtarov, M., Valeeva, G., Khazipov, R., et al. (2016). Developmental changes in electrophysiological properties and a transition from electrical to chemical coupling between excitatory layer 4 neurons in the rat barrel cortex. *Front. Neural Circuits* 10:1. doi: 10.3389/fncir.2016.00001

Wong-Riley, M. T., and Welt, C. (1980). Histochemical changes in cytochrome oxidase of cortical barrels after vibrissal removal in neonatal and adult mice. *Proc. Natl. Acad. Sci. U.S.A.* 77, 2333–2337. doi: 10.1073/pnas.77.4.2333

Conflict of Interest Statement: The authors declare that the research was conducted in the absence of any commercial or financial relationships that could be construed as a potential conflict of interest.

Copyright © 2017 Juzekaeva, Nasretdinov, Gainutdinov, Sintsov, Mukhtarov and Khazipov. This is an open-access article distributed under the terms of the Creative Commons Attribution License (CC BY). The use, distribution or reproduction in other forums is permitted, provided the original author(s) or licensor are credited and that the original publication in this journal is cited, in accordance with accepted academic practice. No use, distribution or reproduction is permitted which does not comply with these terms.

frontiers in Cellular Neuroscience

ORIGINAL RESEARCH
published: 18 December 2018
doi: 10.3389/fncel.2018.00502

Dynamics of the Hypoxia—Induced Tissue Edema in the Rat Barrel Cortex *in vitro*

Elvira Juzekaeva[1†], *Azat Gainutdinov*[1†], *Marat Mukhtarov*[1] *and Roustem Khazipov*[1,2*]

[1] *Laboratory of Neurobiology, Institute of Fundamental Medicine and Biology, Kazan Federal University, Kazan, Russia,* [2] *Aix Marseille Univ, INSERM, INMED, Marseille, France*

Cerebral edema is a major, life threatening complication of ischemic brain damage. Previous studies using brain slices have revealed that cellular swelling and a concomitant increase in tissue transparency starts within minutes of the onset of metabolic insult in association with collective anoxic spreading depolarization (aSD). However, the dynamics of tissue swelling in brain slices under ischemia-like conditions remain elusive. Here, we explored the dynamics of brain tissue swelling induced by oxygen-glucose deprivation (OGD) in submerged rat barrel cortex slices. Video monitoring of the vertical and horizontal position of fluorescent dye-filled neurons and contrast slice surface imaging revealed elevation of the slice surface and a horizontal displacement of the cortical tissue during OGD. The OGD-induced tissue movement was also associated with an expansion of the slice borders. Tissue swelling started several minutes after aSD and continued during reperfusion with normal solution. Thirty minutes after aSD, slice borders had expanded by ∼130 μm and the slice surface had moved up to attain a height of ∼70 μm above control levels, which corresponded to a volume increase of ∼30%. Hyperosmotic sucrose solution partially reduced the OGD-induced slice swelling. Thus, OGD-induced cortical slice tissue swelling in brain slices *in vitro* recapitulates many features of ischemic cerebral edema *in vivo*, its onset is tightly linked to aSD and it develops at a relatively slow pace after aSD. We propose that this model of cerebral edema *in vitro* could be useful for the exploration of the pathophysiological mechanisms underlying ischemic cerebral edema and in the search for an efficient treatment to this devastating condition.

Keywords: brain ischemia, hypoxia, edema, swelling, cortex

OPEN ACCESS

Edited by:
Andrea Nistri,
Scuola Internazionale Superiore di Studi Avanzati (SISSA), Italy

Reviewed by:
John Gordon Ralph Jefferys,
University of Oxford, United Kingdom
Renato Corradetti,
Università degli Studi di Firenze, Italy

***Correspondence:**
Roustem Khazipov
roustem.khazipov@inserm.fr

[†] *These authors have contributed equally to this work*

Received: *08 October 2018*
Accepted: *04 December 2018*
Published: *18 December 2018*

Citation:
Juzekaeva E, Gainutdinov A, Mukhtarov M and Khazipov R (2018) Dynamics of the Hypoxia—Induced Tissue Edema in the Rat Barrel Cortex in vitro. Front. Cell. Neurosci. 12:502. doi: 10.3389/fncel.2018.00502

INTRODUCTION

Cerebral edema is a major life threatening complication of ischemic brain damage (Stokum et al., 2016; Zheng et al., 2016). Cerebral edema causes a mass-effect with distortion, tissue shift and increased intracranial pressure leading to cerebral herniation, further brain damage, and death (Frank, 1995; Schwab et al., 1996; Dostovic et al., 2016). However, efficient medical treatment of edema in stroke patients including hyperventilation, hyperosmotic therapy, diuretics, corticosteroids, or barbiturates is limited. Severe cases of edema require surgical decompression to create space to accommodate the increased volume created by the swollen brain by opening

the cranial vault and dura, or even by removing non-viable or non-essential brain tissue (Dostovic et al., 2016; Zheng et al., 2016).

Cerebral edema is caused by an increase in the brain tissue water content as a result of osmotic changes caused by ionic gradient disturbances and an accumulation of osmotically active metabolites, such as lactate, in the ischemic region (Stokum et al., 2016). Edema develops through several stages starting with cytotoxic edema, or cellular swelling, manifesting minutes after metabolic insult as a result of water translocation from the extracellular to intracellular compartment, generated by the disturbance in the transmembrane ionic gradients during anoxic spreading depolarization (aSD) (Dreier et al., 2018). Cytotoxic edema starts to develop during aSD and it is characterized by swelling of neurons and glial cells, beading of dendrites, shrinkage of the extracellular space, and changes in optical tissue transparency (Vanharreveld, 1957; Murphy et al., 2008; Risher et al., 2009, 2010, 2012). Similar phenomena are also observed in submerged cortical slices exposed to oxygen-glucose deprivation (OGD) (Obeidat et al., 2000; Andrew et al., 2007; Risher et al., 2009; Brisson and Andrew, 2012).

Despite a wealth of knowledge on the dynamics of cellular swelling, whose onset is tightly linked to aSD, the dynamics of tissue swelling are less well-understood. Importantly, cellular swelling may occur without tissue swelling. If water access to the ischemic tissue is limited, cellular swelling occurs through a translocation of water from the extracellular to intracellular space without any change in the total brain tissue volume. For example, during brain ischemia evoked by cardiac arrest, the total volume of brain tissue, and its water content do not change. Similarly, the ischemic core does not increase in size despite cytotoxic swelling reviewed in Klatzo (1987) and Stokum et al. (2016). However, significant tissue edema may occur if external water access to the ischemic tissue is available, for example, in submerged slice preparations, where the slice is exposed to electrolytes and water in the superfusion medium *ad libitum*. Indeed, water content increases in brain slices exposed to the ischemia-like conditions including OGD and other metabolic insults (Kumar et al., 2006; Elkin et al., 2010). Accordingly, an increase in the slice volume after a combination of cyanide poisoning with aglycaemia could already be detected 30 min after metabolic insult (Elkin et al., 2010). Also, previous studies have shown technical challenges in time-lapse imaging from brain slices caused by shifts of the focal plane during OGD which required sampling of the optical section on the fly, and re-centering and adjusting the field of focus prior to acquiring image stacks (Andrew et al., 2007; Risher et al., 2009). A similar technical challenge was indicated in patch-clamp recordings from the intact hippocampus *in vitro*, where electrical access to the neurons being recorded was often lost after OGD-induced aSD likely because of tissue movement (Dzhala et al., 2001). However, the dynamics of ischemic brain mass tissue movement and edema in brain slices have not been previously addressed.

In the present study, we explored the dynamics of the tissue movement and volumetric changes occurring in slices of the rat barrel cortex during ischemia-like OGD conditions. We found that OGD efficiently induces mass tissue movement and swelling that are characteristic of ischemic cerebral edema, that the onset of tissue swelling is tightly linked to aSD and that it develops on a relatively slow time scale after aSD.

MATERIALS AND METHODS

Ethical Approval

All animal-use protocols followed the guidelines of the French National Institute of Health and Medical Research (INSERM, protocol N007.08.01) and the Kazan Federal University on the use of laboratory animals (ethical approval by the Institutional Animal Care and Use Committee of Kazan State Medical University N9-2013).

Brain Slices Preparation

Wistar rats (16–23 days old) of either sex were used. Animals were decapitated under isoflurane anesthesia (5%) and the brain was rapidly removed and placed in ice-cold (2–5°C) slicing solution [modified from, (Dugue et al., 2005)] of the following composition (in mM): K-Gluconate 140, Na-Gluconate 15, NaCl 4, EGTA 0.2, D-AP5 50 μM, and HEPES 10 (pH 7.4). Four hundred μm thick thalamocortical slices were cut using a PELCO easiSlicer™ vibratome (Ted Pella, Inc., Redding, CA, USA). Slices containing the barrel cortex were selected by anatomical coordinates (Khazipov et al., 2015) and the presence of barrel structures in L4. Slices were first kept in oxygenated (95% O_2-5% CO_2) artificial cerebrospinal fluid (ACSF) of the following composition (in mM): NaCl 126, KCl 3.5, $CaCl_2$ 2, $MgCl_2$ 1.3, $NaHCO_3$ 25, NaH_2PO_4 1.2, and glucose 11 (pH 7.4) for 30 min at 32°C and then at room temperature (20–22°C) for at least 1 h before use. For recordings, slices were placed into a submerged chamber and superfused with oxygenated ACSF at 30–32°C at a flow rate of 10 ml/min. Slices were held in place in the recording chamber using a handmade U-shape frame from silver wire (0.025″, A-M Systems, USA). To allow displacement of the tissue during edema, only the two more distant borders of the slice were held by the frame. Oxygen/glucose deprivation (OGD) was induced by superfusion with ACSF in which N_2 replaced O_2 and sucrose replaced glucose at equimolar concentration.

Electrophysiological Recordings

Extracellular recordings of the local field potentials (LFP) were performed in the barrel cortex using single site glass pipette electrodes. Electrodes were pulled from borosilicate glass capillaries (BF150-86-10, Sutter Instrument, Novato, CA, USA) and had resistances of 2–3 MΩ when filled with ACSF. Electrodes were connected via chlorided silver wire to the headstage of a MultiClamp700B patch-clamp amplifier (Axon Instruments, Union City, CA, USA). Recordings were performed in voltage-clamp DC mode, then currents were inverted and voltage calibrated using 5 mV steps.

Time-Lapse Imaging

Time-lapse microscopy recordings were performed using a BX51WI upright microscope equipped with a dry 4x/0.10 Plan N objective and a water immersed 40x/0.80 LUMPlanFL N objective (Olympus, Tokyo, Japan). The slice was illuminated

by a halogen lamp with a 775 nm bandpass filter. Images were acquired using a QIClick-R-F-M-12 CCD camera (QImaging, Surrey, BC, Canada) at 696 × 520 or 1392 × 1040 pixel resolution and 5–10 frames/s acquisition rate.

Time-lapse imaging of the cortical surface with a correction for a change in the surface height was performed either by focusing on the fluorescent dye-filled cells manually or by autofocusing on the highest contrast slice surface images using a home-made Z-correction system. Individual layer 4 neurons located close to the slice surface were labeled with CF™488A fluorescent dye (100 μM) through the patch-pipette in whole-cell mode. The pipette was then removed to enable free cell displacement. The autofocusing system consisted of the step motor, which was attached to the Z-drive of the microscope, and controlled by an Arduino Uno control board, and LabVIEW (National Instruments) software with the Vision Development Module to determine the focal plane of the highest contrast image through online analysis of multiple images taken at different focus distances (range: from +50 to −100 μm, with a 4 μm step). The image was resized to a resolution of 696 × 520 pixels. Then the Sobel operator was used to determine the luminance gradient. The statistical distribution of pixels with different brightness was calculated after the Sobel operator. The average brightness in a given distribution was the criterion for the sharpness of the image. One cycle of autofocusing lasted on average 6.6 ± 0.9 s. Further offline analysis of the position of objects at the cortical surface was used for the detection of tissue drift in the horizontal plane.

LFP and OIS Analysis

Data were analyzed using custom-written procedures in Matlab (MathWorks, Inc., Natick, MA, USA). OIS was calculated using the first-frame subtraction approach: OIS (t) = (I (t) – I_0)/I_0, where I (t)–pixel intensity at the moment t, I_0-time-averaged pixel intensity in the preconditioned baseline period (100 s). The resulting frames were filtered with a 10 × 10 median filter. Regions of interest (ROIs) were selected as square areas near the recording site. OIS traces were calculated as the average OIS signal within selected ROIs.

LFP signals were downsampled to 1 kHz. The continuous running line fit was removed using local linear regression in 300 s windows with a 10 s overlap [*locdetrend* function from the Chronux toolbox (http://chronux.org/)]. Data were smoothed by the 1,000-point moving average filter and the local negative aSD peak was detected. The baseline level was calculated as the mean value of the LFP in the −20 to −10 s time window preceding aSD. aSD amplitude was calculated as the maximal negative LFP peak from the baseline.

Statistical Analysis

Statistical analysis was based on the non-parametric Wilcoxon (paired samples) signed rank sum test with the significance level set at $p < 0.05$. Results are given as medians ± interquartile range, where interquartile range is the difference between 75th and 25th percentiles.

RESULTS

We studied the dynamics of the tissue shifts and volumetric changes in slices of the rat barrel cortex during ischemia-like conditions induced by OGD. To this aim, we used time-lapse imaging of the slice surface and borders with concomitant local field potential and OIS recordings. In keeping with the results of a previous study using this preparation (Juzekaeva et al., 2017), OGD induced aSD at a delay of 9.7 ± 3.2 min ($n = 54$ slices) after the onset of perfusion with OGD solution. aSD attained a peak negative value of 5.8 ± 3.9 mV in L4 ($n = 54$) and it was also associated with a sharp transient increase in slice transparency of 25.7 ± 23.2 % dI/I ($n = 49$) (**Figures 1B,C**; see also summary **Figure 6**).

Mass Tissue Movement: General Observation

In the initial time-lapse imaging of the cortical surface with a constant focal plane (**Figure 1A** and **Video 1**) we observed that during perfusion of slice with OGD solution, the entire cortical tissue started drifting in the horizontal plane as evidenced by the displacement of various objects such as cells and vessels, and vertically as evidenced by the shifting of the objects from the focal plane and the appearance of new moving objects (see also **Video 2** at low magnification for a disappearance of vessels). The images also became blurry, losing contrast objects. Particularly impressive was the tissue movement relative to immobile objects such the pipette for extracellular field potential recordings (**Video 1**). These tissue drifts started in association with aSD, and they continued after aSD (**Figures 1B,C**). We further attempted to quantify the OGD-induced tissue drifts in several imaging settings.

Expansion of the Slice Borders

We first characterized the shifts of the slice borders. To this aim, we analyzed the position of the top (meningeal) and bottom (ventricular) borders of the cortical slice in the region of somatosensory barrel cortex. As shown on **Figures 2A–C** and **Video 2**, slice borders stayed immobile during control conditions, the early phase of OGD, and the OGD-induced aSD. However, immediately after aSD, slice borders started to expand and this process continued after reperfusion of slices with oxygenated, glucose- containing ACSF. Because the onset of the border expansion as well as other volumetric OGD-induced changes (see below) were tightly linked to aSD rather than to the OGD duration, group data analysis was performed in relation to aSD with the aSDs' peak negativity taken as a reference time point T = 0. Borders started to shift from their control position on average 3.5 ± 1.8 min ($n = 21$) after aSD (**Figure 2E**). Following 29 ± 23 min after aSD (a period that included 15.1 ± 4.5 min in OGD and 8.6 ± 4.1 min of reperfusion), the top (meningeal), and bottom (ventricular) borders expanded by 87 ± 44 and 44 ± 68 μm from their initial pre-OGD positions, respectively ($n = 21$). Corresponding slice width (the distance between the top and bottom borders) increased by 132 ± 76 μm, that is to 107 ± 3 % of the control values ($n = 21$; **Figures 2D,F**).

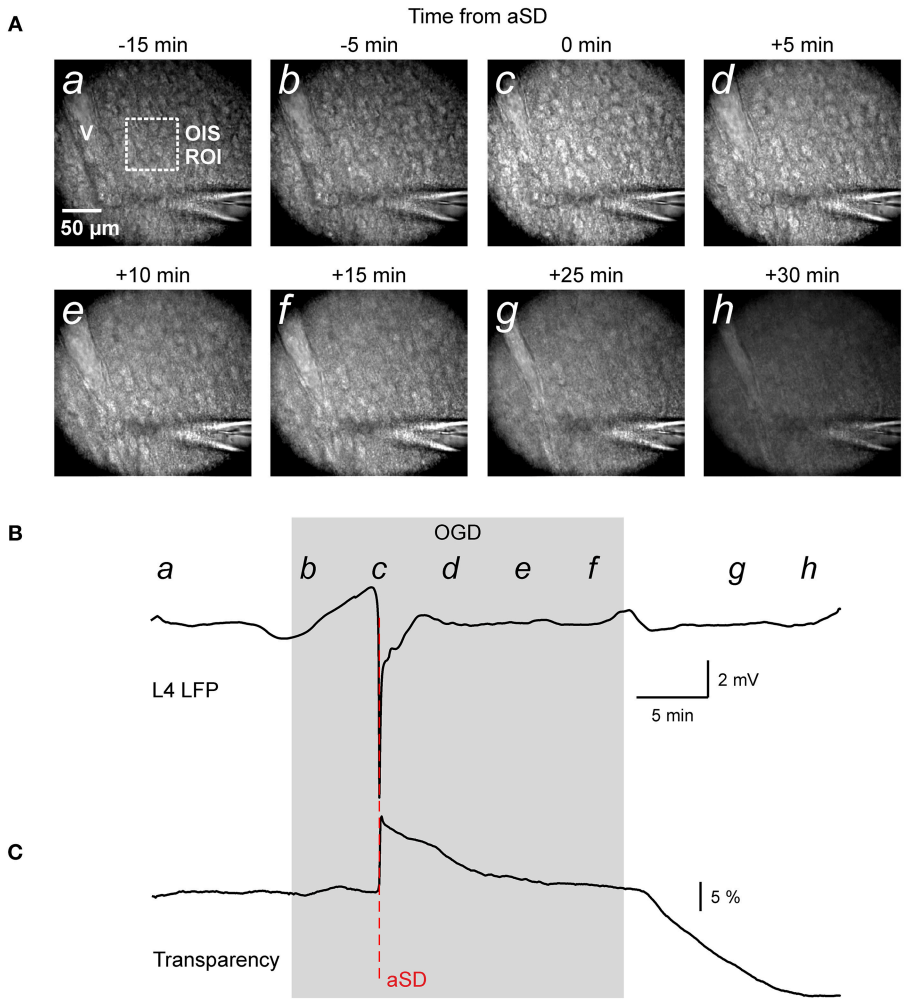

FIGURE 1 | Oxygen-glucose deprivation (OGD) induced mass tissue movement: general observation. **(A)** Snapshots of the cortical slice surface at different time points from the OGD-induced anoxic spreading depolarization (aSD) obtained at constant focal plane set at the slice surface prior to OGD. Note that the tissue starts drifting after aSD and shifts from the focal plane; (a–h) at the top left corner indicate the time points on plot B when the snapshots were taken. Note changes in the vessel (v) appearance due to the vertical tissue displacement. **(B,C)** Corresponding traces of LFP **(B)** and OIS **(C)** recordings from a cortical barrel. Region of interest (ROI) of OIS recording is indicated by dashed box on the snapshot (a). See also corresponding Online **Video 1**.

Elevation of the Slice Surface

We next quantified the OGD-induced tissue mass drifts in the middle of the slice at the level of cortical barrels (layer 4). To this aim, we used two approaches. In the first approach, manual focusing on the fluorescent dye-filled cell was used for the tissue displacement estimation. As shown on **Figure 3A**, the labeled neuron started to drift in the horizontal (x-y) plane shortly after aSD and then disappeared from the focal plane indicating a vertical (z) displacement. Manual correction of the focal plane revealed a displacement of the cell up from the initial position (**Figure 3C**). The first vertical displacement by 14 ± 3 µm was detected 7.0 ± 1.8 min after aSD (n = 7 cells). Continuous manual monitoring of the height of the focal plane of the cell revealed further progressive drift of the cell up and horizontally. In most of the recordings, cells were displaced from the optical field which also required correction of the x-y coordinates of the optical field. Reconstructed cell trajectory in 3D coordinates is shown on **Figure 3B** (see also **Video 3**). On average, cells drifted after aSD to attain their final displacement of 42 ± 7 and 36 ± 5 µm (n = 7 cells) from the pre-OGD position 30 min after aSD in vertical and horizontal planes, respectively (**Figure 3D**).

Because the estimates of tissue drifts using manual correction of the focal plane are of limited spatial and temporal resolution, we further optimized the detection of the height of the cortical surface using a home-made autofocusing system, which enabled adjustment of the focal plane to the highest contrast image coinciding with the slice surface through online analysis of multiple images taken at different focus distances and feedback to an electric z-drive. Further offline analysis of the position of objects at the cortical surface was used for the detection of tissue drifts in the horizontal plane. Time-lapse imaging with this autofocus system provided results that were similar to

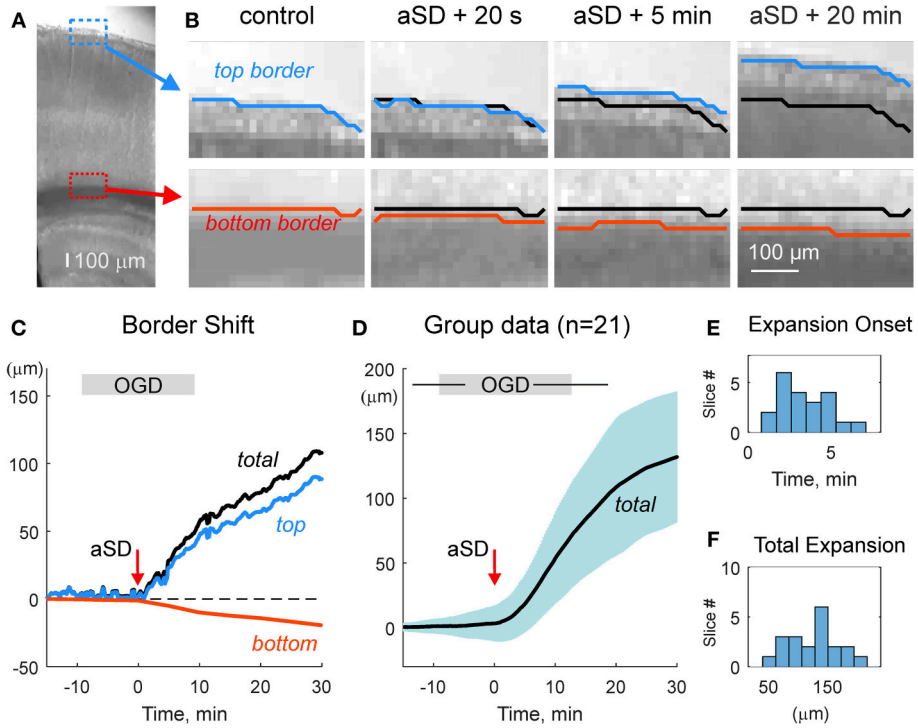

FIGURE 2 | OGD-induced expansion of the cortical slice borders. **(A)** Microphotograph of the cortical slice. ROIs with the meningeal (blue box) and ventricular (red box) borders of the cortical barrel column. **(B)** Snapshots of a position of the top meningeal (blue line) and bottom ventricular (red line) borders of the cortical slice within the ROIs on panel A in control and at different time points from the OGD-induced aSD. Black lines show the pre-OGD borders positions. Note that slice borders start expanding immediately after aSD and continue to expand after reperfusion of the slice with oxygenated glucose-containing ACSF. **(C)** Time course of the OGD-induced top (blue) and bottom (red) borders shift from the control position referenced to aSD as a zero time point in the experiment shown on panels **(A,B)**. Total (black) border shift is a sum of the top and bottom border shifts. Note that shift of the top border is more important than that of the bottom border. **(D)** Average change in the total distance between the top and bottom borders from $n = 21$ slices (shaded area shows SD). Data are referenced to the time aSD = 0. Vertical borders on the gray OGD-box above the plot indicate an average onset and offset of OGD from aSD and horizontal lines indicate SD. **(E,F)** Histograms of the borders expansion onsets **(E)** and total slice border expansion **(F)** 30 min after aSD from $n = 21$ slices. Border movements during the experiment shown on **(A–C)** are also presented in Online **Video 2**.

those obtained using manual focal plane correction using labeled cell monitoring but at higher spatial and temporal resolution (**Figures 4A–C**). We found that the tissue starts to drift 1.8 ± 0.8 min ($n = 4$) after aSD to attain a displacement of 71 ± 3 and 26 ± 10 µm ($n = 4$) 30 min after aSD in vertical and horizontal directions, respectively. An elevation of the slice surface corresponded to an increase in the slice thickness to 115 ± 4 % ($n = 11$) of the control value of 400 µm.

Hyperosmotic Treatment

Osmotic therapy is one of the most frequently used clinical treatments for ischemic brain edema. Therefore, we further explored whether osmotic therapy is also efficient in the case of the OGD-induced edema in cortical slices. To this aim, slices which had been previously exposed to OGD and experienced aSD and swelling, were superfused with hyperosmotic ACSF containing 150 mM sucrose and had osmolarity of 472 mOsm compared to 321 mOsm of control ACSF. As shown on **Figure 5**, hyperosmotic solution evoked a biphasic response with a transient increase in the height of the slice surface attaining a peak of 21 ± 8 µm ($n = 11$) from the pre-sucrose level 2.2 ± 1.0 min after sucrose application, followed by a decrease in the height of the cortical surface to −35 ± 9 µm from the pre-sucrose level 15 min after treatment with hyperosmotic solution. This still remained above the control pre-OGD levels by 35 ± 10 µm ($n = 11$; $p < 0.05$).

Volumetric Changes

From the data on the morphometric changes in the slice thickness and border expansion we further attempted to estimate the OGD-induced volumetric changes. We made several assumptions: (i) horizontal expansion is isotropic and therefore a change in the slice surface is proportional to the square of the change in the distance between the slice borders; (ii) vertical shifts of the cortical surface are also isotropic through the entire slice and therefore vertical swelling through the whole slice equals the change at the level of L4. Slice volume changes were calculated according to this formula:

$$\triangle V = \frac{\triangle Z + Z_0}{Z_0}\left(\frac{\triangle X + X_0}{X_0}\right)^2 \quad (1)$$

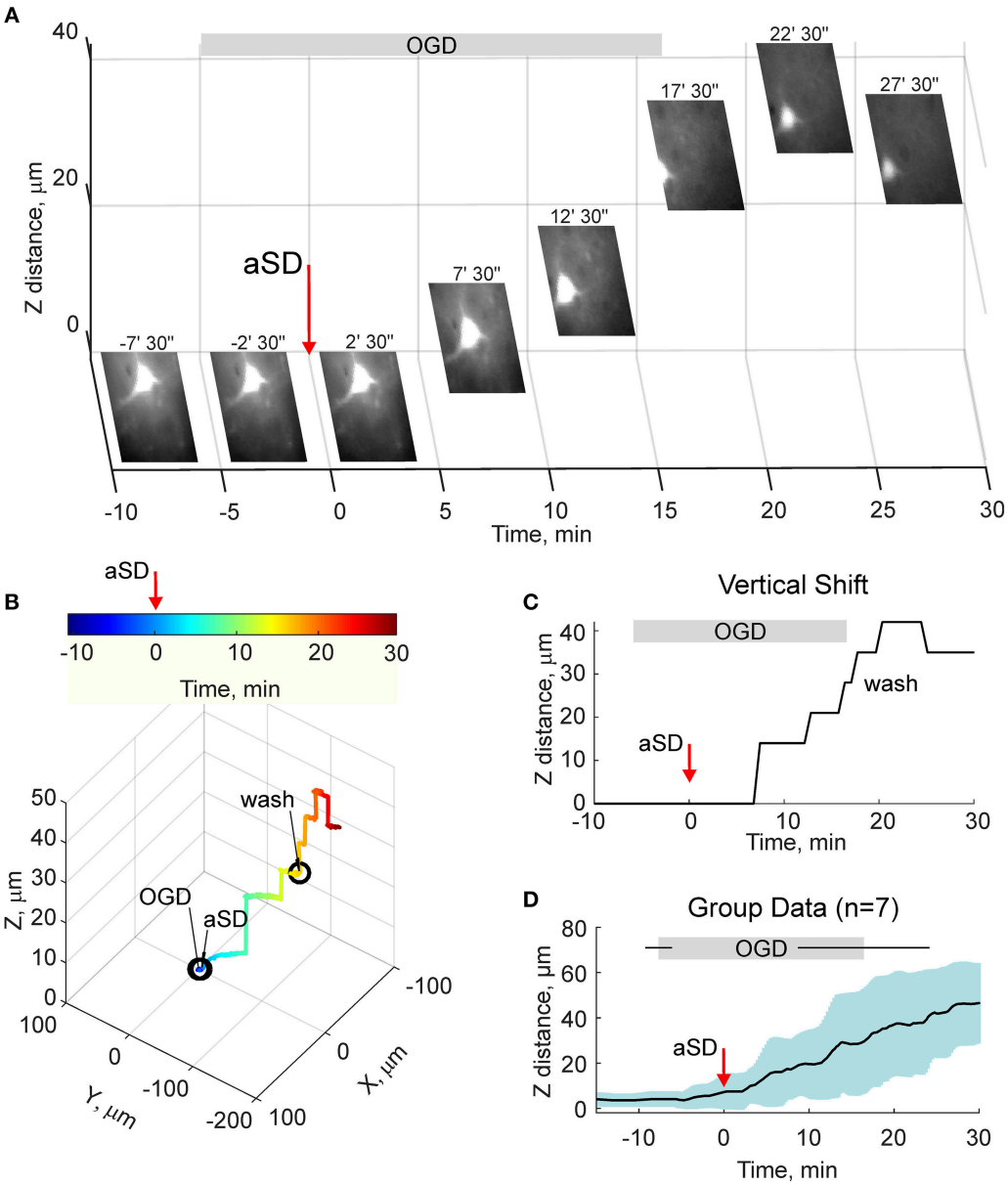

FIGURE 3 | OGD-induced elevation of the cortical slice surface: manual focusing at single cells. **(A)** Snapshots of a CF^{TM}488A-labeled L4 neuron located close to the cortical slice surface at different time points from the OGD-induced aSD (exact time points from aSD are indicated above the snapshots). aSD at time = 0 is indicated by vertical arrow. The focal plane was adjusted manually through the time course of the experiment and the corresponding vertical objective displacement is indicated on Z-scale. Note that the cell moves up and horizontally after aSD. **(B)** Corresponding 3D-trajectory of the OGD-induced cell displacement. Time is color-coded. **(C)** Time course of the vertical displacement of a cell is shown on **(A,B)**. **(D)** Group data on the vertical cell displacement in relation to the OGD-induced aSD. Pooled data from $n = 7$ slices.

where ΔV is slice volume change normalized to the control volume, ΔZ is a change in the slice height, Z_0 is the initial height, ΔX is a change in the slice width, X_0 is initial slice width. The results of these calculations are presented on summary **Figures 6C,D**, were group data on the OGD-induced changes in LFP, slice transparency, slice width (as calculated the from the borders' shifts), and height (from the manual single cell and automatic slice surface shifts pooled together), and slice volume are assembled together, with aSD taken as a reference time point. This plot shows that the slice volume starts increasing almost immediately and linearly after aSD at rate of ∼1% per min to attain 30 min after aSD, 130 ± 10 % (estimated from $n = 21$ slices for the border shifts and $n = 4$ slices for the slice surface shifts) of the pre-OGD volume.

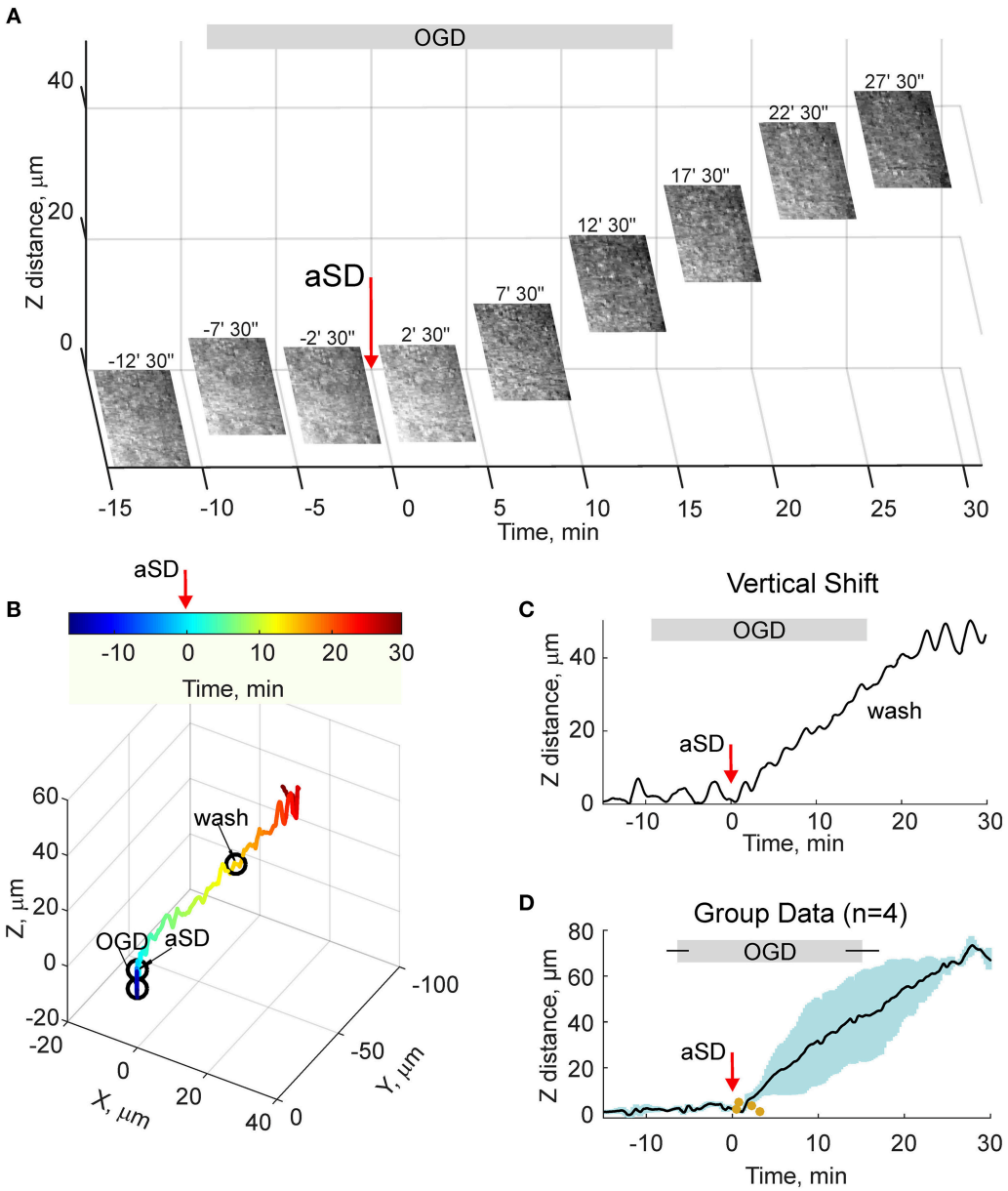

FIGURE 4 | OGD-induced elevation of the cortical slice surface: autofocusing on the slice surface. **(A)** Snapshots of the slice surface at different time points from the OGD-induced aSD (exact time points from aSD are indicated above the snapshots). aSD at time = 0 is indicated by vertical arrow. The focal plane was adjusting automatically during the experiment to the height of the maximal contrast image. Corresponding vertical objective displacement values are indicated on the Z-scale. **(B)** Corresponding 3D-trajectory of the OGD-induced slice surface displacement. Time is color-coded. **(C)** Time course of the vertical displacement of the slice surface. See related Online **Video 3**. **(D)** Group data on the vertical slice surface displacement in relation to the OGD-induced aSD. Pooled data from $n = 4$ slices. Yellow dots indicate the onsets of the vertical displacement from individual experiments. Layout as on **Figure 2D**. See also Online **Video 3**.

DISCUSSION

In the present study, we characterized the dynamics of the mass tissue movement and volumetric changes occurring in slices of the rat barrel cortex under OGD conditions. Our main findings are that OGD efficiently induces the mass tissue movement and swelling that are characteristic of ischemic cerebral edema, that the onset of tissue swelling is tightly linked to aSD and that the cortical slice edema develops on a relatively slow time scale after aSD.

Our findings on the development of the OGD-induced tissue edema in cortical slices are consistent with the results of previous studies, where an increase in a slice volume by ∼20% was observed 30 min after a combination of cyanide poisoning with aglycaemia (Elkin et al., 2010) (present OGD-study: by 30%). This is also in keeping with an increase in the slice water

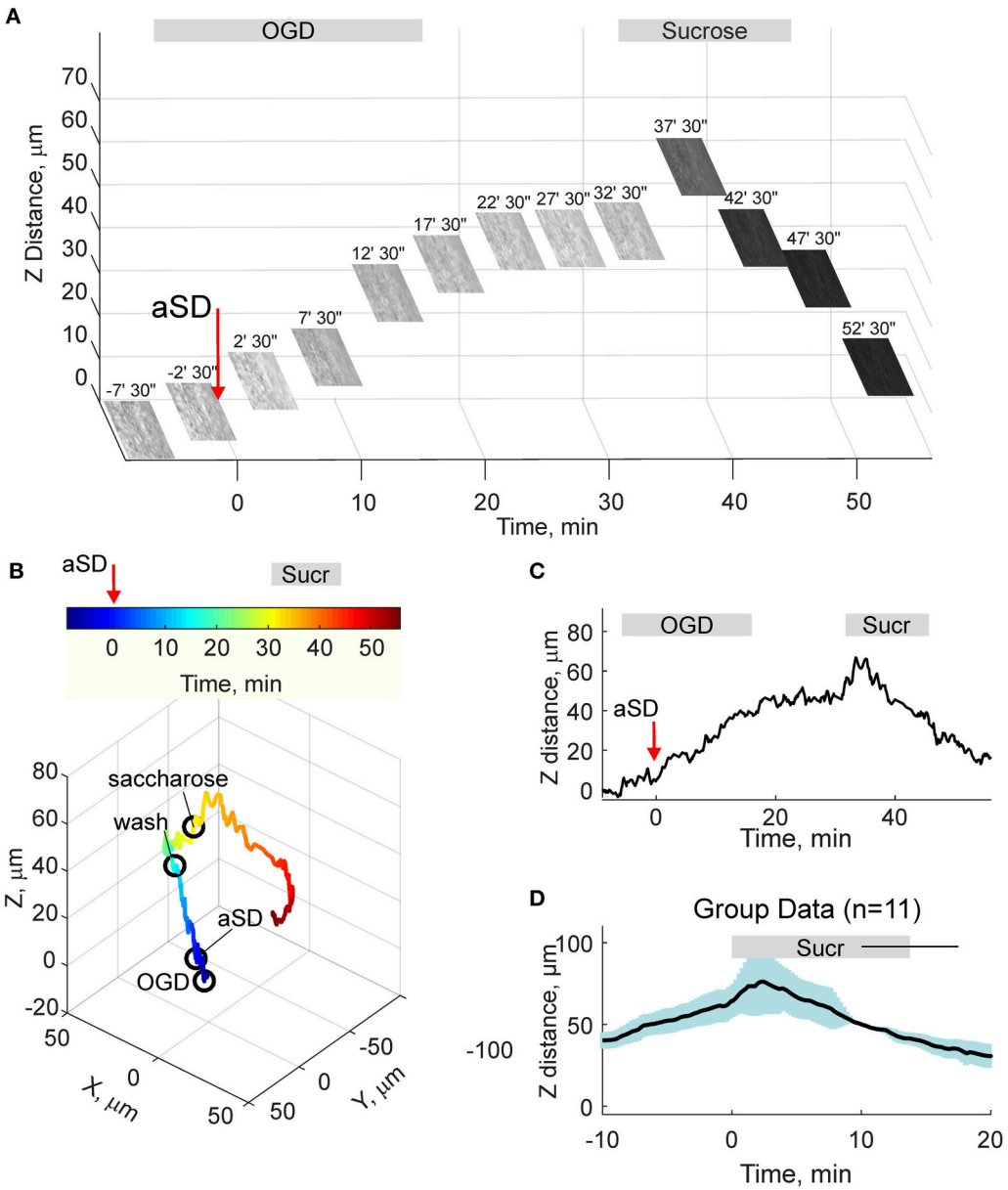

FIGURE 5 | Hyperosmotic treatment reduces OGD-induced slice swelling. **(A)** Snapshots of the slice surface at different time points during experimental osmotic therapy performed after development of the OGD-induced edema. The focal plane was adjusted automatically as on **Figure 4**. Note that superfusion with hyperosmotic sucrose solution reduces the height of the slice surface. **(B)** Corresponding 3D-trajectory of the slice surface displacement. Time is color-coded. **(C)** Time course of the vertical displacement of the slice surface during OGD and following hyperosmotic treatment. **(D)** Group data on the vertical slice surface displacement in relation to the onset of the hyperosmotic treatment. Pooled data from $n = 11$ slices.

content, which was observed 30 min after the metabolic insult (MacGregor et al., 2003; Kumar et al., 2006; Elkin et al., 2010). It is noteworthy that the final increase in slice volume attained ∼75% by 24 h after the onset of metabolic insult (Elkin et al., 2010). Therefore, it is likely that the OGD-induced slice swelling, which was monitored here during the initial stages of the edema formation, also continues after the 30 min interval. The main novelty of the present study consists in showing that the onset of the OGD-induced edema is tightly associated with aSD. Previously, development of cytotoxic edema manifested by swelling of neuronal and glial cell soma, dendritic beading, and shrinkage of the extracellular space was also shown starting minutes after aSD (Vanharreveld, 1957; Murphy et al., 2008; Risher et al., 2009, 2010, 2012). Taking into account these previous findings, our results indicate that the cytotoxic edema and tissue edema in cortical slices develop in parallel, with aSD being their main trigger. We hypothesize that cytotoxic edema is the main driver of the tissue edema in the experimental

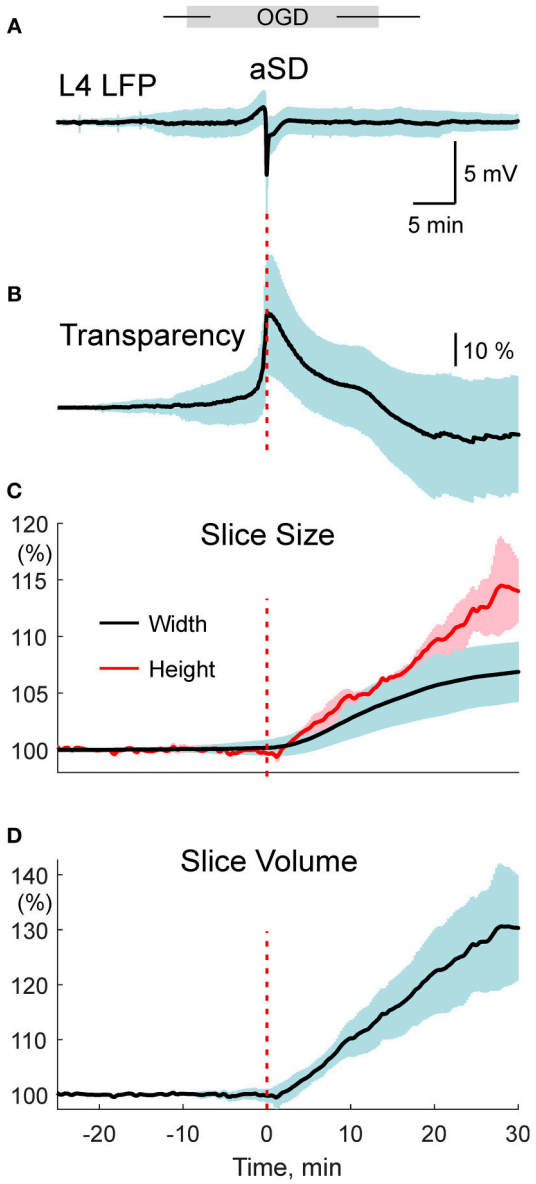

FIGURE 6 | Development of the OGD-induced slice tissue edema in relation to aSD. **(A–D)** Summary plot assembles the time course of the: **(A)** OGD-induced changes in LFP (average of $n = 54$ slices)**, (B)** slice transparency (average of $n = 49$ slices), **(C)** slice size ($n = 21$ slices for the border shifts and $n = 4$ slices for the slice surface shifts with autofocusing method) and **(D)** slice volume estimated from the expansion of the slice borders and elevation of the slice surface. All traces are referenced to electrical aSD.

conditions of submerged brain slice, and that development of cytotoxic edema is supported by continuous and unlimited buffering of the extracellular space by the electrolytes and water contained in the bath medium. This might differ from the *in vivo* settings, where the availability of electrolytes and water in the extracellular space is limited by the lack of blood supply in the ischemic core in the case of focal ischemia or during global brain ischemia caused by cardiac arrest. In the latter cases, cytotoxic edema may develop without prominent tissue edema. However, ionic and water availability through the residual/collateral blood supply, as well as by passive horizontal diffusion may provide substrate for the excessive cytotoxic and tissue swelling that could lead to stronger cellular damage and further aggravate the ischemic state.

Early onset of the tissue swelling after OGD-induced aSD may indicate the particular gravity of this type of metabolic insult in submerged conditions compared to the interface conditions or to the situation *in vivo*. In the submerged slice preparation as used in the present study, the "commitment point" of irreversible damage is achieved during aSD as evidenced by complete and irreversible abolition of synaptic response and membrane potential during OGD episodes with aSD, while shorter OGD episodes without aSD show functional recovery (Rader and Lanthorn, 1989; Tanaka et al., 1997; Joshi and Andrew, 2001; Juzekaeva et al., 2017). Hence, aSD in submerged slices is a terminal event marking neuronal death. In contrast, in brain slices with a gas-fluid interface, where the buffering of the extracellular space is limited (Croning and Haddad, 1998) aSD is not a terminal event and slices can be rescued by reperfusion with oxygen/glucose-containing ACSF several minutes after hypoxia-induced aSD (yet in normal glycemic conditions) (Balestrino and Somjen, 1986; Young et al., 1991; Somjen, 2001). During global ischemia *in vivo*, aSD is also not a terminal event as both morphological and functional impairments to cortical neurons are reversible upon reperfusion started within ∼5 min of aSD (Murphy et al., 2008). Moreover, cortical slices prepared up to 5–6 h after cardiac arrest display quite normal physiological and morphological properties (Charpak and Audinat, 1998). Thus, the OGD-induced aSD in submerged slices appears particularly damaging that may be reflected by the early onset of the tissue swelling in association with aSD.

In conclusion, we have shown that cerebral tissue mass movement, distortion, and swelling also occurs under ischemia-like conditions in a cortical slice *in vitro*, that its onset is tightly linked to aSD and that it develops on a relatively slow time after aSD. Evidently, several important elements of ischemic edema are not present in the reduced system of a brain slice *in vitro*, notably vasogenic mechanisms, mechanical constraints that cause an increase in the intracranial pressure, and the swelling component secondary to glymphatic system dysfunction. Therefore, this model is far from fully able to recapitulate ischemic edema *in vivo*. However, this model reproduces cerebral tissue mass movement and the increase in cerebral tissue volume that occur during ischemic brain edema *in vivo* fairly well. Moreover, we found that the OGD-induced slice swelling could be reduced using hyperosmotic treatment, which is one of the most frequently used medical treatments for ischemic brain edema. Therefore, we propose that this model could be useful for the investigation of cellular and molecular mechanisms including specific ionic channels, transporters, and other proteins involved in maladaptive ion and water transport across neuronal and astrocytic membranes during ischemic edema, as well as in the search for more efficient treatment of this devastating condition.

DATA AVAILABILITY STATEMENT

Original and processed data, and signal processing and analysis routines are available on request from the authors.

AUTHOR CONTRIBUTIONS

RK conceived the project. EJ, AG, and MM performed the experiments. AG and EJ analyzed the data. RK wrote the paper.

FUNDING

This work was supported by RSF # 17-15-01271 (electrophysiology and imaging) and the subsidy allocated to Kazan Federal University for the state assignment in the sphere of scientific activities # 6.2313.2017/4.6 (development of the autofocus system) and performed within the Program of Competitive Growth of Kazan University.

ACKNOWLEDGMENTS

We thank Drs. Sergei Kirov and Igor Medina for helpful suggestions and comments on the manuscript, and David Jappy for editing the manuscript.

SUPPLEMENTARY MATERIAL

The Supplementary Material for this article can be found online at: https://www.frontiersin.org/articles/10.3389/fncel.2018.00502/full#supplementary-material

REFERENCES

Andrew, R.D., Labron, M. W., Boehnke, S. E., Carnduff, L., and Kirov, S. A. (2007). Physiological evidence that pyramidal neurons lack functional water channels. *Cereb. Cortex* 17, 787–802. doi: 10.1093/cercor/bhk032

Balestrino, M., and Somjen, G. G. (1986). Chlorpromazine protects brain tissue in hypoxia by delaying spreading depression-mediated calcium influx. *Brain Res.* 385, 219–226. doi: 10.1016/0006-8993(86)91067-X

Brisson, C.D., and Andrew, R. (2012). A neuronal population in hypothalamus that dramatically resists acute ischemic injury compared to neocortex. *J. Neurophysiol.* 108, 419–430. doi: 10.1152/jn.00090.2012

Charpak, S., and Audinat, E. (1998). Cardiac arrest in rodents: maximal duration compatible with a recovery of neuronal activity. *Proc Natl Acad Sci U.S.A.* 95, 4748–4753. doi: 10.1073/pnas.95.8.4748

Croning, M. D., and Haddad, G. G. (1998). Comparison of brain slice chamber designs for investigations of oxygen deprivation *in vitro*. *J. Neurosci. Methods* 81, 103–111. doi: 10.1016/S0165-0270(98)00023-5

Dostovic, Z., Dostovic, E., Smajlovic, D., Ibrahimagic, O. C., and Avdic, L. (2016). Brain edema after ischaemic stroke. *Med. Arch.* 70, 339–341. doi: 10.5455/medarh.2016.70.339-341

Dreier, J. P., Lemale, C. L., Kola, V., Friedman, A., and Schoknecht, K. (2018). Spreading depolarization is not an epiphenomenon but the principal mechanism of the cytotoxic edema in various gray matter structures of the brain during stroke. *Neuropharmacology* 134, 189–207. doi: 10.1016/j.neuropharm.2017.09.027

Dugue, G. P., Dumoulin, A., Triller, A., and Dieudonne, S. (2005). Target-dependent use of co-released inhibitory transmitters at central synapses. *J. Neurosci.* 25, 6490–6498. doi: 10.1523/JNEUROSCI.1500-05.2005

Dzhala, V., Khalilov, I., Ben Ari, Y., and Khazipov, R. (2001). Neuronal mechanisms of the anoxia-induced network oscillations in the rat hippocampus *in vitro*. *J. Physiol.* 536, 521–531. doi: 10.1111/j.1469-7793.2001.0521c.xd

Elkin, B. S., Shaik, M. A., and Morrison, B. (2010). Fixed negative charge and the Donnan effect: a description of the driving forces associated with brain tissue swelling and oedema. *Philos. Trans. A Math. Phys. Eng. Sci.* 368, 585–603. doi: 10.1098/rsta.2009.0223

Frank, J. I. (1995). Large hemispheric infarction, deterioration, and intracranial pressure. *Neurology* 45, 1286–1290. doi: 10.1212/WNL.45.7.1286

Joshi, I., and Andrew, R. D. (2001). Imaging anoxic depolarization during ischemia-like conditions in the mouse hemi-brain slice. *J. Neurophysiol.* 85, 414–424. doi: 10.1152/jn.2001.85.1.414

Juzekaeva, E., Nasretdinov, A., Gainutdinov, A., Sintsov, M., Mukhtarov, M., and Khazipov, R. (2017). Preferential initiation and spread of anoxic depolarization in layer 4 of rat barrel cortex. *Front. Cell Neurosci.* 11:390 doi: 10.3389/fncel.2017.00390

Khazipov, R., Zaynutdinova, D., Ogievetsky, E., Valeeva, G., Mitrukhina, O., Manent, J. B., et al. (2015). Atlas of the postnatal rat brain in stereotaxic coordinates. *Front. Neuroanat.* 9:161. doi: 10.3389/fnana.2015.00161

Klatzo, I. (1987). Pathophysiological aspects of brain edema. *Acta Neuropathologica* 72, 236–239. doi: 10.1007/BF00691095

Kumar, V., Naik, R. S., Hillert, M., and Klein, J. (2006). Effects of chloride flux modulators in an *in vitro* model of brain edema formation. *Brain Res.* 1122, 222–229. doi: 10.1016/j.brainres.2006.09.012

MacGregor, D. G., Avshalumov, M. V., and Rice, M. E. (2003). Brain edema induced by *in vitro* ischemia: causal factors and neuroprotection. *J. Neurochem.* 85, 1402–1411. doi: 10.1046/j.1471-4159.2003.01772.x

Murphy, T. H., Li, P., Betts, K., and Liu, R. (2008). Two-photon imaging of stroke onset *in vivo* reveals that NMDA-receptor independent ischemic depolarization is the major cause of rapid reversible damage to dendrites and spines. *J. Neurosci.* 28, 1756–1772. doi: 10.1523/JNEUROSCI.5128-07.2008

Obeidat, A. S., Jarvis, C. R., and Andrew, R. D. (2000). Glutamate does not mediate acute neuronal damage after spreading depression induced by O-2/glucose deprivation in the hippocampal slice. *J. Cereb. Blood Flow Metabol.* 20, 412–422. doi: 10.1097/00004647-200002000-00024

Rader, R. K., and Lanthorn, T. H. (1989). Experimental ischemia induces a persistent depolarization blocked by decreased calcium and NMDA antagonists. *Neurosci. Lett.* 99, 125–130. doi: 10.1016/0304-3940(89)90276-0

Risher, W., Ard, D., Yuan, J., and Kirov, S. A. (2010). Recurrent spontaneous spreading depolarizations facilitate acute dendritic injury in the ischemic penumbra. *J. Neurosci.* 30, 9859–9868. doi: 10.1523/JNEUROSCI.1917-10.2010

Risher, W., Croom, D., and Kirov, S. A. (2012). Persistent astroglial swelling accompanies rapid reversible dendritic injury during stroke-induced spreading depolarizations. *Glia* 60, 1709–1720. doi: 10.1002/glia.22390

Risher, W.C., Andrew, R.D., and Kirov, S. A. (2009). Real-time passive volume responses of astrocytes to acute osmotic and ischemic stress in cortical slices and *in vivo* revealed by two-photon microscopy. *Glia* 57, 207–221. doi: 10.1002/glia.20747

Schwab, S., Aschoff, A., Spranger, M., Albert, F., and Hacke, W. (1996). The value of intracranial pressure monitoring in acute hemispheric stroke. *Neurology* 47, 393–398. doi: 10.1212/WNL.47.2.393

Somjen, G. G. (2001). Mechanisms of spreading depression and hypoxic spreading depression-like depolarization. *Physiol. Rev.* 81, 1065–1096. doi: 10.1152/physrev.2001.81.3.1065

Stokum, J. A., Gerzanich, V., and Simard, J. M. (2016). Molecular pathophysiology of cerebral edema. *J. Cereb. Blood Flow Metab.* 36, 513–538. doi: 10.1177/0271678X15617172

Tanaka, E., Yamamoto, S., Kudo, Y., Mihara, S., and Higashi, H. (1997). Mechanisms underlying the rapid depolarization produced by deprivation ofoxygen and glucose in rat hippocampal CA1

neurons *in vitro*. *J. Neurophysiol.* 78, 891–902. doi: 10.1152/jn.1997.78.2.891

Vanharreveld, A. (1957). Changes in volume of cortical neuronal elements during asphyxiation. *Am. J. Physiol.* 191, 233–242. doi: 10.1152/ajplegacy.1957.191.2.233

Young, J. N., Aitken, P. G., and Somjen, G. G. (1991). Calcium, magnesium, and long-term recovery from hypoxia in hippocampal tissue slices. *Brain Res.* 548, 343–345. doi: 10.1016/0006-8993(91)91146-R

Zheng, H., Chen, C., Zhang, J., and Hu, Z. (2016). Mechanism and therapy of brain edema after intracerebral hemorrhage. *Cerebrovasc. Dis.* 42, 155–169. doi: 10.1159/000445170

Conflict of Interest Statement: The authors declare that the research was conducted in the absence of any commercial or financial relationships that could be construed as a potential conflict of interest.

Copyright © 2018 Juzekaeva, Gainutdinov, Mukhtarov and Khazipov. This is an open-access article distributed under the terms of the Creative Commons Attribution License (CC BY). The use, distribution or reproduction in other forums is permitted, provided the original author(s) and the copyright owner(s) are credited and that the original publication in this journal is cited, in accordance with accepted academic practice. No use, distribution or reproduction is permitted which does not comply with these terms.

scientific reports

Check for updates

OPEN

Reappraisal of anoxic spreading depolarization as a terminal event during oxygen–glucose deprivation in brain slices in vitro

Elvira Juzekaeva[1,3], Azat Gainutdinov[1,3], Marat Mukhtarov[1] & Roustem Khazipov[1,2]✉

Anoxic spreading depolarization (aSD) has been hypothesized as a terminal event during oxygen–glucose deprivation (OGD) in submerged cortical slices in vitro. However, mechanical artifacts caused by aSD-triggered edema may introduce error in the assessment of neuronal viability. Here, using continuous patch-clamp recordings from submerged rat cortical slices, we first confirmed that vast majority of L4 neurons permanently lost their membrane potential during OGD-induced aSD. In some recordings, spontaneous transition from whole-cell to out-side out configuration occurred during or after aSD, and only a small fraction of neurons survived aSD with reperfusion started shortly after aSD. Secondly, to minimize artifacts caused by OGD-induced edema, cells were short-term patched following OGD episodes of various duration. Nearly half of L4 cells maintained membrane potential and showed the ability to spike-fire if reperfusion started less than 10 min after aSD. The probability of finding live neurons progressively decreased at longer reperfusion delays at a rate of about 2% per minute. We also found that neurons in L2/3 show nearly threefold higher resistance to OGD than neurons in L4. Our results suggest that in the OGD ischemia model, aSD is not a terminal event, and that the "commitment point" of irreversible damage occurs at variable delays, in the range of tens of minutes, after OGD-induced aSD in submerged cortical slices.

Duration of ischemia is the key factor determining neuronal survival, neurological, and behavioral outcome. During global brain ischemia caused by cardiac arrest, irreversible loss of brain function and legal death are conventionally thought to occur within 5–10 min of cardiac arrest[1]. Paradoxically, however, neuronal function can be restored even after much longer periods of global ischemia under several experimental settings including extracorporeal reperfusion with special cytoprotective reperfusate up to 4 h after cardiac arrest in pigs[2] or maintenance of rat brain slices that were prepared 1–6 h after cardiac arrest[3], or after 30 min middle cerebral artery occlusion[4], in ACSF. These observations raised the hypothesis that neurons may survive much longer episodes of ischemia than traditionally thought, thus opening questions for further research on the possibility of expanding the time window for resuscitation.

Development of brain injury during ischemia proceeds through the initial phase of compensation, during which brain activity ceases but neurons maintain their membrane potential, and recovery of cardiovascular function restores brain activity without major damage to the brain[1,5,6]. Passage to the decompensation phase is associated with a wave of collective and nearly complete neuronal depolarization, so-called anoxic spreading depolarization (aSD) occurring at ~ 5 min after the onset of ischemia[5,7,8]. Generation of aSD is caused by depletion of intracellular reserves of energy metabolites, loss of function of the energy-dependent active ion transporters and rupture in transmembrane ionic gradients[5,7,8]. aSD is a highly energy-demanding event which severely aggravates metabolic status[9]. Considerable evidence indicates that aSD is the key ischemic event that triggers cascades of intracellular reactions leading to acute and delayed neuronal death[5,7,8]. Similarly, periinfarct depolarizations (PIDs) severely compromise the metabolic state in the penumbra and cause expansion of the ischemic core during the development of the focal ischemic injury[10].

The oxygen–glucose deprivation (OGD) model of an ischemia-like condition has been extensively used to explore acute changes in neuronal function during metabolic insult in brain slices in vitro. In this model, metabolite deprivation causes a series of events largely recapitulating the development of ischemic injury

[1]Laboratory of Neurobiology, Kazan Federal University, Kazan 420008, Russia. [2]INMED/INSERM UMR1249, Aix-Marseille University, 163 Avenue de Luminy BP13, 13273 Marseille Cedex 09, France. [3]These authors contributed equally: Elvira Juzekaeva and Azat Gainutdinov. ✉email: roustem.khazipov@inserm.fr

Content courtesy of Springer Nature, terms of use apply. Rights reserved

in vivo, including aSD and ischemic neuronal death. OGD-induced aSD develops within 5–10 min of the onset of perfusion with OGD-solution, it is associated with a wave of collective neuronal depolarization and a drop in electrical membrane resistance, large negative shifts of the extracellular local field potential (LFP) and an increase in tissue light transmittance[11–16]. OGD-induced aSD has been described in slices of neocortex[13,16–20], hippocampus[12,14,15,21–24], striatum[25], thalamus[26,27] and cerebellar cortex[28], but not subthalamic brain structures[18,26,29]. Also, aSD heralds the development of tissue edema manifested by the expansion of brain slice borders, elevation of the slice surface, and massive tissue shifts within the slice[30,31]. However, at difference to ischemia in vivo, where neuronal functions can be, at least partially, preserved when perfusion/oxygen supply is reestablished at delay of 30 min–6 h after the ischemia onset[2–5], occurrence of aSD is considered as a "terminal", i.e. irreversible event during OGD in submerged slices in vitro[8]. Indeed, intracellular sharp electrode recordings from submerged hippocampal slices revealed that CA1 neurons irreversibly lost their membrane potential and synaptic responses during OGD even if reoxygenation started 1 min after aSD[14,15]. Similarly, whole-cell recordings from neocortex and hippocampus in vitro showed that even when oxygen and glucose were reintroduced to the brain slice immediately or few minutes after aSD, the membrane potential was irreversibly lost[12,16,18,21]. Along with these findings, extracellular recordings of responses evoked by afferents electrical stimulation were permanently lost during OGD even if reperfusion with oxygenated ACSF started shortly after aSD both in hippocampus and neocortex[12,13,20–22]. These observations led to the conclusion that at difference to aSD in vivo, aSD in submerged slices of cortex and hippocampus is a lethal terminal event[12–16,18,20–22]. However, massive tissue shifts and mechanical displacement of neurons from the recording electrodes caused by tissue swelling, which starts to develop after aSD[30–32] could severely compromise recordings and introduce error in the assessment of neuronal viability. Therefore, in the present study we reexamined the hypothesis of aSD as a terminal event during OGD, taking into account the methodical constraints imposed by ischemic edema. In this aim, we estimated neuronal survival by short-term patching of neurons following reperfusion started at various delays after aSD. We provide evidence that aSD is not a terminal event during OGD in submerged cortical slices, as previously thought, and that the "commitment point" of irreversible loss of membrane potential and neuronal function occurs at variable and much longer delays, in the range of tens of minutes, after aSD, in the OGD model of ischemia in vitro. Our findings also suggest that the OGD model of ischemia in vitro could be useful in further explorations of neuroprotective interventions that could stop the progression of neuronal damage initiated by aSD during the post-aSD period.

Results

Continuous patch-clamp recordings through OGD and reperfusion. In the present study we explored neuronal survival during OGD in slices of the barrel cortex using whole-cell patch clamp recordings and concomitant extracellular recordings of LFP, and optical intrinsic signals (OIS) imaging. To this aim we used two types of neuronal survival assessment. In the first approach, we performed continuous recordings from a single neuron starting from control conditions and then through OGD and reperfusion. In the second approach, we sampled cells using short-term patch-clamp recordings in control conditions and during reperfusion following OGD of various durations (from 1 to 60 min). Both approaches were used in the same slices (n = 33) of the rat barrel cortex.

During continuous recordings, under control conditions L4 neurons had a membrane potential (E_m) of (median (Q1–Q3): − 68.4 (− 74.8 to − 61.7) mV, a membrane resistance (R_m) of 96.3 (55.7–132.1) MΩ and fired APs in response to suprathreshold depolarizing current steps, which were applied every 10 s to monitor the change in R_m through the entire duration of recordings (Fig. 1a–c, note that E_m traces are low-pass filtered to remove spikes, and that E_m corresponds to the bottom values of the E_m trace). Perfusion with OGD-solution evoked aSD in all neurons at a delay of 5.1 (4.3–8.2) min after OGD onset. aSD was manifested by rapid neuronal depolarization to − 13.6 (− 27.9 to − 7.2) mV (p = 3.0E−12, hereinafter Wilcoxon rank sum test) and occurred simultaneously with a negative shift in extracellular LFP of − 5.6 (− 8.7 to − 3.1) mV in concomitant DC-LFP recordings in the vicinity of the recorded neuron, and an increase in light transparency by 15.3 (9.4–21.3) % in OIS recordings. During aSD, R_m dropped to 10.3 (4.1–29.7) MΩ (p = 6.7E−08). Also, ischemic edema and mechanical slice tissue displacement started developing shortly after aSD as assessed by expansion of the slice borders (Fig. 1d). These observations are in keeping with previous studies using the OGD model[13,16–19,22,31–34]. Further developments after aSD varied between cells and depended on OGD duration (Fig. 1e,f). We sorted neurons into three categories depending on the functional outcome after OGD, based on the parameters E_m, R_m and ability to fire APs in response to depolarizing steps: (1) survivors (Fig. 1a); (2) cells lost during recordings due to a transition from whole-cell to outside-out (Fig. 1b); and (3) cells which apparently did not show functional recovery after OGD, but due to uncertainty in the cause (cell death or cell loss due to a loss of electrical contact with the cell due to displacement during tissue edema) were classified as undetermined cases (Fig. 1c).

Survivors. Only a small minority of L4 neurons recovered during reperfusion (n = 5 neurons of 33, 15%) when reperfusion was started shortly, within a few minutes, after aSD (5.2 (3.7–8.9) min) (Fig. 1a,e,f). Only one neuron survived an OGD episode in which reperfusion started 15 min after aSD. Survivor neurons displayed an E_m of − 70.6 (− 76.1 to − 47.2) mV and R_m of 119.9 (111.5–156.6) MΩ compared to control values for this group of − 75.3 (− 77.9 to − 61.4) mV (p = 0.55) and 100.9 (83.9–132.9) MΩ (p = 0.31), and they recovered their ability to fire APs upon repolarization during reperfusion. Used as a metric of edema, border expansion had a tendency to start later 6.7 (2.4–9.2) min, and attain lower values of 21.2 (18.4–39.6) µm compared to other outcomes: 2.3 (− 1.1 to 4.4) min and 40.6 (29.9–55.0) µm for outside-out cases and 3.7 (1.5–5.4) min and 36.6 (30.2–44.6) µm for undetermined cases, but this difference was not significant (p = 0.29 for Survivors/Outside-out, p = 0.29 for Survivors/Undetermined and p = 0.67 for Outside-out/Undetermined).

Content courtesy of Springer Nature, terms of use apply. Rights reserved

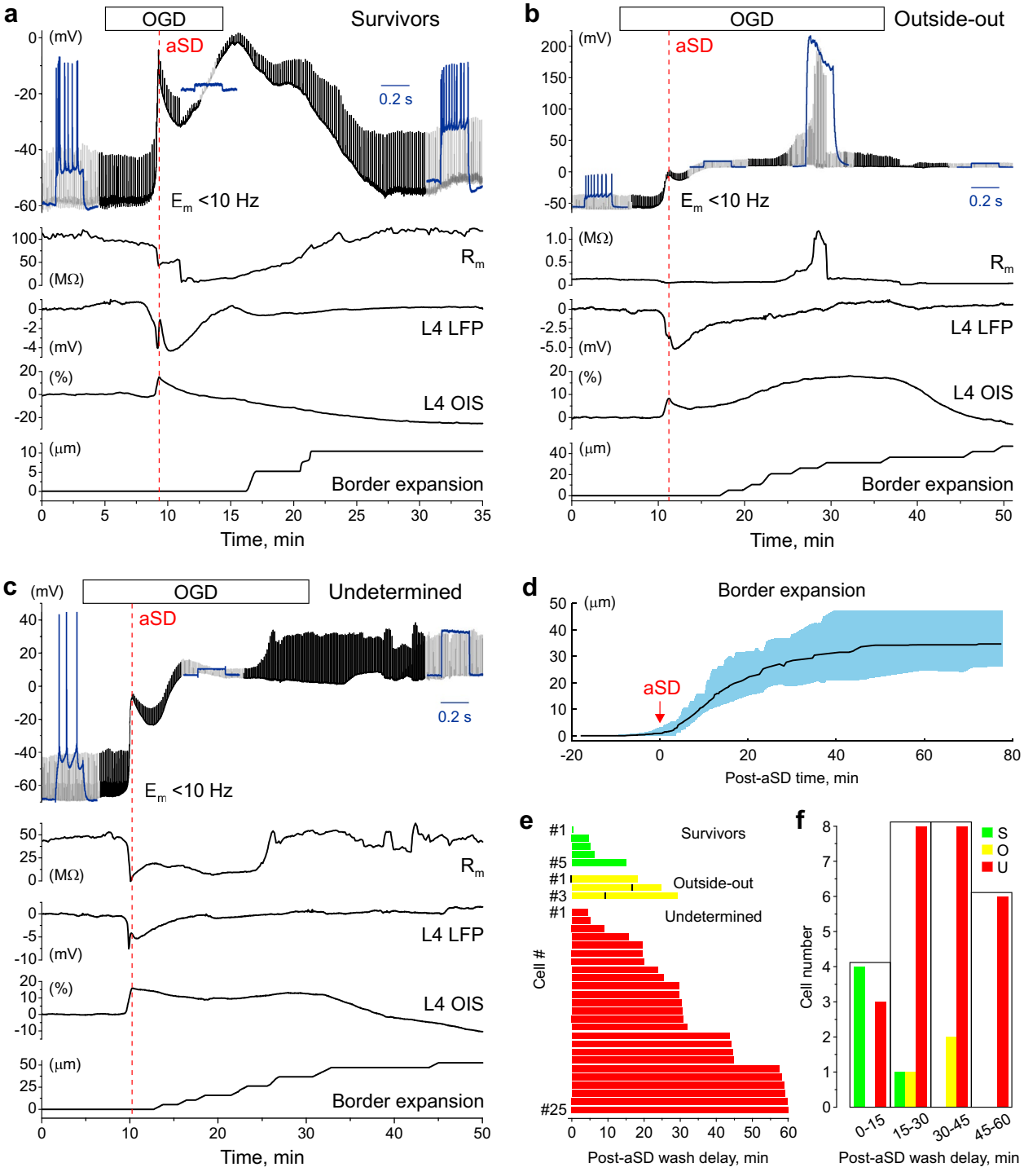

Figure 1. Variety of electrophysiological outcomes during continuous whole-cell recordings through the oxygen–glucose deprivation and reperfusion. **(a–c)** Example traces of continuous recordings from L4 neurons in current-clamp mode starting from control conditions and then through OGD of various durations and then reperfusion. The upper black traces show E_m (10 Hz low-pass filtered to remove spikes), regular upward deflections show E_m deflections evoked by depolarizing steps to monitor cell firing and R_m. Blue insets show cell responses (non-filtered signal) to depolarizing current steps in control conditions, after OGD-induced aSD and after reperfusion. Below, the corresponding changes in membrane resistance, DC-LFP and OIS recordings from L4, and the time course of the OGD-induced border expansion from control position are shown. Example traces for three categories of cells depending on their functional outcome after OGD: (**a**) Survivor, which transiently depolarized during aSD but recovered E_m, R_m and firing ability during reperfusion; (**b**) Cell lost during transition to outside-out, manifested as a sharp increase in R_m during reperfusion to > 1GΩ values and (**c**) Undetermined case which showed no recovery of E_m nor ability for spike firing upon reperfusion. (**d**) Average change in the OGD-induced border expansion (shaded area shows SD). Data are referenced to aSD time = 0. (**e**) Raster plot of outcomes (as shown on panels **a–c**) as a function of reperfusion delay after OGD-induced aSD. For outside-out transitions, the time points of transition to "gigaseal" are indicated by black vertical bars. (**f**) Histograms of the cell count in each outcome category depending on reperfusion delay after aSD. (**d**,**e**) Group data from 33 L4 neurons.

Content courtesy of Springer Nature, terms of use apply. Rights reserved

Lost during transition to outside-out. Three cells of 33 (9%) showed spontaneous transition from whole-cell to outside-out configuration as evidenced by an increase in R_m to > 1 GΩ (1.9 (1.3–2.0) GΩ, range from 1.1 to 2.1 GΩ) (Fig. 1b,e,f). This transition occurred at variable delays after aSD (9.2 (1.9–14.8) min) during OGD episodes in which reperfusion started from 17.6 to 29.3 min (24.8 (19.4–28.1) min) after aSD, and it was typically transient with further rupture of the patch evidenced by a drop in R_m. Neither E_m [− 1.3 (− 5.5 to 6.6) mV] compared to control value of − 57.5 (− 63.7 to − 56.2) mV ($p = 0.029$) nor the ability to fire APs recovered in these cases.

Undetermined. This was the most frequent category of outcomes from OGD (n = 25 cells of 33, 76%) observed through the entire span of OGD durations (reperfusion delay after aSD from 4 to 60 min, average 30.7 (23.6–48.6) min) (Fig. 1c,e,f). All undetermined cases did not show recovery of E_m during reperfusion (− 2.3 (− 8.2 to 6.3) mV), measured 10–15 min after reperfusion onset, compared to control value of − 69.2 (− 74.4 to − 61.9) mV ($p = 1.4E{-}09$) and displayed a variable change in R_m (from 3.4 to 723.1 MΩ), average 54.6 (28.4–208.3) MΩ, compared to control value of 89.0 (54.2–116.6) MΩ ($p = 0.07$). None of these cases showed APs in response to depolarizing steps from negative, close to pre-OGD E_m maintained by constant negative current injection (not shown). These predominant cases of outcomes were classified as dead neurons in previous studies[12,14–16,18]. However, taking into account the major methodical constraints imposed by ischemic edema[31–33] which starts to develop after aSD, and which may severely compromise recordings (as clearly evidenced by transitions to outside-out) we assigned this category as undetermined cases with the hypothesis that some of these cells actually survive but are lost during recordings due to edemic tissue displacement and thus the survival rate is probably underestimated during continuous recordings.

Short-term patch-clamp recordings. To overcome the problem of edema we short-term patched cells during the reperfusion phase after OGD of various durations. Recording sessions started 20 min after reperfusion onset and lasted in each cell for ~ 1 min. According to the estimates of slice surface displacement during OGD-induced edema (~ 2 μm min^{-1}[31]), cell displacement from the patch-pipette during such short-term recordings should not affect assessment of neuronal viability. For each cell patched in these experiments we estimated E_m, R_m and ability to fire APs in response to depolarizing current steps before and after OGD episodes (Fig. 2a). Under control conditions, 122 of 128 (95%) cells from 29 slices patched in L4 displayed features of live neurons with a membrane potential (E_m) of − 71.5 (− 75.9 to − 66.9) mV, membrane resistance (R_m) of 104.8 (73.5–148.8) MΩ, and APs in response to suprathreshold depolarizing current steps (Figs. 2b, 3a,c,d). The remaining 6 (5%) cells had a depolarized E_m of − 31.1 (− 56.6 to − 7.3) mV, R_m of 240.0 (38.0–380.7) MΩ, and did not fire in response to depolarizing steps from − 60/− 70 mV. Cells patched after reperfusion in the post-OGD epoch were classified according to similar criteria as for the continuous recordings above. These included two main categories, (1) Live neurons–survivors, and (2) Others.

(1) Live neurons in post-OGD slices (n = 19, 28% of the total 69 patched cells from 29 slices) were characterized by an E_m of − 65.6 (− 70.6 to − 56.4) mV, that was + 5.9 mV more positive than that in control conditions ($p = 0.0056$)[35,36], R_m of 145.7 (129.9–176.6) MΩ, that was 1.5 fold higher than that in control conditions ($p = 0.0012$), and they all fired APs in response to depolarizing steps from rest (Figs. 2c, 3a,c,d). Neither E_m ($R^2 = 0.000554$, $p = 0.924$) nor R_m ($R^2 = 0.045$, $p = 0.383$) showed any correlation with the time delay of reperfusion after aSD. Live neurons could be found in OGD-exposed slices with reperfusion started at delay of up to 45 min after aSD (Fig. 3a,b). The proportion of live neurons among all cells patched in a slice was highly variable between slices and progressively decreased with increase in the delay of reperfusion onset after aSD (Fig. 3b). The linear fit provided a slope of $-1.9 \pm 0.2\% \cdot min^{-1}$ for the probability of finding live cells in L4 as a function of delay of reperfusion after aSD.

(2) The other L4 cells patched in post-OGD slices (n = 50, 72% of the total 69 patched cells from 29 slices) displayed high variability in electrophysiological characteristics and included live putative glial cells with very negative E_m values, some of them presumably of oligodendrocyte lineage displaying high input resistance and active electrogenic properties (Fig. 2d), and presumably dead cells of unknown origin with strongly depolarized or nearly zero membrane potential and extremely low membrane resistance (Fig. 2e). On average, these other cells in post-OGD slices had an E_m of − 34.9 (− 65.9 to − 10.9) mV ($p = 1E{-}10$) and R_m of 41.2 (28.9–68.6) MΩ ($p = 4.3E{-}12$) (Fig. 3c,d). None of the "other" type cells fired APs in response to depolarizing current steps.

We also sampled cells in L2/3 using a similar approach as for L4. In control conditions 97% of cells (n = 77 of the total 79 patched cells from 16 slices) appeared to be live neurons with an ability to fire action potentials in response to depolarizing steps, E_m of − 71.1 (− 75.5 to − 67.3) mV and R_m of 119.5 (72.2–224.7) MΩ (Fig. 4b,d,e). In slices exposed to OGD and with reperfusion started 5–60 min after aSD, live neurons accounted the vast majority of all cells patched in L2/3 (n = 100, 82% of the total 122 patched cells from 25 slices; Fig. 4a,b) had an E_m of − 69.0 (− 73.8 to − 62.0) mV depolarized by 2.1 mV comparing to the control value ($p = 0.0124$), and R_m of 121.8 (91.7–224.8) MΩ that was not different from the control ($p = 0.38$) (Fig. 4d,e). As in L4, neither E_m ($R^2 = 0.000025$, $p = 0.962$) nor R_m ($R^2 = 0.000909$, $p = 0.769$) of the OGD-surviving neurons showed any correlation with the time delay of reperfusion after aSD (Fig. 4b). With an increase in the OGD duration, the proportion of surviving neurons decreased by a slope of $-0.7 \pm 0.2\% \cdot min^{-1}$ that was about threefold slower than for L4 (Fig. 4c). Even in slices that were reperfused at a delay of 60 min after aSD 54% of patched cells were live neurons (n = 7 of the total 13 patched cells) (Fig. 4b,f). The "other" L2/3 cells patched in post-OGD slices (n = 22, 18% of the total 122 patched cells from 25 slices) fired no APs in response to depolarizing current steps. On average,

Content courtesy of Springer Nature, terms of use apply. Rights reserved

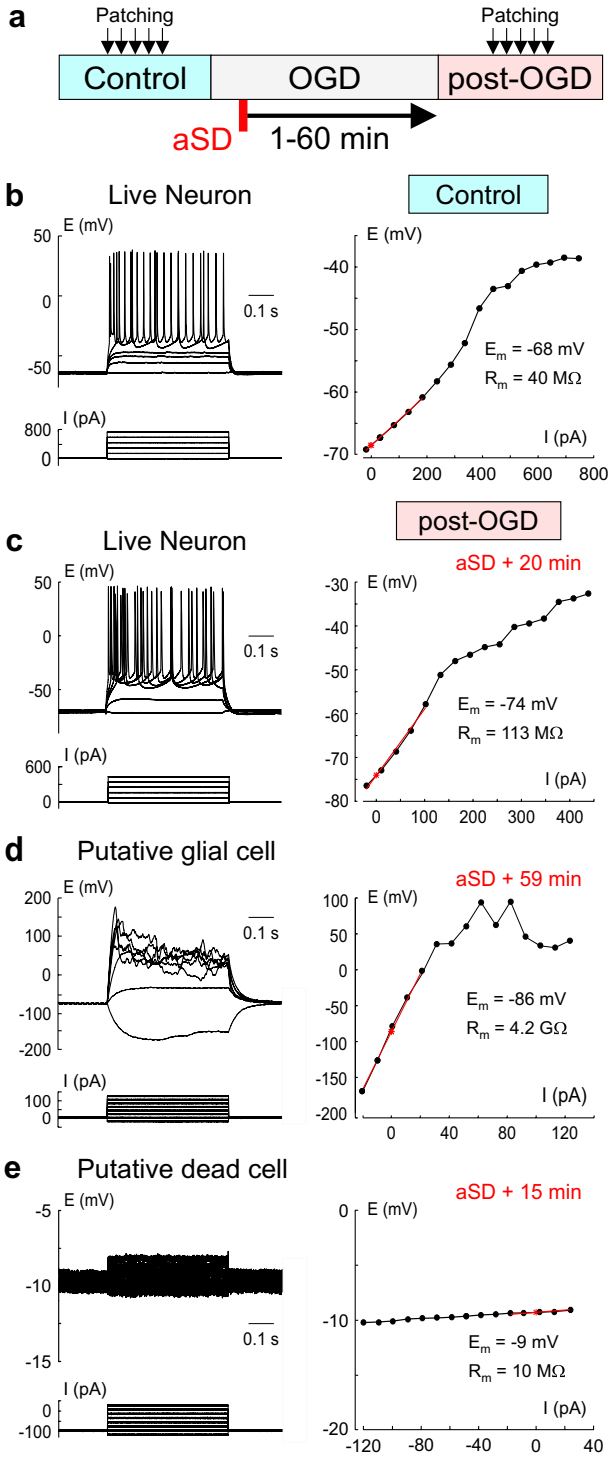

Figure 2. Variety of electrophysiological outcomes from OGD using short-term whole-cell recordings. (**a**) Scheme of the experiment. Cells were sampled using short-term (~ 1 min long) patch-clamp recordings in control conditions and during reperfusion following OGD of various durations (from 1 to 60 min after aSD). (**b**) Voltage responses (top traces) generated by current injections (bottom traces) recorded from a L4 neuron prior to OGD. The corresponding I-V plot is shown on the right, where the red line shows the range in which R_m was measured, and E_m and R_m are indicated on the right of the I-V curve. (**c**) Example traces obtained from a L4 neuron which survived OGD with reperfusion started 20 min after aSD. (**d**) L4 cell which survived OGD with reperfusion started 59 min after aSD, and which has been classified as a putative glial cell due to very negative E_m, high R_m and inability for spike firing. (**e**) Putative dead cell with low R_m and strongly depolarized E_m.

Content courtesy of Springer Nature, terms of use apply. Rights reserved

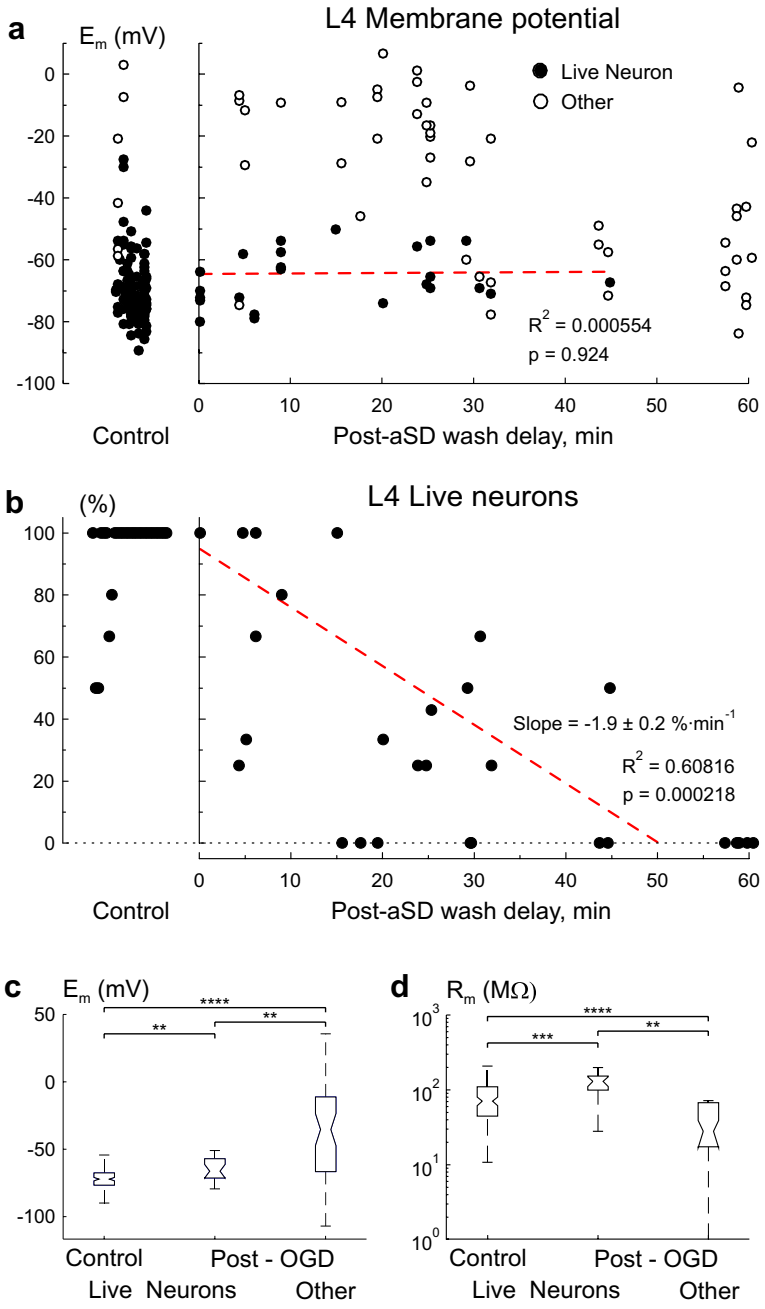

Figure 3. OGD survival in L4 neurons using short-term patching approach. (**a**) E_m of cells patched in L4 before (left) and after OGD episodes (right) as a function of the onset of reperfusion delay after aSD. Each data point corresponds to an individual cell. Filled circles represent live L4 neurons with negative membrane potentials and the ability to fire spontaneously or in response to depolarizing steps. Open circles show data from "other" types of cells which did not fire action potentials as the main criterion for their exclusion from a pool of live neurons. The red dotted line shows no dependence of E_m in survivor neurons on the onset of reperfusion delay after aSD. Data from 128 control and 69 post-OGD cells. (**b**) The corresponding proportion of live neurons among all cells patched in L4 in a given slice (each dot represents one slice). The red dotted line represents a linear fit for the probability of finding a live neuron in L4 as a function of the onset of reperfusion delay after aSD. The intercept was fixed to the control value of cells viability of 95%. Data from 29 slices. (**c**) E_m and (**d**) R_m values in L4 in live neurons before OGD, and live L4 neurons and "other" cells in the post-OGD epoch (boxplots show median and 1st and 3nd quarantiles). Group data from 128 control and 69 post-OGD cells in 29 slices. (**$p < 0.01$, ***$p < 0.001$, ****$p < 0.0001$).

Content courtesy of Springer Nature, terms of use apply. Rights reserved

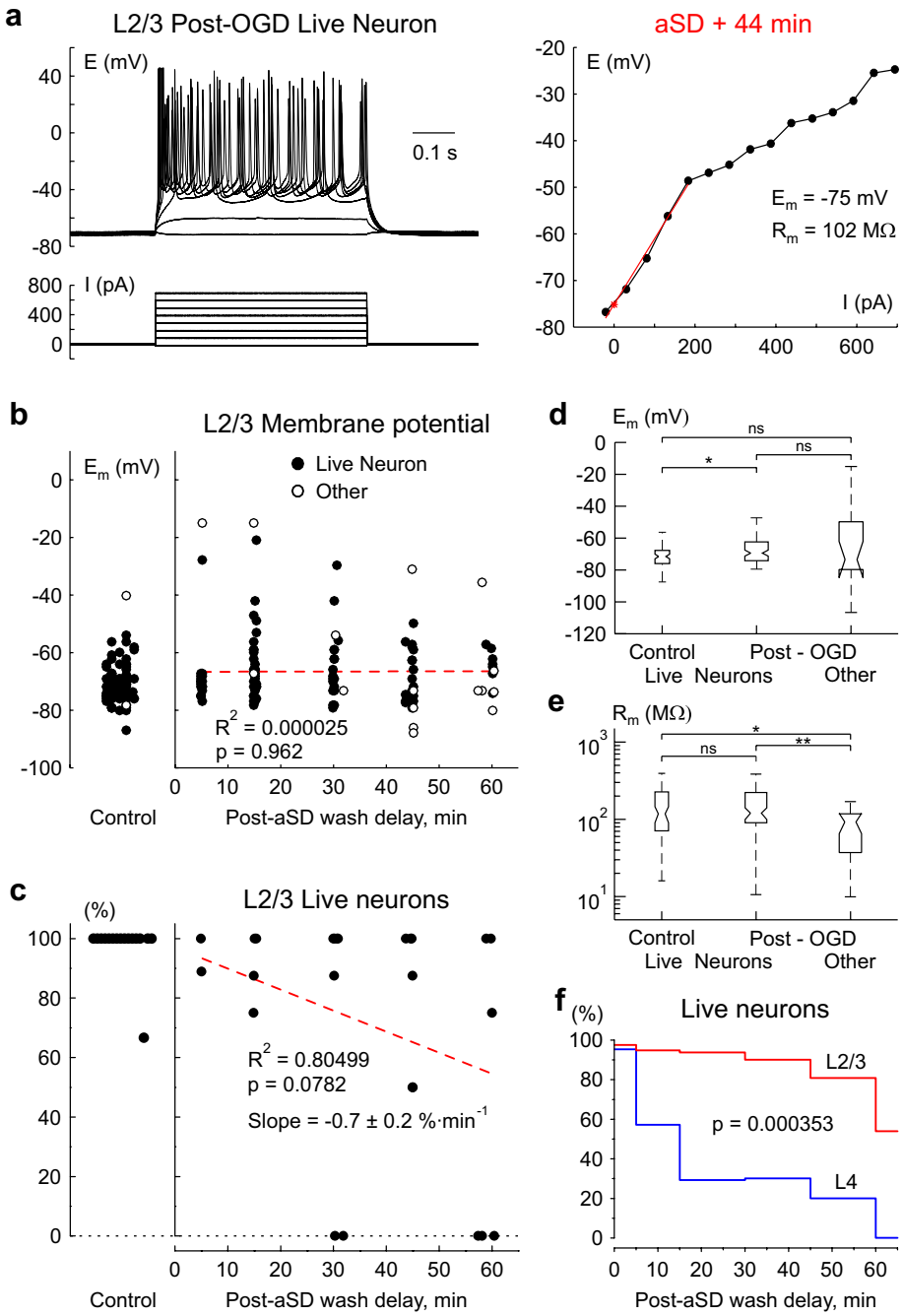

Figure 4. Neurons in L2/3 show higher resistance to OGD than L4 neurons. (**a**) Voltage responses generated by current injections in a L2/3 neuron in a slice which experienced OGD for more than 1 h, and in which reperfusion started at a delay of 59 min after aSD. Right, the corresponding I-V plot. (**b**) E_m values in cells patched in L2/3 before (left) and after OGD of various reperfusion delays after aSD onset (right). Each data point corresponds to an individual cell. Filled circles correspond to live L2/3 neurons, open circles correspond to "other" cells. The red dotted line shows no dependence of E_m in survivor neurons on the onset of reperfusion delay after aSD. Data from 79 control and 122 post-OGD cells. (**c**) The corresponding proportion of live neurons among all cells patched in L2/3 in a given slice (each dot represents one slice). The red dotted line represents a linear fit for the probability of finding a live neuron in L2/3 as a function of the onset of reperfusion delay after aSD. The intercept was fixed to the control value of cells viability of 97%. Data from 16 control and 25 post-OGD slices. (**d**) E_m and (**e**) R_m values in L2/3 in live neurons before OGD, and live L2/3 neurons and "other" cells in the post-OGD epoch (boxplots show median and 1st and 3nd quarantiles). Group data from 79 control cells in 16 slices and 122 post-OGD cells in 25 slices. (*$p < 0.05$, **$p < 0.01$). (**f**) Histogram plots of the probability of finding a live neuron in L2/3 and L4 as a function of the onset of reperfusion delay after aSD. Group data from 122 L2/3 cells in 25 slices and 69 L4 cells in 29 slices. P-value is for a comparison between L2/3 and L4 using Kolmogorov–Smirnov test.

Content courtesy of Springer Nature, terms of use apply. Rights reserved

these "other" cells had an E_m of − 73.0 (− 79.3 to − 49.5) mV ($p = 0.9921$) and R_m of 93.78 (37.9–119.6) MΩ ($p = 0.0104$) (Fig. 4d,e). Analysis of probability of finding live neurons through the post-OGD period revealed that L2/3 neurons showed a much higher survival rate after aSD when compared to L4 neurons ($p = 0.000353$, Kolmogorov–Smirnov test, Fig. 4f).

Discussion

The main conclusion of our study is that aSD is not a terminal event during OGD in submerged cortical slices, and that the "commitment point" of irreversible damage in this model occurs at variable, in the range of tens of minutes, delays after aSD.

Here we used two experimental approaches to assess neuronal survival after transient metabolic insult caused by OGD. Using continuous patch-clamp recordings through the OGD and reperfusion period we found an extremely low survival rate with recovery of negative membrane potential and ability to spike-fire in very few neurons and only if reperfusion started shortly after aSD. This is in line with previous studies where the occurrence of aSD was associated with irreversible loss of membrane potential in submerged slices or intact preparations[12–16,18,21]. However, according to recent observations on the dynamics of tissue edema which starts developing after aSD at a rate of volume increase by ~ 1%/min, irreversible loss of membrane potential after aSD could reflect not only true permanent neuronal depolarization, but also artifacts caused by mechanical displacement of recorded neurons from the recording pipette, and loss of electrical connection between the cell and pipette. This could potentially cause cell survival to be underestimated. In line with these assumptions, we found spontaneous transitions from whole-cell to outside-out configuration following aSD. Normally, transition from whole-cell to outside-out configuration involves slow displacement of the recording pipette from a cell, during which the initial connection between the pipette and cell membrane is preserved and once a relatively small patch is extruded from the plasma membrane, the outside-out formation manifests in an increase in R_m to GΩ values[37]. Although infrequent, cases of transitions from whole-cell to outside-out configuration are highly likely to be indicative of the displacement of the recorded cell from the pipette during edemic tissue shifts. Transition to outside-out is not necessarily indicative of cell damage, however, as neurons can survive this procedure and display quite normal negative E_m values during multiple repatching under normal conditions. Therefore, these cases can only be classified as a fraction of undetermined outcomes, that in total constitute the vast majority of cases during continuous recordings through the OGD and reperfusion phases. To sum up, continuous recordings employed in this, and previous studies show poor neuronal survival after aSD, but this approach may underestimate survival rate due to the artifacts caused by ischemic tissue edema. Likewise irreversible loss of responses evoked by afferents electrical stimulation during extracellular recordings that has been reported after aSD in brain slices[12,13,20–22] could also involve slice tissue displacement relatively the stimulating and recording electrodes as well as mechanical neuronal trauma caused by the brain mass tissue movement against the electrodes during development of ischemic edema.

The short-term patching approach, in which the mechanical artifacts associated with tissue edema were minimized to displacement of only a few microns over ~ 1 min of recording time, showed neuronal death that was more protracted after aSD. Indeed, nearly half of L4 neurons survived OGD episodes during which reperfusion started less than 10 min after aSD, and survival probability decayed with a time constant of 21 min as a function of reperfusion delay after aSD. An even higher survival rate has been found in the supragranular layers, where a half of patched cells were live neurons in slices in which reperfusion was delayed from aSD by 60 min. The higher susceptibility of L4 neurons to OGD is consistent with a "tropism" of aSD to L4 and the higher metabolic demand of this layer as evidenced by the heaviest labelling of L4 by the metabolic level marker 2,3,5-triphenyltetrazolium chloride (TTC)[20], and is in keeping with heterogeneity in sensitivities to ischemia among different neuronal populations and structures[7,11,18,26,29,38–40] that may involve different metabolism in different cell types, but also different neuronal microenvironment which plays a key role in neuronal recovery from OGD[41,42]. Because continuous recordings through the OGD and reperfusion period contain a major source of error caused by tissue edema, we propose that the short-term patching approach, in which this error is minimized, provides more reliable estimates of neuronal survival. However, several points should be taken into account during the interpretation of these results. First, the proportion of surviving neurons could be overestimated with the short-term patching approach because dead cells may change in appearance and ability to establish gigaseal contact and thus can be overlooked during patching. Second, surviving neurons showing functional recovery of membrane potential and firing ability upon reperfusion may have already initiated the cascade of intracellular processes which leads to neuronal death later. Third, cells that were classified as "others" or "undetermined" cases, which show a lack of firing, loss of E_m and low membrane resistance within 1–2 h of reperfusion may regain their function at later time points. Therefore, our conclusions on neuronal survival after OGD are limited to the present experimental settings and may be different with other approaches and at other time points after OGD.

Our findings on significant survival of neurons and their protracted death after aSD reappraise the role of aSD as a terminal event in the OGD model in submerged slices or intact preparations in vitro[12–16,18,20–22,43] and are more consistent with the observations made using other ischemia models. Indeed, in brain slices with a gas-fluid interface, aSD is not a terminal event and slices can be rescued by reperfusion with oxygen/glucose-containing ACSF several minutes after hypoxia-induced aSD (in normal glycemic conditions)[8,44,45]. During global ischemia in vivo, aSD is also not a terminal event as both morphological and functional impairments to cortical neurons are fully reversible upon reperfusion started within ~ 5 min of aSD[6]. Moreover, cortical slices prepared from the rat brain 1–6 h after cardiac arrest display quite normal physiological and morphological properties[3] and sufficient viability for cultures[46–48]. Specific cellular functions, spontaneous synaptic activity, and active cerebral metabolism (yet not global brain activity) was restored in pigs four hours post-mortem after extracorporeal reperfusion using cytoprotective perfusate[2]. Also, reperfusion started after one hour of complete

Content courtesy of Springer Nature, terms of use apply. Rights reserved

global ischemia could result in neuronal, electrophysiological, and metabolic brain resuscitation[49–52]. Also, along with these findings, up to 4 h of reperfusion after a transient (one hour long) focal cerebral ischemia induced by microfilament MCA occlusion, negligible tissue injury was revealed if brain slices prepared from these animals were stained with TTC in vitro[53]. No signs of functional damage were also reported in slices prepared immediately after 30 min of MCAO[4].

Comparing our results with the data obtained in vivo or using *ex-vivo* preparations, it appears that neuronal death occurs at a higher rate during OGD in submerged slices than during ischemia in vivo. The more harmful OGD in submerged slices may involve a stronger cytotoxic edema and calcium load than in vivo. Previously, the development of cytotoxic edema manifested by swelling of neuronal and glial cell soma, dendritic beading and shrinkage of the extracellular space was shown starting minutes after aSD both in vivo and in vitro[6,22,32,54–56]. However, under submerged conditions in vitro, brain tissue is exposed to an unlimited source of calcium, sodium, chloride and water in the extracellular space, through continuous and unlimited buffering of the extracellular space by the electrolytes and water contained in the bath medium[31,34,57,58]. This results in a stronger cytotoxic edema and calcium load than in vivo, where the availability of electrolytes and water in the extracellular space is limited by the lack of blood supply to the ischemic core in the case of focal ischemia or during global brain ischemia caused by cardiac arrest[59]. In the latter case, cytotoxic edema and calcium load are limited by the relatively small amount of electrolytes and water in the narrow extracellular space and are thus less pronounced and less damaging, and occur without tissue swelling in contrast to submerged slices in vitro[31,34,57,58].

In conclusion, the results of the present study suggest that neuronal death evoked by OGD in submerged cortical slices may span a longer time window after aSD than initially thought, and this is more in agreement with the observations made during brain ischemia in vivo. While previously approved strategies for attenuating ischemic injury in the in vitro ischemia models are mainly aimed at delaying aSD onset[12,13,22,24,43], our findings allow in vitro models to be used to explore neuroprotective interventions that could stop the progression of neuronal damage initiated by aSD during the post-aSD period.

Materials and methods

Ethical approval. All animal-use protocols followed the guidelines of the French National Institute of Health and Medical Research (INSERM, protocol N007.08.01) and Kazan Federal University on the use of laboratory animals (ethical approval by the Institutional Animal Care and Use Committee of Kazan State Medical University N9-2013).

Brain slice preparation. Wistar rats (16–23 days old) of either sex were used. Animals were decapitated under isoflurane anaesthesia (5%), the brain was rapidly removed and placed in ice-cold (2–5 °C) slicing solution of the following composition (in mM): KCl 3.5, $CaCl_2$ 2, $MgSO_4$ 2, $NaHCO_3$ 24, NaH_2PO_4 1.25, glucose 10 and sucrose 25.2 (pH 7.4). Four hundred µm thick thalamocortical slices were cut using a PELCO easiSlicer vibratome (Ted Pella, Inc., Redding, CA, USA). Slices containing the barrel cortex were selected by anatomical coordinates[60] and the presence of barrel structures in L4. Slices were first kept in oxygenated (95% O_2–5% CO_2) artificial cerebrospinal fluid (ACSF) of the following composition (in mM): NaCl 126, KCl 3.5, $CaCl_2$ 2, $MgCl_2$ 1.3, $NaHCO_3$ 25, NaH_2PO_4 1.2 and glucose 11 (pH 7.4) for 30 min at 32 °C and then at room temperature (20–22 °C) for at least 1 h before use. For recordings, slices were placed into a submerged chamber and superfused with oxygenated ACSF at 30–32 °C at a flow rate of 10 ml min^{-1}. Oxygen/glucose deprivation (OGD) was induced by superfusion with ACSF in which N_2 replaced O_2 and sucrose replaced glucose at equimolar concentration. OGD durations were fixed prior to each experiment to a pre-defined duration of the post-aSD period, which is a time interval between aSD (monitored using OIS imaging and extracellular field potential recordings) and reperfusion with oxygenated, enriched in glucose ACSF. Pre-defined durations of the post-aSD period were of 0, 5, 10, 15, 20, 25, 30, 45 and 60 min during recordings from L4, and 5, 15, 30, 45 and 60 min during recordings from L2/3. The actual durations of post-aSD period could differ by up to ± 2 min from the pre-defined values due to the time lag between aSD detected online during the experiment and the exact value of the aSD peak determined during post-hoc analysis.

Electrophysiological recordings. *Patch-clamp recordings.* Visual patch-clamp recordings were performed from L4 pyramidal cells using a MultiClamp 700B (Axon Instruments, Union City, CA, USA) amplifier as described previously[31]. Patch electrodes were made from borosilicate glass capillaries (BF150-86-10, Sutter Instrument, Novato, CA, USA) and had a resistance of 4–7 MΩ. The pipette (intracellular) solution contained (in mM) 131 potassium gluconate, 4 KCl, 10 HEPES, 10 phosphocreatine, 4 MgATP, and 0.3 Na_2GTP (adjusted to pH 7.3 with KOH). Extracellular and patch-clamp recordings were digitized at 10 kHz with a Digidata 1440A interface card (Axon Instruments) and analyzed offline using MATLAB (MathWorks, Inc., Natick, MA, USA) routines.

To examine the ability of neurons to fire APs and monitor the membrane resistance (R_m) during continuous patch-clamp recordings 200-ms suprathreshold depolarizing current pulses were applied every 10 s during control, OGD and reperfusion episodes. For short-term patch-clamp recordings in each slice, several neurons were patched before OGD (on average, 4.4 ± 0.4 cells patched per slice in L4 (128 cells in 29 slices) and 4.9 ± 0.4 cells/slice in L2/3 (79 cells in 16 slices) and after OGD (on average, 2.4 ± 0.3 cells/slice in L4 (69 cells in 29 slices) and 4.9 ± 0.7 cells/slice in L2/3 (122 cells in 25 slices). Firing ability, resting membrane potential (E_m) and R_m values in these cells were evaluated by I-V curve analysis.

Extracellular recordings of the local field potentials (LFP) were performed in the barrel cortex using single site glass pipette electrodes. Electrodes were pulled from borosilicate glass capillaries (BF150-86-10, Sutter Instrument, Novato, CA, USA) and had resistances of 2–3 MΩ when filled with ACSF. Electrodes were connected via

Content courtesy of Springer Nature, terms of use apply. Rights reserved

chlorided silver wire to the headstage of a MultiClamp 700B patch-clamp amplifier (Axon Instruments, Union City, CA, USA). Recordings were performed in voltage-clamp DC mode, then currents were inverted and voltage calibrated using 5 mV steps.

Optical intrinsic signal recordings. Optical intrinsic signal (OIS) recordings were performed using slice transillumination as described in[20,31,61]. The slice was illuminated by a halogen lamp with a 775 nm bandpass filter and visualized using a BX51WI upright microscope equipped with a 4x/0.10 Plan N objective (Olympus, Tokyo, Japan). Images were acquired using a QIClick-R-F-M-12 CCD camera (QImaging, Surrey, BC, Canada) every 2.5 s at 348 × 260 pixel resolution.

Data analysis. Data were analyzed using custom-written procedures in MATLAB (MathWorks, Inc., Natick, MA, USA) as described previously[20,31]. OIS was calculated using the first-frame subtraction approach: $OIS(t) = (I(t) - I_0)/I_0$, where I(t)—pixel intensity at the moment t, I_0—time-averaged pixel intensity in the preconditioned baseline period (100 s). The resulting frames were filtered with a 10 × 10 median filter. Regions of interest (ROI) were selected as square areas near recording sites. OIS traces were calculated as the average OIS signal within the selected ROIs. The appearance of the peak value of the OIS signal determined the start time of aSD. The amplitude of aSD during extracellular recordings was calculated as within OIS-detected aSD ± 5 min time window.

Statistical analysis. Statistical analysis was performed using the MATLAB Statistics toolbox (MathWorks, Inc., Natick, MA, USA). Statistical comparisons between the groups were performed using the Wilcoxon rank sum and Kolmogorov–Smirnov tests. The significance level was set at $p < 0.05$. Group data are expressed as median (25th percentile–75th percentile) unless otherwise indicated.

Data availability

Original and processed data, and signal processing and analysis routines are available on request from the authors.

Received: 21 June 2020; Accepted: 22 October 2020

References

1. Allen, B. S. & Buckberg, G. D. Studies of isolated global brain ischaemia: I. overview of irreversible brain injury and evolution of a new concept—redefining the time of brain death. *Eur. J. Cardio-Thoracic Surg.* **41**, 1132–1137 (2012).
2. Vrselja, Z. *et al.* Restoration of brain circulation and cellular functions hours post-mortem. *Nature* **568**, 336–343 (2019).
3. Charpak, S. & Audinat, E. Cardiac arrest in rodents: maximal duration compatible with a recovery of neuronal activity. *Proc. Natl. Acad. Sci. USA* **95**, 4748–4753 (1998).
4. Petrin, D. *et al.* Spreading depolarization and neuronal damage or survival in mouse neocortical brain slices immediately and 12 hours following middle cerebral artery occlusion. *J. Neurophysiol.* **121**, 1650–1663 (2019).
5. Dreier, J. P. & Reiffurth, C. The Stroke-Migraine Depolarization Continuum. *Neuron* **4**, 902–922 (2015).
6. Murphy, T. H., Li, P., Betts, K. & Liu, R. Two-photon imaging of stroke onset in vivo reveals that NMDA-receptor independent ischemic depolarization is the major cause of rapid reversible damage to dendrites and spines. *J. Neurosci.* **28**, 1756–1772 (2008).
7. Lipton, P. Ischemic cell death in brain neurons. *Physiol. Rev.* **79**, 1431–1568 (1999).
8. Somjen, G. G. Mechanisms of spreading depression and hypoxic spreading depression-like depolarization. *Physiol. Rev.* **81**, 1065–1096 (2001).
9. Dreier, J. P. *et al.* Is spreading depolarization characterized by an abrupt, massive release of gibbs free energy from the human brain cortex?. *Neuroscientist* **19**, 25–42 (2013).
10. Hartings, J. A., Rolli, M. L., Lu, X. C. M. & Tortella, F. C. Delayed secondary phase of peri-infarct depolarizations after focal cerebral ischemia: relation to infarct growth and neuroprotection. *J. Neurosci.* **23**, 11602–11610 (2003).
11. Aitken, P. G., Tombaugh, G. C., Turner, D. A. & Somjen, G. G. Similar propagation of SD and hypoxic SD-like depolarization in rat hippocampus recorded optically and electrically. *J. Neurophysiol.* **80**, 1514–1521 (1998).
12. Dzhala, V., Ben-Ari, Y. & Khazipov, R. Seizure accelerate anoxia-induced neuronal death in the neonatal rat hippocampus. *Ann. Neurol.* **48**, 632–640 (2000).
13. Joshi, I. & Andrew, R. D. Imaging anoxic depolarization during ischemia-like conditions in the mouse hemi-brain slice. *J. Neurophysiol.* **85**, 414–424 (2001).
14. Rader, R. K. & Lanthorn, T. H. Experimental ischemia induces a persistent depolarization blocked by decreased calcium and NMDA antagonists. *Neurosci. Lett.* **99**, 125–130 (1989).
15. Tanaka, E., Yamamoto, S., Kudo, Y., Mihara, S. & Higashi, H. Mechanisms underlying the rapid depolarization produced by deprivation of oxygen and glucose in rat hippocampal CA1 neurons in vitro. *J. Neurophysiol.* **78**, 891–902 (1997).
16. Toyoda, H., Kawano, T., Sato, H. & Kato, T. Cellular mechanisms underlying the rapid depolarization caused by oxygen and glucose deprivation in layer III pyramidal cells of the somatosensory cortex. *Neurosci. Res.* **1**, 6. https://doi.org/10.1016/j.neures.2020.03.003 (2020).
17. Anderson, T. R., Jarvis, C. R., Biedermann, A. J., Molnar, C. & Andrew, R. D. Blocking the anoxic depolarization protects without functional compromise following simulated stroke in cortical brain slices. *J. Neurophysiol.* **93**, 963–979 (2005).
18. Devin Brisson, C. & David Andrew, R. A neuronal population in hypothalamus that dramatically resists acute ischemic injury compared to neocortex. *J. Neurophysiol.* **108**, 419–430 (2012).
19. Jarvis, C. R., Anderson, T. R. & Andrew, R. D. Anoxic depolarization mediates acute damage independent of glutamate in neocortical brain slices. *Cereb. Cortex* **11**, 249–259 (2001).
20. Juzekaeva, E. *et al.* Preferential initiation and spread of anoxic depolarization in layer 4 of rat barrel cortex. *Front. Cell. Neurosci.* **11**, 00390. https://doi.org/10.3389/fncel.2017.00390 (2017).
21. Dzhala, V., Khalilov, I., Ben-Ari, Y. & Khazipov, R. Neuronal mechanisms of the anoxia-induced network oscillations in the rat hippocampus in vitro. *J. Physiol.* **536**, 521–531 (2001).
22. Obeidat, A. S., Jarvis, C. R. & Andrew, R. D. Glutamate does not mediate acute neuronal damage after spreading depression induced by O2/glucose deprivation in the hippocampal slice. *J. Cereb. Blood Flow Metab.* **20**, 412–422 (2000).

Content courtesy of Springer Nature, terms of use apply. Rights reserved

23. Tanaka, E., Yamamoto, S., Inokuchi, H., Isagai, T. & Higashi, H. Membrane dysfunction induced by in vitro ischemia in rat hippocampal CA1 pyramidal neurons. *J. Neurophysiol.* **81**, 1872–1880 (1999).
24. Tyzio, R. *et al.* Maternal oxytocin triggers a transient inhibitory switch in GABA signaling in the fetal brain during delivery. *Science* **314**, 1788–1792 (2006).
25. Centonze, D. *et al.* Ionic mechanisms underlying differential vulnerability to ischemia in striatal neurons. *Prog. Neurobiol.* **63**, 687–696 (2001).
26. Brisson, C. D., Lukewich, M. K. & Andrew, R. D. A distinct boundary between the higher brain's susceptibility to ischemia and the lower brain's resistance. *PLoS ONE* **8**, 0079589. https://doi.org/10.1371/journal.pone.0079589 (2013).
27. Senatorov, V. V. & Hu, B. Differential Na+-K+-ATPase activity in rat lemniscal and non-lemniscal auditory thalami. *J. Physiol.* **502**, 387–397 (1997).
28. Hamann, M., Rossi, D. J., Mohr, C., Andrade, A. L. & Attwell, D. The electrical response of cerebellar Purkinje neurons to simulated ischaemia. *Brain* **128**, 2408–2420 (2005).
29. Brisson, C. D., Hsieh, Y. T., Kim, D., Jin, A. Y. & Andrew, R. D. Brainstem neurons survive the identical ischemic stress that kills higher neurons: Insight to the persistent vegetative state. *PLoS ONE* **9**, 0096585. https://doi.org/10.1371/journal.pone.0096585 (2014).
30. Dreier, J. P., Lemale, C. L., Kola, V., Friedman, A. & Schoknecht, K. Spreading depolarization is not an epiphenomenon but the principal mechanism of the cytotoxic edema in various gray matter structures of the brain during stroke. *Neuropharmacology* **134**, 189–207 (2018).
31. Juzekaeva, E., Gainutdinov, A., Mukhtarov, M. & Khazipov, R. Dynamics of the hypoxia—induced tissue edema in the rat barrel cortex in vitro. *Front. Cell. Neurosci.* **12**, 00502. https://doi.org/10.3389/fncel.2018.00502 (2018).
32. Risher, W. C., Andrew, R. D. & Kirov, S. A. Real-time passive volume responses of astrocytes to acute osmotic and ischemic stress in cortical slices and in vivo revealed by two-photon microscopy. *Glia* **57**, 207–221 (2009).
33. Andrew, R. D., Labron, M. W., Boehnke, S. E., Carnduff, L. & Kirov, S. A. Physiological evidence that pyramidal neurons lack functional water channels. *Cereb. Cortex* **17**, 787–802 (2007).
34. Kumar, V., Naik, R. S., Hillert, M. & Klein, J. Effects of chloride flux modulators in an in vitro model of brain edema formation. *Brain Res.* **1122**, 222–229 (2006).
35. Tyzio, R. *et al.* Inhibitory actions of the gamma-aminobutyric acid in pediatric Sturge-Weber syndrome. *Ann. Neurol.* **66**, 209–218 (2009).
36. Luhmann, H. J., Mudrick-Donnon, L. A., Mittmann, T. & Heinemann, U. Ischaemia-induced Long-term Hyperexcitability in Rat Neocortex. *Eur. J. Neurosci.* **7**, 180–191 (1995).
37. Hamill, O. P., Marty, A., Neher, E., Sakmann, B. & Sigworth, F. J. Improved patch-clamp techniques for high-resolution current recording from cells and cell-free membrane patches. *Pflügers Arch. Eur. J. Physiol.* **391**, 85–100 (1981).
38. Basarsky, T. A., Duffy, S. N., Andrew, R. D. & MacVicar, B. A. Imaging spreading depression and associated intracellular calcium waves in brain slices. *J. Neurosci.* **18**, 7189–7199 (1998).
39. Kass, I. S. & Lipton, P. Calcium and long-term transmission damage following anoxia in dentate gyrus and CA1 regions of the rat hippocampal slice. *J. Physiol.* **378**, 313–334 (1986).
40. Kawai, K. *et al.* Global cerebral ischemia associated with cardiac arrest in the rat: I. Dynamics of early neuronal changes. *J. Cereb. Blood Flow Metab.* **12**, 238–249 (1992).
41. Hübel, N., Andrew, R. D. & Ullah, G. Large extracellular space leads to neuronal susceptibility to ischemic injury in a Na+/K + pumps–dependent manner. *J. Comput. Neurosci.* **40**, 177–192 (2016).
42. Ullah, G., Wei, Y., Dahlem, M. A., Wechselberger, M. & Schiff, S. J. The role of cell volume in the dynamics of seizure, spreading depression, and anoxic depolarization. *PLoS Comput. Biol.* **11**, 1004414. https://doi.org/10.1371/journal.pcbi.1004414 (2015).
43. Watson, G. B., Rader, R. K. & Lanthorn, T. H. Epileptiform activity in vitro can produce long-term synaptic failure and persistent neuronal depolarization. *Brain Res.* **498**, 81–88 (1989).
44. Balestrino, M. & Somjen, G. G. Chlorpromazine protects brain tissue in hypoxia by delaying spreading depression-mediated calcium influx. *Brain Res.* **385**, 219–226 (1986).
45. Young, J. N., Aitken, P. G. & Somjen, G. G. Calcium, magnesium, and long-term recovery from hypoxia in hippocampal tissue slices. *Brain Res.* **548**, 343–345 (1991).
46. Onorati, M. *et al.* Zika virus disrupts phospho-TBK1 localization and mitosis in human neuroepithelial stem cells and radial glia. *Cell Rep.* **16**, 2576–2592 (2016).
47. Verwer, R. W. H. *et al.* Cells in human postmortem brain tissue slices remain alive for several weeks in culture. *FASEB J.* **16**, 54–60 (2002).
48. Viel, J. J., McManus, D. Q., Cady, C., Evans, M. S. & Brewer, G. J. Temperature and time interval for culture of postmortem neurons from adult rat cortex. *J. Neurosci. Res.* **64**, 311–321 (2001).
49. Hossmann, K. A. & Sato, K. Recovery of neuronal function after prolonged cerebral ischemia. *Science* **168**, 375–376 (1970).
50. Hossmann, K. A. & Zimmermann, V. Resuscitation of the monkey brain after 1 H complete ischemia. I. Physiological and morphological observations. *Brain Res.* **81**, 59–74 (1974).
51. Kleihues, P., Hossmann, K. A., Pegg, A. E., Kobayashi, K. & Zimmermann, V. Resuscitation of the monkey brain after one hour complete ischemia. III. Indications of metabolic recovery. *Brain Res.* **95**, 61–73 (1975).
52. Zimmermann, V. & Hossmann, K. A. Resuscitation of the monkey brain after one hour's complete ischemia. II. Brain water and electrolytes. *Brain Res.* **85**, 1–11 (1975).
53. Benedek, A. *et al.* Use of TTC staining for the evaluation of tissue injury in the early phases of reperfusion after focal cerebral ischemia in rats. *Brain Res.* **1116**, 159–165 (2006).
54. Risher, W. C., Ard, D., Yuan, J. & Kirov, S. A. Recurrent spontaneous spreading depolarizations facilitate acute dendritic injury in the ischemic penumbra. *J. Neurosci.* **30**, 9859–9868 (2010).
55. Risher, W. C., Croom, D. & Kirov, S. A. Persistent astroglial swelling accompanies rapid reversible dendritic injury during stroke-induced spreading depolarizations. *Glia* **60**, 1709–1720 (2012).
56. Vanhareveld, A. Changes in volume of cortical neuronal elements during asphyxiation. *Am. J. Physiol.* **191**, 233–242 (1957).
57. Elkin, B. S., Shaik, M. A. & Morrison, B. Fixed negative charge and the Donnan effect: a description of the driving forces associated with brain tissue swelling and oedema. *Philos. Trans. R. Soc. A* **368**, 585–603 (2010).
58. MacGregor, D. G., Avshalumov, M. V. & Rice, M. E. Brain edema induced by in vitro ischemia: causal factors and neuroprotection. *J. Neurochem.* **85**, 1402–1411 (2003).
59. Stokum, J. A., Gerzanich, V. & Simard, J. M. Molecular pathophysiology of cerebral edema. *J. Cereb. Blood Flow Metab.* **36**, 513–538 (2016).
60. Khazipov, R. *et al.* Atlas of the postnatal rat brain in stereotaxic coordinates. *Front. Neuroanat.* **9**, 00161. https://doi.org/10.3389/fnana.2015.00161 (2015).
61. Aitken, P. G., Fayuk, D., Somjen, G. G. & Turner, D. A. Use of intrinsic optical signals to monitor physiological changes in brain tissue slices. *Methods A* **18**, 91–103 (1999).

Content courtesy of Springer Nature, terms of use apply. Rights reserved

Acknowledgements
We thank David Jappy for editing the manuscript.

Author contributions
R.K. conceived the project. E.J., A.G. and M.M. performed the experiments. A.G., E.J. and M.M. analyzed the data. R.K. wrote the manuscript. All authors reviewed the manuscript.

Funding
This work was supported by RSF #17-15-01271-P (electrophysiology and imaging) and the subsidy allocated to Kazan Federal University for the state assignment in the sphere of scientific activities #0671-2020-0059 (development of the analytical software) and performed within the Program of Competitive Growth of Kazan University.

Competing interests
The authors declare no competing interests.

Additional information
Correspondence and requests for materials should be addressed to R.K.

Reprints and permissions information is available at www.nature.com/reprints.

Publisher's note Springer Nature remains neutral with regard to jurisdictional claims in published maps and institutional affiliations.

Open Access This article is licensed under a Creative Commons Attribution 4.0 International License, which permits use, sharing, adaptation, distribution and reproduction in any medium or format, as long as you give appropriate credit to the original author(s) and the source, provide a link to the Creative Commons licence, and indicate if changes were made. The images or other third party material in this article are included in the article's Creative Commons licence, unless indicated otherwise in a credit line to the material. If material is not included in the article's Creative Commons licence and your intended use is not permitted by statutory regulation or exceeds the permitted use, you will need to obtain permission directly from the copyright holder. To view a copy of this licence, visit http://creativecommons.org/licenses/by/4.0/.

© The Author(s) 2020

Content courtesy of Springer Nature, terms of use apply. Rights reserved

Terms and Conditions

Springer Nature journal content, brought to you courtesy of Springer Nature Customer Service Center GmbH (“Springer Nature”).
Springer Nature supports a reasonable amount of sharing of research papers by authors, subscribers and authorised users (“Users”), for small-scale personal, non-commercial use provided that all copyright, trade and service marks and other proprietary notices are maintained. By accessing, sharing, receiving or otherwise using the Springer Nature journal content you agree to these terms of use (“Terms”). For these purposes, Springer Nature considers academic use (by researchers and students) to be non-commercial.
These Terms are supplementary and will apply in addition to any applicable website terms and conditions, a relevant site licence or a personal subscription. These Terms will prevail over any conflict or ambiguity with regards to the relevant terms, a site licence or a personal subscription (to the extent of the conflict or ambiguity only). For Creative Commons-licensed articles, the terms of the Creative Commons license used will apply.
We collect and use personal data to provide access to the Springer Nature journal content. We may also use these personal data internally within ResearchGate and Springer Nature and as agreed share it, in an anonymised way, for purposes of tracking, analysis and reporting. We will not otherwise disclose your personal data outside the ResearchGate or the Springer Nature group of companies unless we have your permission as detailed in the Privacy Policy.
While Users may use the Springer Nature journal content for small scale, personal non-commercial use, it is important to note that Users may not:

1. use such content for the purpose of providing other users with access on a regular or large scale basis or as a means to circumvent access control;
2. use such content where to do so would be considered a criminal or statutory offence in any jurisdiction, or gives rise to civil liability, or is otherwise unlawful;
3. falsely or misleadingly imply or suggest endorsement, approval , sponsorship, or association unless explicitly agreed to by Springer Nature in writing;
4. use bots or other automated methods to access the content or redirect messages
5. override any security feature or exclusionary protocol; or
6. share the content in order to create substitute for Springer Nature products or services or a systematic database of Springer Nature journal content.

In line with the restriction against commercial use, Springer Nature does not permit the creation of a product or service that creates revenue, royalties, rent or income from our content or its inclusion as part of a paid for service or for other commercial gain. Springer Nature journal content cannot be used for inter-library loans and librarians may not upload Springer Nature journal content on a large scale into their, or any other, institutional repository.
These terms of use are reviewed regularly and may be amended at any time. Springer Nature is not obligated to publish any information or content on this website and may remove it or features or functionality at our sole discretion, at any time with or without notice. Springer Nature may revoke this licence to you at any time and remove access to any copies of the Springer Nature journal content which have been saved.
To the fullest extent permitted by law, Springer Nature makes no warranties, representations or guarantees to Users, either express or implied with respect to the Springer nature journal content and all parties disclaim and waive any implied warranties or warranties imposed by law, including merchantability or fitness for any particular purpose.
Please note that these rights do not automatically extend to content, data or other material published by Springer Nature that may be licensed from third parties.
If you would like to use or distribute our Springer Nature journal content to a wider audience or on a regular basis or in any other manner not expressly permitted by these Terms, please contact Springer Nature at

onlineservice@springernature.com

frontiers | Frontiers in Cellular Neuroscience

TYPE Original Research
PUBLISHED 09 March 2023
DOI 10.3389/fncel.2023.1106268

Check for updates

OPEN ACCESS

EDITED BY
Yevgeny Berdichevsky,
Lehigh University, United States

REVIEWED BY
Helen E. Scharfman,
Nathan Kline Institute for Psychiatric Research, United States
Michel J.A.M. van Putten,
University of Twente, Netherlands

*CORRESPONDENCE
Roustem Khazipov
✉ roustem.khazipov@inserm.fr

†These authors have contributed equally to this work

SPECIALTY SECTION
This article was submitted to Cellular Neuropathology, a section of the journal Frontiers in Cellular Neuroscience

RECEIVED 23 November 2022
ACCEPTED 16 February 2023
PUBLISHED 09 March 2023

CITATION
Gainutdinov A, Juzekaeva E, Mukhtarov M and Khazipov R (2023) Anoxic spreading depolarization in the neonatal rat cortex *in vitro*.
Front. Cell. Neurosci. 17:1106268.
doi: 10.3389/fncel.2023.1106268

COPYRIGHT
© 2023 Gainutdinov, Juzekaeva, Mukhtarov and Khazipov. This is an open-access article distributed under the terms of the Creative Commons Attribution License (CC BY). The use, distribution or reproduction in other forums is permitted, provided the original author(s) and the copyright owner(s) are credited and that the original publication in this journal is cited, in accordance with accepted academic practice. No use, distribution or reproduction is permitted which does not comply with these terms.

Anoxic spreading depolarization in the neonatal rat cortex *in vitro*

Azat Gainutdinov[1,2†], Elvira Juzekaeva[1†], Marat Mukhtarov[1] and Roustem Khazipov[1,2*]

[1]Laboratory of Neurobiology, Institute of Fundamental Medicine and Biology, Kazan Federal University, Kazan, Russia, [2]INMED—INSERM, Aix-Marseille University, Marseille, France

Anoxic spreading depolarization (aSD) is a hallmark of ischemic injury in the cerebral cortex. In adults, aSD is associated with rapid and nearly complete neuronal depolarization and loss of neuronal functions. While ischemia also evokes aSD in the immature cortex, developmental aspects of neuronal behavior during aSD remain largely unknown. Here, using oxygen-glucose deprivation (OGD) ischemia model in slices of the postnatal rat somatosensory cortex, we found that immature neurons displayed much more complex behaviors: they initially moderately depolarized during aSD, then transiently repolarised (for up to tens of minutes), and only then passed to terminal depolarization. The ability to fire action potentials was maintained in neurons mildly depolarized during aSD without reaching the level of depolarization block, and these functions were regained in the majority of immature neurons during post-aSD transient repolarization. The amplitude of depolarization and the probability of depolarization block during aSD increased, whereas transient post-SD repolarization levels and duration, and associated recovery in neuronal firing decreased with age. By the end of the first postnatal month, aSD acquired an adult-like phenotype, where depolarization during aSD merged with terminal depolarization and the phase of transient recovery was lost. Thus, changes in neuronal function during aSD undergo remarkable developmental changes that may contribute to lower susceptibility of the immature neurons to ischemia.

KEYWORDS

patch-clamp, membrane potential, ischemia, somatosensory cortex, spreading depolarization, neonate, development

Introduction

Anoxic Spreading Depolarization (aSD) is a hallmark of ischemic brain injury (Andrew et al., 2022). aSD develops within several minutes after metabolic deprivation and manifests as a wave of collective and nearly complete neuronal depolarization, and depression of electrical activity largely due to depolarization block of action potentials (APs; Somjen, 2001; Dreier and Reiffurth, 2015). aSD is associated with the large negative shift of the extracellular field potential and an increase in tissue light transmittance caused by cytotoxic cell edema (Rader and Lanthorn, 1989; Aitken et al., 1998; Dzhala et al., 2000; Joshi and Andrew, 2001; Juzekaeva et al., 2017, 2018, 2020; Toyoda et al., 2021; Vinokurova et al., 2022). aSD is a highly energy consuming event which aggravates metabolic deficits and initiates intracellular cascades leading to cell death (Somjen, 2001; Strong et al., 2002; Hartings et al., 2003, 2017; Dreier, 2011; Dreier et al., 2013, 2022; Dreier and Reiffurth, 2015). In the OGD model of brain ischemia using submerged brain slices, which simulates the condition of severe global brain ischemia, cortical neurons typically undergo terminal SD to zero mV without recovery (Rader and Lanthorn, 1989; Tanaka et al., 1997; Toyoda et al., 2021; Andrew et al., 2022).

While an immature brain is more tolerant to metabolic deprivation, ischemic/hypoxic brain damage remains a major problem in peri- and neonatology (Saugstad, 2011; Douglas-Escobar and Weiss, 2015). As in adults, aSD occurs during metabolic deprivation in the neonatal cortex and heralds neuronal death. However, in neonates, aSD occurs at much longer delays (up to tens of minutes in the neonatal neocortex and ∼1 h in the fetal hippocampus at term) from the onset of hypoxia/OGD than in the adults consistent with higher tolerance of the immature brain to metabolic deprivation (Cherubini et al., 1989; Luhmann and Kral, 1997; Dzhala et al., 2000, 2001; Tyzio et al., 2006), and with lower proneness of the neonatal cortex to SD in general (Bures, 1957; Schade, 1959; Richter et al., 1998; Hertelendy et al., 2019; Andrew et al., 2022). However, aSD in the neocortex during the neonatal period [P0–10 in rodents, which corresponds to a period from mid-gestation to term in human fetus (Khazipov and Luhmann, 2006; Clancy et al., 2007; Colonnese et al., 2010; Colonnese and Khazipov, 2012; Luhmann and Khazipov, 2018; Khazipov and Milh, 2018)] at the cellular level remains largely unexplored. Here, we addressed this question using whole-cell recordings from L4 neurons in slices of the somatosensory whisker-related barrel cortex from 3 to 31 days old rats in the OGD model. We chose this area because it is highly sensitive to ischemia and prone to SD (Lin et al., 1990; Bogdanov et al., 2016; Kaufmann et al., 2017; Juzekaeva et al., 2017, 2020). Our main finding is that neonatal neurons only moderately depolarize during aSD, then transiently repolarise, and only then pass to terminal depolarization. The ability to fire action potentials persists in neurons showing mild depolarization during aSD without reaching the level of depolarization block, and these functions are regained in the majority of immature neurons during post-aSD transient repolarization phase. Thus, immature neurons display protracted in time and complex aSD phenotype with a phase of transient recovery. We suggest that these developmentally unique features of aSD contribute to higher tolerance of the immature brain to ischemia.

Materials and methods

Brain slices

Wistar rats (3–31 days old) of either sex were used. Animals were decapitated under isoflurane anesthesia (5%), the brain was rapidly removed and placed in ice-cold (2–5°C) oxygenated (95% O_2–5% CO_2) artificial cerebrospinal fluid (ACSF) of the following composition (in mM): NaCl 126, KCl 3.5, $CaCl_2$ 2, $MgCl_2$ 1.3, $NaHCO_3$ 25, NaH_2PO_4 1.2, and glucose 20 (pH 7.4). Four hundred μm thick thalamocortical slices were cut using a PELCO easiSlicer^{TM} vibratome (Ted Pella, Inc., Redding, CA, USA). A total of n = 58 slices obtained from 43 rats were used (1 slice/rat: n = 29 rats; 2 slices/rat: n = 13 rats; 3 slices/rat: n = 1 rat). Data from all slices were pooled for analysis; n indicates the number of slices. Slices containing the barrel cortex were selected by anatomical coordinates (Khazipov et al., 2015) and the presence of barrel structures in L4. Slices were first kept in ACSF for 30 min at 32°C and then at room temperature (20–22°C) for at least 1 h before use. For recordings, slices were placed into a submerged chamber and superfused with oxygenated ACSF at 30–32°C at a flow rate of 10 ml/min. Oxygen/glucose deprivation (OGD) was induced by superfusion with ACSF in which N_2 replaced O_2 and sucrose replaced glucose at equimolar concentration.

Electrophysiological recordings

For electrophysiological recordings, slices were placed in the recording chamber under an upright microscope BX51WI (Olympus, Tokyo, Japan) equipped with a dry 4×/0.10 Plan N objective and a water immersed 40×/0.80 LUMPlanFL N objective. L4 neurons were identified at 40× magnification using infrared-differential interference contrast (IR-DIC) microscopy. Visual patch-clamp recordings were performed using a MultiClamp 700B (Axon Instruments, Union City, CA, USA) amplifier as described previously (Juzekaeva et al., 2018). Patch electrodes were made from borosilicate glass capillaries (BF150-86-10, Sutter Instrument, Novato, CA, USA) and had a resistance of 4–7 MΩ. The pipette (intracellular) solution contained (in mM) 131 potassium gluconate, 4 KCl, 10 HEPES, 10 phosphocreatine, 4 MgATP, and 0.3 Na_2GTP (adjusted to pH 7.3 with KOH). 200-ms suprathreshold depolarizing current pulses were applied every 10 s to examine the ability of neurons to fire APs and monitor the membrane resistance (R_m). Extracellular DC recordings of the local field potentials (LFP) were performed in the barrel cortex using glass pipette electrodes pulled from borosilicate glass capillaries (BF150-86-10, Sutter Instrument, Novato, CA, USA) with resistances of 2–3 MΩ when filled with ACSF. LFP recordings were performed in voltage-clamp DC mode, then currents were inverted and voltage calibrated using 5 mV steps. Extracellular and patch-clamp recordings were digitized at 32 kHz with a Digidata 1440A interface card (Axon Instruments) and analyzed offline using MATLAB (MathWorks, Natick, MA, USA) routines. Optical intrinsic signal (OIS) recordings were performed at 4× magnification. The boundaries of layer 4 were discerned by barrel-shaped structures at 4× magnification and high cell density in layer 4 at 40× magnification. The slice was illuminated by a halogen lamp with a 775 nm bandpass filter. Images were acquired using a QIClick-R-F-M-12 CCD camera (QImaging, Surrey, BC, Canada) at 696 × 520 or 1,392 × 1,040 pixel resolution at 1 frame/2.5 s acquisition rate.

Data analysis

Experimental data were processed using MATLAB environment (MathWorks, USA). Matlab's Signal Processing Toolbox functions were used for peak detection procedures. Patch-clamp E_m recordings were down-sampled to 1 Hz and filtered using a median filter within sliding 30 s window with 1 s time step to eliminate responses to depolarizing current steps. aSD was detected as a wave of E_m depolarization occurring in association with characteristic negative LFP shifts and OIS signals (Juzekaeva et al., 2020). The time corresponding to the peak depolarization during aSD was defined as aSD time. aSD amplitude was defined as a difference between E_m at the aSD peak and the

baseline E_m values between -3 and -1 min time interval before the aSD peak. The term of transient recovery (TR) was applied for a phase of transient E_m repolarization between aSD and terminal depolarization (TD). TR duration was defined as a time period between aSD peak (TR onset = time of aSD peak) and transition to TD was determined at the peak of the first E_m derivative (dE_m/dt, dt = 1 min). The peak of E_m repolarization during TR was taken as the TR time reference point. Action potentials (AP) in response to suprathreshold current steps were detected from raw signals using *peak detection* function as events with the peak prominence of >3 mV and 5 ms minimum inter-peak interval. Two neurons at P25 with the electrophysiological phenotype of fast spiking interneurons showed no differences in response to OGD and were pooled with other neurons in the P25–31 age group. DC LFP signals were down-sampled to 1 kHz and low-pass filtered using 1 s sliding window. OIS was calculated using the first-frame subtraction approach: OIS (t) = (I (t) − I0)/I0, where I (t)—pixel intensity at the moment t, I0—time-averaged pixel intensity in the preconditioned control period (1 min). The resulting frames were filtered with a 2 × 2 Gaussian filter. Regions of interest (ROIs) were selected as square areas near the recording site. OIS traces were calculated as the average OIS signal in the selected ROIs.

Statistical analysis

Statistical analysis was performed using the MATLAB Statistics toolbox. Pooled data are presented as median, 25th (Q1), and 75th (Q3) percentiles in boxplots or shaded areas. A two-sided Wilcoxon rank sum test was performed to assess the difference between groups. For testing binomial data and proportions we used Two Sample Z-Test for Proportions. Correlations were calculated as Spearman's correlation coefficient with the exact *p*-value. The level of significance was kept at $p < 0.05$.

Results

In the present study, we explored the dynamics of the resting membrane potential (E_m) and neuronal firing during OGD in slices of the barrel cortex of rats aged from P3 to P31 using whole-cell current-clamp recordings of L4 neurons and concomitant extracellular recordings of LFP, and optical intrinsic signals (OIS) imaging. Perfusion with OGD-solution evoked aSD in all neurons at all ages. However, aSD amplitude and aSD delay after OGD onset, and post-aSD E_m dynamics were variable and age-dependent (**Figure 1**). E_m dynamics aligned against aSD peak (marked by red dots) and sorted by the aSD amplitude in neurons from newborn (P3–8) and juvenile (P16–31) rats are shown in **Figures 1A,B**, respectively. Overall, in the newborn animals, aSD was smaller in amplitude, and was typically followed by a remarkable phase of transient recovery (TR) of E_m before a passage to terminal plateau depolarization (TD) near 0 mV. The level and duration of TR were more pronounced in the cases with low-amplitude aSDs, where TR could last for up to 15 min. Only a few neurons with large-amplitude aSD showed "adult-like" aSD phenotype of permanent depolarization without TR in the newborn animals. In contrast, neurons in juvenile rats typically displayed large amplitude aSDs without TR, or, less frequently, with a short and small TR (**Figure 1B**). At the group level, aSD delay from the OGD onset shortened (**Figure 1C**), whereas aSD amplitude increased (**Figure 1D**) with the animals' age. Thus, aSD in the immature neurons is smaller in amplitude and displays a unique intermediate phase of TR before a passage to TD.

We further explored changes in neuronal firing by injecting suprathreshold depolarizing current steps. Exemplary whole-cell recordings from L4 neurons in P4 and P30 rats are presented in **Figure 2**. P4 neuron displayed small-amplitude aSD associated with a mild transient drop in membrane resistance (R_m) followed by 10 min-long TR with a regain in R_m values (**Figures 2A,C**). TR was followed by nearly complete depolarization during TD. Action potentials (APs) could be reliably evoked by depolarizing current in this neuron not only through the pre-aSD period, but also during aSD and TR phase (*nota bene*: no depolarization block in this case!), and were lost only after a passage to TD (**Figure 2E**, **Supplementary Figure 1**). In a P30 neuron (**Figure 2B**), membrane potential rapidly dropped to −20 mV, then showed brief and little recovery during TR phase, followed by TD to 0 mV, during which R_m displayed an apparent increase to ∼1 GOhm (**Figure 2D**) presumably reflecting a passage from whole-cell to outside-out due to tissue displacement caused by aSD-triggered edema (Juzekaeva et al., 2018, 2020). In the P30 neuron, APs were completely suppressed, without any recovery starting from aSD (**Figure 2F**, **Supplementary Figure 1**). Thus, while the P30 neuron displayed an "adult-like" phenotype of rapid and irreversible E_m loss during aSD together with an irreversible depression of APs, P4 neuron showed persistence of APs during aSD and TR, pointing to a qualitative difference of aSD in the immature neuron. All aSDs of different amplitudes were associated with a characteristic negative local field potential shift (**Figure 3B**), and a concomitant wave of increase in the brain tissue light transparency propagating across the entire slice of the cortex during OIS recordings (**Figures 3C,D**). Peak depolarization during aSD in L4 neurons was attained simultaneously with the peak negativity of the local field potential and the peak of light transparency during aSD wave in the vicinity of the recorded neuron (**Figure 3E**).

We next analyzed in detail the age-dependence in the depolarization level attained during aSD and associated changes in the neuronal firing (**Figure 4**). In the newborn animals (P3–8), neurons depolarized, on average, to ∼−40 mV, and APs persisted in their vast majority (73%; n = 16 of 22 cells) at the aSD peak (**Figure 4A**, see also AP raster plots on **Figure 4B**). In the juvenile rats, peak depolarization during aSD attained on average −18 mV at P16–24, and −7 mV at P25–31. Along with a developmental increase in the aSD E_m levels, the proportion of neurons maintaining the ability to fire APs during aSD decreased to 27% at P16–24 (n = 4 of 15 cells), and to 10% at P25–31 (n = 1 of 10 cells; **Figures 4A,B**). Loss of neuronal firing depended on the depolarization level attained during aSD within all age groups, as illustrated by responses to depolarizing steps in different cells on insets in **Figure 4A**. To estimate the AP inactivation threshold, we analyzed neuronal firing during the rising aSD phase. We found that failure in evoking APs by depolarizing current

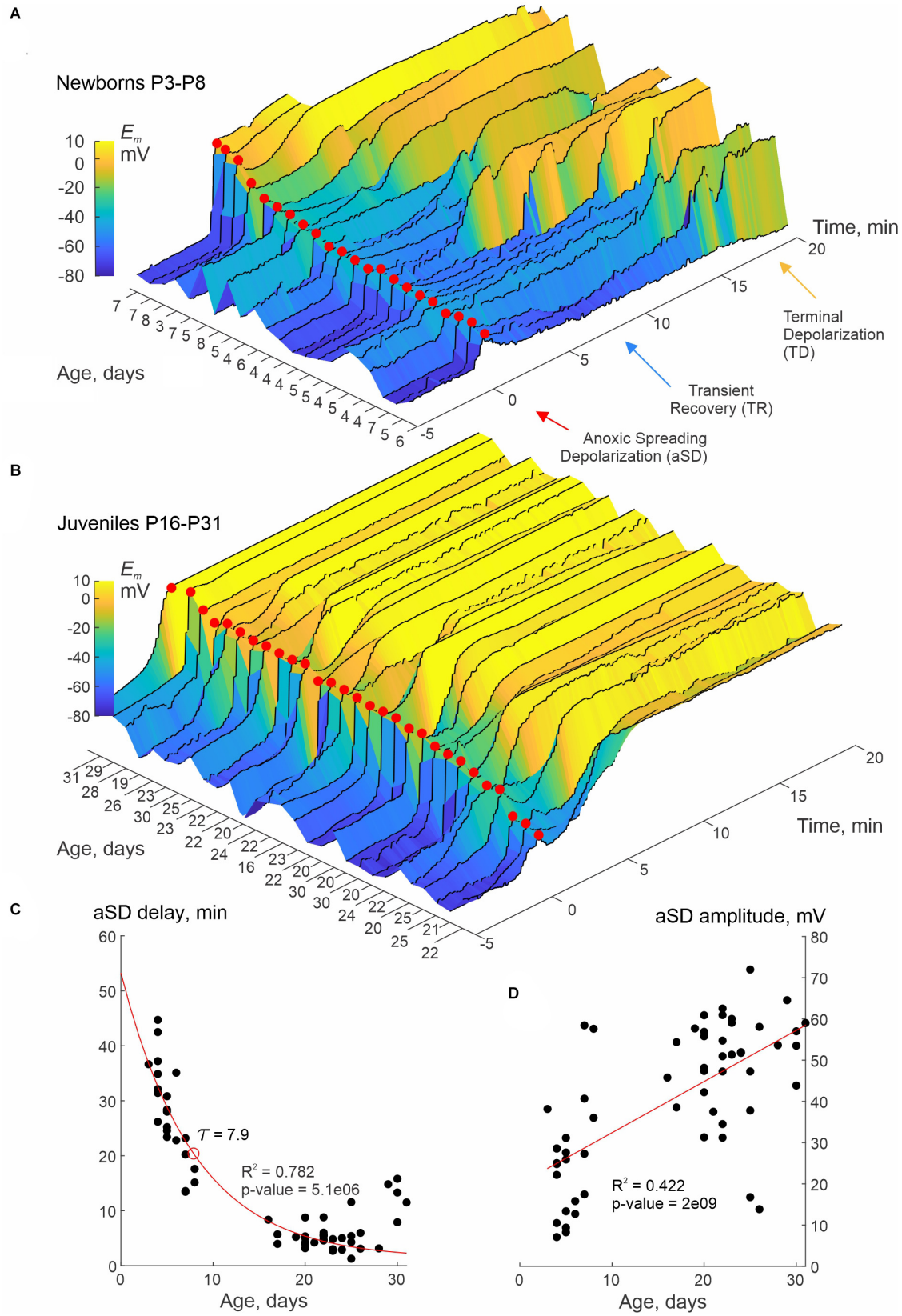

FIGURE 1
Smaller aSD amplitude and transient recovery of membrane potential in neurons of newborn rat cerebral cortex. **(A,B)** Dynamics of membrane potential (E_m) in L4 neurons recorded in whole-cell current-clamp mode during oxygen-glucose deprivation (OGD) in slices of somatosensory cortex prepared from neonatal (P3–8) **(A)** and juvenile (P16–31) **(B)** rats. The E_m signal was low-pass filtered with a median filter using a sliding
(*Continued*)

FIGURE 1 (Continued)
window of 30 s and increment of 1 s to eliminate spikes and the responses to depolarizing current steps. Color-coded E_m values are plotted with reference to aSD (T = 0, red dots). Each trace corresponds to an individual neuron, the age of the animal is indicated on the left horizontal axis. Note the smaller aSD amplitude and the phase of transient E_m recovery (TR) before the transition to terminal depolarization (TD) in the neonatal group. Pooled data from n = 22 **(A)** and n = 29 **(B)** neurons. In some cases, the recordings stopped when the TD reached a plateau. **(C,D)** Delay of aSD peak from the OGD onset **(A)** and aSD amplitude **(B)** as a function of age. Each dot corresponds to an individual neuron. The aSD amplitude was calculated from the baseline E_m values between −3 and −1 min time interval before the aSD peak. The red lines show exponential **(A)** and linear **(B)** regression. Pooled data from n = 58 neurons from P3 to P31 rats.

steps occurred when E_m attained ∼−30 mV (**Figure 4C**). Thus, loss of neuronal firing during aSD critically depends on whether neuronal depolarization attains AP inactivation threshold, which barely occurs in the newborn neurons showing mainly moderate depolarization during aSD.

The phase of transient recovery in E_m and neuronal firing also showed age-dependence. Neurons from newborn rats displayed more negative TR E_m values and longer duration TR phase, and more frequently maintained AP firing than neurons from the juvenile group (**Figures 5A,B**; see also **Figures 2** and **4B**). Group data on the amplitude and time of TR at its peak negativity (the latter taken as a time reference point) and corresponding values of aSD and TD at their onset, neuronal firing during the TR phase, and age-dependence of TR amplitude and duration are summarized in **Figure 5C**. Noteworthy, the level and duration of TR negatively correlated with aSD amplitude and were more prominent in the newborn animals (**Figure 5C**, left and bottom violin plots). Also, TR lasted longer in cells with more negative levels of E_m recovery, and this was associated with longer duration of neuronal firing during the TR phase (**Figures 5D,E**). Similar to aSD, the ability of cells to fire APs during the TR phase depended on whether the cell repolarized below the AP inactivation threshold at around -30 mV, which typically occurred in the newborn group (**Figures 5C,D**). The final TD E_m values also showed an age dependence, reaching more negative values at P3–P8: −7.6 (−14.7 − +0.4) mV (n = 17) than at P16–P24: +4.82 (−2.40 − +7.6) mV (n = 22; p = 0.00055) and at P25–P31: +10.5 (+0.0 − +14.6) mV (n = 11; p = 0.00038).

Discussion

The main finding of the present study is that aSD has several developmentally unique features, including graded levels of depolarization and long-lasting post-aSD phase of transient repolarization preceding TD in the newborn cortical neurons. Furthermore, neuronal functions such as the ability to generate APs are barely depressed during neonatal aSD and TR phase. These results highlight a critical developmental difference in the response of the immature brain to metabolic deprivation and significantly broaden the SD spectrum from a developmental perspective.

Based on studies in the adult brain, aSD has been classically viewed as a binary process, during which neurons rapidly and completely lose their membrane potential (Rader and Lanthorn, 1989; Tanaka et al., 1997; Somjen, 2001; Dreier and Reiffurth, 2015; Toyoda et al., 2021; Andrew et al., 2022). Generative mechanisms of aSD are fundamentally similar to SD in other models and conditions, and involve an increase in extracellular potassium, glutamate, and activation of voltage and ligand—gated conductances (Leao, 1944, 1947; Somjen, 2001; Dreier, 2011; Pietrobon and Moskowitz, 2014; Ayata and Lauritzen, 2015; Dreier and Reiffurth, 2015; Hartings et al., 2017; Andrew et al., 2022). While E_m repolarizes after SD in the metabolically preserved tissue with a pivotal contribution of Na, K—ATPase, under conditions of metabolic deprivation aSD is associated with permanent depolarization as energy sources to fuel Na, K—ATPase are limited. We found that in the immature neurons, aSD was associated with only mild levels of depolarization and was followed by transient repolarization during TR-phase. The stationary state of complete E_m loss, which characterizes full-size aSD in adult neurons, was achieved only during the subsequent TD-phase. Small amplitude aSD likely produces smaller disturbance in the ionic gradients and thus less aggravates the metabolic status of the immature neurons than full-size aSD, leaving energy sources fueling Na, K—ATPase to restore E_m after aSD during the TR phase. This is consistent with the inverse relationships between aSD amplitude and TR: indeed, TR was more prominent in neurons with small amplitude aSDs. Several developmental factors may contribute to unique aSD features in neonates. First, immature neurons have lower metabolic rate and thus are more tolerant to metabolic deprivation consistent with much longer aSD delays than in adults (Cherubini et al., 1989; Luhmann and Kral, 1997; Dzhala et al., 2000, 2001; Tyzio et al., 2006). Second, cortex in the newborns is less prone to SD in general, that could be due to large extracellular space, low levels of synaptic connectivity, the small density of ionic channels, and their different developmental properties (Bures, 1957; Schade, 1959; Richter et al., 1998; Hertelendy et al., 2019; Andrew et al., 2022). We propose that a combination of these developmental factors endows immature neurons with on one hand, higher tolerance to metabolic deprivation, and on the other hand—a lower ability to support mutual depolarization *via* synaptic and ephaptic mechanisms in the SD genesis, explaining small aSD amplitude and TR in the immature neurons. Importantly, these unique developmental aSD features could be only revealed in the present study using whole-cell E_m recordings. aSD *per se* was also reliably detected as a characteristic negative shift of the extracellular field potential and increase in tissue transparency during OIS recordings [**Figure 3** and References Luhmann and Kral, 1997; Dzhala et al., 2000, 2001; Tyzio et al., 2006)], but the magnitude of these signals weakly correlated with the level of neuronal depolarization during aSD (**Supplementary Figure 1**). Also, TR and TD did not have clear manifestations during extracellular field potential and OIS recordings. Because we performed whole-cell recordings from only one neuron in the preparation, we cannot conclude whether the level of depolarization during aSD, level and duration of TR, and transition to TD were uniform in the entire neuronal population. Moreover, the lack of extracellular LFP and OIS manifestations suggests that TR duration and transition to TD are likely desynchronized between neurons. The desynchronized transition to TD in the immature cortex may result from metabolic

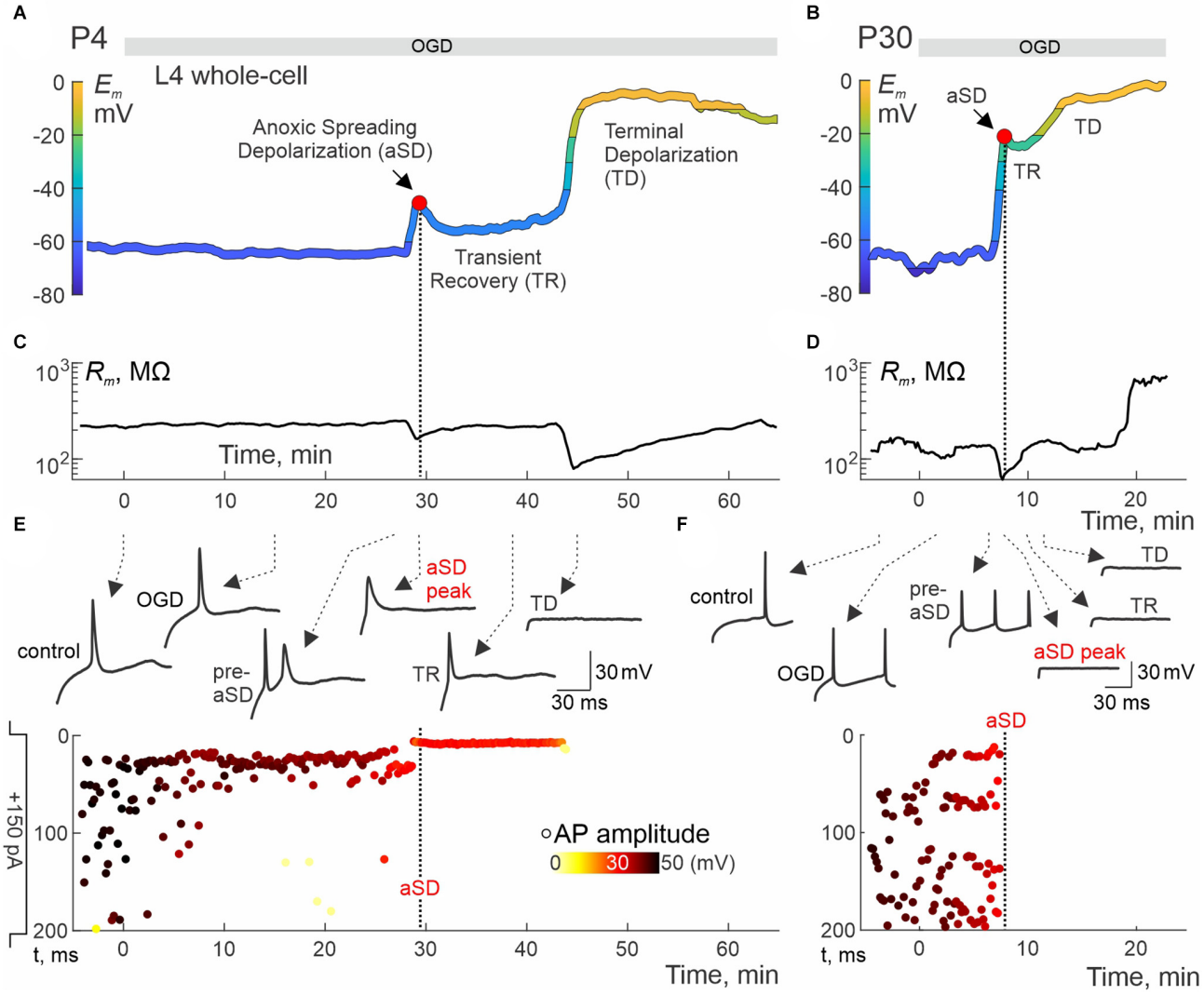

FIGURE 2
Immature neurons remain excitable during aSD and transient recovery phase. **(A,B)** Examples of E_m recordings from L4 neurons in slices from P4 **(A)** and P30 **(B)** rats. E_m traces are low-pass filtered and color-coded as in **Figure 1**. The exposure to OGD is indicated by the horizontal gray bar at the top. **(C,D)** Corresponding changes in input resistance (R_m). **(E,F)** Corresponding example responses to suprathreshold current steps at different time points indicated by arrows (top traces) and raster plots of APs evoked by suprathreshold (+150 pA, 200 ms) current steps (y-axis shows depolarizing step time (top: step start; bottom: step end); APs amplitude is color-coded) (bottom plots). Full trace examples are shown in **Supplementary Figure 1**. Note that the AP firing is maintained through the aSD and TR, and disappears only during the transition to TD in the P4 neuron, whereas in the P30 neuron APs irreversibly disappear as soon as aSD occurs. T = 0 on the x-scale corresponds to the onset of OGD.

heterogeneity between neurons (e.g., due to their different age) and hence the different abilities to maintain E_m during TR, greater extracellular space, low levels of synaptic connectivity, and low density of ion channels and hence smoother increases in extracellular glutamate and potassium. In future studies, it would be of interest to test this hypothesis using multiple whole-cell recordings, or calcium/voltage sensitive dye imaging. The latter approach could be advantageous in overcoming a problem of tissue swelling and displacement that starts after aSD and may cause loss of contact of the electrode with cell and apparent loss of E_m during whole-cell recordings including a transition from whole-cell to outside-out configuration (**Figure 2B** and Juzekaeva et al., 2020). This artifact can lead to an underestimation of the TR duration, which may in fact be even longer than reported here, and can also affect the measurement of TD E_m values. Interestingly, in the P25-P31 age group, we observed that TD E_m reached positive values of ∼+10 mV, which may be due to a greater concentration of impermeable anions in the extracellular than in the intracellular space, a consequence of swelling and shrinkage of the extracellular space.

Our study also revealed that aSD in the neonates lacks the hallmark SD feature—depression of APs. In adults, at the aSD onset, when E_m approaches values close to the AP threshold cortical neurons typically generate one or few APs, and then permanently lose neuronal firing upon further depolarization as a result of voltage-gated sodium channels inactivation and AP depolarization block (Grafstein, 1956; Dzhala et al., 2000, 2001; Canals et al., 2005). Synaptic activity may also display "paradoxical" recovery from

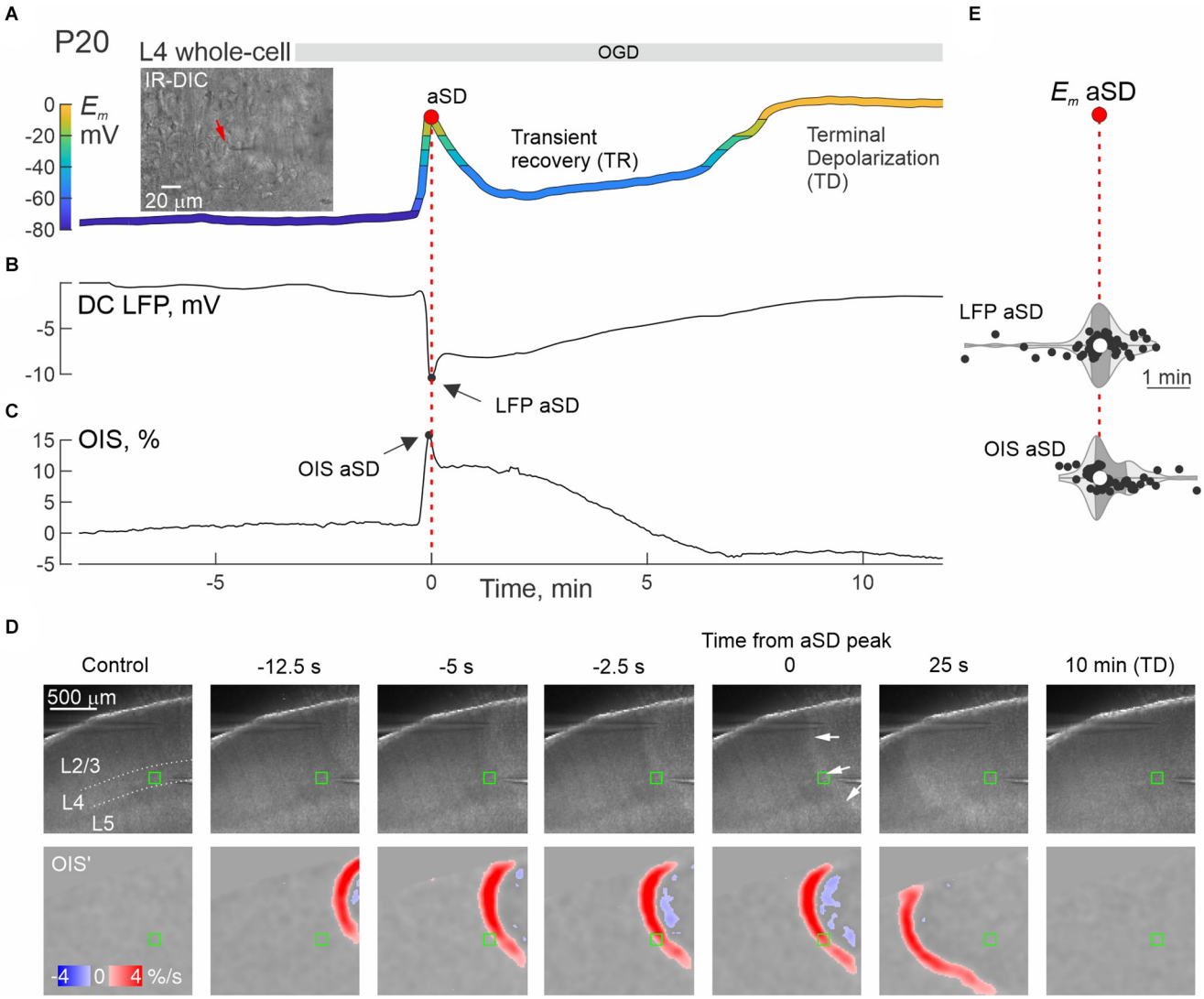

FIGURE 3
aSD correlates with negative LFP shifts and an increase in optical tissue transparency in the developing cortex. **(A–C)** Simultaneous whole-cell E_m recordings from an L4 neuron **(A)**, extracellular DC-LFP recordings **(B)**, and OIS recordings **(C)** near the recorded neuron during OGD in a P20 rat somatosensory cortex slice. T = 0 indicates aSD peak during whole-cell recordings (E_m—aSD). The inset on panel **(A)** shows an IR-DIC image of layer 4 (40x magnification), the neuron being recorded is marked with a red arrow. **(D)** Microphotograph of a slice (4x magnification, raw data, top panels) and the OIS first derivative (bottom panels) at different delays from aSD recorded from the L4 neuron shown on panel **(A)**. The region of interest (ROI) for OIS quantified in panel **(C)** is indicated by a green rectangle. **(E)** Distribution of aSD delays recorded by extracellular electrodes (LFP—aSD) and OIS (OIS—aSD) from aSD during whole-cell recordings (E_m—aSD, vertical dotted line). Hereafter, each dot corresponds to an individual cell/slice, the violin plots show the probability density of the data at different values smoothed by the kernel density estimator, the white circles are the median, and the dark shaded area is the interquartile range. Pooled data from n = 58 cells/slices from P3 to P31 rats. There was no significant time lag between LFP—aSD (p = 0.54), OIS—aSD (p = 0.93, Wilcoxon rank sum test), and E_m—aSD.

non-spreading depression at the aSD onset followed by complete suppression of synaptic responses (Sick et al., 1987; Fowler, 1992; Khazipov et al., 1993; Zhu and Krnjevic, 1999; Dzhala et al., 2001). In contrast, we found that ability to fire APs persists during aSD, and that APs can be reliably triggered during post-aSD TR phase in the majority of neonatal neurons. Our results indicate that the persistence of neuronal firing is primarily due to mild levels of depolarization which barely reaches the threshold of AP inactivation in the immature neurons. Altogether, these findings point to significant developmental differences in aSD properties in immature neurons. We also propose that neonatal aSDs described in the present study broaden the existing SD spectrum (Somjen, 2001; Pietrobon and Moskowitz, 2014; Ayata and Lauritzen, 2015; Dreier and Reiffurth, 2015; Hartings et al., 2017) by adding to a family of full-sized SDs an immature phenotype with its notable mild depolarization levels, TR phase and lack of loss in neuronal functions. In future research, it would be interesting to determine the mechanisms underlying this peculiar phenotype of immature aSD, including the computational modeling approach (Zandt et al., 2013; Herreras and Makarova, 2020; Kalia et al., 2021).

How these unusual aSD features may impact hypoxic/ischemic injury in the neonatal brain? There is general agreement that aSD is a critical event during metabolic deprivation (Andrew et al., 2022).

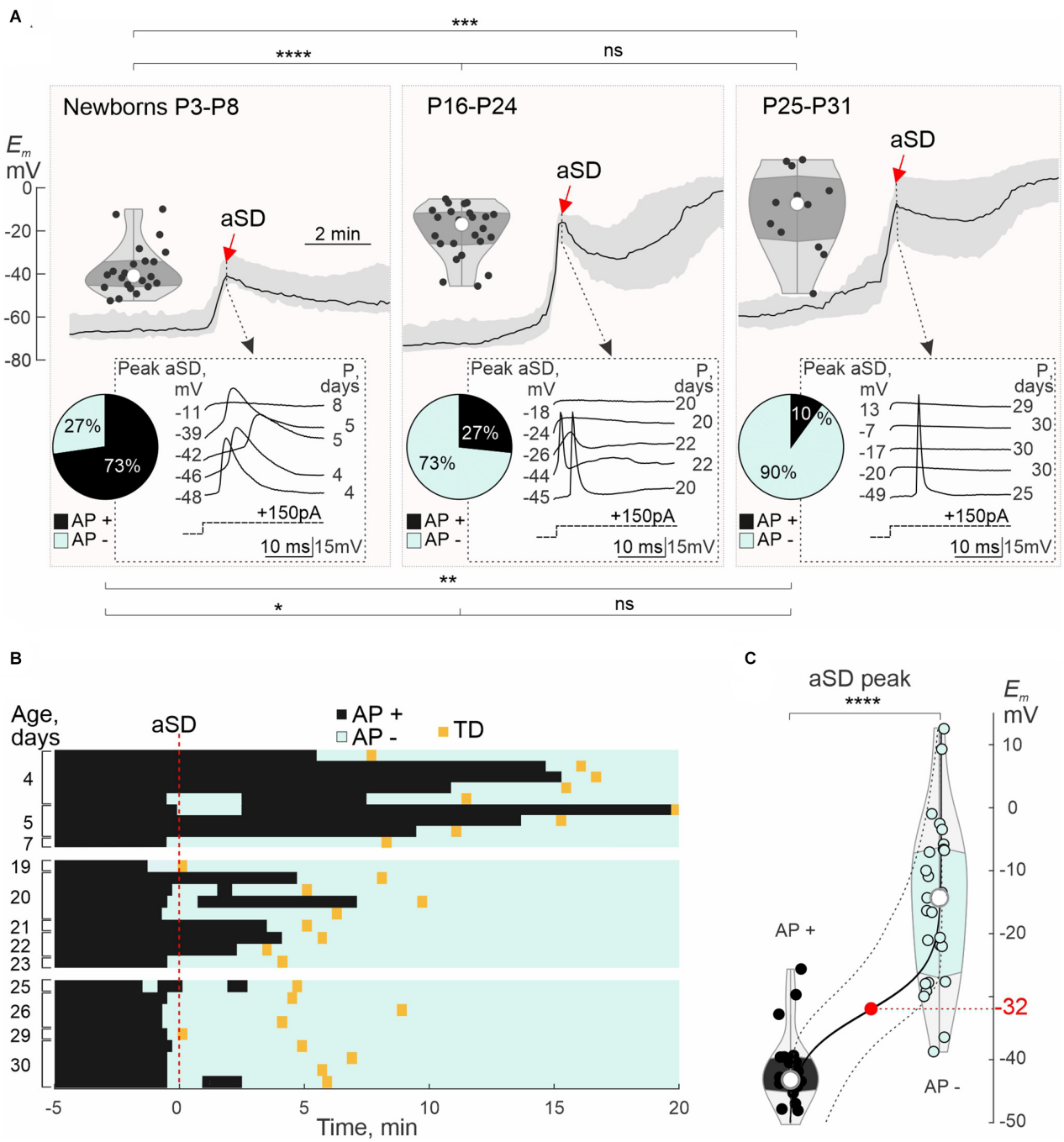

FIGURE 4
Postnatal changes in aSD peak value and neuronal firing during aSD: group data. **(A)** Top traces, grand average aSD (black trace—median *Em*; shaded area—interquartile range) and corresponding statistical plots of E_m values at the aSD peak in L4 neurons from newborn (P3–P8, n = 22 cells), and juvenile rats (P16–P24, n = 24 cells; and P25–P31, n = 12 cells). Gray insets below, examples of responses to depolarizing current steps at the aSD peak in five neurons from each age group, with the corresponding E_m aSD peak value (left) and age (right). Circular histograms show neuronal firing at the aSD peak (black—AP+ neurons responding with APs to depolarizing steps, cyan—AP− neurons not showing APs in response to depolarizing steps). Note that in newborn animals, neuronal depolarization reaches only a weak level during aSD, that most newborn neurons retain neuronal firing during aSD, and that ability to fire APs during aSD diminishes with age. **(B)** Representative raster plots of APs evoked by depolarizing current steps (inter-step interval 10 s) in L4 neurons of different age groups during OGD-induced aSD (T = 0, vertical red dashed line). The black and cyan bins denote responses with AP (AP+) and without AP (AP−), respectively. The transition to TD is indicated by a yellow rectangle. **(C)** Group data on neuronal firing during aSD as a function of peak E_m depolarization during aSD. The black line is a binomial logistic regression fit, dashed lines are 95% confidence intervals for prediction. Half-probability of AP inactivation (or depolarization block) occurs during aSD attaining E_m = −32 (−39/−24) mV [median (interquartile range)]. *, $P < 0.05$; **, $P < 0.01$; ***, $P < 0.0001$; ****, $P < 0.00001$; ns, not significant (Wilcoxon rank sum test).

In adult brain, aSDs are highly energy consuming events associated with a profound depletion of energy sources under conditions of a limited metabolic supply (Somjen, 2001; Strong et al., 2002; Hartings et al., 2003, 2017; Dreier et al., 2013, 2022;

10.3389/fncel.2023.1106268

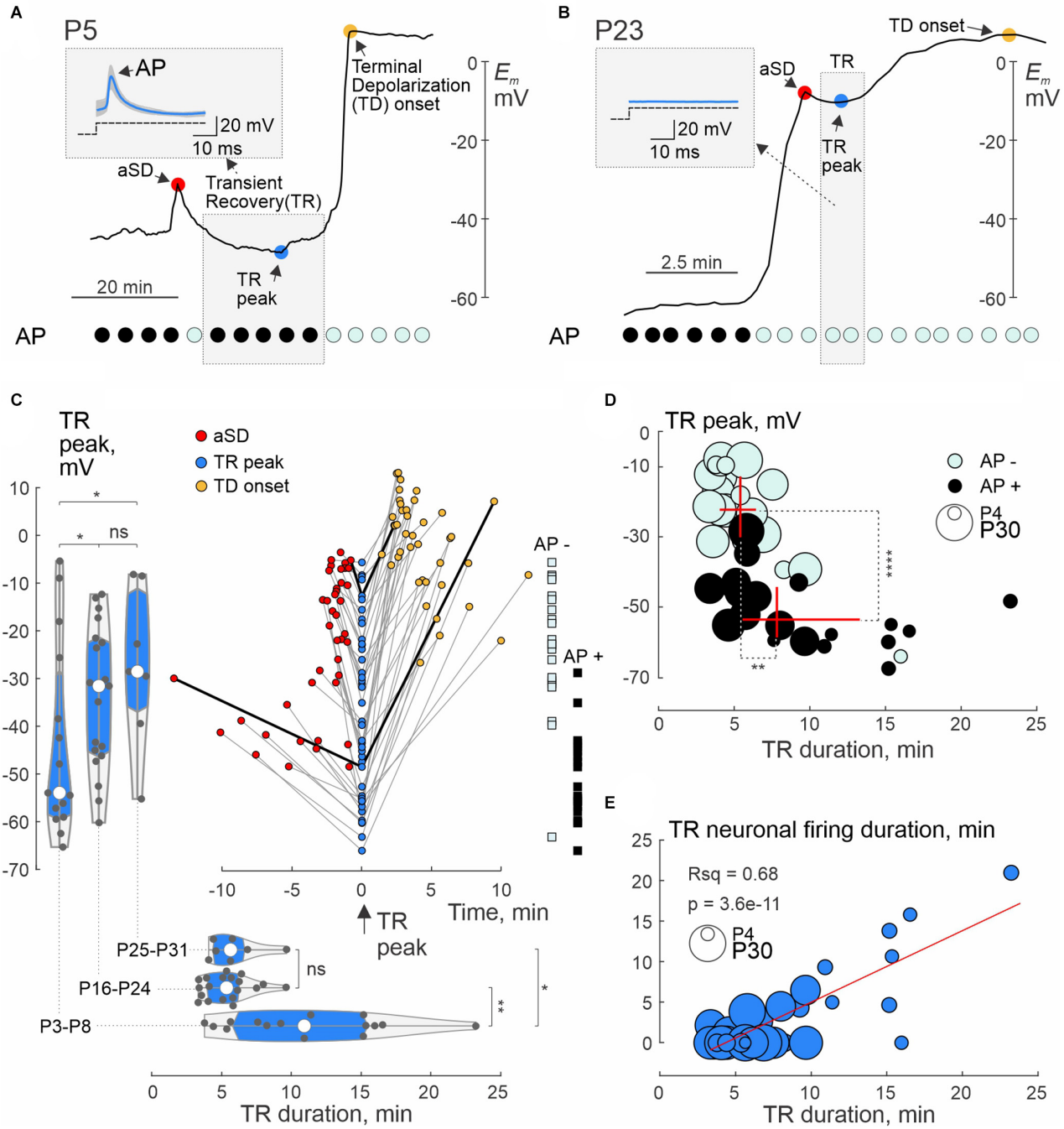

FIGURE 5
Postnatal changes in transient membrane potential recovery following aSD. **(A,B)** Examples of whole-cell recordings from L4 neurons in P5 **(A)** and P23 **(B)** rats. Red circle—peak aSD; blue circle—peak negativity during TR; TD—terminal depolarization. Top left insets—mean responses to depolarizing current steps during TR (median blue traces are superimposed on all gray traces). At the bottom are corresponding graphs indicating responses with APs (black circles) and without APs (cyan circles). Note the long TR with preservation of APs after a small aSD at P5, and weak short TR without APs at P23. **(C)** Summary plot of E_m values achieved during TR, aSD, and TD in individual cells. The peak of negativity during TR is taken as a time reference point. TR, aSD, and TD from individual neurons are connected by gray lines, and values connected by black lines correspond to the examples shown in panels **(A)** and **(B)**. The left and bottom histograms show the distribution of maximum E_m negativity achieved during TR and TR duration, respectively, in the three age groups. On the right, the distribution of TR—E_m values according to the absence (AP–, cyan squares) and presence (AP+, black squares) of APs during TR. **(D)** Relationship between the TR—E_m level and duration of TR as well as neuronal firing during the TR phase. Black (AP+) and cyan (AP–) circles indicate cells that showed or did not show APs in response to depolarizing steps during the TR phase, respectively. The age of the animal is coded by the size of the circle. The red crosses show the median ± interquartile range of TR—E_m levels and duration of TR in the AP+ and AP– cell groups. Note the presence and longer persistence of neuronal firing in cells with more negative E_m values reached during the TR phase. **(E)** The duration of the period within the TR phase, during which neurons retain the ability to fire APs in response to depolarizing steps, correlates with the duration of TR. The red line shows a linear regression fit. **(C–E)**: Pooled data from P3 to P8 (n = 15), P16–P23 (n = 19) and P25–P31 (n = 7). Seventeen cells without TR were excluded from the analysis. *, $P < 0.05$; **, $P < 0.01$; ****, $P < 0.0001$; ns, not significant (Wilcoxon rank sum test).

Dreier and Reiffurth, 2015). Mild level aSDs in the neonatal neurons likely less disturb ionic gradients and thus consume less energy for their restoration. Therefore, it is conceivable that the inability to generate full-size aSDs is beneficial to the neonatal brain and may be a factor contributing to higher tolerance of the neonatal brain to hypoxia/ischemia. Indeed, a similar correlation between weak depolarization and higher tolerance to OGD was also observed in the adult hypothalamus (Brisson and Andrew, 2012). Yet, factors increasing energy consumption such as adenosine A1 receptor antagonists and drugs provoking epileptiform activity are known to accelerate the occurrence of aSD and neuronal death whereas energy-savers such as NKCC1 antagonists and oxytocin exert beneficial actions in the neonatal brain during metabolic deprivation (Dzhala et al., 2000; Tyzio et al., 2006; Khazipov et al., 2008). Even less energy consuming, immature aSD still should jeopardize metabolic status, and inevitably leads to delayed terminal depolarization if metabolic supply is not restored. Indeed, the transition to TD occurred faster in neurons with larger-size aSD. This suggests that aSD occurring simultaneously in the entire population of neurons recruited by aSD wave opens a time window during which neurons attain their cell-specific "commitment point" of irreversible E_m loss and neuronal death at variable delays determined by the aSD size that is consistent with variable survival of neurons following aSD in the juvenile cortex (Juzekaeva et al., 2020). In future studies, it would also be interesting to determine how developmental changes in the composition of the intracellular milieu (notably chloride concentration) and extracellular metabolites (ketone bodies) influence the developmental changes in the aSD described in this study.

In conclusion, our study provides descriptions of aSD in the neonatal cortex at the cellular level. We have shown that aSD in the newborn cortical neurons displays several unique features, including mild levels of depolarization and transient depolarization. We also found that neuronal functions, including the ability to generate APs persist during aSD and TR in neurons with mild aSD. These results highlight a critical developmental difference in the response of the immature brain to metabolic deprivation and are important for understanding the development of cortical damage during hypoxia/ischemia in the neonatal brain.

Data availability statement

The raw data supporting the conclusions of this article will be made available by the authors, without undue reservation.

Ethics statement

The animal study was reviewed and approved by Local Ethical Committee of Kazan Federal University (#24/22.09.2020) and French National Institute of Health and Medical Research (APAFIS #16992-2020070612319346 v2). The animal experiments were carried out in compliance with the ARRIVE guidelines. Animal care and procedures were in accordance with EU Directive 2010/63/EU for animal experiments.

Author contributions

RK conceptualized and drafted the manuscript. EJ, AG, and MM performed the experiments. AG analyzed data. AG, EJ, MM, and RK revised the manuscript and interpreted the data. All authors contributed to the article and approved the submitted version.

Funding

This work was supported by RSF grant #22-15-00236.

Conflict of interest

The authors declare that the research was conducted in the absence of any commercial or financial relationships that could be construed as a potential conflict of interest.

Publisher's note

All claims expressed in this article are solely those of the authors and do not necessarily represent those of their affiliated organizations, or those of the publisher, the editors and the reviewers. Any product that may be evaluated in this article, or claim that may be made by its manufacturer, is not guaranteed or endorsed by the publisher.

Supplementary material

The Supplementary Material for this article can be found online at: https://www.frontiersin.org/articles/10.3389/fncel.2023.1106268/full#supplementary-material.

References

Aitken, P. G., Tombaugh, G. C., Turner, D. A., and Somjen, G. G. (1998). Similar propagation of SD and hypoxic SD-like depolarization in rat hippocampus recorded optically and electrically. *J. Neurophysiol.* 80, 1514–1521. doi: 10.1152/jn.1998.80.3.1514

Andrew, R. D., Hartings, J. A., Ayata, C., Brennan, K. C., wson-Scully, K. D., Farkas, E., et al. (2022). The critical role of spreading depolarizations in early brain injury: consensus and contention. *Neurocrit. Care* 37, 83–101. doi: 10.1007/s12028-021-01431-w

Ayata, C., and Lauritzen, M. (2015). Spreading depression, spreading depolarizations and the cerebral vasculature. *Physiol. Rev.* 95, 953–993. doi: 10.1152/physrev.00027.2014

Bogdanov, V. B., Middleton, N. A., Theriot, J. J., Parker, P. D., Abdullah, O. M., Ju, Y. S., et al. (2016). Susceptibility of primary sensory cortex to spreading depolarizations. *J. Neurosci.* 36, 4733–4743. doi: 10.1523/JNEUROSCI.3694-15.2016

Brisson, D. C., and Andrew, D. R. (2012). A neuronal population in hypothalamus that dramatically resists acute ischemic injury compared to neocortex. *J. Neurophysiol.* 108, 419–430. doi: 10.1152/jn.00090.2012

Bures, J. (1957). The ontogenetic development of steady potential differences in the cerebral cortex in animals. *Electroencephalogr. Clin. Neurophysiol.* 9, 121–130. doi: 10.1016/0013-4694(57)90116-5

Canals, S., Makarova, I., Lopez-Aguado, L., Largo, C., Ibarz, J. M., and Herreras, O. (2005). Longitudinal depolarization gradients along the somatodendritic axis of CA1 pyramidal cells: a novel feature of spreading depression. *J. Neurophysiol.* 94, 943–951. doi: 10.1152/jn.01145.2004

Cherubini, E., Ben-Ari, Y., and Krnjevic, K. (1989). Anoxia produces smaller changes in synaptic transmission, membrane potential and input resistance in immature rat hippocampus. *J. Neurophysiol.* 62, 882–895. doi: 10.1152/jn.1989.62.4.882

Clancy, B., Kersh, B., Hyde, J., Darlington, R. B., Anand, K. J., and Finlay, B. L. (2007). Web-based method for translating neurodevelopment from laboratory species to humans. *Neuroinformatics* 5, 79–94. doi: 10.1385/ni:5:1:79

Colonnese, M. T., Kaminska, A., Minlebaev, M., Milh, M., Bloem, B., Lescure, S., et al. (2010). A conserved switch in sensory processing prepares developing neocortex for vision. *Neuron* 67, 480–498. doi: 10.1016/j.neuron.2010.07.015

Colonnese, M., and Khazipov, R. (2012). Spontaneous activity in developing sensory circuits: Implications for resting state fMRI. *Neuroimage* 62, 2212–2221. doi: 10.1016/j.neuroimage.2012.02.046

Douglas-Escobar, M., and Weiss, M. D. (2015). Hypoxic-ischemic encephalopathy: a review for the clinician. *JAMA Pediatr.* 169, 397–403. doi: 10.1001/jamapediatrics.2014.3269

Dreier, J. P. (2011). The role of spreading depression, spreading depolarization and spreading ischemia in neurological disease. *Nat. Med.* 17, 439–447. doi: 10.1038/nm.2333

Dreier, J. P., Isele, T., Reiffurth, C., Offenhauser, N., Kirov, S. A., Dahlem, M. A., et al. (2013). Is spreading depolarization characterized by an abrupt, massive release of gibbs free energy from the human brain cortex? *Neuroscientist* 19, 25–42. doi: 10.1177/1073858412453340

Dreier, J. P., and Reiffurth, C. (2015). The stroke-migraine depolarization continuum. *Neuron* 86, 902–922. doi: 10.1016/j.neuron.2015.04.004

Dreier, J. P., Winkler, M. K. L., Major, S., Horst, V., Lublinsky, S., Kola, V., et al. (2022). Spreading depolarizations in ischaemia after subarachnoid haemorrhage, a diagnostic phase III study. *Brain* 145, 1264–1284. doi: 10.1093/brain/awab457

Dzhala, V., Ben-Ari, Y., and Khazipov, R. (2000). Seizures accelerate anoxia-induced neuronal death in the neonatal rat hippocampus. *Ann. Neurol.* 48, 632–640. doi: 10.1002/1531-8249(200010)48:4%3C632::AID-ANA10%3E3.3.CO;2-V

Dzhala, V., Khalilov, I., Ben Ari, Y., and Khazipov, R. (2001). Neuronal mechanisms of the anoxia-induced network oscillations in the rat hippocampus *in vitro*. *J. Physiol.* 536, 521–531. doi: 10.1111/j.1469-7793.2001.0521c.xd

Fowler, J. C. (1992). Escape from inhibition of synaptic transmission during in vitro hypoxia and hypoglycemia in the hippocampus. *Brain Res.* 573, 169–173. doi: 10.1016/0006-8993(92)90128-v

Grafstein, B. (1956). Mechanism of spreading cortical depression. *J. Neurophysiol.* 19, 154–171. doi: 10.1152/jn.1956.19.2.154

Hartings, J. A., Rolli, M. L., Lu, X. C., and Tortella, F. C. (2003). Delayed secondary phase of peri-infarct depolarizations after focal cerebral ischemia: relation to infarct growth and neuroprotection. *J. Neurosci.* 23, 11602–11610. doi: 10.1523/JNEUROSCI.23-37-11602.2003

Hartings, J. A., Shuttleworth, C. W., Kirov, S. A., Ayata, C., Hinzman, J. M., Foreman, B., et al. (2017). The continuum of spreading depolarizations in acute cortical lesion development: examining Leao's legacy. *J. Cereb. Blood Flow Metab.* 37, 1571–1594. doi: 10.1177/0271678X16654495

Herreras, O., and Makarova, J. (2020). Mechanisms of the negative potential associated with Leao's spreading depolarization: a history of brain electrogenesis. *J. Cereb. Blood Flow Metab.* 40, 1934–1952. doi: 10.1177/0271678X20935998

Hertelendy, P., Varga, D. P., Menyhart, A., Bari, F., and Farkas, E. (2019). Susceptibility of the cerebral cortex to spreading depolarization in neurological disease states: the impact of aging. *Neurochem. Int.* 127, 125–136. doi: 10.1016/j.neuint.2018.10.010

Joshi, I., and Andrew, R. D. (2001). Imaging anoxic depolarization during ischemia-like conditions in the mouse hemi-brain slice. *J. Neurophysiol.* 85, 414–424. doi: 10.1152/jn.2001.85.1.414

Juzekaeva, E., Gainutdinov, A., Mukhtarov, M., and Khazipov, R. (2018). Dynamics of the hypoxia-induced tissue edema in the rat barrel cortex *in vitro*. *Front. Cell Neurosci.* 12:502. doi: 10.3389/fncel.2018.00502

Juzekaeva, E., Gainutdinov, A., Mukhtarov, M., and Khazipov, R. (2020). Reappraisal of anoxic spreading depolarization as a terminal event during oxygen-glucose deprivation in brain slices *in vitro*. *Sci. Rep.* 10:18970. doi: 10.1038/s41598-020-75975-w

Juzekaeva, E., Nasretdinov, A., Gainutdinov, A., Sintsov, M., Mukhtarov, M., and Khazipov, R. (2017). Preferential initiation and spread of anoxic depolarization in layer 4 of rat barrel cortex. *Front. Cell Neurosci.* 11:390. doi: 10.3389/fncel.2017.00390

Kalia, M., Meijer, H. G. E., van Gils, S. A., van Putten, M. J. A. M., and Rose, C. R. (2021). Ion dynamics at the energy-deprived tripartite synapse. *PLoS Comput. Biol.* 17:e1009019. doi: 10.1371/journal.pcbi.1009019

Kaufmann, D., Theriot, J. J., Zyuzin, J., Service, C. A., Chang, J. C., Tang, Y. T., et al. (2017). Heterogeneous incidence and propagation of spreading depolarizations. *J. Cereb. Blood Flow Metab.* 37, 1748–1762. doi: 10.1177/0271678X16659496

Khazipov, R., Bregestovski, P., and Ben-Ari, Y. (1993). Hippocampal inhibitory interneurons are functionally disconnected from excitatory inputs by anoxia. *J. Neurophysiol.* 70, 2251–2259. doi: 10.1152/jn.1993.70.6.2251

Khazipov, R., and Luhmann, H. J. (2006). Early patterns of electrical activity in the developing cerebral cortex of humans and rodents. *Trends Neurosci.* 29, 414–418. doi: 10.1016/j.tins.2006.05.007

Khazipov, R., and Milh, M. (2018). Early patterns of activity in the developing cortex: focus on the sensorimotor system. *Semin. Cell Dev. Biol.* 76, 120–129. doi: 10.1016/j.semcdb.2017.09.014

Khazipov, R., Tyzio, R., and Ben-Ari, Y. (2008). Effects of oxytocin on GABA signalling in the foetal brain during delivery. *Prog. Brain Res.* 170, 243–257., 243–257. doi: 10.1016/S0079-6123(08)00421-4

Khazipov, R., Zaynutdinova, D., Ogievetsky, E., Valeeva, G., Mitrukhina, O., Manent, J. B., et al. (2015). Atlas of the postnatal rat brain in stereotaxic coordinates. *Front. Neuroanat.* 9:161. doi: 10.3389/fnana.2015.00161

Leao, A. A. P. (1944). Spreading depression of activity in the cerebral cortex. *J. Neurophysiol.* 7, 359–390. doi: 10.1152/jn.1944.7.6.359

Leao, A. A. P. (1947). Further observations on the spreading depression of activity in the cerebral cortex. *J. Neurophysiol.* 10, 409–414. doi: 10.1152/jn.1947.10.6.409

Lin, C. S., Polsky, K., Nadler, J. V., and Crain, B. J. (1990). Selective neocortical and thalamic cell death in the gerbil after transient ischemia. *Neuroscience* 35, 289–299. doi: 10.1016/0306-4522(90)90083-g

Luhmann, H. J., and Khazipov, R. (2018). Neuronal activity patterns in the developing barrel cortex. *Neuroscience* 368, 256–267. doi: 10.1016/j.neuroscience.2017.05.025

Luhmann, H. J., and Kral, T. (1997). Hypoxia-induced dysfunction in developing rat neocortex. *J. Neurophysiol.* 78, 1212–1221. doi: 10.1152/jn.1997.78.3.1212

Pietrobon, D., and Moskowitz, M. A. (2014). Chaos and commotion in the wake of cortical spreading depression and spreading depolarizations. *Nat. Rev. Neurosci.* 15, 379–393. doi: 10.1038/nrn3770

Rader, R. K., and Lanthorn, T. H. (1989). Experimental ischemia induces a persistent depolarization blocked by decreased calcium and NMDA antagonists. *Neurosci. Lett.* 99, 125–130. doi: 10.1016/0304-3940(89)90276-0

Richter, F., Lehmenkühler, A., Fechner, R., Manveljan, L., and Haschke, W. (1998). Postnatal conditioning for spreading cortical depression in the rat brain. *Brain Res. Dev. Brain Res.* 106, 217–221. doi: 10.1016/s0165-3806(98)00018-2

Saugstad, O. D. (2011). Reducing global neonatal mortality is possible. *Neonatology* 99, 250–257. doi: 10.1159/000320332

Schade, J. P. (1959). Maturational aspects of EEG and of spreading depression in rabbit. *J. Neurophysiol.* 22, 245–257. doi: 10.1152/jn.1959.22.3.245

Sick, T. J., Solow, E. L., and Roberts, E. L. J. (1987). Extracellular potassium ion activity and electrophysiology in the hippocampal slice: paradoxical recovery of synaptic transmission during anoxia. *Brain Res.* 418, 227–234. doi: 10.1016/0006-8993(87)90090-4

Somjen, G. G. (2001). Mechanisms of spreading depression and hypoxic spreading depression-like depolarization. *Physiol. Rev.* 81, 1065–1096. doi: 10.1152/physrev.2001.81.3.1065

Strong, A. J., Fabricius, M., Boutelle, M. G., Hibbins, S. J., Hopwood, S. E., Jones, R., et al. (2002). Spreading and synchronous depressions of cortical activity in acutely injured human brain. *Stroke* 33, 2738–2743. doi: 10.1161/01.str.0000043073.69602.09

Tanaka, E., Yamamoto, S., Kudo, Y., Mihara, S., and Higashi, H. (1997). Mechanisms underlying the rapid depolarization produced by deprivation of oxygen and glucose in rat hippocampal CA1 neurons *in vitro*. *J. Neurophysiol.* 78, 891–902. doi: 10.1152/jn.1997.78.2.891

Toyoda, H., Kawano, T., Sato, H., and Kato, T. (2021). Cellular mechanisms underlying the rapid depolarization caused by oxygen and glucose deprivation in layer III pyramidal cells of the somatosensory cortex. *Neurosci. Res.* 164, 1–9. doi: 10.1016/j.neures.2020.03.003

Tyzio, R., Cossart, R., Khalilov, I., Minlebaev, M., Hubner, C. A., Represa, A., et al. (2006). Maternal oxytocin triggers a transient inhibitory switch in GABA signaling in the fetal brain during delivery. *Science* 314, 1788–1792. doi: 10.1126/science.1133212

Vinokurova, D., Zakharov, A., Chernova, K., Burkhanova-Zakirova, G., Horst, V., Lemale, C. L., et al. (2022). Depth-profile

of impairments in endothelin-1 - induced focal cortical ischemia. *J. Cereb. Blood Flow Metab.* 42, 1944–1960. doi: 10.1177/0271678X221107422

Zandt, B.-J., Haken, B. t., and van Putten, M. J. A. M. (2013). Diffusing substances during spreading depolarization: analytical expressions for propagation speed, triggering and concentration time courses. *J. Neurosci.* 33, 5915–5923. doi: 10.1523/JNEUROSCI.5115-12.2013

Zhu, P. J., and Krnjevic, K. (1999). Persistent block of CA1 synaptic function by prolonged hypoxia. *Neuroscience* 90, 759–770. doi: 10.1016/s0306-4522(98)00495-3